

Dissertation zur Erlangung des Doktorgrades
der Fakultät für Chemie und Pharmazie
der Ludwig-Maximilians-Universität München

**The High-Pressure Metathesis Route for the Preparation of
Rare-Earth and Transition Metal Nitridophosphates**

Simon David Kloß

aus

Geseke, Deutschland

2018

Erklärung

Diese Dissertation wurde im Sinne von § 7 der Promotionsordnung vom 28. November 2011 von Herrn Prof. Dr. Wolfgang Schnick betreut.

Eidesstattliche Versicherung

Diese Dissertation wurde eigenständig und ohne unerlaubte Hilfe erarbeitet.

München, 5.11.2018

.....

(Simon David Kloß)

Dissertation eingereicht am 5.11.2018

1. Gutachter:

Prof. Dr. Wolfgang Schnick

2. Gutachter:

Prof. Dr. Oliver Oeckler

Mündliche Prüfung am

14.12.2018

Dedicated to my beloved family.

“Decide in your heart of hearts what really excites and challenges you, and start moving your life in that direction. Every decision you make, from what you eat to what you do with your time tonight, turns you into who you are tomorrow, and the day after that.”

Col. Chris Hadfield, Commander of the International Space Station, Expedition 34/35

&

“You can’t get lost in space.”

Lathan Devers (Foundation and Empire, Isaac Asimov)

Dank

Mein besonderer Dank gilt Prof. Dr. Wolfgang Schnick für die Möglichkeit in seiner Arbeitsgruppe meine Dissertation anfertigen zu können. Die zahlreichen zur Verfügung stehenden Mittel und die vielen Freiheiten bei der Gestaltung der eigenen Forschung haben das ohnehin schon äußerst spannende Thema bereichert. Ich danke auch für die zahlreichen und hilfreichen Fachgespräche.

Vielen Dank an Prof. Dr. Oliver Oeckler für die Übernahme der Rolle des 2. Gutachters meiner Dissertation.

Ich danke des weiteren Prof. Dr. Hubert Huppertz, Prof. Dr. Achim Hartschuh, Prof. Dr. Dirk Johrendt, und Prof. Dr. Konstantin Karaghiosoff für die bereitwillige Teilnahme als Prüfer in meinem Rigorosum.

Ich möchte Prof. Dr. Oliver Oeckler, Priv.-Doz. Dr. Constantin Hoch, Dr. Thomas Bräuniger, Prof. Dr. Robert Glaum für zahlreiche Fachgespräche/Kooperationen danken durch die ich sehr viel lernen konnte.

Besonders möchte ich auch Dr. Dominik Baumann danken. Von ihm habe ich während Bachelor- und Masterarbeit sowie in den Anfängen meiner Promotion vieles gelernt, was mir den Einstieg in das wissenschaftliche Arbeiten erheblich erleichtert hat.

Meinen Praktikanten Simon Wanninger, Niels Weidmann, Andreas Weis, und Sophia Wandelt danke ich für unermüdlichen Fleiß und Neugierde an der anorganischen Chemie. Aus ihren tatkräftigen Beiträgen sind schöne Arbeiten hervorgegangen.

Bei Herr Christian Minke möchte ich mich für die Betreuung von NMR und Rasterelektronenmikroskop bedanken, bei Herr Thomas Miller für die Betreuung von den Röntgendiffraktometern sowie

sicherheitstechnischen Angelegenheiten, und bei Herr Wolfgang Wünschheim für die Meisterung zahlreicher EDV-technischer Herausforderungen sowie der Hochdruckpressenproblemen.

Herrn Dr. Peter Mayer danke ich für die geduldige Messung von vielen kleinen und kleinsten Kristallen.

Frau Olga Lorenz danke ich für die zuverlässige Bewältigung allerlei organisatorischer Aufgaben.

Den Herren Dr. Markus Döblinger, Markus Nentwig, Dr. Roman Pobel, Tobias Rackl, und Prof. Dirk Johrendt danke ich für die Durchführung von diversen Messungen und Unterstützung bei einigen Auswertungen.

Meinen Arbeitskollegen und Kooperationspartnern Dr. Lukas Neudert und Robin Niklaus möchte ich für die sorgfältigen und teils sehr langwierigen (S)TEM-Messungen und DFT-Berechnungen danken.

Meinen ehemaligen und derzeitigen Laborkollegen Dr. Dominik Baumann, Dr. Alexey Marchuk, Dr. Frank Tambornino, Dr. Matthias Wörsching, Dr. Eva-Maria Bertschler, Tobias Gifthaler, Philipp Biel-ec, Sebastian Vogel, Sebastian Wendl, und Stefanie Schneider möchte ich für eine unglaublich witzige und kurzweilige Zeit in Labor D2.110 danken. In unserem Labor kamen Spaß und wissenschaftliche Neugier nie zu kurz. Desweiteren möchte ich meinen geschätzten Arbeitskollegen und Freunden Christian Maak und Mathias Mallmann für ihre tatkräftige Unterstützung in allen Belangen danken.

Zuletzt, aber vielleicht am wichtigsten, will ich noch meinen Eltern, Cornelia und Hartmut, sowie meinen Geschwister Franziska und Benjamin, sowie Janina Graf danken. Ohne deren Unterstützung während all der langen Jahre des Studium und der Promotion wäre ich sicher nicht da wo ich jetzt bin.

Table of Contents

1. Introduction	2
1.1 Of serendipity and explorative solid-state chemistry.....	2
1.2 The nitridophosphate class of compounds.....	4
1.3 Challenges to synthesis.....	8
1.4 High-pressure metathesis, the remedy?.....	12
1.5 References.....	15
2. Rare-Earth-Metal Nitridophosphates Through High-Pressure Metathesis	20
2.1 Introduction with Results and Discussion.....	22
2.2 Conclusion.....	28
2.3 References.....	29
3. High-pressure Synthesis of Melilite-Type Rare-Earth Nitridophosphates	
$RE_2P_3N_7$ and a $Ba_2Cu[Si_2O_7]$-type Polymorph	32
3.1 Introduction.....	34
3.2 Experimental Section.....	36
3.2.1 Synthesis of P_3N_5	36
3.2.2 Preparation of $LiPN_2$	36
3.2.3 Synthesis of <i>mcm</i> -type and <i>bex</i> -type $RE_2P_3N_7$ ($RE_{mcm} = Pr, Nd, Sm, Eu, Ho, Yb$; $RE_{bex} = La, Ce, Pr$) Phases.....	36
3.2.4 Spectroscopic Analysis.....	37
3.2.5 Single-Crystal X-ray Diffraction.....	38
3.2.6 Powder X-ray Diffraction.....	38
3.2.7 Computational Details.....	39
3.3 Results and Discussion.....	40
3.3.1 Synthesis and Characterization of <i>mcm</i> - $RE_2P_3N_7$ and <i>bex</i> - $RE_2P_3N_7$	40
3.3.2 Crystal Structure Determination of <i>mcm</i> - and <i>bex</i> - $RE_2P_3N_7$	41
3.3.3 Structure Description of <i>mcm</i> - $RE_2P_3N_7$ ($RE = Pr, Nd, Sm, Eu, Ho, Yb$).....	43

3.3.4	Structure Description of <i>bex</i> -Pr ₂ P ₃ N ₇	45
3.3.5	Structural Evolution of <i>mcm</i> - and <i>bex</i> -RE ₂ P ₃ N ₇ Phases.....	49
3.3.6	Density Functional Theory Calculations.....	50
3.3.7	High-Temperature Powder Diffraction.....	52
3.4	Conclusion.....	53
3.5	References.....	54
4.	Antiperovskite Nitridophosphate Oxide Ho₃[PN₄]O by High-Pressure Metathesis	58
4.1	Introduction.....	60
4.2	Results and Discussion.....	62
4.2.1	Preparation and Chemical Analysis.....	62
4.2.2	Structure Determination.....	62
4.2.3	Structure Description.....	65
4.2.4	Optical Properties.....	68
4.2.5	Thermal Properties.....	71
4.2.6	Magnetic Properties.....	71
4.2.7	DFT Calculations.....	72
4.3	Conclusions.....	74
4.4	Experimental Section.....	75
4.4.1	Synthesis of P ₃ N ₅	75
4.4.2	Synthesis of LiPN ₂	75
4.4.3	Synthesis of Li ₂ O.....	75
4.4.4	Synthesis of Ho ₃ [PN ₄]O.....	76
4.4.5	Spectroscopic Analysis.....	76
4.4.6	Magnetometry.....	77
4.4.7	Powder X-ray Diffraction.....	77
4.4.8	Computational Details.....	78
4.5	References.....	79

5. Puzzling Intergrowth in Cerium Nitridophosphate Unraveled by Joint Venture of Aberration-Corrected Scanning Transmission Electron Microscopy and Synchrotron Diffraction	82
5.1 Introduction.....	84
5.2 Experimental Details.....	86
5.2.1 Preparation of P_3N_5	86
5.2.2 Preparation of $LiPN_2$	86
5.2.3 Preparation of $Ce_{4-0.5x}Li_3P_{18}N_{35-1.5x}O_{1.5x}$ ($x \approx 0.72$).....	86
5.2.4 Spectroscopic Analysis.....	87
5.2.5 Magnetometry	87
5.2.6 Powder X-ray Diffraction	88
5.2.7 Single-Crystal X-ray Diffraction.....	88
5.2.8 Transmission Electron Microscopy	89
5.2.9 Optical Properties	89
5.3 Results and Discussion	90
5.3.1 Preparation and Chemical Analysis	90
5.3.2 Determination of the Average Structure	91
5.3.3 Description of the Average Structure.....	94
5.3.4 Transmission Electron Microscopy	97
5.3.5 Superstructure Determined from Synchrotron Data	102
5.3.6 (3 + 2)D Superspace Description	104
5.3.7 Superstructure Discussion.....	106
5.3.8 Optical Properties	106
5.3.9 Magnetic Properties.....	108
5.4 Conclusion	109
5.5 References.....	110
6. $LiPr_2P_4N_7O_3$: Structural Diversity of Oxonitridophosphates Accessed by High-Pressure Metathesis	114
6.1 Introduction.....	116

6.2	Experimental Section	119
6.2.1	LiPN ₂	119
6.2.2	Li ₂ O	119
6.2.3	a-PON	119
6.2.4	LiPr ₂ P ₄ N ₇ O ₃	119
6.2.5	Single-Crystal Diffraction.....	120
6.2.6	Powder X-Ray Diffraction.....	120
6.2.7	Spectroscopy.....	121
6.3	Results and Discussion	122
6.3.1	Synthesis	122
6.3.2	Structure Determination.....	122
6.3.3	Structure Description.....	123
6.3.4	Optical properties.....	127
6.3.5	High-Temperature Powder X-Ray Diffraction	129
6.4	Conclusion	130
6.5	References	131
7.	Accessing Tetravalent Transition-Metal Nitridophosphates through High-Pressure Metathesis	134
7.1	Introduction with Results and Discussion	136
7.2	Conclusion	142
7.3	References.....	143
8.	High-Pressure Metathesis of the M_{1-x}PO_{3+4x}N_{1-4x} (x ≈ 0.05) and M_{0.75}PO₄ (M = Zr, Hf) Orthophosphates	146
8.1	Introduction.....	148
8.2	Experimental Section	151
8.2.1	Li ₂ O	151
8.2.2	Phosphoric Triamide	151
8.2.3	a-PON	151

8.2.4	cri-PON.....	152
8.2.5	Oxo(nitrido)phosphates	152
8.2.6	Spectroscopy.....	152
8.2.7	Solid State NMR.....	153
8.2.8	Single-Crystal Diffraction	153
8.2.9	Powder Diffraction.....	154
8.3	Results and Discussion	155
8.3.1	Synthesis	155
8.3.2	Structure Determination	156
8.3.3	Structure Discussion	157
8.3.4	Thermal Properties.....	159
8.3.5	Optical Properties	160
8.3.6	Alternative synthesis methods	161
8.4	Conclusion	162
8.5	References.....	163
9.	Open-shell 3d Transition Metal Nitridophosphates $M^{II}P_8N_{14}$	
	($M^{II} = Fe, Co, Ni$) by High-pressure Metathesis	166
9.1	Introduction with Results and Discussion.....	168
9.2	Conclusion	176
9.3	References.....	177
10.	Summary	180
11.	Discussion and Outlook	190
11.1	Advancements in nitridophosphate chemistry.....	190
11.2	Prospects for rare-earth nitridophosphates.....	192
11.3	Prospects for transition metal nitridophosphates	194
11.4	Concluding remarks	197
11.5	References.....	198

A. Supporting Information for Chapter 1	200
A.1 List of published (oxo)nitridophosphates	201
A.2 References	207
B. Supporting Information for Chapter 2	212
B.1 Experimental details of the HP/HT-metathesis of LiNdP_4N_8	213
B.2 Information on data collection and structure elucidation of LiNdP_4N_8	214
B.3 Details of scanning electron microscopy	216
B.4 Additional crystallographic data for LiNdP_4N_8	217
B.5 Details of the Rietveld refinement.	219
B.6 Detailed Rietveld plot	220
B.7 Additional information on the structure	221
B.8 Detailed high-angle Rietveld plot	222
B.9 Comparison of paracelsian-type $\text{BaAl}_2\text{Si}_2\text{O}_8$ and LiNdP_4N_8	224
B.10 Temperature dependent powder X-ray diffraction.	225
B.11 FTIR spectrum	226
B.12 Details on the magnetic characterization of LiNdP_4N_8	227
B.13 Light-microscopy of a LiNdP_4N_8 sample	230
B.14 References	231
C. Supporting Information for Chapter 3	232
C.1 <i>bex</i> - $\text{La}_2\text{P}_3\text{N}_7$	233
C.2 <i>bex</i> - $\text{Ce}_2\text{P}_3\text{N}_7$	235
C.3 <i>bex</i> - $\text{Pr}_2\text{P}_3\text{N}_7$	239
C.4 <i>mcm</i> - $\text{Pr}_2\text{P}_3\text{N}_7$	244
C.5 <i>mcm</i> - $\text{Nd}_2\text{P}_3\text{N}_7$	247
C.6 <i>mcm</i> - $\text{Sm}_2\text{P}_3\text{N}_7$	250
C.7 <i>mcm</i> - $\text{Eu}_2\text{P}_3\text{N}_7$	253
C.8 <i>mcm</i> - $\text{Ho}_2\text{P}_3\text{N}_7$	255
C.9 <i>mcm</i> - $\text{Yb}_2\text{P}_3\text{N}_7$	260

C.10 Rietveld Refinement of a <i>mcm/bex</i> -Pr ₂ P ₃ N ₇ phase mixture.....	263
D. Supporting Information for Chapter 4	264
D.1 Chemical analysis table containing EDX and ICP data	265
D.2 Additional crystallographic information on Ho ₃ [PN ₄]O.....	266
D.3 Maple calculations.....	267
D.4 Rietveld refinement of Ho ₃ [PN ₄]O at 123 K	268
D.5 References.....	270
E. Supporting Information for Chapter 5	272
E.1 Infrared spectroscopy.....	273
E.2 High-Temperature Powder XRD.....	274
E.3 Details of Rietveld refinement.....	275
E.4 Additional Crystallographic data for Ce _{4-0.5x} Li ₃ P ₁₈ N _{35-1.5x} O _{1.5x}	276
E.5 MAPLE and BVS	278
E.6 Difference Fourier Maps.....	280
E.7 Network topology	283
E.8 Coordination polyhedra.....	285
E.9 TEM.....	287
E.10 Synchrotron Data	294
E.11 References.....	300
F. Supporting Information for Chapter 6	302
F.1 Rietveld refinement.....	303
F.2 Infrared spectroscopy.....	305
F.3 Crystallographic tables.....	306
F.4 Electrostatics	308
F.5 High-temperature X-ray powder diffraction.....	310
F.6 References.....	311

G. Supporting Information for Chapter 7	312
G.1 Experimental	313
G.2 Additional information on synthesis	317
G.3 Powder X-ray diffraction	318
G.4 Scanning Electron Microscopy	320
G.5 Crystallographic tables.....	321
G.6 EEL and NMR spectroscopy	324
G.7 Magnetic measurements	329
G.8 Infrared spectroscopy.....	331
G.9 Bond valence sums	332
G.10 Additional information on structure solution	333
G.11 High-temperature PXRD.....	337
G.12 References.....	338
H. Supporting information for Chapter 8.	340
H.1 Rietveld refinement data.....	341
H.2 Infrared spectroscopy.....	344
H.3 Crystallographic tables.....	345
H.4 Details on structure determination.....	349
H.5 Temperature-dependent powder X-ray diffraction	357
H.6 UV-vis spectroscopy	361
H.7 References.....	362
I. Supporting information for Chapter 9.	364
I.1 Experimental Procedures.....	365
I.2 Structure Determination.....	368
I.3 Crystallographic tables.....	371
I.4 Charge distribution (CHARDI) calculations	376
I.5 Scanning electron microscopy.....	378
I.6 Fourier transform infrared spectroscopy.....	379

I.7	Temperature-dependent powder X-ray diffraction	380
I.8	Addition to the structure discussion	382
I.9	Magnetic measurements.....	383
I.10	Mössbauer spectroscopy.....	386
I.11	Electronic absorption spectra	387
I.12	References.....	392
J.	Miscellaneous	396
J.1	List of Publications	397
J.2	Contributions to Conferences and Seminars	400
J.3	Deposited crystallographic data	402
J.4	Curriculum Vitae.....	403

Table of Figures

Chapter 1

- Figure 1.1** Periodic system of elements with elements highlighted that form ternary compounds with P and N.5
- Figure 1.2** Selected landmarks in κ occurring in nitridophosphates.6

Chapter 2

- Figure 2.1** Projection of the LiNdP_4N_8 crystal structure along [010].24
- Figure 2.2** Coordination polyhedra around Nd, Li, P1, and P2.25
- Figure 2.3** Susceptibility measurement carried out at 20 kOe.26

Chapter 3

- Figure 3.1** SEM micrographs. (a) An *mcm*- $\text{Ho}_2\text{P}_3\text{N}_7$ crystal. (b) A *bex*- $\text{Pr}_2\text{P}_3\text{N}_7$ crystal.40
- Figure 3.2** (left) Four unit cells of $\text{Ho}_2\text{P}_3\text{N}_7$ in projection along the *c*-axis. (right) Projection along the *b*-axis, parallel to the tetrahedral monolayers.44
- Figure 3.3** N-coordination polyhedra in *mcm*- $\text{Ho}_2\text{P}_3\text{N}_7$44
- Figure 3.4** (left) Four unit cells of *bex*- $\text{Pr}_2\text{P}_3\text{N}_7$ in projection along the *b*-axis. (right) Projection along the *c*-axis, parallel to the monolayers.45
- Figure 3.5** N-coordination polyhedra in *bex*- $\text{Pr}_2\text{P}_3\text{N}_7$ around Pr1 (top), P1 (bottom left), and P2 (bottom right) with respective bond lengths.46
- Figure 3.6** Deduction of the *mcm* (top) and *bex* (bottom) tiling pattern from monolayers of the respective $\text{RE}_2\text{P}_3\text{N}_7$ structures.48
- Figure 3.7** Lattice parameters *a*, *c*, and *V* obtained from Rietveld refinement of respective *mcm*- $\text{RE}_2\text{P}_3\text{N}_7$ compounds.49
- Figure 3.8** Density of both polymorphs as determined by Rietveld refinement.50
- Figure 3.9** Energy–volume diagram for the *bex*- and *mcm*- $\text{Pr}_2\text{P}_3\text{N}_7$51
- Figure 3.10** Enthalpy–pressure diagram obtained by fitting the Murnaghan equation of state from the Energy–Volume diagram for the *mcm* and *bex* modifications.52

Chapter 4

Figure 4.1	SEM micrographs of a representative $\text{Ho}_3[\text{PN}_4]\text{O}$ sample.....	62
Figure 4.2	Result of the Rietveld Refinement of a $\text{Ho}_3[\text{PN}_4]\text{O}$ sample plotted in Q-space versus absolute intensity.	63
Figure 4.3	(a) Side view on the unit cell of $\text{Ho}_3[\text{PN}_4]\text{O}$ and (b) projection along c	66
Figure 4.4	Coordination polyhedra of (a) O1, (b) P1, (c) Ho1, and (d) Ho2.	67
Figure 4.5	UV/Vis spectrum of $\text{Ho}_3[\text{PN}_4]\text{O}$ recorded from $\lambda = 240$ to 800 nm in reflection geometry.	69
Figure 4.6	IR (top) and Raman (bottom) spectra of $\text{Ho}_3[\text{PN}_4]\text{O}$ recorded in the ranges $\tilde{\nu} = 600$ to 4000 and 50 to 3500 cm^{-1}	70
Figure 4.7	Magnetic susceptibility of $\text{Ho}_3[\text{PN}_4]\text{O}$ recorded from 3.3 to 300 K at a field of 2 T.	72
Figure 4.8	DFT calculations on $\text{Ho}_3[\text{PN}_4]\text{O}$	73

Chapter 5

Figure 5.1	(a) Single-crystal of $\text{Ce}_{4-0.5x}\text{Li}_3\text{P}_{18}\text{N}_{35-1.5x}\text{O}_{1.5x}$ under excitation with 390 nm UV light, emitting blue light. (b) SEM micrograph of a $\text{Ce}_{4-0.5x}\text{Li}_3\text{P}_{18}\text{N}_{35-1.5x}\text{O}_{1.5x}$ single-crystal.	90
Figure 5.2	Rietveld refinement for a sample with $\text{Ce}_{4-0.5x}\text{Li}_3\text{P}_{18}\text{N}_{35-1.5x}\text{O}_{1.5x}$ as the main component and LiPN_2 and h-BN as side phases.....	91
Figure 5.3	Crystal structure of $\text{Ce}_{4-0.5x}\text{Li}_3\text{P}_{18}\text{N}_{35-1.5x}\text{O}_{1.5x}$ in projection along [001].	94
Figure 5.4	(a) Side-view of the triangular columns running perpendicular to [001], tetrahedra bridged by $\text{N}^{[3]}$ highlighted in royal blue. (b) One repetition unit of the stacks of six-membered rings.	95
Figure 5.5	(top, left) P–P connection pattern; (top, right) <i>natural tiling</i> in projection along [001], consisting of six individual tiles. (bottom) Cross section through one unit cell of the tiling.....	96
Figure 5.6	Coordination polyhedra around the sites of Li (a), Ce1 (b), and Ce2 (c); two coordination polyhedra are shown for Ce2, as they appear in stacks along [001] in the structure.	97

Figure 5.7	(a–c) Aberration-corrected STEM-HAADF Fourier filtered images along zone axes [100], [001], and [120]. (d) Drift corrected EDX mappings along [120] in juxtaposition to a HAADF image of the same section.	98
Figure 5.8	(a) Dark-field STEM micrograph of a representative crystallite of ground powder of $\text{Ce}_{4-0.5x}\text{Li}_3\text{P}_{18}\text{N}_{35-1.5x}\text{O}_{1.5x}$. (b, c) SAED along the along [120] zone axis and EDX for the highlighted regions in panel a.	98
Figure 5.9	(a) Experimental STEM-HAADF image along [001] of a domain with increased O content showing Ce atom columns. Region of intensity line scan (b) highlighted in red in panels a and c. (c) Intensity map of panel a enhanced by interpolation of brightness over 4 pixels followed by augmenting the bright areas for 9 pixels.	100
Figure 5.10	(a) SAED pattern of a superstructure domain along the [120] zone axis of the average structure (red indices and cell outlines); this corresponds to the [110] zone axis of the supercell (green, note the 30° rotation). (b) STEM-HAADF image along this direction showing a displacement of certain Ce2 atoms.	101
Figure 5.11	General reciprocal hkn ($n = 2, 4$, etc.) lattice plane, in which the basic cell (red), supercell (green), and modulation vectors \mathbf{q}_1 and \mathbf{q}_2 (blue) are marked.	102
Figure 5.12	(a) Projection of the (3 + 2)D superstructure model onto 3D space along [001] direction in a section corresponding to a $3 \times 3 \times 1$ multiple (black) of the basic cell (red). (b) Ce2 displacement along [001] and along the additional direction of (3 + 2)D superspace $\times 4$, atoms related by symmetry are marked with color.	105
Figure 5.13	$\text{Ce}_{4-0.5x}\text{Li}_3\text{P}_{18}\text{N}_{35-1.5x}\text{O}_{1.5x}$ emission spectrum (blue) in the range 410–700 nm, excitation spectrum (red) in the range 240–400 nm, and reflectance (black) in the range of 240–700 nm.	107
Figure 5.14	Molar magnetic susceptibility of $\text{Ce}_{4-0.5x}\text{Li}_3\text{P}_{18}\text{N}_{35-1.5x}\text{O}_{1.5x}$ determined at 20 kOe in the range of 1.85–300 K.	108

Chapter 6

Figure 6.1	(a) Digital micrograph of a single-crystal used for the SCXRD affixed to a glass rod. (b) SEM micrograph of another crystal, revealing smooth crystal surfaces.	122
Figure 6.2	(a) Unit cell of $\text{LiPr}_2\text{P}_4\text{N}_7\text{O}_3$. (b) Projection of a supercell along [100]. (c) Archimedean <i>fes</i> tiling consistent of regular squares and octagons with vertex symbol 4.8.8.	125

Figure 6.3	(a) Coordination polyhedron around Pr. (b) Coordination polyhedron around Li.	126
Figure 6.4	(a) UV-vis spectrum of $\text{LiPr}_2\text{P}_4\text{N}_7\text{O}_3$ obtained with a step width of 1 nm/step. (b) Region around the absorptions stemming from f-f transitions were measured with a step width of 0.025 nm/step.	127
Figure 6.5	Tauc-plot calculated from the UV-vis spectrum.	128

Chapter 7

Figure 7.1	a) Unit cell of $\text{Hf}_{7.16}\text{P}_{24}\text{N}_{44.64}\text{O}_{7.36}$. b) One hollow truncated supertetrahedron and the underlying P-P connection pattern. c) Centres of gravity of truncated supertetrahedra marked by light gray and dark gray spheres, respectively, for both diamond-type nets. d) Sphere packing of centres of gravity (light/dark gray spheres) of the diamond-type nets, forming a NaTl structure type.	139
Figure 7.2	Coordination spheres around a) Hf1 and b) Hf2 (in black) in a 3 Å radius.	140
Figure 7.3	Top: UV/Vis spectrum of $\text{Hf}_{9-x}\text{P}_{24}\text{N}_{52-4x}\text{O}_{4x}$ ($x \approx 1.84$). Bottom: Tauc plot of $\text{Hf}_{9-x}\text{P}_{24}\text{N}_{52-4x}\text{O}_{4x}$ ($x \approx 1.84$).	141

Chapter 8

Figure 8.1	SEM micrographs of representative crystals of (a) $\text{Zr}_{1-x}\text{PO}_{3+4x}\text{N}_{1-4x}$, (b) $\text{Zr}_{0.75}\text{PO}_4$, (c) $\text{Hf}_{1-x}\text{PO}_{3+4x}\text{N}_{1-4x}$, and (d) $\text{Hf}_{0.75}\text{PO}_4$	156
Figure 8.2	Unit cell of the Zr and Hf orthophosphates. Figure based on structure model of $\text{Zr}_{1-x}\text{PO}_{3+4x}\text{N}_{1-4x}$, with metal atoms in green, P in black and N in orange: (a) random orientation of the unit cell; (b) projection along [100].	157
Figure 8.3	Heavy-atom $M(\text{O/N})_8$ coordination polyhedron based on structure model of $\text{Zr}_{1-x}\text{PO}_{3+4x}\text{N}_{1-4x}$, with metal atom in green and N in orange: (a) polyhedron in random orientation; (b) polyhedron in projection along the $\bar{4}$ rotoreflection.	158
Figure 8.4	Comparison of lattice parameters a and c , unit cell volumes V , and P-(X) and M-(X) ($X = \text{O/N}$) distances of all title compounds as well as ZrSiO_4 and HfSiO_4	159
Figure 8.5	Tauc-plots of all compounds, generated from UV-vis reflectance data.	160

Chapter 9

- Figure 9.1** Crystal structure of MP_8N_{14} , MN_6 octahedra displayed in light gray, PN_4 tetrahedra in dark gray, M as light gray spheres, P as black spheres, N omitted for clarity.170
- Figure 9.2** Magnetic properties of FeP_8N_{14} : (a) χ and χ^{-1} data measured at 10 kOe, (b) zero-field-cooled / field-cooled measurements (ZFC/FC) at 100 Oe and (c) magnetization isotherms recorded at 3, 10 and 50 K..172
- Figure 9.3** Powder reflectance spectra of CoP_8N_{14} (top) and NiP_8N_{14} (bottom).174

Chapter 10

Chapter 11

- Figure 11.1** Periodic system of elements for nitridophosphates.191

Appendix A

Appendix B

- Figure B.1** Scanning electron micrograph of a $LiNdP_4N_8$ single crystal.216
- Figure B.2** Rietveld refinement of $LiNdP_4N_8$ in space group $Pnma$ (no. 62)..220
- Figure B.3** Rietveld refinement of $LiNdP_4N_8$ in space group $Pnma$ (no. 62) in the range of $2\theta = 60-93.5^\circ$222
- Figure B.4** Double Crankshaft chain running along [010].223
- Figure B.5** Temperature dependent powder X-ray diffractogram of $LiNdP_4N_8$225
- Figure B.6** FTIR spectrum of $LiNdP_4N_8$ 226
- Figure B.7** Susceptibility measurements of $LiNdP_4N_8$ carried out at 0.1, 1, 5, 10 and 20 kOe. ...228
- Figure B.8** Field dependent magnetization measurement of $LiNdP_4N_8$ carried out at 1.8 and 300 K.228
- Figure B.9** Field-cooled, Zero-field-cooled magnetization measurement of $LiNdP_4N_8$ carried out at 30 Oe.....229
- Figure B.10** Light-microscope image of a representative $LiNdP_4N_8$ sample.....230

Appendix C

Figure C.1	Rietveld plot of <i>bex</i> -La ₂ P ₃ N ₇	234
Figure C.2	Rietveld plot of <i>bex</i> -Ce ₂ P ₃ N ₇	237
Figure C.3	Rietveld plot of <i>bex</i> -Pr ₂ P ₃ N ₇	240
Figure C.4	IR spectrum of <i>bex</i> -Pr ₂ P ₃ N ₇ obtained in ATR geometry.	242
Figure C.5	Temperature Programmed PXRD of a <i>bex</i> -Pr ₂ P ₃ N ₇ sample.	242
Figure C.6	Rietveld plot of <i>mcm</i> -Pr ₂ P ₃ N ₇	246
Figure C.7	Rietveld plot of <i>mcm</i> -Nd ₂ P ₃ N ₇	249
Figure C.8	Rietveld plot of <i>mcm</i> -Sm ₂ P ₃ N ₇	252
Figure C.9	Rietveld plot of <i>mcm</i> -Eu ₂ P ₃ N ₇	254
Figure C.10	Rietveld plot of <i>mcm</i> -Ho ₂ P ₃ N ₇	256
Figure C.11	IR spectrum of <i>mcm</i> -Ho ₂ P ₃ N ₇ obtained in ATR Geometry.	258
Figure C.12	Temperature Programmed PXRD of a <i>mcm</i> -Ho ₂ P ₃ N ₇ sample.	258
Figure C.13	Rietveld plot of <i>mcm</i> -Yb ₂ P ₃ N ₇	262
Figure C.14	Rietveld plot of <i>mcm</i> - and <i>bex</i> -Pr ₂ P ₃ N ₇	263

Appendix D

Figure D.1	Rietveld refinement of data from a Ho ₃ [PN ₄]O sample, collected at 123 K.....	268
-------------------	--	-----

Appendix E

Figure E.1	FTIR spectrum of Ce _{4-0.5x} Li ₃ P ₁₈ N _{35-1.5x} O _{1.5x}	273
Figure E.2	Top view of high-temperature powder X-ray diffraction patterns of Ce _{4-0.5x} Li ₃ P ₁₈ N _{35-x} O _{1.5x}	274
Figure E.3	Difference Fourier maps ($F_{\text{obs}} - F_{\text{calc}}$) calculated for a structure model in space group $P6_3$, in which the atom positions of the inter-tetrahedra-bridging N were deleted.	281
Figure E.4	Difference Fourier maps ($F_{\text{obs}} - F_{\text{calc}}$) calculated for a structure model in space group $P6_3/m$, in which the atom positions of the inter-tetrahedra bridging N were deleted.	282

Figure E.5	Tiles occurring in $\text{Ce}_{4-0.5x}\text{Li}_3\text{P}_{18}\text{N}_{35-1.5x}\text{O}_{1.5x}$, face symbols and volume given in Table D.8.....	284
Figure E.6	Electron diffraction along [001] (a) and [100] (b), both SAED (left) and nanodiffraction (right) whole pattern symmetry in accordance to space group $P6_3/m$ derived from X-ray data.....	287
Figure E.7	Reciprocal lattice sections (see also Figure D.12, D.13) reconstructed from single crystal X-ray diffraction data (left) compared to SAED patterns along special directions from different crystallites (middle) with corresponding simulations (right) based on single crystal X-ray data,	288
Figure E.8	Fourier filtered STEM-HAADF images (a-c) including structure projection as overlay (P atoms in orange, Ce1 atoms in green, Ce2 atoms in light green) and drift corrected EDX mappings (d) both with atomic resolution viewed along zone axis [100], [001] and [120]	289
Figure E.9	Top: Experimental unfiltered STEM-HAADF image along [001] showing Ce2 atom columns with varying intensity. Bottom: Same figure, visually enhanced by interpolating brightness over four pixels, followed by extrapolation of bright areas over nine pixels.	290
Figure E.10	SAED patterns along [120] (a) and [121] (b) zone axis containing superstructure reflections, pattern indexed with the average structure model (red). Unfiltered STEM-HAADF image (c) along [120] with corresponding Fourier transform (d) showing superstructure reflections (green arrows) similar to those in SAED above based on different Ce2 positions. STEM-HAADF image (e) along [120] with corresponding Fourier transform (e) of a domain without superstructure, superstructure reflections are missing (red arrows) and no different Ce2 positions can be observed.	291
Figure E.11	(a) EELS spectrum of $\text{Ce}_{4-0.5x}\text{Li}_3\text{P}_{18}\text{N}_{35-1.5x}\text{O}_{1.5x}$ ($x \approx 0.72$), red arrows represent positions of the $\text{Ce}^{3+}\text{-M}_5$ and $\text{Ce}^{3+}\text{-M}_4$ edges. (b) Reference EELS spectra of CeF_3 and CeO_2 from Arai et al.	292
Figure E.12	Top to bottom: $hk2$, $hk4$ and $hk6$ planes.	295
Figure E.13	hhl plane. Visual enhancement (as stated above) reveals superstructure reflections for every lattice plane hkl with $l = 2n$, except for the $hk0$ plane.....	296
Figure E.14	Results of the superstructure refinement: Ce2 atoms related by symmetry highlighted by the same color.	296

Figure E.15	F_{obs} maps of the Ce2 position (blue line) in superspace. Top: x3 vs. x4; bottom: x3 vs. x5 map.	299
--------------------	---	-----

Appendix F

Figure F.1	Rietveld refinement of $\text{LiPr}_2\text{P}_4\text{N}_7\text{O}_3$. Experimental data as black crosses, Rietveld fit in red, difference plot in blue.	303
Figure F.2	FTIR spectrum of $\text{LiPr}_2\text{P}_4\text{N}_7\text{O}_3$ obtained in ATR geometry.	305
Figure F.3	Temperature-dependent powder diffraction pattern.	310

Appendix G

Figure G.1	Rietveld refinement of a $\text{Hf}_{9-x}\text{P}_{24}\text{N}_{52-4x}\text{O}_{4x}$ ($x \approx 1.84$) sample, datapoints as black crosses, fit as red line, difference plot as blue line, ($\lambda(\text{Mo-K}_{\alpha 1}) = 0.709300 \text{ \AA}$).	318
Figure G.2	SEM micrograph of a $\text{Hf}_{9-x}\text{P}_{24}\text{N}_{52-4x}\text{O}_{4x}$ ($x \approx 1.84$) crystal.	320
Figure G.3	EDX spectrum of the title compound.	324
Figure G.4	EEL spectrum in light blue, background subtracted spectrum dark blue, red line background.	326
Figure G.5	EEL spectrum in light blue, background subtracted spectrum dark blue, red line background.	326
Figure G.6	High-loss EEL spectrum in light blue, background subtracted spectrum dark blue, red line background.	327
Figure G.7	^7Li NMR spectra of two samples of the title compound recorded at room temperature.	327
Figure G.8	^7Li NMR spectra of a LiCl reference (left) and the sample (right) recorded at room temperature.	328
Figure G.9	Top left: effective magnetic moment per formula unit at 300 K. Top right: effective magnetic moment per formula unit at 1.9 K. Bottom: molar susceptibility obtained in the temperature range of 1.9 to 300 K.	330
Figure G.10	Fourier transform infrared spectrum of a $\text{Hf}_{9-x}\text{P}_{24}\text{N}_{52-4x}\text{O}_{4x}$ ($x \approx 1.84$) sample measured in ATR geometry.	331
Figure G.11	(a) Planes through a Hf2 electron density distribution. (b) One plane through the Hf2 electron density distribution at 2.9 \AA from origin.	334

Figure G.12	Difference Fourier map at Hf2's position in projection along [001] obtained from refinement in space group $I4_122$ (no. 98).....	335
Figure G.13	Difference Fourier map at Hf2's position in projection along [001] obtained from refinement in space group $\bar{I}4$ (no. 82).	336
Figure G.14	Difference Fourier map at Hf2's position obtained from refinement in space group $P1$ (no. 1).	336
Figure G.15	High-temperature powder diffraction patterns of a $\text{Hf}_{9-x}\text{P}_{24}\text{N}_{52-4x}\text{O}_{4x}$ ($x \approx 1.84$) sample ($\lambda(\text{Mo-K}\alpha_1) = 0.709300 \text{ \AA}$).	337

Appendix H

Figure H.1	Rietveld refinement of a $\text{Zr}_{1-x}\text{PO}_{3+4x}\text{N}_{1-4x}$ sample.	341
Figure H.2	Rietveld refinement of a $\text{Zr}_{0.75}\text{PO}_4$ sample.	341
Figure H.3	Rietveld refinement of a $\text{Hf}_{1-x}\text{PO}_{3+4x}\text{N}_{1-4x}$ sample.	342
Figure H.4	Rietveld refinement of a $\text{Hf}_{0.75}\text{PO}_4$ sample.	342
Figure H.5	Infrared spectra of samples of (a) $\text{Zr}_{1-x}\text{PO}_{3+4x}\text{N}_{1-4x}$, (b) $\text{Zr}_{0.75}\text{PO}_4$, (c) $\text{Hf}_{1-x}\text{PO}_{3+4x}\text{N}_{1-4x}$, (d) $\text{Hf}_{0.75}\text{PO}_4$	344
Figure H.6	Reconstructed reciprocal lattice planes of $\text{Zr}_{1-x}\text{PO}_{3+4x}\text{N}_{1-4x}$, maximum index is two.	350
Figure H.7	Reconstructed reciprocal lattice planes of $\text{Zr}_{0.75}\text{PO}_4$, maximum index is two.	351
Figure H.8	Reconstructed reciprocal lattice planes of $\text{Hf}_{1-x}\text{PO}_{3+4x}\text{N}_{1-4x}$, maximum index is two.	352
Figure H.9	Reconstructed reciprocal lattice planes of $\text{Hf}_{0.75}\text{PO}_4$, maximum index is two.	353
Figure H.10	^{31}P MAS NMR spectra of the $M_{0.75}\text{PO}_4$ ($M = \text{Zr, Hf}$) samples.	354
Figure H.11	Second coordination sphere around P in $M_{0.75}\text{PO}_4$ ($M = \text{Zr, Hf}$).	355
Figure H.12	High-temperature powder diffraction patterns of $\text{Zr}_{1-x}\text{PO}_{3+4x}\text{N}_{1-4x}$	357
Figure H.13	High-temperature powder diffraction patterns of $\text{Zr}_{0.75}\text{PO}_4$	357
Figure H.14	High-temperature powder diffraction patterns of $\text{Hf}_{1-x}\text{PO}_{3+4x}\text{N}_{1-4x}$	358
Figure H.15	High-temperature powder diffraction pattern of $\text{Hf}_{0.75}\text{PO}_4$	358
Figure H.16	Powder diffraction pattern of the phase transformation product of $\text{Zr}_{0.75}\text{PO}_4$ at 1000 °C.	359

Figure H.17	Powder diffraction pattern of the phase transformation product of $\text{Hf}_{0.75}\text{PO}_4$ at 1000 °C.	359
Figure H.18	Powder diffraction pattern of the phase transformation product of $\text{Zr}_{1-x}\text{PO}_{3+4x}\text{N}_{1-4x}$ and $\text{Zr}_{0.75}\text{PO}_4$ at 740 and 1000 °C.	360
Figure H.19	UV-vis spectra of samples of (a) $\text{Zr}_{1-x}\text{PO}_{3+4x}\text{N}_{1-4x}$, (b) $\text{Zr}_{0.75}\text{PO}_4$, (c) $\text{Hf}_{1-x}\text{PO}_{3+4x}\text{N}_{1-4x}$, (d) $\text{Hf}_{0.75}\text{PO}_4$	361

Appendix I

Figure I.1	Rietveld refinement of $\text{FeP}_8\text{N}_{14}$	369
Figure I.2	Rietveld refinement of $\text{CoP}_8\text{N}_{14}$	369
Figure I.3	Rietveld refinement of $\text{NiP}_8\text{N}_{14}$	370
Figure I.4	(a) Observed electron density (F_{obs}) map with boundaries around a CoN_6 octahedron obtained from the $\text{CoP}_8\text{N}_{14}$ powder data. (b) Observed electron density (F_{obs}) map with boundaries around a NiN_6 octahedron obtained from the $\text{NiP}_8\text{N}_{14}$ powder data.	370
Figure I.5	Scanning electron microscopy micrographs of representative samples of (a) $\text{FeP}_8\text{N}_{14}$, (b) $\text{CoP}_8\text{N}_{14}$, (c) $\text{NiP}_8\text{N}_{14}$	378
Figure I.6	FTIR spectra of (a) $\text{FeP}_8\text{N}_{14}$, (b) $\text{CoP}_8\text{N}_{14}$, (c) $\text{NiP}_8\text{N}_{14}$ obtained in ATR geometry.	379
Figure I.7	Temperature-dependent powder X-ray diffraction pattern of $\text{FeP}_8\text{N}_{14}$	380
Figure I.8	Temperature-dependent powder X-ray diffraction pattern of $\text{CoP}_8\text{N}_{14}$	381
Figure I.9	Temperature-dependent powder X-ray diffraction pattern of $\text{NiP}_8\text{N}_{14}$	381
Figure I.10	(a)–(d) Honeycomb-type layers of PN_4 tetrahedra forming the tetra-layers of the MP_8N_{14} structures along [001]. (e) Tetra-layer along the [010] direction.	382
Figure I.11	Magnetic properties of $\text{CoP}_8\text{N}_{14}$: (top) χ and χ^{-1} data measured at 10 kOe and (bottom) magnetization isotherms recorded at 3, 10 and 50 K.	383
Figure I.12	Magnetic properties of $\text{NiP}_8\text{N}_{14}$: (top) χ and χ^{-1} data measured at 10 kOe, (middle) zero-field-cooled / field-cooled measurements (ZFC/FC) at 100 Oe and (bottom) magnetization isotherms recorded at 3, 10 and 50 K.	384
Figure I.13	Temperature dependence of the effective magnetic moment of the Fe^{2+} cations in $\text{FeP}_8\text{N}_{14}$	385

Figure I.14	Experimental (dots) and simulated (red line) ^{57}Fe Mössbauer spectrum of $\text{FeP}_8\text{N}_{14}$ at 6 K.....	386
Figure I.15	Orbital energies in coordination environments of different symmetry compared to the free ion for (a) a d^7 system and (b) a d^8 system.	387
Figure I.16	MN_6 octahedra of MP_8N_{14} ($M = \text{Fe, Co, Ni}$) with second coordination sphere, visualizing the trigonal-planar [$\text{c.n.}(\text{N}^{3-}) = 3$] coordination of N by one metal atom M and two P atoms.	389

Appendix J

Chapter 1

Introduction



1.1 Of serendipity and explorative solid-state chemistry

Mass marketing, or shotgun marketing, is a viable strategy in advertisement, in which the product is broadcasted via mass media to the largest possible audience. The aim is to locate potential buyers within a large crowd, meaning the larger the audience the more customers will be reached. A similar approach exists in inorganic chemistry, simply coined explorative chemistry. Chemists and materials scientists, driven by human desire for exploration and the increasing demand for high-performance materials, screen vast amount of elemental compositions, and temperature and pressure conditions, with numerous synthesis procedures to find local minima on the global energy hypersurface, which contains stable and metastable compounds.^[1]

The combinatorial possibilities offered by the periodic system of elements, however, are insurmountable. Taking into account the 86 elements with sufficient reactivity and isotope stability yields 2^{86} possible element combinations that would require 10^{80} – 10^{90} experiments to screen at a decent step width of parameters.^[1] These decimal potencies are comparable with the number of atoms in the universe, which would require recycling of matter used in previous experiments. Despite the odds, explorative chemistry, of course fused with chemical intuition and varying degrees of serendipity, has been the key to the discovery of remarkable materials, for example the cuprate family of high- T_C superconductors or perovskite-type solar-cells.^[2–4] After identification of a promising material, the related material family is systematically screened for compounds with similar or better properties. The

reason for finding compounds with similar properties within one material family is vividly highlighted by modern data-mining techniques. The review of numerous thermoelectric materials belonging to several classes of materials revealed that properties and performance tend to cluster within one material family.^[5] This relation, however, also implies that drastic improvements of performance cannot be expected within one class of compounds, as for that switching the class is imperative. Hence, with the increasing demand for high-performance materials, the role of explorative chemistry remains ever-important.

Despite the sheer endless combinations possible with the 86 stable elements, materials of few constituents are desirable as they serve as model systems of manageable size and oftentimes have a better performance than multinary compounds. Diamond, for example, is still the hardest known material with a microhardness of 9000 kg/mm² followed by cubic boron nitride with 4800 kg/mm².^[6] Hematite Fe₂O₃, though not having the best of performances, is intensely studied as a model system for the physics of water splitting.^[7] Technologic advances like third generation synchrotrons, powerful in-house diffractometers, and readily available high-resolution transmission electron microscopes concomitant with new strategies for material characterization like rotation electron diffraction and microfocused synchrotron beams form the foundation for an increasing pace of exploration.^[8-12] However, as the number of materials with fewer constituent elements is limited, the increasing pace might lead to a scarcity of such compounds being discovered. Opening new classes of materials postpones a shortage of discoveries, an important task for explorative chemists and materials scientists. New areas on the energy hypersurface can be accessed by materials synthesis at extreme conditions. This can, for example, mean reacting precursors at prior neglected temperatures and pressures using for example high-frequency furnaces, hot isostatic presses, ammonothermal environments, or, as was used in this dissertation, large volume presses. The synthesis strategy is another important aspect in explorative chemistry as local energy minima of desired phases can be shrouded by thermodynamically stable compounds. To avoid these thermodynamic sinkholes, the invention of a new synthesis strategy involving reactive precursors is oftentimes the only way to prepare the targeted materials. In this dissertation, a systematic access to the vast but scarcely explored materials families of rare-earth and transition metal nitridophosphates is opened by the combination of extreme reaction conditions achieved with large volume presses and the establishment of a novel synthesis strategy.

1.2 The nitridophosphate class of compounds

Outlined below are the motivations for nitridophosphate research encompassing structural and compositional diversity, relation to similar materials families, and physical properties. Moreover, key aspects of the research advancements, implemented synthesis strategies, their advantages and limitations with regard to granting a systematic access, are discussed. Most important, the central problem of nitridophosphate synthesis, the thermally induced redox activity of nitridophosphates through N_2 elimination, is addressed.

Nitridophosphates theoretically constitute a vast family of materials, but despite over 25 years of research it is still for a large part unexplored. As the element combinations P/N and Si/O are isoelectronic, the structures and properties of nitridophosphates are related to those of (alumo)silicates. The fundamental building unit in both cases is the tetrahedron, and multiple isotypic or homeotypic structures are observed in both materials families, such as paracelsian-type $BaAl_2Si_2O_8$ and $NdLiP_4N_8$, phenakite-type BeP_2N_4 and Be_2SiO_4 , and diverse phosphorus oxide nitride (PON) and silica (SiO_2) polymorphs, e.g. β -cristobalite, α -quartz, moganite, coesite, and the stishovite-related post-coesite-type.^[13–21] Hence nitridophosphates feature similar properties as silicates and were discussed as Li-ion conductors, such as most Li–P–N nitridophosphates, phosphors for solid-state lighting like $Ba_3P_5N_{10}Br:Eu^{2+}$, colour pigments like the transition metal nitrido-sodalites, and host compounds for guest molecules like the nitridic clathrate $P_4N_4(NH)_4(NH_3)$.^[22–26]

Despite their close relation to silicates, nitridophosphates constitute a purely synthetic class of compounds. Hence the structural and compositional diversity of known nitridophosphates does not yet compare to the vast numbers of known silicates. A colour-coded periodic system of elements (PSE, Figure 1.1) highlights elements with which ternary nitridophosphates M –P–N have been published prior to this dissertation. But even this scarcely featured PSE obscures that only for group 1 and 2 a partly systematic access has been achieved as there are 34 group 1 and 21 group 2 (oxo)nitridophosphates crystallizing in 27 and 10 different structure types, the majority share of all known nitridophosphate compounds. Table A.1 contains a list of all published (oxo)nitridophosphates to this date, a list with less than one hundred entries. Due to the structural kinship to silicates, nitridophosphates are also expected to readily incorporate transition and rare-earth metals. Rare-earth compounds,

however, have been completely unknown and only few transition metals have been successfully incorporated.

To understand the critique expressed towards the diversity of hitherto prepared nitridophosphates, the range of compounds that are expected to exist, with all conceivable structures and element combinations, has to be evaluated. A systematic access given by one preparation method is hereby coined as the ability to prepare a large range of structures within one sub-family of nitridophosphates, e.g. the rare-earth nitridophosphates. In tetrahedra-based structure families, such as silicates and nitridophosphates, the tetrahedra can be either non-condensed or interconnected to form frameworks, layers, rings or chains, and complex anions.

The type of network obtained can, to some degree, be controlled through the atomic ratio of tetrahedra-centres to tetrahedra-corners within the network. For a framework with all-side vertex-sharing tetrahedra this ratio, namely the degree of condensation κ , has to be at least 1/2, like in SiO_2 or NdLiP_4N_8 .^[14,27] While κ is a useful measure for the connectivity of a tetrahedra network, it cannot strictly predict the network type as exceptions such as $\text{Li}_{10}\text{P}_4\text{N}_{10}$ exist, which features adamantane-like cages despite $\kappa = 2/5$ that usually is found for layered networks.^[28]

Group	1	2	3	4	5	6	7	8	9	10	11	12	13	14	15	16	17	18													
1	1 H																	2 He													
2	3 Li	4 Be											5 B	6 C	7 N	8 O	9 F	10 Ne													
3	11 Na	12 Mg											13 Al	14 Si	15 P	16 S	17 Cl	18 Ar													
4	19 K	20 Ca	21 Sc	22 Ti	23 V	24 Cr	25 Mn	26 Fe	27 Co	28 Ni	29 Cu	30 Zn	31 Ga	32 Ge	33 As	34 Se	35 Br	36 Kr													
5	37 Rb	38 Sr	39 Y	40 Zr	41 Nb	42 Mo	43 Tc	44 Ru	45 Rh	46 Pd	47 Ag	48 Cd	49 In	50 Sn	51 Sb	52 Te	53 I	54 Xe													
6	55 Cs	56 Ba		72 Hf	73 Ta	74 W	75 Re	76 Os	77 Ir	78 Pt	79 Au	80 Hg	81 Tl	82 Pb	83 Bi	84 Po	85 At	86 Rn													
7	87 Fr	88 Ra		104 Rf	105 Db	106 Sg	107 Bh	108 Hs	109 Mt	110 Ds	111 Rg	112 Cn	113 Uut	114 Uuq	115 Uup	116 Uuh	117 Uus	118 Uuo													
				Lanthanides													57 La	58 Ce	59 Pr	60 Nd	61 Pm	62 Sm	63 Eu	64 Gd	65 Tb	66 Dy	67 Ho	68 Er	69 Tm	70 Yb	71 Lu
				Actinides													89 Ac	90 Th	91 Pa	92 U	93 Np	94 Pu	95 Am	96 Cm	97 Bk	98 Cf	99 Es	100 Fm	101 Md	102 No	103 Lr

Figure 1.1. Periodic system of elements with elements highlighted that form ternary compounds with P and N. Blue: 29 group 1 and 2 nitridophosphates, orange: 4 transition metal nitridophosphates, purple, 2 group 14 nitridophosphates. O is highlighted due to the 8 P/O/N compounds. A complete list of all nitridophosphates is given in Table A.1.

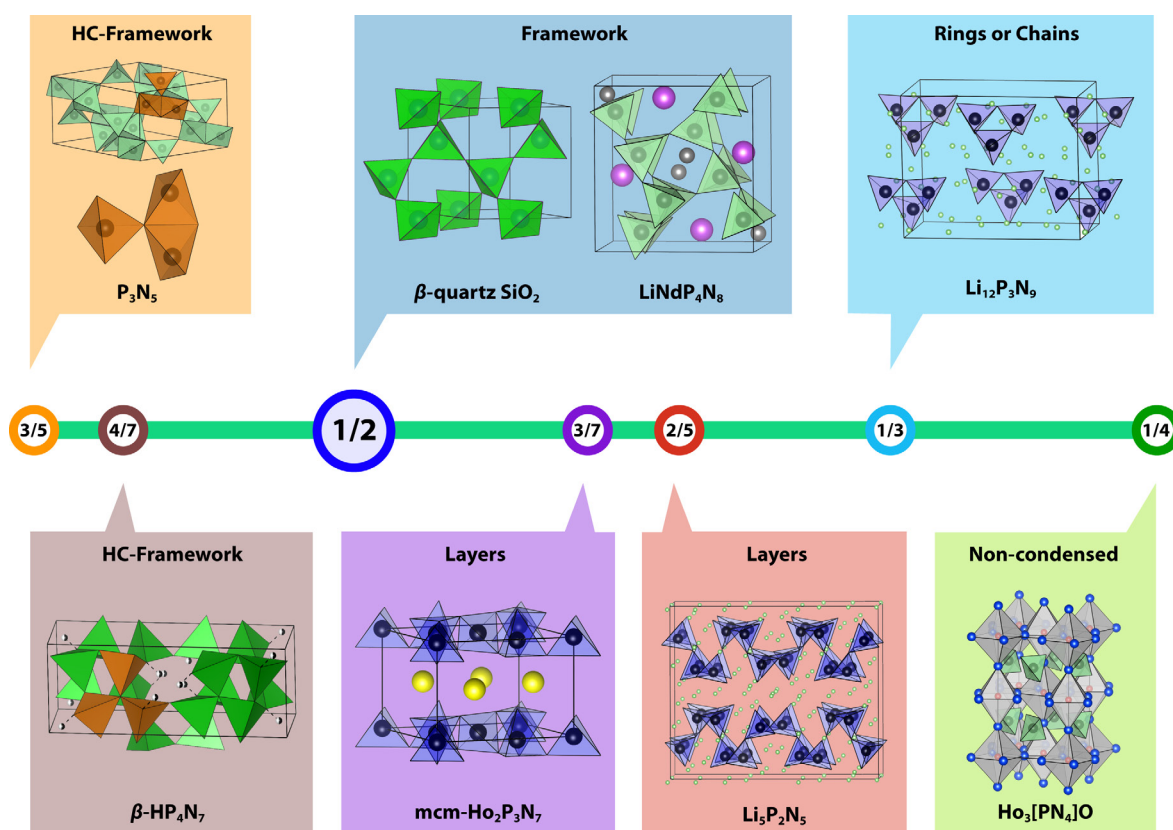


Figure 1.2. Selected landmarks in κ occurring in nitridophosphates; 6/11 has been omitted for clarity.^[14,27,29–34] For oxosilicates, κ terminates in SiO_2 . HC stands for highly-condensed, representing frameworks with $\kappa > 1/2$, which necessarily feature triply-bridging N atoms.

The range of κ is individual for each class of materials. While the low end of κ naturally is $1/4$, representing non-condensed tetrahedra, the high end is determined by electrostatics and terminates in the κ of the binary parent compounds, for silicates and nitridophosphates that being SiO_2 and P_3N_5 .^[29] A higher degree of condensation would either necessitate a change in the oxidation state of e.g. P, or would result in tetrahedra networks with positive formal charge. Landmarks in κ are shown in Figure 1.2, and, as it reveals, nitridophosphates encompass a greater electrostatic range than silicates.

Nitridophosphates are able to form higher-condensed structures, which in theory give rise to a greater structural diversity than silicates can offer. These higher-condensed structures with $\kappa > 1/2$ necessitate the introduction of a new structural motif, the triply-bridging N atom. All vertices of the tetrahedra are in the regular case doubly bridging for $\kappa = 1/2$. Increasing the degree of condensation necessitates that more than two tetrahedra centres share a common vertex, which in nitridophosphates results in $\text{N}^{[3]}$ atoms (coordination number in superscripted square brackets). Examples for $\text{N}^{[3]}$ atoms within phosphorus nitrides and nitridophosphates are the P_3N_5 polymorphs, the HP_4N_7

polymorphs, and the $M_3P_6N_{11}$ ($M = \text{Na, K, Rb, Cs}$) phases.^[29,30,35–40] $N^{[3]}$ was observed in two arrangements, as the vertex of three vertex-sharing PN_4 tetrahedra (e.g. $\beta\text{-HP}_4\text{N}_7$, MP_6N_{11} ($M = \text{Na, K, Rb, Cs}$)), and as the vertex of two edge-sharing and one vertex-sharing tetrahedra (e.g. $\alpha\text{-P}_3\text{N}_5$, $\alpha\text{-HP}_4\text{N}_7$, P_4N_6O).^[29,30,36,38–41] In high-pressure polymorphs $N^{[3]}$ atoms were observed to be one vertex of two edge-sharing PN_5 trigonal-bipyramids ($\gamma\text{-HP}_4\text{N}_7$) or square pyramids ($\gamma\text{-P}_3\text{N}_5$) and one tetrahedron.^[35,37] The readily occurring $N^{[3]}$ atoms concomitant with edge-sharing polyhedra reflect the electrostatic properties of the less polarized P–N bond in comparison with the more ionic Si–O bond.^[42] Edge-sharing tetrahedra have not yet been observed in silicates, only claimed for fibrous SiO_2 that could not yet be reproduced, most likely due to electrostatic repulsion of the highly-charged Si^{4+} ions.^[43,44]

1.3 Challenges to synthesis

Taking under consideration κ and the structural motif of triply-bridging N atoms, the structural diversity of nitridophosphates is in theory greater than that of oxosilicates. As nitridophosphates are a purely synthetic class of compounds, however, all compounds have to be prepared by chemists. The preparation of the nitridophosphates has been the progress limiting step due to several cumulative reasons. The central problem is the negative electron affinity of N, which makes nitride ions prone to oxidation as they are only stabilized by their surrounding coordination environment.^[45] During synthesis an oxidation results in the elimination of N₂ and reduction of P to oxidation state +III or 0. Common precursors like P₃N₅ are therefore thermally labile. P₃N₅ decomposes at around 850 °C (P₃N₅ → 3 “PN” + N₂), which is well below the crystallization temperature of most nitridophosphates, especially the higher-condensed ones with $\kappa > 1/2$.^[29,46,47]

To discuss the synthesis methods developed over the years to tackle or to bypass the problem of N₂ elimination, a comprehensive list of nitridophosphates is given in Table A1.1. The table includes the synthesis route, precursors, structural information, and year of publishing of approximately 80 nitridophosphates crystallizing in 64 structure types. Prior to methods incorporating a large volume press and pressures in the gigapascal (GPa) range, ampoule synthesis gave access to various nitridophosphates, predominantly in the Li–P–N system. Li₇PN₄, Li₁₂P₃N₉, α -/ β -Li₁₀P₄N₁₀, Li₁₃P₄N₁₀X₃ (X = Cl, Br), and LiPN₂, are examples of solid-solid reactions between P₃N₅ and varying amounts of Li₃N, a method coined the Li₃N self-flux method.^[22,33,48–50] The reactivity of Li₃N certainly favours low reaction temperatures below the decomposition temperature of P₃N₅ and thus enables a rich Li–P–N chemistry. The need for reactive starting materials was discovered early on and implemented via decomposition and condensation of molecular precursors in sealed fused-silica ampoules. α -P₃N₅, for example, has been prepared in phase-pure and crystalline form through decomposition of tetraaminophosphoric iodide [P(NH₂)₄]I.^[29] The condensation byproducts are gaseous HI and ammonia, which raise the pressure in the reaction container, yielding the so-called pressure-ampoule. Further, NH₄I is argued to suppress the formation of β -P₃N₅ and aided the crystallization of α -P₃N₅; ammonium halides are thus often added to the starting materials as mineralisers.^[51,52] The phosphorus imide nitride α -HPN₂ was prepared through ammonolysis of P₃N₅ inside a pressure ampoule, in which ammonia was formed *in situ* through reaction of a mixture of Mg₃N₂ and NH₄Cl.^[53] An analogous

reaction with a Zn_3N_2/NH_4Cl mixture did not yield α -HPN₂, but the sodalites $Zn_{7-x}H_{2x}[P_{12}N_{24}]Cl_2$ with $0 \leq x \leq 3$ since $ZnCl_2$ is volatile under reaction conditions allowing its incorporation into the nitridophosphate network.^[54] Several other metals could also be stabilized in the low-density sodalite framework, always concomitant with halides or chalcogenides and through reaction of reactive precursors; the $M_{(6+(y/2)-x)}H_{2x}[P_{12}N_{24}]Z_y$ with $M = Mn, Fe, Co, Ni$; $Z = Cl, Br, I$; $0 \leq x \leq 4$; $y \leq 2$ phases were prepared from a $MZ_2/NH_4Z/(PNZ_2)_3$ mixture, while the nitridophosphate sulfides $M_8[P_{12}N_{24}]S_2$ ($M = Mg, Fe, Co, Cd$) could be obtained from ammonolysis of a MS/P_4S_{10} mixture.^[24,55,56]

The highly-condensed α -HP₄N₇ and silicon phosphorus nitride SiPN₃ were prepared in pressure ampoules by decomposition and condensation of elaborate molecular precursors, $(NH_2)_2P(S)NP(NH_2)_3$ and $SiPN(NH)(NH_2)_4$, respectively, which already contained the correct elemental ratio of the products considering volatile species as well.^[36,57] More universal molecular precursors proved to be the phosphoric triamid $OP(NH_2)_3$ and the thiophosphoric triamid $SP(NH_2)_3$. The low-density framework structures of zeolites nitridophosphate one (NPO) and nitridophosphate two (NPT) were accessible upon reaction of these triamids with Li_2S and BaS , respectively.^[58,59] Moreover, oxonitridophosphates with densely packed tetrahedra networks like SrP_3N_5O and $BaP_{12}N_{17}O_9Br_3$ have been prepared in this way.^[51,60] Key to the preparation of nitridophosphates at ambient or medium pressures (well below 1 GPa) seems to be the use of reactive starting materials, mineralisers like ammonium halides, and/or high ammonia partial pressures. Oftentimes, however, only low-density frameworks or low degrees of condensation are accessible, a drawback of gas flow and pressure-ampoule methods. Ostwald's step rule might indicate the reason for this shortcoming: during synthesis metastable phases tend to form first and then rearrange to the thermodynamically stable ones.^[61] In hydrothermal synthesis of zeolites, for example, prolonged reaction can cause the formed porous frameworks to collapse to denser structures. Collapsing the nanoporous β -cages of above mentioned nitrido-sodalites to denser structures would require higher temperatures, which is prevented by N_2 elimination under ambient- to medium-pressure ($p < 1$ GPa) conditions.^[54-56]

The point of N_2 elimination is shifted through pressure following Le Chatelier's principle. Hence, reactions carried out at higher pressures allow for higher reaction temperatures that in turn allow the use of starting materials that are less reactive than for example Li_3N . Le Chatelier's principle was used early on and realized with the ammonothermal synthesis of $K_3P_6N_{11}$ and a reproduction

of α -HPN₂.^[39,62] Ammonothermal synthesis, however, is limited in temperature and pressure by the autoclave material. State of the art materials are nickel-based superalloys Inconel® 718 (max. 600 °C, 0.3 GPa) and Haynes® 282® (max. 800 °C, 0.17 GPa).^[63] Large volume presses, such as the Voggenreiter hydraulic 1000 t presses used in this work, proved to be a compelling alternative. With the multianvil technique reaction pressures of up to 25 GPa and temperatures of up to 1500 °C can be achieved.^[64] The augmented window of temperature-stability of nitridophosphates is exemplified by the preparation of the highly-condensed MP_4N_7 ($M = \text{Na, K, Rb, Cs}$) phases in a belt-apparatus at pressures of 4 GPa and temperatures ranging from 1800 to 2000 °C.^[65]

With the multianvil technique as state of the art preparation method, several synthesis strategies emerged that led to the discovery of most nowadays known nitridophosphates. Molecular precursors were mostly abandoned, in favour of metal nitrides and metal azides, which are reacted with P₃N₅, PON, and/or HPN₂.^[28,65,66] The metal nitrides found only niche applications, mostly when stability would not allow the use of the azides, which was the case in the preparation of BeP₂N₄ and Zn₂PN₃.^[15,67] Starting from sodium, chemistry with the heavier alkali metals necessitated the use of the azides, since of the nitrides only Na₃N and K₃N are known but not easily accessible, while Rb₃N and Cs₃N are still unknown.^[40,65,68,69] The reaction of alkali azides and P₃N₅ lead to the preparation of MP_4N_7 ($M = \text{Na, K, Rb, Cs}$) and $M_3P_6N_{11}$ ($M = \text{Rb, Cs}$).^[40,65] Moreover, ternary group 1 and 2 nitridophosphates with $\kappa = 1/2$, NaPN₂, CaP₂N₄, SrP₂N₄, and BaP₂N₄ were prepared with the azide route.^[15,47,66,70,71]

As nitridophosphate networks consisting of PN_2^- ($\kappa = 1/2$) are isoelectronic to SiO₂, they often-times crystallize in silica- or aluminosilicate-analogous structures. LiPN₂ and NaPN₂ enter a filled β -cristobalite-type, while CaP₂N₄ and SrP₂N₄ crystallize in the megakalsilite-type.^[49,66,70,71] BaP₂N₄ has not been affiliated with any known silicate, however is isotypic to HP-CaB₂O₄.^[72] Next to the 3d transition metal nitridophosphate-sodalites, a few transition metal nitridophosphates, namely MnP₂N₄, CdP₂N₄, CuPN₂, and Zn₂PN₃, with dense P/N frameworks have been prepared.^[67,73,74] The compounds with $\kappa = 1/2$ also crystallize in the megakalsilite- and filled β -cristobalite-type, respectively. Zn₂PN₃ is a double nitride forming the wurtzite-type and was recently discussed as a potential nitride semiconductor made of earth-abundant elements.^[75]

Despite the variety of structures discovered with the azide and nitride routes using large volume

presses, a systematic access to nitridophosphates has not been achieved. Structural diversity in terms of exhausting the full range of condensation from $1/4$ to $3/5$ (cf. Figure 1.2) was not yet shown for either synthesis route. Non-condensed PN_4 tetrahedra have only been observed in Li_7PN_4 , while PO_3N tetrahedra were realized in $M_2\text{PO}_3\text{N}$ ($M = \text{Ca}, \text{Sr}$).^[48,76] Layered networks, related to phyllosilicates with $\kappa = 2/5$, have not yet been prepared with group 2 metals as most of these nitridophosphates have a degree of condensation of $\kappa = 1/2$. Only $\kappa = 6/11$ and $4/7$ has been observed for K, Rb, and Cs nitridophosphates and no lower-condensed structures as present in the Li–P–N system.^[39,40,65]

The attainable elemental diversity is the second issue of the azide and nitride routes. Rare-earth nitrides, for example, are stable interstitial metals, while the azides are unknown since they are too instable.^[77,78] Most transition metal azides are similarly instable and unsuitable for synthesis; $\text{Cd}(\text{N}_3)_2$ has been used for the synthesis of CdP_2N_4 but with a warning label attached.^[73] The structure chemistry of the transition metal nitrides varies within the third period, from ionic compounds till group 3, to metallic bonding to group 9, and covalent bonding thereafter. The stability of the nitrides decreases beyond group 5, which manifests in increasing M/N ratios and attainable oxidation states. The highest oxidation state was observed in Ta_3N_5 with Ta^{+V} .^[79] Mn, Fe, Co, and Ni do not form or only form metastable 1:1 nitrides, the two existing polymorphs of FeN for example have been prepared by direct current reactive sputtering and by high-pressure synthesis in a diamond anvil cell.^[79–81] Reasons for the lack of transition metal nitridophosphates prepared from the nitrides, only CuPN_2 was prepared from Cu_3N , are speculative.^[74] Since most of the transition metal nitrides are interstitial metals, oxidation of the metals is mandatory during synthesis. However, oxidation requires a reduction partner. This narrows the use of, nowadays known, starting materials to HPN_2 that has successfully been used in reaction with Mn and Sn metal resulting in MnP_2N_4 and the $\text{Sn}_6[\text{P}_{12}\text{N}_{24}]$ sodalite.^[73,82] The challenge here is for HPN_2 to oxidize the metal while not oxidizing the nitride ions. The stable oxidation states Mn^{2+} and Sn^{2+} with half-filled d-shell, and filled d-shell/filled s-shell, respectively, might be a reason for the success with MnP_2N_4 and $\text{Sn}_6[\text{P}_{12}\text{N}_{24}]$. Moreover, 3d transition metals readily form phosphides through oxidation of nitride ions when in the vicinity of P. These thermodynamic sinkholes have to be circumvented, necessitating the use of starting materials that are reactive in a narrow window of temperature and pressure. Favorable are precursors with metals in the correct oxidation states, to exclude additional redox reactions and to prevent the oxidation of nitride ions.

1.4 High-pressure metathesis, the remedy?

In the light of above discussion, this dissertation is concerned with the development of a new and highly adaptable synthesis route, the high-pressure metathesis, which may grant a systematic access to rare-earth and transition metal nitridophosphates.^[14] The general idea of high-pressure metathesis is the reaction of metal halides with LiPN_2 to form the corresponding nitridophosphate and a lithium halide, as schematically shown in Equation 1.1.



To suppress elimination of N_2 , the metathesis reaction is carried out under pressures of several GPa (usually around 5–10 GPa) achieved with the multianvil technique. The advantage of metathesis is the thermodynamic driving force generated by the ion-exchange forming thermodynamically more stable products, in nitridophosphate synthesis that being the lithium halides. This driving force has been taken advantage of to target even metastable compounds since lower external temperatures are required to start the reaction.

Solid-state metathesis reactions form a branch of the prior developed self-propagating high-temperature (combustion) synthesis route (SHS). The SHS route uses a mixture of reactive precursors in a fast and exothermic reaction and was initially developed in the 1960s to alleviate the cost and time resources of conventional high-temperature synthesis.^[83,84] The thermite reactions (e.g. $\text{Fe}_2\text{O}_3 + \text{Al}$) are probably the best-known examples for SHS, but also intermetallics, refractory nitrides, borides, and carbides can be so prepared.^[83–85] SHS oftentimes produces porous products due to the formation of volatile species, but for Ti borides and carbides it was shown that densification could be achieved by reaction at pressures of up to 250 bar.^[83] Solid-state metathesis reactions were developed in the 1990s by the groups of Kaner, and Parkin targeting metal borides, silicides, pnictides and chalcogenides, usually starting from respective metal halides.^[86,87] More recently, metathesis has been used for the preparation of otherwise inaccessible nitridoborates, carbodiimides, tetracyanoborates, tetracyanamidosilicates, and carbon-nitride materials.^[88,89] To overcome the drawbacks of solid-state metathesis reactions, that are combustible precursors, poor product crystallinity, non-stoichiometric product formation, and an uncontrollable reaction pathway, the metathesis can also be carried out under pressures of several GPa, leading to the discovery of new metal nitrides like VN, Fe_3N , and Re_3N , or

single-crystal growth of important functional nitrides like GaN.^[90,91] Lei and He thus coined the term high-pressure solid-state metathesis reaction. Next to the nitridophosphates presented in this work, a ternary double nitride ZnSnN₂ has been prepared by high-pressure metathesis reaction.^[92]

Prior to the development of the high-pressure metathesis, most synthesis routes of nitridophosphates yielded microcrystalline samples, which necessitate an oftentimes challenging structure determination from powder diffraction data. This problem has been tackled by adding ammonium halides as mineralisers to the starting materials, a procedure rendered unnecessary by the high-pressure metathesis route.^[51,52] As will be shown in this dissertation, the lithium halides formed as byproduct greatly enhance the formation of single-crystals under high-pressure conditions: single-crystals of up to 250 μm in size have been observed.^[14,93] As explorative synthesis in uncharted systems usually leads to multi-component samples, single-crystals can greatly simplify structure determination of the constituent phases. The structural and compositional information obtained from the crystal structure can then be used to refine the synthesis strategy to obtain single-phase materials for further characterization of its physical properties. This procedure, sustained by the enhanced crystal growth, has the prospect of notably enhancing the speed of nitridophosphate research.

Next to the motivation of overcoming the challenge of difficult synthesis, rare-earth and transition metal nitridophosphates pose the opportunity to study fundamental structural and physical properties of completely unknown compounds in an explorative approach as outlined in Section 1.1. The rare-earth nitridophosphates reported here were the first to be described in literature, the group 4 nitridophosphates are the first transition metal nitridophosphates with tetravalent cations, and the MP_8N_{14} phases with $M = \text{Fe, Co, Ni}$ are the first nitridophosphates with open-shell transition metals without a half-filled d-shell (MnP_2N_4).^[73] Incorporating metals with states of valence unobserved before into nitridophosphate networks is likely to yield hitherto unprecedented structures within nitridophosphates or tetrahedra-based compounds in general. The correlation of the thermal stability of the nitridophosphate network and the charge of the ion has only been investigated for mono- and divalent cations, but with rare-earth and group 4 metals this correlation can be expanded to tri- and tetravalent cations as well. Open-shell systems give rise to electronic transitions in the visible part of the spectrum. Properties like the ligand-field strength of nitride ions in nitridophosphates or the nephelauxetic effect could be determined and possibly even applications as low-band gap material for

photocatalysis could follow. Magnetic properties like spin-ordering phenomena can now be studied for the first time on nitridophosphates. Further, ion conductivity and luminescent properties upon doping with for example Eu^{2+} , Ce^{3+} , $\text{Mn}^{2+/3+/4+}$, $\text{Cu}^{+/2+}$, Bi^{3+} , or Pb^{2+} could be probed in these novel structures. Especially alluring is the preparation of 3d transition metal nitridophosphates, since those systems, e.g. Fe–P–N, consist of earth-abundant elements only. Since sustainability is a pressing global issue, developing such systems becomes increasingly important. LiFePO_4 , for example, is already used as cathode material in commercially available Li-ion conductors, while cobalt phosphates are currently being investigated for application in photocatalytic water splitting as catalyst for the oxygen evolution reaction.^[94,95]

The content of this dissertation is presented in logical order with regards to the development of a systematic access to rare-earth and transition metal nitridophosphates. Chapter 2 deals with the basic high-pressure metathesis reaction between rare-earth halide and LiPN_2 leading to NdLiP_4N_8 . General ideas and future prospects are presented there. Chapters 3 to 6 show the ability of high-pressure metathesis to produce networks of rare-earth nitridophosphates ranging from non-condensed tetrahedra to highly-condensed frameworks with triply-bridging N atoms and $\kappa > 1/2$ by addition of further starting materials like Li_3N , P_3N_5 , Li_2O , and PON. Chapter 6 deals with the expansion of structural diversity in nitridophosphates by incorporating oxygen atoms into the network structures. The work carried out on the compound $\text{Ce}_4\text{Li}_3\text{P}_{18}\text{N}_{35}$ in Chapter 5 surpasses routine structure determination and is a benchmark for the resolution limit of nowadays possible structure analysis. A very weak and domain-localized superstructure could only be elucidated by joint venture of synchrotron diffraction on large single-crystals and scanning transmission electron microscopy.^[96]

Chapter 7 and 8 include the advancement of high-pressure metathesis to the first oxonitridophosphates with tetravalent ions, Zr and Hf, stabilized once in a framework structure and once concomitant with non-condensed tetrahedra. In Chapter 9 the open-shell transition metal compounds with sum formula MP_8N_{14} and $M = \text{Fe}, \text{Co}, \text{Ni}$ are presented. The circumvention of phosphide formation through high-pressure metathesis, optical properties including the determination of the ligand field strength of nitride ions in nitridophosphates, and measurement of the magnetic properties are the highlights of this work.

1.5 References

- [1] M. Jansen, *Angew. Chem., Int. Ed.* **2002**, *41*, 3746–3766; *Angew. Chem.* **2002**, *114*, 3896–3917.
- [2] J. G. Bednorz, K. A. Müller, *Z. Phys. B: Condens. Matter* **1986**, *64*, 189–193.
- [3] M. K. Wu, J. R. Ashburn, C. J. Torng, P. H. Hor, R. L. Meng, L. Gao, Z. J. Huang, Y. Q. Wang, C. W. Chu, *Phys. Rev. Lett.* **1987**, *58*, 908–910.
- [4] H. J. Snaith, *J. Phys. Chem. Lett* **2013**, *4*, 3623–3630.
- [5] M. W. Gaultois, T. D. Sparks, C. K. H. Borg, R. Seshadri, W. D. Bonificio, D. R. Clarke, *Chem. Mater.* **2013**, *25*, 2911–2920.
- [6] C. M. Sung, M. Sung, *Mater. Chem. Phys.* **1996**, *43*, 1.
- [7] A. G. Tamirat, J. Rick, A. A. Dubale, W.-N. Su, B.-J. Hwang, *Nanoscale Horiz.* **2016**, *1*, 243–267.
- [8] S. Hovmöller, X. Zou, *Cryst. Res. Technol.* **2011**, *46*, 535–541.
- [9] W. Zhou, H. F. Greer, *Eur. J. Inorg. Chem.* **2016**, 941–950.
- [10] J. Sun, Z. He, S. Hovmöller, X. Zou, F. Gramm, C. Baerlocher, L. B. McCusker, *Z. Kristallogr. - Cryst. Mater.* **2010**, *225*, 77–85.
- [11] F. Fahrnbauer, T. Rosenthal, T. Schmutzler, G. Wagner, G. B. M. Vaughan, J. P. Wright, O. Oeckler, *Angew. Chem., Int. Ed.* **2015**, *54*, 10020–10023; *Angew. Chem.* **2015**, *127*, 10158–10161.
- [12] W. Wan, J. Sun, J. Su, S. Hovmöller, X. Zou, *J. Appl. Crystallogr.* **2013**, *46*, 1863–1873.
- [13] J. V. Smith, *Acta Crystallogr.* **1953**, *6*, 613–620.
- [14] S. D. Klotz, W. Schnick, *Angew. Chem., Int. Ed.* **2015**, *54*, 11250–11253; *Angew. Chem.* **2015**, *127*, 11402–11405.
- [15] F. J. Pucher, R. Römer, F. W. Karau, W. Schnick, *Chem. - Eur. J.* **2010**, *16*, 7208–7214.
- [16] L. W. Bragg, *Z. Kristallogr. - Cryst. Mater.* **1930**, *72*, 518–528.
- [17] J. M. Léger, J. Haines, C. Chateau, G. Bocquillon, M. W. Schmidt, S. Hull, F. Gorelli, A. Lesauze, R. Marchand, *Phys. Chem. Miner.* **2001**, *28*, 388–398.
- [18] J.-M. Léger, J. Haines, L. S. de Oliveira, C. Chateau, A. Le Sauze, R. Marchand, S. Hull, *J. Phys. Chem. Solids* **1999**, *60*, 145–152.
- [19] J. Haines, C. Chateau, J.-M. Léger, A. Le Sauze, N. Diot, R. Marchand, S. Hull, *Acta Crystallogr., Sect. B: Struct. Sci.* **1999**, *55*, 677–682.
- [20] S. Vogel, D. Baumann, R. Niklaus, E. Bykova, M. Bykov, N. Dubrovinskaia, L. Dubrovinsky, W.

- Schnick, *Angew. Chem., Int. Ed.* **2018**, *57*, 6691–6695; *Angew. Chem.* **2018**, *130*, 6801–6805.
- [21] D. Baumann, R. Niklaus, W. Schnick, *Angew. Chem., Int. Ed.* **2015**, *54*, 4388–4391; *Angew. Chem.* **2015**, *127*, 4463–4466.
- [22] E.-M. Bertschler, C. Dietrich, T. Leichtweiß, J. Janek, W. Schnick, *Chem. - Eur. J.* **2018**, *24*, 196–205.
- [23] A. Marchuk, W. Schnick, *Angew. Chem., Int. Ed.* **2015**, *54*, 2383–2387; *Angew. Chem.* **2015**, *127*, 2413–2417.
- [24] N. Stock, J. Lücke, M. Volkmann, M. Jansen, W. Schnick, *Z. Anorg. Allg. Chem.* **1995**, *621*, 987–992.
- [25] F. Karau, W. Schnick, *Angew. Chem., Int. Ed.* **2006**, *45*, 4505–4508; *Angew. Chem.* **2006**, *118*, 4617–4620.
- [26] M. Pouchard, *Nature* **2006**, *442*, 878–879.
- [27] R. W. G. Wyckoff, *Z. Kristallogr., Kristallgeom., Kristallphys., Kristallchem.* **1926**, *63*, 507–537.
- [28] A. Marchuk, V. R. Celinski, J. Schmedt auf der Günne, W. Schnick, *Chem. - Eur. J.* **2015**, *21*, 5836–5842.
- [29] S. Horstmann, E. Irran, W. Schnick, *Angew. Chem., Int. Ed. Engl.* **1997**, *36*, 1873–1875; *Angew. Chem.* **1997**, *109*, 1938–1940.
- [30] D. Baumann, W. Schnick, *Inorg. Chem.* **2014**, *53*, 7977–7982.
- [31] S. D. Kloß, N. Weidmann, R. Niklaus, W. Schnick, *Inorg. Chem.* **2016**, *55*, 9400–9409.
- [32] E.-M. Bertschler, R. Niklaus, W. Schnick, *Chem. - Eur. J.* **2018**, *24*, 736–742.
- [33] E.-M. Bertschler, R. Niklaus, W. Schnick, *Chem. - Eur. J.* **2017**, *23*, 9592–9599.
- [34] S. D. Kloß, N. Weidmann, W. Schnick, *Eur. J. Inorg. Chem.* **2017**, 1930–1937.
- [35] K. Landskron, H. Huppertz, J. Senker, W. Schnick, *Angew. Chem., Int. Ed.* **2001**, *40*, 2643–2645; *Angew. Chem.* **2001**, *113*, 2713–2716.
- [36] S. Horstmann, E. Irran, W. Schnick, *Angew. Chem., Int. Ed. Engl.* **1997**, *36*, 1992–1994; *Angew. Chem.* **1997**, *109*, 2085–2087.
- [37] D. Baumann, W. Schnick, *Angew. Chem., Int. Ed.* **2014**, *53*, 14490–14493; *Angew. Chem.* **2014**, *126*, 14718–14721.
- [38] A. Vitola, J. Ronis, T. Millers, *Latv. PSR Zinat. Akad. Vestis, Kim. Ser.* **1990**, *90*, 299–301.

- [39] R. Nymwegen, H. Jacobs, *Z. Anorg. Allg. Chem.* **1997**, 623, 429–433.
- [40] K. Landskron, W. Schnick, *J. Solid State Chem.* **2001**, 156, 390–393.
- [41] J. Ronis, B. Bondars, A. Vitola, T. Millers, *J. Solid State Chem.* **1995**, 115, 265–269.
- [42] R. Marchand, F. Tessier, A. Le Sauze, N. Diot, *Int. J. Inorg. Mater.* **2001**, 3, 1143–1146.
- [43] A. Weiss, A. Weiss, *Z. Anorg. Allg. Chem.* **1954**, 301, 95–112.
- [44] L. Pauling, *J. Am. Chem. Soc.* **1929**, 51, 1010–1026.
- [45] T. Andersen, H. K. Haugen, H. Hotop, *J. Phys. Chem. Ref. Data* **1999**, 28, 1511–1533.
- [46] W. Schnick, J. Lücke, F. Krumeich, *Chem. Mater.* **1996**, 8, 281–286.
- [47] F. W. Karau, W. Schnick, *J. Solid State Chem.* **2005**, 178, 135–141.
- [48] W. Schnick, J. Luecke, *J. Solid State Chem.* **1990**, 87, 101–106.
- [49] W. Schnick, J. Lücke, *Z. Anorg. Allg. Chem.* **1990**, 588, 19–25.
- [50] W. Schnick, U. Berger, *Angew. Chem., Int. Ed. Engl.* **1991**, 30, 830–831; *Angew. Chem.* **1991**, 103, 857–858.
- [51] S. J. Sedlmaier, E. Mugnaioli, O. Oeckler, U. Kolb, W. Schnick, *Chem. - Eur. J.* **2011**, 17, 11258–11265.
- [52] A. Marchuk, F. J. Pucher, F. W. Karau, W. Schnick, *Angew. Chem., Int. Ed.* **2014**, 53, 2469–2472; *Angew. Chem.* **2014**, 126, 2501–2504.
- [53] J. Lücke, W. Schnick *Z. Anorg. Allg. Chem.* **1992**, 610, 121–126.
- [54] W. Schnick, J. Lücke, *Z. Anorg. Allg. Chem.* **1994**, 620, 2014–2019.
- [55] J. Ronis, V. Krasnikov, B. Bondars, A. Vitola, T. Millers, *Latv. PSR Zinat. Akad. Vestis, Kim. Ser.* **1989**, 1989, 139–144.
- [56] J. Ronis, V. V. Krasnikov, B. Y. Bondars, A. A. Vitola, T. Millers, *Latv. PSR Zinat. Akad. Vestis, Kim. Ser.* **1988**, 1988, 643–646.
- [57] H. P. Baldus, W. Schnick, J. Lücke, U. Wannagat, G. Bogedain, *Chem. Mater.* **1993**, 5, 845–850.
- [58] S. Correll, N. Stock, O. Oeckler, J. Senker, T. Nilges, W. Schnick, *Z. Anorg. Allg. Chem.* **2004**, 630, 2205–2217.
- [59] S. J. Sedlmaier, M. Doeblinger, O. Oeckler, J. Weber, J. S. A. Der Guenne, W. Schnick, *J. Am. Chem. Soc.* **2011**, 133, 12069–12078.
- [60] E. Mugnaioli, S. J. Sedlmaier, O. Oeckler, U. Kolb, W. Schnick, *Eur. J. Inorg. Chem.* **2012**, 2012,

- 121–125.
- [61] W. Ostwald, *Z. Phys. Chem.* **1879**, 22, 289–330.
- [62] H. Jacobs, R. Nymwegen, S. Doyle, T. Wroblewski, W. Kockelmann, *Z. Anorg. Allg. Chem.* **1997**, 623, 1467–1474.
- [63] J. Häusler, S. Schimmel, P. Wellmann, W. Schnick, *Chem. - Eur. J.* **2017**, 23, 12275–12282.
- [64] H. Huppertz, *Z. Kristallogr.* **2004**, 219, 330–338.
- [65] K. Landskron, E. Irran, W. Schnick, *Chem. - Eur. J.* **1999**, 5, 2548–2553.
- [66] F. W. Karau, L. Seyfarth, O. Oeckler, J. Senker, K. Landskron, W. Schnick, *Chem. - Eur. J.* **2007**, 13, 6841–6852.
- [67] S. J. Sedlmaier, M. Eberspächer, W. Schnick, *Z. Anorg. Allg. Chem.* **2011**, 637, 362–367.
- [68] D. Fischer, M. Jansen, *Angew. Chem., Int. Ed.* **2002**, 41, 1755–1756; *Angew. Chem.* **2002**, 114, 1777–1778.
- [60] D. Fischer, Z. Cancarevic, J. C. Schön, M. Jansen, *Z. Anorg. Allg. Chem.* **2004**, 630, 156–160.
- [70] K. Landskron, S. Schmid, W. Schnick, *Z. Anorg. Allg. Chem.* **2001**, 627, 2469–2472.
- [71] F. J. Pucher, A. Marchuk, P. J. Schmidt, D. Wiechert, W. Schnick, *Chem. - Eur. J.* **2015**, 21, 6443–6448.
- [72] M. Marezio, J. P. Remeika, P. D. Dernier, *Acta Crystallogr., Sect. B: Struct. Crystallogr. Cryst. Chem.* **1969**, 25, 965–970.
- [73] F. J. Pucher, F. W. Karau, J. Schmedt auf der Günne, W. Schnick, *Eur. J. Inorg. Chem.* **2016**, 1497–1502.
- [74] F. J. Pucher, F. Hummel, W. Schnick, *Eur. J. Inorg. Chem.* **2015**, 1886–1891.
- [75] Y. Hinuma, T. Hatakeyama, Y. Kumagai, L. A. Burton, H. Sato, Y. Muraba, S. Iimura, H. Hiramatsu, I. Tanaka, H. Hosono, F. Oba, *Nat. Commun.* **2016**, 7.
- [76] A. Marchuk, P. Schultz, C. Hoch, O. Oeckler, W. Schnick, *Inorg. Chem.* **2016**, 55, 974–982.
- [77] N. Sclar, *J. Appl. Phys.* **1964**, 35, 1534–1538.
- [78] W. Klemm, G. Winkelmann, *Z. Anorg. Allg. Chem.* **1956**, 288, 87–90.
- [79] R. Dronskowski, S. Kikkawa, A. Stein, *Handbook of Solid State Chemistry*, WILEY-VCH, Weinheim, Germany, **2017**.
- [80] K. Suzuki, H. Morita, T. Kaneko, H. Yoshida, H. Fujimori, *J. Alloys Compd.* **1993**, 201, 11–16.

- [81] W. P. Clark, S. Steinberg, R. Dronskowski, C. McCammon, I. Kuppenko, M. Bykov, L. Dubrovinsky, L. G. Akselrud, U. Schwarz, R. Niewa, *Angew. Chem., Int. Ed.* **2017**, *56*, 7302–7306; *Angew. Chem.* **2017**, *129*, 7408–7412.
- [82] F. J. Pucher, C. Frhr. von Schirnding, F. Hummel, V. R. Celinski, J. Schmedt auf der Günne, B. Gerke, R. Pöttgen, W. Schnick, *Eur. J. Inorg. Chem.* **2015**, 382–388.
- [83] H. C. Yi, J. J. Moore, *J. Mater. Sci.* **1990**, *25*, 1159–1168.
- [84] R. W. Cahn, *Adv. Mater.* **1990**, *2*, 314–316.
- [85] J. D. Walton, N. E. Poulos, *J. Am. Ceram. Soc.* **1959**, *42*, 40–49.
- [86] J. B. Wiley, R. B. Kaner, *Science* **1992**, *255*, 1093–1097.
- [87] I. P. Parkin, *Chem. Soc. Rev.* **1996**, *25*, 199.
- [88] H.-J. Meyer, *Dalton Trans.* **2010**, *39*, 5973–5982.
- [89] B. Blaschkowski, H. Jing, H.-J. Meyer, *Angew. Chem., Int. Ed.* **2002**, *41*, 3322–3336; *Angew. Chem.* **2002**, *114*, 3468–3483.
- [90] L. Lei, D. He, *Cryst. Growth Des.* **2009**, *9*, 1264–1266.
- [91] L. Lei, W. Yin, X. Jiang, S. Lin, D. He, *Inorg. Chem.* **2013**, *52*, 13356–13362.
- [92] F. Kawamura, N. Yamada, M. Imai, T. Taniguchi, *Cryst. Res. Technol.* **2016**, *51*, 220–224.
- [93] S. D. Kloß, W. Schnick, *Inorg. Chem.* **2018**, *57*, 4189–4195.
- [94] B. Kang, G. Ceder, *Nature* **2009**, *458*, 190–193.
- [95] M. W. Kanan, D. G. Nocera, *Science* **2008**, *321*, 1072–1075.
- [96] S. D. Kloß, L. Neudert, M. Döblinger, M. Nentwig, O. Oeckler, W. Schnick, *J. Am. Chem. Soc.* **2017**, *139*, 12724–12735.

Chapter 2

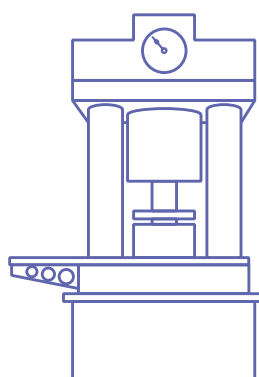
Rare-Earth-Metal Nitridophosphates Through High-Pressure Metathesis

Simon D. Kloß, Wolfgang Schnick

published in: *Angew. Chem., Int. Ed.* **2015**, *54*, 11250–11253. DOI: 10.1002/anie.201504844

published in: *Angew. Chem.* **2015**, *127*, 11402–11405. DOI: 10.1002/ange.201504844

Reprinted (adapted) with permission from *Angewandte Chemie*. Copyright 2015 John Wiley and Sons.



Trivalent rare-earth-metal nitridophosphates are a completely uncharted family of materials and can feature intriguing properties. The first member of this family, LiNdP_4N_8 , was prepared through high-pressure metathesis starting from NdF_3 and LiPN_2 . LiNdP_4N_8 was studied as a model system to demonstrate the potential of high-pressure metathesis in the synthesis of such nitridophosphates.

Abstract

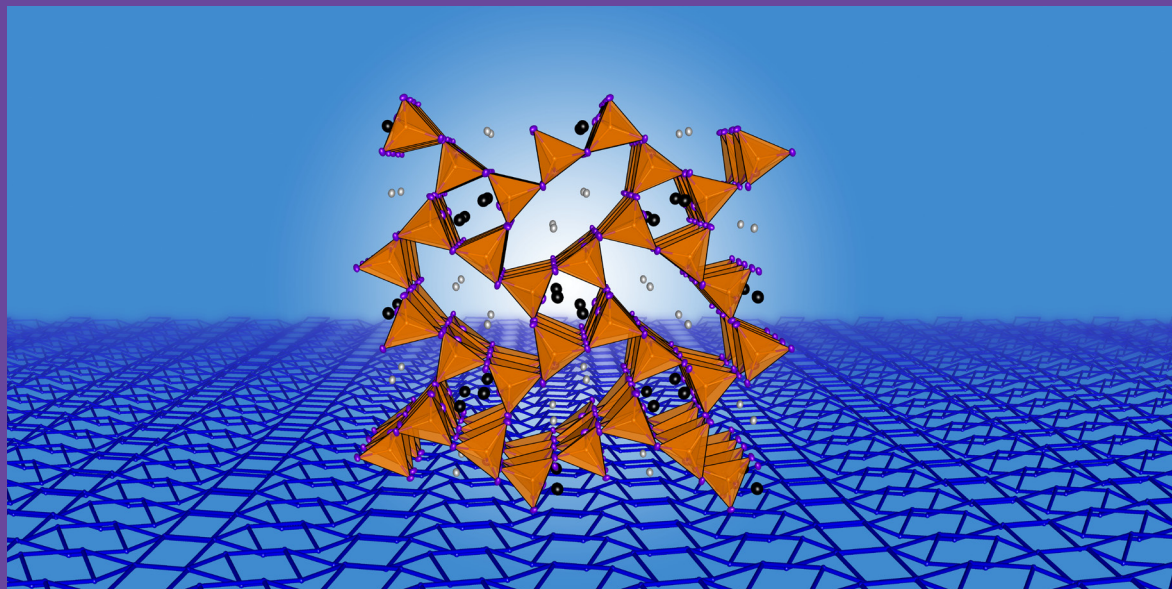


Table-of-contents graphic.

Developing a synthetic method to target a broad spectrum of unknown phases can lead to fascinating discoveries. The preparation of the first rare-earth-metal nitridophosphate LiNdP_4N_8 is reported. High-pressure solid-state metathesis between LiPN_2 and NdF_3 was employed to yield a highly crystalline product. The in situ formed LiF is believed to act both as the thermodynamic driving force and as a flux to aiding single-crystal formation in dimensions suitable for crystal structure analysis. Magnetic properties stemming from Nd^{3+} ions were measured by SQUID magnetometry. LiNdP_4N_8 serves as a model system for the exploration of rare-earth-metal nitridophosphates that may even be expanded to transition metals. High-pressure metathesis enables the systematic study of these uncharted regions of nitride-based materials with unprecedented properties.

2.1 Introduction with Results and Discussion

Nitridophosphates are believed to be one of the largest uncharted compound classes despite their proven structural versatility, which rivals even that of silicates, and their intriguing properties. Owing to their framework structure of PN₄ tetrahedra, nitridophosphates are closely related to silicates but they offer a broader structural diversity because of the possibility of triply bridging N^[3] atoms.^[1-4] To date, nitridophosphates of the first and second main groups have been thoroughly investigated. However, the number of hitherto discovered compounds (23 ternary ones, 15 structure types) is small when compared to the vast number of known silicate minerals,^[5] but simultaneously highlights the potential for explorative chemistry. This general approach has been key to the discovery of high-performance materials, as demonstrated by the cuprate family of high T_c superconductors or the recent upsurge in perovskite-type solar cells.^[6-8] Moreover, data-mining techniques have revealed that materials within the same structural family exhibit similar performances.^[9] Hence the exploration of new materials families like nitridophosphates with transition or rare earth metals is anticipated to lead to the discovery of intriguing materials.

Nitridophosphate research has already produced functional materials like the clathrate P₄N₄(NH)₄(NH₃), which is an open-framework structure hosting trapped ammonia molecules.^[10] This clathrate has been discussed as a possible gas-storage material.^[11] Furthermore, the zeolitic Ba₃P₅N₁₀Br:Eu²⁺ is a promising luminescent material for solid-state lighting that emits natural white light.^[12]

However, the accessibility of nitridophosphates through conventional solid-state synthesis is limited by the thermal stability of common starting materials like P₃N₅, which tend to decompose below the crystallization temperature of the targeted phases. High-pressure synthesis using the multianvil technique has promoted the exploration of alkaline earth nitridophosphates like MP₂N₄ ($M = \text{Be, Ca, Sr, Ba}$) and high-pressure polymorphs of the silica analogous PON.^[13-17] However, the structural elucidation can be laborious owing to microcrystalline products that require elaborate powder diffraction and electron microscopy methods for structure determination.^[14,16]

Synthetic success with alkali-metal and alkaline-earth-metal nitridophosphates could not yet be expanded to trivalent rare earth metals. In order to tackle the aforementioned problems, we tailored a new synthetic pathway by means of high-pressure metathesis and targeted rare-earth-metal nitrido-

phosphates as a model system. Owing to their f electrons, such lanthanide materials offer more versatile properties, such as magnetism, than the already known nitridophosphates. We found that solid-state metathesis (SSM) is crucial for the preparation of rare-earth-metal nitridophosphates since it is imperative for phase formation and greatly aids crystal growth. SSM is an exchange reaction that capitalizes on the formation energy of a stable byproduct to generate the driving force for powering a less favored reaction. For example, rare-earth-metal nitridoborates, carbodiimides, and tetracyanoborates, as well as the functional materials GaN and Si₃N₄, are accessible by SSM.^[18–20]

Herein, we report on the preparation of the first nitridophosphate with a trivalent cation, namely LiNdP₄N₈, by high-pressure metathesis. Stoichiometric amounts of NdF₃ and LiPN₂ were reacted at 5 GPa and approximately 1300 °C to yield LiNdP₄N₈ and LiF as described by the following Equation 2.1.



The reaction conditions were achieved through a 1000 t hydraulic press combined with a modified Walker-Type multianvil module.^[21a–e] A colorless transparent product containing single crystals with a diameter of up to 100 μm was obtained after dissolving the byproduct LiF in H₂O (Figure B.10 in the Supporting Information). The growth of such large crystals under high pressure can be attributed to in situ formed LiF, which is molten under these reaction conditions and can act as a flux.^[22] The achievable crystal size easily exceeds the efficiency of the extrinsic mineralizer NH₄Cl, which was applied in the syntheses of β-HPN₂, β-P₄N₆(NH), and γ-P₄N₆(NH).^[23–25]

The elemental composition, as determined by energy dispersive X-ray spectroscopy (EDX), is in good agreement with the theoretical atomic ratio of Nd/P/N=1:4:8. Details of the EDX analysis can be found in Table B.7 of the Supporting Information.

The crystal structure of LiNdP₄N₈ was solved in the orthorhombic space group *Pnma* (no. 62) from single-crystal X-ray diffraction data.^[26] LiNdP₄N₈ crystallizes in a variant of the pseudo-orthorhombic structure of the mineral paracelsian (BaAl₂Si₂O₈, space group *P2₁/a*).^[27] Additional information that rules out a monoclinic crystal system in LiNdP₄N₈ can be found in the Supporting Information. In order to quantify the similarity between paracelsian in an orthorhombic crystal system and LiNdP₄N₈, the two structures were compared by using the COMPSTRU tool of the Bilbao Crystallo-

graphic Server.^[28] The mean shift of atomic positions is only 0.11 Å. The resulting measure of similarity Δ ^[29] of 0.073 emphasizes the close relation between the two structures.

The established structural model was confirmed by Rietveld refinement on X-ray powder diffraction data (Figure B.2), which also indicates that LiNdP₄N₈ was prepared as a phase-pure compound. Further high-temperature powder diffraction experiments (Figure B.5) reveal phase stability of at least 1000 °C in air, thus suggesting that LiNdP₄N₈ is not a high-pressure phase.

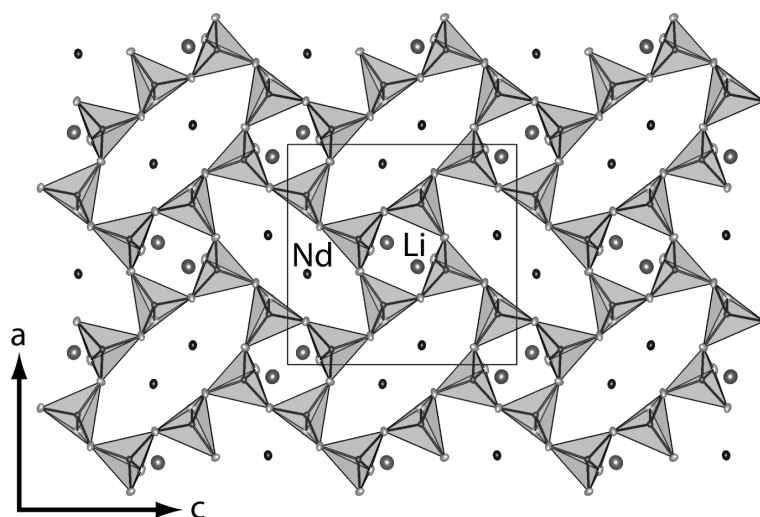


Figure 2.1. Projection of the LiNdP₄N₈ crystal structure along [010]. The unit cell is highlighted by black lines and the atoms are displayed with anisotropic displacement parameters set at 90% probability.

The structure of LiNdP₄N₈ consists of a network of all-side vertex-sharing PN₄ tetrahedra (Figure 2.1), which is best described as interconnected double crankshaft chains (Figure B.4) running along [010]. These chains consist of stacked *vierer*-rings (as defined by Liebau^[5]) connected to adjacent layers by two up- and two down-pointing tetrahedra.^[5] Li⁺ and Nd³⁺ ions occupy the 4- and 8-membered-ring channels running along *b* (Figure 2.1), with the 8-membered-ring channels created by interconnection of the crankshaft chains. The framework topology is the same as in paracelsian and is characterized by the point symbol 4².6³.8, as calculated with TOPOS.^[30,31] Because of the loop-branched double crankshaft chains, the paracelsian framework can be described by the Liebau classification LiNd{*lb*1³_∞}[P₄N₈].^[5]

The 7-fold coordination sphere of Nd (Figure 2.2) is an augmented triangular prism with Nd–N distances of between 2.49 and 2.59 Å, which is in good agreement with the Nd–N distances in NdN ($d(\text{Nd–N})=2.58$ Å).^[32] Li is coordinated in a slightly distorted square pyramid with Li–N distances

ranging from 1.96 to 2.17 Å. This Li coordination polyhedron is unprecedented for nitrogen-containing framework structures and is only known within the complex structure of $\text{Li}_3\text{Ni}_4[\text{NH}_2]_{11}[\text{NH}_3]$.^[33]

The FTIR spectrum of LiNdP_4N_8 (Figure B.6) reveals characteristic P–N framework vibrations between 600–1500 cm^{-1} . The absence of N–H valence vibrations indicates that no N–H groups are contained in the sample.

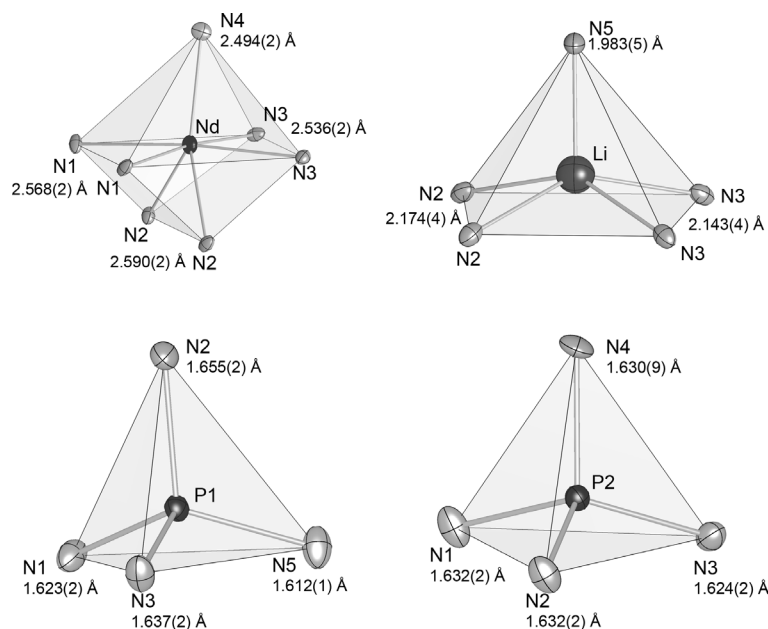


Figure 2.2. Coordination polyhedra around Nd, Li, P1, and P2. The thermal ellipsoids are set to 90% probability.

Owing to the three unpaired electrons of Nd^{3+} (electron configuration $[\text{Xe}]4f^3$), SQUID magnetometry was employed to examine the magnetic properties of LiNdP_4N_8 . The susceptibility data obtained at a constant magnetic field of 20 kOe follows the expected trend for paramagnetic substances in the range of 300 to 1.8 K (Figure 2.3). To calculate the effective magnetic moment μ_{eff} with the Curie–Weiß law, a linear regression was fitted to the inverse molar susceptibility χ_{mol}^{-1} in the range of 300 to 50 K. The experimental μ_{eff} value of 3.815 μ_{B} is in good agreement with the theoretical value of 3.618 μ_{B} calculated from Hund’s laws.^[34] The Curie temperature Θ was determined to be -4 K, which is close to the theoretical value of 0 K. The deviations may stem from additional magnetic contributions caused by the amorphous phase visible in the powder pattern (Figure B.2). Additionally, no magnetic ordering effects were observed in experiments with lower magnetic field strengths (Figure B.7). LiNdP_4N_8 is thus the first confirmed paramagnetic nitridophosphate.

As mentioned above, we studied LiNdP₄N₈ as a model system to fathom the applicability of high-pressure metathesis in the development of new material families, in this case the rare-earth-metal nitridophosphates. We were able to demonstrate that this preparation method is capable of effortlessly producing a magnetic nitridophosphate with a trivalent cation. The synthetic complexity was deliberately kept minimalistic by the use of only two reactants, one of them commercially available, to emphasize the simplicity of this approach. However, the synthesis route can also be highly adaptive when the starting materials are carefully chosen. While the use of metal halides seems mandatory, the alkali-metal-containing compounds can be exchanged. For example, the degree of condensation of the PN₄ tetrahedral framework can be tuned by adding Li₃N as a reactant, which could result in compounds with the sum formula LiLn₂PN₄ that contain isolated PN₄ tetrahedra. Combined with the ability of high-pressure metathesis to grow single crystals, as demonstrated with LiNdP₄N₈, this flexibility enables rapid screening of a vast composition space. Fast structural elucidation is especially desired when searching for useful properties like body color, luminescence, or magnetism.

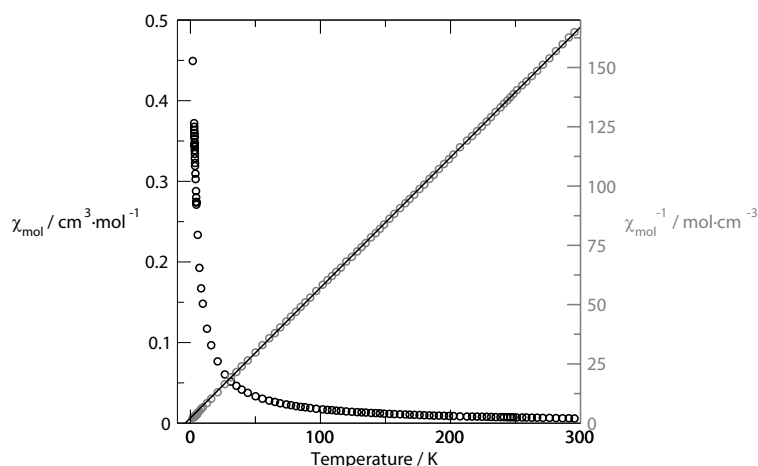


Figure 2.3. Susceptibility measurement carried out at 20 kOe. The data are displayed as χ_{mol} versus T (black circles) and χ_{mol}^{-1} versus T (gray circles). A linear regression (black line) was fit to the χ_{mol}^{-1} versus T data with the formula $y=0.5494(4) + 2.20(8)$.

With the focus on exploring materials for general applications, it is advantageous to use compounds consisting of economical elements, such as transition metals.^[9] Our high-pressure metathesis route is currently being expanded to metals such as iron, through which we hope to establish a gateway system to transition-metal nitridophosphates. Moreover, the idea of high-pressure metathesis can also be transferred to the structurally related family of nitridosilicates, since starting materials in the form

of Li_2SiN_2 are readily available.^[35] Transition-metal nitridosilicates are also a little explored substance class and may offer similar features to transition-metal nitridophosphates.

2.2 Conclusion

In conclusion, we prepared the first rare-earth-metal nitridophosphate LiNdP₄N₈ through high-pressure metathesis. The compound crystallizes in an undistorted orthorhombic variant of the paracelsian structure type, which is related to the feldspar type. By conducting a metathesis reaction, we were able to grow large single crystals at high pressure owing to the in situ formed mineralizer LiF. The growth of crystals suitable for X-ray crystallography greatly accelerates structure analysis. These results could form the basis for the discovery of a substantial number of interesting rare-earth- and transition-metal nitridophosphates, thereby stimulating progress in this exciting branch of chemistry.

2.3 References

- [1] A. Stock, H. Grüneberg, *Ber. Dtsch. Chem. Ges.* **1907**, 40, 2573–2578.
- [2] S. Horstmann, E. Irran, W. Schnick, *Angew. Chem., Int. Ed. Engl.* **1997**, 36, 1873–1875; *Angew. Chem.* **1997**, 109, 1938–1940.
- [3] S. Horstmann, E. Irran, W. Schnick, *Z. Anorg. Allg. Chem.* **1998**, 624, 620–628.
- [4] S. Horstmann, E. Irran, W. Schnick, *Angew. Chem., Int. Ed. Engl.* **1997**, 36, 1992–1994; *Angew. Chem.* **1997**, 109, 2085–2087.
- [5] F. Liebau, *Structural Chemistry of Silicates: Structure, Bonding, and Classification*, Springer, Berlin, Germany, **1985**.
- [6] J. G. Bednorz, K. A. Müller, *Z. Phys. B Con. Mat.* **1986**, 64, 189–193.
- [7] M. K. Wu, J. R. Ashburn, C. J. Torng, P. H. Hor, R. L. Meng, L. Gao, Z. J. Huang, Y. Q. Wang, C. W. Chu, *Phys. Rev. Lett.* **1987**, 58, 908–910.
- [8] H. J. Snaith, *J. Phys. Chem. Lett.* **2013**, 4, 3623–3630.
- [9] M. W. Gaultois, T. D. Sparks, C. K. H. Borg, R. Seshadri, W. D. Bonificio, D. R. Clarke, *Chem. Mater.* **2013**, 25, 2911–2920.
- [10] F. Karau, W. Schnick, *Angew. Chem., Int. Ed.* **2006**, 45, 4505–4508; *Angew. Chem.* **2006**, 118, 4617–4620.
- [11] M. Pouchard, *Nature* **2006**, 442, 878–879.
- [12] A. Marchuk, W. Schnick, *Angew. Chem., Int. Ed.* **2015**, 54, 2383–2387; *Angew. Chem.* **2015**, 127, 2413–2417.
- [13] F. W. Karau, W. Schnick, *J. Solid State Chem.* **2005**, 178, 135–141.
- [14] D. Baumann, S. J. Sedlmaier, W. Schnick, *Angew. Chem., Int. Ed.* **2012**, 51, 4707–4709; *Angew. Chem.* **2012**, 124, 4785–4787.
- [15] F. J. Pucher, S. Rebecca Römer, F. W. Karau, W. Schnick, *Chem. - Eur. J.* **2010**, 16, 7208–7214.
- [16] F. W. Karau, L. Seyfarth, O. Oeckler, J. Senker, K. Landskron, W. Schnick, *Chem. - Eur. J.* **2007**, 13, 6841–6852.
- [17] F. J. Pucher, A. Marchuk, P. J. Schmidt, D. Wiechert, W. Schnick, *Chem. - Eur. J.* **2015**, 21, 6443–6448.
- [18] H. J. Meyer, *Dalt. T.* **2010**, 39, 5973–5982.

- [19] C. H. Wallace, S. H. Kim, G. Rose, L. Rao, J. R. Heath, M. Nicol, R. B. Kaner, *Appl. Phys. Lett.* **1998**, 72, 596–598.
- [20] M. P. Shemkunas, G. H. Wolf, K. Leinenweber, W. T. Petuskey, *J. Am. Ceram. Soc.* **2004**, 85, 101–104.
- [21] a) N. Kawai, S. Endo, *Rev. Sci. Instrum.* **1970**, 41, 1178–1181; b) D. Walker, M. A. Carpenter, C. M. Hitch, *Am. Mineral.* **1990**, 75, 1020–1028; c) D. Walker, *Am. Mineral.* **1991**, 76, 1092–1100; d) D. C. Rubie, *Phase Transitions* **1999**, 68, 431–451; e) H. Huppertz, *Z. Kristallogr.* **2004**, 219, 330–338.
- [22] I. Jackson, *Phys. Earth Planet. Inter.* **1977**, 14, 86–94.
- [23] D. Baumann, W. Schnick, *Inorg. Chem.* **2014**, 53, 7977–7982.
- [24] D. Baumann, W. Schnick, *Angew. Chem., Int. Ed.* **2014**, 53, 14490–14493; *Angew. Chem.* **2014**, 126, 14718–14721.
- [25] A. Marchuk, F. J. Pucher, F. W. Karau, W. Schnick, *Angew. Chem., Int. Ed.* **2014**, 53, 2469–2472; *Angew. Chem.* **2014**, 126, 2501–2504.
- [26] Crystal data for LiNdP₄N₈: crystal size: 0.020 x 0.030 x 0.030 mm³, space group *Pnma* (no. 62), $a = 8.7305(17)$, $b = 7.8783(16)$, $c = 9.0881(18)$ Å, $V = 625.1(2)$ Å³, $Z = 4$, $\rho_{diffm} = 4.114$ g cm⁻³, Bruker D8 Venture, Mo-K α -radiation (71.073 pm), multi-scan absorption correction, 12131 reflections, 1262 independent reflections, least squares refinement on F^2 , R-values (all data/ $F_0^2 \geq 2\sigma(F_0^2)$): $R_1 = 0.0135/0.0128$, $wR_2 = 0.0343/0.0341$, GooF = 1.159 for 1224 observed reflections ($F_0^2 \geq 2\sigma(F_0^2)$) and 70 parameters. Further details of the crystal structure investigation(s) may be obtained from Fachinformationszentrum Karlsruhe, 76344 Eggenstein-Leopoldshafen, Germany (fax: (+49)7247-808-666; e-mail: crysdata@fiz-karlsruhe.de) on quoting the deposition number CSD-429542.
- [27] J. V. Smith, *Acta Crystallogr.* **1953**, 6, 613–620.
- [28] E. S. Tasci, G. de La Flor, D. Orobengoa, C. Capillas, M. Perez-Mato, M. I. Aroyo, *EPJ Web Conf.* **2012**, 22, 00009.
- [29] G. Bergerhoff, M. Berndt, K. Brandenburg, T. Degen, *Acta Crystallogr. Sect. B Struct. Sci.* **1999**, 55, 147–156.
- [30] V. A. Blatov, *IUCr CompComm Newsl.* **2006**, 7, 4–38.

- [31] V. A. Blatov, M. O’Keeffe, D. M. Proserpio, *CrystEngComm* **2010**, *12*, 44–48.
- [32] W. Klemm, G. Winkelmann, *Z. Anorg. Allg. Chem.* **1956**, *288*, 87–90.
- [33] A. Tenten, H. Jacobs, *J. Alloys Compd.* **1991**, *177*, 193–217.
- [34] F. Hund, *Z. Phys.* **1925**, *33*, 855–859.
- [35] S. Pagano, M. Zeuner, S. Hug, W. Schnick *Eur. J. Inorg. Chem.* **2009**, *2009*, 1579–1584.

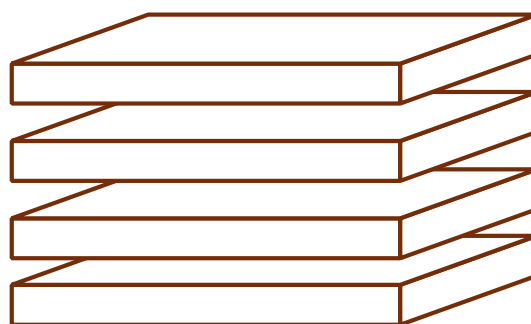
Chapter 3

High-pressure Synthesis of Melilite-Type Rare-Earth Nitridophosphates $RE_2P_3N_7$ and a $Ba_2Cu[Si_2O_7]$ -type Polymorph

Simon D. Kloß, Niels Weidmann, Robin Niklaus, and Wolfgang Schnick

published in: *Inorg. Chem.* **2016**, *55*, 9400–9409. DOI: 10.1021/acs.inorgchem.6b01611

Reprinted (adapted) with permission from *Inorganic Chemistry*. Copyright 2016 American Chemical Society.



The first ternary rare-earth nitridophosphates $RE_2P_3N_7$ ($RE = La, Ce, Pr, Nd, Sm, Eu, Ho, Yb$) were prepared by high-pressure solid-state metathesis. The compounds are the first instances of layered rare-earth nitridophosphates. The structural relation of the melilite-type ($RE = Pr, Nd, Sm, Eu, Ho, Yb$) and the $BaCu[Si_2O_7]$ -type ($RE = La, Ce, Pr$) $RE_2P_3N_7$ was investigated by experiment and verified by DFT calculations based on the $Pr_2P_3N_7$ polymorphs.

Abstract

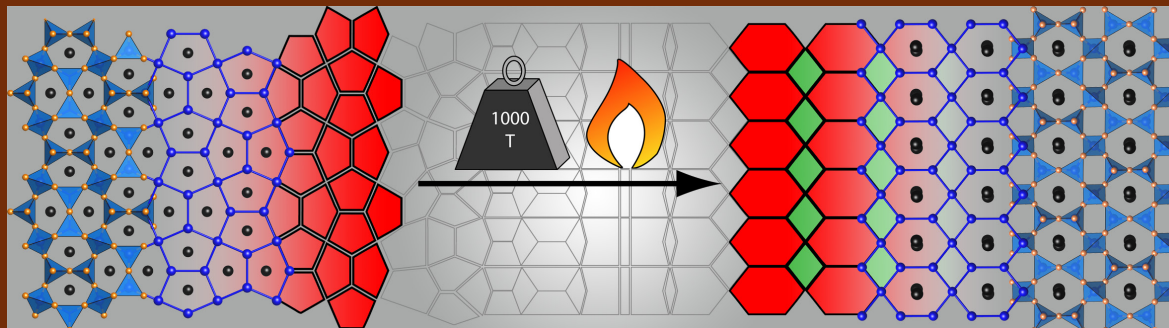


Table-of-contents graphic.

High-pressure metathesis was proposed to be a gateway to the elusive class of rare-earth nitridophosphates. With this method the first ternary compounds of this class with sum formula $RE_2P_3N_7$ were prepared, a melilite-type with $RE = \text{Pr, Nd, Sm, Eu, Ho, Yb}$ ($\text{Ho}_2\text{P}_3\text{N}_7$; $P\bar{4}2_1m$, $a = 7.3589(2)$, $c = 4.9986(2)$ Å, $Z = 2$) and a $\text{Ba}_2\text{Cu}[\text{Si}_2\text{O}_7]$ structure type with $RE = \text{La, Ce, Pr}$ ($\text{Pr}_2\text{P}_3\text{N}_7$; monoclinic, $C2/c$, $a = 7.8006(3)$, $b = 10.2221(3)$, $c = 7.7798(3)$ Å, $\beta = 111.299(1)^\circ$, $Z = 4$). The phase relation between the two structure types was prior unknown and is here evidenced by experimental data as well as density functional theory calculations performed for the $\text{Pr}_2\text{P}_3\text{N}_7$ compounds. Adequate classification of both structures types with regard to *Liebau* nomenclature, vertex symbol, and point symbol is made. Additionally, the tiling patterns of the monolayered structures are deduced. We demonstrate that high-pressure metathesis offers a systematic access to rare-earth nitridophosphates with an atomic ratio of P/N between 1/2 and 1/4.

3.1 Introduction

Nitridophosphates constitute an ample compound class that, however, is little explored. Their structural multiformity stems from the synergy of P and N; the ability to form networks of corner- and edge-sharing PN_4 -tetrahedra and PN_5 -pyramids^[1–6] concomitant with higher cross-linking network structures by triply bridging $N^{[3]}$ clearly distinguishes nitridophosphates from silicates^[7,8] and creates diversity. Numerous first- and second-group element compounds were discovered,^[6,9,10] but simple transition-metal-containing nitridophosphates, for example, $CuPN_2$ ^[11] or Zn_2PN_3 ,^[12] are scarcely known, and rare-earth nitridophosphates were completely unknown. The latter tempt with a combination of potentially unprecedented structures and open-shell cations, which engender properties like magnetism, luminescence, and body color. As a remedy for the elusive rare-earth nitridophosphates, we proposed a high-pressure metathesis route and proved its viability on precedence of $LiNdP_4N_8$.^[13]

High-pressure metathesis deliberately accesses rare-earth nitridophosphates by a combination of beneficial attributes. In the synthesis rare-earth halides, preferably fluorides, are reacted under pressure with $LiPN_2$ to yield the desired nitridophosphate and Li halide as byproduct (Equation 3.1).



The halide formation releases lattice energy that is the thermodynamic driving force for the nitridophosphate synthesis.^[14] Additionally, the halide acts as a flux, oftentimes yielding macroscopic single crystals of the main phases, facilitating structure determination. Reactions of Equation 3.1, also used for the preparation of $LiNdP_4N_8$, are restricted to a degree of condensation (the ratio of P and N, which gives an estimate of the tetrahedra network) equal to 1/2, which usually yields a three-periodic network. To attain less condensed (e.g., layered, chain, ring, and ortho-type) nitridophosphates with a molar P/N ratio smaller than 1/2 we propose to add Li_3N to the metathesis; Equation 3.2 displays the reaction for the two here presented monophyllo compounds.



Two polymorphs of the layered nitridophosphates $RE_2P_3N_7$ were obtained, a melilite-type with $RE = Pr, Nd, Sm, Eu, Ho, Yb$ and a $Ba_2Cu[Si_2O_7]$ -type with $RE = La, Ce, Pr$.^[15,16] Since both structures constitute a single-layer PN-network their topological symbol, as defined by the *Reticular Chemistry*

Structure Resource (RCSR),^[17] is used to differentiate them. The melilite-type $RE_2P_3N_7$ phases are denominated *mcm-RE₂P₃N₇*, and the $Ba_2Cu[Si_2O_7]$ -type phases are *bex-RE₂P₃N₇*.^[17] The deduction of the topological symbol from the monolayers is later discussed with regard to the underlying tiling pattern of respective structures.

The tetragonal melilite structure type with sum formula $M_2A[B_2X_7]$ is common for materials classes forming tetrahedra networks. An abundance of examples are known from silicates (e.g., natural melilite and its end members åkermanite $Ca_2Mg[Si_2O_7]$ ^[16] and gehlenite $Ca_2Al[AlSiO_7]$ ^[18]), oxonitridosilicates (e.g., $Sm_2Si[Si_2O_3N_4]$ ^[19]), gallates (e.g., $Ca_2Ga[GaSiO_7]$ ^[20]), germanates (e.g., $Sr_2Mg[Ge_2O_7]$ ^[21]), and vanadates (e.g., $Na_2Zn[V_2O_7]$ ^[22]). High-pressure investigations of diverse melilite-type compounds included the incommensurate-to-normal structure transition in åkermanite^[23,24] and a reconstructive high-pressure phase of åkermanite and gehlenite,^[25] also found in $Sr_2Zn[Ge_2O_7]$.^[26] The structure type of *bex-RE₂P₃N₇* was established in Ba-containing silicates with sum formula $Ba_2A[Si_2O_7]$ ($A = Co, Cu, Mg, Zn$)^[15,27–29] that is an indication for a melilite polymorph. However, an immaculate phase relationship has not yet been proposed; the *inverse relationship*^[30] between pressure and temperature in $Ba_2Mg[Si_2O_7]$ ^[28] and the high-pressure behavior of the solid solution $Sr_{2-x}Ba_xMg[Si_2O_7]$ ($0 < x < 2$), in which the Sr compound crystallizes in the melilite-type, was examined to no final conclusion.^[31]

We argue that the *bex*-type is the high-pressure polymorph of the *mcm*-type based on our experimental results and DFT calculations; we evaluate the influence of cation size, pressure, and temperature on the formation of the $RE_2P_3N_7$ ($RE = La, Ce, Pr, Nd, Sm, Eu, Ho, Yb$) phases and examine density and stability development of the phases. Moreover, the crystal structures are subsumed regarding their topology, vertex configuration, and *Liebau* classification because of the dearth of such information in literature. Additionally, the advantages of using tiling patterns for classification of tetrahedral networks are discussed.

3.2 Experimental Section

3.2.1 Synthesis of P_3N_5

The binary nitridophosphate P_3N_5 , starting material for $LiPN_2$ synthesis, was prepared by reaction of phosphorus pentasulfide P_4S_{10} (Sigma-Aldrich, 99.99%) with NH_3 gas (Air Liquide, 5.0) flowing at a constant rate.^[32] A tube furnace with a quartz tube containing a quartz boat was dried for 4 h at 1000 °C under reduced pressure of 1×10^{-3} mbar. To prevent clogging of the tubing due to sublimation of byproducts, the quartz boat can only be loaded, in an Ar counterflow, with a limited amount of P_4S_{10} . The tubing was saturated with NH_3 gas before firing the starting material at 850 °C for 4 h. Temperature ramps for heating and cooling were set to 5 °C/min, and the system was flushed with Ar after reaching room temperature. The obtained P_3N_5 was washed with water/ethanol/acetone and characterized by X-ray powder diffraction and Fourier transform infrared (FTIR) spectroscopy.^[2]

3.2.2 Preparation of $LiPN_2$

$LiPN_2$ was prepared by a solid-state reaction of P_3N_5 with a 1.2 times excess of Li_3N (Rockwood Lithium, 94%). The starting materials were thoroughly mixed and ground under inert conditions and then transferred into a Ta-crucible residing in a dried quartz tube with N_2 atmosphere. The sealed quartz ampule is fired in a tube furnace at 800 °C for 96 h. Temperature ramps for heating and cooling were set to 5 °C/min. The product was washed with diluted hydrochloric acid, water, and ethanol. The purity of $LiPN_2$ was confirmed by means of X-ray powder diffraction and FTIR spectroscopy.^[9]

3.2.3 Synthesis of *mcm*-type and *bex*-type $RE_2P_3N_7$ ($RE_{mcm} = Pr, Nd, Sm, Eu, Ho, Yb$; $RE_{bex} = La, Ce, Pr$) Phases

Both $RE_2P_3N_7$ phases were prepared by high-pressure metathesis starting from $LiPN_2$, Li_3N (Rockwood), and the respective rare-earth fluorides REF_3 (Alfa Aesar, 99.99%). Note that Li_3N was added in a 2 times excess to cope with side reactions of the crucible. High-pressure conditions of 4 to 6 GPa were achieved with the multianvil technique using a 1000 ton hydraulic press (Voggenreiter, Mainleus, Germany) and a modified Walker-type module. The starting materials were thoroughly ground and mixed before being packed in an h-BN crucible (Henze, Kempten, Germany). The crucible was placed in the pressure medium consisting of a specially prepared Cr_2O_3 -doped (6%) MgO-octahe-

dron (Ceramic Substrates & Components, Isle of Wight, U.K) with 18 mm edge length. This work was performed under inert conditions in an Ar-filled glovebox (Unilab, MBraun, Garching, Germany) with O₂ and H₂O < 1 ppm concentrations. Eight Co-doped (7%) tungsten carbide cubes (Hawedia, Marklkofen, Germany) with truncated edges (11 mm) forward the pressure to the eight sides of the sample octahedron, causing quasi-hydrostatic pressure conditions. Additional information regarding this high-pressure setup may be found in literature.^[33–37] The reaction conditions for each rare-earth element can be found in the synthesis part of the Discussion Section along with respective body colors of the products (Table 3.1). Some products were washed with water to reduce the LiF content.

Table 3.1. List of Reaction Conditions for Each Prepared Phase and Body Color of the Samples.

compound	pressure, GPa	temperature, °C	dwel, min	heat, min	cool, min	color
<i>bex-RE₂P₃N₇</i>						
La ₂ P ₃ N ₇	5	900	300	120	120	colorless
Ce ₂ P ₃ N ₇	5	1150	20	20	20	burgundy
Pr ₂ P ₃ N ₇	5	1250	300	120	120	pale green
<i>mcm-RE₂P₃N₇</i>						
Pr ₂ P ₃ N ₇	4	1000	360	120	60	pale green
Nd ₂ P ₃ N ₇	5	1200	60	120	80	colorless
Sm ₂ P ₃ N ₇	5	1200	60	120	80	pale yellow
Eu ₂ P ₃ N ₇	5	1200	60	120	80	colorless
Ho ₂ P ₃ N ₇	5	1200	60	120	80	pale yellow
Yb ₂ P ₃ N ₇	5	1250	300	60	180	colorless

3.2.4 Spectroscopic Analysis

Morphologies and elemental compositions of prepared compounds were determined by scanning electron microscopy (SEM) coupled with energy-dispersive X-ray (EDX) spectroscopy. A JEOL JSM 6500F microscope equipped with a field emission electron source and Oxford Instruments 7418 Si/Li EDX detector was used for these characterizations. Owing to their insulating properties the samples were sputtered with carbon to reduce electric charging with an electron beam evaporator (BAL-TEC MED 020, Bal Tex AG). FTIR spectra were recorded in the range of 400–4000 cm⁻¹ using a PerkinElmer Spectrum BX II spectrometer with ATR geometry.

3.2.5 Single-Crystal X-ray Diffraction

X-ray diffraction on single crystals were performed either with a D8 Quest diffractometer (Bruker, Billerica MA, USA) or an IPDS1 (Stoe & Cie, Darmstadt, Germany) using Mo K α radiation. The unit cells were determined and integrated with APEX2 and X-Area, for D8 Quest and IPDS data, respectively. The space group was determined with XPREP;^[38] structure solution using direct methods was executed with SHELXS-97 and structure refinement with SHELXL-97.^[39,40] Structure solution resulted in identification of heavy atom sites as well as P-sites. Missing N-sites were identified from difference Fourier maps and subsequently refined. Absorption correction was performed with the MulScanAbs function of PLATON.^[41] All atom sites were refined anisotropically. Crystal structures were visualized using VESTA.^[42]

3.2.6 Powder X-ray Diffraction

X-ray powder diffraction for bulk analysis, structure refinement, and structure confirmation was performed on a Stadi P diffractometer (Stoe, Darmstadt, Germany) in parafocusing Debye–Scherrer geometry. The instrument was equipped with a MYTHEN 1K silicon strip detector (Dectris, Baden, Switzerland; angular range $\Delta 2\theta = 12.5^\circ$) and a Ge(111) monochromator selecting Mo K α_1 radiation. Homogenous powder samples were loaded to 0.3 mm diameter glass capillaries with 0.01 mm wall thickness (Hilgenberg GmbH, Malsfeld, Germany). Rietveld refinement was performed using the *TOPAS-Academic V4.1* software.^[43] The peak shape function was modeled using a fundamental parameters approach including direct convolution of source emission profiles, axial instrument contributions, crystallite size, and microstrain effects. Possible preferred orientation of crystallites within the capillary was treated using the spherical harmonics model of fourth order. The background was handled using a shifted Chebychev function. Capillary absorption correction was performed taking the calculated absorption coefficient and capillary diameter into account. Crystal structures were visualized using VESTA.^[42]

High-temperature powder diffraction was performed on a Stoe Stadi P diffractometer equipped with a graphite furnace and an image plate position sensitive detector. The Mo radiation was monochromatized with a Ge(111) single crystal (Mo K α_1 , $\lambda = 70.930$ pm). The samples were heated to a maximum of 1000 °C in steps of 25 °C. Data were collected at constant temperature.

3.2.7 Computational Details

The total energies and atomic structures of both $\text{Pr}_2\text{P}_3\text{N}_7$ polymorphs were calculated using density functional theory (DFT) in the generalized gradient approximation (GGA) of *Perdew, Burke, and Ernzerhof*^[44,45] together with the projector-augmented-wave method^[46,47] that is implemented in the Vienna ab initio simulation package.^[48-50] GGA potentials were chosen since they are usually superior in reproducing transition pressures of solid-state materials.^[51,52] Initial ionic relaxation of the *bex*-polymorph was performed by relaxing all internal coordinates with a constant cell volume, and relaxation of the *mcm*-polymorph was performed by additionally relaxing all cell parameters, while using a plane-wave cutoff of 535 eV. The *Brillouin* zone was sampled on a dense γ -centered k-mesh (*bex*- $\text{Pr}_2\text{P}_3\text{N}_7$: $8 \times 6 \times 8$, *mcm*- $\text{Pr}_2\text{P}_3\text{N}_7$: $7 \times 7 \times 10$) produced from the method of *Monkhorst and Pack*^[53] to ensure sufficient precision. The energy convergence criterium was set to 1×10^{-8} eV per unit cell to ensure accurate electronic convergence, while the residual atomic forces were converged below values of 2×10^{-3} eV/Å.

3.3 Results and Discussion

3.3.1 Synthesis and Characterization of $mcm-RE_2P_3N_7$ and $bex-RE_2P_3N_7$

The general reaction scheme for the preparation of mcm - and $bex-RE_2P_3N_7$ ($RE = La, Ce, Pr, Nd, Sm, Eu, Ho, Yb$) phases is displayed in Equation 3.2. The reaction conditions achieving the largest phase fraction of respective $RE_2P_3N_7$ compound are listed in Table 3.1.

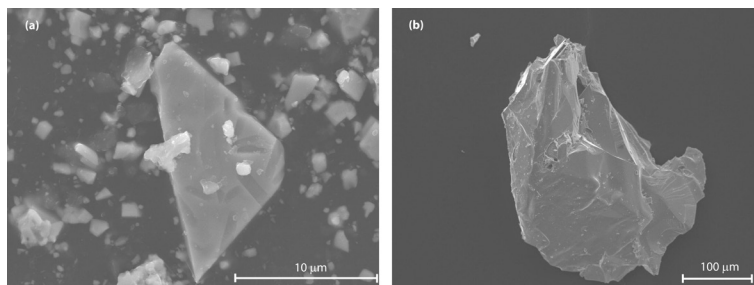


Figure 3.1. SEM micrographs. (a) An $mcm-Ho_2P_3N_7$ crystal. (b) A $bex-Pr_2P_3N_7$ crystal.

$mcm-Ho_2P_3N_7$ was prepared as a single phase according to X-ray powder diffraction (Figure C.10); the other samples contained byproducts. $mcm-Eu_2P_3N_7$ is accompanied by EuF_2 , which can be explained by the reductive reaction environment created by nitrides under high pressure. The Sm and Nd mcm -samples are accompanied by an oxonitridophosphate that accretes in mass fraction with increasing rare-earth ion size, which may be an indication for diminishing phase stability (see Supporting Information Figures C.8 and C.9). The destabilization culminates in $Pr_2P_3N_7$, that at 4 GPa and 1000 °C crystallizes in the mcm -modification and at 5 GPa and 1250 °C in the bex -modification. Lowering the temperature to 900 °C and increasing the pressure to 5.5 GPa yielded a heterogeneous mixture of mcm - and $bex-RE_2P_3N_7$ (Figure C.14). The phase formation is therefore dependent on temperature. Pr is the only lanthanide for which we prepared both polymorphs. Ce and Pr bex phases are formed concomitant with little of a colorless (oxo)phosphate, $mcm-Yb_2P_3N_7$ with a small $YbPO_4$ byproduct. The burgundy colored $bex-Ce_2P_3N_7$ could be manually separated from the side phase to obtain a phase-pure sample for powder diffraction measurements. The oxygen impurities may be explained by a partially hydrolyzed boron nitride crucible (forming boric acid) and the oxophilia of the rare-earth metal.

Prolonged dwelling and cooling times (300 and 120 min) promote the growth of larger single crystals, which was necessary for $Ho_2P_3N_7$ owing to the observed reluctant crystallization of the heavy-

rare-earth phases. Twenty micrometer $\text{Ho}_2\text{P}_3\text{N}_7$ crystals could be grown in this way (Figure 3.1a). The light-rare-earth compounds showed better crystallization; 200 μm *bex*- $\text{Pr}_2\text{P}_3\text{N}_7$ single crystals were obtained after a 300 min dwell (Figure 3.1b), and *bex*- $\text{Ce}_2\text{P}_3\text{N}_7$ achieved similar sizes after 20 min of dwell.

Elemental distribution obtained from EDX measurements on crystals of *mcm*- $\text{Ho}_2\text{P}_3\text{N}_7$ and *bex*- $\text{Pr}_2\text{P}_3\text{N}_7$ (Figure 3.1) confirmed the theoretical atomic ratio Pr/P/N of 2:3:7 (Table C.16 and C.38 of the Supporting Information). Infrared spectroscopy performed on samples of *mcm*- $\text{Ho}_2\text{P}_3\text{N}_7$ and *bex*- $\text{Pr}_2\text{P}_3\text{N}_7$ ruled out the presence of any O–H or N–H groups (Figures C.4 and C.11).

Table 3.2. Crystallographic Information for Single-Crystal X-ray Diffraction of *mcm*- $\text{Ho}_2\text{P}_3\text{N}_7$.

Formula	$\text{Ho}_2\text{P}_3\text{N}_7$
Crystal system	tetragonal
Space group	$P\bar{4}2_1m$ (No. 113)
Cell parameters, Å	$a = 7.3589(2)$ $c = 4.9986(2)$
Cell volume, Å ³	270.691(18)
Formula units per unit cell Z	2
Formula mass, g·mol ⁻¹	520.84
Calculated density, g·cm ⁻³	6.390
Absorption coefficient μ/mm^{-1}	29.825
diffractometer	Bruker D8 Quest
Radiation	Mo Ka ($\lambda = 71.073$ pm)
Temperature, K	293(2)
$F(000)$	456
θ range, deg	$3.916 \leq \theta \leq 37.675$
Total no. of reflections	6905
Independent reflections	791
Refined parameters	35
Goodness-of-fit	1.121
$R_{\text{int}}, R_{\sigma}$	0.0402, 0.0250
R_1 (all data), $R_1 [F^2 > 2\sigma(F^2)]$	0.0232, 0.0190
wR_2 (all data), $wR_2 [F^2 > 2\sigma(F^2)]$	0.0321, 0.0313
$\Delta\rho_{\text{max}}, \Delta\rho_{\text{min}}, \text{e}\cdot\text{Å}^{-3}$	1.037, -0.624

3.3.2 Crystal Structure Determination of *mcm*- and *bex*- $\text{RE}_2\text{P}_3\text{N}_7$.

The structural model for *mcm*- $\text{RE}_2\text{P}_3\text{N}_7$ was established by single-crystal X-ray diffraction of $\text{Ho}_2\text{P}_3\text{N}_7$. As mentioned, $\text{Ho}_2\text{P}_3\text{N}_7$ crystallizes in the tetragonal melilite structure type with lattice constants of $a = 7.3589(2)$ and $c = 4.9986(2)$ Å.^[54] The space group $P\bar{4}2_1m$ was unequivocally determined from

systematically absent reflections, and the structure was solved using direct methods, which yielded the positions of Ho and P, while N atom sites were obtained from difference Fourier maps. All atoms were refined with anisotropic displacement parameters. The crystallographic data can be found in Table 3.2, atomic positions, isotropic displacement parameters, anisotropic displacement parameters, and geometric values in Tables C.33–C.36. The isotypic structure models of *mcm*-RE₂P₃N₇ with RE = Pr, Nd, Sm, Eu, and Yb were refined from powder diffraction data by the Rietveld method based on the Ho₂P₃N₇ model.

Table 3.3. Crystallographic Information for Single-Crystal X-ray Diffraction of *bex*-Pr₂P₃N₇.

Formula	Pr ₂ P ₃ N ₇
Crystal system	monoclinic
Space group	C2/c (no. 15)
Cell parameters / Å, °	$a = 7.8006(3)$ $b = 10.2221(3)$ $c = 7.7798(3)$ $\beta = 111.299(1)$
Cell volume / Å ³	577.98(4)
Formula units per unit cell Z	4
Formula mass, g·mol ⁻¹	472.80
Calculated density, g·cm ⁻³	5.433
Absorption coefficient μ / mm ⁻¹	17.417
Diffractometer	Bruker D8 Quest
Radiation	Mo-K α ($\lambda = 71.073$ pm)
Temperature, K	293(2)
$F(000)$	848
θ range / °	$3.440 \leq \theta \leq 40.247$
Total no. of reflections	10 211
Independent reflections	1823
Refined parameters	57
Goodness-of-fit	1.251
$R_{\text{int}}, R_{\sigma}$	0.0300, 0.0188
R_1 (all data), $R_1 [F^2 > 2\sigma(F^2)]$	0.0177, 0.0164
wR_2 (all data), $wR_2 [F^2 > 2\sigma(F^2)]$	0.0402, 0.0398
$\Delta\rho_{\text{max}}, \Delta\rho_{\text{min}} / \text{e}\cdot\text{\AA}^{-3}$	2.129, -1.641

An unknown side phase in the *mcm*-Pr₂P₃N₇ sample prohibited the refinement of fractional coordinates, but the cell dimensions were reliably obtained. Details of the Rietveld refinement data as well as lists of bond angles and bond lengths are provided in the Supporting Information.

The crystal structures of *bex*-Pr₂P₃N₇ and *bex*-Ce₂P₃N₇ were solved ab initio from single-crystal X-ray diffraction; the La-compound's structure model was refined by Rietveld refinement (see Support-

ing Information for further details). The following structure description is based on the *bex*-Pr₂P₃N₇ model, which crystallizes in the Ba₂Cu[Si₂O₇] structure type^[15] with a monoclinic unit cell of $a = 7.8006(3)$, $b = 10.2221(3)$, $c = 7.7798(3)$ Å, and $\beta = 111.299(1)^\circ$.

Space group *C2/c* was assigned to the structure considering systematic absence of reflections. Structure solution with direct methods yielded the position of Pr as well as P; N-sites were identified from difference Fourier maps, and anisotropic displacement parameters could be refined for all atomic positions. The crystallographic data, atomic positions, isotropic displacement parameters, anisotropic displacement parameters, and bond lengths/angles of *bex*-Pr₂P₃N₇ are listed in Tables 3.3 and Tables C.11–C.14, respectively.

3.3.3 Structure Description of *mcm*-RE₂P₃N₇ (RE = Pr, Nd, Sm, Eu, Ho, Yb)

Following silicate nomenclature *mcm*-RE₂P₃N₇ and *bex*-RE₂P₃N₇ are best categorized as monophyllo-nitridophosphates and of such are the first instances within the nitridophosphate materials class. The melilite group of naturally occurring silicates is distinctly assorted to the sorosilicates, since the Q⁴ tetrahedron is centered by nonsilicon cations, for example, Fe or Mg, leaving isolated [Si₂O₇]⁶⁻ units.^[55] Thus, the naturally occurring minerals åkermanite and gehlenite are not considered as phyllo contrary to precedents like Sm₂Si₃O₃N₄, in which condensed [Si₃O₃N₄]⁶⁻ layers are observed.^[19] *mcm*-Ho₂P₃N₇ crystallizes in the melilite structure type with a tetragonal unit cell that includes single [P₃N₇]⁶⁻ monolayers and four Ho atoms between the layers (Figure 3.2).

The non-centrosymmetric space group $\overline{P4}2_1m$ (No. 113) is in accordance with the AA stacking arrangement of the monolayers, in which the tetrahedra vertices point in the same direction preempting a mirror plane. The Ho atoms arrange with pseudo-inversion symmetry due to a z close to 0.5. The suggested supergroup *P4/mbm* (No. 127) is, however, impossible for the entire structure owing to the missing mirror plane between the AA monolayer stacks. The monolayers comprise condensed five-membered rings (*fünfer*-rings after *Liebau*)^[55] with vertex-sharing Q³- and Q⁴-type PN₄-tetrahedra in a molar ratio of 2:1. Hence the two-periodic layer can be described by the vertex symbol (5³)₂(5⁴) or point symbol (5³)₂(5⁴.8²), the latter being determined by TOPOS.^[56] The coexistence of Q³- and Q⁴-type bridging tetrahedra within a plane layer results in the degree of condensation $\kappa = P/N = 3:7$.

An unbranched fundamental *dreier* chain running along [100] subsumes the single-layer tetrahedra network as $\{\mathbf{uB}, 1^2_{\infty}\}[\text{P}_3\text{N}_7]$ according to *Liebau*.^[55]

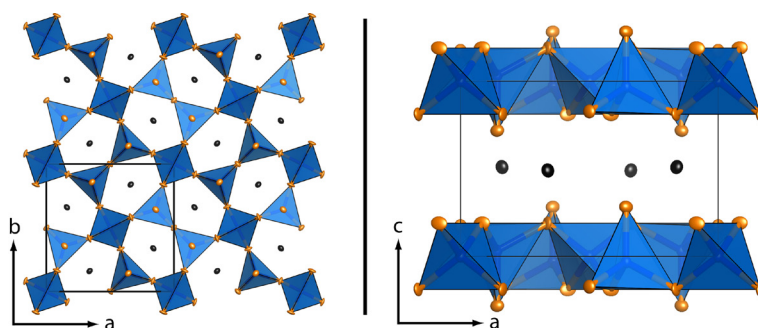


Figure 3.2. (left) Four unit cells of *mcm*-Ho₂P₃N₇ in projection along the *c*-axis. (right) Projection along the *b*-axis, parallel to the tetrahedral monolayers. All anisotropic displacement ellipsoids are displayed with 95% probability.

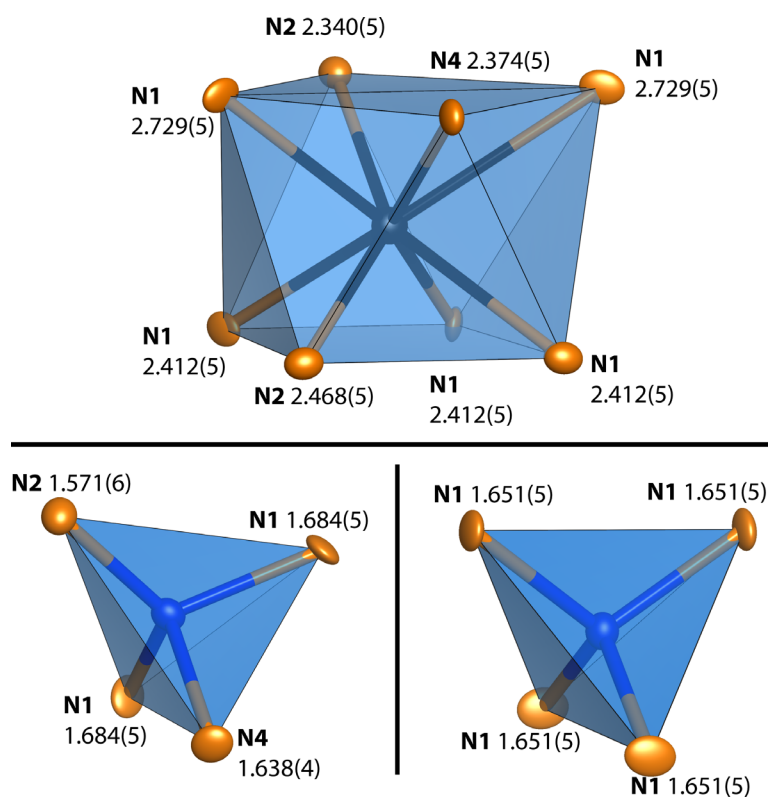


Figure 3.3. N-coordination polyhedra in *mcm*-Ho₂P₃N₇ around Ho1 (top), P1 (bottom left), and P2 (bottom right) with respective bond lengths.

Eight N atoms coordinate Ho1 in form of a quadratic antiprism, analogous to other melilite-type compounds (Figure 3.3). The Ho–N distances within this semiregular polyhedron range from 2.34 to 2.73 Å and are similar to those found in the oxonitridosilicate Ho₆Si₁₁N₂₀O ($d(\text{Ho}-\text{N}) = 2.36\text{--}2.53$

Å).^[57] Owing to terminal and single-bridging N atoms, two sets of P–N distances are observed (Figure 3.3). The P1–N2^[1] bond (superscripted numbers in square brackets following element symbols give coordination numbers) is with $d(\text{P1–N2}^{[1]}) = 1.57 \text{ \AA}$ expectedly shorter than the P–N^[2] bonds with bridging N atoms ($d(\text{P–N}^{[2]}) = 1.64\text{--}1.68 \text{ \AA}$).^[55] These values are in good agreement with those reported in comparable structures.^[10,13,58] The angles of Q⁴-tetrahedra, centered by P2, vary from 109.1 to 110.2°, which is exceptionally close to the regular value 109.5°. The P1-tetrahedra, exhibiting the one terminal N^[1]-atom, is distorted with N–P1–N angles ranging from 100.1 to 117.7° and a *bond angle variance*^[59] of 79.25°².

3.3.4 Structure Description of *bex*-Pr₂P₃N₇

As mentioned above, the *bex*-RE₂P₃N₇ phase is classified as a monophyllo nitridophosphate and crystallizes in the Ba₂Cu[Si₂O₇] structure type.^[15] Its unit cell contains two identical monolayers of vertex-sharing PN₄-tetrahedra, which are shifted one-half of a *c*-translation against each other according to the *c*-glide-plane of space group C2/*c* (Figure 3.4).

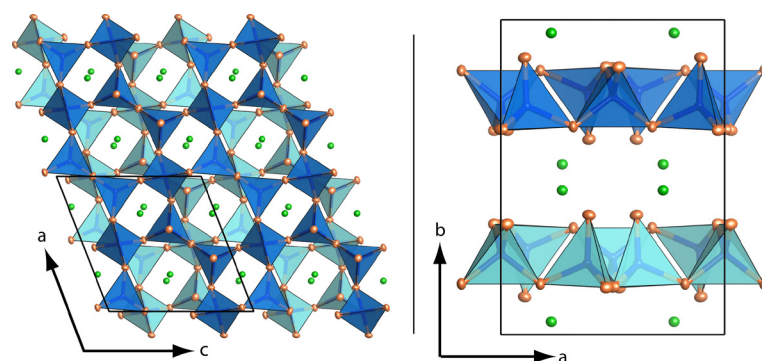


Figure 3.4. (left) Four unit cells of *bex*-Pr₂P₃N₇ in projection along the *b*-axis. (right) Projection along the *c*-axis, parallel to the monolayers. All anisotropic displacement ellipsoids are displayed with 95% probability.

The Pr-atoms are residing between the layers, more precisely, between rings created by the PN₄-tetrahedra connection pattern. The vertex-sharing PN₄-tetrahedra within a monolayer form an alternating pattern of contiguous four- and six-membered rings (*vierer*- and *sechser*-rings after Liebau^[55]) with vertex symbol (4.6.4.6)(4.6²)₂.

The Liebau nomenclature for this two-dimensional net is {**uB**, 1_∞²}[P₃N₇] due to a repetition unit consisting of an unbranched *dreier*-chain running along [100].^[55] The Pr₂P₃N₇ structure comprises

two different P-sites that are part of Q³- and Q⁴-bridging tetrahedra in the ratio 2:1. Reminiscent of the melilite structure type, this causes a degree of condensation of P/N = 3:7, which is rather unusual; in silicates, monolayered nets usually exhibit a molar ratio 2:5. The resulting topology, with comprehensible point symbol (4.6²)₂(4².6².8²) (calculated with TOPOS),^[56] is, to the authors knowledge, unprecedented for tetrahedral phyllo-networks; the Ba₂A[Si₂O₇] (A = Co, Cu, Mg, Zn)^[15,27-29] compounds are classified as sorosilicates, since a non-Si atom occupies the Q⁴-tetrahedron. However, the point symbol of the phyllo-net is established in the structural chemistry of metal–organic frameworks (MOFs) under topological type 3,4L13, which is not unexpected, since MOFs usually constitute of atavistic nets.^[60,61]

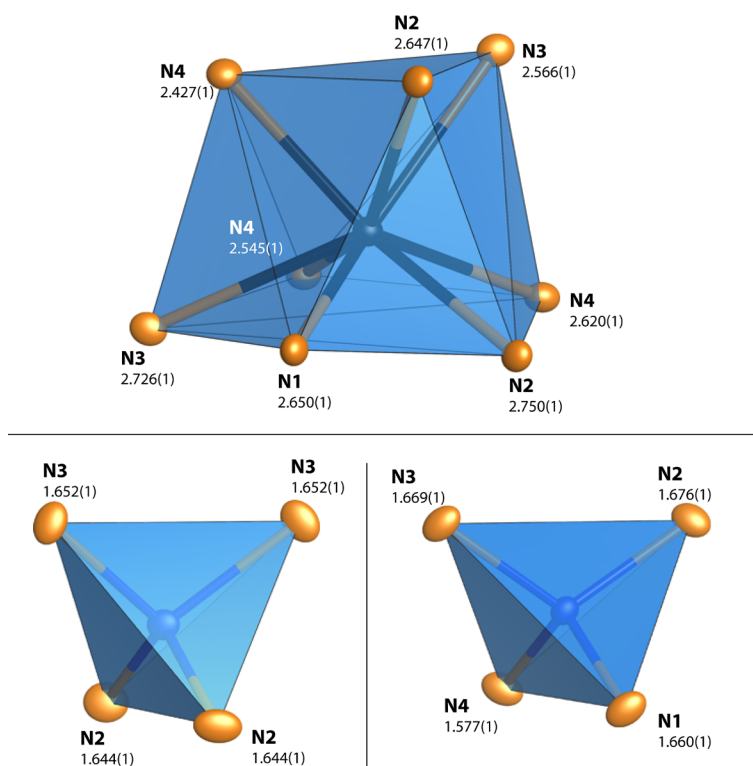


Figure 3.5. N-coordination polyhedra in *bex*-Pr₂P₃N₇ around Pr1 (top), P1 (bottom left), and P2 (bottom right) with respective bond lengths.

The bond geometry is similar to the *mcm*-case (Figure 3.5), with little skewed N–P–N bond angles in the P1 Q⁴-tetrahedra (between 106.0 and 114.7°) and distorted P2 Q³-tetrahedra with angles ranging from 101.1 to 117.8°. The P2–N^[1] bond length (1.57 Å) is shorter than the P2–N^[2] distances (1.64–1.68 Å) causing this distortion yielding a *bond angle variance*^[59] of 60.1°.

The Pr-atom is coordinated by eight N atoms forming an irregular PrN_8 -polyhedron. The Pr–N distances range from 2.43 to 2.75 Å, which is in good agreement with the sum of the ionic radii^[62] and values found in nitridosilicate PrSi_3N_5 (2.41–2.82 Å).^[63]

Driven by means to simplify and aid understanding chemists consider the topology of crystal structures. Traditionally, net-topologies derived from graph theory are used,^[64,65] but with advances in tiling theory^[66,67] the description of network structures as tessellations proves to be an advantageous alternative.^[68] For this purpose, two- and three-periodic chemical structures can be abstracted to mathematical tiling patterns,^[56,67–69] which are gap-free tessellations of the Euclidian plane or the Euclidian space by convex polygons or polyhedra (the tiles). Figure 3.6 displays the breaking down of the complex tetrahedral network of both $\text{RE}_2\text{P}_3\text{N}_7$ polymorphs into their respective tiling pattern with maximal symmetry embedding, which are listed under symbol *mcm* and *bex* of the RCSR database.^[17] The tiling symbols were determined with TOPOS.^[56]

This additional structure description is complementary in its function as a visualized archetype to the inherently cryptic classifications of vertex and point symbols,^[70] which consolidate structural information in a string of numbers. The reduction of two- or even three-periodic nets into their highly symmetric tiling pattern offers an intuitive understanding of intricate structures.^[68] Concomitant with conversion to a tiling pattern is, to a certain degree, the effacement of chemical information, which allows comparing structures of different materials families. For instance, a *bex* tiling pattern is found in $\text{K}_2\text{MoO}_2\text{As}_2\text{O}_7$, which exhibits Q^4 -type MoO_6 octahedra instead of Q^4 -type tetrahedra.^[71] Moreover, divergences from the maximum-symmetry embedding of the tiling pattern reveal distortions; for example, plane group of the *bex*-tiling pattern is *p2mm*, but *bex-RE}_2\text{P}_3\text{N}_7* monolayers have *p2* symmetry (Figure 3.6, bottom). Abstract classification symbols lack such symmetry information.

The incorporation of all-side vertex-sharing Q^4 -tetrahedra in a two-periodic net has interesting structural implications revealed by tiling theory. The method for enumerating the tile-k-transitive tiling patterns of the Euclidian plane has been published by Huson,^[66] and the solutions for up to three symmetry-inequivalent tiles are contained in the program *2Dtiler*.^[72] This list contains the topology of all two-periodic structures with up to three symmetry-inequivalent tiles. Relevant for two-periodic phyllosilicates, with a degree of condensation of 2:5, are the tessellations constructed solely from three-coordinated vertices (Q^3 -tetrahedra). The numbers of tessellations with three-coordinated ver-

tices can be extracted and yield a total of three uninodal, 17 binodal, and 103 trinodal tiling patterns (uninodal denoting tilings with one symmetry inequivalent vertex, binodal with two, etc).^[67,72] The inclusion of four-coordinated vertices, as found in both of the here discussed $RE_2P_3N_7$ polymorphs, in this enumeration multiplies the theoretical number of tiling patterns to a total of seven uninodal, 129 binodal, and 1585 trinodal nets.^[66,72] Thus, a successful incorporation of Q^4 -tetrahedra in a two-periodic structure theoretically proliferates the structural possibilities, of course bearing in mind that not all tiling patterns are realizable due to the limitations of bond lengths and angles.^[73]

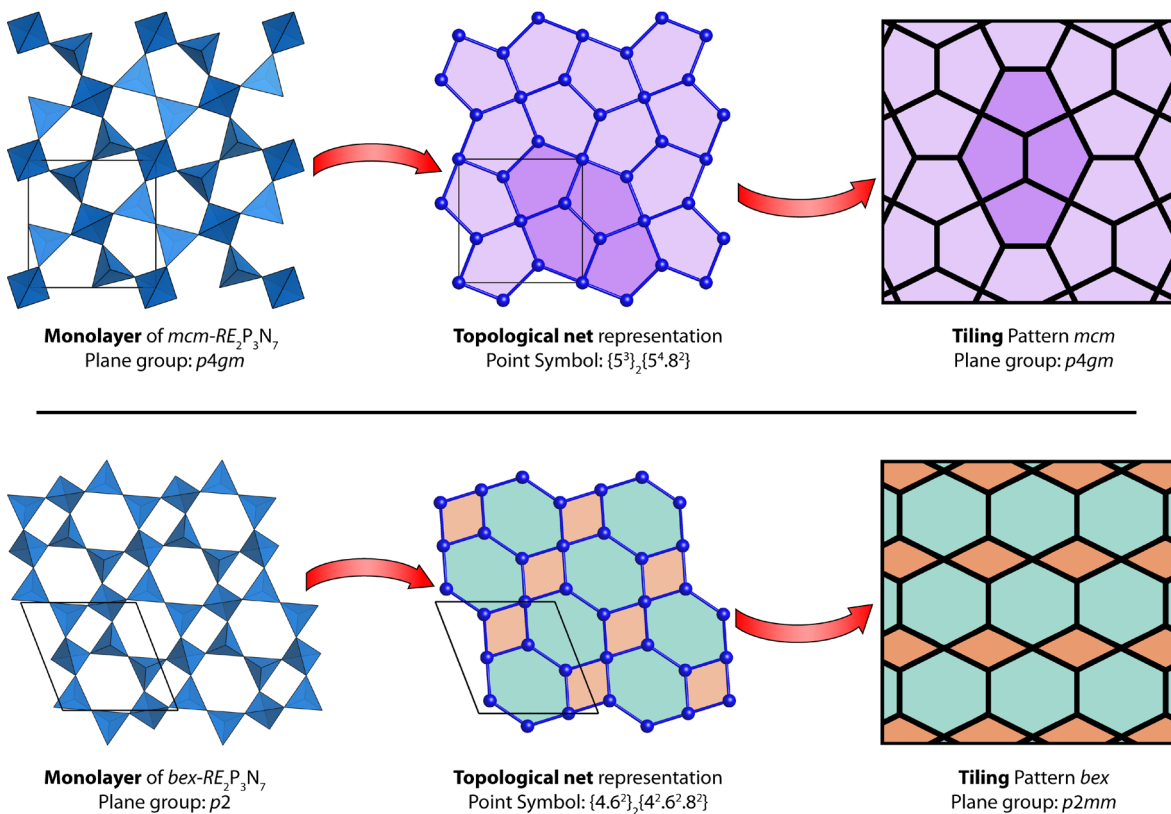


Figure 3.6. Deduction of the mcm (top) and bex (bottom) tiling pattern from monolayers of the respective $RE_2P_3N_7$ structures. The structures' topologies (P network) are drawn in the middle, the tiles already colored as they appear in the tiling pattern on the right.

3.3.5 Structural Evolution of mcm - and bex - $RE_2P_3N_7$ Phases

Figure 3.7 shows the lattice parameters and unit cell volume of mcm - $RE_2P_3N_7$ ($RE = Pr, Nd, Sm, Eu, Ho, Yb$) obtained from Rietveld refinement. All parameters linearly decline in the row from Pr to Yb. The abundance of Vegard's law^[73] is expected owing to the lanthanide contraction, which delineates atomic and ionic radii decrease with atomic number.^[74] Reminiscent of the high-pressure compress-

ibility of $\text{Sr}_{2-x}\text{Ba}_x\text{Mg}[\text{Si}_2\text{O}_7]$, the unit cell parameter's alteration is anisotropic.^[31] The lateral strain (parameter a) parallel to the monolayers is smaller than the vertical strain perpendicular to the layers, the contraction amounts to $-0.0148 \text{ \AA}/\text{atom}$ in lateral and $-0.0223 \text{ \AA}/\text{atom}$ in vertical direction, indicating an anisotropic compressibility. The resulting average volume drop of the unit cells is $-2.3384 \text{ \AA}^3/\text{atom}$. This anisotropic strain is explained by the layered structure of $mcm\text{-RE}_2\text{P}_3\text{N}_7$; the exchange of cations can be compared to an intercalation process, in which the intercalated component widens the layer spacing but barely effects the lateral spread.^[75]

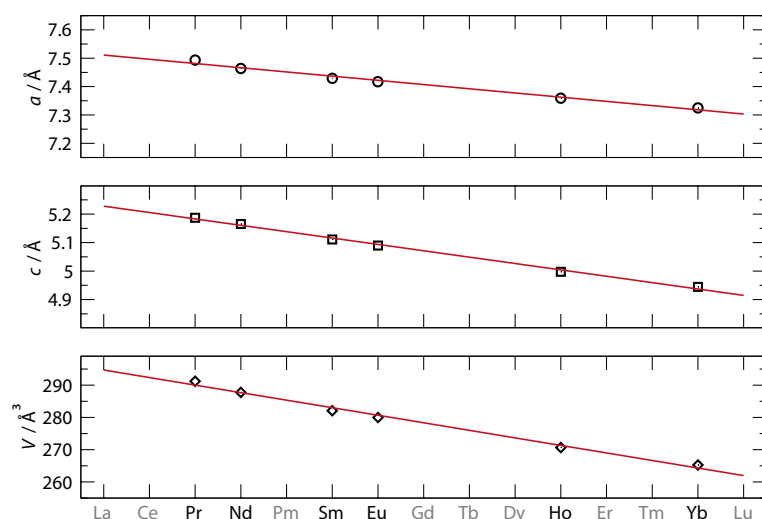


Figure 3.7. Lattice parameters a , c , and V obtained from Rietveld refinement (see Supporting Information) of respective $mcm\text{-RE}_2\text{P}_3\text{N}_7$ compounds. A linear regression (red line) is fit to the data.

The density's increase with atomic number is depicted in Figure 3.8 for both $mcm\text{-}$ and $bex\text{-}$ type $\text{RE}_2\text{P}_3\text{N}_7$. Comparison of the $mcm\text{-}$ and $bex\text{-Pr}_2\text{P}_3\text{N}_7$ polymorphs reveals that bex , which was prepared at higher pressures, is the denser structure. The difference is but marginal, in compliance with the structural changes; the monolayers reconstructively rearrange, splitting five-membered rings into four- and six-membered rings, and the cation coordination alters from the $4 + 4$ of a quadratic anti-prism to a $5 + 3$ of an irregular polyhedron (Figures 3.3 and 3.5). Embedding of the cations between the four- and six-membered rings of the monolayers leads to a smaller layer-spacing and a denser structure. Energetically, both structures are expected to be close; the mentioned $\text{Ba}_2\text{Cu}[\text{Si}_2\text{O}_7]$ can be prepared in both polymorphs at ambient pressure.^[15,76]

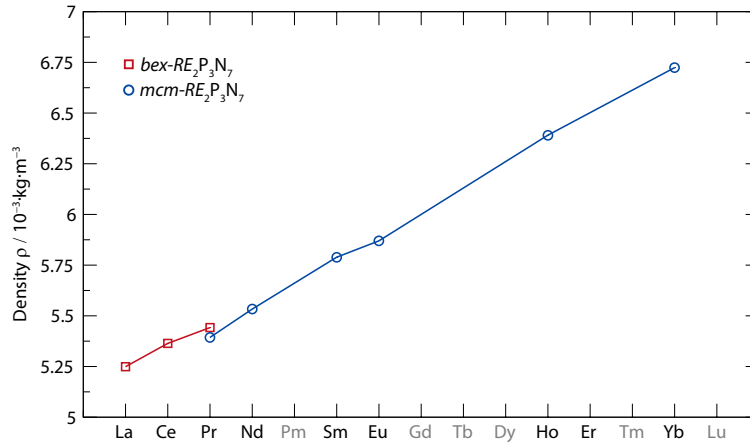


Figure 3.8. Density of both polymorphs as determined by Rietveld refinement.

3.3.6 Density Functional Theory Calculations

To corroborate the observed high-pressure phase transition from *mcm*- to *bex*- $Pr_2P_3N_7$ we performed additional ab initio DFT calculations.

To study the structural behavior at elevated pressures, the total energies of the relaxed structures were recalculated, approximating the compression and expansion of volume in a range from 96% to 103%, which simulates synthesis pressures up to 7 GPa. The calculations were performed at constant volume.

Table 3.4. Results^a of the Murnaghan Equation of State Fit for Relaxed *mcm*- and *bex*- $Pr_2P_3N_7$.

model	<i>bex</i> - $Pr_2P_3N_7$	<i>mcm</i> - $Pr_2P_3N_7$
energy E_0 / eV	-96.12	-96.14
volume V_0 / \AA^3	148.16	149.03
bulk modulus B_0 / GPa	156.5	173.7
B'	3.8	4.0

(a) Obtained by the GGA

The energy–volume (E – V) curves for both polymorphs (Figure 3.9) indicate that at lower pressures *mcm*- $Pr_2P_3N_7$ is slightly energetically favored compared to *bex*- $Pr_2P_3N_7$ (0.01 eV/formula unit (1.14 kJ/mol)). At higher pressures (lower volumes) the E – V curves intersect, indicating a possible phase transition. The bulk modulus B_0 as depicted in Table 3.4 for both polymorphs is obtained by fitting the total energies of the resulting E – V curves with the Murnaghan equation of state.^[77]

Following previous works, the entropy part of ΔG is usually neglected for solid-state transitions, enabling accurate estimations of ΔH from $H = E + pV$, by only regarding the energy, volume, and pressure of the system.^[78]

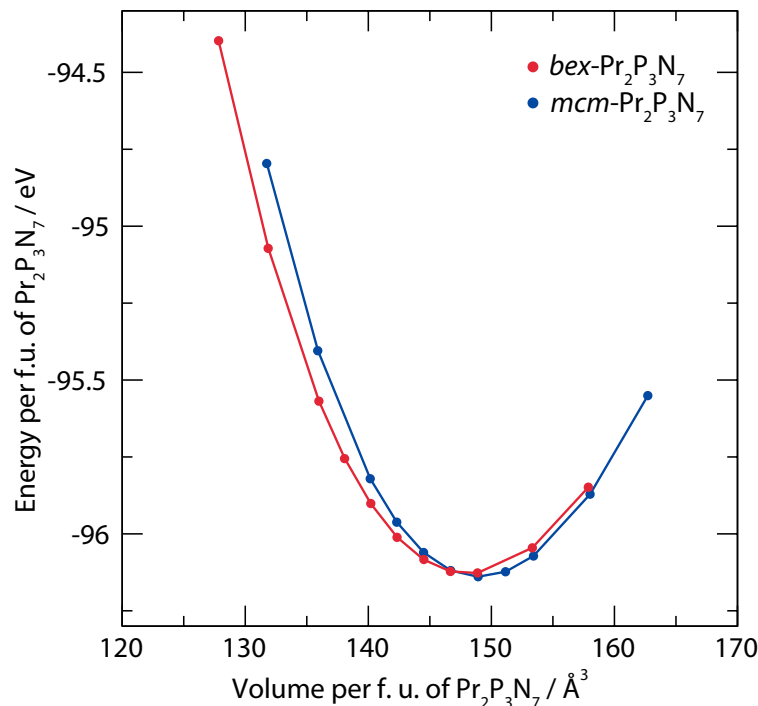


Figure 3.9. Energy–volume diagram for the *bex*- and *mcm*- $\text{Pr}_2\text{P}_3\text{N}_7$. Results were obtained with the GGA. Each point represents one structural optimization at constant volume. Energy and volume are given per formula unit (f.u.) of $\text{Pr}_2\text{P}_3\text{N}_7$.

The prevailing pressure is obtained from the E – V diagram in terms of a simple numerical differentiation: $p = -\partial E/\partial V$. The enthalpy difference of both polymorphs ΔH is subsequently plotted in Figure 3.10, normalized to ΔH of *mcm*- $\text{Pr}_2\text{P}_3\text{N}_7$. Neglecting the influence of temperature, the pressure at which *bex*- $\text{Pr}_2\text{P}_3\text{N}_7$ becomes the energetically favored polymorph is ~ 1.8 GPa, corroborating that *bex*- $\text{Pr}_2\text{P}_3\text{N}_7$ is the high-pressure polymorph in accordance with above-discussed experimental results.

The *bex*- $\text{RE}_2\text{P}_3\text{N}_7$ phase is the second high-pressure modification of the melilite structure type. The first is a polymorph of åkermanite and gehlenite composed of four-, five-, and six-membered rings in molar ratio of 1:1:1.^[25] Structurally, it is related to the melilite-type by splitting half of the five-membered rings into four- and six-membered rings. This polymorph might be a frozen transition state between a reconstructive phase transition from the *mcm* to the *bex* modification, since in the *bex*-modification all five-membered rings are split into four- and six-membered ones.

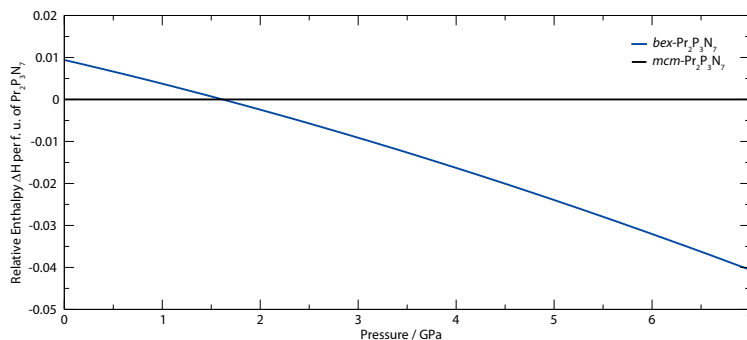


Figure 3.10. Enthalpy–pressure diagram obtained by fitting the Murnaghan equation of state from the Energy–Volume diagram for the *mcm* and *bex* modifications. The enthalpy difference of *bex*- $Pr_2P_3N_7$ relative to *mcm*- $Pr_2P_3N_7$ is given per formula unit of $Pr_2P_3N_7$.

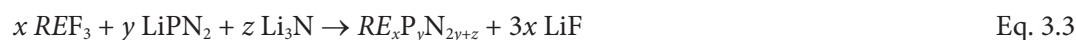
3.3.7 High-Temperature Powder Diffraction

To study the phase stability of the *bex*- and *mcm*-polymorphs high-temperature powder diffraction was performed. At 850 °C *bex*- $Pr_2P_3N_7$ decomposes (Figure C.13), and *mcm*- $Ho_2P_3N_7$ decomposes at 750 °C (Figure C.5) forming unidentified products. The experiment on *bex*- $Pr_2P_3N_7$ was conducted under Ar atmosphere to detect a possible phase transition to the *mcm* form. The stability of both compounds is significantly lower than for $NdLiP_4N_8$, which is stable to at least 1000 °C in air.^[13] This is expected, since $NdLiP_4N_8$ is composed of a three-periodic tetrahedra network, while the two polymorphs at hand are only two-periodic.

3.4 Conclusion

Two polymorphs of $RE_2P_3N_7$ ($RE = La, Ce, Pr, Nd, Sm, Eu, Ho, Yb$) were prepared by solid-state high-pressure metathesis. We showed that the $BaCu[Si_2O_7]$ -type *bex*- $Pr_2P_3N_7$ is a reconstructive high-pressure polymorph of the tetragonal *mcm*- $Pr_2P_3N_7$. This phase relation was deduced from the experimental data as well as stability DFT calculations. We subsumed both polymorphs with regard of their *Liebau* classification, vertex and point symbol, and tiling pattern. The tiling pattern is an intuitive way for the classification of intricate structures, since it provides a concrete picture of the underlying structure. Especially for three-periodic structures with extensive point symbols, a tiling pattern could be a promising alternative to easily grasp the underlying net.

Moreover, with successful preparation of two nitridophosphates with a low degree of condensation, the here proposed expanded high-pressure metathesis route opens the pathway to a host of new structures. The generalized Equation 3.3 suggests that, by adding Li_3N , degrees of condensation ranging from $1/4$ to $1/2$ are attainable, and novel chain, ring, and ortho nitridophosphates are to be expected from this approach.



3.5 References

- [1] S. Horstmann, E. Irran, W. Schnick, *Angew. Chem., Int. Ed. Engl.* **1997**, *3*, 1873–1875; *Angew. Chem.* **1997**, *109*, 1938–1940.
- [2] W. Schnick, J. Lücke, F. Krumeich, *Chem. Mater.* **1996**, *8*, 281–286.
- [3] K. Landskron, H. Huppertz, J. Senker, W. Schnick, *Angew. Chem., Int. Ed.* **2001**, *40*, 2643–2645; *Angew. Chem.* **2001**, *113*, 2713–2716.
- [4] K. Landskron, H. Huppertz, J. Senker, W. Schnick, *Z. Anorg. Allg. Chem.* **2002**, *628*, 1465–1471.
- [5] D. Baumann, W. Schnick, *Angew. Chem., Int. Ed.* **2014**, *53*, 14490–14493; *Angew. Chem.* **2014**, *126*, 14718–14721.
- [6] S. Horstmann, E. Irran, W. Schnick, *Angew. Chem., Int. Ed. Engl.* **1997**, *36*, 1992–1994; *Angew. Chem.* **1997**, *109*, 2085–2087.
- [7] K. Landskron, W. Schnick, *J. Solid State Chem.* **2001**, *156*, 390–393.
- [8] K. Landskron, E. Irran, W. Schnick, *Chem. - Eur. J.* **1999**, *5*, 2548–2553.
- [9] W. Schnick, J. Lücke, *Z. Anorg. Allg. Chem.* **1990**, *588*, 19–25.
- [10] A. Marchuk, W. Schnick, *Angew. Chem., Int. Ed.* **2015**, *54*, 2383–2387; *Angew. Chem.* **2015**, *127*, 2413–2417.
- [11] F. J. Pucher, F. Hummel, W. Schnick, *Eur. J. Inorg. Chem.* **2015**, *2015*, 1886–1891.
- [12] S. J. Sedlmaier, M. Eberspächer, W. Schnick, *Z. Anorg. Allg. Chem.* **2011**, *637*, 362–367.
- [13] S. D. Kloß, W. Schnick, *Angew. Chem., Int. Ed.* **2015**, *54*, 11250–11253; *Angew. Chem.* **2015**, *127*, 11402–11405.
- [14] H.-J. Meyer, *Dalton Trans.* **2010**, *39*, 5973–5982.
- [15] Y. A. Malinovskii, *Sov. Phys. Dokl.* **1984**, *29*, 706–708.
- [16] M. Kimata, N. Ii, *Neues Jb. Mineral. Monat.* **1981**, *1981*, 1–10.
- [17] M. O’Keeffe, M. A. Peskov, S. J. Ramsden, O. M. Yaghi, *Acc. Chem. Res.* **2008**, *41*, 1782–1789.
- [18] F. Raaz, *Mineral. und Petrogr.* **1932**, *42*, 72–78.
- [19] R. Lauterbach, W. Schnick, *W. Z. Anorg. Allg. Chem.* **1999**, *625*, 429–434.
- [20] N. A. Toropov, T. S. Lin, *Russ. J. Inorg. Chem.* **1960**, *5*, 1194–1196.
- [21] N. A. Sirazhiddinov, N. N. Mirbabaeva, R. G. Grebenschikov, E. V. Stroganov, *Inorg. Mater.* **1973**, *9*, 1236–1238.

- [22] A. P. Tyutyunnik, V. G. Zubkov, L. L. Surat, B. V. Slobodin, G. Svensson, *Powder Diffr.* **2005**, *20*, 189–192.
- [23] J. D. C. McConnell, C. A. McCammon, R. J. Angel, F. Seifert, *Z. Kristallogr.* **2000**, *215*, 669–677.
- [24] H. Yang, R. M. Hazen, R. T. Downs, L. W. Finger, *Phys. Chem. Miner.* **1997**, *24*, 510–519.
- [25] M. Merlini, M. Gemmi, M. Hanfland, W. Crichton, *Am. Mineral.* **2009**, *94*, 704–709.
- [26] S. N. Achary, D. Errandonea, D. Santamaria-Perez, O. Gomis, S. J. Patwe, F. J. Manjón, P. R. Hernandez, A. Muñoz, A. K. Tyagi, *Inorg. Chem.* **2015**, *54*, 6594–6605.
- [27] R. D. Adams, R. Layland, C. Payen, T. Datta, *Inorg. Chem.* **1996**, *35*, 3492–3497.
- [28] M. Ardit, C. Zanelli, M. Dondi, G. Cruciani, *Period. di Mineral.* **2011**, *80*, 155–165.
- [29] J. W. Kaiser, W. Jeitschko, *Z. Kristallogr. - New Cryst. Struct.* **2002**, *217*, 25–26.
- [30] R. M. Hazen, R. T. Downs, C. T. Prewitt, *Rev. Mineral. Geochem.* **2000**, *41*, 1–33.
- [31] M. Ardit, M. Dondi, M. Merlini, G. Cruciani, *Phys. Chem. Miner.* **2011**, *39*, 199–211.
- [32] A. Stock, H. Grüneberg, *Ber. Dtsch. Chem Ges.* **1907**, *40*, 2573–2578.
- [33] H. Huppertz, *Z. Kristallogr.* **2004**, *219*, 330–338.
- [34] N. Kawai, S. Endo, *Rev. Sci. Instrum.* **1970**, *41*, 1178–1181.
- [35] D. C. Rubie, *Phase Transitions* **1999**, *68*, 431–451.
- [36] D. Walker, *Am. Mineral.* **1991**, *76*, 1092–1100.
- [37] D. Walker, M. A. Carpenter, C. M. Hitch, *Am. Mineral.* **1990**, *75*, 1020–1028.
- [38] Bruker-AXS, *XPREP Reciprocal Space Exploration*, Karlsruhe, **2001**.
- [39] G. M. Sheldrick, *Acta Crystallogr., Sect. A: Found. Crystallogr.* **2008**, *64*, 112–122.
- [40] G. M. Sheldrick, *SHELXS - A Program for Crystal Structure Solution*, University of Göttingen, **1997**.
- [41] L. J. Farrugia, *PLATON*, University of Glasgow, **1995**.
- [42] K. Momma, F. Izumi, *J. Appl. Crystallogr.* **2011**, *44*, 1272–1276.
- [43] A. A. Coelho, *TOPAS-Academic V4.1*, **2007**.
- [44] J. P. Perdew, K. Burke, M. Ernzerhof, *Phys. Rev. Lett.* **1996**, *77*, 3865–3868.
- [45] J. P. Perdew, K. Burke, M. Ernzerhof, *Phys. Rev. Lett.* **1997**, *78*, 1396–1396.
- [46] P. E. Blöchl, *Phys. Rev. B: Condens. Matter Mater. Phys.* **1994**, *50*, 17953–17979.
- [47] G. Kresse, D. Joubert, *Phys. Rev. B: Condens. Matter Mater. Phys.* **1999**, *59*, 1758–1775.

- [48] G. Kresse, J. Hafner, *Phys. Rev. B: Condens. Matter Mater. Phys.* **1993**, *47*, 558–561.
- [49] G. Kresse, J. Hafner, *Phys. Rev. B: Condens. Matter Mater. Phys.* **1994**, *49*, 14251–14269.
- [50] G. Kresse, J. Furthmüller, *Mater. Sci.* **1996**, *6*, 15–50.
- [51] J. E. Jaffe, J. A. Snyder, Z. Lin, A. C. Hess, *Phys. Rev. B* **2000**, *62*, 1660–1665.
- [52] P. Kroll, W. Schnick, *Chem. - Eur. J.* **2002**, *8*, 3530–3537.
- [53] H. J. Monkhorst, J. D. Pack, *Phys. Rev. B* **1976**, *13*, 5188–5192.
- [54] *Further details on the crystal structure investigations may be obtained from the Fachinformati-
onszentrum Karlsruhe, 76344 Eggenstein-Leopoldshafen, Germany (fax: (+49)7247-808-666; e-
mail:crysdata@fiz-karlsruhe.de), on quoting the depository numbers CSD-431287, CSD-431288
and CSD-431289 for bex-Ce₂P₃N₇, bex-Pr₂P₃N₇ and mcm-Ho₂P₃N₇, respectively.*
- [55] F. Liebau, *Structural Chemistry of Silicates: Structure, Bonding, and Classification*; Springer:
Berlin, Germany, **1985**.
- [56] V. A. Blatov, A. P. Shevchenko, D. M. Proserpio, *Cryst. Growth Des.* **2014**, *14*, 3576–3586.
- [57] M. Woike, W. Jeitschko, *J. Solid State Chem.* **1997**, *129*, 312–319.
- [58] A. Marchuk, F. J. Pucher, F. W. Karau, W. Schnick, *Angew. Chem., Int. Ed.* **2014**, *53*, 2469–2472;
Angew. Chem. **2014**, *126*, 2501–2504.
- [59] K. Robinson, G. V. Gibbs, P. H. Ribbe, *Science* **1971**, *172*, 567–570.
- [60] T. G. Mitina, V. A. Blatov, *Cryst. Growth Des.* **2013**, *13*, 1655–1664.
- [61] N. W. Ockwig, O. Delgado-Friedrichs, M. O’Keeffe, O. M. Yaghi, *Acc. Chem. Res.* **2005**, *38*,
176–182.
- [62] R. D. Shannon, *Acta Crystallogr., Sect. A: Cryst. Phys., Diffr., Theor. Gen. Crystallogr.* **1976**, *32*,
751–767.
- [63] M. Woike, W. Jeitschko, *Inorg. Chem.* **1995**, *34*, 5105–5108.
- [64] A. F. Wells, *Acta Crystallogr.* **1954**, *7*, 535–544.
- [65] W. E. Klee, *MATCH Commun. Math. Comput. Chem.* **1980**, *9*, 105–120.
- [66] D. H. Huson, *Geom. Dedicata* **1993**, *47*, 269–296.
- [67] O. Delgado-Friedrichs, A. W. M. Dress, D. H. Huson, J. Klinowski, A. L. Mackay, *Nature* **1999**,
400, 644–647.
- [68] V. A. Blatov, O. Delgado-Friedrichs, M. O’Keeffe, D. M. Proserpio, *Acta Crystallogr., Sect. A:*

- Found. Crystallogr.* **2007**, *63*, 418–425.
- [69] O. Delgado-Friedrichs, M. O’Keeffe, *Acta Crystallogr., Sect. A: Found. Crystallogr.* **2007**, *63*, 344–347.
- [70] V. A. Blatov, M. O’Keeffe, D. M. Proserpio, *CrystEngComm.* **2010**, *12*, 44–48.
- [71] M. F. Zid, T. Jouini, *Acta Crystallogr., Sect. C: Cryst. Struct. Commun.* **1996**, *52*, 1334–1336.
- [72] D. H. Huson, *Program 2DTiler*, **2005**.
- [73] L. Z. Vegard, *Z. Phys.* **1921**, *5*, 17–26.
- [74] P. Pyykkö, *Chem. Rev.* **1988**, *88*, 563–594.
- [75] M. S. Dresselhaus, G. Dresselhaus, *Adv. Phys.* **1981**, *51*, 1–186.
- [76] J. Du, H. Zeng, L. Song, Z. Dong, H. Ma, G. Guo, J. Huang, *Chin. J. Struct. Chem.* **2003**, *22*, 33–36.
- [77] F. D. Murnaghan, *Proc. Natl. Acad. Sci. U.S.A.* **1944**, *30*, 244–247.
- [78] D. Baumann, R. Niklaus, W. Schnick, *Angew. Chem., Int. Ed.* **2015**, *54*, 4388–4391; *Angew. Chem.* **2015**, *127*, 4463–4466.

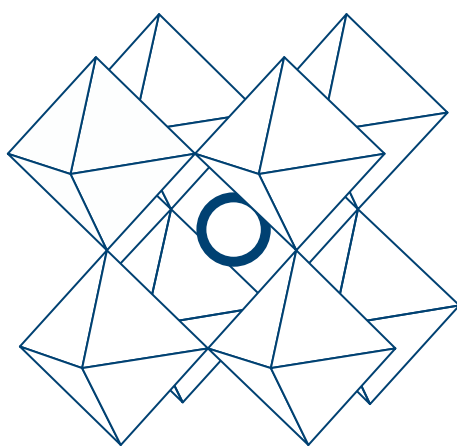
Chapter 4

Antiperovskite Nitridophosphate Oxide $\text{Ho}_3[\text{PN}_4]\text{O}$ by High-Pressure Metathesis

Simon D. Kloß, Niels Weidmann, and Wolfgang Schnick

published in: *Eur. J. Inorg. Chem.* **2017**, 1930–1937. DOI: 10.1002/ejic.201601425

Reprinted (adapted) with permission from *European Journal of Inorganic Chemistry*. Copyright 2017 John Wiley and Sons.



$\text{Ho}_3[\text{PN}_4]\text{O}$, a rare-earth nitridophosphate oxide with isolated PN_4 tetrahedra, is prepared by high-pressure metathesis. $\text{Ho}_3[\text{PN}_4]\text{O}$ adopts an antiperovskite structure with PN_4 tetrahedra in the cuboctahedral voids. This synthesis is a stepping stone for the high-pressure metathesis of nitridophosphates as it shows its capability to produce low-condensed nitridophosphates.

Abstract

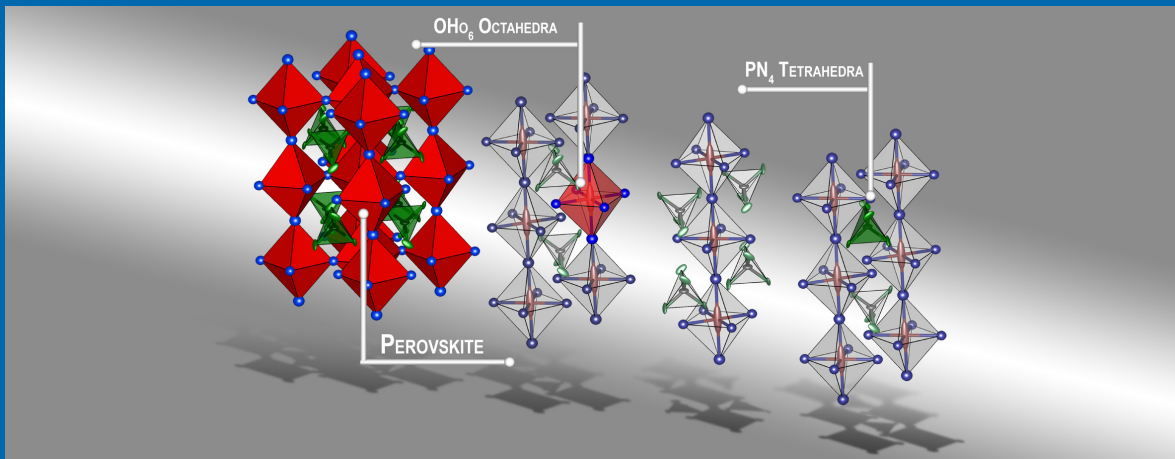


Table-of-contents graphic.

Rare-earth nitridophosphates are a recently discovered class of materials, which are accessible by high-pressure metathesis. Antiperovskite-type $\text{Ho}_3[\text{PN}_4]\text{O}$ was synthesized from HoF_3 , LiPN_2 , Li_3N , and Li_2O at 5 GPa and ca. 1025 °C by this method and the multianvil technique. $\text{Ho}_3[\text{PN}_4]\text{O}$ contains rarely observed isolated PN_4 tetrahedra and can be derived by the hierarchical substitution of the ABX_3 perovskite, in which Ho occupies the X positions, O occupies the B position, and the PN_4 tetrahedra occupy the A position. The structure was refined on the basis of powder diffraction data [$I4/mcm$, $a = 6.36112(3)$, $c = 10.5571(1)$ Å, $Z = 4$, $R_{\text{wp}} = 0.04$, $R_{\text{Bragg}} = 0.01$, $\chi^2 = 2.275$] starting from the structural model of isotypic $\text{Gd}_3[\text{SiN}_3]\text{O}$. To characterize $\text{Ho}_3[\text{PN}_4]\text{O}$, elemental analyses were performed through energy-dispersive X-ray spectroscopy (EDX) and inductively coupled plasma optical emission spectroscopy (ICP-OES). $\text{Ho}_3[\text{PN}_4]\text{O}$ is paramagnetic down to low temperatures with $\mu_{\text{eff}} = 10.43(1) \mu_{\text{B}}$ and a Curie temperature (Θ) of 0.11(4) K. It shows the optical characteristics of Ho^{3+} ions and vibrations corresponding to isolated PN_4 tetrahedra. On the basis of DFT calculations [generalized gradient approximation (GGA)], $\text{Ho}_3[\text{PN}_4]\text{O}$ has an indirect band gap of 1.87 eV. We demonstrate the versatility of high-pressure metathesis by attaining the low end of the P/N atomic ratio $\kappa = 1/4$. This confirms the previous assumption that rare-earth nitridophosphates with $\kappa = 1/2$ to $1/4$ are feasible by this method.

4.1 Introduction

The recently opened family of rare-earth (RE) nitridophosphates offers an abundance of structural possibilities owing to the close relation of nitridophosphates and silicates.

For the preparation of rare-earth nitridophosphates, the adaptable high-pressure metathesis route has been demonstrated for NdLiP₄N₈ and two RE₂P₃N₇ polymorphs^[1,2] Adaptability refers to the feasible systematic variation of the P/N atomic ratio κ , which grants control over the degree of condensation of the PN network. This is achieved by reacting the readily available precursors LiPN₂, Li₃N, and rare-earth fluorides in the desired stoichiometry under high-pressure conditions of several GPa (Equation 4.1):^[2]



Here, $x = 1/3y + z$ to retain a ternary compound. The P/N atomic ratio κ influences the attained type of PN network but does not strictly determine it; three-periodic frameworks can possess $\kappa = 1/2$, and layered, chain, ring, and noncondensed ortho structures have values of 2/5, 1/3, 1/3, and 1/4, respectively. However, exceptions to this are common, for example, in layered CaH₄P₆N₁₂ with P/N equal to 1/2.^[3]

Regarding the hitherto known rare-earth nitridophosphates, NdLiP₄N₈, with $\kappa = 1/2$, is a three-periodic network of all-side vertex-sharing PN₄ tetrahedra, whereas the RE₂P₃N₇ polymorphs are two-periodic layered compounds.^[1,2] Generally, nitridophosphates at the low end with P/N = 1/4 are scarcely known; Li₇PN₄ is the only exclusively nitridic example followed by the oxonitridophosphate M₂PO₃N (M = Ca, Sr).^[4,5]

In this contribution, we report on the nitridophosphate oxide Ho₃[PN₄]O, which exhibits isolated PN₄ tetrahedra. Ho₃[PN₄]O crystallizes in a tetragonally distorted antiperovskite structure with PN₄ tetrahedra at the A position, O at the B position, and Ho at the X positions of the normal ABX₃ perovskite structure. For the preparation of Ho₃[PN₄]O, Equation 4.1 was modified to Equation 4.2:



The incorporation of oxygen in the structure seems to be a necessity, as no oxygen-free structure with isolated PN₄ tetrahedra, for example, a hypothetical Ho₇(PN₄)₃, could be obtained by high-pressure

metathesis with the exclusion of oxygen-containing precursors and the temperature and pressure ranges applied here. This might be due to the structural problem of arranging large and highly charged ions, in this case Ho^{3+} and PN_4^{7-} ions, in three-dimensional space without electrostatic repulsion. We argue that the oxygen atoms, which reside in the centers of the Ho_6 octahedra, buffer the positive charge of the Ho ions.

An abundance of oxides with general formula $\text{M}_3[\text{TO}_4]\text{X}$ are known, and their structures span all crystal systems and large composition spaces.^[6,7] The diverse $\text{M}_3[\text{TO}_4]\text{X}$ structures have been described on the basis of the stacking arrangement of closely packed $\text{M}_3[\text{TO}_4]$ layers, in which the orientation of the tetrahedra and the occupation of the X site direct the stacking order.^[6,8] The tetragonal structure type with space group $I4/mcm$ of $\text{Ho}_3[\text{PN}_4]\text{O}$ has been realized in several tetrahedra-based material classes, for example, sulfates ($\text{K}_3[\text{SO}_4]\text{F}$),^[6] selenates ($\text{K}_3[\text{SeO}_4]\text{F}$),^[9] aluminates ($\text{Sr}_3[\text{AlO}_4]\text{F}$),^[10] silicates ($\text{Ba}_3[\text{SiO}_4]\text{O}$),^[7,11] and oxonitridosilicates ($\text{Gd}_3[\text{SiN}_3\text{O}]\text{O}$).^[12] All $\text{M}_3[\text{TO}_4]\text{X}$ structures feature XM_6 octahedra; $\text{Gd}_3[\text{SiN}_3\text{O}]\text{O}$ is electrostatically closest to the present $\text{Ho}_3[\text{PN}_4]\text{O}$, and both contain $[\text{OLn}_6]^{16+}$ complex ions.^[12]

In this contribution, the crystal structure and physical properties of $\text{Ho}_3[\text{PN}_4]\text{O}$ are characterized and corroborated by powder diffraction, energy-dispersive X-ray spectroscopy (EDX), Fourier transform infrared (FTIR) spectroscopy, Raman spectroscopy, UV/Vis spectroscopy, magnetometry, chemical analysis through inductively coupled plasma optical emission spectroscopy (ICP-OES), and DFT calculations. The O/N assignment was based on electrostatic MAPLE (Madelung part of the lattice energy) calculations.

4.2 Results and Discussion

4.2.1 Preparation and Chemical Analysis

Ho₃[PN₄]O was prepared by following Equation 4.2 at 5 GPa and ca. 1025 °C through the multianvil technique. An air- and water-stable, pale yellow microcrystalline product was obtained and washed with water to reduce the content of the LiF side-product. The morphology and elemental composition were examined through electron microscopy and associated EDX. The elemental analysis for Ho/P/O/N by EDX (see the Supporting Information, Table D.1) deviated from the theoretical composition, but a correct Ho/P atomic ratio of 3:1 was observed. Powder diffraction revealed an amorphous side phase, but the SEM micrographs (Figure 4.1) show a homogeneous sample, which indicates that the amorphous parts and the crystalline phase coalesce. Therefore, EDX detects a superposition of both phases, and this explains the divergence. To analyze the chemical composition further, ICP-OES was performed to determine the Ho, P, and Li content of the sample (Table D.1).

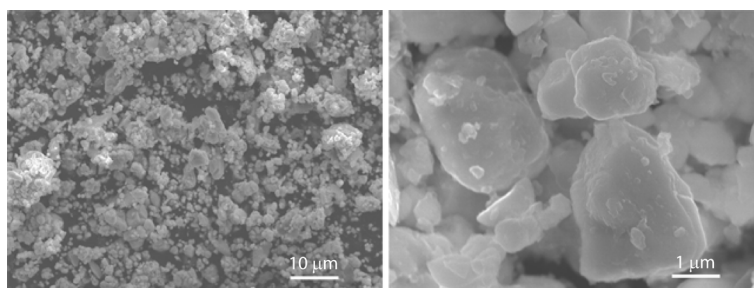


Figure 4.1. SEM micrographs of a representative Ho₃[PN₄]O sample.

The Ho and P concentrations match the expected Ho/P atomic ratio of 3:1, and the amount of Ho₃[PN₄]O in the sample was determined to be 60 wt.-% from the Ho content. Li is present either as a constituent of the amorphous phase or as part of formed LiF; however, powder diffraction methods could not resolve LiF because the sample was washed with water as mentioned above. Therefore, the amorphous phase accounts for 40 wt.-% of the sample.

4.2.2 Structure Determination

The crystal structure of Ho₃[PN₄]O was determined solely by powder diffraction methods owing to the microcrystalline nature of the sample.^[13] The powder diffraction pattern (Figure 4.2) was indexed with the SVG algorithm^[14] included in the TOPAS-Academic V4.1 program,^[15] which yielded a te-

tragonal body-centered unit cell with dimensions $a = 6.36112(3)$ and $c = 10.5571(1)$ Å. A query in the International Crystal Structure Database (ICSD)^[16,17] matched the unit-cell parameters with those of $\text{Gd}[\text{SiN}_3\text{O}]$.^[12] Based on this structural model, a Rietveld refinement^[18,19] was performed (TOPAS-Academic V4.1)^[15] with Gd replaced with Ho, Si replaced with P, and mixed N/O replaced with N. To acquire the maximum information from a powder pattern collected with a laboratory X-ray diffractometer, the diffraction pattern was recorded with $\text{Mo-K}_{\alpha 1}$ radiation in the range $2\theta = 2\text{--}76^\circ$ ($Q = 10.95 \text{ \AA}^{-1}$) and a sufficient collection time to ensure satisfactory counting statistics in the high-angle regime [$R_{\text{exp}}(50\text{--}76^\circ) = 0.023$]. The absorption was treated with a cylindrical absorption correction, and the peak profiles were modeled with the fundamental parameters approach, which is a direct convolution of source emission profiles, axial instrument contributions, crystallite size, and microstrain effects. The background was handled with a shifted Chebyshev function with 18 polynomials. It was possible to refine all five Wyckoff positions with anisotropic displacement parameters, which revealed a disorder of the O1 position, as was also observed for $\text{Gd}[\text{SiN}_3\text{O}]$.^[12]

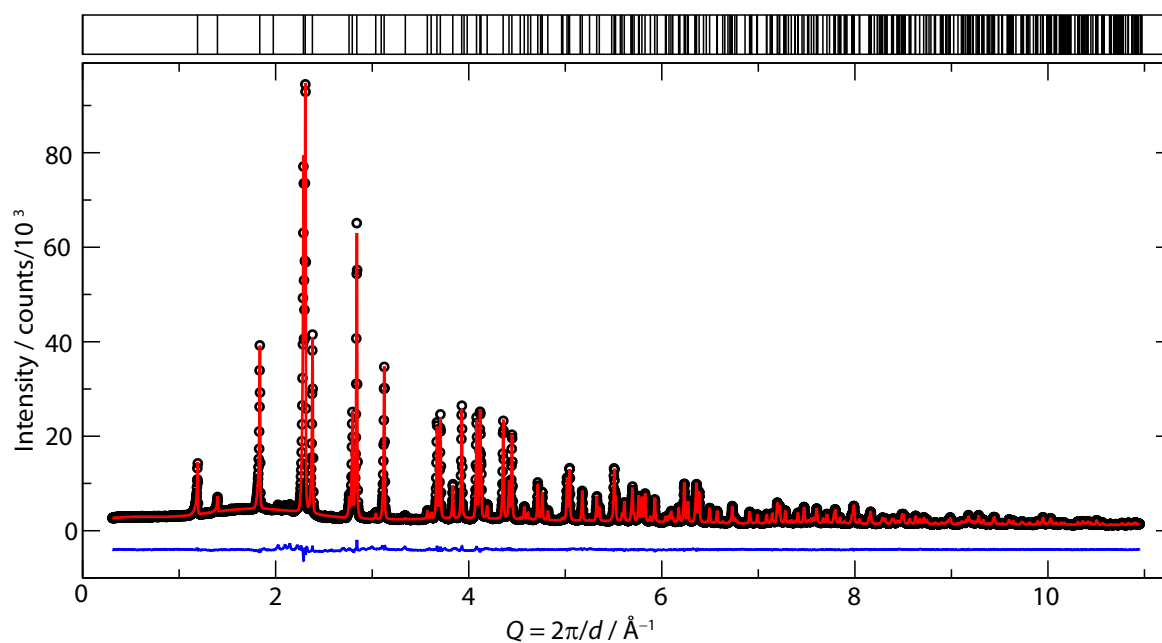


Figure 4.2. Result of the Rietveld Refinement of a $\text{Ho}_3[\text{PN}_4]\text{O}$ sample plotted in Q -space versus absolute intensity. Data points are displayed as black circles, the calculated pattern from the fitted model is shown as a red line, and the difference plot $I_{\text{obs}} - I_{\text{calc}}$ is the blue line below the pattern. The theoretical Bragg positions are displayed as vertical lines above the pattern.

Table 4.1. Crystallographic data for the refinement of Ho₃[PN₄]O.

Formula	Ho ₃ [PN ₄]O
Formula weight / g·mol ⁻¹	597.80
Crystal system, space group	tetragonal, <i>I4/mcm</i> (no. 140)
Lattice parameters / Å	<i>a</i> = 6.36112(3) <i>c</i> = 10.5571(1)
Cell volume / Å ³	427.181(5)
Formula units per cell <i>Z</i>	4
X-ray density / g·cm ⁻³	9.2949(1)
Absorption coefficient / mm ⁻¹	55.266
Radiation	Mo-K _{α1} (λ = 70.9300 pm)
Monochromator	Ge(111)
Diffractometer	Stoe Stadi P
Detector	MYTHEN 1K
<i>F</i> (000)	1008
2θ range / °	2–76
Temperature / K	297(2)
Data points	4958
Number of observed reflections	346
Number of parameters	50
Constraints	0
Program used	TOPAS-Academic V4.1
Structure refinement	Rietveld method
Profile function	fundamental parameters model
Background function	shifted Chebyshev with 18 polynomials
<i>R</i> _{wp}	0.039
<i>R</i> _{exp}	0.017
<i>R</i> _p	0.026
<i>R</i> _{Bragg}	0.010
χ ²	2.275

The result of the Rietveld refinement is displayed in Figure 4.2, the crystallographic data are summarized in Table 4.1, the atomic positions are listed in Table 4.2, and lists of bond lengths and angles as well as anisotropic displacement parameters are contained in Tables D.2–D.4. Owing to their similar atomic form factors, the positions of the O and N atoms cannot be determined reliably from X-ray diffractometry. The assignment of the O position is based on calculations of the Coulomb part of the lattice energy with the Madelung part of the lattice energy (MAPLE) concept and Shannon ionic radii.^[20-23] The MAPLE values were calculated for each ion type and for the complete structure. The sum formula Ho₃[PN₄]O was tripled and formally decomposed to Ho₂P₃N₇, Ho₂O₃, and five HoN formula units.^[2,24,25]

Table 4.2. Atomic positions and isotropic displacement parameters of Ho₃[PN₄]O.

Atom	Wyckoff position	Site symmetry	x	y	z	$U_{eq}/\text{\AA}^2$	Occupancy
Ho1	4a	422	0	0	1/4	0.0118(3)	1
Ho2	8h	<i>m.2m</i>	0.1756(1)	0.6756(1)	0	0.0087(2)	1
P1	4b	42 <i>m</i>	0	1/2	1/4	0.0069(7)	1
O1	4c	4/ <i>m</i>	0	0	0	0.031(4)	1
N1	16 <i>l</i>	.. <i>m</i>	0.6401(6)	0.1401(6)	0.1503(4)	0.0077(13)	1

The deviation of the total lattice energies (Table D.5) of Ho₃[PN₄]O and its decomposition constituents is 0.17 %, which is an excellent electrostatic consistency. The partial MAPLE values found for the N1 (5256 kJ/mol) and O1 (1971 kJ/mol) positions are consistent with reference values and indicate a correct O/N assignment (Table D.5).^[26,27] The validity of this approach has been shown for nitridosilicates with the aid of neutron diffraction.^[26,28,29]

4.2.3 Structure Description

As mentioned above, Ho₃[PN₄]O crystallizes in the tetragonal body-centered antiperovskite structure type with space group *I4/mcm*, in analogy with Gd[SiN₃O]O.^[12] The structure is displayed in Figure 4.3 in the antiperovskite depiction with corner-sharing OHo₆ octahedra. The PN₄ tetrahedra reside on the A site of a regular ABX₃ perovskite, forming concomitant with the Ho atoms (X site) a face-centered-cubic packing, whereas the O atoms occupy 1/4 of the octahedral voids (B sites). The corner-sharing OHo₆ octahedra are skewed by 16.57(4)° around the *c* axis with respect to the unit-cell alignment and by 56.85(7)° with respect to one another. The distortion might be due to the mismatched sizes of the ions on the basis of the Goldschmidt tolerance factor. This assumption seems reasonable considering that the mentioned isostructural K₃[SO₄]F undergoes a displacive phase transition to a cubic polymorph at elevated temperatures.^[6] Moreover, the electrostatic repulsion of P⁵⁺ ions and the surrounding twelve Ho³⁺ ions might be the cause for the displacive twisting distortion of the octahedra, which otherwise could enter a cubic arrangement. Additionally, the orientation of the tetrahedra was mentioned as a cause of distortion in M₃[TO₄]X materials.^[6,7] Symmetry reduction from the archetypical perovskite in space group *Pm3m* (no. 221) to space group *I4/mcm* of Ho₃[PN₄]O has been stated before and involves a *k2* transition to *Fm3c* (no. 226) with a subsequent *t3* transition to *I4/mcm*.^[12]

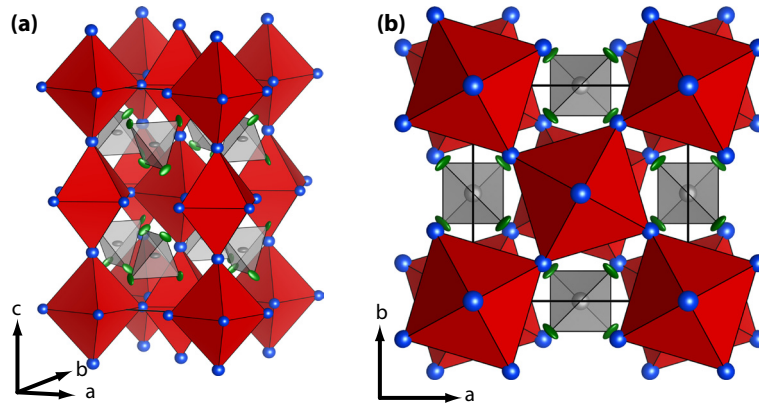


Figure 4.3. (a) Side view on the unit cell of Ho₃[PN₄]O and (b) projection along *c*. The Ho atoms are displayed in blue, P atoms are gray, and N atoms are green. The oxygen atoms are at the centers of the red-faced octahedra, and the PN₄ tetrahedra are displayed with translucent gray faces. The displacement ellipsoids of all atoms are set to a probability of 95 %.

The OHo₆ octahedra, displayed in Figure 4.4a, are elongated along the *c* axis with Ho–O distances of $d(\text{Ho}2\text{--O}1) = 2.347(1) \text{ \AA}$ in the equatorial direction and $d(\text{Ho}1\text{--O}1) = 2.639(1) \text{ \AA}$ in axial direction. Typical Ho–O distances, such as those in cubic Ho₂O₃, are slightly shorter at 2.227 Å.^[24] The elongation may stem from electrostatic repulsion between the highly charged Ho³⁺ ions. As a consequence, the central O atom is liberated to thermal motion parallel to *c*. Strongly anisotropic O displacement has also been observed in the OGd₆ octahedra of Gd[SiN₃O]O, for which the room-temperature single-crystal data indicated dynamic disorder, and a crystallographic splitting was resolved at 123 K.^[12] Such splitting of the O position from room- and low-temperature (123 K) powder diffraction data was not possible (see Thermal Properties section). Moreover, DFT calculations with symmetry restrictions omitted and starting from the refined model did not converge in a distorted structure but retained the original one.

As mentioned above, only one other instance of isolated PN₄ tetrahedra, namely Li₇PN₄, is known.^[4] The high negative formal charge of the PN₄⁷⁻ unit permits the implementation of trivalent cations in the M₃[TX₄]Y family, whereas the electrostatic limit in oxides, for example, Ba₃[SiO₄]O, is divalent cations.^[7,13] The P1–N1 bond lengths in the PN₄ tetrahedron (Figure 4.4b) of 1.642(4) Å is comparable to the values found in other rare-earth nitridophosphates, for example, LiNdP₄N₈ [$d(\text{P--N}) = 1.61\text{--}1.65 \text{ \AA}$] and Ho₂P₃N₇ [$d(\text{P--N}) = 1.57\text{--}1.68 \text{ \AA}$], and slightly shorter than that in Li₇PN₄ [$d(\text{P--N}) = 1.69\text{--}1.73 \text{ \AA}$].^[1,2,4] The PN₄ tetrahedron resides in a cuboctahedron of Ho atoms, which is distorted

by the skewing of the octahedra. This is expressed in the Ho–P distances, which range from 3.076(1) to 3.935(1) Å.

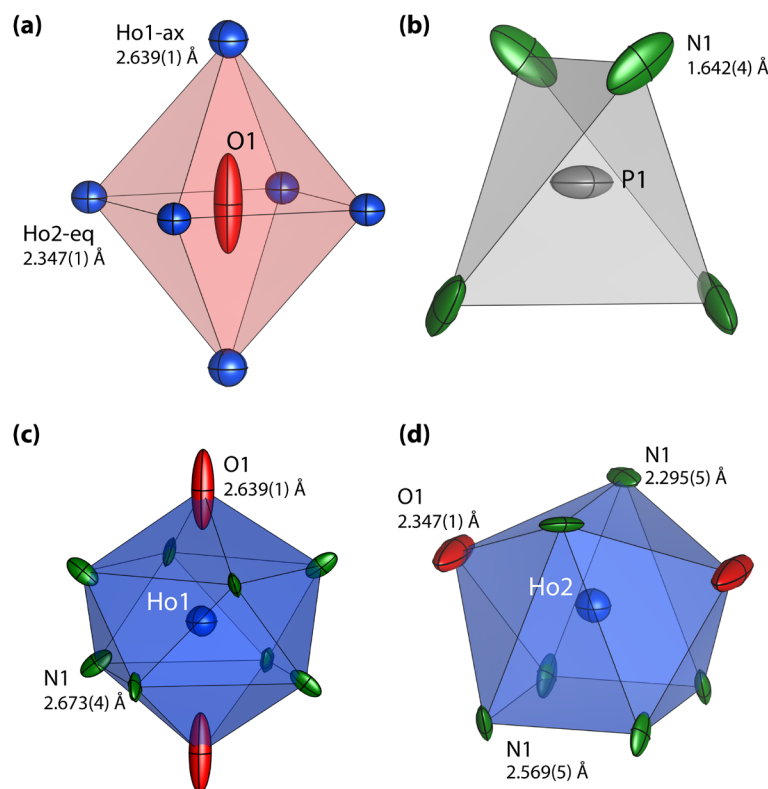


Figure 4.4. Coordination polyhedra of (a) O1, (b) P1, (c) Ho1, and (d) Ho2. Ho atoms are displayed in blue, P atoms are gray, O atoms are red, and N atoms are green. All of the atoms are displayed with their respective anisotropic displacement parameters with 95% probability. O1 is coordinated octahedrally by Ho, and P1 is coordinated tetrahedrally by N. Ho1 is surrounded by a gyroelongated square bipyramid of N and O atoms, whereas Ho2 is coordinated in a biaugmented trigonal prism.

Ho1 and Ho2 are coordinated in a HoN_8O_2 gyroelongated square bipyramid and a HoN_6O_2 biaugmented trigonal prism (Figure 4.4c–d), which correspond to the Johnson solids J_{17} and J_{50} , respectively.^[30] The gyroelongated square bipyramid can be derived from the gyroelongation of an octahedron or by capping a square antiprism. It belongs to the subgroup of deltahedra, which are polyhedra constructed solely from equilateral triangles. The vertex symbol^[31] of J_{17} is $(3^4)_2(3^5)_8$ with two kinds of vertices; the N atoms occupy the eight (3^5) (square antiprism) vertices, the O atoms occupy both (3^4) vertices (the augmentations), and J_{17} has a total of two times eight triangular faces. The holoedry of a gyroelongated square bipyramid with regular polygons as faces is D_{4d} in Schönflies notation; however, this is noncrystallographic because of an eightfold roto-reflection parallel to c . In the

HoN₈O₂ deltahedra, the symmetry is reduced as all of the triangles are distorted and not equilateral and, thus, preempt the roto-reflection and dihedral reflection planes. The resulting point group is D_4 or 422 in Hermann–Mauguin notation.

A biaugmented trigonal antiprism comprises one square face and ten triangular faces arranged in vertex symbol $(3^5)_2(3^4)_2(3^3.4)_4$, in which O atoms occupy both (3^4) vertices (the augmentations). J_{50} has crystallographic point group C_{2v} ($mm2$), which is also true for the HoN₆O₂ polyhedra and is reflected in the $m.2m$ site symmetry of Ho2. However, the HoN₆O₂ polyhedra have irregular (non-equilateral) faces, indicative of a symmetry-abiding distortion.

The Ho–O/N bond lengths differ significantly for the Ho1 and Ho2 coordination spheres, which can be explained by the coordination numbers [CNs; CN(Ho1) = 10 and CN(Ho2) = 8]. As Ho1 is coordinated by ten anions, the Ho1–O/N distances [$d(\text{Ho1–O/N}) = 2.639\text{--}2.673 \text{ \AA}$] are larger than those in the Ho2 coordination polyhedra with CN = 8 [$d(\text{Ho2–O/N}) = 2.259\text{--}2.569 \text{ \AA}$]. The mean bond lengths for the Ho2 biaugmented trigonal prism [$d_o(\text{Ho2–O/N}) = 2.445 \text{ \AA}$] are in the range of values found in the square-antiprismatic HoN₈ polyhedra of Ho₂P₃N₇ [$d(\text{Ho–N}) = 2.340\text{--}2.729 \text{ \AA}$, $d_o(\text{Ho–N}) = 2.492 \text{ \AA}$].^[2]

4.2.4 Optical Properties

UV/Vis Spectroscopy

The optical absorption of Ho³⁺ ions in an inorganic matrix or in solution is well known, and the emerging absorption bands have been assigned to the corresponding electronic transitions.^[32] As the 4f states of rare-earth ions are scarcely influenced by the surrounding ligand field, the absorption bands shift negligibly from the energies of a free ion.^[32,33] Therefore, the observed electronic transitions in Figure 4.5 can be assigned to the literature-known Russel–Saunders terms. The ground state of the Ho³⁺ ion with electron configuration [Xe]4f¹⁰, which is retained for all transitions, is ⁵I₈ in accordance with Hund's rules. The strong transition visible at $\lambda \approx 650 \text{ nm}$ arises from the ⁵I₈ → ⁵F₅ excitation, whereas that at $\lambda \approx 540 \text{ nm}$ corresponds to a superposition of ⁵I₈ → ⁵S₂ and ⁵I₈ → ⁵F₄.^[32,33] The latter transitions are responsible for the alexandrite effect observed in Ho-containing materials.^[34] The LaPO₄:Tb³⁺,Ce³⁺ phosphor in fluorescent lamps has a narrow emission band in the green part of the visible spectrum at $\lambda = 540 \text{ nm}$, at which Ho³⁺ ions absorb strongly.^[35] Thus, Ho³⁺-containing com-

pounds appear pink under fluorescent lamps and pale yellow under black-body radiation. The third strong absorption band at $\lambda = 453$ nm is due to the ${}^5I_8 \rightarrow {}^5G_6$ and possibly the ${}^5I_8 \rightarrow {}^5F_1$ excitations, which have similar energies and are not resolved. The weaker transitions are assigned in Figure 4.5. The reflectance spectrum is a superposition of the f-electron excitations of Ho^{3+} ions and valence band to conduction band transitions, as evidenced by the increasing absorption at $\lambda \approx 400$ nm.

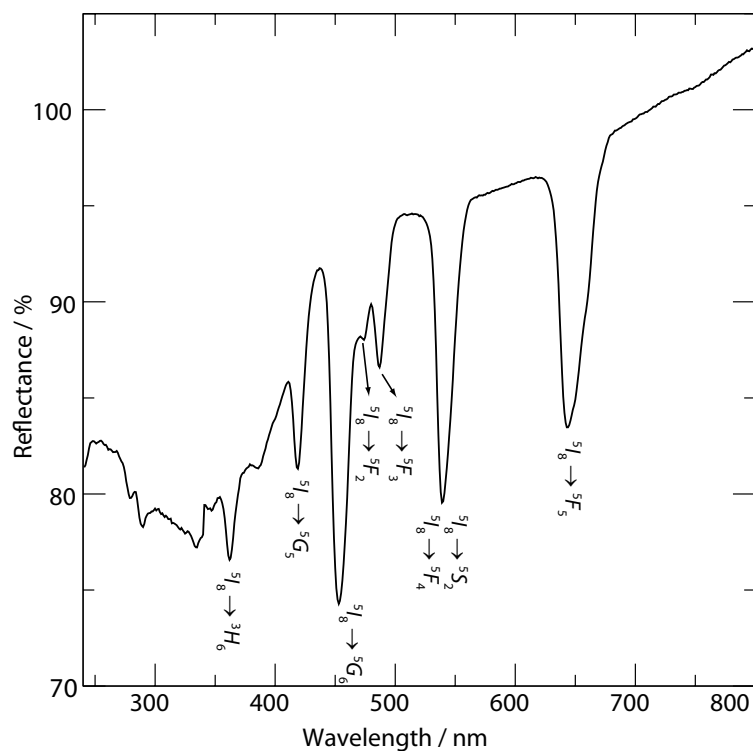


Figure 4.5. UV/Vis spectrum of $\text{Ho}_3[\text{PN}_4]\text{O}$ recorded from $\lambda = 240$ to 800 nm in reflection geometry.

Infrared and Raman Spectroscopy

Vibrational spectroscopy studies of orthophosphates in solid matrices and in aqueous solution have been reported previously, and the spectra should be similar to those of orthonitridophosphates, as all of the possible vibrational modes of the tetrahedron are retained after the O/N substitution.^[36,37] Jastrzebski et al. pointed out that isolated PO_4^{3-} ions with T_d symmetry have four types of vibrations, namely, symmetric (A_1) and asymmetric [$F_2^{(2)}$] stretching of the P–O bonds and scissor (E) and bending deformation [$F_2^{(1)}$] of O–P–O fragments, all of which are Raman-active and two are IR-active [$F_2^{(1)}$ and $F_2^{(2)}$].^[37] The same vibrations should be visible for isolated PN_4 tetrahedra. The Raman and IR spectra of $\text{Ho}_3[\text{PN}_4]\text{O}$ (displayed in juxtaposition in Figure 4.6) were recorded in the ranges $\tilde{\nu} = 3500$

to 50 and 4000–600 cm⁻¹, respectively. In the IR spectrum, the asymmetric stretching vibration is located at $\tilde{\nu} \approx 925$ cm⁻¹. Similarly to crystalline K₃PO₄ hydrate, the magnification reveals that this vibration is split into two bands at $\tilde{\nu} = 906$ and 930 cm⁻¹.^[37] This is a result of the crystal field, which distorts the PN₄ tetrahedra and reduces the symmetry from tetrahedral point group T_d to D_{2d} . The asymmetric vibration is excited at a lower energy than that observed for crystalline K₃PO₄ hydrate ($\tilde{\nu} = 1006$ and 1037 cm⁻¹).^[37] The band position is influenced by the crystal field but also by the bond strength. A P–N bond in a nitridophosphate is expected to be weaker than a P–O bond in a phosphate, as P–N bonds are usually longer [e.g., LiNdP₄N₈ $d(\text{P–N}) = 1.61\text{--}1.65$ Å, Al(PO₄) $d(\text{P–O}) = 1.51\text{--}1.52$ Å].^[1,38] The two strong Raman bands at $\tilde{\nu} = 943$ and 883 cm⁻¹ can be assigned to the asymmetric and symmetric P–N bond stretching vibrations, respectively. The two other Raman-active modes cannot be discerned from the spectra because of contributions of the amorphous side phase.

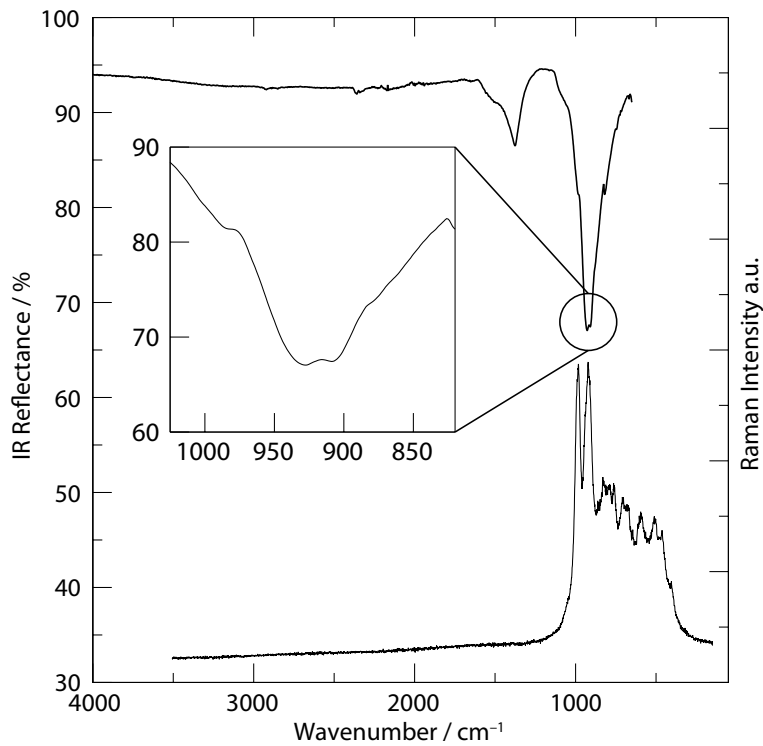


Figure 4.6. IR (top) and Raman (bottom) spectra of Ho₃[PN₄]O recorded in the ranges $\tilde{\nu} = 600$ to 4000 and 50 to 3500 cm⁻¹. The magnified region of the IR spectrum from $\tilde{\nu} = 820$ to 1025 cm⁻¹ displays the asymmetric stretching vibration of the PN₄ tetrahedron.

Similarly, the second visible band in the IR spectrum at $\tilde{\nu} = 1375$ cm⁻¹ cannot be attributed to PN₄ tetrahedral vibrations and, thus, stems either from lattice vibrations or the amorphous side phase. The

absence of vibration modes in the $\tilde{\nu} = 3000$ to 4000 cm^{-1} range in the IR and Raman spectra indicates that no H is present in the sample.

4.2.5 Thermal Properties

High-Temperature Stability

The thermal stability of $\text{Ho}_3[\text{PN}_4]\text{O}$ was examined by high-temperature X-ray powder diffraction (HTXRD). The data were obtained at temperature increments of 20 K, and a full powder pattern was recorded at each temperature up to $1000 \text{ }^\circ\text{C}$ (Figure D.1). At $800 \text{ }^\circ\text{C}$, the degradation of $\text{Ho}_3[\text{PN}_4]\text{O}$ begins, as indicated by diminishing reflection intensities, and the reflections of an unidentified product emerge; however, these reflections are not retained upon cooling to room temperature and could not be attributed to a cubic $\text{Ho}_3[\text{PN}_4]\text{O}$ phase. The stability of $\text{Ho}_3[\text{PN}_4]\text{O}$ is remarkable compared with that of the other orthonitridophosphate, Li_7PN_4 , which decomposes in air or above $650 \text{ }^\circ\text{C}$ under inert conditions.^[4]

Low-Temperature Behavior

An X-ray powder diffraction pattern was collected at 123 K to investigate the highly anisotropic O displacement ellipsoid (Figure D.1 and Table D.5). However, no anisotropic splitting of the O position could be detected in the difference Fourier map. This is either due to the absence of such splitting at 123 K or the insufficient resolution of the collected powder pattern (collected in the same 2θ range as that for the room-temperature diffractogram). Detailed investigations of such splitting would require single-crystal data. The unit-cell parameters decreased slightly by 0.2% in the a direction and 0.05% in the c direction, as expected from normal thermal expansion behavior.

The respective thermal expansion coefficients are $\alpha_a = 1.097 \times 10^{-5} \text{ K}^{-1}$ and $\alpha_c = 0.285 \times 10^{-5} \text{ K}^{-1}$.

4.2.6 Magnetic Properties

The magnetic properties of $\text{Ho}_3[\text{PN}_4]\text{O}$ stem from the open-shell configuration of the Ho^{3+} ion with four unpaired electrons. The electronic ground state $^5\text{I}_8$ is in accordance with Hund's rules, and the resulting theoretical effective magnetic moment, incorporating spin-orbit coupling, of the Ho^{3+} ions is $\mu_{\text{eff}} = 10.61 \mu_{\text{B}}$. The magnetic susceptibility of the sample was measured between 3.3 and 300 K at a

constant field of 2 T (Figure 4.7), and the results reveal paramagnetic behavior down to low temperatures.

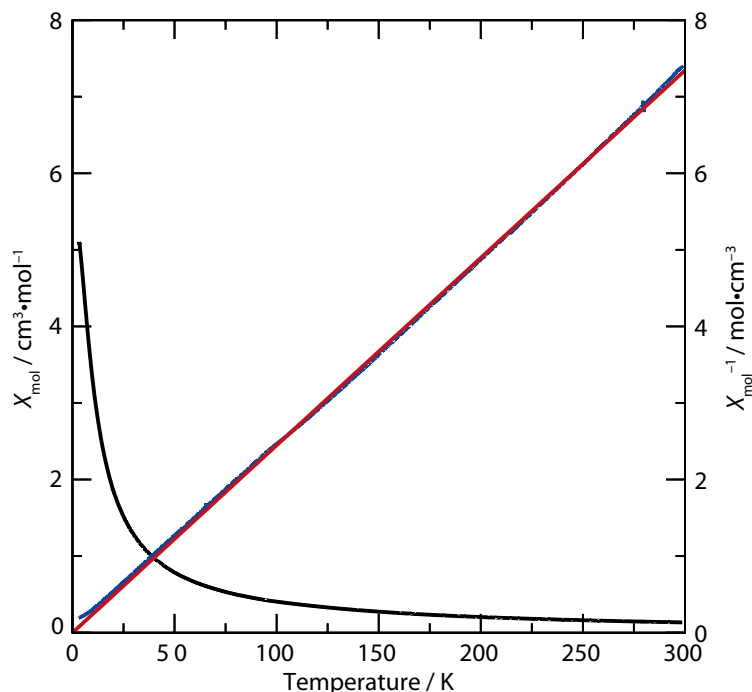


Figure 4.7. Magnetic susceptibility of Ho₃[PN₄]O recorded from 3.3 to 300 K at a field of 2 T. The black line represents the data displayed as χ_{mol} versus T , and the blue line represents χ_{mol}^{-1} versus T . A Curie–Weiss fit (red line) was performed for the χ_{mol}^{-1} versus T data.

The inverse molar susceptibility χ_{mol}^{-1} was used to perform a Curie–Weiss fit of the data in the region from 50 to 300 K. As the sample contained an amorphous side phase, the Ho content was determined by ICP-OES (Table D.1). The μ_{eff} value of 10.43(1) μ_{B} obtained from the fit coincides well with the theoretical value. The Curie temperature Θ of 0.11(4) K is close to the expected value of 0 for a paramagnetic substance. The data diverge from the fit at low temperatures, which can be explained by weak antiferromagnetic coupling.

4.2.7 DFT Calculations

The electronic structure of Ho₃[PN₄]O was determined through DFT calculations with the GGA-PBE functional. The bond lengths of the structural model obtained after the initial ionic relaxation differ from those of the X-ray diffraction model by a maximum of 0.01 Å. This indicates a successful relaxation and correct O/N assignment. The band structure and density of states (DOS) of the valence

and conduction bands near the Fermi energy E_F is displayed in Figure 4.8. E_F was set to zero to match the highest energy of the valence-band states. The conduction-band minimum and valence-band maximum are located at the Γ point and within the X–N path of the first Brillouin zone to form an indirect band gap with $E_{\text{gap}} = 1.87$ eV. This value is expected to be smaller than the actual band gap of the material, as E_{gap} is usually underestimated by DFT calculations within the generalized gradient approximation (GGA).^[39] Moreover, the material is optically transparent, which is indicative of a larger band gap. However, the pathways of the band do not change, and the band structure yields information about the orbital contributions of the individual atom types to the electronic structure. As is evident from the partial DOS, the N 2p orbitals contribute substantially to the valence band. The configuration of the Ho^{3+} ion predicts empty 5d, 6s, and 6p shells, which are populated to some extent here and add to the valence band through overlap with the O and N 2p orbitals. The conduction band is dominated by empty bands arising from the Ho 5d orbitals, as expected as the structure consists mostly of Ho^{3+} ions.

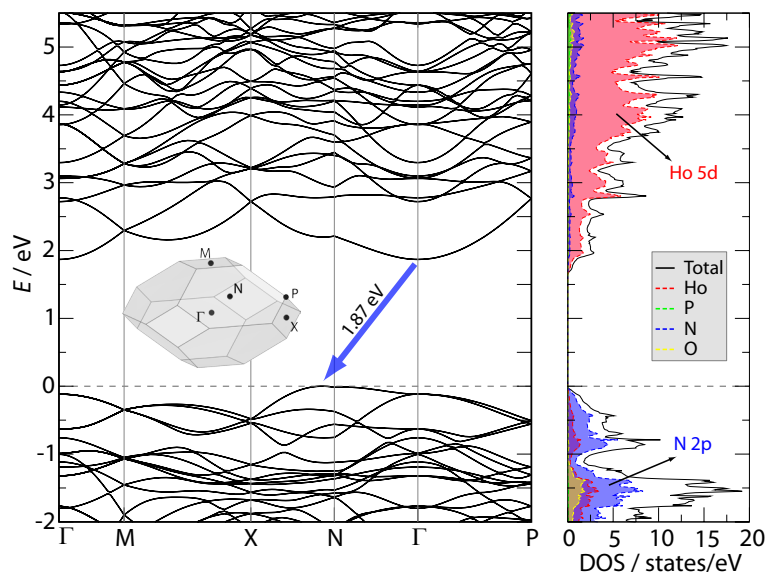


Figure 4.8. DFT calculations on $\text{Ho}_3[\text{PN}_4]\text{O}$. Displayed is the band structure (left) of $\text{Ho}_3[\text{PN}_4]\text{O}$ in the energy region from -2 to 5.5 eV around E_F along a Brillouin zone path of high-symmetry points. The indirect band gap of 1.87 eV is indicated by an arrow. The DOS and partial DOS (right) are displayed as solid and dashed lines, respectively, and the area under the partial DOS is filled in. E_F is indicated by a gray dashed line.

4.3 Conclusions

The orthonitridophosphate oxide Ho₃[PN₄]O has been prepared by solid-state high-pressure metathesis with the multianvil technique. Ho₃[PN₄]O adds to the existing family of M₃[TX₄]O structures and exhibits the rarely observed isolated PN₄ tetrahedron. Thus, the adaptability of the P/N atomic ratio by high-pressure metathesis has been expanded to the low end of P/N = 1/4, and this opens the pathway to a large spectrum of new rare-earth nitridophosphates.

The antiperovskite structure of Ho₃[PN₄]O has been refined on the basis of powder diffraction data. Ho₃[PN₄]O exhibits paramagnetic behavior down to low temperatures, absorbs visible light in the fashion of free Ho³⁺ ions, and has vibrations corresponding to distorted PN₄ tetrahedra. The O/N assignment was based on MAPLE calculations, which were corroborated by DFT calculations.

4.4 Experimental Section

4.4.1 Synthesis of P_3N_5

P_3N_5 was prepared through the reaction of P_4S_{10} (Sigma–Aldrich 99.99 %) with a constant flow of ammonia gas (Air Liquide 5.0) in a tube furnace lined with a fused silica tube.^[40] The fused silica tube, containing a fused silica boat, was dried at 1000 °C for 4 h under reduced pressure ($<10^{-3}$ mbar). To prevent clogging of the tubing by volatile sublimated byproducts, a limited amount of P_3N_5 was loaded into the fused silica boat under an Ar counterflow. The tubing was saturated with ammonia gas for 4 h, after which the starting material was fired at 850 °C for 4 h. The temperature ramp for heating and cooling was 5 °C/min. After the system reached room temperature again, the residual ammonia was flushed with Ar. The obtained orange P_3N_5 was washed with water/ethanol/acetone and characterized by X-ray powder diffraction and FTIR spectroscopy.^[41]

4.4.2 Synthesis of $LiPN_2$

$LiPN_2$ was prepared through the reaction of P_3N_5 and a 1.2 times excess of Li_3N (Rockwood Lithium, 94 %) in a Ta crucible. The starting materials were mixed thoroughly and ground under inert conditions in an Ar-filled glovebox (Unilab, MBraun, Germany). The Ta crucible was placed in a fused silica ampoule and dried before the reaction mixture was conveyed into the crucible under Ar counterflow. The ampoule was sealed and fired in a tube furnace at 800 °C for 96 h with a temperature ramp of 5 °C/min. The obtained brownish powder was washed with dilute hydrochloric acid/water/ethanol and characterized by X-ray powder diffraction and FTIR spectroscopy.^[42]

4.4.3 Synthesis of Li_2O

Li_2O was prepared by the thermal decarboxylation of Li_2CO_3 .^[43] Li_2CO_3 (Sigma–Aldrich 99.99 %) was ground and filled in a Ag boat, which was placed in a quartz tube. The quartz tube, residing in a tube furnace, was connected to a Schlenk line with Ar and vacuum valves. The decarboxylation was performed under reduced pressure ($<10^{-3}$ mbar) and at 725 °C for 100 h or until the reaction finished. The colorless reaction product was stored under inert conditions in a glovebox and characterized by powder diffraction.^[43]

4.4.4 Synthesis of Ho₃[PN₄]O

Ho₃[PN₄]O was prepared by high-pressure metathesis from stoichiometric amounts of HoF₃ (chem-PUR 99.9%), Li₃N (Rockwood Lithium, 94%), LiPN₂, and Li₂O at ca. 1025 °C and 5 GPa. The starting materials were mixed and ground under inert conditions with H₂O and O₂ concentrations below 1 ppm. The temperature was attained over 120 min, maintained for 60 min, and decreased to room temperature over 80 min.

The reaction pressure was achieved with a hydraulic 1000 t press (Voggenreither, Mainleus, Germany) by the multianvil technique with a modified Walker-type module. A specially prepared Cr₂O₃-doped (6%) MgO octahedron (Ceramic Substrates & Components, Isle of Wight, UK) with 18 mm edge length served as the pressure medium. The h-BN crucible (Henze, Kempten, Germany) was placed inside the octahedron under inert conditions. Two cylindrical graphite sleeves (Schunk Kohlenstofftechnik GmbH, Gießen, Germany) were used for resistance heating. The uniaxial pressure of the hydraulic press was redirected onto the four axes of the Mg octahedron by eight Co-doped (7%) tungsten carbide cubes (Hawedia, Marklkofen, Germany) with truncated edges (11 mm). Further information regarding synthetic multianvil methods can be found in refs.^[44-48]

4.4.5 Spectroscopic Analysis

The SEM and EDX measurements were performed with a JEOL JSM 6500F microscope equipped with a field-emission electron source and an Oxford Instruments 7418 Si/Li EDX detector. The samples were carbon-sputtered with an electron-beam evaporator (BAL-TEC MED 020, Bal Tex AG) to avoid electrostatic charging.

The ICP-OES was performed with a Varian Vista RL instrument for the elements Ho, P, and Li.

The FTIR spectra were recorded in the wavenumber range 600–4000 cm⁻¹ with a Perkin–Elmer Spectrum BX II spectrometer with an attenuated total reflectance (ATR) attachment.

The Raman spectra were recorded with a confocal Raman microscope (LabRAM HG UV/Vis, Horiba Jobin Yvon GmbH, combined with a Olympus BX 41 microscope) equipped with a He–Ne laser with a 1 mm focus and a CCD detector. The sample was contained in a glass capillary.

The UV/Vis spectra were recorded with an Edinburgh Photonics FLS920-s spectrometer equipped with a Xe900 450 W arc lamp, a single-photon photomultiplier detector, and a Czerny–Turner mono-

chromator with triple-grating turret. The spectra covered the wavelength range from 240 to 800 nm with a 5 nm step size.

4.4.6 Magnetometry

The magnetic susceptibility measurements were performed with a Cryogenic VSM 5T miniCFM magnetometer at a constant field of 2 T in the temperature range from 3.3 to 300 K. The sample was placed in a gelatine capsule with known diamagnetic properties.

4.4.7 Powder X-ray Diffraction

The powder X-ray diffraction pattern of a homogeneous sample with small crystallite sizes was recorded with a Stadi P diffractometer (Stoe, Darmstadt, Germany) in parafocusing Debye–Scherrer geometry equipped with a MYTHEN 1K silicon strip detector (Dectris, Baden, Switzerland; angular range $\Delta 2\theta = 12.5^\circ$). The Mo X-ray radiation was monochromated to Mo- $K_{\alpha 1}$ radiation by a Ge(111) single crystal. The samples were loaded in a glass capillary with 0.3 mm diameter and a wall thickness of 0.01 mm (Hilgenberg GmbH, Malsfeld, Germany). Indexing with the SVD-algorithm^[14] and Rietveld refinement^[18] of the diffractograms was performed with the TOPAS-Academic V4.1 software.^[15] The fundamental parameters approach (direct convolution of source emission profiles, axial instrument contributions, crystallite size, and microstrain effects) was used to model the peak shape function. The absorption was treated with a cylindrical correction to take into account the calculated absorption coefficient and the capillary diameter. Potential preferred orientation was handled with a fourth-order spherical harmonics model. The background was handled with a shifted Chebyshev function. The crystal structures were visualized with VESTA.^[49]

High-temperature powder diffraction was performed with a Stoe Stadi P diffractometer equipped with a graphite furnace and an image-plate position-sensitive detector. The employed Mo- $K_{\alpha 1}$ radiation was selected by a Ge(111) monochromator. The diffractograms were recorded at constant temperature in the range 25 to 1000 °C in steps of 20 K.

4.4.8 Computational Details

The electronic structure of Ho₃[PN₄]O was calculated by first-principles density functional theory (DFT)^[50] as implemented in the Vienna Ab Initio Simulation Package (VASP)^[51-54] within the generalized gradient approximation as parameterized by Perdew, Burke, and Ernzerhof (GGA-PBE).^[55,56] The projector augmented wave (PAW) method was used to model the electron–ion interactions.^[57,58] A kinetic energy cutoff of 535 eV was used for the expansion of the electronic wave functions in a plane-wave basis set. Initial ionic relaxation was performed by relaxing all internal coordinates and cell parameters. The first Brillouin zone was sampled on a dense γ -centered $8 \times 8 \times 5$ k -mesh obtained by the Monkhorst–Pack method.^[59] The energy convergence criterion of the electronic relaxation was set to 10^{-8} eV per unit cell, and the residual atomic forces were converged below 10^{-4} eV/Å. The DOS was obtained by integration over the first Brillouin zone, and the bands along the path Γ –M–X–N– Γ –P were calculated with 25 k -point spacing.

4.5 References

- [1] S. D. Kloß, W. Schnick, *Angew. Chem., Int. Ed.* **2015**, *54*, 11250–11253; *Angew. Chem.* **2015**, *127*, 11402–11405.
- [2] S. D. Kloß, N. Weidmann, R. Niklaus, W. Schnick, *Inorg. Chem.* **2016**, *55*, 9400–9409.
- [3] A. Marchuk, V. R. Celinski, J. Schmedt auf der Günne, W. Schnick, *Chem. - Eur. J.* **2015**, *21*, 5836–5842.
- [4] W. Schnick, J. Luecke, *J. Solid State Chem.* **1990**, *87*, 101–106.
- [5] A. Marchuk, P. Schultz, C. Hoch, O. Oeckler, W. Schnick, *Inorg. Chem.* **2016**, *55*, 974–982.
- [6] J. M. S. Skakle, J. G. Fletcher, A. R. West, *J. Chem. Soc., Dalton Trans.* **1996**, 2497–2501.
- [7] M. Mansmann, *Z. Anorg. Allg. Chem.* **1965**, *339*, 52–56.
- [8] W. Eysel, K. Breuer, *Z. Kristallogr. - Cryst. Mater.* **1983**, *163*, 1–18.
- [9] J. M. S. Skakle, J. G. Fletcher, A. R. West, *An. Quim. Int. Ed.* **1996**, *92*, 358–361.
- [10] T. Vogt, P. M. Woodward, B. A. Hunter, A. K. Prodjosantoso, B. J. Kennedy, *J. Solid State Chem.* **1999**, *144*, 228–231.
- [11] E. Tillmanns, H.-P. Grosse, *Acta Crystallogr., Sect. B: Struct. Crystallogr. Cryst. Chem.* **1978**, *34*, 649–651.
- [12] H. A. Höpfe, G. Kotzyba, R. Pöttgen, W. Schnick, *J. Solid State Chem.* **2002**, *167*, 393–401.
- [13] Further details on the crystal structure investigations may be obtained from the Fachinformationszentrum Karlsruhe, 76344 Eggenstein-Leopoldshafen, Germany (fax: (+49)7247–808–666; e-mail: @fiz-karlsruhe.de), on quoting the depository number CSD-432168.
- [14] A. A. Coelho, *J. Appl. Crystallogr.* **2003**, *36*, 86–95.
- [15] A. A. Coelho, *TOPAS-Academic V4.1*, Coelho Software, Brisbane, Australia, **2007**.
- [16] F. H. Allen in *Crystallographic Databases*, Eds.: G. Bergerhoff, I. Brown, *International Union of Crystallography*, Chester, **1987**.
- [17] A. Belsky, M. Hellenbrandt, V. L. Karen, P. Luksch, *Acta Crystallogr., Sect. B: Struct. Sci.* **2002**, *58*, 364–369.
- [18] H. M. Rietveld, *J. Appl. Crystallogr.* **1969**, *2*, 65–71.
- [19] H. M. Rietveld, *Z. Kristallogr. - Cryst. Mater.* **2010**, *225*, 545–547.
- [20] R. D. Shannon, *Acta Crystallogr., Sect. A: Cryst. Phys., Diffraction, Theor. Gen. Crystallogr.* **1976**, *32*,

- 751–767.
- [21] R. Hoppe, *Angew. Chem., Int. Ed. Engl.* **1966**, *5*, 95–106; *Angew. Chem.* **1966**, *78*, 52–63.
- [22] R. Hoppe, *Angew. Chem., Int. Ed. Engl.* **1970**, *9*, 25–34; *Angew. Chem.* **1970**, *82*, 7–16.
- [23] R. Hübenthal, *MAPLE, Programm zur Berechnung des Madelunganteils der Gitterenergie*, Vers. 4, University Giessen, Germany, **1993**.
- [24] H. Bommer, *Z. Anorg. Allg. Chem.* **1939**, *241*, 273–280.
- [25] W. Klemm, G. Winkelmann, *Z. Anorg. Allg. Chem.* **1956**, *288*, 87–90.
- [26] K. Köllisch, Dissertation, *Neue Beiträge Zur Strukturchemie Der Sione Und Sialone*, LMU Munich, Germany, **2001**.
- [27] H. Höpfe, Dissertation, *Optische, Magnetische Und Strukturelle Eigenschaften von Nitridosilicaten, Oxonitridosilicaten Und Carbidonitridosilicaten*, LMU Munich, Germany, **2003**.
- [28] R. Lauterbach, E. Irran, P. F. Henry, M. T. Weller, W. Schnick, *J. Mater. Chem.* **2000**, *10*, 1357–1364.
- [29] E. Irran, K. Köllisch, S. Leoni, R. Nesper, P. F. Henry, M. T. Weller, W. Schnick, *Chem. - Eur. J.* **2000**, *6*, 2714–2720.
- [30] N. W. Johnson, *Canad. J. Math.* **1966**, *18*, 169–200.
- [31] V. A. Blatov, M. O’Keeffe, D. M. Proserpio, *CrystEngComm.* **2010**, *12*, 44–48.
- [32] T. Som, B. Karmakar, *Spectrochim. Acta, Part A* **2011**, *79*, 1766–1782.
- [33] A. Kramida, Y. Ralchenko, J. Reader, NIST ASD Team, *NIST Atomic Spectra Database*, National Institute Of Standards And Technology, Gaithersburg, MD, USA, **2016**.
- [34] Y. Liu, J. Shigley, E. Fritsch, S. Hemphill, *Color Res. Appl.* **1994**, *19*, 186–191.
- [35] C. Feldmann, T. Jüstel, C. R. Ronda, P. J. Schmidt, *Adv. Funct. Mater.* **2003**, *13*, 511–516.
- [36] F. A. Miller, C. H. Wilkins, *Anal. Chem.* **1952**, *24*, 1253–1294.
- [37] W. Jastrzbski, M. Sitarz, M. Rokita, K. Bułat, *Spectrochim. Acta, Part A* **2011**, *79*, 722–727.
- [38] D. Schwarzenbach, *Z. Kristallogr.* **1966**, *123*, 161–185.
- [39] J. P. Perdew, *Int. J. Quantum Chem.* **1986**, *19*, 497–523.
- [40] A. Stock, H. Grüneberg, *Ber. Dtsch. Chem Ges.* **1907**, *40*, 2573–2578.
- [41] W. Schnick, J. Lücke, F. Krumeich, *Chem. Mater.* **1996**, *8*, 281–286.

- [42] W. Schnick, J. Lücke, *Z. Anorg. Allg. Chem.* **1990**, 588, 19–25.
- [43] E. Zintl, A. Harder, B. Dauth, *Z. Elektrochem. Angew. Phys. Chem.* **1934**, 40, 588–593.
- [44] H. Huppertz, *Z. Kristallogr.* **2004**, 219, 330–338.
- [45] N. Kawai, S. Endo, *Rev. Sci. Instrum.* **1970**, 41, 1178–1181.
- [46] D. C. Rubie, *Phase Transitions* **1999**, 68, 431–451.
- [47] D. Walker, *Am. Mineral.* **1991**, 76, 1092–1100.
- [48] D. Walker, M. A. Carpenter, C. M. Hitch, *Am. Mineral.* **1990**, 75, 1020–1028.
- [49] K. Momma, F. Izumi, *J. Appl. Crystallogr.* **2011**, 44, 1272–1276.
- [50] W. Kohn, L. J. Sham, *Phys. Rev.* **1965**, 140, 1133–1138.
- [51] G. Kresse, J. Hafner, *Phys. Rev. B* **1993**, 47, 558–561.
- [52] G. Kresse, J. Hafner, *Phys. Rev. B* **1994**, 49, 14251–14269.
- [53] G. Kresse, J. Furthmüller, *Mater. Sci.* **1996**, 6, 15–50.
- [54] G. Kresse, J. Furthmüller, *Phys. Rev. B* **1996**, 54, 11169–11186.
- [55] J. P. Perdew, K. Burke, M. Ernzerhof, *Phys. Rev. Lett.* **1996**, 77, 3865–3868.
- [56] J. P. Perdew, K. Burke, M. Ernzerhof, *Phys. Rev. Lett.* **1997**, 78, 1396.
- [57] G. Kresse, D. Joubert, *Phys. Rev. B* **1999**, 59, 1758–1775.
- [58] P. E. Blöchl, *Phys. Rev. B* **1994**, 50, 17953–17979.
- [59] H. J. Monkhorst, J. D. Pack, *Phys. Rev. B* **1976**, 13, 5188–5192.

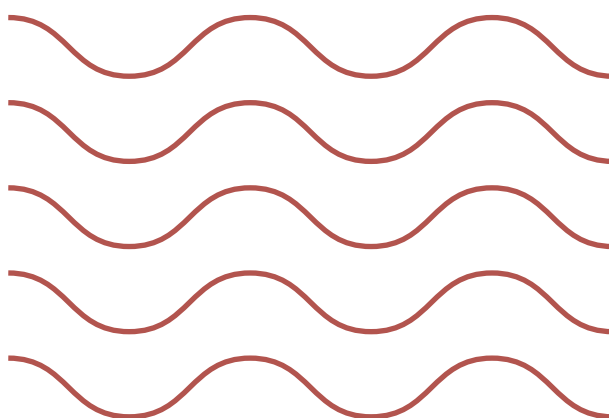
Chapter 5

Puzzling Intergrowth in Cerium Nitridophosphate Unraveled by Joint Venture of Aberration-Corrected Scanning Transmission Electron Microscopy and Synchrotron Diffraction

Simon D. Kloß, Lukas Neudert, Markus Döblinger, N. Nentwig, Oliver Oeckler, Wolfgang Schnick

published in: *J. Am. Chem. Soc.* **2017**, *139*, 12724–12735. DOI: 10.1021/Jacs.7b07075

Reprinted (adapted) with permission from *Journal of the American Chemical Society*. Copyright 2017 American Chemical Society.



The compound $\text{Ce}_{4-0.5x}\text{Li}_3\text{P}_{18}\text{N}_{35-1.5x}\text{O}_{1.5x}$ ($x \approx 0.72$) is the first higher-condensed rare-earth nitridophosphate and incorporated triply bridging N atoms. High-pressure metathesis can thus be used for the preparation of nitridophosphates over a large range of degrees of condensation. The structural elucidation of $\text{Ce}_{4-0.5x}\text{Li}_3\text{P}_{18}\text{N}_{35-1.5x}\text{O}_{1.5x}$ ($x \approx 0.72$) required a joint venture of synchrotron diffraction and aberration-corrected scanning transmission electron microscopy due to the occurrence of two slightly different domains, one of which featuring a modulated superstructure.

Abstract

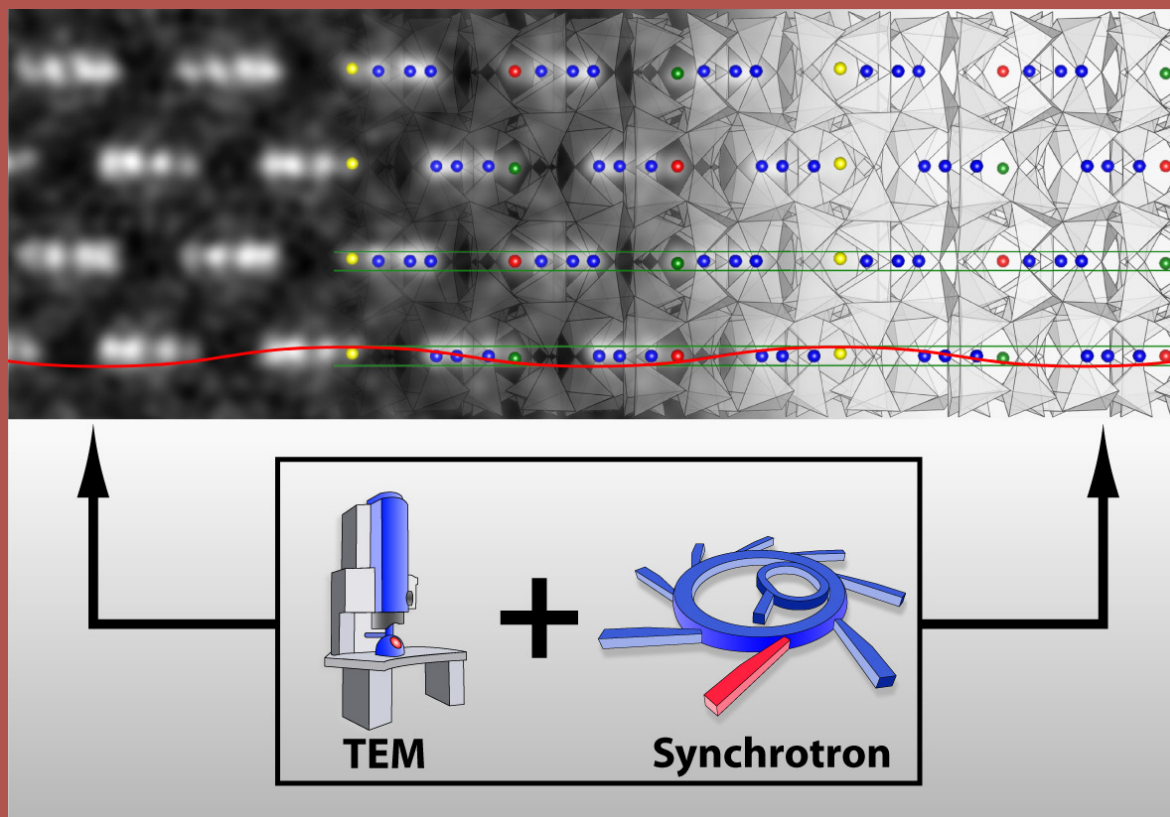


Table-of-contents graphic.

Thorough investigation of nitridophosphates has rapidly accelerated through development of new synthesis strategies. Here we used the recently developed high-pressure metathesis to prepare the first rare-earth metal nitridophosphate, $\text{Ce}_4\text{Li}_3\text{P}_{18}\text{N}_{35}$, with a high degree of condensation $>1/2$. $\text{Ce}_4\text{Li}_3\text{P}_{18}\text{N}_{35}$ consists of an unprecedented hexagonal framework of PN_4 tetrahedra and exhibits blue luminescence peaking at 455 nm. Transmission electron microscopy (TEM) revealed two intergrown domains with slight structural and compositional variations. One domain type shows extremely weak superstructure phenomena revealed by atomic-resolution scanning TEM (STEM) and single-crystal diffraction using synchrotron radiation. The corresponding superstructure involves a modulated displacement of Ce atoms in channels of six-membered tetrahedra rings. The displacement model was refined in a supercell as well as in an equivalent commensurate $(3 + 2)$ -dimensional description in superspace group $P6_3(\alpha, \beta, 0)0(-\alpha - \beta, \alpha, 0)0$. In the second domain type, STEM revealed disordered vacancies of the same Ce atoms that were modulated in the first domain type, leading to sum formula $\text{Ce}_{4-0.5x}\text{Li}_3\text{P}_{18}\text{N}_{35-1.5x}\text{O}_{1.5x}$ ($x \approx 0.72$) of the average structure. The examination of these structural intricacies may indicate the detection limit of synchrotron diffraction and TEM. We discuss the occurrence of either Ce displacements or Ce vacancies that induce the incorporation of O as necessary stabilization of the crystal structure.

5.1 Introduction

The yet little explored nitridophosphates, however, which are derived from silicates by isoelectronic substitution of Si–O by P–N bonds, have shown promising developments. Thorough investigation of first and second main group element nitridophosphates revealed several dozens of structures, some as straightforward as the single-chain comprising Ca₂PN₃, and some complex as zeolitic Ba₃P₅N₁₀Br:Eu²⁺ and nitride imide clathrate P₄N₄(NH)₄(NH₃).^[4-6] The last two were discussed for their potential application as a warm-white emitting phosphor for solid-state lighting and as a gas storage material, respectively.^[5,7] Moreover, distinct structural building blocks such as triply bridging N atoms, edge-sharing tetrahedra, and pentacoordinated P prove that structural diversity is, in theory, no impediment in rivaling silicates.^[8-10] Still, a sincere competition for diversity necessitates a comparable number of structure types and size of composition space.

Recently, the latter was extended by accessing rare-earth nitridophosphates through an adaptive high-pressure metathesis route.^[11] In high-pressure metathesis rare-earth halides are reacted with alkali-metal-containing nitridophosphates such as LiPN₂ to yield the desired rare-earth nitridophosphate and an alkali metal halide under pressures of several gigapascal (GPa).^[11] It effectively circumvents the use of thermodynamically stable and unreactive starting materials like rare-earth nitrides and prevents the formation of phosphides, which can result from the reductive environment created by nitride ions. LiNdP₄N₈, two Ln₂P₃N₇ polymorphs, and the nitridophosphate oxide Ho₃[PN₄]O were already identified, all crystallizing in silicate-analogous structures.^[11-13]

Formal oxidation states limit the attainable degree of condensation, κ (ratio of tetrahedra centers to tetrahedra corners per sum formula), of a material family; while the minimum κ in all tetrahedra-based structures is 1/4, oxosilicates have a maximum κ of 1/2 (SiO₂) and nitridophosphates one of 3/5 (P₃N₅).^[14] High-pressure metathesis reliably produced rare-earth metal nitridophosphates with $\kappa = 1/4-1/2$, while higher condensed structures have remained unobserved.^[12,13] The latter also have never been realized in oxosilicates because they would lead to cationic SiO₂ frameworks. In nitridophosphates higher condensed frameworks intrigue with structural motifs like triply bridging N and edge-sharing tetrahedra. Currently, the alkali metal nitridophosphates MP₄N₇ and M₃P₆N₁₁ (*M* = Na–Cs) are the only reported cases of such frameworks comprising metal ions.^[15-18] Hence, closing the gap between $\kappa = 1/2$ and 3/5 in rare-earth nitridophosphates is likely to uncover unprecedented

tetrahedra networks. Such compounds feature rigid frameworks of all-side vertex-sharing tetrahedra, making them, for example, promising candidates as host lattices for inorganic solid-state lighting.^[19]

The diversity of three-dimensional frameworks is, in theory, infinite,^[20] and a general task of modern synthetic chemistry is to combine new structural motifs and complex elemental compositions in order to realize increasingly sophisticated materials. But as the materials become more numerous, structure elucidation frequently encounters various challenges including microcrystalline heterogeneous samples, pseudosymmetry, and weak superstructures.^[21-23] Through technological advances, methods for solving these latter problems like aberration-corrected transmission electron microscopy (TEM), application of third generation synchrotrons, and refractive X-ray lenses producing microfocused beams for X-ray diffraction became available.^[24-27] Atomic resolution *Z*-contrast scanning TEM (STEM) now enables the direct observation of vacancies or superstructures to derive atom positions and first structure models.^[28-31]

Pushing TEM and synchrotron diffraction to their detection limits became necessary in the structure determination of here presented $\text{Ce}_4\text{Li}_3\text{P}_{18}\text{N}_{35}$, which is the first higher condensed ($\kappa = 0.514$) rare-earth metal nitridophosphate. $\text{Ce}_4\text{Li}_3\text{P}_{18}\text{N}_{35}$, which consists of a framework of all-side vertex-sharing PN_4 tetrahedra, was prepared following the high-pressure metathesis route. The microstructure of $\text{Ce}_4\text{Li}_3\text{P}_{18}\text{N}_{35}$ consists of two slightly different types of domains, one with randomly distributed Ce vacancies and one in which the Ce atoms enter a long-range ordered superstructure correlated to decreased O content. The elucidation of this superstructure was achieved by combined efforts of atomic-resolution STEM and synchrotron diffraction with a PILATUS pixel detector.^[32-34] Owing to the Ce vacancies, the average structure has the sum formula $\text{Ce}_{4-0.5x}\text{Li}_3\text{P}_{18}\text{N}_{35-1.5x}\text{O}_{1.5x}$ ($x \approx 0.72$). Curiously, the compound encompasses blue Ce^{3+} luminescence and paramagnetism as determined with superconducting quantum interference device (SQUID) magnetometry.

5.2 Experimental Details

5.2.1 Preparation of P₃N₅

The binary starting material P₃N₅ was prepared by an adapted synthesis route according to Grüneberg.^[35] Phosphorus pentasulfide, P₄S₁₀ (Sigma-Aldrich, 99.99%), was reacted with constantly flowing NH₃ gas (Air Liquide, 5.0). A tube furnace equipped with a fused silica tube was dried together with a fused silica boat at 1000 °C for 4 h under reduced pressure of 10⁻³ mbar to exclude moisture and O₂. The fused silica boat was loaded in an Ar counterflow with a limited amount of P₄S₁₀ to prevent clogging of the tube by subliming byproducts. The tubing and the P₄S₁₀ were saturated by a constant flow of ammonia over the course of 4 h after which the material was fired at 850 °C for additional 4 h. Temperature ramps for heat-up and cool-down were set to 5 °C/min. P₃N₅ was obtained as an orange-brown powder, which was successively washed with water/ethanol/acetone and characterized with powder X-ray diffraction (PXRD) and Fourier transform infrared spectroscopy (FTIR).

5.2.2 Preparation of LiPN₂

Lithium nitridophosphate, LiPN₂, was prepared by solid state reaction of P₃N₅ with a 1.2-fold excess of Li₃N (Rockwood Lithium, 94%).^[36] Starting materials were mixed and thoroughly ground under the inert conditions of an Ar-filled glovebox (Unilab, MBraun, Garching, Germany) with partial pressures of O₂/H₂O < 1 ppm and then placed in a Ta crucible. The crucible was transferred to a dried fused silica tube under N₂ atmosphere, and the ampule was sealed and fired at 800 °C with 96 h dwell and 5 °C/min ramp times. The obtained light-brown powder was successively washed with diluted hydrochloric acid/water/ethanol and characterized by means of PXRD and FTIR spectroscopy.

5.2.3 Preparation of Ce_{4-0.5x}Li₃P₁₈N_{35-1.5x}O_{1.5x} (x ≈ 0.72)

Ce_{4-0.5x}Li₃P₁₈N_{35-1.5x}O_{1.5x} (x ≈ 0.72) was prepared by high-pressure metathesis, following Equation 5.1 (see below). CeF₃ (Alfa Aesar, 99.99%) and 4 equiv of LiPN₂ were reacted for 5 h at 1300 °C under a pressure of 5 GPa achieved with a 1000 ton hydraulic press (Voggenreiter, Mainleus, Germany) using a Walker-type module and the multianvil technique. A cylindrical and thick-walled hexagonal boron nitride (h-BN) crucible (Henze, Kempten, Germany) with outer diameter $d_{\text{outer}} = 3.67$ mm, inner diameter $d_{\text{inner}} = 2.00$ mm, outer length $l_{\text{outer}} = 6$ mm, inner length $l_{\text{inner}} = 5$, total volume $V_{\text{all}} =$

63 mm³, and sample volume $V_{\text{sample}} = 15 \text{ mm}^3$ was used and closed with a 1.5 mm thick h-BN lid. The temperature ramps were set to 120 min heat-up and cool-down. Starting materials were mixed and thoroughly ground in the Ar-filled glovebox. The sample-filled crucible was placed inside a Cr₂O₃-doped (6%) MgO octahedron with 18 mm edge-length (Ceramic Substrates & Components, Isle of Wight, U.K.). Co-doped (7%) tungsten carbide cubes (Hawedia, Marklkofen, Germany) with truncated edges (11 mm) were used as anvils to ensure quasi-hydrostatic pressure conditions. Additional information about the high-pressure multianvil technique can be found in literature.^[37-41] The product was obtained in the form of small colorless and transparent crystals. The sample was washed with H₂O to remove byproduct LiF.

5.2.4 Spectroscopic Analysis

Morphology and elemental composition were examined with a JEOL JSM 6500F scanning electron microscope (SEM) equipped with a field-emission electron source and an Oxford Instruments 7418 Si/Li energy dispersive X-ray (EDX) detector. The sample was coated (BAL-TEC MED 020, BalTec AG) with carbon to reduce electrical charging of the insulating material. Details of the results of the analysis can be found in the article and the Supporting Information.

FTIR spectra were recorded on a Spectrum BX II spectrometer (PerkinElmer, Waltham MA, USA) with ATR setup in the range of 600–4000 cm⁻¹. Details of the results of the analysis can be found in the article.

Inductively coupled plasma optical emission spectroscopy (ICP-OES) was carried out with a Varian Vista RL instrument for Ce, P, and Li. Details of the results of the analysis can be found in the article.

5.2.5 Magnetometry

Magnetic measurements were performed with a MPM-XL SQUID magnetometer (Quantum Design, San Diego, USA). Magnetic susceptibility was measured at a constant magnetic field of $M = 20 \text{ kOe}$, in the range of 1.8 to 300 K. The sample was placed inside gelatin capsules of known diamagnetic properties.

5.2.6 Powder X-ray Diffraction

PXRD was recorded on powdered Ce_{4-0.5x}Li₃P₁₈N_{35-1.5x}O_{1.5x} ($x \approx 0.72$) samples using a Stadi P diffractometer (Stoe & Cie GmbH, Darmstadt, Germany) in modified Debye–Scherrer geometry equipped with a MYTHEN 1K silicon strip detector (Dectris, Baden, Switzerland; angular range $\Delta 2\theta = 12.5^\circ$) and Mo K α 1 radiation ($\lambda = 0.7093 \text{ \AA}$, Ge(111) monochromator). The samples were filled into glass capillaries with 0.5 mm diameter and ~ 0.01 mm wall thickness. Data were collected in the range of $2^\circ \leq 2\theta \leq 76^\circ$, and the average structural model of Ce_{4-0.5x}Li₃P₁₈N_{35-1.5x}O_{1.5x} ($x \approx 0.72$) obtained from single-crystal diffraction was used to fit the data with the Rietveld method.^[42] The peak shape was modeled using the fundamental parameters approach, which is a convolution of source emission profiles, axial instrument contributions, crystallite size, and microstrain effects. The background was modeled with a shifted Chebychev function and preferred orientation was treated with spherical harmonics of fourth order. Cylindrical absorption correction was performed taking into account capillary diameter and linear absorption coefficients of all phases present in the sample.

A Stoe Stadi P diffractometer (Stoe & Cie GmbH, Darmstadt, Germany) equipped with a graphite furnace and image plate position sensitive detector was used for temperature dependent PXRD. Samples were filled into fused silica capillaries with 0.5 mm diameter. Data were collected at constant temperature with 20 °C/step intervals up to 1000 °C and a 20 min collection time per step.

5.2.7 Single-Crystal X-ray Diffraction

High-intensity X-ray diffraction data of a Ce_{4-0.5x}Li₃P₁₈N_{35-1.5x}O_{1.5x} ($x \approx 0.72$) single crystal were obtained at the Swiss-Norwegian Beamline (SNBL), ESRF, Grenoble, on the multipurpose PILATUS@SNBL diffractometer ($\lambda = 0.68010 \text{ \AA}$) with a Dectris Pilatus 2M detector.^[32] Data of multiple runs were summed up and binned with the SNBL toolbox. Integration was done with CrysAlis Pro^[43] and semiempirical absorption correction with SADABS.^[44]

Solution and refinement of the average structure was done with SHELX-97.^[45,46] Further details on the crystal structure analysis can be obtained from the Fachinformationszentrum Karlsruhe, 76344 Eggenstein-Leopoldshafen, Germany (fax: +49-7247-808-666; e-mail: crysdata@fiz-karlsruhe.de) on quoting the depository number CSD-433141.

Refinements of the superstructure and the commensurately modulated model in (3 + 2)D superspace was carried out with JANA2006.^[47] Crystal structures were visualized with VESTA and Diamond.^[48,49]

5.2.8 Transmission Electron Microscopy

For sample preparation, crystals of $\text{Ce}_{4-0.5x}\text{Li}_3\text{P}_{18}\text{N}_{35-1.5x}\text{O}_{1.5x}$ ($x \approx 0.72$) were ground in absolute ethanol and drop-cast on copper grids covered with holey carbon film (S166-2, Plano GmbH, Germany). For STEM and electron energy loss spectroscopy (EELS), the samples were plasma cleaned for 20 s. The grids were mounted on a double-tilt holder and transferred into a Cs DCOR probe corrected Titan Themis 300 (FEI, USA) TEM equipped with a X-FEG, a postcolumn filter (Enfinium ER-799), a US1000XP/FT camera system (Gatan, Germany) and a windowless, 4-quadrant Super-X energy dispersive X-ray (EDX) detector. TEM images were recorded using a $4\text{k} \times 4\text{k}$ FEI Ceta CMOS camera. The microscope was operated at 300 kV accelerating voltage for selected area electron diffraction (SAED), STEM-HAADF (convergence angle of 16.6 mrad, 50 μm aperture, detector inner half angle 63 mrad for 100 mm and 105 mrad for 60 mm camera length) and EELS. For drift corrected EDX mapping with atomic resolution, the microscope was operated at 120 kV accelerating voltage. For the evaluation of the TEM data, the following software was used: Digital Micrograph (Fourier filtering of STEM images, EELS spectra), ProcessDiffraction7 (geometric calculations for SAED), JEMS (SAED simulations), and ES Vision (EDX spectra).^[50-54]

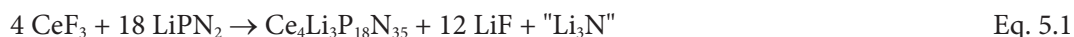
5.2.9 Optical Properties

Images of luminescent single-crystals mounted in glass capillaries were obtained on a Horiba Fluorimax4 spectrofluorimeter system attached to an Olympus BX51 microscope via fiber optics. Photoluminescence was determined on powdered samples with an in-house-built system based on a 5.3 in. integrating sphere and a spectrofluorimeter equipped with a 150 W Xe lamp, two 500 mm Czerny–Turner monochromators, 1800 1/mm lattices and 250/500 nm lamps, with a spectral range from 230 to 820 nm.

5.3 Results and Discussion

5.3.1 Preparation and Chemical Analysis

The reaction of a molar ratio 1:4.5 of CeF₃ and LiPN₂ aimed to synthesize Ce₄Li₃P₁₈N₃₅ (see Experimental Details section) as the ratio P/N in LiPN₂ is close to the required atomic ratio of 18:35; following Equation 5.1, Li₃N could be eliminated for a stoichiometric reaction.



As will be shown later, the actual sum formula is Ce_{4-0.5x}Li₃P₁₈N_{35-1.5x}O_{1.5x} ($x \approx 0.72$) due to Ce vacancies. The presence of O probably stems from the crucible material since h-BN slowly decomposes in air to boric acid and B₂O₃.^[55] The crucible used in the experiment had a small sample to h-BN volume ratio (see Experimental Details section), allowing the diffusion of sufficient amounts of O into the sample.

Ce_{4-0.5x}Li₃P₁₈N_{35-1.5x}O_{1.5x} ($x \approx 0.72$) crystallizes in block-like colorless and transparent crystals up to ~100 μm in size. The latter emit blue light upon excitation with UV or near-UV radiation (Figure 5.1a, see Optical Properties). Morphology and elemental composition were determined by means of SEM (Figure 5.1b) and EDX. The EDX values are in accordance with the theoretical sum formula (Ce_{3.7(4)}P_{17.4(11)}N_{34.3(14)}O_{1.3(5)}/Ce_{3.64}P₁₈N_{33.92}O_{1.08}, measured (12 points)/calculated without taking Li into account).

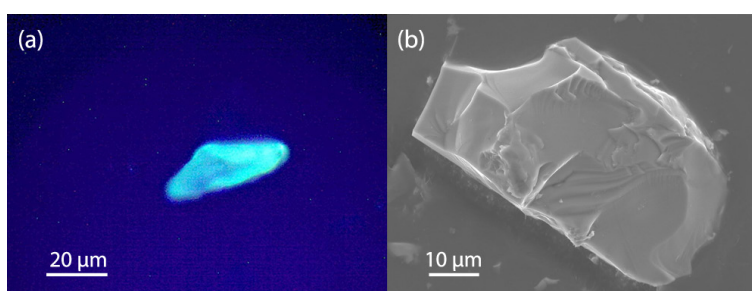


Figure 5.1. (a) Single-crystal of Ce_{4-0.5x}Li₃P₁₈N_{35-1.5x}O_{1.5x} under excitation with 390 nm UV light, emitting blue light. (b) SEM micrograph of a Ce_{4-0.5x}Li₃P₁₈N_{35-1.5x}O_{1.5x} single-crystal

IR spectroscopy indicated the absence of N–H or O–H bonds; only the typical fingerprint region of nitridophosphates was observed (Figure E.1). Temperature dependent powder diffraction showed that the phase is stable in air up to at least 1000 °C (Figure E.2).

Rietveld refinement (Figure 5.2, Table E.1) carried out on powder X-ray diffraction data confirms the average-structure model. Residual LiPN_2 is expected since the ratio 1:4 of the starting materials is nonstoichiometric with respect to sum formula $\text{Ce}_4\text{Li}_3\text{P}_{18}\text{N}_{35}$; h-BN stems from the crucible.^[36,56]

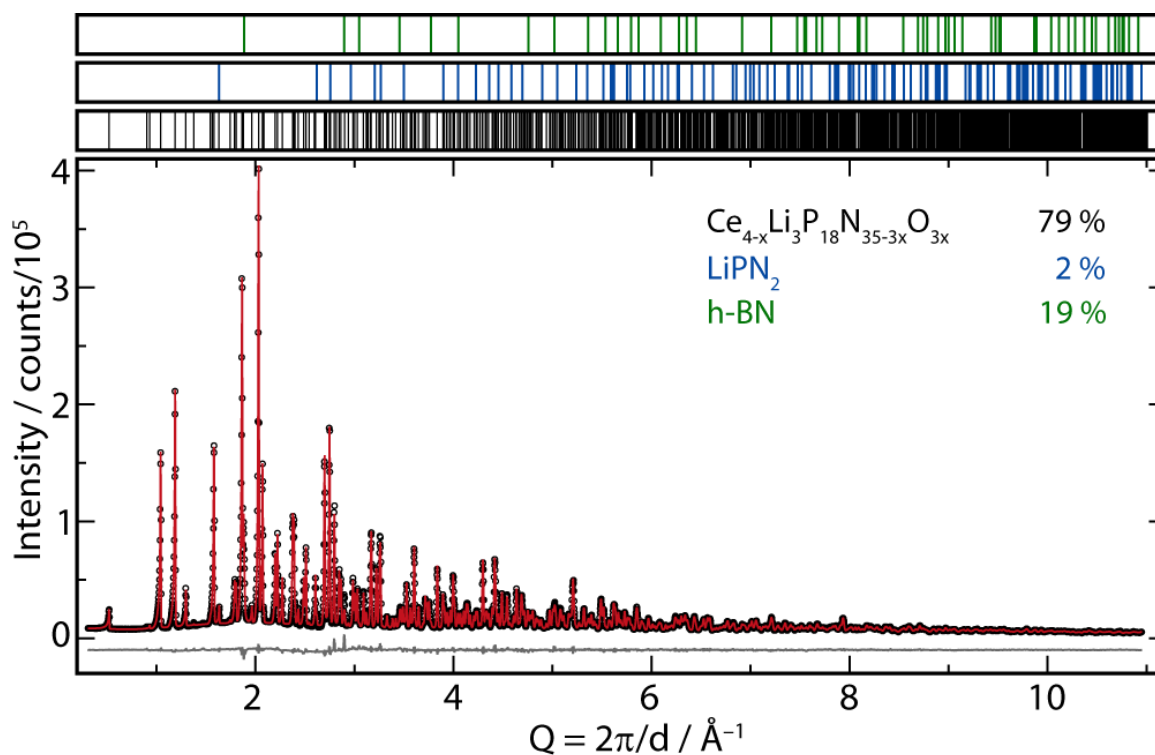


Figure 5.2. Rietveld refinement for a sample with $\text{Ce}_{4-0.5x}\text{Li}_3\text{P}_{18}\text{N}_{35-1.5x}\text{O}_{1.5x}$ as the main component and LiPN_2 and h-BN as side phases,^[36,56] observed pattern displayed with black circles, calculated pattern as a red line, difference plot as a gray line, positions of Bragg reflections above.

In thin-walled crucibles, $\text{Ce}_{4-0.5x}\text{Li}_3\text{P}_{18}\text{N}_{35-1.5x}\text{O}_{1.5x}$ could be prepared as the major constituent of the sample after introducing an O source in the form of amorphous PON.^[57] Oxygen, therefore, seems either to facilitate the formation of the compound or to stabilize it as it induces Ce vacancies. Such vacancy-stabilization is reminiscent of yttria-stabilized zirconia, in which the larger Y^{3+} cations stabilize the CaF_2 -type high-temperature phase.^[58]

5.3.2 Determination of the Average Structure

$\text{Ce}_{4-0.5x}\text{Li}_3\text{P}_{18}\text{N}_{35-1.5x}\text{O}_{1.5x}$ crystallizes in a hexagonal lattice with parameters $a = 13.9318(1)$ and $c = 8.1355(1)$ Å. The unit cell metrics and the average structure model were confirmed by TEM as discussed in the corresponding section. Space group $P6_3/m$ (no. 176) was assigned by analysis of system-

atically absent reflections in XPREP^[59] and with superiority over $P6_3$ (no. 173), as refinement revealed. The structure was solved by direct methods,^[46] yielding the positions of all heavy atoms. The positions of the light atoms Li and N were determined from difference Fourier maps.

Table 5.1. Crystallographic Data for the Average Structure of Ce_{4-0.5x}Li₃P₁₈N_{35-1.5x}O_{1.5x} ($x \approx 0.72$).

Crystal Data	
Formula	Ce _{4-0.5x} Li ₃ P ₁₈ N _{35-1.5x} O _{1.5x} ($x \approx 0.72$)
Formula mass / g·mol ⁻¹	1580.11
Crystal system	hexagonal
Space group	$P6_3/m$ (no. 176)
Cell parameters / Å	$a = 13.9318(1)$ $c = 8.1355(1)$
Cell volume / Å ³	1367.51(3)
Formula units per unit cell, Z	2
$F(000)$	1472
Calcd density, ρ / g·cm ⁻³	3.837
Abs. coefficient, μ / mm ⁻¹	6.235
Data Collection	
Radiation	synchrotron, $\lambda = 0.68010$ Å
Temperature / K	293(2)
θ range / °	$1.615 \leq \theta \leq 31.971$
Total no. of reflns	11325
Independent reflns	1795
Absorption correction	semiempirical ^[44]
R_{intr} R_{sigma}	0.019, 0.007
Refinement	
Extinction coefficient	0.0053(5)
Refined parameters	101
GOF	1.233
R_1 (all data), $R_1 [F^2 > 2\sigma(F^2)]$	0.019, 0.019
wR_2 (all data), $wR_2 [F^2 > 2\sigma(F^2)]$	0.047, 0.047
$\Delta\rho_{\text{max}}$ $\Delta\rho_{\text{min}}$ e·Å ⁻³	1.008, -2.025

All atoms were refined anisotropically, taking into account dispersion correction terms for X-rays with $\lambda = 0.6801$ Å. Table 5.1 contains the crystallographic data and Table 5.2 the atom parameters. Anisotropic displacement parameters as well as bond lengths and angles can be found in Tables E.2–E.4. The site occupancy of position Ce2 is 0.635(2), and the atom has a prolate displacement ellipsoid elongated along [001]. At full occupation, the sum formula Ce₄Li₃P₁₈N₃₅ would be charge-balanced,

but a Ce deficit necessitates O for N substitution, as inferred from EDX (see above), in order to maintain charge neutrality.

Since X-rays cannot differentiate between N and O, the distribution of O atoms was derived from electrostatic calculations employing the Madelung part of lattice energy (MAPLE). Accordingly, the N4 position has the smallest partial MAPLE value, and bond valence sum (BVS) calculations also indicate an O share on the N4 position (Tables E.5–7).^[60] As MAPLE and BVS depend strongly on the atomic positions and considering that N4 belongs to the first coordination sphere of Ce2 with its prolate displacement ellipsoid, this is only conjecture. O atoms in close proximity to Ce2, however, are reasonable as they are required for charge compensation. The N4 position was therefore mixed with a fixed amount of 0.36O, yielding the sum formula $\text{Ce}_{4-0.5x}\text{Li}_3\text{P}_{18}\text{N}_{35-1.5x}\text{O}_{1.5x}$ with $x \approx 0.72$.

Table 5.2. Atom sites of $\text{Ce}_{4-0.5x}\text{Li}_3\text{P}_{18}\text{N}_{35-1.5x}\text{O}_{1.5x}$

Atom	Wyckoff pos.	Site sym.	x	y	z	$U_{eq} (\text{Å}^3)$	Occ.
Ce1	6h	<i>m</i> ..	0.44029(2)	0.04225(2)	1/4	0.00866(6)	1
Ce2	2a	$\bar{6}$..	0	0	1/4	0.02020(17)	0.635(2)
P1	12i	1	0.02032(4)	0.20721(4)	0.06775(6)	0.00775(9)	1
P2	12i	1	0.33965(4)	0.54801(4)	0.07504(6)	0.00607(9)	1
P3	12i	1	0.43947(4)	0.30795(4)	0.06620(6)	0.00643(9)	1
N1	4f	3..	1/3	2/3	0.0750(4)	0.0066(4)	1
N2	6h	<i>m</i> ..	0.2995(2)	0.48706(19)	1/4	0.0080(4)	1
N3	12i	1	0.46921(14)	0.20913(13)	0.0692(2)	0.0095(3)	1
N4	6h	<i>m</i> ..	0.2080(2)	0.03965(19)	1/4	0.0113(4)	0.64
O4	6h	<i>m</i> ..	0.2080(2)	0.03965(19)	1/4	0.0113(4)	0.36
N5	12i	1	0.11661(13)	0.53492(13)	0.0319(2)	0.0096(3)	1
N6	6h	<i>m</i> ..	0.4296(2)	0.3469(2)	1/4	0.0140(5)	1
N7	12i	1	0.04775(19)	0.33260(16)	0.0406(3)	0.0185(4)	1
N8	12i	1	0.1293(2)	0.1946(3)	0.0725(3)	0.0377(8)	1
Li1	6h	<i>m</i> ..	0.2540(5)	0.3193(5)	1/4	0.0208(12)	1

The atom sites N6, N7, and N8 (Figures 5.3 and 5.4) exhibit prolate displacement ellipsoids, which are likely a consequence of the Ce2 displacement discussed later in the section “Superstructure Determined from Synchrotron Data”. A possible lower symmetry, in which the afflicted N atoms are not mapped onto themselves by the horizontal mirror plane of space group $P6_3/m$, was ruled out by refinement in $P6_3$ (Figures E.3 and E.4 for more information), which did not yield any improvement. Other models of twinning and associated symmetry reduction were ruled out by a refinement in $P1$ including all appropriate twin laws that would lead to Laue symmetry $6/m$.

5.3.3 Description of the Average Structure

The structure of $\text{Ce}_{4-0.5x}\text{Li}_3\text{P}_{18}\text{N}_{35-1.5x}\text{O}_{1.5x}$ consists of a framework built up from all-side vertex-sharing PN_4 tetrahedra (Figure 5.3). Their interconnection pattern is a combination of stacks of six-membered rings and triangular columns running along [001] (Figures 5.3 and 5.4). This formal decomposition emerges from comparison with the oxonitridophosphates $\text{Ba}_6\text{P}_{12}\text{N}_{17}\text{O}_9\text{Br}_3$ and $\text{SrP}_3\text{N}_5\text{O}$; both comprise similar triangular columns.^[61,62] While the columns in $\text{Ba}_6\text{P}_{12}\text{N}_{17}\text{O}_9\text{Br}_3$ are not interconnected and therefore only periodic in one direction, they are interconnected via 2/3 of the triangles' vertices in $\text{SrP}_3\text{N}_5\text{O}$, forming layered anions with periodicity in two directions.^[63]

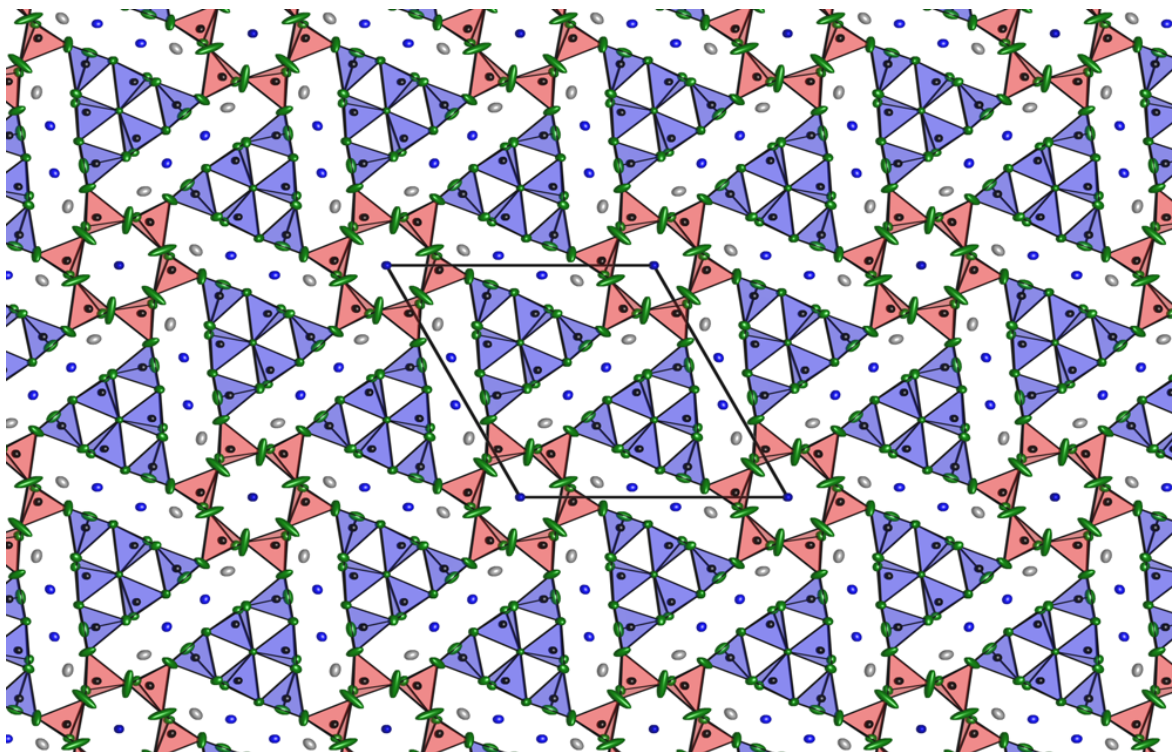


Figure 5.3. Crystal structure of $\text{Ce}_{4-0.5x}\text{Li}_3\text{P}_{18}\text{N}_{35-1.5x}\text{O}_{1.5x}$ in projection along [001]. The stacks of 6-membered rings and triangular columns are highlighted by red and blue tetrahedra, respectively. Atoms are displayed as their displacement ellipsoid at 90% probability level, Ce in blue, Li in gray, P in black, and N in green.

In $\text{Ce}_{4-0.5x}\text{Li}_3\text{P}_{18}\text{N}_{35-1.5x}\text{O}_{1.5x}$, the triangular columns are interconnected via stacks of six-membered rings and vice versa. Hence, an extended three-dimensional anionic framework with a molar ratio 1:2 of stacks of six-membered rings and triangular columns is formed. The triangular columns

$^1[(P_{12}^{[4]}N_2^{[3]}N_{24}^{[2]})^{18-}]$, displayed in Figure 5.4a, comprise triply bridging $N^{[3]}$ atoms, which are the reason for $\kappa = 0.514$. The 6-rings form stacks by sharing tetrahedra vertices, which alternately point up and down (Figure 5.4b).

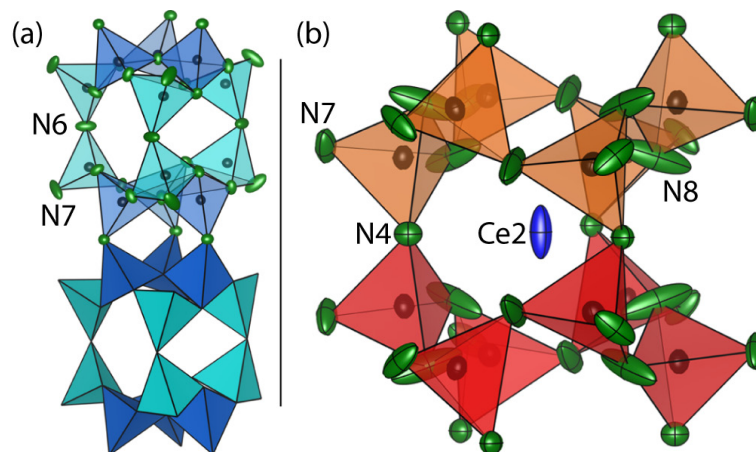


Figure 5.4. (a) Side-view of the triangular columns running perpendicular to [001], tetrahedra bridged by $N^{[3]}$ highlighted in royal blue. (b) One repetition unit of the stacks of six-membered rings. Ellipsoids are displayed at 90% probability level.

The P–P connection pattern represents the framework of the structure (Figure 5.5, top left) and is referred to as the net topology. The P–P net is subsumed by point symbol^[64] $(3.6^5)(3^3.4^4.5^3)(6^6)$, which enumerates the shortest cycles originating from P-vertex angles (calculated by TOPOS^[65]). The analysis of point and vertex symbols (for the latter see Supporting Information) revealed that this net topology has been neither experimentally realized nor theoretically predicted.

For an intuitive understanding of $Ce_{4-0.5x}Li_3P_{18}N_{35-1.5x}O_{1.5x}$'s topology, the three-dimensional *natural tiling* in its maximum symmetry embedding was derived from the P–P connection pattern (Figure 5.5, top right and bottom).^[66,67] The 3D tiles' faces consist of *locally strong rings* (built up from P–P adjacencies) so that the *natural tiling* retains the full symmetry of the net it carries and the tiles represent chemically meaningful cavities in the structure.^[67] The *natural tiling* consists of six tiles subsumed with signature $3[6^3]+[3^2.4^3]+3[3^2.4.6^2]+[6^5]+3[6^5.10^2]+[3^8.6^3]$ (face symbols) and transitivity symbol 3796 (number of symmetry inequivalent vertices, edges, faces, and tiles, in that order). The cations Ce1 and Li1 reside in the large $[6^5.10^2]$ cage ($V = 148 \text{ \AA}^3$, volume in crystal structure), and Ce2 resides in the $[6^5]$ cage ($V = 62 \text{ \AA}^3$, volume in crystal structure). A detailed description and view of the tiles can be found in the Supporting Information.

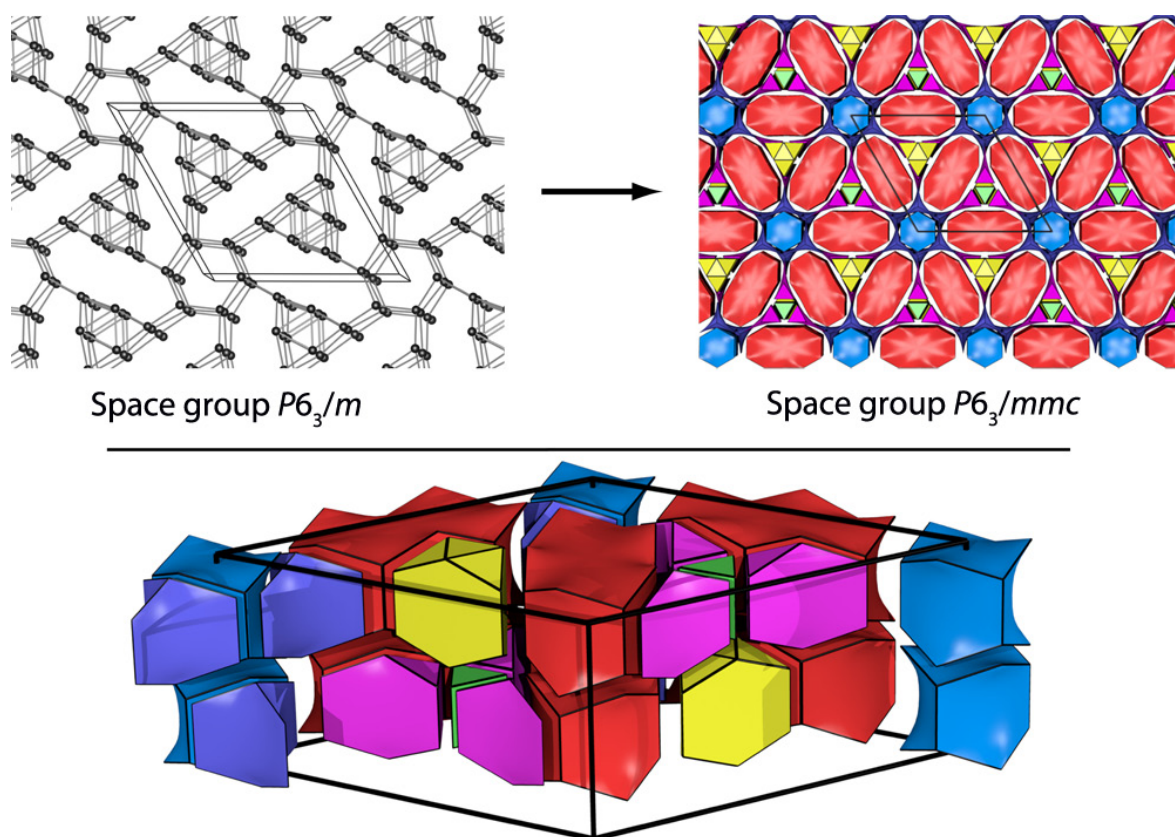


Figure 5.5. (top, left) P–P connection pattern; (top, right) *natural tiling* in projection along [001], consisting of six individual tiles. (bottom) Cross section through one unit cell of the tiling. Tiles are light blue [6⁵], dark blue [6³], yellow [3⁸.6³], pink [3².4.6²], green [3².4³], and red [6⁵.10²].^[66]

The maximum symmetry embedding of the tiling is in $P6_3/mmc$ (no. 194), which is also the maximum symmetry of a theoretical archetype (Figure 5.5). In Ce_{4-0.5x}Li₃P₁₈N_{35-1.5x}O_{1.5x}, the mirror plane perpendicular to $\langle 100 \rangle$ is absent due to a rotational twist of the six-membered ring with respect to the triangular columns causing the interconnecting P–N–P angles to be 139.4° instead of 180°. Hence, the structure has symmetry $P6_3/m$, which is a subgroup of $P6_3/mmc$ by t_2 transition.

The coordination polyhedra surrounding the metal ions are displayed in Figure 5.6. Li1 is coordinated by six N atoms forming a distorted pentagonal pyramid (Johnson solid J_2), Ce1 by nine N atoms in an irregular polyhedron, and Ce2 by nine N atoms arranged in a distorted triaugmented triangular prism (Johnson solid J_{51}).^[68] To approximate the magnitude of distortion, the polyhedra were compared to their holohedral counterparts as described in the Supporting Information (section Coordination Polyhedra). The bond lengths in these polyhedra (Figure 5.6) are typical for N coordination.

They are comparable to those found in NdLiP_4N_8 [$d(\text{Li}-\text{N}) = 1.96$ to 2.17 Å], $\text{LiCa}_4[\text{BN}_2]_3$ [$d(\text{Li}-\text{N}) = 2.22$ Å], and $\text{Ba}_2\text{Cu}[\text{Si}_2\text{O}_7]$ -type $\text{Ce}_2\text{P}_3\text{N}_7$ [$d(\text{Ce}-\text{N}) = 2.44$ – 2.75 Å].^[11,13,69]

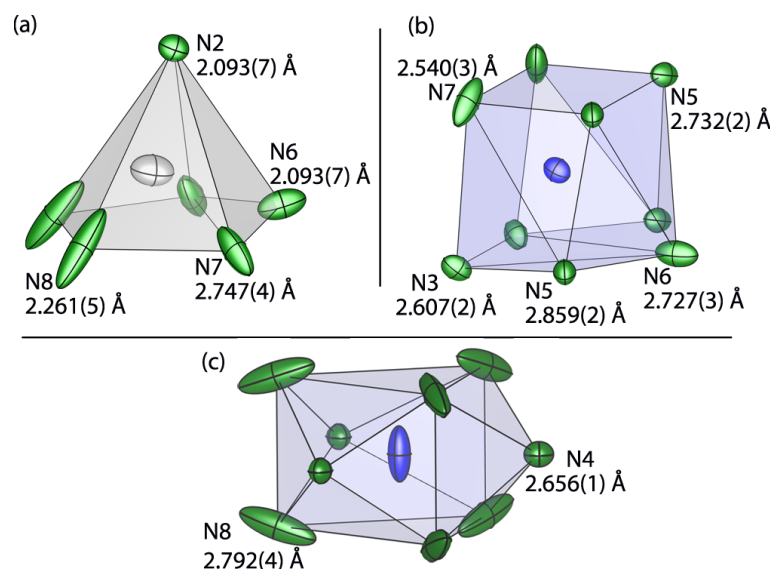


Figure 5.6. Coordination polyhedra around the sites of Li (a), Ce1 (b), and Ce2 (c); two coordination polyhedra are shown for Ce2, as they appear in stacks along [001] in the structure. Ce–N and Li–N distances are given for all independent N positions; the ellipsoids are displayed with 90% probability.

In the average structure model discussed above, vacancies are present on the Ce2 site, and as can be seen from Figure 5.6, Ce2 and certain N displacement ellipsoids are elongated. A similar case was reported for $\text{Ba}_{0.85}\text{Ca}_{2.15}\text{In}_6\text{O}_{12}$ ($P6_3/m$, no. 176), in which Ba atoms residing in analogous six-membered-ring channels entered a long-range periodic order resulting in a (3 + 1)D incommensurate modulation.^[70] In the following sections, the causes and effects of the Ce2 vacancies and displacements are analyzed.

5.3.4 Transmission Electron Microscopy

$\text{Ce}_{4-0.5x}\text{Li}_3\text{P}_{18}\text{N}_{35-1.5x}\text{O}_{1.5x}$ was investigated by TEM to gain information about the Ce2 position. SAED patterns along zone axes [100] and [001] exhibit symmetry $2mm$ and 6, respectively, and correspond to reciprocal lattice sections reconstructed from single-crystal X-ray data, confirming hexagonal symmetry (Figures E.6 and E.7). Z-Contrast HAADF-STEM images and drift-corrected EDX mappings differentiate between Ce and P atoms; maxima coincide with the heavy-atom positions of the average

structure model (Figure 5.7, enlarged in Figure E.8). In the Fourier filtered micrographs, the intensities of the different Ce atom columns match the theoretical atom ratios along the different projections in consideration of the average structure model and the under-occupancy of Ce2.

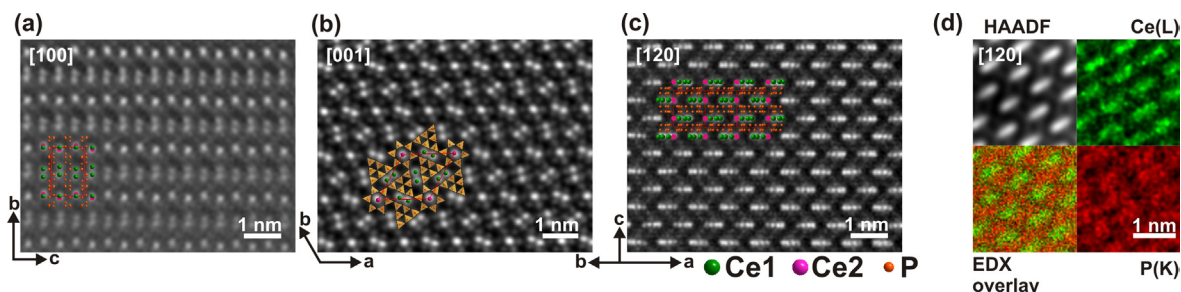


Figure 5.7. (a–c) Aberration-corrected STEM-HAADF Fourier filtered images along zone axes [100], [001], and [120]. Brighter contrast corresponds to Ce1 (green) and Ce2 (light green) atom columns, darker contrast to P columns (orange). The unit cells of the average structure in corresponding projections were overlaid in red. (d) Drift corrected EDX mappings along [120] in juxtaposition to a HAADF image of the same section. An enlarged version of this figure is Figure E.8.

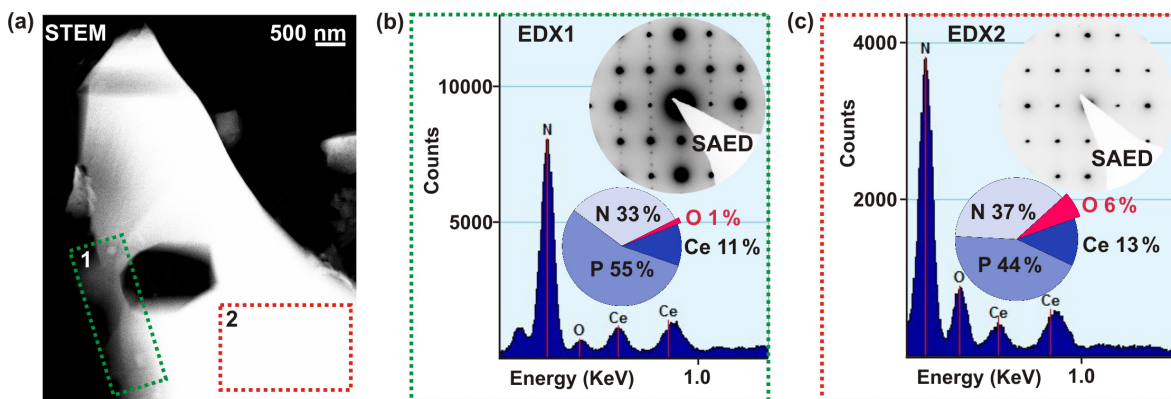


Figure 5.8. (a) Dark-field STEM micrograph of a representative crystallite of ground powder of Ce_{4-0.5x}Li₃P₁₈N_{35-1.5x}O_{1.5x}. The area in which the superstructure was observed is highlighted in green, the area without superstructure highlighted in red. (b, c) SAED along the along [120] zone axis and EDX for the highlighted regions in panel a. EDX element ratios shown here were obtained from highlighted regions. The dark area is a hole in the crystal.

Further EDX and SAED combined with high resolution STEM-HAADF suggested two different types of domains in Ce_{4-0.5x}Li₃P₁₈N_{35-1.5x}O_{1.5x}. The first revealed a lower O content, relative to the second, and additionally showed diffraction spots suggesting a superstructure (Figure 5.8). Since the quantification of little amounts of O by TEM EDX is difficult, several different crystallites were analyzed corroborating the suggested trend (Table E.9). Within the standard deviation, the measured

amounts of Ce fit the average structure model. In the unfiltered STEM images of the second domain type with increased O content, the contrast of the Ce₂ atom columns viewed along [001] varies significantly. In a wedge-shaped edge of a crystal some Ce₂ atom columns are missing completely (Figure 5.9, larger and thinner region represented in Figure E.9). This direct observation of the Ce atom columns confirms a random distribution of Ce₂ vacancies as suggested by the average structure model.

In the superstructure domains, the additional reflections hinted at hexagonal metrics with $a = 24.08$, $c = 8.1$ Å as later determined by synchrotron diffraction on single crystals (see below). Superstructure reflections are most pronounced in SAED patterns along zone axes [120] of the average structure (Figures 5.10a and E.10). Z-Contrast STEM images along this direction revealed a displacement of Ce₂ atoms in [001] direction. Three different locked-in positions (nondynamic displacement) of the Ce₂ atoms are directly discernible; one atom resides below (A), one atom above (C), and one atom (B) roughly at the Ce₂ position of the average structure model. The distance between atoms at height A and C was measured to be roughly 0.3(1) Å based on 10 measurement points (details in Supporting Information).

The Fourier transform of the STEM image (Figure E.10) shows small additional peaks indicating a periodicity of the Ce₂ displacement within the boundaries of the obtained image. As the displacement is repetitive, they are likely the cause for the superstructure reflections observed in the SAEDs. Since EDX and SAED showed that the superstructure domains with very low O content are only a fraction of the crystal volume (Figure 5.8), the superstructure reflections of macroscopic single crystals are expected to have extremely weak intensity. A model of the superstructure will therefore be derived in the next section from synchrotron diffraction data.

The Ce₂ positions appear less bright than other Ce₁ positions, which might indicate the presence of vacancies in the superstructure domains. Though such vacancies cannot be ruled out based on O contents due to the lacking accuracy of TEM EDX (Table E.9), they appear to be less frequent than in domains without superstructure. The [120] zone-axis images of domains without superstructure even indicate completely missing Ce₂ atom columns (Figure E.10). The Fourier transform of those images do not suggest the presence of a further periodic ordering of Ce₂ in accordance with the above-mentioned SAEDs.

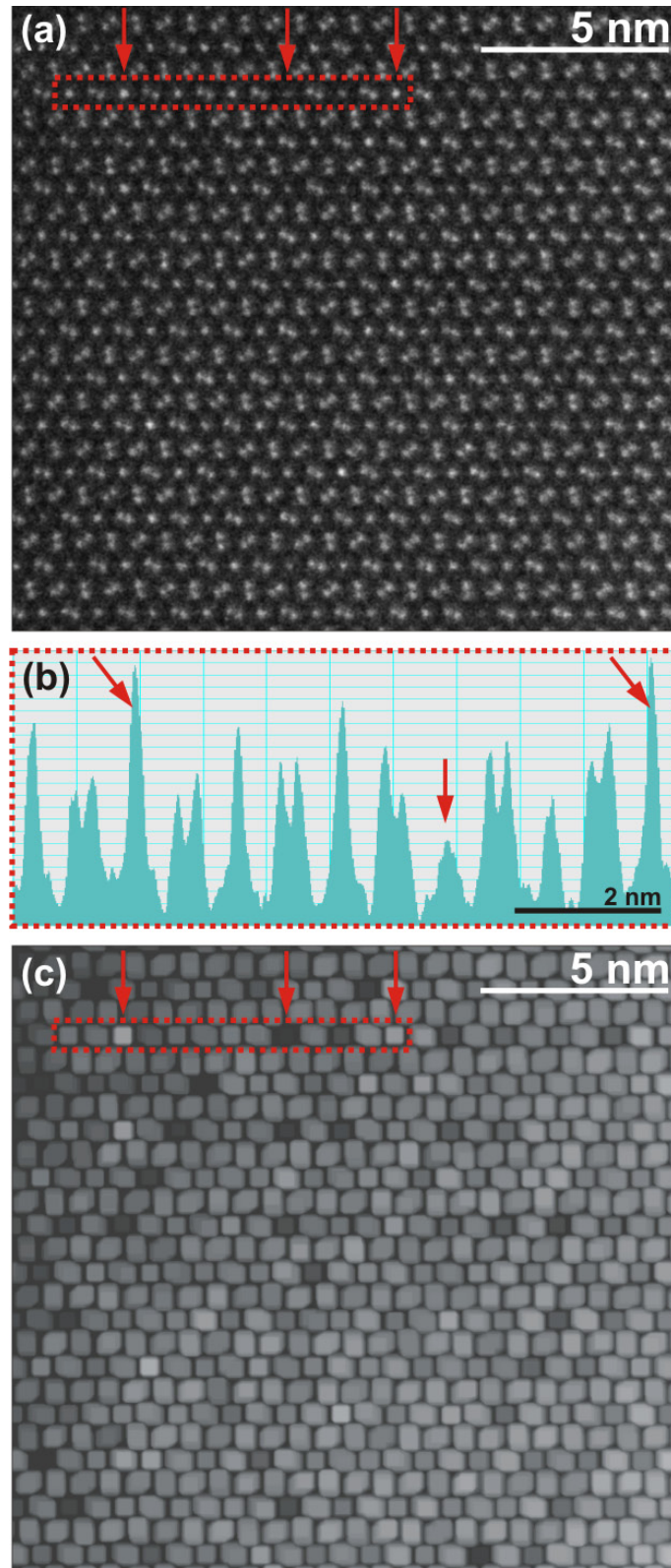


Figure 5.9. (a) Experimental STEM-HAADF image along [001] of a domain with increased O content showing Ce atom columns. Region of intensity line scan (b) highlighted in red in panels a and c. (c) Intensity map of panel a enhanced by interpolation of brightness over 4 pixels followed by augmenting the bright areas for 9 pixels. The intensity contrast represents the number of Ce atoms in the columns, highlighting a random distribution of Ce₂ vacancies in accordance with the average structure.

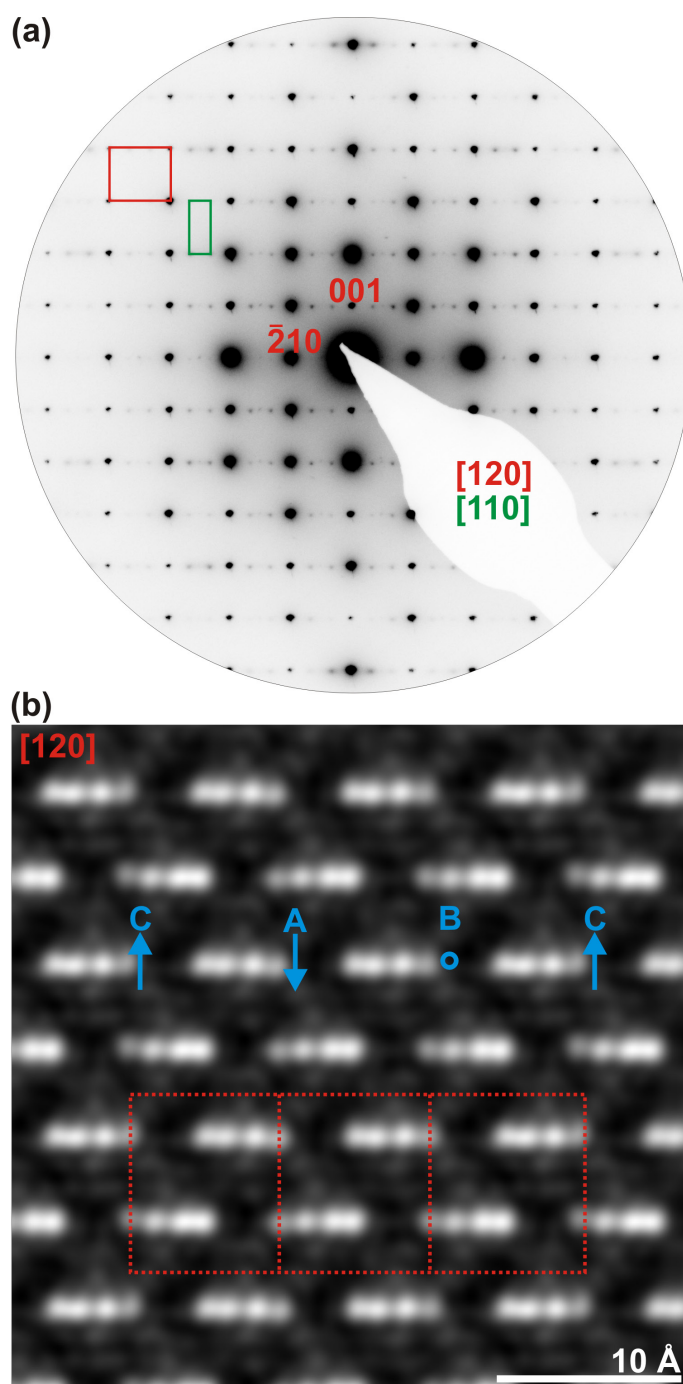


Figure 5.10. (a) SAED pattern of a superstructure domain along the $[120]$ zone axis of the average structure (red indices and cell outlines); this corresponds to the $[110]$ zone axis of the supercell (green, note the 30° rotation). (b) STEM-HAADF image along this direction showing a displacement of certain Ce2 atoms. Three different locked-in positions of Ce2 atoms along $[001]$ are highlighted with arrows: A (displaced downward), B (roughly in the middle), C (displaced upward); maximum distance between A and C $\approx 0.3(1)$ Å.

In order to balance the charge difference caused by the Ce2 vacancies, the presence of Ce^{4+} is conceivable. Therefore, EELS was performed to gain information about the formal oxidation states of the

Ce atoms. EELS quantification of domains with a lower O content determined an atomic ratio Ce/P/N of 1:3.2:8.8 close to the ratio of 1:4.5:8.8 based on the sum formula of the average structure. In the examined domains, no Li and O could be quantified with EELS. Off-axis EELS spectra do not indicate the presence of Ce⁴⁺ (Figure E.11). They show the Ce-M₅ and Ce-M₄ edges at 882.0 and 899.5 eV energy loss, respectively, very close to typical values for Ce³⁺ (M₅ at 882.0 eV, M₄ at 899.7 eV) in Ce₂Zr₂O₈ or CeO₂ doped with lanthanides.^[71,72] A M₅ to M₄ ratio near to one and more asymmetrically shaped M₄ edge compared to the M₅ edge are characteristic for Ce³⁺.^[73]

5.3.5 Superstructure Determined from Synchrotron Data

Synchrotron diffraction data were collected in sufficient quality for analysis of the superstructure suggested by SAED (for a detailed description of X-ray data analysis, the reader is referred to the Supporting Information). From the reciprocal lattice section $hk0$ shown schematically in Figure 5.11 (experimental patterns are shown in Figure E.12), it is apparent that the superstructure is commensurate. The reciprocal lattice of the supercell as defined by vectors $\mathbf{a}^{*} = 2/3 \mathbf{a}^{*} - 1/3 \mathbf{b}^{*}$, $\mathbf{b}^{*} = 1/3 \mathbf{a}^{*} + 1/3 \mathbf{b}^{*}$ and $\mathbf{c}^{*} = \mathbf{c}^{*}$ allows indexing of the whole diffraction pattern. These vectors span a hexagonal ($\sqrt{3} \times \sqrt{3}$)R30° supercell ($a' = 24.1306(1)$, $c' = 8.1335(1)$ Å) with three times the volume of the basic cell.

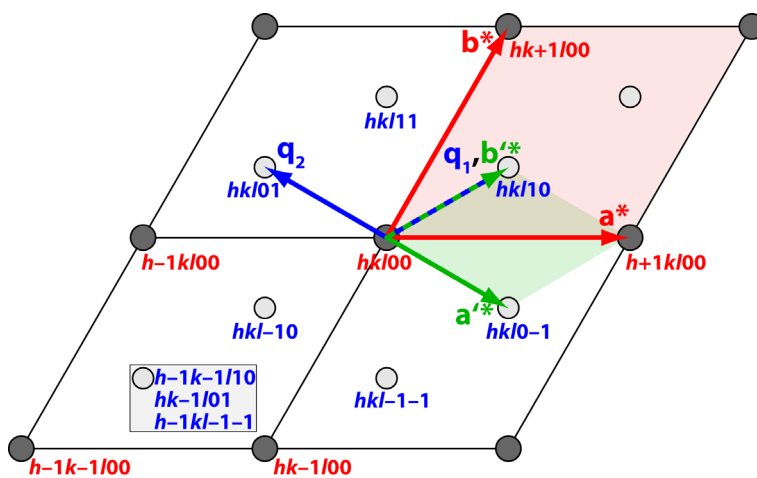


Figure 5.11. General reciprocal hkn ($n = 2, 4$, etc.) lattice plane, in which the basic cell (red), supercell (green), and modulation vectors \mathbf{q}_1 and \mathbf{q}_2 (blue) are marked (\mathbf{q}_1 and \mathbf{b}^{*} are equal and thus highlighted by a dashed blue green vector). Several reflections (dark gray and light gray) carry indices for orientation, for one satellite; its three superspace indices are given.

An initial supercell model for tentative structure refinement was obtained by $i3$ subgroup transformation of the basic structure model according to

$$\begin{pmatrix} a' \\ b' \\ c' \end{pmatrix} = \begin{pmatrix} a \\ b \\ c \end{pmatrix} \begin{pmatrix} 1 & -1 & 0 \\ 1 & 2 & 0 \\ 0 & 0 & 1 \end{pmatrix}$$

Due to pronounced parameter correlation, a conventional refinement of the superstructure in space groups $P6_3/m$ and its subgroup $P6_3$ failed, no significant deviation from the average model could be obtained. This failure is due to the extreme difference in intensity and counting statistics between basic and superstructure reflection (intensity to sigma ratio of the basic structure reflections and the ratio of the superstructure reflections: $I_b/\sigma = 23.7$ to $I_s/\sigma = 1.8$, Figure E.12). Moreover, the space group of the superstructure could not be determined unequivocally from the diffraction pattern since the satellite reflections are only observed in hkl planes with $l = 2n$ and $n \neq 0$ (Figure E.13).

Note that SAED patterns (Figure 5.10a) show superstructure reflections in all planes, most likely due to multiple diffraction. Assuming that mainly Ce2 atoms contribute to the superstructure, the reflections in the hkl with $l = \text{odd}$ planes are expected to be weak or absent since the Ce2 atoms in the average structure can be described by a smaller unit cell with $1/2c$ translation. The unobserved reflections in the $hk0$ plane indicate that the Ce2 atoms are displaced solely along $[001]$, which is reasonable considering their coordination in a triaugmented triangular prism (Figure 5.6c).

To resolve these issues, only the z coordinates of the Ce2 atoms in the supercell were refined^[47] in $P1$ using the superstructure reflections, while all other atom parameters, which were already well-established by the average structure, remained fixed. Ce2 displaced from its average position (Figure E.14) and hence corroborated the STEM findings. However, the z coordinates and thus the amplitude of the displacement cannot be determined since they are strongly correlated with the scale factor of the superstructure reflections, whose true value is unknown since the superstructure exists only in domains that correspond to an unknown fraction of the crystal. Setting the superstructure scale factor equal to that of the average structure (corresponding to a superstructure encompassing the whole crystal) yielded the minimal displacement of the Ce2 atoms of 0.1 \AA , whereas STEM suggested approximately $0.3(1) \text{ \AA}$. From the refined Ce2 atom positions and their correlation matrix, space group symmetry $P6_3$ was determined for the superstructure; the mirror symmetry is broken by displacement from the

special position on the horizontal mirror plane, and the inversion symmetry is broken by unidirectional displacement of the Ce2 atoms on unit cell edges (Figure E.14). A subsequent refinement, with symmetry restrictions and additional translational symmetry applied, included the other atoms as well, yielding the same Ce2 displacement.

5.3.6 (3 + 2)D Superspace Description

A (3 + 2)D superspace model may be a more elegant description of the superstructure and can better illustrate the long-range order of the Ce2 displacements. Moreover, it can corroborate the supercell refinement. As (3 + *d*) superspace groups are supergroups of the 3D space groups, the corresponding structure models often require fewer parameters, which is especially favorable when refining a weak superstructure. Since the modulation is refined in the basic cell, no artificial centering has to be introduced by manual parameter constraints as was done in the supercell refinement. A more detailed derivation of the superspace description can be found in the Supporting Information.

Since the displaced, that is, modulated Ce2 atoms have $P6_3$ symmetry, the superspace group $P6_3(\alpha, \beta, 0)0(-\alpha - \beta, \alpha, 0)0$ was chosen for the (3 + 2)D modulation description. The diffraction pattern was indexed based on the basic cell with two modulation vectors $\mathbf{q}_1 = (1/3, 1/3, 0)$ and $\mathbf{q}_2 = (-2/3, 1/3, 0)$ (Figure 5.11) resulting in diffraction vectors $\mathbf{h} = h\mathbf{a}^* + k\mathbf{b}^* + l\mathbf{c}^* + m\mathbf{q}_1 + n\mathbf{q}_2$. Since the superstructure is commensurate, the indexing is ambiguous as one satellite is shared by three basic structure reflections. This might be regarded as merohedry in 5D but does not impede structure refinement as the reflections were treated as overlapped.^[74] We are aware that an equivalent description in (3 + 1)D superspace could be possible due to the commensurate modulation vectors, which allow a description in the higher symmetric commensurate Bravais class $P6/mmm(1/3, 1/3, 0)$.^[75] Because this is more difficult to implement in the refinement and because a commensurate description would not be applicable to possible related structures with incommensurate modulations, we favor the (3 + 2)D description. The (3 + 1)D case, however, is discussed in the Supporting Information and a commensurate (3 + 1)D superspace group is deduced there.

A displacive modulation in superspace is an arbitrarily shaped wave running parallel to the higher dimensional basis vectors, which projected onto physical space are the modulation vectors. Transferred to the superstructure domains of Ce₄Li₃P₁₈N₃₅, the modulation vectors \mathbf{q}_1 , \mathbf{q}_2 and their linear

combination $\mathbf{q}_1 + \mathbf{q}_2$ give direction and wavelength of the modulation waves (Figure 5.11). Since Ce2 was shown to displace along [001], the modulated description necessitates a set of three purely z -polarized plane waves. Those modulation waves are expanded in sine and cosine functions, whose amplitudes are determined in the refinement. Since the waves are related by symmetry and the satellite order is one, only two amplitudes of one wave had to be determined. The refinement (Supporting Information for details) yielded the qualitative displacements of Ce2 atoms, corroborating the supercell description. The superstructure can be conceived as the superposition of three z -polarized plane waves with directions \mathbf{q}_{1d} , \mathbf{q}_{2d} , and $\mathbf{q}_{1d} + \mathbf{q}_{2d}$, wavelength $\lambda_m = 3a$ and mutual origin (Figure 5.12a). Ce2 atoms occur in three unique positions, one below, one above, and one approximately at the average z -coordinate (Figure 5.12b). Since the \mathbf{q} -vectors are commensurate, the supercell contains all structural variations but the long-range order of a domain can intuitively be grasped with the modulation-description.

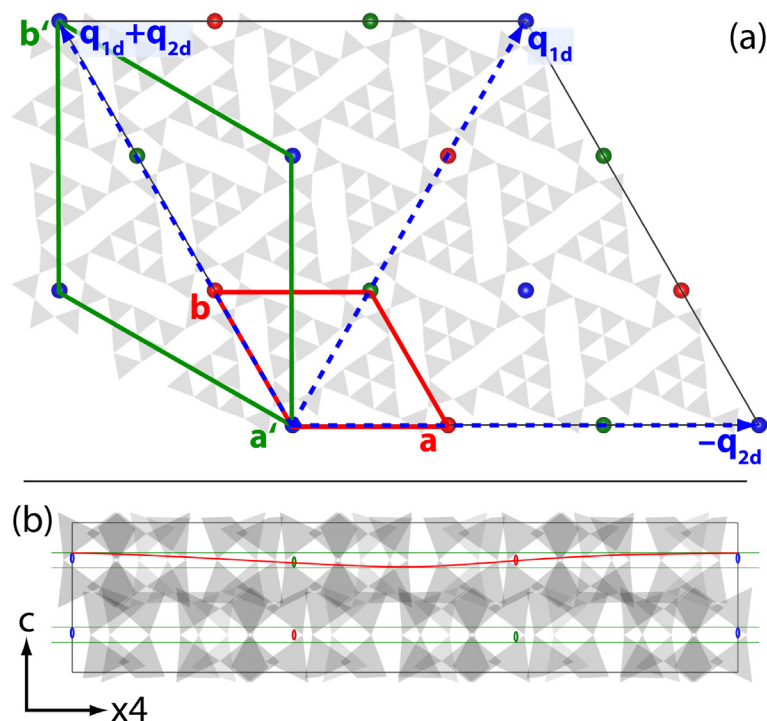


Figure 5.12. (a) Projection of the $(3 + 2)$ D superstructure model onto 3D space along [001] direction in a section corresponding to a $3 \times 3 \times 1$ multiple (black) of the basic cell (red). The $(\sqrt{3} \times \sqrt{3})R30^\circ$ supercell is given in green, and the modulation waves are indicated by dashed blue vectors. Atoms of equivalent displacement are marked with color (red, green, blue). (b) Ce2 displacement along [001] and along the additional direction of $(3 + 2)$ D superspace $\times 4$, atoms related by symmetry are marked with color.

5.3.7 Superstructure Discussion

Presumably, the Ce2 displacement causes the elongated N6, N7, and N8 ellipsoids observed in the basic structure (Figures 5.3, 5.4, and 5.6). The N8 atoms evade the nearing Ce2 atoms by rotating further from the center of the six-membered ring; a displacement that in turn induced a twisting of N6 and N7, which are in close proximity to the six-membered rings (Figure 5.4a,b). However, the P atoms are unaffected by the Ce2 disposition, as indicated by regular displacement ellipsoids and can be interpreted as centers of rotation for the N atoms. Since the P atoms are indifferent to the conformation of the six-membered rings and no intratetrahedra N–P–N angles distort, this N-induced distortion seems to have a low energetic barrier. A displacive modulation of the N atoms, however, cannot be refined from the synchrotron data because the reflections in the $hk0$ plane that would carry such information are not observed even with the combination of PILATUS detector and third generation synchrotron.

Displacement of heavy atoms in channel-like coordination environments has been reported before; a stabilization of Ba through modulation was suggested as the driving force in Ba_{0.85}Ca_{2.15}In₆O₁₂.^[70] Similarly, the Ce2 displacement might be driven by electrostatics. By moving up and down the channels, Ce2 leaves the Ce2N₉ coordination sphere and enters a distorted octahedral coordination (Figure 5.6c), also evading the trigonal planar surrounding of N4 atoms. The octahedral coordination mimics the bonding situation in CeN and thus might be the driving force for the displacement.^[76]

A long-range modulation can arise since the framework is condensed with all-side vertex-sharing tetrahedra, conducting the displacement information from one six-membered-ring channel to the other via the bridging triangular columns. The strength of this long-range ordering, however, is small as can be inferred from the small displacement ellipsoids of all atoms except N6, N7, N8, and Ce2. Thus, an accumulation of Ce2 vacancies might interrupt the transfer of information on the modulation and create the nonmodulated domains.

5.3.8 Optical Properties

The emission spectrum of Ce_{4-0.5x}Li₃P₁₈N_{35-1.5x}O_{1.5x} (Figure 5.13) reveals optical emission in the range of 410 nm (detector start) to 526 nm with a maximum at 455 nm corresponding to a full width at half-maximum of 71 nm (3520 cm⁻¹). The peak shape is anisotropic and cannot be modeled by one

Gaussian function. Owing to Ce^{3+} 's electron configuration of $[\text{Xe}]4f^1$, the electronic ground state is split in two states of similar energy, $^2F_{5/2}^0$ and $^2F_{7/2}^0$, which usually results in a broadening of the Ce^{3+} emission. Moreover, in the near-UV region, re-excitation might occur due to the small Stokes shift, explaining the anisotropy. As the Ce2 atom position is modulated, so is the coordination environment around the corresponding atom. This could also take effect on peak broadening.

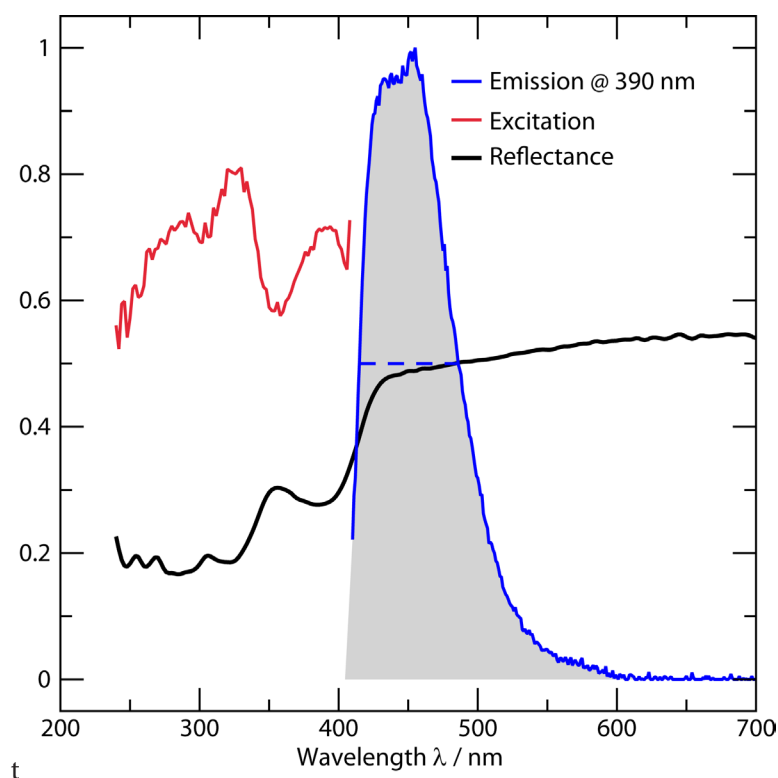


Figure 5.13. $\text{Ce}_{4-0.5x}\text{Li}_3\text{P}_{18}\text{N}_{35-1.5x}\text{O}_{1.5x}$ emission spectrum (blue) in the range 410–700 nm, excitation spectrum (red) in the range 240–400 nm, and reflectance (black) in the range of 240–700 nm.

Usually, luminescence is observed from Ce^{3+} -doped inorganic host frameworks since pure Ce-containing compounds tend to exhibit concentration quenching (although exceptions like the UV or blue luminescence of several Ce salts are known).^[77] The suggested mechanism for concentration quenching involves a transfer of excitation energy between active ions in close spatial proximity, which increases the chance of a nonradiative decay of the excited state.^[78,79] The Ce–Ce distances might be too large for concentration quenching ($d(\text{Ce}1\text{–}\text{Ce}1) = 4.760$, $d(\text{Ce}2\text{–}\text{Ce}2) = 4.068$, $d(\text{Ce}1\text{–}\text{Ce}2) = 5.862$ Å) as the Ce atoms are separated by a rigid tetrahedra framework. Moreover, the Ce2 vacancies increase the interatomic distance between adjacent Ce2 atoms, which might facilitate luminescence.

The UV–vis reflectance spectrum (Figure 5.13, black line) follows the inverse trend of the excitation spectrum, low reflectivity at high excitation and vice versa.

5.3.9 Magnetic Properties

The predicted effective magnetic moment, μ_{eff} of Ce³⁺ in electronic ground state $^2F_{5/2}^0$ is $\mu_{\text{eff}} = 2.54 \mu_{\text{B}}$ according to Hund's laws and Russel-Saunders' spin–orbit-coupling approximation. The effective magnetic moment of Ce_{4–0.5x}Li₃P₁₈N_{35–1.5x}O_{1.5x} was determined with SQUID magnetometry by measuring the temperature dependent susceptibility at a constant magnetic field of 20 kOe (1 kOe = $7.96 \times 10^4 \text{ A}\cdot\text{m}^{-1}$). Because of the nonstoichiometric reaction of Ce_{4–0.5x}Li₃P₁₈N_{35–1.5x}O_{1.5x}, the total Ce content of the sample (0.5495 mmol/g) was determined with ICP-OES. A linear regression fit to the χ_{m}^{-1} data in the range of 50 to 200 K (Figure 5.14) yielded a $\mu_{\text{eff,exp}} = 2.71(1) \mu_{\text{B}}$, which is slightly larger than the theoretical value, and a Curie temperature of $\theta = -2.9(2) \text{ K}$. The 7% deviation in theoretical and experimental μ_{eff} might be due to a slight under-determination of the sample's Ce content, which was solved with aqua regia at 200 °C. The electronic state of Ce_{4–0.5x}Li₃P₁₈N_{35–1.5x}O_{1.5x} is paramagnetic.

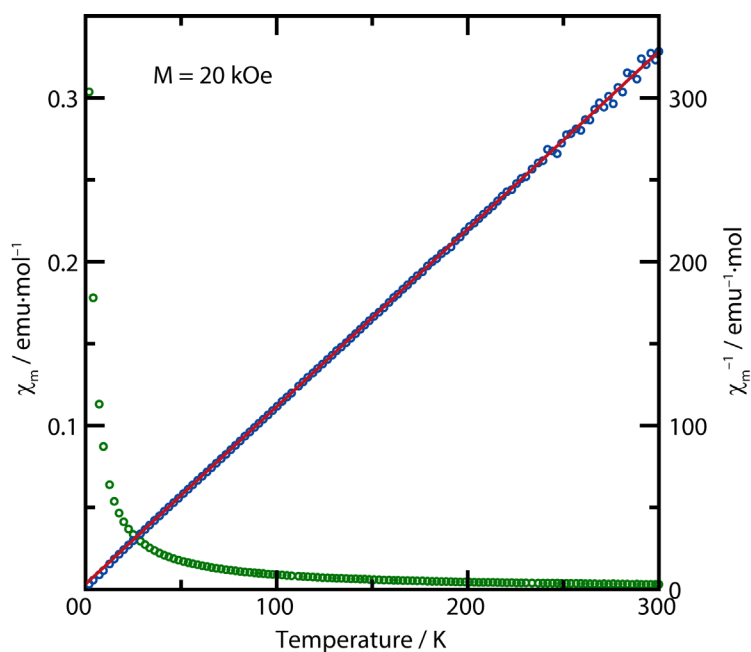


Figure 5.14. Molar magnetic susceptibility of Ce_{4–0.5x}Li₃P₁₈N_{35–1.5x}O_{1.5x} determined at 20 kOe in the range of 1.85–300 K. Green circles χ_{m} vs T , blue circles χ_{m}^{-1} vs T , and a Curie–Weiss fit displayed as a red line.

5.4 Conclusion

Nitridophosphates with a degree of condensation larger than 1/2 are scarcely known. $\text{Ce}_{4-0.5x}\text{Li}_3\text{P}_{18}\text{N}_{35-1.5x}\text{O}_{1.5x}$ ($x \approx 0.72$) is the first non-alkaline earth nitridophosphate comprising a framework with $\kappa > 1/2$; an example showing that high-pressure metathesis gives access to a large unexplored structure space. In retrospect to the here observed blue light emission, these expectedly rigid structures could lead to a new class of host frameworks for inorganic solid state lighting.

The joint venture of aberration-corrected STEM and synchrotron diffraction showed that $\text{Ce}_{4-0.5x}\text{Li}_3\text{P}_{18}\text{N}_{35-1.5x}\text{O}_{1.5x}$ ($x \approx 0.72$) contains two different domains, one with a higher and one with a lower O content, which we correlated to the amount of Ce2 vacancies. In the domains of low O content, the Ce2 atoms enter a long-range periodic order. Due to this Ce2 deficiency, the average structure has the sum formula $\text{Ce}_{4-0.5x}\text{Li}_3\text{P}_{18}\text{N}_{35-1.5x}\text{O}_{1.5x}$ ($x \approx 0.72$). In the superstructure domains TEM EDX revealed only negligible amounts of O, which could also stem from surface hydrolysis. Therefore, Ce2 vacancies cannot be ruled out but to our conjecture some domains exhibit full Ce2 occupation and sum formula $\text{Ce}_4\text{Li}_3\text{P}_{18}\text{N}_{35}$. Seemingly, the structure is stabilized either by forming a superstructure or by introducing vacancies on the Ce2 position.

Both supercell and superspace refinements yielded the same, due to the domains qualitative, superstructure model. With STEM, we directly observed the Ce2 displacement and measured a distance of ca. 0.3(1) Å between lowest and highest atom. The small variation between the two domains necessitated an investigation at the detection limit of state of the art analysis methods that may indicate the frontier of structure analysis.

5.5 References

- [1] F. H. Allen, *Crystallographic Databases* (Eds.: Bergerhoff, G., Brown, I. D.), International Union of Crystallography: Chester, **1987**.
- [2] F. Liebau, *Structural Chemistry of Silicates: Structure, Bonding, and Classification*; Springer: Berlin, Germany, 1985.
- [3] A. Belsky, M. Hellenbrandt, V. L. Karen, P. Luksch, *Acta Crystallogr., Sect. B: Struct. Sci.* **2002**, 58, 364–369.
- [4] W. Schnick, V. Schultz-Coulon, *Angew. Chem., Int. Ed. Engl.* **1993**, 32, 280–281; *Angew. Chem.* **1993**, 105, 308–309.
- [5] A. Marchuk, W. Schnick, *Angew. Chem., Int. Ed.* **2015**, 54, 2383–2387; *Angew. Chem.* **2015**, 127, 2413–2417.
- [6] F. Karau, W. Schnick, *Angew. Chem., Int. Ed.* **2006**, 45, 4505–4508; *Angew. Chem.* **2006**, 118, 4617–4620.
- [7] M. Pouchard, *Nature* **2006**, 442, 878–879.
- [8] K. Landskron, H. Huppertz, J. Senker, W. Schnick, *Angew. Chem., Int. Ed.* **2001**, 40, 2643–2645; *Angew. Chem.* **2001**, 113, 2713–2715.
- [9] S. Horstmann, E. Irran, W. Schnick, *Angew. Chem., Int. Ed. Engl.* **1997**, 36, 1992–1994; *Angew. Chem.* **1997**, 109, 2085–2087.
- [10] D. Baumann, W. Schnick, *Angew. Chem., Int. Ed.* **2014**, 53, 14490–14493; *Angew. Chem.* **2014**, 126, 14718–14721.
- [11] S. D. Kloß, W. Schnick, *Angew. Chem., Int. Ed.* **2015**, 54, 11250–11253; *Angew. Chem.* **2015**, 127, 11402–11405.
- [12] S. D. Kloß, N. Weidmann, W. Schnick, *Eur. J. Inorg. Chem.* **2017**, 1930–1937.
- [13] S. D. Kloß, N. Weidmann, R. Niklaus, W. Schnick, *Inorg. Chem.* **2016**, 55, 9400–9409.
- [14] S. Horstmann, E. Irran, W. Schnick, *Angew. Chem., Int. Ed. Engl.* **1997**, 36, 1992–1994; *Angew. Chem.* **1997**, 109, 2085–2087.
- [15] K. Landskron, E. Irran, W. Schnick, *Chem. - Eur. J.* **1999**, 5, 2548–2553.
- [16] R. Nymwegen, H. Jacobs, *Z. Anorg. Allg. Chem.* **1997**, 623, 429–433.
- [17] A. Vitola, J. Ronis, T. Millers, *Latv. PSR Zinat. Akad. Vestis, Kim. Ser.* **1990**, 90, 299–301.

- [18] K. Landskron, W. Schnick, *J. Solid State Chem.* **2001**, *156*, 390–393.
- [19] K. A. Denault, J. Brgoch, S. D. Kloß, M. W. Gaultois, J. Siewenie, K. Page, R. Seshadri, *ACS Appl. Mater. Interfaces* **2015**, *7*, 7264–7272.
- [20] O. Delgado-Friedrichs, A. W. M. Dress, D. H. Huson, J. Klinowski, A. L. Mackay, *Nature* **1999**, *400*, 644–647.
- [21] D. Durach, L. Neudert, P.J. Schmidt, O. Oeckler, W. Schnick, *Chem. Mater.* **2015**, *27*, 4832–4838.
- [22] F. Gramm, C. Baerlocher, L. B. McCusker, S. J. Warrender, P. Wright, B. Han, S. B. Hong, Z. Liu, T. Ohsuna, O. Terasaki, *Nature* **2006**, *444*, 79–81.
- [23] D. Batuk, M. Batuk, A. M. Abakumov, J. Hadermann, *Acta Crystallogr., Sect. B: Struct. Sci., Cryst. Eng. Mater.* **2015**, *71*, 127–143.
- [24] S. Hovmöller, X. Zou, *Cryst. Res. Technol.* **2011**, *46*, 535–541.
- [25] W. Zhou, H. F. Greer, *Eur. J. Inorg. Chem.* **2016**, *2016*, 941–950.
- [26] J. Sun, Z. He, S. Hovmöller, X. Zou, F. Gramm, C. Baerlocher, L. B. McCusker, *Z. Kristallogr. – Cryst. Mater.* **2010**, *225*, 77–85.
- [27] F. Fahrnbauer, T. Rosenthal, T. Schmutzler, G. Wagner, G. B. M. Vaughan, J. P. Wright, O. Oeckler, *Angew. Chem., Int. Ed.* **2015**, *54*, 10020–10023; *Angew. Chem.* **2015**, *127*, 10158–10161.
- [28] F. Azough, R. Freer, *J. Am. Ceram. Soc.* **2010**, *93*, 1237–1240.
- [29] R. Huang, T. Mizogushi, K. Sugiura, H. Ohta, K. Koumoto, T. Hirayama, *Appl. Phys. Lett.* **2008**, *93*, 181907.
- [30] F. Yang, D. R. Coughlin, P. J. Phillips, Y. Yang, A. Devaraj, L. Kovarik, R. D. Noebe, M. J. Mills, *Acta Mater.* **2013**, *61*, 3335–3346.
- [31] K. Z. Baba-Kishi, *J. Appl. Cryst.* **2011**, *44*, 111–121.
- [32] V. Dyadkin, P. Pattison, V. Dmitriev, D. Chernyshov, *J. Synchrotron Radiat.* **2016**, *23*, 825–829.
- [33] B. Henrich, A. Bergamaschi, C. Broennimann, R. Dinapoli, E. F. Eikenberry, I. Johnson, M. Kobas, P. Kraft, A. Mozzanica, B. Schmitt, *Nucl. Instrum. Methods Phys. Res., Sect. A* **2009**, *607*, 247–249.
- [34] E. F. Eikenberry, C. Brönnimann, G. Hülsen, H. Toyokawa, R. Horisberger, B. Schmitt, C. Schulze-Briese, T. Tomizaki, *Nucl. Instrum. Methods Phys. Res., Sect. A* **2003**, *501*, 260–266.

- [35] A. Stock, H. Grüneberg, *Ber. Dtsch. Chem. Ges.* **1907**, *40*, 2573–2578.
- [36] W. Schnick, J. Lücke, *Z. Anorg. Allg. Chem.* **1990**, *588*, 19–25.
- [37] N. Kawai, S. Endo, *Rev. Sci. Instrum.* **1970**, *41*, 1178–1181.
- [38] H. Z. Huppertz, *Kristallogr.* **2004**, *219*, 330–338.
- [39] D. Walker, *Am. Mineral.* **1991**, *76*, 1092–1100.
- [40] D. Walker, M. A. Carpenter, C. M. Hitch, *Am. Miner.* **1990**, *75*, 1020–1028.
- [41] D. C. Rubie, *Phase Transitions* **1999**, *68*, 431–451.
- [42] A. A. Coelho, *TOPAS-Academic V4.1*, Coelho Software, Brisbane, Australia, **2007**.
- [43] Agilent Technologies, *CrysAlis Pro*, Yarnton, Oxfordshire, England, **2011**.
- [44] Bruker AXS, Inc., *SADABS*, Madison, Wisconsin, USA, **2001**.
- [45] G. M. Sheldrick, *Acta Crystallogr., Sect. A: Found. Crystallogr.* **2008**, *64*, 112–122.
- [46] G. M. Sheldrick, *SHELXS – A Programm for Crystal structure Solution*, University of Göttingen, Germany, **1997**.
- [47] V. Petříček, M. Dušek, L. Z. Palatinus, *Kristallogr. – Cryst. Mater.* **2014**, *229*, 345–352.
- [48] K. Momma, F. J. Izumi, *Appl. Crystallogr.* **2011**, *44*, 1272–1276.
- [49] K. Brandenburg, *Diamond*, Crystal Impact GbR, Bonn, Germany **2014**.
- [50] Gatan, Inc., *Digital Micrograph*, Pleasanton, California, USA, **1999**.
- [51] J. L. Lábár, *Ultramicroscopy* **2005**, *103*, 237–249.
- [52] P. A. Stadelmann, *JEMS*, CIME-EPFL, Saas-Fee, Switzerland **2008**.
- [53] Emispec Systems, Inc. *ES Vision*, Tempe, Arizona, USA, **2002**.
- [54] EDAX AMETEK, *TEAM*, Wiesbaden, Germany **2013**.
- [55] C. G. Cofer, *Economy, J. Carbon* **1995**, *33*, 389–395.
- [56] O. Hassel, *Nor. Geol. Tidsskr.* **1927**, *9*, 266–270.
- [57] R. Klement, O. Koch, *Chem. Ber.* **1954**, *87*, 333–340.
- [58] J. Goff, W. Hayes, S. Hull, M. Hutchings, K. Clausen, *Phys. Rev. B* **1999**, *59*, 14202–14219.
- [59] Bruker AXS, Inc., *XPREP*, Karlsruhe, Germany, **2001**.
- [60] R. Hübenthal, *MAPLE, Programm zur Berechnung des Madelunganteils der Gitterenergie*, Vers. 4, University of Giessen, **1993**.
- [61] E. Mugnaioli, S. J. Sedlmaier, O. Oeckler, U. Kolb, W. Schnick, *Eur. J. Inorg. Chem.* **2012**, *2012*,

- 121–125.
- [62] S. J. Sedlmaier, E. Mugnaioli, O. Oeckler, U. Kolb, W. Schnick, *Chem. Eur. J.* **2011**, *17*, 11258–11265.
- [63] O. Delgado-Friedrichs, M. O’Keeffe, *J. Solid State Chem.* **2005**, *178*, 2480–2485.
- [64] V. A. Blatov, M. O’Keeffe, D. M. Proserpio, *CrystEngComm* **2010**, *12*, 44–48.
- [65] V. A. Blatov, A. P. Shevchenko, D. M. Proserpio, *Cryst. Growth Des.* **2014**, *14*, 3576–3586.
- [66] O. Delgado-Friedrichs, *3dt*, <http://www.gavrog.org/>, **2013**.
- [67] V. A. Blatov, O. Delgado-Friedrichs, M. O’Keeffe, D. M. Proserpio, *Acta Crystallogr., Sect. A: Found. Crystallogr.* **2007**, *63*, 418–425.
- [68] N. W. Johnson, *Can. J. Math.* **1966**, *18*, 169–200.
- [69] M. Somer, U. Herterich, J. Curda, K. Peters, H. G. von Schnering, *Z. Kristallogr.* **1994**, *209*, 182.
- [70] G. Baldinozzi, F. Goutenoire, M. Hervieu, E. Suard, D. Grebille, *Acta Crystallogr., Sect. B: Struct. Sci.* **1996**, *52*, 780–789.
- [71] L. A. J. Gravie, P. R. Buseck, *J. Phys. Chem. Solids* **1999**, *60*, 1943–1947.
- [72] S. Arai, S. Muto, J. Murai, T. Sasaki, Y. Ukyo, K. Kuroda, H. Saka, *Mater. Trans.* **2004**, *45*, 2951–2955.
- [73] A. M. D’Angelo, A. C. Y. Liu, A. L. Chaffee, *J. Phys. Chem. C* **2016**, *120*, 14382–14389.
- [74] L. Bindi, P. Bonazzi, M. Dušek, V. Petříček, G. Chapuis, *Acta Crystallogr., Sect. B: Struct. Sci.* **2001**, *57*, 739–746.
- [75] S. Van Smaalen, *Acta Crystallogr., Sect. A: Found. Crystallogr.* **1987**, *43*, 202–207.
- [76] W. Klemm, G. Winkelmann, *Z. Anorg. Allg. Chem.* **1956**, *288*, 87–90.
- [77] F. A. Kröger, J. Bakker, *Physica* **1941**, *8*, 628–646.
- [78] D. L. Dexter, J. H. Schulman, *J. Chem. Phys.* **1954**, *22*, 1063–1070.
- [79] F. Benz, H. P. Strunk, *AIP Adv.* **2012**, *2*, 2–7.

Chapter 6

LiPr₂P₄N₇O₃: Structural Diversity of Oxonitridophosphates Accessed by High-Pressure Metathesis

Simon D. Kloß, Wolfgang Schnick

published in: *Inorg. Chem* **2018**, *57*, 4189–4195. DOI: 10.1021/acs.inorgchem.8b00455

Reprinted (adapted) with permission from *Inorganic Chemistry*. Copyright 2018 American Chemical Society.



The oxonitridophosphate LiPr₂P₄N₇O₃ was prepared by high-pressure metathesis. LiPr₂P₄N₇O₃ exemplifies the enhancement of structural diversity that can be accomplished by deliberately incorporating N and O anions into a tetrahedra framework. The crystal structure of LiPr₂P₄N₇O₃ consists of single-layered P(N/O)₄ tetrahedra nets with a degree of condensation of 2/5, which has not yet been observed for rare-earth nitridophosphates.

Abstract

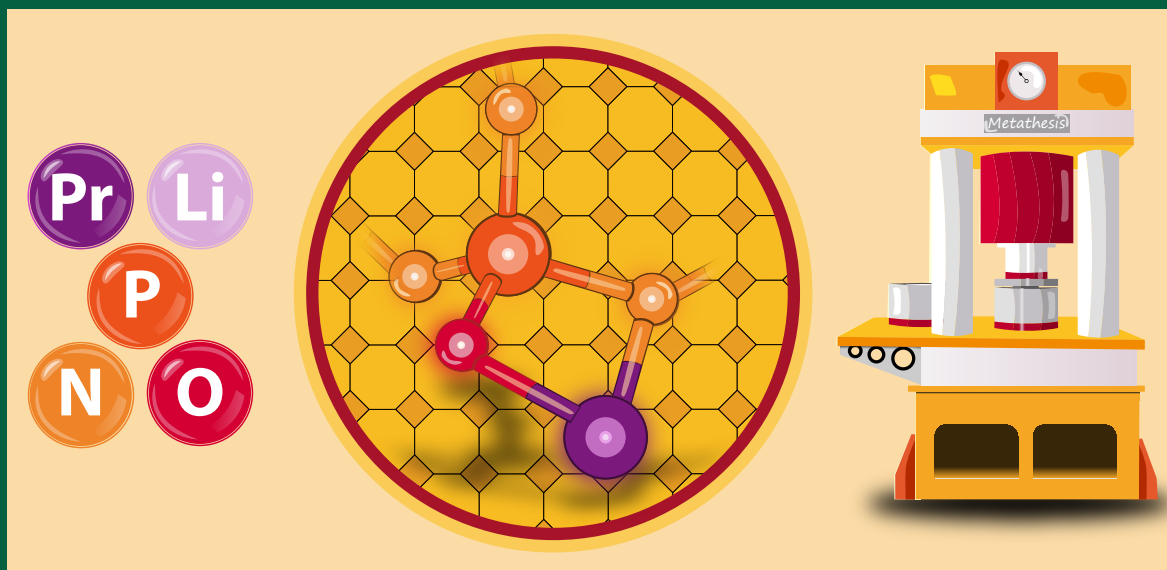


Table-of-contents graphic.

The structural diversity of tetrahedra networks of phosphates can greatly be enhanced by introduction of mixed N/O anion positions. $\text{LiPr}_2\text{P}_4\text{N}_7\text{O}_3$ exemplifies the benefits of N/O mixed anion positions as it is the first rare-earth (oxo)nitridophosphate with a single-layered structure and a degree of condensation (atomic ratio of tetrahedra centers (P) to tetrahedra corners (N/O atoms)) of 2/5. The compound was prepared through high-pressure metathesis starting from PrF_3 , LiPN_2 , Li_2O , and PON using a hydraulic 1000t press and the multianvil technique. $\text{LiPr}_2\text{P}_4\text{N}_7\text{O}_3$ crystallizes as pale-green single-crystals, from which its structure was determined (space group $P2_1/c$ (no. 14), $a = 4.927(1)$, $b = 7.848(2)$, $c = 10.122(2)$ Å, $\beta = 91.55(3)^\circ$, $Z = 2$, $R_1 = 0.020$, $wR_2 = 0.045$). The structure consists of single-layers of vertex-sharing Q^3 -type $\text{P}(\text{N/O})_4$ tetrahedra forming four- and eight-membered rings arranged in the fashion of the Archimedean *fes* net. UV-vis spectroscopy revealed the typical Pr^{3+} f-f transitions, leading to a pale-green color of the crystals. Moreover, the optical band gap was determined to 4.1(1) eV, assuming a direct transition. High-temperature powder X-ray diffraction showed the beginning of a gradual decomposition starting at ca. 500 °C.

6.1 Introduction

The continued interest of chemists, mineralogists, and materials scientists in compound classes with tetrahedra-based network structures such as silicates or phosphates arises, next to applications, from their immense structural versatility.^[1] Some variables to navigate the large explorative fields encompass the type of cation compensating the network's negative charge, the tetrahedra constituents, e.g. (Al,Si,P)/(N,O), and the degree of condensation κ , which is the ratio between the sum of tetrahedra centers to the sum of tetrahedra corners. The best example for the vastness such a materials family can take on is the numerous natural and synthetic (alumo)silicates known, incorporating almost all metals and encompassing innumerable structure types.^[1,2] The potential size of such a materials family might be estimated by taking into account the attainable κ together with the number of incorporable metal ions. While the low end of κ is 1/4, representing noncondensed tetrahedra, its high end is determined by electrostatics and terminates in the binary parent compound. For example, the combination P/O has the maximum κ of 2/5, that being the binary P₂O₅.^[3] Due to N's higher formal charge, substituting O with N leads to an increased span of κ and access to higher condensed networks, which becomes apparent when comparing, e.g., the molecular adamantane-type P₄O₁₀ with the highly condensed framework of P₃N₅.^[4,5]

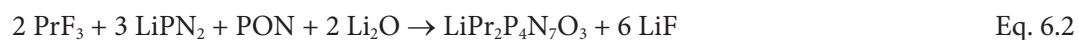
This increased span of κ from 1/4 to 3/5 and, stemming from this, additional building units such as edge-sharing tetrahedra or triply bridging N^[3] allow nitridophosphates to theoretically rival even the diversity of silicates.^[6-9] Nitridophosphates are, however, a young class of materials, their research inhibited by experimental obstacles like the necessity of high-pressure techniques, the lack of viable synthesis routes, or microcrystalline samples. The latter two issues have been tackled in recent years through development of the azide and ammonium chloride routes for alkaline earth nitridophosphates and the high-pressure metathesis route for rare-earth and transition-metal nitridophosphates, which was used in this work.^[6,10-12] In high-pressure metathesis, rare-earth halides are reacted with LiPN₂ at pressures of several GPa achieved with a hydraulic press and the multianvil technique (Equation 6.1).^[6]



The resulting type of tetrahedra network can be directed by adding Li_3N to lower or by adding P_3N_5 to increase the degree of condensation, giving access to a broad range of κ , as exemplified by the series $\text{Ho}_3[\text{PN}_4]\text{O}$ with $\kappa = 1/4$, $\text{RE}_2\text{P}_3\text{N}_7$ with $\kappa = 3/7$, NdLiP_4N_8 with $\kappa = 1/2$, and $\text{Ce}_4\text{Li}_3\text{P}_{18}\text{N}_{35}$ with $\kappa = 18/35$.^[7–9]

Hence, the substitution of O with N in phosphates enlarges the structural possibilities, and one might even be inclined to subsume oxophosphates and nitridophosphates to two distinct classes of materials. Such distinction, however, would be ill-suited for explorative chemistry as it deprives the possibility of multinary compounds with mixed N/O anion positions. In our opinion, pure oxophosphates and pure nitridophosphates should be seen as the endmembers of a multidimensional phase system. A few of these oxonitridophosphates like $\text{Sr}_3\text{P}_6\text{O}_6\text{N}_8$ and $\text{SrP}_3\text{N}_5\text{O}$ have already been realized with alkaline earth metals.^[13,14] One issue is that the limitation to either N or O as the sole anion might impede the exploration of new structure types and tetrahedra connection patterns. For example, two polymorphs of single-layered $\text{RE}_2\text{P}_3\text{N}_7$ compounds with $\kappa = 3/7$ are known.^[7] However, no rare-earth nitridophosphate with $\kappa = 2/5$, the ratio single-layered structures are usually observed for, has been discovered yet. This is surprising because the number of tessellations of the Euclidean plane with three-connected vertices, which effectively describe all possible arrangements of Q^3 tetrahedra based monolayers with $\kappa = 2/5$, sums up to 3 uninodal, 17 binodal, and 103 trinodal patterns.^[7,15,16] Not including the patterns with more nodes (symmetry inequivalent vertices), there are 123 possible tetrahedra arrangements, but none could have been realized with exclusively PN_4 tetrahedra and rare-earth ions.

The reasons for this shortcoming can be manifold. Naturally, not all of the patterns described by tiling theory are feasible under the restraints of proper bond lengths and angles or they have not been discovered because of unsuitable synthesis methods and reaction conditions. But single-layers composed of PN_4 tetrahedra with $\kappa = 2/5$ might also not be stable with rare-earth ions due to electrostatic or geometric reasons. In this contribution, we show with the preparation of the oxonitridophosphate $\text{LiPr}_2\text{P}_4\text{N}_7\text{O}_3$ ($\kappa = 2/5$) how the inclusion of O into the PN_4 tetrahedra network can enhance the structural versatility of nitridophosphates in general. $\text{LiPr}_2\text{P}_4\text{N}_7\text{O}_3$ was prepared with high-pressure metathesis and the multianvil technique starting from PrF_3 , LiPN_2 , PON , and Li_2O following Equation 6.2.



Similar to Li₃N and P₃N₅ in pure nitridophosphates, Li₂O and PON are used as starting materials to set κ to 2/5. The compound crystallizes in large single-crystals, from which the structure was determined by X-ray diffraction. The phase composition of the powder sample and the physical properties of LiPr₂P₄N₇O₃ were analyzed by powder X-ray diffraction (PXRD), UV-vis, and infrared (IR) spectroscopy. The elemental composition was determined with scanning electron microscopy (SEM) and energy dispersive X-ray (EDX) spectroscopy. The temperature stability was investigated with high-temperature powder X-ray diffraction (HTPXRD).

6.2 Experimental Section

6.2.1 LiPN₂

LiPN₂ was prepared through solid–solid reaction of P₃N₅ and a 1.2 times excess Li₃N (94%, Rockwood Lithium, Langelsheim, Germany) under Ar atmosphere. P₃N₅ was synthesized by reaction of P₄S₁₀ (Sigma-Aldrich, 99.99%) with ammonia gas (Air Liquide 5.0) at 850 °C.^[6,17] P₃N₅ and Li₃N were thoroughly mixed and ground under inert conditions in an Ar filled glovebox with concentrations of O₂ and H₂O < 1 ppm. The ground mixture was conveyed into a Ta crucible residing in fused silica ampule, which was dried in vacuum beforehand. The sealed ampule was fired in a tube furnace at 800 °C with 5 °C/min temperature ramps and a 90 h dwell. After stepwise washing with water/ethanol, the product was obtained as a brownish powder, which was characterized by PXRD and IR.

6.2.2 Li₂O

Li₂O was obtained from thermal decarboxylation of Li₂CO₃ (Sigma-Aldrich, 99.99%).^[18] The Li₂CO₃ was loaded on an Ag boat and heated to 700 °C for 72 h under dynamic vacuum conditions (<0.1 Pa) within a fused silica tube. The product was characterized by PXRD and stored in the glovebox.

6.2.3 a-PON

OP(NH₂)₃, which was prepared from reaction of POCl₃ with liquid ammonia (Air Liquide 5.0), was fired in a constant flow of ammonia (Air Liquide 5.0) to yield amorphous PON (a-PON).^[19,20] For this purpose, a fused silica tube was dried in vacuum (<0.1 Pa) at 1000 °C and then loaded with the OP(NH₂)₃ + 3NH₄Cl mixture, which is the direct reaction product of the POCl₃ ammonolysis. The NH₄Cl was sublimated at 300 °C in a constant flow of ammonia over the course of 5 h, after which the temperature was raised to 620 °C and maintained for 12 h. The obtained a-PON was characterized by IR and PXRD (to exclude residual NH₄Cl).

6.2.4 LiPr₂P₄N₇O₃

LiPr₂P₄N₇O₃ was prepared by high-pressure metathesis starting from stoichiometric amounts of PrF₃ (Alfa Aesar, 99.99%), LiPN₂, PON, and Li₂O at 8 GPa and ca. 1200 °C. Compression time was 208

min, followed by the temperature program at constant pressure with a 30 min heating/cooling ramps and 120 min dwell. Decompression was conducted over a period of 624 min. The reaction conditions were achieved with a 1000t hydraulic press (Voggenreiter, Mainleus, Germany) and the multianvil setup using a modified Walker-type module (Voggenreiter). The multianvil setup consisted of an 18/11 octahedra-within-cubes load, which was driven by steel wedges. A Cr₂O₃-doped MgO octahedron was used as pressure medium with pyrophyllite as gasket material (Ceramic Substrates & Components, Isle of Wight, U.K.) and tungsten carbide cubes (11 mm truncation of edges, Hawedia, Marklkofen, Germany). The starting materials were thoroughly ground in a glovebox then loaded into an h-BN crucible (Henze, Kempten, Germany). Heating was done by graphite sleeves. (Schunk Kohlenstofftechnik GmbH, Zolling, Germany). Additional information regarding the employed high-pressure technique can be found in literature.^[21–25]

6.2.5 Single-Crystal Diffraction

X-ray diffraction data of single-crystals (SCXRD) were collected on a D8 Quest diffractometer (Bruker, Billerica, MA, United States) equipped with a microfocus Mo K α X-ray source. Data were reduced, and semiempirical absorption correction was applied with the program APEX2.^[26] The space group was determined with XPREP based on systematically absent reflections.^[27] Structure solution and refinement was carried out with SHELX-97.^[28,29] Crystal structures were visualized with VESTA.^[30]

CCDC 1824687 contains the supplementary crystallographic data for this paper. The data can be obtained free of charge from The Cambridge Crystallographic Data Centre via www.ccdc.cam.ac.uk/structures.

Further details on the crystal structure analysis can be obtained from the Fachinformationszentrum Karlsruhe, 76344 Eggenstein-Leopoldshafen, Germany (fax: + 49-7247-808-666; e-mail: crysdata@fiz-karlsruhe.de) on quoting the depository number CSD 434268.

6.2.6 Powder X-Ray Diffraction

PXRD data were obtained with a Stadi P diffractometer (STOE & Cie GmbH, Darmstadt, Germany) in parafocusing Debye–Scherrer Geometry. Mo K α 1 radiation was used, singled out with a Ge(111) monochromator. Diffractograms were recorded with a Mythen 1K Si-strip detector (Dectris, Baden,

Switzerland). Rietveld refinement was performed with TOPAS-Academic V4.1.^[31] The background was handled with a shifted Chebychev function, and the peak shape was modeled with the fundamental parameters approach, convoluting source emission profile, crystallite size, microstrain, and peak asymmetry from axial instrument contributions. Data were corrected with a capillary absorption correction.^[32] Samples were loaded to glass capillaries 0.3 mm in diameter (Hilgenberg GmbH, Malsfeld, Germany).

High-temperature PXRD data were collected with the same radiation source as the PXRD data on a Stadi P diffractometer mounted with a graphite furnace and an image-plate position-sensitive detector. The diffractograms were recorded in the range of 25–1000 °C in steps of 20 °C.

6.2.7 Spectroscopy

Fourier transform IR spectra were recorded on a Spectrum BX II spectrometer (PerkinElmer, Waltham, MA, United States) with an attenuated total reflectance (ATR) unit in the range of 600–4500 cm^{-1} .

UV–vis spectra were obtained with a FLS920-s spectrometer (Edinburgh Instruments, Livingston, Scotland) featuring a Xe900 450 W arc lamp, a single-photon photomultiplier detector, and a Czerny–Turner monochromator with triple-grating turret. Spectra were recorded in the range of 240–800 nm with a 1 nm step width and in the range of 410–630 nm with a step width of 0.025 nm.

SEM and EDX spectroscopy were carried out on a Helios Nanolab G3 Dualbeam UC (FEI, Hillsboro, OR, United States) equipped with an X-Max 80 SDD detector (Oxford Instruments, Abingdon, United Kingdom). Samples were placed on adhesive conducting carbon foil affixed to a metal carrier and coated with a thin layer of carbon.

6.3 Results and Discussion

6.3.1 Synthesis

LiPr₂P₄N₇O₃ crystallizes, after synthesis outlined in the Experimental Section, in pale-green single-crystals up to 200 μm in size (Figure 6.1), which are stable against air and water. PXRD could not detect any other phases than LiPr₂P₄N₇O₃ (Figure F.1) after the reaction product had been washed with water to remove residual LiF formed in the metathesis reaction. The elemental composition, determined with EDX on smooth surfaces of the single crystals, fits to the theoretical values within the standard deviations: experiment/theory Pr_{2.1(2)}P_{3.9(2)}N_{6.9(5)}O_{3.1(4)}/Pr₂P₄N₇O₃, 10 points of measurement. No indication for N–H or O–H bonds was found by IR spectroscopy (Figure F.2).

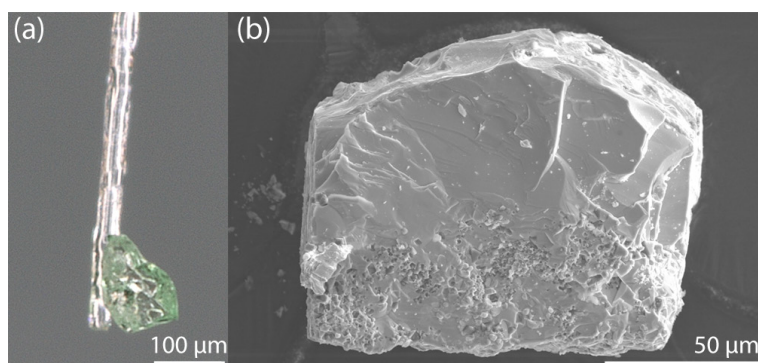


Figure 6.1. (a) Digital micrograph of a single-crystal used for the SCXRD affixed to a glass rod. (b) SEM micrograph of another crystal, revealing smooth crystal surfaces

6.3.2 Structure Determination

The structure was solved from single-crystal data in space group $P2_1/c$ (no. 14) using direct methods yielding the positions of Pr and P. Atom sites of N/O and Li were identified from difference Fourier maps. All atoms could be refined anisotropically. Crystallographic data are summarized in Table 6.1, atom positions are given in Table 6.2, anisotropic displacement parameters and tables of interatomic distances and angles in Tables F.2 to F.4. As O and N cannot be distinguished with X-ray diffraction due to the similar atomic form factors, the assignment of the N/O mixed positions was based on bond valence sum (BVS) and charge distribution (with VESTA) calculations, which indicated a shared position on site N1/O1 and N5/O5 (Tables F.5 and F.6).^[30,33] As a restrained refinement (with the SUMP instruction) of the N/O occupancy did not converge, they were set to N/O 0.25/0.75 to account for the charge balancing.

Table 6.1. Crystallographic Data for the Refinement of $\text{LiPr}_2\text{P}_4\text{N}_7\text{O}_3$.

Crystal data	
Formula	$\text{LiPr}_2\text{P}_4\text{N}_7\text{O}_3$
Formula mass / $\text{g}\cdot\text{mol}^{-1}$	558.71
Crystal system	monoclinic
Space group	$P2_1/c$ (no. 14)
Cell parameters / $\text{\AA},^\circ$	$a = 4.927(1)$ $b = 7.848(2)$ $c = 10.122(2)$ $\beta = 91.55(3)$
Cell volume / \AA^3	391.3(2)
Formula units per unit cell Z	2
$F(000)$	508
Calculated density ρ / $\text{g}\cdot\text{cm}^{-3}$	4.74
Abs. coefficient μ / mm^{-1}	13.1
Data collection	
Radiation	Mo-K α
Temperature / K	293(2)
θ range / $^\circ$	$3.285 \leq \theta \leq 45.263$
Total no. of reflections	30850
Independent reflections	3279
Absorption correction	semiempirical ^[26]
$R_{\text{intr}}, R_{\text{sigma}}$	0.044, 0.020
Refinement	
Refined parameters	80
Goodness of fit	1.150
R_1 (all data), $R_1 [F^2 > 2\sigma(F^2)]$	0.024, 0.020
wR_2 (all data), $wR_2 [F^2 > 2\sigma(F^2)]$	0.046, 0.045
$\Delta\rho_{\text{max}}, \Delta\rho_{\text{min}}/\text{e}\cdot\text{\AA}^{-3}$	1.60, -1.59

6.3.3 Structure Description

Following silicate nomenclature, $\text{LiPr}_2\text{P}_4\text{N}_7\text{O}_3$ can be classified as a monophyllo-oxonitridophosphate, of which only the two *bex*- and *mcm*- $\text{RE}_2\text{P}_3\text{N}_7$ modifications and $\text{Li}_5\text{P}_2\text{N}_5$ have been known.^[1,7,34]

The structure consists of vertex-sharing Q^3 -type $\text{P}(\text{ON})_4$ tetrahedra, condensed to four- and eight-membered rings to form one planar single-layer per unit cell (Figure 6.2a). The Pr atoms reside between the single layers on a general Wyckoff position, and as can be seen from projection along the *a* direction (Figure 6.2b), are located in between the voids created by the eight-membered rings, as

would be expected. Li, residing on a special Wyckoff position on the unit cell edges, are similarly located in between two four-membered rings.

Table 6.2. Positions, Equivalent Displacement Parameters, and Occupancy of the Atoms in LiPr₂P₄N₇O₃.^a

Atom	Wyckoff position	x	y	z	$U_{eq}/\text{Å}^2$	Occupancy
Pr1	4e	0.00067(2)	0.60908(2)	0.67233(2)	0.00774(2)	1
P1	4e	0.47490(8)	0.23585(5)	0.08271(3)	0.00559(5)	1
P2	4e	0.53807(8)	0.09178(5)	0.33902(4)	0.00623(6)	1
O1	4e	0.2469(3)	0.10736(15)	0.04150(12)	0.00891(17)	0.75
N1	4e	0.2469(3)	0.10736(15)	0.04150(12)	0.00891(17)	0.25
N2	4e	0.3207(3)	0.40369(16)	0.13935(13)	0.00843(18)	1
N3	4e	0.3399(3)	0.71949(17)	0.04389(13)	0.00894(18)	1
N4	4e	0.6773(3)	0.15801(17)	0.19969(12)	0.00794(17)	1
O5	4e	0.2212(3)	0.09014(15)	0.33258(12)	0.00953(17)	0.75
N5	4e	0.2212(3)	0.09014(15)	0.33258(12)	0.00953(17)	0.25
Li1	2c	0	0	1/2	0.0209(11)	1

^aSites N1/O1 and N5/O5 are shared positions.

The connection pattern of the contiguous four- and eight-membered rings can be subsumed by point symbol 4.8² and vertex symbol 4.8.8.^[35] To further classify the topology of the P(N/O)₄ net, it can be related to a mathematical tessellation of the Euclidean plane. The tiling pattern with maximum symmetry embedding of the 4.8.8-net is the Archimedean *fes*, in nomenclature of the Reticular Chemistry Structure Resource (RCSR) database (Figure 6.2c).^[35–37] The mathematical *fes* tiling in holohedral symmetry has plane group *p4mm* (no. 11), while the symmetry of LiPr₂P₄N₇O₃ along the special [100] projection is the lower symmetric *p2gg* (no. 8) group. The distortions, visible in the elongated and stretched four- and eight-membered rings of tetrahedra, are probably necessitated through the incorporation of one- and trivalent metal ions, Li and Pr, into the structure.

A comparison of LiPr₂P₄N₇O₃ with the apophyllite group of silicates, which also feature the *fes*-related tetrahedra net, may emphasize the flexibility of tetrahedra anion networks with regard to spatial arrangement and symmetry. The apophyllites, e.g. fluorapophyllite Ca₄K(Si₈O₂₀)F(H₂O)₈, crystallize in space group *P4/mnc* (no. 128).^[38]

Their *fes*-related tetrahedra net, though having a higher symmetry group *p4gm* (no. 12) along the special [001] projection, enters a corrugated boat-like conformation by alternating the direction in which the terminal O atoms of the four-membered rings point. Curiously, the special projection of

the apophyllite net has a higher symmetry group than the mathematical *fes* tiling. This is because the four- and eight-membered rings of the silicate are not regular. Regular polygons, from which the *fes* tiling is composed, are transitive on their vertices and edges, which means they only have one vertex and edge that are equivalent through the automorphism group of the polygon.^[35,39]

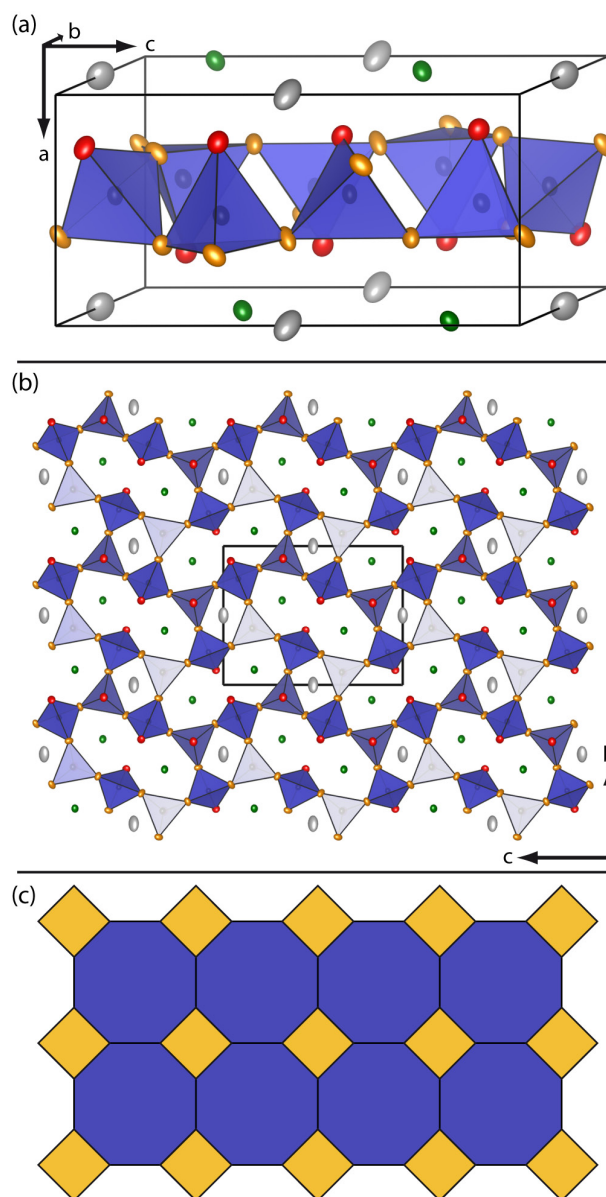


Figure 6.2. (a) Unit cell of $\text{LiPr}_2\text{P}_4\text{N}_7\text{O}_3$, Li displayed as gray, Pr as green, P as black, N as orange, N/O as red displacement ellipsoids at 95% probability level. (b) Projection of a supercell along [100], revealing the tetrahedra connection pattern. (c) Archimedean *fes* tiling consistent of regular squares and octagons with vertex symbol 4.8.8.

Because the apophyllites and $\text{LiPr}_2\text{P}_4\text{N}_7\text{O}_3$ have different Si–Si and P–P interatomic distances ($d(\text{P–P}) = 2.837(1)$ to $2.905(1)$ Å) the polygons spanned by their connection net are not regular and thus

may be arranged with higher symmetry. The *fes*-related net conformations observed in apophyllites, and LiPr₂P₄N₇O₃ might be influenced by the incorporated metal ions and the different type of bonds between Si–O and P–N. P–N bonds are more covalent, Si–O bonds more ionic, according to the electronegativity differences.^[40] The P–N ($d(\text{P–N}) = 1.631(1)–1.668(1) \text{ \AA}$) and P–(N/O) bond lengths ($d(\text{P–(N/O)}) = 1.558(1)–1.561(1) \text{ \AA}$) in LiPr₂P₄N₇O₃ are in the range of typically observed values of, for example, layered oxonitridophosphate Sr₃P₆O₆N₈: $d(\text{P–O}) = 1.528(7)$, $d(\text{P–N}) = 1.637(7) \text{ \AA}$.^[13]

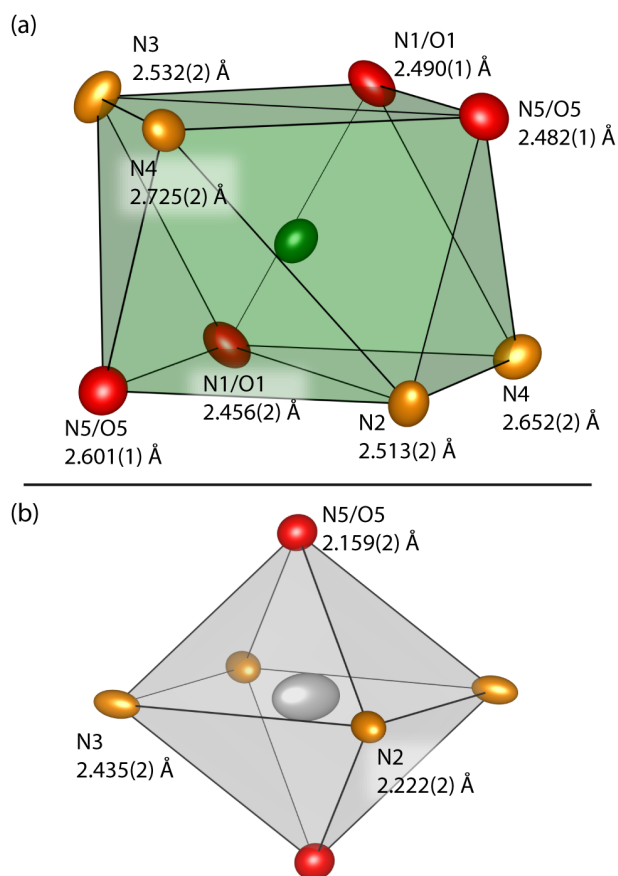


Figure 6.3. (a) Coordination polyhedron around Pr. (b) Coordination polyhedron around Li. Pr in green, Li in gray, N in orange, N/O in red. Ellipsoids displayed at 95% probability level.

BVS calculations indicated that the O occupies the terminal position of the tetrahedra net, as expected from comparison with Sr₃P₆O₆N₈.^[13,33] Pr is thus coordinated by N/O in a distorted quadratic antiprism (Figure 6.3a). This coordination of rare-earth ions has been reported for the melilite-type RE₂P₃N₇ polymorph,^[7] and the here observed Pr–(N/O) distances, $d(\text{Pr–(N/O)}) = 2.456(2)–2.725(2) \text{ \AA}$, are in good agreement with the values of RE₂P₃N₇ ($RE = \text{Pr, Nd, Sm, Eu, Ho, Yb}$), $d(\text{RE–N}) = 2.32–2.84 \text{ \AA}$.^[7] Li is surrounded by a distorted octahedron of N/O (Figure 6.2b) with atomic dis-

tances ($d(\text{Li}-(\text{N/O})) = 2.159(2)\text{--}2.435(2) \text{ \AA}$) in the typically observed range for 6-fold coordination (e.g., $\text{Ce}_4\text{Li}_3\text{P}_{18}\text{N}_{35}$, $d(\text{Li}-(\text{N})) = 2.093(7)\text{--}2.747(4) \text{ \AA}$).^[9]

6.3.4 Optical properties

Figure 6.4 shows the UV–vis spectrum of $\text{LiPr}_2\text{P}_4\text{N}_7\text{O}_3$. Typical absorption features are visible, which can be attributed to the f–f transitions in Pr^{3+} ions. This absorption is accountable for the pale-green color of the crystals (Figure 6.1a). The assignment of the individual electronic transitions is based on the reference given in the NIST Atomic Spectra Database, which is feasible because the energy levels of the f electrons are only slightly influenced by the crystal field.^[41–43]

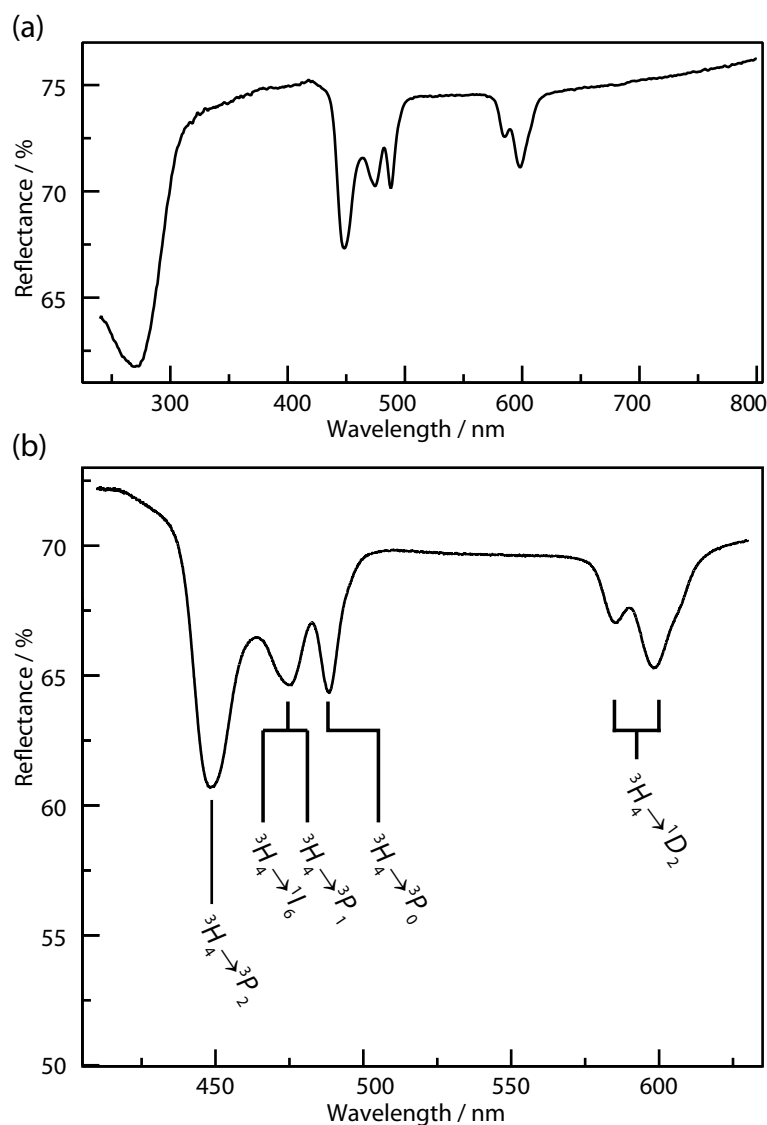


Figure 6.4. (a) UV–vis spectrum of $\text{LiPr}_2\text{P}_4\text{N}_7\text{O}_3$ obtained with a step width of 1 nm/step. (b) Region around the absorptions stemming from f–f transitions were measured with a step width of 0.025 nm/step. The transitions are marked with the corresponding energy terms.

The transitions, always from ground state 3H_4 , are observed at 585 and 598 nm (1D_2), 488 nm (3P_0), 474 nm (3P_1 and 1I_6), and 448 nm (3P_2). The 3P_1 and 1I_6 transitions could not unambiguously be resolved in the spectrum (Figure 6.4b); only a small shoulder is visible in the transition. The 1D_2 transition is most likely split in two by the crystal field, as has been reported in literature.^[42,43]

The optical band gap can be estimated from the valence to conduction band transition visible in the UV-region of the spectrum (below 300 nm) by converting the reflectance data into the Kubelka–Munk function and plotting it in a Tauc-plot (Figure 6.5).^[44,45]

For the calculations a direct band gap was assumed ($[h\nu \cdot F(R_\infty)]^2$, with h as Planck's constant, ν as frequency, and $F(R_\infty)$ as the Kubelka–Munk function) and a linear regression fit to the region of steepest slope. The band gap value can be read off the x -axis intersection with $E_g \approx 4.1(1)$ eV. This estimate of the band gap indicates that LiPr₂P₄N₇O₃ is an electronically insulating material, which is in accordance with the optical transparency of the single-crystals (Figure 6.1a).

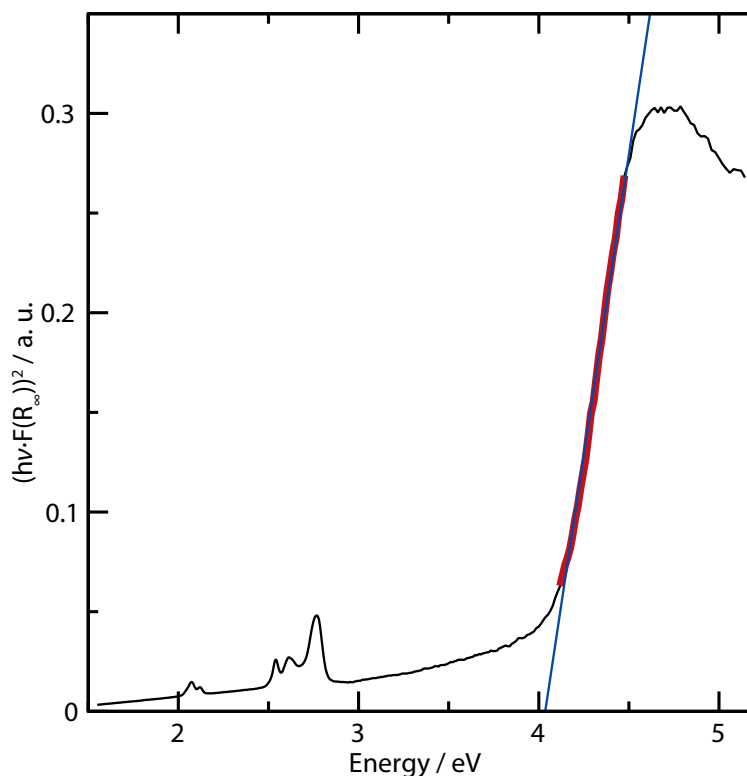


Figure 6.5. Tauc-plot calculated from the UV–vis spectrum. The Kubelka–Munk function is displayed as black line, the linear regression (blue) fit to the data points highlighted in red. Absorption onset is read off of the x -axis intersection (ca. 4.1(1) eV).

6.3.5 High-Temperature Powder X-Ray Diffraction

The temperature-dependent powder diffraction pattern (Figure F.3) indicates a slow and gradual decomposition of $\text{LiPr}_2\text{P}_4\text{N}_7\text{O}_3$ starting at ca. 500 °C. As a decomposition product only Pr_2O_3 could be identified next to unknown phases.^[46] The reaction progress, however, can be well monitored by the increase in intensity of the main Pr_2O_3 reflection at ca. $2\theta \approx 14^\circ$, as highlighted in Figure F.3. As the data were collected over the course of 12 h, the decomposition starting at 500 °C is relatively slow and completed at ca. 850 °C. The thermal decomposition temperature is in the range of the expected value, as the $\text{RE}_2\text{P}_3\text{N}_7$ compounds decompose between 750 and 850 °C.^[7]

6.4 Conclusion

LiPr₂P₄N₇O₃ is an oxonitridophosphate consistent of single-layers, in which the tetrahedra are arranged in a net related by distortion to the *fes* tiling. UV–vis revealed that the pale-green color of the single-crystals stem from Pr³⁺ ion f–f transitions. The optical band gap of ca. 4.1(1) eV indicates an electronic insulating material. HTPXRD showed a gradual decomposition starting at ca. 500 °C. The preparation of LiPr₂P₄N₇O₃ highlights the additional structural diversity accessible with mixed N/O anion positions in phosphates. The number of yet undiscovered rare-earth nitridophosphates spiraling from the adapted high-pressure metathesis route can only be estimated. By carefully adjusting variables like N/O ratio, degree of condensation, and incorporated metal ion, a wide range of materials is to be expected. The mixing of N and O further allows a better adjustability of the compounds' compositions and hence is favorable for a closer-gridded search for desirable properties such as ion conductivity or luminescence.

6.5 References

- [1] F. Liebau *Structural Chemistry of Silicates: Structure, Bonding, and Classification*; Springer: Berlin, Germany, **1985**.
- [2] A. Belsky, M. Hellenbrandt, V. L. Karen, P. Luksch, *Acta Crystallogr., Sect. B: Struct. Sci.* **2002**, *58*, 364–369.
- [3] H. C. J. de Decker, *Recl. Trav. Chim. Pays-Bas.* **1941**, *60*, 413–427.
- [4] S. Horstmann, E. Irran, W. Schnick, *Angew. Chem., Int. Ed. Engl.* **1997**, *36*, 1873–1875; *Angew. Chem.* **1997**, *109*, 1938–1940.
- [5] H. C. J. de Decker, C. H. Mac Gillavry, *Recl. Trav. Chim. Pays-Bas* **1941**, *60*, 153–175.
- [6] S. D. Kloß, W. Schnick, *Angew. Chem., Int. Ed.* **2015**, *54*, 11250–11253; *Angew. Chem.* **2015**, *127*, 11402–11405.
- [7] S. D. Kloß, N. Weidmann, R. Niklaus, W. Schnick, *Inorg. Chem.* **2016**, *55*, 9400–9409.
- [8] S. D. Kloß, N. Weidmann, W. Schnick, *Eur. J. Inorg. Chem.* **2017**, *2017*, 1930–1937.
- [9] S. D. Kloß, L. Neudert, M. Döblinger, M. Nentwig, O. Oeckler, W. Schnick, *J. Am. Chem. Soc.* **2017**, *139*, 12724–12735.
- [10] F. W. Karau, L. Seyfarth, O. Oeckler, J. Senker, K. Landskron, W. Schnick, *Chem. – Eur. J.* **2007**, *13*, 6841–6852.
- [11] A. Marchuk, F. J. Pucher, F. W. Karau, W. Schnick, *Angew. Chem., Int. Ed.* **2014**, *53*, 2469–2472; *Angew. Chem.* **2014**, *126*, 2501–2504.
- [12] S. D. Kloß, S. Wandelt, A. Weis, W. Schnick, *Angew. Chem., Int. Ed.* **2018**, *57*, 3192–3195; *Angew. Chem.* **2018**, *130*, 3246–3249.
- [13] S. J. Sedlmaier, J. Schmedt a. d. Günne, W. Schnick, *Dalton Trans.* **2009**, *21*, 4081–4084.
- [14] S. J. Sedlmaier, E. Mugnaioli, O. Oeckler, U. Kolb, W. Schnick, *Chem. – Eur. J.* **2011**, *17*, 11258–11265.
- [15] D. H. Huson, *Geom. Dedicata* **1993**, *47*, 269–296.
- [16] D. H. Huson, *2dTiler V2.0.*, University of Tübingen, Germany, **2005**.
- [17] A. Stock, H. Grüneberg, *Ber. Dtsch. Chem. Ges.* **1907**, *40*, 2573–2578.
- [18] E. Zintl, A. Harder, B. Dauth, *Z. Elektrochem.* **1934**, *40*, 588–593.
- [19] R. Klement, O. Koch, *Chem. Ber.* **1954**, *87*, 333–340.

- [20] D. Baumann, R. Niklaus, W. Schnick, *Angew. Chem., Int. Ed.* **2015**, *54*, 4388–4391; *Angew. Chem.*, **2015**, *127*, 4463–4466.
- [21] H. Huppertz, *Z. Kristallogr.* **2004**, *219*, 330–338.
- [22] N. Kawai, S. Endo, *Rev. Sci. Instrum* **1970**, *41*, 1178–1181.
- [23] D. Walker, *Am. Mineral.* **1991**, *76*, 1092–1100.
- [24] D. Walker, M. A. Carpenter, C. M. Hitch, *Am. Mineral.* **1990**, *75*, 1020–1028.
- [25] D. C. Rubie, *Phase Transitions* **1999**, *68*, 431–451.
- [26] Bruker AXS, Inc., SADABS, Madison, Wisconsin, USA, **2001**.
- [27] Bruker AXS, Inc., XPREP, Karlsruhe, Germany, **2001**.
- [28] G. M. Sheldrick, *SHELXS: A Program for Crystal Structure Solution*. University of Göttingen, Göttingen, Germany, **1997**.
- [29] G. M. Sheldrick, *Acta Crystallogr., Sect. A: Found. Crystallogr.* **2008**, *64*, 112–122.
- [30] K. Momma, F. Izumi, *J. Appl. Crystallogr.* **2011**, *44*, 1272–1276.
- [31] A. A. Coelho, *TOPAS-Academic V4.1*, Coelho Software, Brisbane, Australia, **2007**.
- [32] M. Bowden, M. Ryan, *J. Appl. Crystallogr.* **2010**, *43*, 693–698.
- [33] A. S. Wills, *VaList*, Program available from www.ccp14.ac.uk, **2011**.
- [34] E.-M. Bertschler, R. Niklaus, W. Schnick, *Chem. – Eur. J.* **2018**, *24*, 736–742.
- [35] V. A. Blatov, M. O’Keeffe, D. M. Proserpio, *CrystEngComm* **2010**, *12*, 44–48.
- [36] V. A. Blatov, A. P. Shevchenko, D. M. Proserpio, *Cryst. Growth Des.* **2014**, *14*, 3576–3586.
- [37] M. O’Keeffe, M. A. Peskov, S. J. Ramsden, O. M. Yaghi, *Acc. Chem. Res.* **2008**, *41*, 1782–1789.
- [38] W. H. Taylor, S. Naray-Szabo, *Z. Kristallogr., Cryst. Mater.* **1931**, *77*, 146–159.
- [39] O. Delgado-Friedrichs, M. O’Keeffe, *J. Solid State Chem.* **2005**, *178*, 2480–2485.
- [40] R. Marchand, F. Tessier, A. Le Sauze, N. Diot, *Int. J. Inorg. Mater.* **2001**, *3*, 1143–1146.
- [41] A. Kramida, Y. Ralchenko, J. Reader, NIST ASD Team, *NIST Atomic Spectra Database*, vers. 5.4.; National Institute of Standards and Technology: Gaithersburg, MD, USA, **2016**.
- [42] T. Som, B. Karmakar, *Spectrochim. Acta, Part A* **2011**, *79*, 1766–1782.
- [43] R. D. Mclaughlin, J. G. Conway, *J. Chem. Phys.* **1963**, *38*, 1037–1038.
- [44] J. Tauc, R. Grigorovici, A. Vancu, *Phys. Status Solidi* **1966**, *15*, 627–637.
- [45] E. A. Davis, N. F. Mott, *Philos. Mag.* **1970**, *22*, 903–922.

- [46] O. Greis, R. Ziel, B. Breidenstein, A. Haase, T. Petzel, *J. Alloys Compd.* **1995**, *216*, 255–258.

Chapter 7

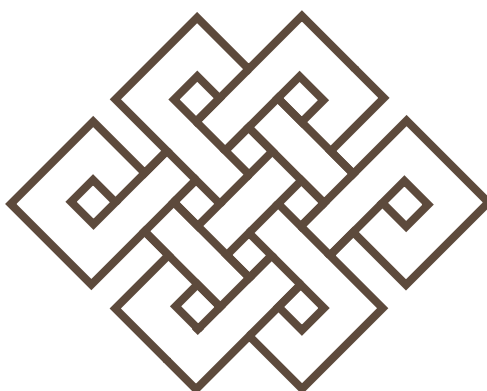
Accessing Tetravalent Transition-Metal Nitridophosphates through High-Pressure Metathesis

Simon D. Kloß, Sophia Wandelt, Andreas Weis, Wolfgang Schnick

published in: *Angew. Chem., Int. Ed.* **2018**, 57, 3192-3195. DOI: 10.1002/anie.201712006

published in: *Angew. Chem.* **2018**, 130, 3246-3249. DOI: 10.1002/ange.201712006

Reprinted (adapted) with permission from *Angewandte Chemie*. Copyright 2018 John Wiley and Sons.



The oxonitridophosphate $\text{Hf}_{9-x}\text{P}_{24}\text{N}_{52-4x}\text{O}_{4x}$ ($x \approx 1.84$) is the first one to incorporate a tetravalent metal into its P/N framework. The high-pressure metathesis route is thus being expanded to transition metals, emphasizing the great flexibility the route has to offer. The complex structure of $\text{Hf}_{9-x}\text{P}_{24}\text{N}_{52-4x}\text{O}_{4x}$ ($x \approx 1.84$) consists of two interpenetrating P/N frameworks, each adopting a highly decorated diamond-like net.

Abstract

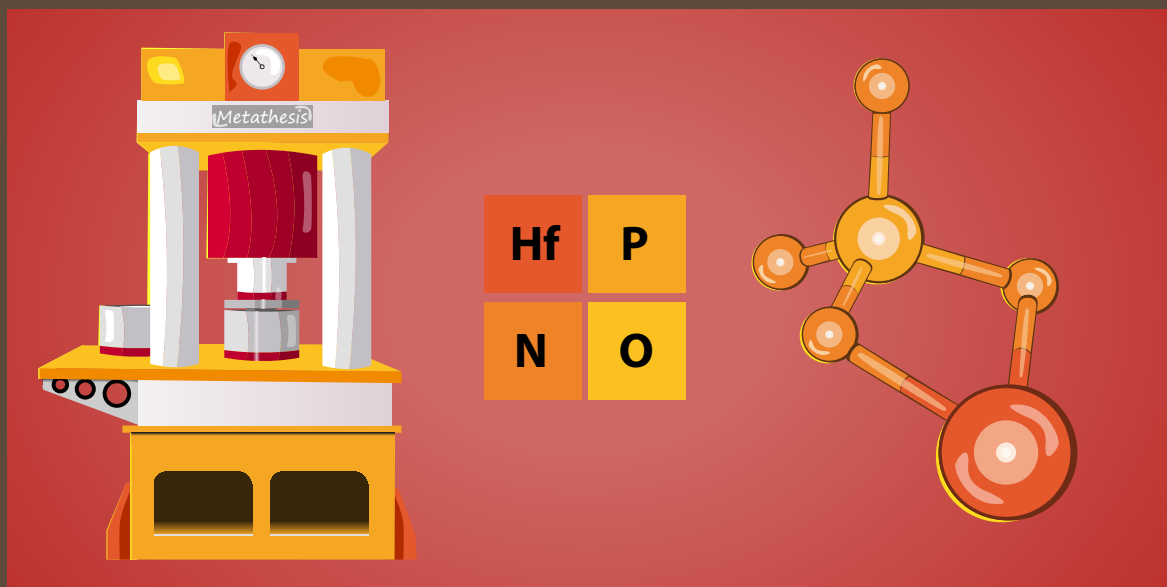


Table-of-contents graphic.

Advancing the attainable composition space of a compound class can lead to fascinating materials. The first tetravalent metal nitridophosphate, namely $\text{Hf}_{9-x}\text{P}_{24}\text{N}_{52-4x}\text{O}_{4x}$ ($x \approx 1.84$), was prepared by high-pressure metathesis. The Group 4 nitridophosphates are now an accessible class of compounds. The high-pressure metathesis reaction using a multianvil setup yielded single crystals that were suitable for structure analysis. Magnetic properties of the compound indicate Hf in oxidation state +IV. Optical measurements show a band gap in the UV region. The presented route unlocks the new class of Group 4 nitridophosphates by significantly improving the understanding of this nitride chemistry. $\text{Hf}_{9-x}\text{P}_{24}\text{N}_{52-4x}\text{O}_{4x}$ ($x \approx 1.84$) is a model system and its preparation is the first step towards a systematic exploration of the transition-metal nitridophosphates.

7.1 Introduction with Results and Discussion

Transition-metal nitridophosphates are a long-sought-for class of compounds that could give chemists and materials scientists decades of exploring.^[1] As their structures are expected to be similar to oxophosphates or oxosilicates, so could be their properties. Well-known applications of transition-metal phosphates are, for example, ion conductors or cathode materials.^[2-5] Research into transition-metal nitridophosphates, however, is impeded by their challenging synthesis. Nitride ions are prone to oxidation, as indicated by the positive electron affinity of N, and they are only stabilized by their surrounding coordination environment.^[6] With transition metals, the formation of nitridophosphates is competed by this oxidation and the consequential formation of metal phosphides. Only few instances of successful synthesis of transition-metal nitridophosphates have been reported; for example, the series $M_3^I M^{III} P_3 O_9 N$ ($M^I = \text{Na, K}$, $M^{III} = \text{Al, Ga, Cr, Fe, Mn}$), nitrido-sodalites with 3d transition-metal ions, and $M^I P N_2 / M P_2 N_4$ with $M^I = \text{Mn, Cu, Cd}$.^[7-11] All of these compounds were prepared by specialized synthetic approaches, resulting in the individual type of material, but none of the methods has proven to be adaptable to yield a systematic access to transition-metal nitridophosphates, with control over structure and composition.

We believe that among the problems of synthesizing transition-metal nitridophosphates is the competing N₂ elimination, and a lack of suitable starting materials and reaction conditions. $M_3^I M^{III} P_3 O_9 N$ and the nitrido-sodalites were obtained at ambient pressure, which can be a drawback since temperature-labile starting materials such as P₃N₅ may decompose ($P_3N_5 \rightarrow 3 PN + N_2$, $T > 850^\circ\text{C}$) prior to the formation of the targeted phases.^[7-9] $M^I P N_2 / M^I P_2 N_4$ ($M = \text{Mn, Cu, Cd}$), prepared from the metal nitrides and P₃N₅/HPN₂, required pressures of several gigapascals, controlling the chemical equilibrium by the principle of Le Chatelier.^[10,11] This high-pressure technique, typically realized with a multianvil setup, was also used for the preparation of nitridophosphates of the first and second main group. Nowadays, several dozens of these compounds have been identified through high-pressure reaction of metal nitrides or metal azides with P₃N₅ or HPN₂.^[12]

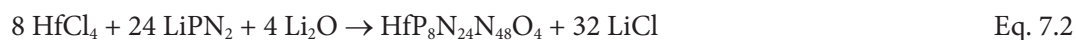
Some nitridophosphate systems, however, have been inaccessible with the common nitride starting materials. Rare-earth nitridophosphates, for example, could only be prepared by the newly developed high-pressure metathesis route.^[13] In this approach, the metal halides are reacted with alkali metal nitridophosphates, for example, LiPN₂, as displayed in Equation 7.1:



The stable Li halide is the thermodynamic driving force and acts as flux at the same time. Addition of, for example, Li_3N , Li_2O , or P_3N_5 influences the resulting atomic ratio of P/N and hence one can control the type of material formed. Anion networks ranging from isolated PN_4 tetrahedra to dense frameworks have been reported, which show that high-pressure metathesis grants a systematic access to rare-earth nitridophosphates.^[13-16]

Herein, we show the feasibility of high-pressure metathesis to prepare nitridophosphates with a Group 4 metal. The closest existing relative to this compound class are the Zr and Hf trimetaphosphimates, molecular structures in which the $(PO_2NH)_3^{3-}$ trimetaphosphimate anions are tridentate ligands to the metals.^[17] The coordination, however, is by O not N, and furthermore, a successful condensation to framework structures, oxonitridophosphates, has never been reported. Therefore, the $Hf_{9-x}P_{24}N_{52-4x}O_{4x}$ ($x \approx 1.84$) presented herein is the first oxonitridophosphate with a tetravalent metal ion.

$Hf_{9-x}P_{24}N_{52-4x}O_{4x}$ ($x \approx 1.84$) was prepared by high-pressure metathesis following Equation 7.2:



The reaction conditions of 8 GPa and 1300 °C were achieved using a 1000 t hydraulic press and the multianvil technique. Detailed information on the experimental setup are given in the Supporting Information.^[18]

The compound was obtained as the only crystalline phase present in the sample; a slightly curved background in the powder diffraction pattern, however, indicates an amorphous side phase (Supporting Information, Figure G.1, Table G.1). The title compound crystallizes in transparent, colourless crystals, 20–30 μm in size (Supporting Information, Figure G.2), from which the crystal structure was elucidated by single-crystal X-ray diffraction.^[19] The structure was solved and refined (Supporting Information, Tables G.2–G.6 and Experimental Section) in space group $I4_1/acd$ (no. 142). The structure features two not fully occupied Hf positions (Supporting Information, Table G.3): Hf1 with about 88 % and Hf2 with about 6 % occupancy, leading to sum formula $Hf_{7.16}P_{24}N_{44.64}O_{7.36}$. The small electron density on the Hf2 position might also be explained by a Li occupation. Refinement with Li on this position, however, was not possible as it led to a negative thermal displacement ellipsoid stem-

ming from a too large electron density (0.06 Hf ≡ 1.44 Li, based on electrons/element). A Hf/Li split position is also not suggested by additional electron energy-loss spectroscopy (EELS) measurements, which could not detect any Li (for a detailed discussion about Li analysis with EELS and NMR, see the Supporting Information, Figures G.3–G.8).

Isothermal magnetization measurements indicate that the sample is diamagnetic, which probably stems from paired core electrons. Hence, the formal oxidation state Hf^{IV} is assumed for the electrostatic charge balancing. Further details regarding the magnetic measurement are given in the Supporting Information, Figure G.9. The amount of O/N needed for electrostatic charge balancing was determined from the refined Hf content in the measured crystal. The O/N assignment to the crystallographic anion positions was based on electrostatic bond valence sum (BVS) calculations (Supporting Information, Table G.7).^[20]

Energy-dispersive X-ray (EDX) spectroscopy confirmed the theoretical elemental composition (theoretical/ measured Hf_{7.16}P₂₄N_{44.64}O_{7.36}/ Hf_{7.1(1.2)}P_{27.1(2.4)}N_{44.0(4.0)}O_{6.3(1.3)}; 8 points of measurement), while the presence of N–H/O–H vibrations was not suggested by Fourier transform infrared (FTIR) spectroscopy (Supporting Information, Figure G.10). The compound showed no pronounced phase width when prepared with differing starting material compositions, as can be expected from a structure with deficient heavy metal position. A discussion about the element ratio variation with regards to stoichiometry of the starting materials and reaction conditions is given in the Supporting Information.

The Hf2 position, with an occupation of only 6 %, is split into closely adjacent electron density peaks, two larger ones and two smaller shoulders, as displayed in the Supporting Information, Figure G.11. An anharmonic refinement of the observed electron density failed, and thus it was approximated by a regular ellipsoid. The single-crystal data does not suggest a possible overlooked pseudosymmetry by twinning leading to this electron density distribution, as discussed in the SI (Supporting Information, Figure G.11 to G.14).

Hf_{7.16}P₂₄N_{44.64}O_{7.36} crystallizes in a defect variant of the Ti₅B₁₂O₂₆ structure type, which consists of two separate interpenetrating nets of vertex sharing tetrahedra (Figure 7.1a).^[21] Each individual net comprises Q⁴ and Q³ tetrahedra in the molar ratio 2:1 with point symbol (3.4.5.6².8)₂(3.6²) (calculated with TOPOS), resulting in a degree of condensation $\kappa \approx 0.46$.^[22] The secondary building units of the

nets are composed of twelve tetrahedra forming one hollow truncated supertetrahedron, each interconnected to four additional truncated supertetrahedra via two P–N–P bridges (Figure 7.1b,c).

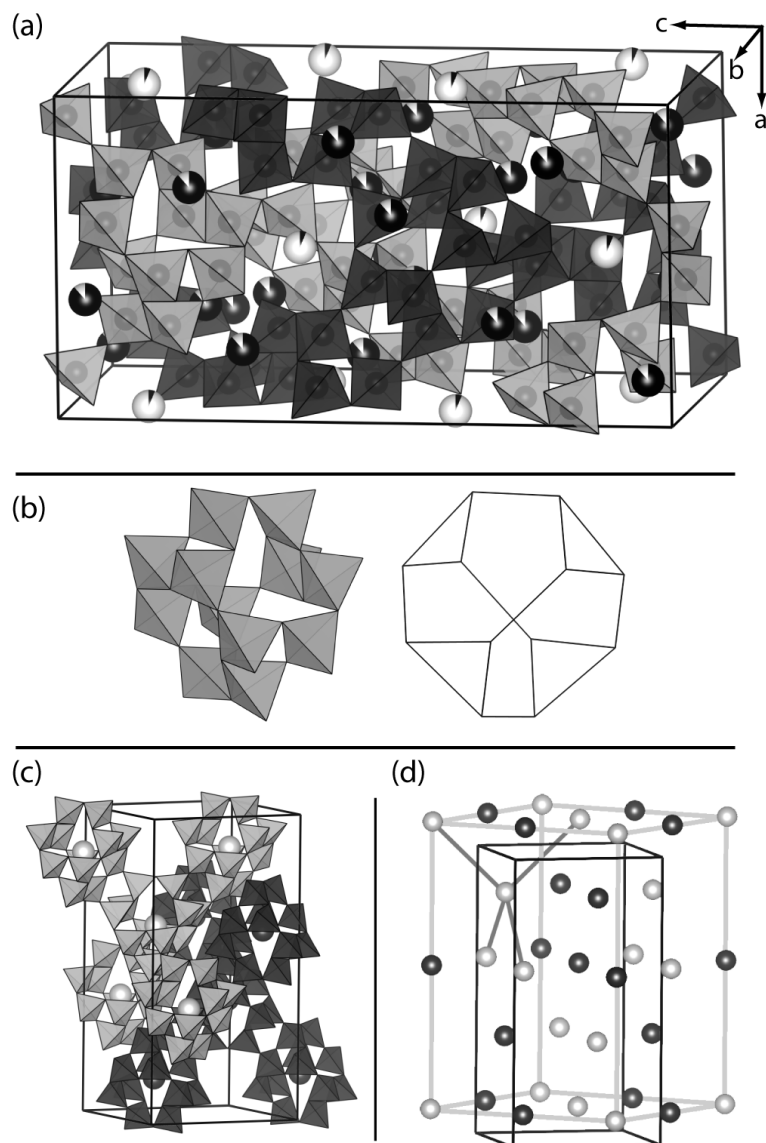


Figure 7.1. a) Unit cell of $\text{Hf}_{7.16}\text{P}_{24}\text{N}_{44.64}\text{O}_{7.36}$. Hf atoms are in black and diamond-type nets are highlighted in dark gray/light gray, respectively. Occupancy of Hf atoms indicated by partly filled-in spheres. b) One hollow truncated supertetrahedron and the underlying P–P connection pattern. c) Centres of gravity of truncated supertetrahedra marked by light gray and dark gray spheres, respectively, for both diamond-type nets. d) Sphere packing of centres of gravity (light/dark gray spheres) of the diamond-type nets, forming a NaTl structure type. Unit cell of sphere packing in light gray, one tetrahedral coordination highlighted by gray connections.

The centres of gravity of the truncated supertetrahedra of one net form a diamond packing, so that the topology of the nitridophosphate nets can be seen as a heavily decorated NaTl-type (Figure 7.1d).^[23] Interpenetration of nets in inorganic compounds is rare, but the most frequent type

(total count 64 structure types, about 44 % of all interpenetration cases, based on the ICSD in 2005) is with diamond nets or augmented diamond nets.^[24] The space group $I4_1/acd$ (no. 142) harbours several instances of such interpenetrating networks such as HgI₂, while in the nitridophosphate-related class of nitridoaluminates a case of interpenetrating nets of *T5* supertetrahedra has been reported.^[25,26]

The Hf atoms are coordinated in an octahedral fashion. The Hf1 coordination polyhedron is additionally capped by the remote N3 and N6 atoms, leading to a Hf(O/N)₈ bicapped octahedron (Figure 7.2a). The Hf–(O/N) interatomic distances justify this formal grouping, as the distances to the capping atoms are by over one half angstrom larger than those of the octahedron. Hf–O distances in comparable materials like Hf₂[PO₄]₂O range from 2.035 to 2.362 Å and are similar to the values found for the atoms constituting the octahedral coordination.^[27]

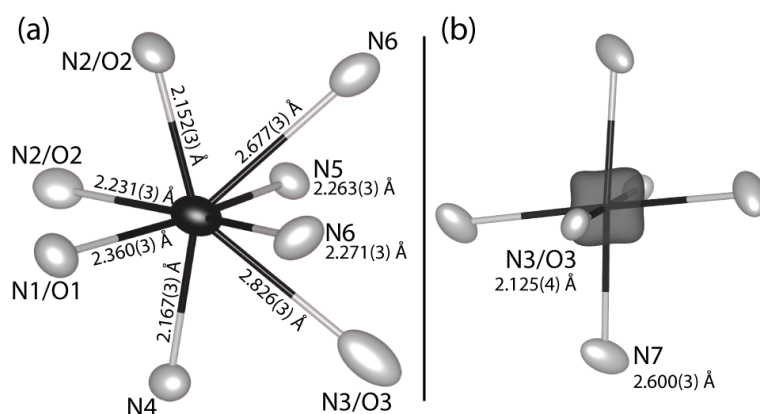


Figure 7.2. Coordination spheres around a) Hf1 and b) Hf2 (in black) in a 3 Å radius. Atoms displayed with a probability of 95 %, Hf2 displayed as an isosurface at a 1.5 electrons/ a_0^3 level (a_0 =Bohr radius) owing to the unusual split position into four peaks.

Hf2 is also coordinated in a distorted octahedron; the Hf–(O/N) interatomic distances, however, form two sets. Two atoms (N3 in Figure 7.2b) are at a comparable distance found in the Hf1 coordination polyhedron, but four atoms (N7, atoms in paper plane in Figure 7.2b) are relatively remote with an interatomic distance of 2.600(3) Å. The elongated Hf2–N7 distances may cause the Hf2 atom to split in four positions, resulting in the cushion-like electron density distribution (Supporting Information, Figure G.11). The coordination environment seems to be too large for the Hf atoms, which might also indicate a reason for the low Hf2 occupancy.

The optical properties of Hf_{9-x}P₂₄N_{52-4x}O_{4x} (x ≈ 1.84) were determined with UV/Vis spectroscopy (Figure 7.3). The valence-to-conduction band transition occurs in the UV part of the spectrum. The

optical band gap was approximated by converting the reflectance spectrum to the Kubelka–Munk function and calculation of the Tauc plot under assumption of a direct band gap.^[28,29] As the point of inflection could not clearly be determined, a linear regression was fit to the steep sloped region between 4.00 and 4.33 eV, yielding an estimated optical band gap of ca. 3.8 eV.

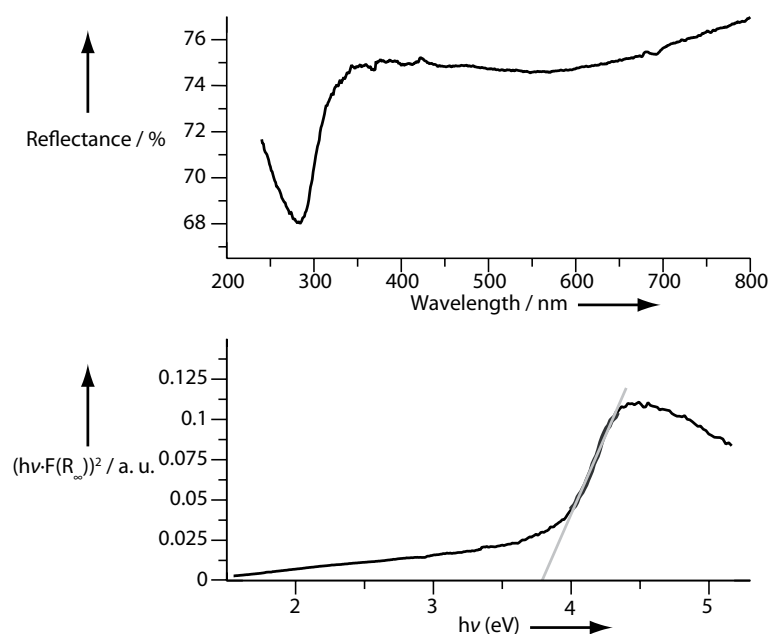


Figure 7.3. Top: UV/Vis spectrum of $\text{Hf}_{9-x}\text{P}_{24}\text{N}_{52-4x}\text{O}_{4x}$ ($x \approx 1.84$). Bottom: Tauc plot of $\text{Hf}_{9-x}\text{P}_{24}\text{N}_{52-4x}\text{O}_{4x}$ ($x \approx 1.84$). Linear regression (light gray line) was fit to the datapoints highlighted in dark gray. The band gap was estimated from the intersection of regression line and x-axis.

The thermal stability of $\text{Hf}_{9-x}\text{P}_{24}\text{N}_{52-4x}\text{O}_{4x}$ ($x \approx 1.84$) in air was investigated by high-temperature PXRD (Supporting Information, Figure G.15, Experimental Section), which indicates that the compound is stable up to at least the maximum measured temperature of 1000 °C. This stability is expected since nitridophosphates with metal ions with formal oxidation states larger than one usually show high thermal stability.^[13,14]

7.2 Conclusion

The successful preparation of the first nitridophosphate with a Group 4 transition metal is a landmark in the exploration of nitridophosphates. By opening a new class of compounds with lots of explorative potential the elemental diversity in nitridophosphates is increased. The immediate task is a systematic access to the Group 4 nitridophosphates, which means directing the synthesized anion network by control over the ratio of P/N/O. The exploration of the rare-earth nitridophosphates set the guideline for doing so, addition of nitrides and oxides like Li_2O and Li_3N , or P_3N_5 and PON to the starting materials was shown to influence the resulting anion network.^[15,16] Li^+ -containing structures likely to show ion conductivity could for example be targeted, as in the structurally related class of NASICON materials.^[2]

The understanding of the underlying nitridophosphate chemistry obtained herein can help to tackle the aforementioned synthesis problems of the other transition-metal nitridophosphates with an open-shell electron configuration. Those have been notoriously difficult to prepare, as only transition metals with an empty, half-filled, or closed d-shell have been incorporated. Fe^{2+} , Co^{2+} , or Ni^{2+} systems, for example, also undergo phosphide formation through N_2 elimination. Hence the next step is to advance the high-pressure metathesis method to these completely uncharted systems.

7.3 References

- [1] R. Marchand, W. Schnick, N. Stock, *Adv. Inorg. Chem.* **2000**, *50*, 193–233.
- [2] N. Anantharamulu, K. K. Rao, G. Rambabu, B. V. Kumar, V. Radha, M. Vithal, *J. Mater. Sci.* **2011**, *46*, 2821–2837.
- [3] O. Paschos, J. Kunze, U. Stimming, F. Maglia, *J. Phys. Condens. Matter* **2011**, *23*, 234110.
- [4] B. Kang, G. Ceder, *Nature* **2009**, *458*, 190–193.
- [5] S.-Y. Chung, J. T. Bloking, Y.-M. Chiang, *Nat. Mater.* **2002**, *1*, 123–128.
- [6] T. Andersen, H. K. Haugen, H. Hotop, *J. Phys. Chem. Ref. Data* **1999**, *28*, 1511–1533.
- [7] W. Feldmann, *Z. Chem.* **1987**, *27*, 182–183.
- [8] W. Schnick, J. Lücke, *Angew. Chem., Int. Ed. Engl.* **1992**, *31*, 213–215; *Angew. Chem.* **1992**, *104*, 208–209.
- [9] N. Stock, J. Lücke, M. Volkmann, M. Jansen, W. Schnick, *Z. Anorg. Allg. Chem.* **1995**, *621*, 987–992.
- [10] F. J. Pucher, F. Hummel, W. Schnick, *Eur. J. Inorg. Chem.* **2015**, *2015*, 1886–1891.
- [11] F. J. Pucher, F. W. Karau, J. Schmedt auf der Günne, W. Schnick, *Eur. J. Inorg. Chem.* **2016**, *2016*, 1497–1502.
- [12] F. W. Karau, L. Seyfarth, O. Oeckler, J. Senker, K. Landskron, W. Schnick, *Chem. - Eur. J.*, **2007**, *13*, 6841–6852.
- [13] S. D. Kloß, W. Schnick, *Angew. Chem., Int. Ed.* **2015**, *54*, 11250–11253; *Angew. Chem.* **2015**, *127*, 11402–11405.
- [14] S. D. Kloß, L. Neudert, M. Döblinger, M. Nentwig, O. Oeckler, W. Schnick, *J. Am. Chem. Soc.* **2017**, *139*, 12724–12735.
- [15] S. D. Kloß, N. Weidmann, R. Niklaus, W. Schnick, *Inorg. Chem.* **2016**, *55*, 9400–9409.
- [16] S. D. Kloß, N. Weidmann, W. Schnick, *Eur. J. Inorg. Chem.* **2017**, *2017*, 1930–1930.
- [17] N. Stock, W. Herrendorf, J. Beck, W. Schnick, *Eur. J. Inorg. Chem.* **1998**, *1998*, 469–476.
- [18] H. Huppertz, *Z. Kristallogr.* **2004**, *219*, 330–338.

- [19] Further details of the crystal structure investigation(s) may be obtained from FIZ Karlsruhe, 76344 Eggenstein-Leopoldshafen, Germany (fax: (+49)7247-808-666; e-mail: crysdata@fiz-karlsruhe.de, on quoting the deposition number CSD-433753.
- [20] A. S. Wills, *VaList*, Program available from www.ccp14.ac.uk, **2011**.
- [21] A. Haberer, H. Huppertz, *J. Solid State Chem.* **2009**, *182*, 484–490.
- [22] V. A. Blatov, A. P. Shevchenko, D. M. Proserpio, *Cryst. Growth Des.* **2014**, *14*, 3576–3586.
- [23] E. Zintl, W. Dullenkopf, *Z. Phys. Chem., Abt. B* **1932**, *16*, 195–205.
- [24] I. A. Baburin, V. A. Blatov, L. Carlucci, G. Ciani, D. M. Proserpio, *J. Solid State Chem.*, **2005**, *178*, 2452–2474.
- [25] M. Hostettler, D. Schwarzenbach, *Acta Crystallogr. Sect. B Struct. Sci.* **2002**, *58*, 914–920.
- [26] P. Wagatha, P. Pust, V. Weiler, A. S. Wochnik, P. J. Schmidt, C. Scheu, W. Schnick, *Chem. Mater.* **2016**, *28*, 1220–1226.
- [27] G. Wallez, J.-P. Souron, M. Quarton, *Solid State Sci.* **2006**, *8*, 1061–1066.
- [28] J. Tauc, R. Grigorovici, A. Vanacu, *Phys. Status Solidi* **1966**, *15*, 627–637.
- [29] E. A. Davis, N. F. Mott, *Philos. Mag.* **1970**, *22*, 903–922.

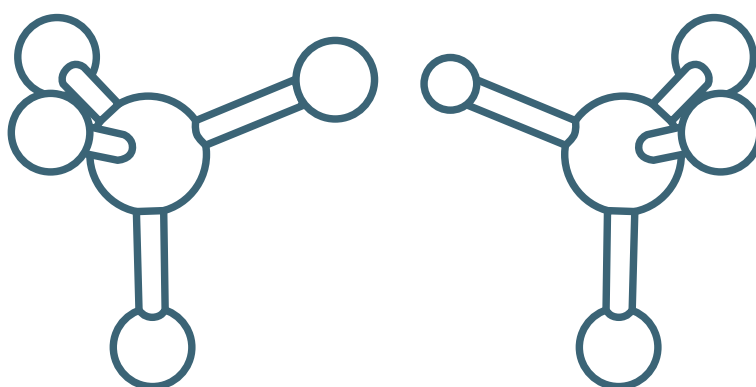
Chapter 8

High-Pressure Metathesis of the $M_{1-x}PO_{3+4x}N_{1-4x}$ ($x \approx 0.05$) and $M_{0.75}PO_4$ ($M = Zr, Hf$) Orthophosphates

Simon D. Kloß, Andreas Weis, Sophia Wandelt, Wolfgang Schnick

published in: *Inorg. Chem.* **2018**, 57, 4164–4170. DOI: 10.1021/acs.inorgchem.8b00373

Reprinted (adapted) with permission from *Inorganic Chemistry*. Copyright 2018 American Chemical Society.



The $M_{1-x}PO_{3+4x}N_{1-4x}$ ($x \approx 0.05$) and $M_{0.75}PO_4$ ($M = Zr, Hf$) orthophosphates were prepared through high-pressure metathesis using a multianvil setup. The nitride-containing compounds show that high-pressure metathesis gives a systematic access to group 4 nitridophosphates. The $M_{0.75}PO_4$ compounds are thermally labile and metastable at ambient pressures. High-pressure metathesis is a promising route to numerous such metastable oxophosphates.

Abstract



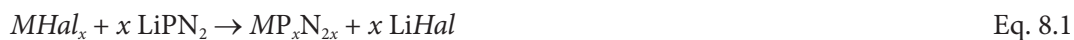
Table-of-contents graphic.

We describe the oxonitridophosphates $M_{1-x}\text{PO}_{3+4x}\text{N}_{1-4x}$ ($x \approx 0.05$) and the isotypic oxophosphates $M_{0.75}\text{PO}_4$ ($M = \text{Zr}, \text{Hf}$) obtained by high-pressure metathesis. The structures (ZrSiO₄-type, space group $I4_1/amd$ (no. 141), $a = 6.5335(7)$ – $6.6178(12)$, $c = 5.7699(7)$ – $5.8409(9)$ Å, $Z = 4$) were refined from single-crystal X-ray diffraction data, and the powder samples were examined with quantitative Rietveld refinement. Infrared spectroscopy did not indicate the presence of X–H ($X = \text{O}, \text{N}$) bonds. The optical band gaps, between 3.5 and 4.3 eV, were estimated from UV–vis data using the Kubelka–Munk function under assumption of a direct band gap. Temperature-dependent powder X-ray diffraction showed a phase transformation of the $M_{0.75}\text{PO}_4$ ($M = \text{Zr}, \text{Hf}$) compounds to ambient pressure polymorphs at 780 (Zr) and 900 °C (Hf). The preparation of the nitrogen containing compounds exemplifies the systematic access to the new class of group 4 nitridophosphates granted by high-pressure metathesis. Moreover, we show that high-pressure metathesis can also be used for the preparation of metastable oxophosphates.

8.1 Introduction

High-pressure metathesis using the multianvil technique was the first synthesis route to offer fast and efficient access to oxonitridophosphates with trivalent rare-earth metals and, moreover, providing the means to systematically direct the structures' anion networks.^[1–4] Recently, high-pressure metathesis was successfully expanded to nitridophosphates with the group 4 metal Hf. As the first instance of this class of compounds the oxonitridophosphate $\text{Hf}_{9-x}\text{P}_{24}\text{N}_{52-4x}\text{O}_{4x}$ ($x \approx 1.84$), which consists of two interpenetrating diamond-like anion frameworks, has been prepared.^[5] While this compound has been a first proof of principle, one strong-point of high-pressure metathesis for nitridophosphates, however, is the granted control over the formed anion network. For the rare earths, for example, the flexible anion networks range from highly condensed frameworks down to noncondensed tetrahedra.^[1–4] This systematic tuning of the network type has yet to be proven for group 4 nitridophosphates.

The inherent challenge during synthesis of transition metal nitridophosphates is a competitive redox reaction by which the nitride ion is oxidized and transition metal phosphides are formed.^[5] Previous synthesis routes to transition metal nitridophosphates led only to scarce success most likely due to unsuitable reaction conditions, e.g. lack of high-pressure methods, or unsuitable starting materials, e.g. lack of metal azides or reactive nitrides.^[6–9] The existence of nitridosodalites, which were prepared at ambient pressures, showed stability of transition metals embedded in a nitridophosphate network.^[10,11] No synthesis route, however, was discovered yet that grants control over the formed anion network. High-pressure metathesis may remedy these problems. It starts from reaction of readily available metal halides with LiPN_2 under pressures of several GPa (Equation 8.1), a concept which is in principle transferable to almost all metals of the periodic system:^[1]



The starting material LiPN_2 constitutes a preformed tetrahedra network made up of PN_4 -units, which breaks down and reforms the new network.^[12] The high-pressure conditions suppress the elimination of N_2 and preserve the formed metal nitridophosphate. Moreover, the Li halide produced during the reaction is at the same time the thermodynamic driving force and flux aiding the crystallization process of the nitridophosphate.^[1] Flexibility and further control over stoichiometry and structure can be achieved by addition of oxides or nitrides such as Li_2O , Li_3N , P_3N_5 , or PON as starting materials.^[2–4]

The targeted degree of condensation κ , i.e. the atomic ratio of tetrahedra centers to tetrahedra corners, influences the anionic network formed and can be controlled by the stoichiometry of the starting materials. Naturally, the low end of κ is 1/4, representing noncondensed tetrahedra, while the high end is determined by electrostatics. For the element combination P and N the highest κ is 3/5, that being the binary parent compound P_3N_5 .^[13]

In this contribution we show that high-pressure metathesis may offer a systematic access to oxonitridophosphates containing a group 4 element by preparation of Zr and Hf compounds with noncondensed tetrahedra and $\kappa = 1/4$, namely $Zr_{1-x}PO_{3+4x}N_{1-4x}$ and $Hf_{1-x}PO_{3+4x}N_{1-4x}$ ($x \approx 0.05$).

As these nitridophosphates have vacancies on the metal position, the end members of the O/N solid solution series, the oxophosphates $Zr_{0.75}PO_4$ and $Hf_{0.75}PO_4$, are also fathomable. These are missing members of group 4 phosphates, which is curious since this group was intensively investigated because of their ion exchange and ion conductivity properties.^[14] The subsolidus phase diagrams of the pseudobinary system $ZrO_2-P_2O_5$ and several pseudoternary $ZrO_2-P_2O_5-MO_x$ have extensively been investigated in the literature.^[15,16] Hitherto, only three ternary structure-types, the diphosphate MP_2O_7 and the orthophosphate oxide $M_2[PO_4]_2O$ with $M = Zr, Hf$, as well as the chain phosphate $Zr(PO_3)_4$ were structurally characterized.^[17-21] ZrP_2O_7 , among other tetravalent metal phosphates, was discussed as a H^+ ion conductor for fuel cells.^[22] We were able to prepare these curious $Zr_{0.75}PO_4$ and $Hf_{0.75}PO_4$ compounds with the high-pressure metathesis route and so advance the chemistry of the group 4 oxophosphates.

$Zr_{0.75}PO_4$ and $Hf_{0.75}PO_4$ are isotypic to $Zr_{1-x}PO_{3+4x}N_{1-4x}$ and $Hf_{1-x}PO_{3+4x}N_{1-4x}$ ($x \approx 0.05$) and crystallize in a defect variant of the $ZrSiO_4$ structure type. The structural feature of noncondensed tetrahedra is reminiscent of the important class of NASICON materials ($Na_{1-x}Zr_2P_{3-x}Si_xO_{12}$ ($0 \leq x \leq 3$)), which are known for their ion conduction properties and nuclear waste immobilization.^[14,23,24] Incorporation of Na into oxonitridophosphates or metastable oxophosphates through high-pressure metathesis could lead to compounds with similar properties.

In the following, we report the structures and properties of $M_{1-x}PO_{3+4x}N_{1-4x}$ ($x \approx 0.05$), and $M_{0.75}PO_4$ ($M = Zr, Hf$) by means of single-crystal and powder X-ray diffraction (SCXRD, PXRD), scanning electron microscopy (SEM) with energy dispersive X-ray (EDX) spectroscopy, infrared (IR) spectroscopy, and UV-vis spectroscopy. We discuss stabilities of the compounds based on high-temperature

XRD (HTXRD) and possible alternative synthesis routes of the $M_{0.75}\text{PO}_4$ ($M = \text{Zr, Hf}$) to determine reasons for their late discovery.

8.2 Experimental Section

8.2.1 Li₂O

Li₂O was prepared by thermal decarboxylation of Li₂CO₃ (Sigma-Aldrich 99.99%) under dynamic vacuum conditions (<10⁻³ mbar).^[25] For this purpose, a fused silica tube residing in a tube furnace was loaded with a Li₂CO₃-filled Ag boat. The tube was connected to an Ar/vacuum Schlenk line and subsequently heated to 700 °C for 72 h in dynamic vacuum with temperature ramps set to 5 °C/min. Moisture sensitive Li₂O was recovered and then stored in a glovebox. The purity of the colorless product was confirmed by PXRD to check for residual Li₂CO₃.

8.2.2 Phosphoric Triamide

The phosphoric triamide OP(NH₂)₃ is a starting material for the synthesis of PON and was prepared by ammonolysis of phosphorus oxychloride POCl₃ in liquid ammonia.^[26] A three-necked flask equipped with one connection to an inert gas/vacuum/ammonia line and one connection to an overpressure valve was dried in vacuum. Approximately 200 mL NH₃ (Air Liquide 5.0) was condensed into the flask with an acetone/CO₂ freezing mixture. Approximately 10 mL of POCl₃ was added dropwise through a septum into the stirred liquid ammonia. Excess ammonia was evaporated overnight and the product OP(NH₂)₃ was obtained as a colorless powder in a 1:3 mixture with NH₄Cl. The product was characterized by PXRD.

8.2.3 a-PON

Amorphous PON (a-PON) was prepared by condensation of OP(NH₂)₃ in a constant flow of ammonia.^[27] A fused silica tube was prepared by drying at 1000 °C for 8 h under dynamic vacuum <0.1 Pa. The above obtained 1:3 mixture of OP(NH₂)₃ and NH₄Cl was loaded on a fused silica boat in an Ar-filled glovebox (O₂ and H₂O < 1 ppm) and conveyed into the tube furnace in an Ar counterflow via transporter. The gas flow was switched to ammonia and the starting materials fired at 300 °C for 5 h to sublime the NH₄Cl; then the temperature was increased to 620 °C with a 12 h dwell. All temperature ramps were set to 5 °C/min. The colorless a-PON was characterized by PXRD (check for residual NH₄Cl) and IR.

8.2.4 cri-PON

Cristobalite phosphorus oxonitride (cri-PON) was prepared by crystallizing amorphous PON.^[27,28] A dried fused silica tube with fused silica boat (tube furnace setup, 1000 °C for 8 h under dynamic vacuum <0.1 Pa) was loaded with a-PON. The condensation was carried out for 168 h in dynamic vacuum (<0.1 Pa) at 750 °C with temperature ramps set to 5 °C/min. cri-PON was obtained as a colorless powder and characterized by PXRD and IR.

8.2.5 Oxo(nitrido)phosphates

$Zr_{1-x}PO_{3+4x}N_{1-4x}$ ($x \approx 0.05$), $Hf_{1-x}PO_{3+4x}N_{1-4x}$ ($x \approx 0.05$), $Zr_{0.75}PO_4$, and $Hf_{0.75}PO_4$ were prepared by high-pressure metathesis using a hydraulic 1000t press (Voggenreiter, Mainleus, Germany) and the multianvil technique. The setup included a modified Walker-type module (Voggenreiter) with an octahedron-within-cubes load driven by steel wedges. The here used 18/11 assembly consisted of Co-doped (7%) tungsten carbide cubes (Hawedia, Marklkofen, Germany) with truncated edges (11 mm), a Cr_2O_3 -doped (6%) MgO octahedron as pressure medium (18 mm edge length), and pyrophyllite gaskets (Ceramic Substrates & Components, Isle of Wight, U.K.). The samples resided inside a h-BN crucible (Henze, Kempten, Germany), and they were heated through resistance heating with a graphite sleeve (Schunk Kohlenstofftechnik GmbH, Zolling, Germany). Additional information regarding the employed high-pressure technique can be found in the literature.^[29–33]

Starting materials were mixed and ground in a glovebox (O_2 and $H_2O < 1$ ppm). All samples were prepared by high-pressure metathesis starting from stoichiometric mixtures of $ZrCl_4$ (99.99%, Sigma-Aldrich), $HfCl_4$ (99.9%, abcr GmbH), P_4O_{10} (99.99% Sigma-Aldrich), cri-PON, and Li_2O . The samples were recovered as colorless products and washed with H_2O to remove the LiCl byproduct. Additional information regarding synthesis can be found in the Synthesis section.

8.2.6 Spectroscopy

A Helios Nanolab G3 Dualbeam UC (FEI, Hillsboro, OR, United States) equipped with an X-Max 80 SDD detector (Oxford Instruments, Abingdon, United Kingdom) was used for scanning electron microscopy and the recording of EDX spectra. The samples were placed on an adhesive conducting carbon foil affixed to a metal carrier and coated with carbon.

Infrared spectra were recorded on a Spectrum BX II spectrometer (PerkinElmer Waltham, MA, United States) with a DuraSampler ATR-unit in the range of 650–4500 cm^{-1} .

UV–vis spectra were recorded in reflection geometry on a V-650 UV–vis spectrophotometer (JASCO, Gross-Umstadt, Germany) equipped with a photomultiplier tube detector and a single monochromator with 1200 lines/mm. The detected spectral range was from 240 to 800 nm, scanned with a deuterium lamp (240–330 nm) and a halogen lamp (330–800 nm) with a 1 nm resolution and a scan speed of 400 nm/min. The device was controlled with the Spectra Manager II software. Samples were loaded onto a sample holder consisting of a fused silica slide and a BaSO_4 -coated stamp. The baseline was recorded prior each measurement.

8.2.7 Solid State NMR

^{31}P NMR spectra of $M_{0.75}\text{PO}_4$ ($M = \text{Zr}, \text{Hf}$) were recorded on a DSX Avance spectrometer (Bruker) at a magnetic field of 11.7 T. The samples were loaded into a 2.5 mm rotor made of ZrO_2 . The rotor was mounted on a commercial MAS probe (Bruker). Spectra were recorded at a rotation frequency of 20 kHz and at room temperature. The raw data were analyzed with the device-specific software.

8.2.8 Single-Crystal Diffraction

X-ray diffraction on single-crystals was carried out on a D8 Venture diffractometer (Bruker, Billerica, MA, United States) with a fine-focus sealed tube X-ray source. Cell determination, data reduction, and multiscan absorption correction (SADABS), as well as calculation of planes through reciprocal space were carried out using the APEX3 software.^[34,35] Crystals were affixed on a MicroMount (MiTeGen, Ithaca, NY, United States). The space groups were determined based on systematic absences analyzed with XPREP.^[36] Structure solution and refinement were carried out with SHELX-97.^[37,38] Crystal structures were visualized with VESTA.^[39] Further details on the crystal structure analysis can be obtained from the Fachinformationszentrum Karlsruhe, 76344 Eggenstein-Leopoldshafen, Germany (fax: + 49-7247-808-666; e-mail: crysdata@fiz-karlsruhe.de) on quoting the depository numbers CSD-433854, -433855, -433856, and -433857. **CCDC 1816010–1816013 contain the supplementary crystallographic data for this paper.** The data can be obtained free of charge from The Cambridge Crystallographic Data Centre via www.ccdc.cam.ac.uk/structures.

8.2.9 Powder Diffraction

PXRD on microcrystalline samples was carried out on a Stadi P diffractometer (Stoe & Cie GmbH, Darmstadt, Germany) in parafocusing Debye–Scherrer geometry with Mo $K_{\alpha 1}$ radiation. The instrument was equipped with a Ge single-crystal monochromator, singling out the $K_{\alpha 1}$ emission line, and a MYTHEN 1K silicon strip detector (Dectris, Baden, Switzerland). Samples were loaded into glass capillaries (Hilgenberg GmbH, Malsfeld, Germany) with diameters ranging from 0.1 to 0.3 mm, depending on absorption, and a wall thickness of 0.01 mm. Diffractograms were recorded in the angular range of $2\theta = 2\text{--}76^\circ$.

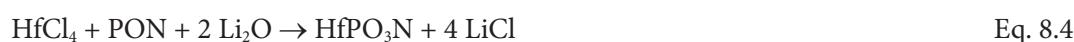
Rietveld refinement was carried out with the program TOPAS-Academic V4.1.^[40,41] Peak shapes were modeled using a fundamental parameters approach featuring a direct convolution of source emission profiles, axial instrument contributions, crystallite size, and microstrain effects. The background was handled using a shifted Chebychev polynomial.

High-temperature PXRD was recorded on a Stadi P diffractometer (Stoe & Cie GmbH, Darmstadt, Germany) with Mo $K_{\alpha 1}$ radiation source and equipped with a graphite furnace and an image-plate position-sensitive detector. The diffractograms were recorded in the range of $2\theta = 3\text{--}65^\circ$ in temperature steps of 20 K starting from room temperature to a maximum of 1000 °C. Samples were loaded into fused silica capillaries (Hilgenberg GmbH, Malsfeld, Germany) with 0.5 mm diameter and 0.01 mm wall thickness.

8.3 Results and Discussion

8.3.1 Synthesis

The title compounds were prepared by high-pressure metathesis starting from the metal chlorides, Li₂O, and PON or P₂O₅, respectively. Reaction equations are as follows:



The conditions for each reaction are listed in Table 8.1. All compounds were obtained as colorless and transparent single-crystals large enough for XRD (Figure 8.1). Zr_{0.75}PO₄ and Hf_{0.75}PO₄ were prepared as crystallographically phase-pure materials, Zr_{1-x}PO_{3+4x}N_{1-4x} had a minor, not-quantifiable, side phase of ZrO₂ and Hf_{1-x}PO_{3+4x}N_{1-4x} has an 8 wt % side phase of HfO₂.^[42] Rietveld refinements are shown in the Supporting Information (Figures H.1 to H.4, Table H.1). The thermodynamic stability of respective metal dioxides impeded the preparation of phase pure compounds, but their formation can be, to a good amount, circumvented by careful grinding of the starting materials. Structure analysis (see Structure Determination) showed that the nitrogen containing compounds both have defects on the heavy atom positions, necessitating a surplus of O for charge balancing and thus leading to sum formulas M_{1-x}PO_{3+4x}N_{1-4x} (*x* ≈ 0.05, *M* = Zr, Hf). Infrared spectroscopy did not indicate the presence of N–H or O–H bonds (Figure H.5).

Table 8.1. Reaction conditions for reactions in Eqs 8.2 to 8.5

Reaction	Pressure/GPa	Temp/°C	Dwell/min	Temp up/down/min
Eq 8.2	6	1200	160	30/150
Eq 8.3	6	1200	160	30/150
Eq 8.4	6	1100	160	30/150
Eq 8.5	6	1100	160	30/150

EDX of the compounds showed that the experimentally determined composition is in good agreement with the theoretical values: experiment/theory Zr_{1.17(1)}P_{1.08(7)}O_{2.99(17)}N_{0.72(23)}/Zr_{0.95}P₁O_{3.2}N_{0.8} (three

points), $Zr_{0.85(6)}P_{0.85(9)}O_{4.04(15)}/Zr_{0.75}P_1O_4$ (three points), $Hf_{1.08(10)}P_{1.01(4)}O_{3.11(16)}N_{0.72(13)}/Hf_{0.95}P_1O_{3.2}N_{0.8}$ (nine points), $Hf_{0.87(10)}P_{0.94(8)}O_{3.94(16)}/Hf_{0.75}P_1O_4$ (eight points). EDX and single-crystal analysis indicate that the amount of Zr/Hf and N/O incorporated in $M_{1-x}PO_{3+4x}N_{1-4x}$ seems to favor a structure with vacancies on the heavy atom position. We found no experimental evidence for the existence of the end members $ZrPO_3N$ and $HfPO_3N$. This could have electrostatic causes, in which for energy minimization vacancies are required. Single-crystal diffraction and EDX, however, are not methods for generating statistics; hence, the real compositional variance can only be estimated. The composition certainly varies to some degree around the postulated value of $x \approx 0.05$, and in domains the end members $ZrPO_3N$ and $HfPO_3N$ might be present. The analysis of this, however, is beyond the scope of this report.

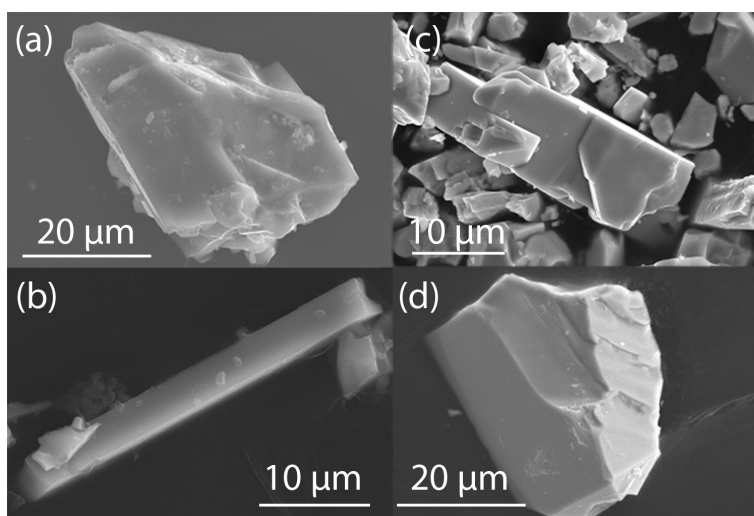


Figure 8.1. SEM micrographs of representative crystals of (a) $Zr_{1-x}PO_{3+4x}N_{1-4x}$ (b) $Zr_{0.75}PO_4$, (c) $Hf_{1-x}PO_{3+4x}N_{1-4x}$, and (d) $Hf_{0.75}PO_4$.

8.3.2 Structure Determination

The crystal structures of all compounds were solved and refined from single-crystal data. Crystallographic data is summarized in Table H.2, atom positions in Table H.3, lists of anisotropic displacement parameters, bond lengths, and angles can be found in the Supporting Information (Tables H.4–H.6). The structures were solved in space group $I4_1/amd$ (no. 141), determined from systematically absent reflections, yielding the positions of all heavy atoms including P, O and, respectively, N were determined through difference Fourier maps. The occupancy of the single Zr and Hf positions in

$M_{1-x}\text{PO}_{3+4x}\text{N}_{1-4x}$ ($x \approx 0.05$, $M = \text{Zr, Hf}$) was freely refined and the O/N occupancy adjusted to maintain charge neutrality. The $M_{0.75}\text{PO}_4$ structures were tested for additional vacancies on the P and M positions; however, none were found, and therefore, both occupancies were fixed to 1 and 3/4, respectively (details in Supporting Information). As the heavy atom positions of all products are not fully occupied, they might form an ordered vacancy distribution. Such an ordering would require either a lowering of the space group symmetry, as only one Zr/Hf Wyckoff-position exists in $I4_1/amd$ (no. 141), or an enlarged unit cell. Reconstructed planes through reciprocal space (Figures H.6 to H.9) indicate neither the existence of superstructure reflections nor reflections breaking the systematic absences, as would be required for the maximal *translationengleiche* subgroups of $I4_1/amd$ (no. 141). Hence, a random distribution of vacancies was assumed. The structure models with a random distribution of vacancies were also corroborated by ^{31}P solid state NMR measurements carried out on the $M_{0.75}\text{PO}_4$ compounds (Figure H.10).

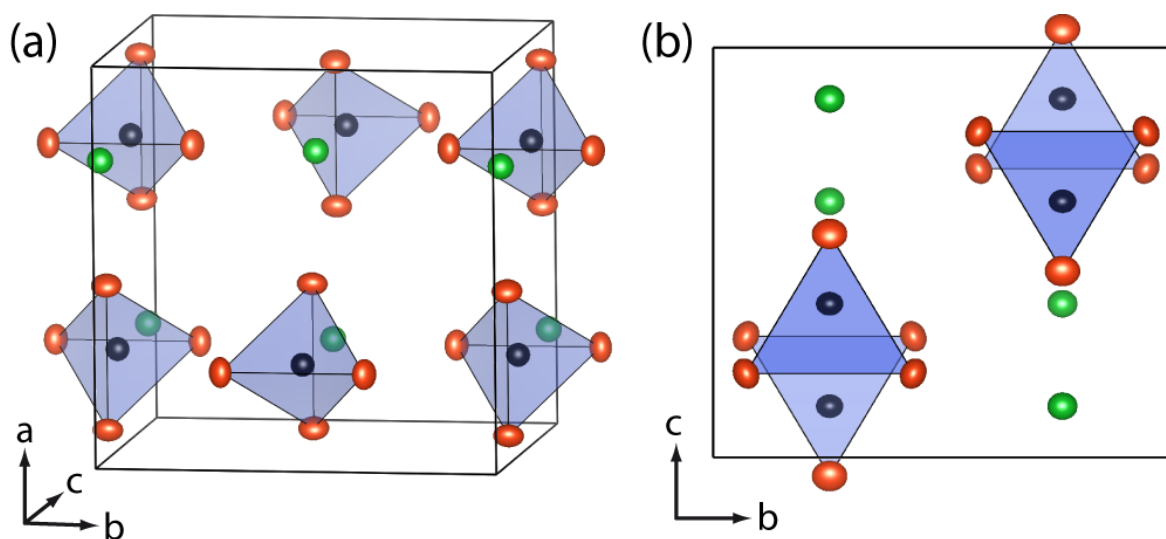


Figure 8.2. Unit cell of the Zr and Hf orthophosphates. Figure based on structure model of $\text{Zr}_{1-x}\text{PO}_{3+4x}\text{N}_{1-4x}$, with metal atoms in green, P in black and N in orange: (a) random orientation of the unit cell; (b) projection along [100]. Ellipsoids are set to a 90% probability level.

8.3.3 Structure Discussion

All title compounds crystallize in the ZrSiO_4 structure-type, space group $I4_1/amd$ (no. 141), albeit being defect variants as the heavy atom positions are not fully occupied. The crystal structure comprises noncondensed $\text{P}(\text{O}/\text{N})_4$ tetrahedra, as illustrated in projection along [100], alternatingly pointing up and downward (Figure 8.2). The tetrahedra are separated by heavy atoms, which are coordinated in

a $M(O/N)_8$ bisdisphenoid (also called dodecadeltahedron, Johnson solid J_{84} , Figure 8.3).^[43] The bisdisphenoid is common in structures with noncondensed tetrahedra and has been observed in the room temperature modification of $AgClO_4$ as well as anhydrite $CaSO_4$ and scheelite $CaWO_4$.^[44–46] A mathematical bisdisphenoid is a deltahedron with symmetry D_{2d} in Schönflies notation and vertex symbol $(3^4)_4(3^5)_4$; in the $M(O/N)_8$ polyhedra of presented orthophosphates this symmetry is retained (Figure 8.3b) but two different $M-(O/N)$ distances lead to irregular triangles as faces of the polyhedra.^[47]

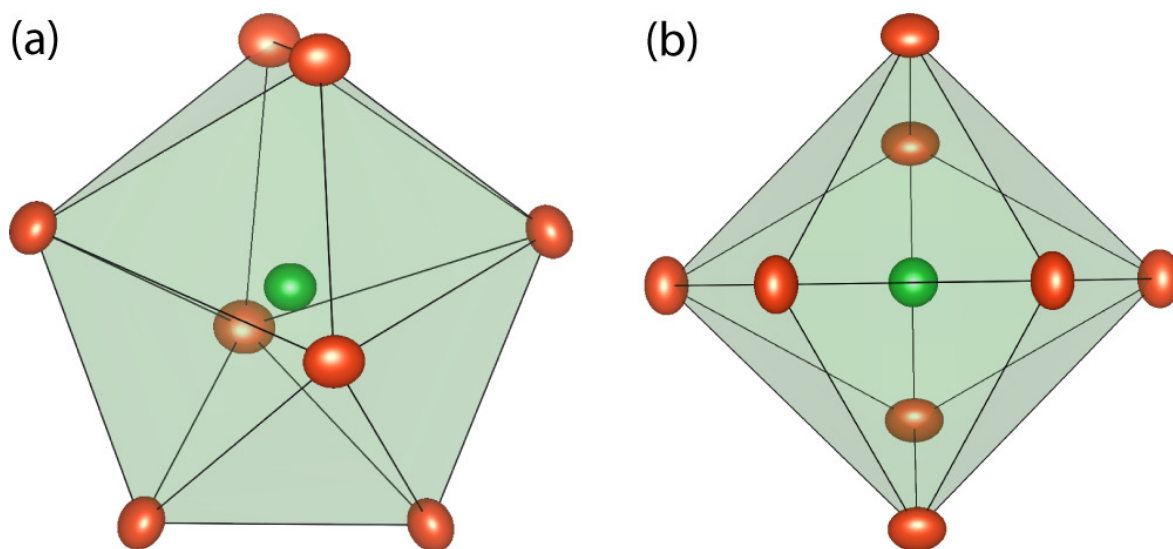


Figure 8.3. Heavy-atom $M(O/N)_8$ coordination polyhedron based on structure model of $Zr_{1-x}PO_{3+4x}N_{1-4x}$ with metal atom in green and N in orange: (a) polyhedron in random orientation; (b) polyhedron in projection along the $\bar{4}$ rotoreflection. Ellipsoids are set to a 90% probability level.

A comparison of the title compounds with $ZrSiO_4$ and $HfSiO_4$ shows that the Hf compounds have a smaller unit cell than their Zr counterparts (Figure 8.4).^[48,49] This shrinkage is due to the increased relativistic contraction of the 5d Hf atoms compared to the lighter 4d Zr atoms, resulting in slightly smaller Hf atoms.^[50] Chemically, Hf and Zr are very similar, unlike, e.g. Mo and W; the relativistic contraction and the shell-structure expansion cancel each other out, which might explain why Hf and Zr adopt the same structure-type.^[51] Since the heavy-atom positions in $M_{0.75}PO_4$ are occupied to 3/4, their unit cell volume is expectedly smaller than that of the oxonitridophosphates. The P–(O/N) bond lengths are longer for the nitrogen containing compounds than in the pure oxophosphates, but all bond lengths are shorter than the respective Si–O interatomic distances of zircon and hafnon.

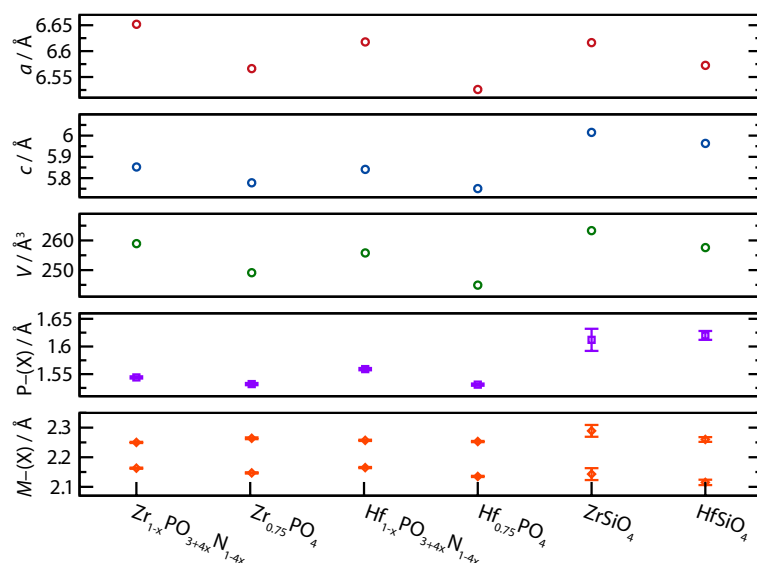


Figure 8.4. Comparison of lattice parameters a and c , unit cell volumes V , and P-(X) and M-(X) ($X = \text{O/N}$) distances of all title compounds as well as ZrSiO_4 and HfSiO_4 .^[48,49] Cell parameters of the title compounds were extracted from Rietveld refinement and interatomic distances from single-crystal refinement. Standard deviations are displayed for interatomic distances, not for lattice parameters as they are too small to be visualized.

The P-(O/N) bond lengths found here are in good agreement with values found in $\beta\text{-K}_2\text{SO}_4$ -type $\text{Sr}_2\text{PO}_3\text{N}$ ($d(\text{P}-(\text{O/N})) = 1.569\text{--}1.574$).^[52] For the M-(O/N) distances no trend can be postulated, and the values of the two different distances range from 2.135 to 2.163 Å and from 2.250 to 2.264 Å, respectively.

8.3.4 Thermal Properties

High-temperature PXRD diffractograms (Figures H.12 to H.15) were recorded to a maximum temperature of 1000 °C to investigate the thermal stability of the compounds in air. The oxophosphates $M_{0.75}\text{PO}_4$ seem to undergo a phase transformation to ambient pressure polymorphs with the same composition at ca. 900 °C for $\text{Zr}_{0.75}\text{PO}_4$ and at ca. 780 °C for $\text{Hf}_{0.75}\text{PO}_4$. The diffraction pattern of the $\text{Zr}_{0.75}\text{PO}_4$ phase transformation matches a unit cell reported by Alamo et al. reported for Zr orthophosphate $\text{Zr}_{2.25}(\text{PO}_4)_3$. This $\text{Zr}_{2.25}(\text{PO}_4)_3$ was reported to enter the NASICON structure-type as the unit cell is similar to that of $\text{NaZr}_2(\text{PO}_4)_3$ (Figure H.16).^[21] The phase transformation of $\text{Hf}_{0.75}\text{PO}_4$ yields a similar powder pattern (Figure H.17), but no corresponding $\text{Hf}_{2.25}(\text{PO}_4)_3$ structure has been reported. Since the unit cell reported for $\text{Zr}_{2.25}(\text{PO}_4)_3$ also matches the reflection pattern after the phase transformation, a similar structure can be assumed.

While no decomposition was observed for the $\text{Hf}_{1-x}\text{PO}_{3+4x}\text{N}_{1-4x}$ up to 1000 °C, the oxonitridophosphate $\text{Zr}_{1-x}\text{PO}_{3+4x}\text{N}_{1-4x}$ decomposes at ca. 680 °C. Most of the diffraction pattern can be explained by the $\text{Zr}_{2.25}(\text{PO}_4)_3$ reference; however, several reflections could not be assigned to any known phase (Figure H.18). From the chemical composition the unknown phase should be rich in Zr, but the pattern did not match that of ZrO_2 .^[42]

8.3.5 Optical Properties

The UV–vis spectra recorded for each compound reveal valence to conduction band transitions in the UV range (Figure H.19). To obtain an estimate of the optical band gap, the reflectance spectra were transformed into the Kubelka–Munk function and plotted in a Tauc-plot (Figure 8.5).^[53,54] A direct band gap was assumed for the structures. A linear regression was fit to the regions of steep slope and the estimated band gap value read off at the x -axis intersection.

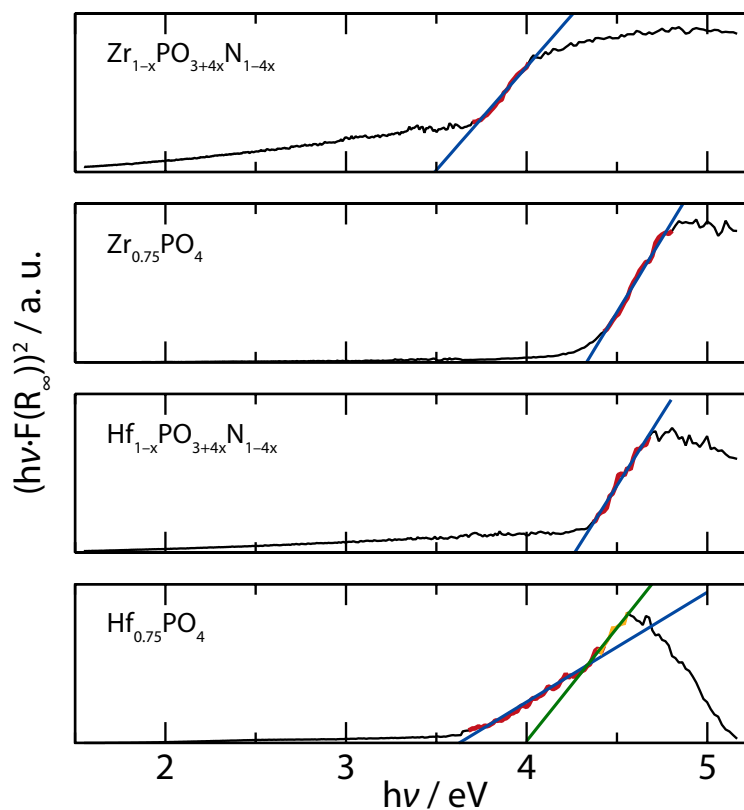


Figure 8.5. Tauc-plots of all compounds, generated from UV–vis reflectance data. Kubelka–Munk function in black, linear regression (blue) fit to data points highlighted in red. Special case for $\text{Hf}_{0.75}\text{PO}_4$ as two slopes are discernible; two regression lines (blue and green) were fit to the data points (red and orange) yielding adsorption onset values of 3.6 and 4 eV, respectively.

The values for the $M_{1-x}\text{PO}_{3+4x}\text{N}_{1-4x}$ ($M = \text{Zr}, \text{Hf}$) are $E_g \approx 3.5$ and 4.3 eV, respectively, while $\text{Zr}_{0.75}\text{PO}_4$ has a value of $E_g \approx 4.2$ eV. The band gap of $\text{Hf}_{0.75}\text{PO}_4$ cannot unambiguously be derived since the UV-vis spectra shows no clear beginning of the valence to conduction band transition (Figure H.19d), which leads to a Kubelka–Munk function with an additional point of inflection in the region of steepest slope (Figure 8.5, bottom). Two different slopes are discernible, both leading to different values of E_g , 3.6 and 4 eV, respectively. This absorption might not only be caused by the valence to conduction band transition but could also be influenced by local defects. Hence, a true optical band gap cannot be derived here, only the beginning of absorption, which is at ≈ 3.6 eV.

8.3.6 Alternative synthesis methods

Metathesis reactions were successfully applied in the synthesis of temperature labile compounds of, e.g., metal borides, nitrides, and carbides.^[55] The energy for the product formation is generated through the exothermic nature of the metathesis reaction, allowing for lower furnace temperatures. Since $\text{Hf}_{0.75}\text{PO}_4$ and $\text{Zr}_{0.75}\text{PO}_4$ are ternary phosphates they might be accessible without applying high pressures. Analogous metathesis reactions were therefore carried out in alumina crucibles in sealed Ar ampules at 700 °C. This temperature was chosen since the HTXRD data indicate that both phosphates do not start to undergo a phase transformation at that temperature. The reactions, however, did not yield the desired orthophosphate as $M_2(\text{PO}_4)_2\text{O}$ ($M = \text{Hf}, \text{Zr}$), and unidentified side phases were formed.^[19] Hence, formation of the orthophosphate, with its defect ZrSiO_4 structure, seemed to be stabilized under high-pressure conditions. As mentioned in the HTXRD section, the phosphates undergo a phase transformation to the ambient pressure form of $\text{Zr}_{2.25}(\text{PO}_4)_3$.^[21] Hence the oxophosphates reported here might be the high-pressure polymorphs of this structure-type and metastable under ambient pressure conditions. Hence they were not previously discovered despite the thorough investigation of the group 4 phosphates. Thus high-pressure metathesis opens a route to compounds that are thermally labile and potentially metastable at ambient pressures.

8.4 Conclusion

The preparation of the oxonitridophosphates with group 4 metals comprising noncondensed $\text{P}(\text{N/O})_4$ tetrahedra, $M_{1-x}\text{PO}_{3+4x}\text{N}_{1-4x}$ ($M = \text{Zr, Hf}$) shows that high-pressure metathesis can grant a systematic access to this class of compounds. Naturally, more types of anion network have to be prepared to underline the capability of the high-pressure metathesis route.

Moreover, high-pressure metathesis could be a viable route to unknown oxophosphates, as shown with the preparation of $\text{Zr}_{0.75}\text{PO}_4$ and $\text{Hf}_{0.75}\text{PO}_4$. The latter are inaccessible by ambient pressure synthesis methods and are probable high-pressure polymorphs of the $M_{2.25}(\text{PO}_4)_3$ phases crystallizing in the NASICON structure-type. $\text{Zr}_{0.75}\text{PO}_4$ and $\text{Hf}_{0.75}\text{PO}_4$ have, most likely, not been discovered before since they are metastable at ambient pressures and could not be prepared without high-pressure techniques. Hence, high-pressure metathesis could also be used to target metastable systems of oxophosphates, which were previously only accessible via kinetic control of ambient pressure synthesis methods.

The orthophosphates reported here are an intriguing starting point for the search for ion conduction properties within the group 4 (nitrido)phosphates, as are known from the structurally related class of NASICON materials.

8.5 References

- [1] S. D. Kloß, W. Schnick, *Angew. Chem., Int. Ed.* **2015**, *54*, 11250–11253; *Angew. Chem.* **2015**, *127*, 11402–11405.
- [2] S. D. Kloß, N. Weidmann, R. Niklaus, W. Schnick, *Inorg. Chem.* **2016**, *55*, 9400–9409.
- [3] S. D. Kloß, N. Weidmann, W. Schnick, *Eur. J. Inorg. Chem.* **2017**, 1930–1937.
- [4] S. D. Kloß, L. Neudert, M. Döblinger, M. Nentwig, O. Oeckler, W. Schnick, *J. Am. Chem. Soc.* **2017**, *139*, 12724–12735.
- [5] S. D. Kloß, S. Wandelt, A. Weis, W. Schnick, *Angew. Chem., Int. Ed.* **2018**, *57*, 3192–3195; *Angew. Chem.* **2018**, *130*, 3246–3249.
- [6] R. Marchand, W. Schnick, N. Stock, *Adv. Inorg. Chem.* **2000**, *50*, 193–233.
- [7] W. Feldmann, *Z. Chem.* **1987**, *27*, 182–183.
- [8] F. J. Pucher, F. Hummel, W. Schnick, *Eur. J. Inorg. Chem.* **2015**, 1886–1891.
- [9] F. J. Pucher, F. Karau, J. Schmedt auf der Günne, W. Schnick, *Eur. J. Inorg. Chem.* **2016**, 1497–1502.
- [10] W. Schnick, J. Lücke, *Angew. Chem., Int. Ed. Engl.* **1992**, *31*, 213–215; *Angew. Chem.* **1992**, *104*, 208–209.
- [11] N. Stock, J. Lücke, M. Volkmann, M. Jansen, W. Schnick, *Z. Anorg. Allg. Chem.* **1995**, *621*, 987–992.
- [12] W. Schnick, J. Lücke, *Z. Anorg. Allg. Chem.* **1990**, *588*, 19–25.
- [13] S. Horstmann, E. Irran, W. Schnick, *Angew. Chem., Int. Ed. Engl.* **1997**, *36*, 1873–1875; *Angew. Chem.* **1997**, *109*, 1938–1940.
- [14] B. E. Scheetz, D. K. Agrawal, E. Breval, R. Roy, *Waste Manage.* **1994**, *14*, 489–505.
- [15] C. A. Martinek, F. A. Hummel, *J. Am. Ceram. Soc.* **1970**, *53*, 159–161.
- [16] K. R. Laud, F. A. Hummel, *J. Am. Ceram. Soc.* **1971**, *54*, 407–409.
- [17] G. W. Stinton, M. R. Hampson, J. S. O. Evans, *Inorg. Chem.* **2006**, *45*, 4352–4358.
- [18] W. Gebert, E. Tillmanns, *Acta Crystallogr., Sect. B: Struct. Crystallogr. Cryst. Chem.* **1975**, *31*, 1768–1770.
- [19] G. Wallez, J.-P. Souron, M. Quarton, *Solid State Sci.* **2006**, *8*, 1061–1066.
- [20] Y. E. Gorbunova, V. V. Ilyukhin, V. G. Kuznetsov, A. V. Lavrov, S. A. Linde, *Dokl. Akad. Nauk*

- SSSR **1976**, 228, 1329–1331.
- [21] J. Alamo, R. Rustum, *J. Am. Ceram. Soc.* **1984**, 67, 80–82.
- [22] O. Paschos, J. Kunze, U. Stimming, F. Maglia, *J. Phys. Condens. Matter* **2011**, 23, 234110.
- [23] N. Anantharamulu, K. Koteswara Rao, G. Rambabu, B. Vijaya Kumar, V. Radha, M. A. Vithal, *J. Mater. Sci.* **2011**, 46, 2821–2837.
- [24] N. Dacheux, R. Podor, V. Brandel, M. Genet, *J. Nucl. Mater.* **1998**, 252, 179–186.
- [25] E. Zintl, A. Harder, B. Dauth, *B. Z. Elektrochem.* **1934**, 40, 588–593.
- [26] R. Klement, O. Koch, *Chem. Ber.* **1954**, 87, 333–340.
- [27] D. Baumann, R. Niklaus, W. Schnick, *Angew. Chem., Int. Ed.* **2015**, 54, 4388–4391; *Angew. Chem.*, **2015**, 127, 4463–4466.
- [28] J. M. Léger, J. Haines, C. Chateau, G. Bocquillon, M. W. Schmidt, S. Hull, F. Gorelli, A. Lesauze, R. Marchand, *Phys. Chem. Miner.* **2001**, 28, 388–398.
- [29] H. Huppertz, *Z. Kristallogr.* **2004**, 219, 330–338.
- [30] D. C. Rubie, *Phase Transitions* **1999**, 68, 431–451.
- [31] D. Walker, M. A. Carpenter, C. M. Hitch, *Am. Mineral.* **1990**, 75, 1020–1028.
- [32] D. Walker, *Am. Mineral.* **1991**, 76, 1092–1100.
- [33] N. Kawai, S. Endo, *Rev. Sci. Instrum* **1970**, 41, 1178–1181.
- [34] Bruker AXS, Inc., SADABS, Madison, Wisconsin, USA, **2001**.
- [35] Bruker AXS, Inc., APEX3, Madison, Wisconsin, USA, **2016**.
- [36] Bruker AXS, Inc., XPREP, Karlsruhe, Germany, **2001**.
- [37] G. M. Sheldrick, *Acta Crystallogr., Sect. A: Found. Crystallogr.* **2008**, 64, 112–122.
- [38] G. M. Sheldrick, *SHELXS - A Program for Crystal Structure Solution*, University of Göttingen, Göttingen, Germany, **1997**.
- [39] K. Momma, F. Izumi, *J. Appl. Crystallogr.* **2011**, 44, 1272–1276.
- [40] H. M. Rietveld, *J. Appl. Crystallogr.* **1969**, 2, 65–71.
- [41] A. A. Coelho, *TOPAS-Academic V4.1*, Coelho Software, Brisbane, Australia, **2007**.
- [42] J. Adam, M. D. Rogers, *Acta Crystallogr.* **1959**, 12, 951–951.
- [43] N. W. Johnson, *Canad. J. Math.* **1966**, 18, 169–200.
- [44] D. Errandonea, L. Gracia, A. Beltrán, A. Vegas, Y. Meng, *Phys. Rev. B: Condens. Matter Mater.*

- Phys.* **2011**, *84*, 1–11.
- [45] F. C. Hawthorne, R. B. Ferguson, *Can. Mineral.* **1975**, *13*, 289–292.
- [46] M. I. Kay, B. C. Frazer, I. Almodovar, *J. Chem. Phys.* **1964**, *40*, 504–506.
- [47] V. A. Blatov, M. O’Keeffe, D. M. Proserpio, *CrystEngComm.* **2010**, *12*, 44–48.
- [48] I. R. Krstanović, *Acta Crystallogr.* **1958**, *11*, 896–897.
- [49] J. A. Speer, B. J. Cooper, *Am. Mineral.* **1982**, *67*, 804–808.
- [50] P. Pyykko, *Chem. Rev.* **1988**, *88*, 563–594.
- [51] P. Pyykkö, J.-P. Desclaux, *Acc. Chem. Res.* **1979**, *12*, 276–281.
- [52] A. Marchuk, P. Schultz, C. Hoch, O. Oeckler, W. Schnick, *Inorg. Chem.* **2016**, *55*, 974–982.
- [53] J. Tauc, R. Grigorovici, A. Vanacu, *Phys. Status Solidi B* **1966**, *15*, 627–637.
- [54] E. A. Davis, N. F. Mott, *Philos. Mag.* **1970**, *22*, 903–922.
- [55] H.-J. Meyer, *Dalton Trans.* **2010**, *39*, 5973–5982.

Chapter 9

Open-shell 3d Transition Metal Nitridophosphates $M^{\text{II}}\text{P}_8\text{N}_{14}$ ($M^{\text{II}} = \text{Fe}, \text{Co}, \text{Ni}$) by High-pressure Metathesis

Simon D. Kloß, Oliver Janka, Theresa Block, Rainer Pöttgen, Robert Glaum, Wolfgang Schnick

published in: *Angew. Chem., Int. Ed.* **2018**, DOI: 10.1002/anie.201809146

published in: *Angew. Chem.* **2018**, DOI: 10.1002/ange.201809146

Reprinted (adapted) with permission from *Angewandte Chemie*. Copyright 2018 John Wiley and Sons.



The ternary MP_8N_{14} ($M = \text{Fe}, \text{Co}, \text{Ni}$) nitridophosphates were prepared by high-pressure metathesis. Transition metal nitridophosphates are a new class of materials consistent of earth-abundant elements. Magnetic and optical properties of these compounds were studied for the first time. The ligand field properties of nitride ions were investigated on $[MN_6]$ chromophores.

Abstract

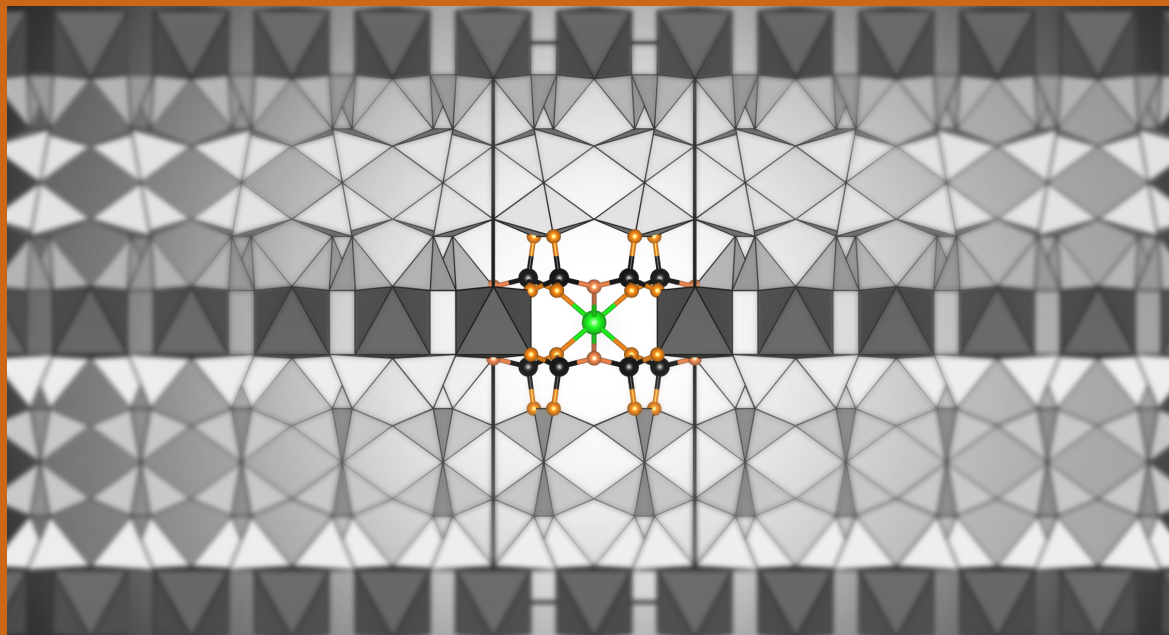


Table-of-contents graphic.

3d transition metal nitridophosphates $M^{\text{II}}\text{P}_8\text{N}_{14}$ ($M^{\text{II}} = \text{Fe, Co, Ni}$) were prepared by high-pressure metathesis indicating that this route might give a systematic access to a structurally rich family of $M\text{-P-N}$ compounds. Their structures, which are stable in air up to at least 1273 K, were determined through powder X-ray diffraction and consist of highly condensed tetra-layers of PN_4 tetrahedra and MN_6 octahedra. Magnetic measurements revealed paramagnetic behavior of $\text{CoP}_8\text{N}_{14}$ and $\text{NiP}_8\text{N}_{14}$ down to low temperatures while, $\text{FeP}_8\text{N}_{14}$ exhibits an antiferromagnetic transition at $T_{\text{N}} = 3.5(1)$ K. Curie-Weiss fits of the paramagnetic regime indicate that the transition metal cations are in a oxidation state +II, which was corroborated by Mössbauer spectroscopy for $\text{FeP}_8\text{N}_{14}$. The ligand field exerted by the nitride ions in $\text{CoP}_8\text{N}_{14}$ and $\text{NiP}_8\text{N}_{14}$ was determined from UV/Vis/NIR data and is comparable to that of aqua-ligands and oxophosphates.

9.1 Introduction with Results and Discussion

Nowadays, group one and two nitridophosphates are well-studied but the progress of exploration beyond these two groups, towards transition metal compounds, is limited. As a consequence, the knowledge about the underlying chemistry of such compounds, from structural to electronic properties, is scarce. Here we report the first ternary open-shell 3d transition metals nitridophosphates $M^{\text{II}}P_8N_{14}$ ($M = \text{Fe, Co, Ni}$). Taking advantage of the open-shell electron configuration of these metal ions, we present, based on magnetic susceptibility data and electronic spectra, the first ligand field analysis for transition metal ions in nitridophosphates. That these compounds were discovered only now, is in part owed to the difficult synthesis of nitridophosphates, whose challenges are briefly introduced in the following.^[1–4]

The element combination P/N is isoelectronic to Si/O, hence nitridophosphates form tetrahedra networks similar to silicates. However, unlike silicates, nitridophosphates are usually not refractory and melt incongruently at ambient pressures. This is owed to the positive electron affinity of N, making nitride ions prone to oxidation, the major challenge in nitridophosphate synthesis.^[5] Hence, common starting materials like P_3N_5 decompose above ca. 1100 K ($P_3N_5 \rightarrow 3 \text{PN} + \text{N}_2$), well-below the crystallization temperatures of most nitridophosphates.^[6] High-pressure reaction conditions, usually achieved with a multianvil setup, are mandatory for most syntheses as the counter-pressure suppresses decomposition of the nitrides following the principle of Le Chatelier.^[2]

For non-main group nitridophosphates it is challenging to find suitable starting materials as the use of metal azides and nitrides is dependent upon their stability.^[4,7] For example, for trivalent rare-earths, these precursors are not practicable, as the azides are too unstable (or unknown) and the nitrides too unreactive.^[8] An alternative is the recently applied high-pressure metathesis, which we reported for rare-earth and group four nitridophosphates. The metathesis starts from metal halides and LiPN_2 , e.g. Eq. 9.1, yielding the nitridophosphate and a lithium halide as byproduct.^[9,10]

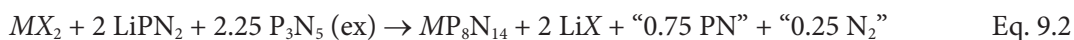


The formed lithium halide is the thermodynamic driving force of the exothermic reaction and flux medium enhancing the growth of single crystals.^[9] By addition of nitrides or oxides like Li_3N , P_3N_5 , Li_2O , PON , or P_2O_5 to this route, a systematic access to rare-earth nitridophosphates has been estab-

blished resulting in compounds with structural motifs ranging from highly condensed frameworks (e.g. $\text{Ce}_4\text{Li}_3\text{P}_{18}\text{N}_{35}$) down to non-condensed tetrahedra (e.g. $\text{Ho}_3[\text{PN}_4]\text{O}$).^[11,12]

Transition metal nitridophosphates are more difficult to prepare because the competing N_2 elimination reaction is favored by the formation of stable phosphides. While phosphide formation is reportedly a minor problem with group four oxonitridophosphates prepared by high-pressure metathesis at moderate pressures, it affects the late 3d transition metals.^[10] Up to now, Fe, Co, and Ni were only stabilized with a pressure-ampoule route in $M_{(6+(y/2)-x)}\text{H}_{2x}[\text{P}_{12}\text{N}_{24}]X_y$ with $X = \text{Cl, Br, I}$; $0 \leq x \leq 4$; $y \leq 2$ sodalites, which, however, have a low framework density.^[13] Structures with a higher density require higher temperatures, which in turn triggers the oxidation of nitride ions, and have thus not been reported yet.

With high-pressure metathesis we could prepare the $M^{\text{II}}\text{P}_8\text{N}_{14}$ ($M = \text{Fe, Co, Ni}$) compounds following Eq. 9.2, requiring pressures of 9 GPa and temperatures of ca. 1473 K (achieved with the multianvil technique, experimental details in the Supporting Information).^[14]



with $X = \text{Cl}$ for Fe, Ni and $X = \text{Br}$ for Co. A slight excess of P_3N_5 was used to suppress phosphide formation and to obtain crystallographically pure compounds. The excess P_3N_5 may undergo amorphization or side reactions with the crucible releasing N_2 , which further shifts the chemical equilibrium according to Le Chatelier, similar to the mechanism proposed for the azide route.^[4] Pressures below 9 GPa yielded mainly metal phosphides. The here used reaction conditions are unprecedentedly extreme for the stabilization of any metal in nitridophosphates, underlining the severity of the redox chemistry problem.

The isotopic compounds crystallize as colorless ($\text{FeP}_8\text{N}_{14}$), pale-blue ($\text{CoP}_8\text{N}_{14}$), and pale-green ($\text{NiP}_8\text{N}_{14}$) microcrystalline powders that are resistant to air, water, and concentrated acids. Their structure was solved and refined from powder X-ray diffraction (PXRD) data (Tables I.1–I.5, Figures I.1–I.3).^[15] The theoretical composition was confirmed by energy dispersive X-ray (EDX) spectroscopy (measured: $\text{FeP}_{7.8(6)}\text{N}_{12.6(7)}$ (10 points), $\text{CoP}_{8.0(7)}\text{N}_{14.1(7)}$ (5 points), $\text{NiP}_{8.2(6)}\text{N}_{12.8(7)}$ (4 points)). Some small oxygen impurities were detected, which, however, might be due to passivating surface hydrolysis/oxidation of the small crystallites or traces of residual moisture (Figure I.5). FTIR spectroscopy

indicated no N–H bonds present in the samples (Figure I.6). The compounds are stable in air up to 1273 K (Figure I.7–I.9).

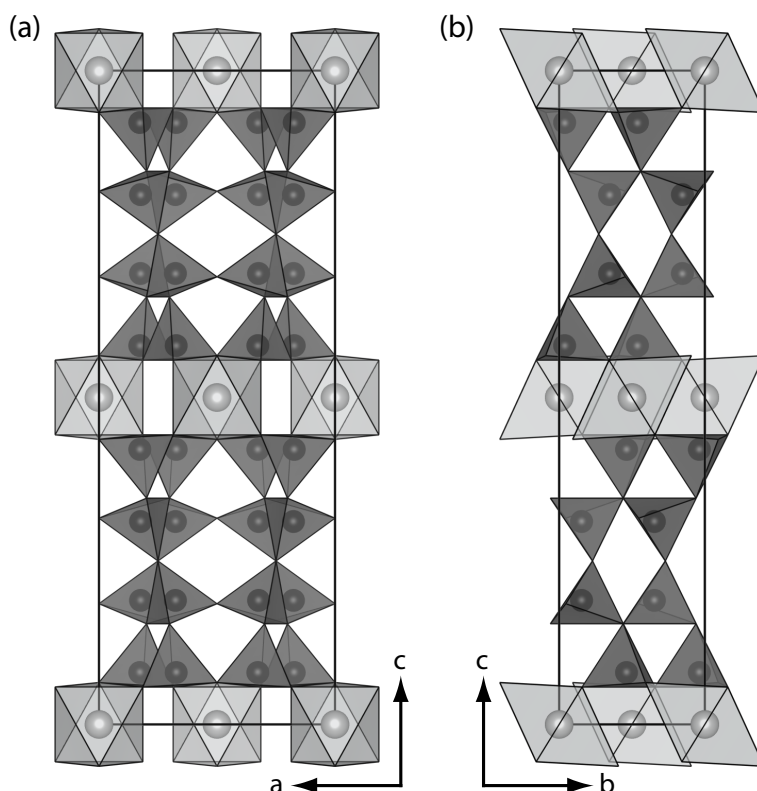


Figure 9.1. Crystal structure of MP_8N_{14} , MN_6 octahedra displayed in light gray, PN_4 tetrahedra in dark gray, M as light gray spheres, P as black spheres, N omitted for clarity. (a) Projection along b , (b) projection along a .

The crystal structure of MP_8N_{14} is related to that of SrP_8N_{14} (details in SI) and consists of vertex-sharing PN_4 tetrahedra forming highly-condensed tetra-layers, which are separated by metal ions (Figure 9.1).^[16] Each tetra-layer consists of four single-layers, which are composed of six-membered rings arranged in a distorted honeycomb net (Figure I.10). The stacking sequence is ABCD, as the second and third layers are related by the e glide plane of space group $Cmce$.

Three coordination environments of N are present in the structure, one with coordination by two P ($N^{[2]}$), one with coordination by three P ($N^{[3]}$), and one with coordination by two P and one M atom ($N^{[3M]}$). Moreover, the coordination of the $N^{[3M]}$ atoms are close to trigonal-planar, suggesting sp^2 hybridization of N (Figure I.15), which will be discussed later concomitant with the UV/Vis/NIR data. The interatomic P – N distances mirror the coordination environments: the P – $N^{[2]}$ distances are the shortest with $1.533(2) \leq d(P-N) \leq 1.564(3)$ Å, the P – $N^{[3]}$ the longest with $1.681(3) \leq d(P-N) \leq$

1.725(3) Å and the P–N^[3M] are intermediate with $1.607(2) \leq d(\text{P–N}) \leq 1.634(5)$ Å (Tables I.6–I.8). These variations can be explained within *Pauling's* rule of Coulomb repulsion in complex ionic crystals and the pressure-distance-paradox of *Kleber*.^[17,18] Similar interatomic distances have been found in nitridophosphates with comparable tetrahedra connection patterns such as β -HP₄N₇ and MP₄N₇ (*M* = Na, K, Rb, Cs; $1.528 \leq d(\text{P–N}) \leq 1.755$ Å).^[1,19]

The metal ions are coordinated in elongated MN₆ octahedra with separate sets of equatorial and axial *M*–N interatomic distances ($d_{\text{eq}}(\text{(Fe; Co; Ni)–N}) = 2.201(4); 2.188(3); 2.164(3)$ Å, $d_{\text{ax}}(\text{(Fe; Co; Ni)–N}) = 2.585(7); 2.605(4); 2.535(4)$ Å, Tables I.6–I.8). The trend in equatorial distances agrees with the sum of ionic radii (Shannon) if high-spin states are present for Fe²⁺ and Co²⁺ and further charge distribution (CHARDI) calculations are consistent with the structure model (Tables I.12–I.14).^[20,21,22] For Fe²⁺ the high-spin state was shown with Mössbauer spectroscopy (Figure I.14). Further corroboration will be given along with the magnetochemistry and UV/Vis/NIR spectroscopy presented below.

The magnetic properties of the MP₈N₁₄ compounds were determined using the Vibrating Sample Magnetometry (VSM) option of a Quantum Design Physical Property Measurement System (PPMS). Susceptibility measurements reveal a linear behavior in χ^{-1} above 100 K for all compounds, which indicates paramagnetism (Figures 9.2 for *M* = Fe, I.11, I.12 for *M* = Co, Ni). The iron compounds susceptibility additionally features a slight bent below 100 K indicating a temperature dependency of the magnetic moment (Figure I.13). The effective magnetic moments μ_{eff} extracted from Curie-Weiss fits, indicate upon comparison with the calculated spin-only values, that Fe, Co, and Ni are in oxidation state +II, and in high-spin states for Fe and Co (Table 9.1). The values for CoP₈N₁₄ and NiP₈N₁₄ are, however, slightly higher than the spin-only values, a circumstance that could be traced back to spin-orbit coupling and low-symmetry components of the ligand field. This assessment is based upon the UV/Vis/NIR analysis through angular overlap modeling (AOM) discussed later and in the Supporting Information.

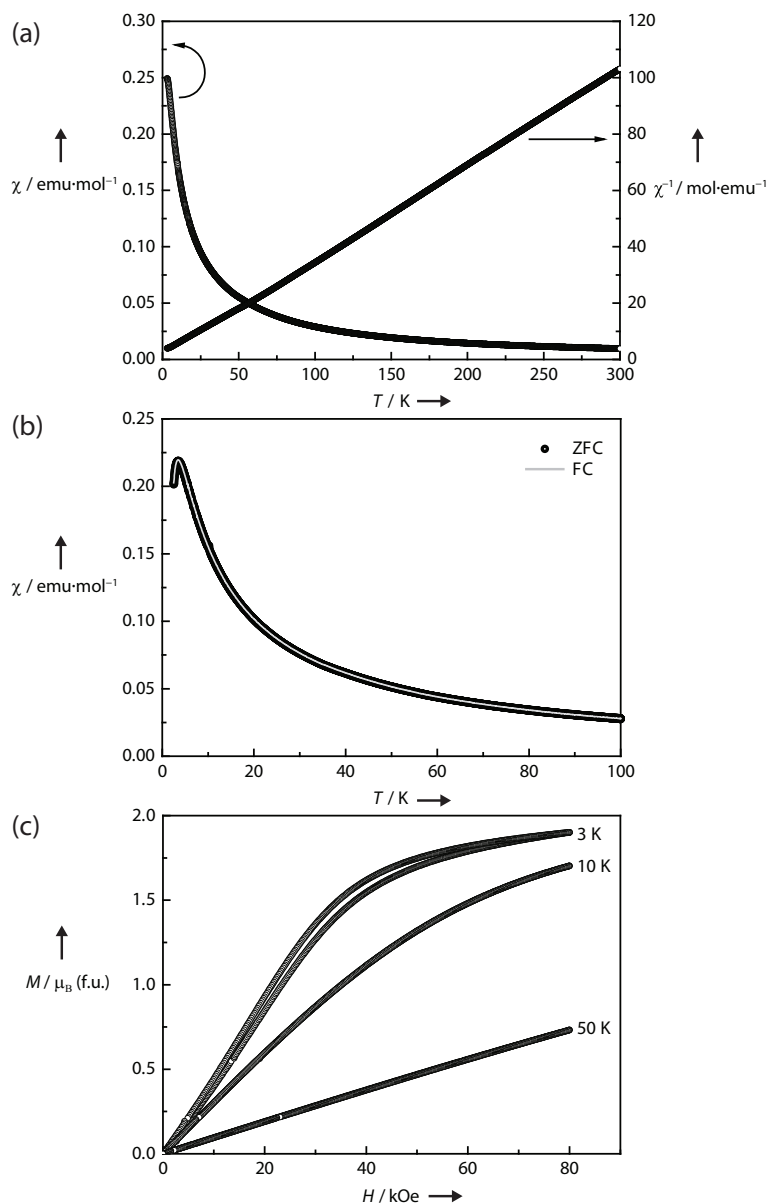


Figure 9.2. Magnetic properties of $\text{FeP}_8\text{N}_{14}$: (a) χ and χ^{-1} data measured at 10 kOe, (b) zero-field-cooled / field-cooled measurements (ZFC/FC) at 100 Oe and (c) magnetization isotherms recorded at 3, 10 and 50 K. In the isotherm at 3 K the lower line is increasing field, upper line decreasing field.

Interestingly, $\text{FeP}_8\text{N}_{14}$ shows an antiferromagnetic (AFM) transition at $T_N = 3.5(1)$ K in the low-field (100 Oe) zero-field-cooled / field-cooled measurements (ZFC/FC, Figure 9.2b). It is the first nitridophosphate in which a cooperative magnetic ordering phenomenon has been observed. The AFM state is also visible in the magnetization isotherms at 3 K (Figure 9.2c). Its S-shape indicates a spin-reorientation from and to the AFM ordering, in contrast to the slightly bent and linear curves at 10 and 50 K. Moreover, the 3 K isotherm features a small hysteresis between the increasing and decre-

asing field curve indicating a weak permanent magnetism. The magnetic measurements are discussed further in the Supporting Information.

Table 9.1. Magnetic data for MP_8N_{14} ($M = \text{Fe, Co, Ni}$) with T_N being the Néel temperature, μ_{eff} the effective magnetic moment, μ_{calc} the calculated spin-only moments, μ_{AOM} the calculated (AOM) moments in the range of 100 to 300 K accounting quantitatively for spin-orbit coupling, μ_{sat} the saturation moment at 3 K and 80 kOe, and θ_p the Weiss constant.

Compound	T_N / K	μ_{eff} / μ_B	$\mu_{\text{calc}} / \mu_B$	μ_{AOM} / μ_B	μ_{sat} / μ_B	θ_p / K
FeP₈N₁₄	3.5(1)	4.84(1)	4.90	5.30	1.90(1)	−0.9(1)
CoP₈N₁₄	–	4.27(1)	3.87	4.24–4.30	1.69(1)	−9.6(1)
NiP₈N₁₄	–	3.22(1)	2.83	3.17–3.22	0.63(1)	−12.8(1)

To investigate the optical properties of the pale-blue $\text{CoP}_8\text{N}_{14}$ and light-green $\text{NiP}_8\text{N}_{14}$, UV/Vis/NIR spectra were recorded (Figure 9.3). The color of the compounds stems from the d-d-electron transitions but the assignment of the transitions to term symbols is, however, not straight forward (Table I.15, I.16). The $[\text{MN}_6]$ chromophores do not exhibit O_h symmetry but are strongly elongated along one axis (point symmetry $2/m$, Figure I.16, Tables I.6–I.11). This elongation presumably leads to a lowering of the energy of the $d(z^2)$, $d(xz)$, and $d(yz)$ orbitals resulting in splitting of the $^4\text{T}_{1g}(\text{P})$ ($\text{CoP}_8\text{N}_{14}$) and the $^3\text{T}_{2g}(\text{F})$ states ($\text{NiP}_8\text{N}_{14}$, Figure I.15). Such severe geometric influence on d-electron energies has similarly been observed for $[\text{Ni}^{\text{II}}\text{O}_6]$ chromophores.^[23]

With assignment of the transitions to electronic states, the ligand field splitting Δ_o (energy difference between t_{2g} and e_g orbitals) and the Racah-parameter B (measure of interelectronic repulsion of the d-electrons) were determined with Tanabe-Sugano (TS) diagrams (Table 9.2, details in Supporting Information).^[24]

Table 9.2. Ligand field splitting parameter Δ_o , Racah-parameter B , and nephelauxetic ratios from Tanabe-Sugano and from AOM, β and β_{AOM} .^[28]

Compound	$\Delta_o / \text{cm}^{-1}$	B / cm^{-1}	β	β_{AOM}
CoP₈N₁₄	7915	842	0.85	0.75
NiP₈N₁₄	7300	820	0.78	0.78

B indicates that Co is in a high-spin state, in line with the magnetic measurements. The nephelauxetic ratio $\beta = B/B_{\text{free ion}}$ (Table 9.2), which is the reduction of the inter-d-electron repulsion compared to the free ion, points for the $[\text{MN}_6]$ chromophores to a slightly higher covalency than observed for

oxo-ligands ($\beta = 0.8$ or above).^[25] For nitride ions in typical solid-state compounds this value has to our knowledge never been reported.

Discrepancies in β (Table 9.2) from the TS evaluation and AOM (explained below) point to the limitations of the two-parameter model (Δ_o and B) in describing the ligand field splitting in the low-symmetry $[MN_6]$ chromophores.^[24,25] In addition to the dramatic elongation (radial distortion) of the chromophores the symmetry of the ligand field is further lowered by a second-sphere ligand-field effect.^[26] The latter occurs since the $N^{[3M]}$ ligands are trigonal-planarly coordinated (see above, Figure I.15) and therefore probably sp^2 hybridized. Only the p-orbital (of nitrogen) perpendicular to the trigonal plane will interact with the metal d-orbitals, while the in-plane p-bonding can be neglected.

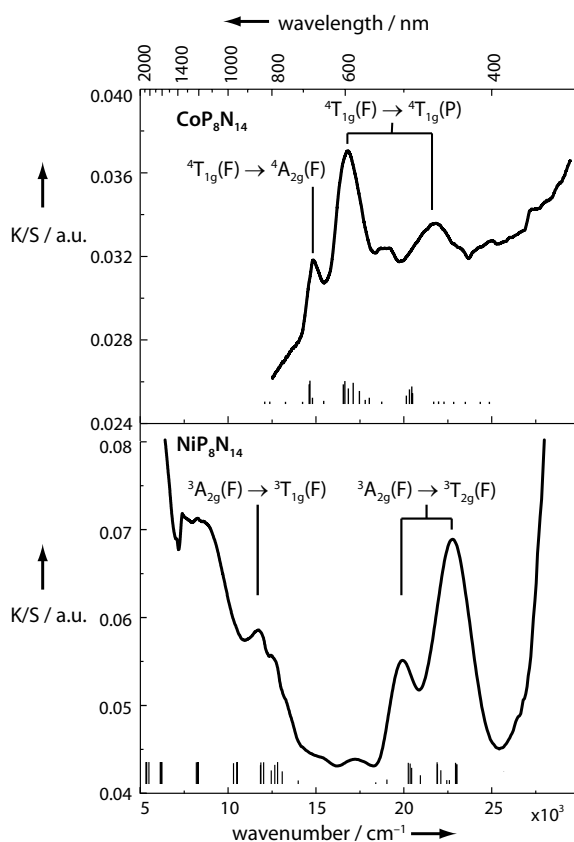


Figure 9.3. Powder reflectance spectra of CoP_8N_{14} (top) and NiP_8N_{14} (bottom). Tick marks at the bottom of each spectrum indicate calculated (AOM) transition energies for the $[M^{II}N_6]$ ($M^{II} = Co, Ni$) chromophores. Length of tick marks indicate the ratio of spin-allowed to spin-forbidden transition resulting from configuration interactions.

Low-symmetry ligand fields can be described by angular overlap modeling (AOM), which uses a molecular orbital approach and describes the metal-ligand interaction in terms of covalent σ - and π -bonding.^[25] For each ligand, one σ - and two π -interactions are used with energies $e_{\sigma}(M^{II}-N)$ and

$e_{\pi}(M^{II}-N)$. Here, the actual geometric structure of the chromophore, as obtained from crystal structure analysis, is accounted for by attenuation of the energy of each interaction. The remote axial N ligands naturally have weaker interactions. Furthermore, the angular dependence of the interactions is thus accounted for quantitatively. Further details about AOM, its validity in the present case and the parameters for the calculation for all three MP_8N_{14} compounds, and detailed results are given in the Supporting Information.

The AO modelling of the spectra provides quantitative evidence for the influence of the geometric distortion of the $[MN_6]$ chromophores and to a lesser extent of the p-anisotropy on the splitting of the states, which would be degenerate in a ligand field of O_h symmetry. Moreover, more accurate nephelauxetic ratios $\beta = 0.75$ and 0.78 for the $[CoN_6]$ and $[NiN_6]$ chromophores, respectively (Figure 9.3) were thus obtained. According to this study values $e_{\sigma}(M^{II}-N)$ are quite similar to $e_{\sigma}(M^{II}-O)$ in oxophosphates despite approximately 10% longer interatomic distances $d(M^{II}-N)$ compared to $d(M^{II}-O)$. As one might have anticipated from the higher polarizability of the nitride ion in comparison to oxide a slightly stronger nephelauxetic effect (lower β ; higher covalency) is evidenced for the nitrido ligands.

The ligand field analysis by AOM using the computer program CAMMAG with its quantitative treatment of spin-orbit coupling yields also magnetic moments for the $[M^{II}N_6]$ chromophores (Table 9.1).^[27] For CoP_8N_{14} , the larger μ_{eff} could only be modeled when incorporating the assumed anisotropic π -bonding (only one contributing p-orbital). Hence, this is the first evidence for sp^2 hybridization of nitride ions in nitridophosphates based on experimental data (details in SI).

9.2 Conclusion

High-pressure metathesis is a viable route to difficult to prepare open-shell 3d transition metal nitridophosphates. Reminiscent of this route is the ion-exchange reaction towards the transition metal nitridosilicate $\text{Fe}_2\text{Si}_5\text{N}_8$.^[28] In the ion-exchange, starting from FeCl_2 and $\alpha\text{-Mg}_2\text{Si}_5\text{N}_8$ at moderate 1253 K, no Si–N bond cleavage and formation has to take place, which prevents decomposition into the binary compounds and elements. In high-pressure metathesis of nitridophosphates the ion-exchange is concomitant with a reformation of the tetrahedra network, enabling explorative structure chemistry. The high-pressures in the GPa range increase the temperature of N_2 elimination/phosphide formation, while the metathesis allows a reaction at lower temperatures. The onset of the formation of MP_8N_{14} could be pinpointed to 9 GPa, which leaves a large potential for further investigation of transition-metal-rich phases as it is well below the maximum achievable pressure of the multianvil technique ($p_{\text{max}} \approx 25$ GPa).

9.3 References

- [1] K. Landskron, E. Irran, W. Schnick, *Chem. - Eur. J.* **1999**, *5*, 2548–2553.
- [2] F. Karau, W. Schnick, *Angew. Chem., Int. Ed.* **2006**, *45*, 4505–4508; *Angew. Chem.* **2006**, *118*, 4617–4620.
- [3] F. W. Karau, L. Seyfarth, O. Oeckler, J. Senker, K. Landskron, W. Schnick, *Chem. - Eur. J.* **2007**, *13*, 6841–6852.
- [4] A. Marchuk, F. J. Pucher, F. W. Karau, W. Schnick, *Angew. Chem., Int. Ed.* **2014**, *53*, 2469–2472; *Angew. Chem.* **2014**, *126*, 2501–2504.
- [5] T. Andersen, H. K. Haugen, H. Hotop, *J. Phys. Chem. Ref. Data* **1999**, *28*, 1511–1533.
- [6] S. Horstmann, E. Irran, W. Schnick, *Angew. Chem., Int. Ed. Engl.* **1997**, *36*, 1873–1875; *Angew. Chem.* **1997**, *109*, 2085–2087.
- [7] F. J. Pucher, S. R. Römer, F. W. Karau, W. Schnick, *Chem. - Eur. J.* **2010**, *16*, 7208–7214.
- [8] N. Sclar, *J. Appl. Phys.* **1964**, *35*, 1534–1538.
- [9] S. D. Kloß, W. Schnick, *Angew. Chem., Int. Ed.* **2015**, *54*, 11250–11253; *Angew. Chem.* **2015**, *127*, 11402–11405.
- [10] S. D. Kloß, S. Wandelt, A. Weis, W. Schnick, *Angew. Chem., Int. Ed.* **2018**, *57*, 3192–3195; *Angew. Chem.* **2018**, *130*, 3246–3249.
- [11] S. D. Kloß, L. Neudert, M. Döblinger, M. Nentwig, O. Oeckler, W. Schnick, *J. Am. Chem. Soc.* **2017**, *139*, 12724–12735.
- [12] S. D. Kloß, N. Weidmann, W. Schnick, *Eur. J. Inorg. Chem.* **2017**, 1930–1937.
- [13] N. Stock, J. Lücke, M. Volkmann, M. Jansen, W. Schnick, *Z. Anorg. Allg. Chem.* **1995**, *621*, 987–992.
- [14] H. Huppertz, *Z. Kristallogr.* **2004**, *219*, 330–338.
- [15] Crystal data for $\text{FeP}_8\text{N}_{14}$: $a = 8.26930(13)$, $b = 5.10147(8)$, $c = 23.0776(4)$ Å, $V = 973.54(3)$ Å³, $Cmce$ (no. 64), $Z = 4$, $R_{\text{Bragg}} = 2.76$ %. Crystal data for $\text{CoP}_8\text{N}_{14}$: $a = 8.25183(8)$, $b = 5.10337(5)$, $c = 22.9675(2)$ Å, $V = 967.21(2)$ Å³, $Cmce$, $Z = 4$, $R_{\text{Bragg}} = 2.27$ %. Crystal data for $\text{NiP}_8\text{N}_{14}$: $a = 8.23105(9)$, $b = 5.08252(6)$, $c = 22.8516(3)$ Å, $V = 973.54(3)$ Å³, $Cmce$, $Z = 4$, $R_{\text{Bragg}} = 2.76$ %. E.s.d.'s as obtained from TOPAS do not represent physically meaningful standard deviations. Details on data collection and refinement are located in the Supporting Information

(Table I.1). Further details on the crystal structure investigations may be obtained from the Fachinformationszentrum Karlsruhe, 76344 Eggenstein-Leopoldshafen, Germany (fax: (+49)7247-808-666; e-mail: crysdata@fiz-karlsruhe.de), on quoting the depository numbers CSD-1856625-1856627.

- [16] S. Wendl, W. Schnick, *Chem. - Eur. J.* **2018**, *24*, 15889–15896.
- [17] L. Pauling, *J. Am. Chem. Soc.* **1929**, *51*, 1010–1026.
- [18] W. Kleber, *Krist. Tech* **1967**, *2*, 13–14.
- [19] D. Baumann, W. Schnick, *Inorg. Chem.* **2014**, *53*, 7977–7982.
- [20] R. D. Shannon, *Acta Crystallogr., Sect. A: Cryst. Phys., Diffr., Theor. Gen. Crystallogr.* **1976**, *32*, 751–767.
- [21] K. Momma, F. Izumi, *J. Appl. Crystallogr.* **2011**, *44*, 1272–1276.
- [22] R. Hoppe, S. Voigt, H. Glaum, J. Kissel, H. P. Müller, K. Bernet, *J. Less-Common Met.* **1989**, *156*, 105–122.
- [23] K. Maaß, Dissertation, Gießen University, Gießen, Germany, **2002**.
- [24] Y. Tanabe, S. Sugano, *J. Phys. Soc. Jpn.* **1954**, *9*, 753–766.
- [25] B. N. Figgis, M. A. Hitchman, *Ligand Field Theory and Its Applications*, Wiley-VCH, Weinheim, Germany, **2000**.
- [26] D. Reinen, M. Atanasov, S. L. Lee, *Coord. Chem. Rev.* **1998**, *175*, 91–158.
- [27] a) D. A. Cruse, J. E. Davies, J. H. Harding, M. Gerloch, D. J. Mackey, R. F. McMeeking *CAMMAG, a FORTRAN program*, Cambridge, UK, 1980; b) M. Gerloch, *Magnetism and Ligand Field Theory*; Cambridge Univ. Press 1983; c) M. Riley, *CAMMAG for PC*, v4.0, University of Queensland, St. Lucia, Australia, 1997.
- [28] P. Bielec, O. Janka, T. Block, R. Pöttgen, W. Schnick, *Angew. Chem., Int. Ed.* **2018**, *57*, 2409–2412; *Angew. Chem.* **2018**, *130*, 2433–2436.

Chapter 10

Summary

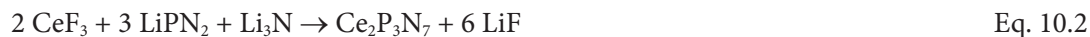
The publications within this cumulative dissertation thesis illustrate the successive progress made in gaining systematic access to rare-earth and transition metal nitridophosphates through high-pressure metathesis. Prior to this work no synthesis route to rare-earth nitridophosphates was known and very few transition metal nitridophosphates were described in literature. The obstacles to overcome included the development of a new synthesis route, devising alternative starting materials, as rare-earth and transition metal nitrides and azides were not suitable, and the elimination of N₂ during synthesis, which especially for open-shell transition metal nitridophosphates is favoured due to formation of stable metal phosphides. The here introduced high-pressure metathesis route employs readily available starting materials; in the simplest case (cf. Chapter 2), a metal halide, which is reacted with LiPN₂ under high-pressure conditions achieved with large volume presses and the multianvil technique. One advantage of the metathesis route is the thermodynamic driving force generated through co-formation of a stable lithium halide, which propels the nitridophosphate formation. Moreover, flux properties are ascribed to the lithium halide, supporting the growth of nitridophosphate crystals. Readily available single-crystals greatly speed up the process of materials characterization, from identifying the components of a multi-phase reaction product, to elucidating their crystal structures and to the preparation of phase-pure samples that can be used for determining the physical properties of interest.

The systematic access to rare-earth and transition metal nitridophosphates was achieved by a step-wise expansion of the high-pressure metathesis route. The fundamental reaction pathway starts from salt metathesis between rare-earth halides and LiPN₂ as presented in Chapter 2, e.g. Eq. 10.1.



By addition of Li₃N to the starting materials, lower-condensed networks were created such as the layered RE₂P₃N₇ polymorphs (Chapter 3) and Ho₃[PN₄]O featuring non-condensed tetrahedra

(Chapter 4), e.g. Eq. 10.2.



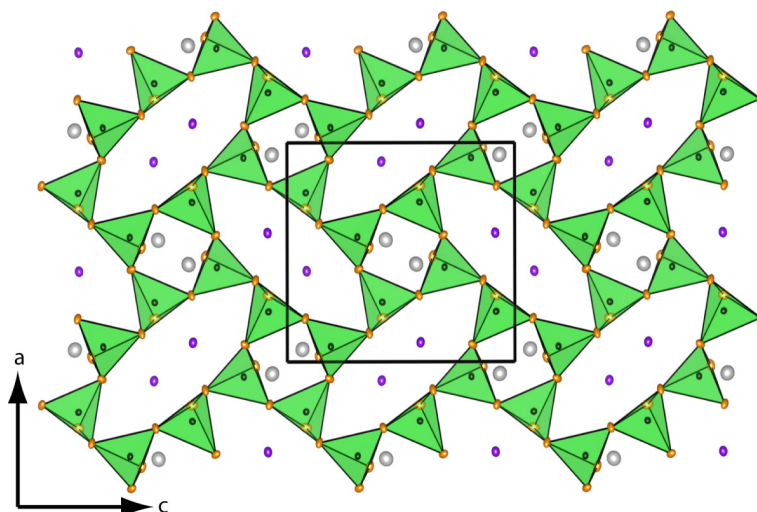
In Chapter 5, the highly-condensed framework structure of $\text{Ce}_4\text{Li}_3\text{P}_{18}\text{N}_{35}$ with $\kappa > 1/2$ was realized through addition of P_3N_5 to the reaction. $\text{LiPr}_2\text{P}_4\text{N}_7\text{O}_3$ in Chapter 6 highlights the possible proliferation of structural variation in nitridophosphates if O is incorporated into the tetrahedra network. The addition of Li_2O to the starting materials resulted in the formation of a layered structure with $\kappa = 2/5$, whose topology has not yet been realized with solely nitride anion.

The focus of research in Chapters 7 to 9 is switched to the preparation of transition metal nitridophosphates by high-pressure metathesis. The oxonitridophosphates $\text{Hf}_{9-x}\text{P}_{24}\text{N}_{52-4x}\text{O}_{4x}$ and $M_{1-x}\text{PO}_{3+4x}\text{N}_{1-4x}$ with $M = \text{Zr}, \text{Hf}$ are the first examples of oxonitridophosphate frameworks incorporating tetravalent metals. The $M\text{P}_8\text{N}_{14}$ phases with $M = \text{Fe}, \text{Co}, \text{Ni}$ of Chapter 9 exemplify the disposition of nitridophosphates toward N_2 elimination, as the formation of transition metal phosphides could only be suppressed at pressures of 9 GPa. The successful synthesis of nitridophosphates with open-shell transition metals allowed a detailed study of the electronic properties of nitride ions and P–N bonds. Using the d-electron energies of the transition metals as local probes the nitride ligands could be placed in the nephelauxetic series, as slightly more covalent than comparable oxo ligands. This was the first time that the ligand field strength of nitride ions was experimentally investigated on typical solid state compounds.

Rare-Earth-Metal Nitridophosphates through High-Pressure Metathesis

published in: S. D. Klotz, W. Schnick, *Angew. Chem., Int. Ed.* 2015, 54, 11250–11253
DOI: 10.1002/anie.201504844

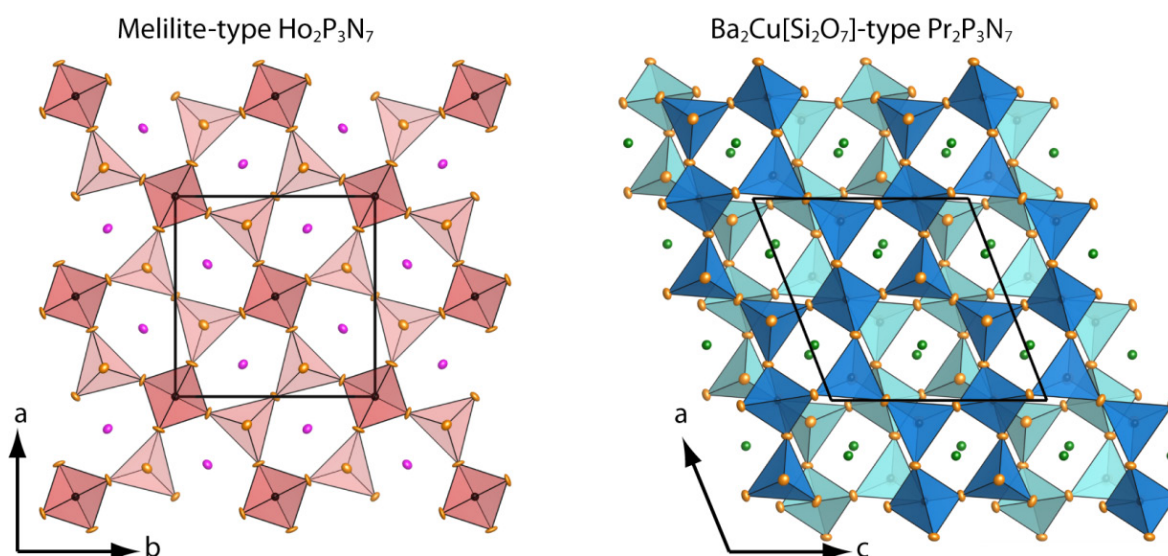
published in: S. D. Klotz, W. Schnick, *Angew. Chem.* 2015, 127, 11402–11405.
DOI: 10.1002/ange.201504844



The first rare-earth nitridophosphate, LiNdP_4N_8 , was prepared by high-pressure metathesis at 5 GPa and 1300 °C achieved with a large volume press employing the Walker-type multianvil technique. NdF_3 and four equivalents of LiPN_2 served as starting materials. The framework of LiNdP_4N_8 crystallizes in an orthorhombic variant of the monoclinic paracelsian ($\text{BaAl}_2\text{Si}_2\text{O}_8$) structure type (space group $Pnma$, no. 62, $a = 8.7305(17)$, $b = 7.8783(16)$, $c = 9.0881(18)$ Å, $V = 625.1(2)$ Å³, $Z = 4$). The structure was solved and refined from single-crystal X-ray diffraction data and consists of all-side vertex-sharing PN_4 tetrahedra forming a framework with $\kappa = 1/2$. The compound was additionally characterized by FTIR, SEM, and magnetometry (SQUID), the latter revealing that LiNdP_4N_8 is paramagnetic down to the lowest measured temperature of 1.8 K.

High-Pressure Synthesis of Melilite-type Rare-Earth Nitridophosphates $RE_2P_3N_7$ and a $Ba_2Cu[Si_2O_7]$ -type Polymorph

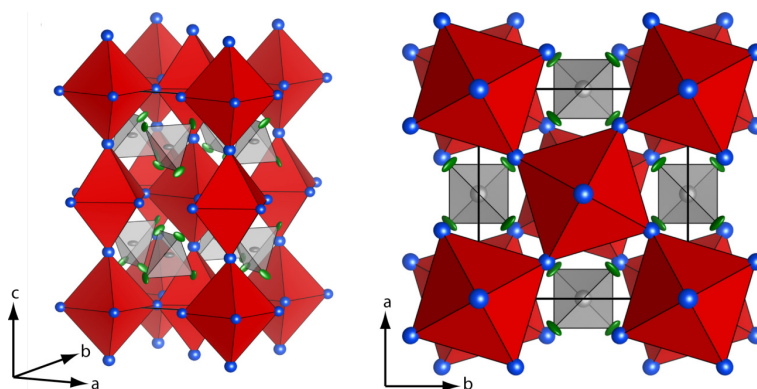
published in: S. D. Klotz, N. Weidmann, R. Niklaus, W. Schnick, *Inorg. Chem.* 2016, 55, 9400–9409.
DOI: 10.1021/acs.inorgchem.6b01611



Two polymorphs with sum formula $RE_2P_3N_7$ are described, one being a homeotype of the melilite-type (e.g. åkermanite $Ca_2Mg[Si_2O_7]$) with $RE = Pr, Nd, Sm, Eu, Ho, Yb$ and one being a homeotype of the $Ba_2Cu[Si_2O_7]$ -type with $RE = La, Ce, Pr$. The compounds were prepared via high-pressure metathesis with reaction conditions ranging from 4 to 5 GPa and from 900 to 1250 °C achieved with a large volume press. Stoichiometric ratios of the rare-earth halides, $LiPN_2$, and Li_3N served as starting materials. The crystal structures were determined from single-crystal and powder X-ray diffraction (SCXRD melilite-type $Ho_2P_3N_7$: space group $P2_1m$, no. 113, $a = 7.3589(2)$, $c = 4.9986(2)$ Å, $V = 270.691(18)$ Å³, $Z = 2$; SCXRD $Ba_2Cu[Si_2O_7]$ -type $Pr_2P_3N_7$: space group $C2/c$, no. 15, $a = 7.8006(3)$, $b = 10.2221(3)$, $c = 7.7798(3)$ Å, $\beta = 111.299(1)^\circ$, $V 577.98(4)$ Å³, $Z = 4$). The structures of both polymorphs consist of Q^3 and Q^4 vertex-sharing PN_4 tetrahedra forming single-layers with $\kappa = 3/7$. While in the melilite-type materials the tetrahedra are interconnected forming five-membered rings, the tetrahedra in the $Ba_2Cu[Si_2O_7]$ -type materials form four- and six-membered rings in a ratio 1:1. The phase relationship of the polymorphs was studied by DFT-calculations, which revealed that the $Ba_2Cu[Si_2O_7]$ -type $Pr_2P_3N_7$ is most likely a high-pressure polymorph of the melilite-type $Pr_2P_3N_7$.

Antiperovskite Nitridophosphate Oxide $\text{Ho}_3[\text{PN}_4]\text{O}$ by High-Pressure Metathesis

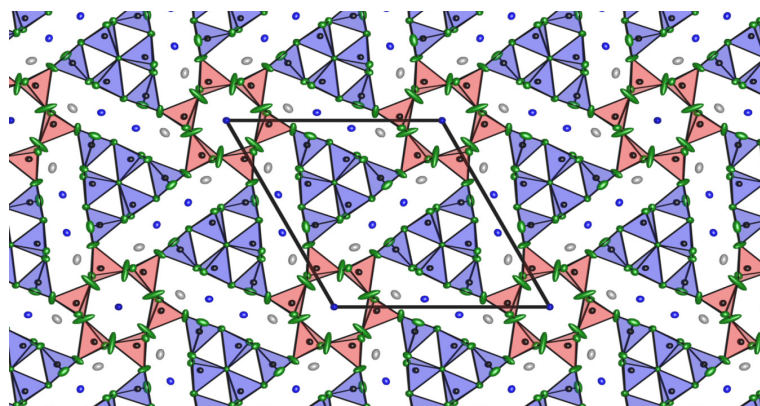
published in: **S. D. Kloß**, N. Weidmann, W. Schnick, *Eur. J. Inorg. Chem.* 2017, 1930–1937.
DOI: 10.1002/ejic.201601425



$\text{Ho}_3[\text{PN}_4]\text{O}$ was prepared by reaction of stoichiometric amounts of HoF_3 , LiPN_2 , Li_3N , and Li_2O at 5 GPa and 1025 °C achieved with a large volume press and the multianvil technique. The structure was refined from powder X-ray diffraction data (space group $I4/mcm$, no. 140, $a = 6.36112(3)$, $c = 10.5571(1)$ Å, $V = 427.181(5)$ Å³, $Z = 4$), and forms a hierarchical variant of an antiperovskite, in which Ho atoms occupy the X, O atoms the B, and non-condensed PN_4 tetrahedra ($\kappa = 1/4$) the A position of the regular ABX_3 perovskite. The compound was further characterized using UV-vis, FTIR, Raman, SEM, and magnetic measurements (VSM), as well as DFT-calculations.

Puzzling Intergrowth in Cerium Nitridophosphate Unraveled by Joint Venture of Aberration-Corrected Scanning Transmission Electron Microscopy and Synchrotron Diffraction

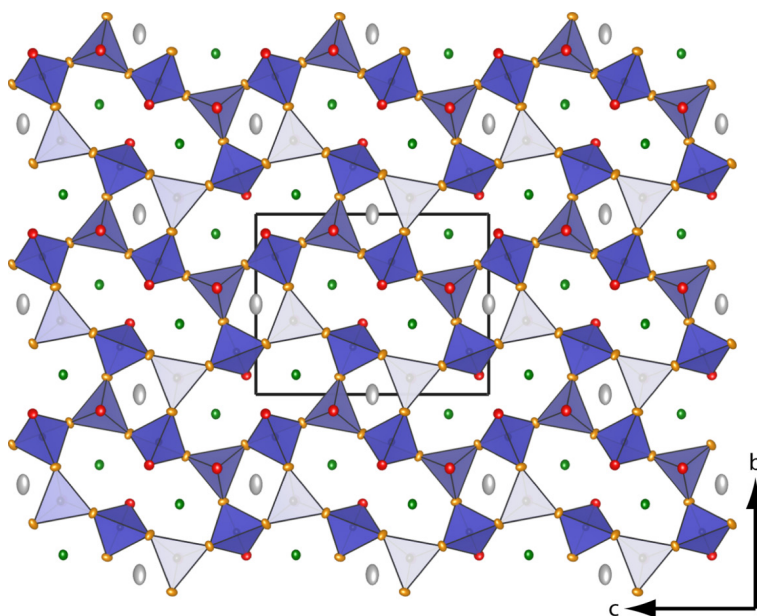
published in: S. D. Kloß, L. Neudert, M. Döblinger, N. Nentwig, O. Oeckler, W. Schnick, *J. Am. Chem. Soc.* 2017, 139, 12724–12735.
DOI: 10.1021/Jacs.7b07075



The nitridophosphate $\text{Ce}_4\text{Li}_3\text{P}_{18}\text{N}_{35}$ was prepared by high-pressure metathesis starting from a 1:4 ratio of CeF_3 and LiPN_2 at 5 GPa and 1300 °C (multi-anvil method). The compound crystallizes in large single-crystals (>100 μm), which feature two structurally slightly different domains. One domain shows an increased O content leading to sum formula $\text{Ce}_{4-0.5x}\text{Li}_3\text{P}_{18}\text{N}_{35-1.5x}\text{O}_{1.5x}$ ($x \approx 0.72$) of the average structure (space group $P6_3/m$, no. 176, $a = 13.9318(1)$, $c = 8.1355(1)$ Å, $1367.51(3)$ Å³, $Z = 2$). It consists of a highly-condensed framework of all-side vertex-sharing PN_4 tetrahedra with $\kappa \approx 0.514$ effectuated by triply-bridging N atoms. The slightly increased O content of domain-type one could be detected in STEM and HRTEM experiments, which also revealed random vacancies on the Ce2 position. In domain-type two a non-significant amount of O was present concomitant with a long-range periodic order of Ce2 atoms, which gives rise to a commensurate $(\sqrt{3} \times \sqrt{3})R30^\circ$ superstructure. The second domain-type was characterized by STEM and HRTEM experiments as well. The very weak superstructure was refined from synchrotron diffraction data by treating average structure and superstructure reflections with individual scale factors. The refinement was once conducted in a supercell, in space group $P6_3$ (no. 173) and once in a modulation of the basic structure in superspace group $P6_3(\alpha, \beta, 0)0(-\alpha-\beta, \alpha, 0)0$. A commensurate superspace group $P6_3(1/3, 1/3, 0)0$ of the commensurate Bravais-class $P6/mmm(1/3, 1/3, 0)$ was also discussed as a viable symmetry. Additional characterization involved FTIR, UV-vis, luminescence, SEM, and magnetic measurements.

LiPr₂P₄N₇O₃: Structural Diversity of Oxonitridophosphates Accessed by High-Pressure Metathesis

published in: S. D. Klotz, W. Schnick, *Inorg. Chem* 2018, 57, 4189–4195.
DOI: 10.1021/acs.inorgchem.8b00455

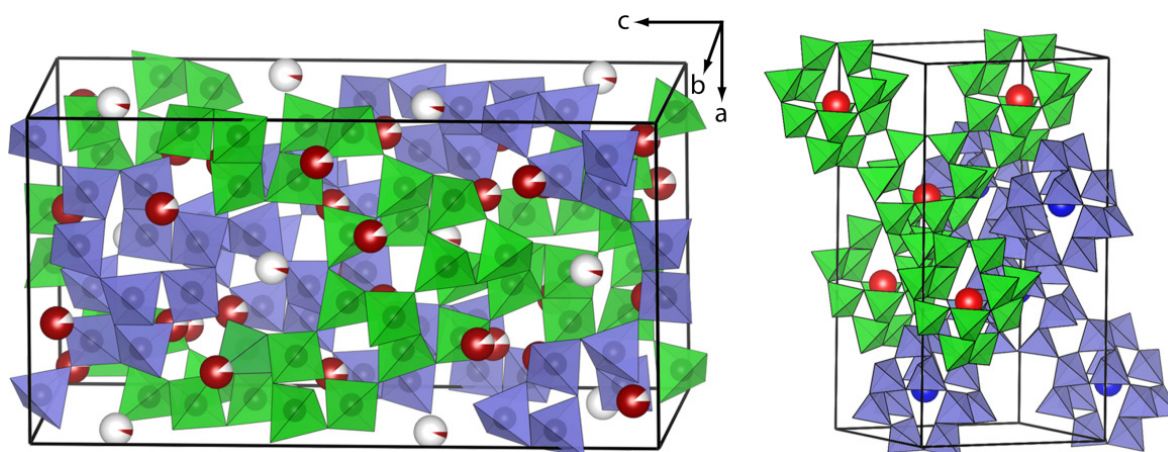


The reaction of stoichiometric amounts of PrF₃, LiPN₂, Li₂O, and PON at pressures of 8 GPa and temperatures of 1200 °C lead to the formation of the oxonitridophosphate LiPr₂P₄N₇O₃. The crystal structure was solved and refined from single-crystal X-ray diffraction data (space group *P2₁/c*, no. 14, $a = 4.927(1)$, $b = 7.848(2)$, $c = 10.122(2)$ Å, $\beta = 91.55(3)^\circ$, $V = 391.3(2)$ Å³, $Z = 2$). The structure consists of Q³ vertex-sharing tetrahedra forming single-layers with $\kappa = 2/5$. The tetrahedra are interconnected to form four- and eight-membered rings, a topology previously observed in the apophyllite group of silicates, e.g. fluorapophyllite Ca₄K(Si₈O₂₀)F(H₂O)₈. Additional characterization involved FTIR, UV-vis, SEM, and temperature-dependent PXRD measurements.

Accessing Tetravalent Transition-Metal Nitridophosphates through High-Pressure Metathesis

published in: S. D. Kloß, S. Wandelt, A. Weis, W. Schnick, *Angew. Chem., Int. Ed.* 2018, 57, 3192-3195
DOI: 10.1002/anie.201712006

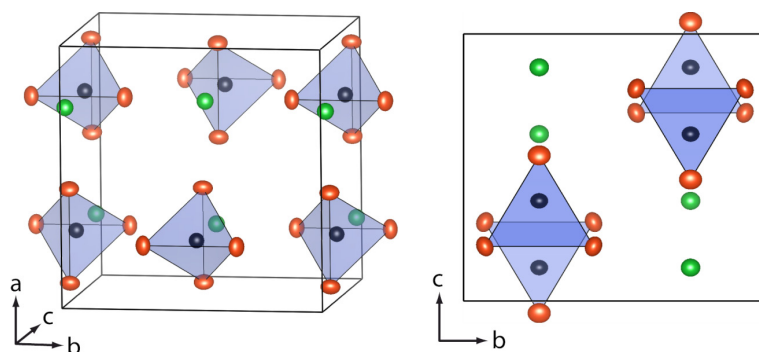
published in: S. D. Kloß, S. Wandelt, A. Weis, W. Schnick, *Angew. Chem.* 2018, 130, 3246-3249.
DOI: 10.1002/ange.201712006



Tetravalent Hf atoms were incorporated into an oxonitridophosphate network by reaction of HfCl_4 , LiPN_2 , and Li_2O at 8 GPa and 1300 °C achieved with the multianvil technique. The crystal structure of $\text{Hf}_{9-x}\text{P}_{24}\text{N}_{52-4x}\text{O}_{4x}$ ($x \approx 1.84$) was solved and refined from single-crystal X-ray diffraction data (space group $I4_1/acd$, no. 142, origin choice 2, $a = 12.466(1)$, $c = 23.719(2)$ Å, $V = 3685.7(9)$ Å³, $Z = 4$). The structure is isotypic to $\text{Ti}_5\text{B}_{12}\text{O}_{26}$ and consists of two interpenetrating networks of Q^3 and Q^4 vertex-sharing tetrahedra. The individual networks enter the topology of heavily decorated diamond-nets. The compound was further characterized by FTIR, UV-vis, ³¹P NMR, magnetometry (PPMS VSM), SEM, and STEM measurements. The magnetic measurements detected diamagnetism of core-electrons, thus corroborating the assumption of tetravalent Hf atoms.

High-Pressure Metathesis of the $M_{1-x}\text{PO}_{3+4x}\text{N}_{1-4x}$ ($x \approx 0.05$) and $M_{0.75}\text{PO}_4$ ($M = \text{Zr, Hf}$) Orthophosphates

published in: **S. D. Klotz**, A. Weis, S. Wandelt, W. Schnick, *Inorg. Chem* 2018, 57, 4164–4170.
DOI: 10.1021/acs.inorgchem.8b00373

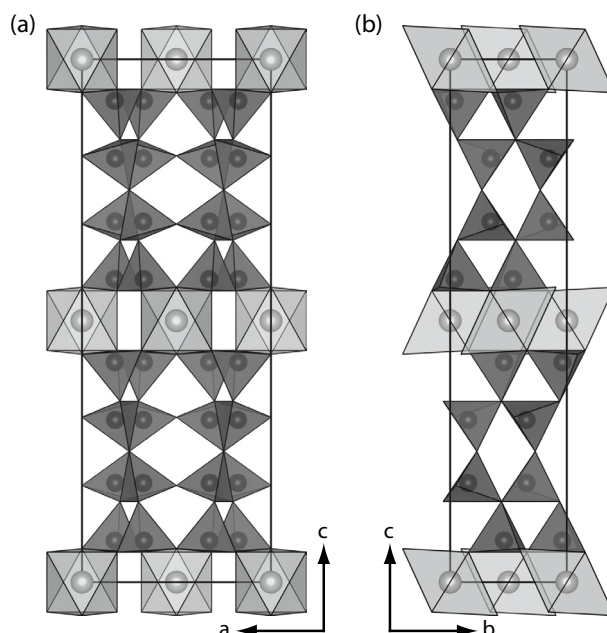


The $M_{1-x}\text{PO}_{3+4x}\text{N}_{1-4x}$ ($x \approx 0.05$) and $M_{0.75}\text{PO}_4$ ($M = \text{Zr, Hf}$) orthophosphates ($\kappa = 1/4$) are defect variants of the ZrSiO_4 and HfSiO_4 structures. They were prepared by metathesis starting from the metal chlorides, PON, and Li_2O in case of the nitride containing compounds, and metal chlorides, P_2O_5 , and Li_2O in case of the oxophosphates. Reactions were carried out at 6 GPa and temperatures between 1100 and 1200 °C, achieved with the multianvil technique. The structures were solved and refined from single-crystal X-ray diffraction data (space group $I4_1/amd$ (no. 141), $Z = 4$; $\text{Zr}_{0.950(6)}\text{PO}_{3.2}\text{N}_{0.8}$: $a = 6.596(1)$, $c = 5.805(1)$ Å, $V = 252.59(9)$ Å³; $\text{Zr}_{0.75}\text{PO}_4$: $a = 6.567(1)$, $c = 5.783(2)$ Å, $V = 249.3(1)$ Å³; $\text{Hf}_{0.947(4)}\text{PO}_{3.2}\text{N}_{0.8}$: $a = 6.6178(12)$, $c = 5.8409(9)$ Å, $V = 255.8(1)$ Å³; $\text{Hf}_{0.75}\text{PO}_4$: $a = 6.5335(7)$, $c = 5.7699(7)$ Å, $V = 246.30(6)$ Å³). Upon heating $M_{0.75}\text{PO}_4$ ($M = \text{Zr, Hf}$) in air, a phase transformation to the $M_{2.25}(\text{PO}_4)_3$ phases that crystallize in the NASICON structure type was observed. This might indicate that the $M_{0.75}\text{PO}_4$ ($M = \text{Zr, Hf}$) structures are high-pressure polymorphs of the NASICON-type. FTIR, UV-vis, and SEM measurements were carried out to further characterize the materials.

Open-shell 3d Transition Metal Nitridophosphates $M^{\text{II}}\text{P}_8\text{N}_{14}$ ($M^{\text{II}} = \text{Fe}, \text{Co}, \text{Ni}$) by High-pressure Metathesis

published in: S. D. Kloß, O. Janka, T. Block, R. Pöttgen, R. Glaum, W. Schnick, *Angew. Chem., Int. Ed.* **2018**, DOI: 10.1002/anie.201809146

published in: S. D. Kloß, O. Janka, T. Block, R. Pöttgen, R. Glaum, W. Schnick, *Angew. Chem.* **2018**, DOI: 10.1002/ange.201809146



The $M^{\text{II}}\text{P}_8\text{N}_{14}$ ($M = \text{Fe}, \text{Co}, \text{Ni}$) compounds were prepared by high-pressure metathesis starting from LiPN_2 , P_3N_5 , and FeCl_2 , CoBr_2 , and NiCl_2 , respectively. The reaction conditions of 9 GPa and 1200 °C were achieved with a 1000t hydraulic press and the multianvil technique. The isotypic structures were solved and refined from powder X-ray diffraction data (space group *Cmce* (no. 64), $Z = 4$, $\text{FeP}_8\text{N}_{14}$: $a = 8.26930(13)$, $b = 5.10147(8)$, $c = 23.0776(4)$ Å, $V = 973.54(3)$ Å³; $\text{CoP}_8\text{N}_{14}$: $a = 8.25183(8)$, $b = 5.10337(5)$, $c = 22.9675(2)$ Å, $V = 967.21(2)$ Å³; $\text{NiP}_8\text{N}_{14}$: $a = 8.23105(9)$, $b = 5.08252(6)$, $c = 22.8516(3)$ Å, $V = 973.54(3)$ Å³). All metal atoms are in oxidation state +II, and Fe and Co are in high-spin states, corroborated by several techniques including magnetometry, UV/Vis/NIR spectroscopy, and Mössbauer spectroscopy. $\text{FeP}_8\text{N}_{14}$ shows an antiferromagnetic ordering at 3.5(1) K. The ligand field properties of nitride ions were determined with UV/Vis/NIR spectra of the Co and Ni compound. Angular overlap modelling led to reliable nephelauxetic ratios, which showed that the metal-nitride bond present in these compounds are slightly more covalent than metal-oxide bonds of comparable compounds.

Chapter 11

Discussion and Outlook

11.1 Advancements in nitridophosphate chemistry

This dissertation laid the foundation for a systematic exploration of rare-earth and transition metal nitridophosphates through the development of the necessary preparative tool, the high-pressure metathesis. Chapters 2 to 6 deal with the establishment of a systematic access of rare-earth nitridophosphates and highlight suitable reaction conditions and starting materials such as LiPN_2 , Li_3N , Li_2O , P_3N_5 , and PON . Chapters 6 to 9 deal with the transfer of the high-pressure metathesis concept to transition metal nitridophosphates and the development of a suitable understanding of the underlying chemistry from which applicable reaction conditions can be deduced. The compounds prepared show the capability of high-pressure metathesis to produce nitridophosphates with unprecedented metal atoms and networks in various degrees of condensation, from non-condensed tetrahedra to highly-condensed framework. The overview on elements with which nitridophosphates can be formed The periodic system of elements depicted in Figure 1.1, which highlights all elements that were stabilized in ternary nitridophosphates, can thus be updated, showing that the compositional diversity of nitridophosphates has been greatly improved.

Next to the structural advancements, high-pressure metathesis opened the possibility of studying the electronic properties of nitridophosphates. In Chapter 9 the d-electrons of the transition metals incorporated into the nitridophosphate networks are used as local probes. The attenuation of the d-electron energies observed with UV/Vis/NIR spectroscopy allowed deep insights into the ligand field properties of nitride ions and the electronic properties of the P–N bond. It was possible to place the nitride ligands in the nephelauxetic series, as slightly more covalent than comparable oxo ligands, and the first experimental evidence for sp^2 hybridization of nitrogen is presented. Hence, because the access to systems with open-shell configurations is now available with high-pressure metathesis,

an increased effort can be made to investigate them. This might lead to additional unprecedented insights into nitridophosphate chemistry. An outline for the systematic exploration of such systems is given in Chapter 11.3.

Group →	1	2	3	4	5	6	7	8	9	10	11	12	13	14	15	16	17	18	
Period ↓																			
1	1 H																		2 He
2	3 Li	4 Be											5 B	6 C	7 N	8 O	9 F	10 Ne	
3	11 Na	12 Mg											13 Al	14 Si	15 P	16 S	17 Cl	18 Ar	
4	19 K	20 Ca	21 Sc	22 Ti	23 V	24 Cr	25 Mn	26 Fe	27 Co	28 Ni	29 Cu	30 Zn	31 Ga	32 Ge	33 As	34 Se	35 Br	36 Kr	
5	37 Rb	38 Sr	39 Y	40 Zr	41 Nb	42 Mo	43 Tc	44 Ru	45 Rh	46 Pd	47 Ag	48 Cd	49 In	50 Sn	51 Sb	52 Te	53 I	54 Xe	
6	55 Cs	56 Ba		72 Hf	73 Ta	74 W	75 Re	76 Os	77 Ir	78 Pt	79 Au	80 Hg	81 Tl	82 Pb	83 Bi	84 Po	85 At	86 Rn	
7	87 Fr	88 Ra		104 Rf	105 Db	106 Sg	107 Bh	108 Hs	109 Mt	110 Ds	111 Rg	112 Cn	113 Uut	114 Uuq	115 Uup	116 Uuh	117 Uus	118 Uuo	
Lanthanides				57 La	58 Ce	59 Pr	60 Nd	61 Pm	62 Sm	63 Eu	64 Gd	65 Tb	66 Dy	67 Ho	68 Er	69 Tm	70 Yb	71 Lu	
Actinides				89 Ac	90 Th	91 Pa	92 U	93 Np	94 Pu	95 Am	96 Cm	97 Bk	98 Cf	99 Es	100 Fm	101 Md	102 No	103 Lr	

Figure 11.1. Periodic system of elements for nitridophosphates. Elements highlighted in dark-green are ternary compounds presented in this work. Half-filled squares represent multinary compounds presented in this work, or elements for which a systematic access is probably possible, based on the findings within this dissertation.

11.2 Prospects for rare-earth nitridophosphates

The here presented rare-earth nitridophosphates are, despite their diversity, only the tip of the iceberg. A plethora of phases certainly has remained amiss by the crude step width, with which the hypersurface of the global energy landscape has been screened. Even compounds with readily observed degrees of condensation such as 4/7, 6/11, and 1/3 have not yet been discovered. Through deft choice of starting materials and reaction conditions such compounds should be accessible. Moreover, the range of pressures offered by the 1000 t hydraulic press with the multianvil technique ($p_{\max} \approx 25$ GPa) has not been exhausted yet, as the rare-earth (oxo)nitridophosphates of Chapters 2 to 6 were prepared at pressures up to 8 GPa. Increasing the pressure could lead to denser-packed tetrahedra networks and a rich family of high-pressure polymorphs, as was already shown for the $RE_2P_3N_7$ polymorphs (Chapter 3). Phosphorus in coordination number > 4 has yet to be observed for nitridophosphates containing a metal atom, as γ - P_3N_5 , pc-PON, γ - HP_4N_7 , and $TiPO_4$ -V are the only reported cases of P in a five-fold coordination, next to octahedrally coordinated P in a $CaCl_2$ -type high-pressure polymorph of $AlPO_4$.^[1-5]

The compounds presented in this dissertation show that metathesis is a viable synthesis strategy; however, properties like reaction mechanisms and thermodynamics were not studied. Conclusions were drawn based on observation of the reaction outcome, which leaves unanswered questions. Oftentimes, Li seems to be incorporated into rare-earth nitridophosphates when using the high-pressure metathesis route ($LiNdP_4N_8$, $Ce_4Li_3P_{18}N_{35}$, $LiPr_2P_4N_7O_3$). The reason for this phenomenon is not yet elucidated since the control group of prepared compounds is still too small to allow a statistical analysis. The incorporation of Li into rare-earth nitridophosphates might be favoured since it helps to balance the evenly distributed negative charge of the tetrahedra network, which otherwise has to be countered solely by the point charges of coarsely spread trivalent rare-earth ions. The screening of the energy hypersurface will determine whether Li is an important component to the stability of rare-earth nitridophosphates.

The lithium halide, which is formed in situ during the metathesis reaction, seems to be a flux facilitating crystal growth. Large single-crystals are favourable since many applications and measurements of physical properties such as second harmonic generation and (ion)conductivity require single crystalline materials. The fluxing properties are reminiscent of the lithium self-flux mechanism used for

the preparation of several lithium nitridophosphates, in which a surplus of Li_3N favours crystal growth and phase formation.^[6–10] The presence of a lithium salt seems to play a crucial role in the crystallization process. The underlying mechanism, however, is unknown. For ammonium halides, for example, reversible P–N bond cleavage and formation and the increase of the ammonia partial pressures in ampoule synthesis are the suggested principles of operation.^[11,12] Nitride ions have an excellent solubility in molten lithium salts: for example, the portion of Li_3N soluble in a LiCl melt at $650\text{ }^\circ\text{C}$ amounts to 0.15 mol/mol LiCl .^[13] No studies are available regarding the solubility of PN_4^{7-} orthoanions in such melts, nor whether lithium halides might be able to catalyze the P–N bond cleavage and formation. Moreover, the aggregate state of the lithium halides under reaction conditions of several GPa is in question. At 5 GPa LiF melts at temperatures exceeding $1300\text{ }^\circ\text{C}$, conditions which are not fulfilled in all experiments.^[14] However, lower temperatures for melting might be required due to initially small particle sizes of the in situ formed lithium halides. Moreover, the literature melting temperatures apply to pure substances, the dissolution of nitride ions, PN_4^{7-} tetrahedra, or larger fragments of the P/N tetrahedra framework would lead to a decrease in the melting point, as dictated by thermodynamics. Hence, monitoring the metathesis reaction with in situ experiments at a synchrotron beamline might shed light onto the reaction mechanism. Such experiments would also yield the ignition temperature of the metathesis and the timeline of phase formation under real reaction conditions. An interesting issue to examine is the aggregation state and therefore mobility of the lithium salt that ultimately determines the role of the lithium halide in the metathesis.

11.3 Prospects for transition metal nitridophosphates

Three Chapters (7 to 9) of this dissertation are concerned with the high-pressure metathesis of transition metal nitridophosphates, a first glimpse at a vast family of materials. A new synthetic access to such systems naturally raise uncountable intriguing questions and with an immense potential for investigations. With limited resources, equipment, time, and personnel, the next steps have to be carefully planned. The first course of action should still be advancing the high-pressure metathesis route, gaining experience with reaction conditions and starting materials, towards the consequential establishment of a systematic access. Unlike rare-earth metals, the transition metals are expected to feature a different chemistry based on their position in the periodic system. Early transition metals like Group 4 feature a more ionic bonding with N than the late transition metals like Fe, Co, and Ni.^[15] Effectively, each transition metal has to be treated individually. This impacts reaction conditions, as was shown by the different synthesis strategies for the Group 4 nitridophosphates (Chapter 7 and 8) and the MP_8N_{14} phases (Chapter 9). But, despite the complexity of transition metal chemistry, the results presented in this dissertation should give a reasonable starting point for the continued exploration.

Based on the published transition metal nitridophosphates (c.f. Table A.1), the hitherto disregarded 3d transition metals, Sc, Ti, V, and Cr might also be incorporated into a nitridophosphate network by high-pressure metathesis.^[16] Moreover, due to the great stability of the metal nitrides in Group 5, metathesis might also be feasible with Ta and Nb. Stabilizing Ta^{5+} in nitridophosphates is a worthwhile challenge as Ta^{5+} in Ta_3N_5 is the highest oxidation state of a metal achieved with nitride ions.^[15] Moreover early transition metal nitridophosphates might feature rich structural chemistry similar to the rare-earth and the alkaline earth compounds due to their rather ionic $M-N$ bond. Chapter 7 and 8 already present Zr^{4+} and Hf^{4+} stabilized in compounds with a framework structure and a structure of non-condensed tetrahedra.

The preparation of low-condensed open-shell 3d transition metal compounds might pose a greater challenge because the necessary increase in N content might favour N_2 elimination. Adjusting the pressure at which the reaction is carried out certainly plays a crucial role for the synthesis of these compounds. N_2 elimination might also be prevented by conducting a similar ion-exchange reaction as was used for the preparation of transition metal nitridosilicate FeP_8N_{14} .^[17,18] Transition metal ni-

tridosilicates face similar preparative challenges as nitridophosphates: beyond a certain threshold temperature a redox reaction occurs, in which N_2 is eliminated and the transition metal is reduced to M^0 with Si_3N_4 as byproduct.^[19] As this decomposition occurs prior to the formation of the targeted nitridosilicate phases, the usual high-temperature routes employing a high-frequency furnace are not feasible. When α - $Ca_2Si_5N_8$ is exposed to a stoichiometric surplus of molten $FeCl_2$ an ion-exchange of Ca and Fe towards $Fe_2Si_5N_8$ occurs well below the decomposition temperature of the Si/N network.^[18] Relatively low temperatures are required for the ion-exchange since the preformed nitridosilicate network is retained and no Si/N bond breaking and formation takes place. Due to the two properties, exchange of ion A with ion B and framework preservation, the ion-exchange reaction can be regarded as a specialized form of a metathesis. In the light of explorative chemistry, the ion-exchange was certainly not created for exploring new structure types; however, its purpose is to access thermodynamically less stable phases through a kinetically controlled reaction. Therefore, if the expansion of the high-pressure metathesis to the specialized ion-exchange proves to be feasible, such kinetically controlled reaction products can greatly enrich the structural and compositional portfolio of nitridophosphates. A drawback of the ion-exchange reaction is that a proof of concept was yet only shown for the $M_2Si_5N_8$ framework.^[17,18] Thus, suitable nitridophosphates systems have to be established and investigated whether the ion-exchange also works with less-condensed networks. Due to the lower thermal stability of nitridophosphates in comparison to nitridosilicates, ambient pressure reactions might still not be practicable so that the ion-exchange has to be conducted under high-pressure conditions.

After obtaining a sufficient understanding of the chemistry of transition metal nitridophosphates, an active search for functional materials can follow. In a sustainable energy infrastructure based on renewable energies, batteries play a crucial role in energy storage. Hence enormous amounts of resources are spent for the development of more efficient components and materials, such as high-performance ion-conductors. As nitridophosphates are chemically similar to oxophosphates, so should be their properties. Hence transition metal nitridophosphates might harbour intriguing materials for model systems.

The $M_{1-x}PO_{3+4x}N_{1-4x}$ ($x \approx 0.05$) and $M_{0.75}PO_4$ ($M = Zr, Hf$) phases presented in Chapter 8 crystallize in a high-pressure polymorph of $Zr_{2.25}P_3O_{12}$, a structure related to the NASICON materials (Na_{1-x}

$x\text{Zr}_2\text{P}_{3-x}\text{Si}_x\text{O}_{12}$ ($0 \leq x \leq 3$). The NASICON materials feature high-ion conductivities and have been discussed for application in Na-ion batteries and for nuclear waste immobilization.^[20–23] By addition of alkali metals, e.g. Na, to Group 4 oxonitridophosphates one arrives at a multinary phase system Na–M–P–N–O ($M = \text{Zr, Hf}$) that could feature potential ion-conductors.

Similarly, there is an ongoing search for ion-conductors for Li-ion accumulators. Solid-state ion-conductors are favourable since they circumvent the use of toxic and inflammable organic solvents and they are impenetrable by dendrites that form when using lithium metal as cathode. LiFePO_4 is already in use as such a solid-state lithium ion-conductor because it has high lithium bulk mobility, which allows fast charge and discharge rates.^[24] To increase the conductivity of LiFePO_4 , iron and phosphorus deficiencies were introduced in the material. In the Li–Fe–P–N system a similar material could be devised, for example a $\text{Li}_x\text{Fe}_{y-0.5x}\text{PN}_4$ with $0 \leq x \leq 7$ and $0 \leq y \leq 3.5$. Such a material is expected to be structurally similar to LiFePO_4 , would also consist mainly of earth-abundant elements, but feature more degrees of compositional variation. Because of the higher formal charge of N, more Li can be incorporated into such a material, easily fathomable when comparing Li_7PN_4 to Li_3PO_4 . Additionally, the atomic ratio Li to Fe could be adjusted and, by introduction of O into the structure, cation vacancies could be achieved, which might be favourable for the ion-conductivity as in LiFePO_4 .

11.4 Concluding remarks

The establishment of a new synthesis route paving the way to such extensive and unexplored materials families naturally raises far more questions than can be answered in this already prolonged eleven chapter discourse. Luckily, the raising of questions is the fuel of scientific research. Every examination and experiment is based on previous unanswered questions, and they should thus be regarded as a facet of progress. The aim of this dissertation was to lay the foundation and set the direction for the future exploration of nitridophosphates, while giving enough substance to fuel this research for the years to come. The sections in this last chapter give but a brief overview over all the prospects of high-pressure metathesis, sufficient for initial orientation for successors, as the routes to choose from are manifold. Not all could be covered, such as revisiting Group 1 and Group 2 nitridophosphates with the high-pressure metathesis. However, time, creativity, and serendipity will determine to what end the tools presented here will be used.

11.5 References

- [1] K. Landskron, H. Huppertz, J. Senker, W. Schnick, *Angew. Chem., Int. Ed.* **2001**, *40*, 2643–2645; *Angew. Chem.* **2001**, *113*, 2713–2716.
- [2] S. Vogel, D. Baumann, R. Niklaus, E. Bykova, M. Bykov, N. Dubrovinskaia, L. Dubrovinsky, W. Schnick, *Angew. Chem., Int. Ed.* **2018**, *57*, 6691–6695; *Angew. Chem.* **2018**, *130*, 6801–6805.
- [3] D. Baumann, W. Schnick, *Angew. Chem., Int. Ed.* **2014**, *53*, 14490–14493; *Angew. Chem.* **2014**, *126*, 14718–14721.
- [4] M. Bykov, E. Bykova, M. Hanfland, H.-P. Liermann, R. K. Kremer, R. Glaum, L. Dubrovinsky, S. van Smaalen, *Angew. Chem., Int. Ed.* **2016**, *55*, 15053–15057; *Angew. Chem.* **2016**, *128*, 15277–150281.
- [5] J. Pellicer-Porres, A. M. Saitta, A. Polian, J. P. Itié, M. Hanfland, *Nat. Mater.* **2007**, *6*, 698–702.
- [6] E.-M. Bertschler, C. Dietrich, T. Leichtweiß, J. Janek, W. Schnick, *Chem. - Eur. J.* **2018**, *24*, 196–205.
- [7] E. M. Bertschler, T. Bräuniger, C. Dietrich, J. Janek, W. Schnick, *Angew. Chem., Int. Ed.* **2017**, *56*, 4806–4809; *Angew. Chem.* **2017**, *129*, 4884–4887.
- [8] E.-M. Bertschler, R. Niklaus, W. Schnick, *Chem. - Eur. J.* **2017**, *23*, 9592–9599.
- [9] E. M. Bertschler, C. Dietrich, J. Janek, W. Schnick, *Chem. - Eur. J.* **2017**, *23*, 2185–2191.
- [10] E.-M. Bertschler, R. Niklaus, W. Schnick, *Chem. - Eur. J.* **2018**, *24*, 736–742.
- [11] A. Marchuk, F. J. Pucher, F. W. Karau, W. Schnick, *Angew. Chem., Int. Ed.* **2014**, *53*, 2469–2472; *Angew. Chem.* **2014**, *126*, 2501–2504.
- [12] S. J. Sedlmaier, E. Mugnaioli, O. Oeckler, U. Kolb, W. Schnick, *Chem. - Eur. J.* **2011**, *17*, 11258–11265.
- [13] W. Sundermeyer, *Angew. Chem., Int. Ed. Engl.* **1965**, *4*, 222–238; *Angew. Chem.* **1965**, *77*, 241–258.
- [14] I. Jackson, *Phys. Earth Planet. Inter.* **1977**, *14*, 86–94.
- [15] R. Dronskowski, S. Kikkawa, A. Stein, *Handbook of Solid State Chemistry*, WILEY-VCH, Weinheim, Germany, **2017**.
- [16] N. Stock, J. Lücke, M. Volkmann, M. Jansen, W. Schnick, *Z. Anorg. Allg. Chem.* **1995**, *621*, 987–992.

- [17] P. Bielec, W. Schnick, *Angew. Chem., Int. Ed.* **2017**, *56*, 4810–4813; *Angew. Chem.* **2017**, *129*, 4888–4891.
- [18] P. Bielec, O. Janka, T. Block, R. Pöttgen, W. Schnick, *Angew. Chem., Int. Ed.* **2018**, *57*, 2409–2412; *Angew. Chem.* **2018**, *130*, 2433–2436.
- [19] H. Huppertz, N. Stock, W. Schnick, *Adv. Mater.* **1996**, *8*, 844–847.
- [20] B. E. Scheetz, D. K. Agrawal, E. Breval, R. Roy, *Waste Manage.* **1994**, *14*, 489–505.
- [21] J. Alamo, R. Rustum, *J. Am. Ceram. Soc.* **1984**, *67*, 80–82.
- [22] N. Anantharamulu, K. Koteswara Rao, G. Rambabu, B. Vijaya Kumar, V. Radha, M. Vithal, *J. Mater. Sci.* **2011**, *46*, 2821–2837.
- [23] O. Paschos, J. Kunze, U. Stimming, F. Maglia, *J. Phys. Condens. Matter* **2011**, *23*, 234110.
- [24] B. Kang, G. Ceder, *Nature* **2009**, *458*, 190–193.

Appendix A. Supporting Information for Chapter 1

A.1 List of published (oxo)nitridophosphates

Table A.1. The table contains (oxo)nitridophosphates sorted by number of constituent elements and affiliation to either Group/section of the periodic system of elements. Sodalites and oxygen-rich compounds are listed individually. Within each group the compounds are listed in order of increasing atomic number. The table lists degree of condensation (κ), synthesis method (AP, MP, and HP stand for ambient, medium and high pressure, respectively), synthesis route including starting materials, structure-type, type of network (NW stands for network), special building blocks, and year of publication. Degrees of condensation for double nitrides are given for P and for P+M in parenthesis. NC stands for non-condensed.

Sum formula	κ	Synthesis method	Synthesis route	Structure type	Type of network	Special building blocks	Year	Citation
Binary/								
Quasi-binary								
α -P ₃ N ₅	3/5	AP: Ampoule	Condensation of [P(NH ₂) ₄]	α -P ₃ N ₅	Framework	Edge-sharing tetrahedra	1997	[1]
γ -P ₃ N ₅	3/5	HP: Multianvil	Transformation of α -P ₃ N ₅	γ -P ₃ N ₅	Framework	Edge-sharing square pyramids	2001	[2]
P ₄ N ₆ O	4/7	AP: Gas flow	Ammonolysis of PON	P ₄ N ₆ O	Framework	Edge-sharing tetrahedra	1995	[3]
<i>cri</i> -PON	1/2	AP: Gas flow	Crystallization of α -PON	β -Cristobalite	Framework	-	1989	[4]
<i>coe</i> -PON	1/2	HP: Multianvil	Transformation of <i>cri</i> -PON	Coesite	Framework	-	2015	[5]
<i>mog</i> -PON	1/2	HP: Belt	Transformation of <i>cri</i> -PON	Moganite	Framework	-	1999	[6]
δ -PON	1/2	HP: Multianvil	Condensation of H-P-O-N	δ -PON	Framework	-	2012	[7]
α -quartz PON	1/2	HP: Belt	Transformation of <i>cri</i> -PON	α -quartz	Framework	-	1999	[8]
<i>pc</i> -PON	1/2	HP: Multianvil	Transformation of <i>cri</i> -PON	<i>pc</i> -PON	Framework	Edge-sharing square pyramids	2018	[9]
<i>o</i> -PON*	1/2	HP: Diamond anvil	Transformation of <i>cri</i> -PON	CaCl ₂ *	Framework	Edge-sharing octahedra	2018	[9]
SiPN ₃	2/3	AP: Gas flow MP: Crystallization	Condensation of SiPN(NH)(NH ₂) ₄	Sinoite Si ₂ N ₂ O	Framework	Triply-bridging N	1993	[10]
BP ₃ N ₆	2/3	HP: Multianvil	Azide route [(PNC _{1/2}) ₃ , NH ₄ N ₃ , BN]	BP ₃ N ₆	Framework	Edge-sharing tetrahedra	2018	[11]
Ternary								
Group 1								
α -HPN ₂	1/2	MP: Ampoule	Ammonolysis of P ₃ N ₅	β -Cristobalite	Framework	-	1992	[12]
β -HPN ₂	1/2	HP: Multianvil	Transformation of amorphous HPN ₂	β -HPN ₂	Framework	-	2014	[13]

α -HP ₄ N ₇	4/7	MP: Ampoule	Decomposition of (NH ₃) ₂ P(S)	α -HP ₄ N ₇	Framework	Edge-sharing tetrahedra	1997	[14]
β -HP ₄ N ₇	4/7	HP: Multianvil	NP(NH ₃) ₃	β -HP ₄ N ₇	Framework	Triply-bridging N	2014	[15]
γ -HP ₄ N ₇	4/7	HP: Multianvil	P ₃ N ₅ /NH ₄ Cl	γ -HP ₄ N ₇	Framework	Edge-sharing trigonal-bipyramids	2014	[16]
LiPN ₂	1/2	AP: Ampoule	P ₃ N ₅ /NH ₄ Cl	Filled b-Cristobalite	Framework	-	1990	[17]
α -Li ₁₀ P ₄ N ₁₀	2/5	AP: Ampoule	P ₃ N ₅ /Li ₃ N	α -Li ₁₀ P ₄ N ₁₀	NC complex ions	[P ₄ N ₁₀] ¹⁰⁻ adamantane-cages	1991	[18]
β -Li ₁₀ P ₄ N ₁₀	2/5	AP: Ampoule	Self-flux LiPN ₂ /Li ₃ PN ₄	β -Li ₁₀ P ₄ N ₁₀	NC complex ions	Adamantane-cages	2018	[19]
Li ₃ P ₂ N ₅	2/5	HP: Multianvil	Transformation of β -Li ₁₀ P ₄ N ₁₀	Li ₃ P ₂ N ₅	Layer	Corrugated honeycomb layers	2018	[20]
Li ₁₈ P ₆ N ₁₆	3/8	HP: Multianvil	Self-flux P ₃ N ₅ /Li ₃ N	Li ₁₈ P ₆ N ₁₆	NC complex ions	[P ₆ N ₁₆] ¹⁸⁻ anion	2017	[21]
Li ₁₂ P ₃ N ₉	1/3	AP: Ampoule	Self-flux P ₃ N ₅ /Li ₃ N	Li ₁₂ P ₃ N ₉	NC complex ions	[P ₃ N ₉] ¹²⁻ anion	2017	[22]
Li ₄ PN ₃	1/3	HP: Multianvil	Transformation of Li ₁₂ P ₃ N ₉	Li ₄ PN ₃	Chain	-	2017	[22]
Li ₂ PN ₄	1/4	AP: Ampoule	P ₃ N ₅ /Li ₃ N	Li ₂ PN ₄	NC tetrahedra	-	1990	[23]
NaP ₄ N ₇	4/7	HP: Belt	Azide route (P ₃ N ₅)	CaAl ₂ O ₇	Framework	Triply-bridging N	1999	[24]
Na ₃ P ₆ N ₁₁	6/11	?	?	Na ₃ P ₆ N ₁₁	Framework	Triply-bridging N	1990	[25]
NaPN ₂	1/2	HP: Multianvil	Azide route (P ₃ N ₅)	Filled β -Cristobalite	Framework	-	2001	[26]
KP ₄ N ₇	4/7	HP: Belt	Azide route (P ₃ N ₅)	Barylite BaBe ₂ Si ₂ O ₇	Framework	Triply-bridging N	1999	[24]
K ₃ P ₆ N ₁₁	6/11	MP: Ammonothermal	P ₃ N ₅ /KNH ₂	K ₃ P ₆ N ₁₁ (FW of Na ₃ P ₆ N ₁₁)	Framework	Triply-bridging N	1997	[27]
RbP ₄ N ₇	4/7	HP: Belt	Azide route (P ₃ N ₅)	Barylite BaBe ₂ Si ₂ O ₇	Framework	Triply-bridging N	1999	[24]
Rb ₃ P ₆ N ₁₁	6/11	HP: Multianvil	Azide route (P ₃ N ₅)	K ₃ P ₆ N ₁₁	Framework	Triply-bridging N	2001	[28]
CsP ₄ N ₇	4/7	HP: Belt	Azide route (P ₃ N ₅)	Barylite BaBe ₂ Si ₂ O ₇	Framework	Triply-bridging N	1999	[24]
Cs ₃ P ₆ N ₁₁	6/11	HP: Multianvil	Azide route (P ₃ N ₅)	K ₃ P ₆ N ₁₁	Framework	Triply-bridging N	2001	[28]
P ₄ N ₄ (NH ₄)(NH ₃)	1/2	HP: Multianvil	Azide route (P ₃ N ₅)	P ₄ N ₄ (NH ₄)(NH ₃)	Framework	Porous cages	2006	[29]
Group 2								
BeP ₂ N ₄	1/2 (3/4)	HP: Multianvil	Nitride route (P ₃ N ₅)	Phenakite	Framework	-	2010	[30]
Mg ₂ PN ₃	1/3 (1/1)	AP: Ampoule	Nitride route (P ₃ N ₅)	Wurtzite (SS)	Chain (Framework)	Chains of [PN ₃] ⁴⁻	1997	[31]
CaP ₂ N ₄	1/2	HP: Multianvil	Azide route (P ₃ N ₅)	Megakalsilite KAISO ₄ (SS)	Framework	-	2015	[32]
Ca ₂ PN ₃	1/3 (1/1)	AP: Ampoule	Nitride route (P ₃ N ₅)	Wurtzite (SS)	Chain (Framework)	Chains of [PN ₃] ⁴⁻	1997	[31]
SrP ₂ N ₄	1/2	HP: Multianvil	Azide route (P ₃ N ₅)	Megakalsilite KAISO ₄ (SS)	Framework	-	2007	[33]
SrP ₈ N ₁₄	4/7	HP: Multianvil	Azide route (P ₃ N ₅)	SrP ₈ N ₁₄	Layers	Triply-bridging N	2018	[34]
BaP ₂ N ₄	1/2	HP: Multianvil	Azide route (P ₃ N ₅)	HP-CaB ₂ O ₄	Framework	-	2005	[35]

Transition metals									
MnP ₂ N ₄	1/2	HP: Multianvil	Mn/HPN ₂	Megakalsilite KAISiO ₄ (SS)	Framework	-	2016	[36]	
MP ₈ N ₁₄ (M = Fe, Co, Ni)	4/7	HP: Multianvil	Metathesis	FeP ₈ N ₁₄	Layer	Triply-bridging N	2018	[37]	
CuPN ₂	1/2	HP: Multianvil	Nitride route (P ₃ N ₅)	Filled β-Cristobalite	Framework	-	2015	[38]	
Zn ₂ PN ₃	1/3 (1/1)	HP: Multianvil	Nitride route (P ₃ N ₅)	Wurtzite (SS)	Chain (Framework)	Chains of [PN ₃] ⁴⁻	2011	[39]	
CdP ₂ N ₄	1/2	HP: Multianvil	Azide route (P ₃ N ₅)	Megakalsilite KAISiO ₄ (SS)	Framework	-	2016	[36]	
Rare-earth									
bex-RE ₂ P ₃ N ₇ (RE = La, Ce, Pr)	3/7	HP: Multianvil	Metathesis	α-Ba ₂ Cu ₂ [Si ₅ O ₇]	Layer	-	2016	[40]	
mcm-RE ₂ P ₃ N ₇ (RE = Pr, Nd, Sm, Eu, Ho, Yb)	3/7	HP: Multianvil	Metathesis	Mellite Ca ₂ MgSi ₂ O ₇	Layer	-	2016	[40]	
Quaternary									
Group 1									
H ₃ P ₈ O ₈ N ₉	8/17	HP: Multianvil	Condensation of amorphous PON	H ₃ P ₈ O ₈ N ₉	Framework	-	2012	[41]	
Li ₁₇ B ₃ P ₁₄ N ₄₂	17/42	HP: Multianvil	Self-flux LiPN ₂ /Li ₇ PN ₇ /BN	Li ₁₇ B ₃ P ₁₄ N ₄₂	NC complex ions	[B ₃ P ₃ N ₁₃] ¹⁵⁻ anion	2017	[42]	
Li ₁₃ P ₄ N ₁₀ X ₃ (X = Cl, Br)	2/5	AP: Ampoule	Self-flux P ₃ N ₅ /Li ₃ N/LiX	Li ₁₃ P ₄ N ₁₀ Cl ₃	NC complex ions	Adamantane-cages	2018	[19]	
Li ₂ [PO ₂ N]	1/3	AP: Ampoule	Li ₂ O/P ₂ O ₅ /P ₃ N ₅	Li ₂ [PO ₂ N]	Chain	-	2013	[43]	
Li _{2,881} PO _{3,73} N _{0,14}]	1/4	AP: Inert gas flow	Li ₃ N + LiPO ₃	γ-Li ₃ PO ₄	NC tetrahedra	-	1995	[44]	
Li ₁₄ [PON ₃] ₂ O	1/4	MP: Ampoule	PO(NH ₂) ₃ + LiNH ₂	Li ₁₄ Cr ₂ N ₆ O	NC tetrahedra	-	2015	[45]	
Na ₁₀ (P ₄ (NH) ₈ N ₄)(NH ₂) ₆ (NH ₃) _{0,5}	2/5	MP: Autoclave	P ₃ N ₅ /NaNH ₂	Na ₁₀ (P ₄ (H) ₆ N ₄)(NH ₂) ₆ (NH ₃) _{0,5}	NC complex ions	Adamantane-cages	1994	[46]	
Rb ₈ (P ₄ N ₆ (NH) ₂)(NH ₂) ₂	2/5	MP: Autoclave	P ₃ N ₅ /RbNH ₂	Rb ₈ (P ₄ N ₆ (NH) ₂)(NH ₂) ₂	NC complex ions	Adamantane-cages	1995	[47]	
Cs ₅ [P(NH) ₄](NH ₂) ₂	1/4	MP: Autoclave	P ₃ N ₅ /CsNH ₂	Cs ₅ [P(NH) ₄](NH ₂) ₂	NC tetrahedra	-	1994	[48]	
Group 2									
Mg ₄ P ₈ N ₁₂ (M = Mg, Ca)	1/2	HP: Multianvil	Nitride route (HPN ₂ , P ₃ N ₅)	Mg ₄ P ₈ N ₁₂	Layer	-	2015	[49]	
MPO ₃ N (M = Ca, Sr)	1/4	HP: Multianvil AP: Ampoule	MO/amorphous PON	β-K ₂ SO ₄	NC tetrahedra	-	2016	[50]	
SrH ₄ P ₈ N ₁₂	1/2	HP: Multianvil	Azide route (HPN ₂ , P ₃ N ₅)	SrH ₄ P ₈ N ₁₂	Layer	-	2018	[34]	
SrP ₃ N ₃ NH	1/2	HP: Multianvil	Azide route (P ₃ N ₅ , NH ₄ Cl)	SrP ₃ N ₃ NH	Framework	-	2018	[51]	

$\text{SrP}_3\text{N}_5\text{O}$	1/2	MP: Ampoule	Condensation of $\text{SrS}/\text{OP}(\text{NH}_3)_2/\text{SP}(\text{NH}_3)_2/\text{NH}_4\text{Cl}$	$\text{SrP}_3\text{N}_5\text{O}$	Layer	Triply-bridging N	2011	[52]	
$\text{Sr}_3\text{P}_6\text{O}_6\text{N}_6$	3/7	HP: Multianvil	Azide route (PON)	$\text{Sr}_3\text{P}_6\text{O}_6\text{N}_6$	Layer	-	2009	[53]	
$\text{Ba}_3\text{P}_6\text{O}_6\text{N}_6$	3/7	HP: Multianvil	Azide route (PON)	$\text{Sr}_3\text{P}_6\text{O}_6\text{N}_6$	Layer	-	2012	[54]	
$\text{Ba}_3\text{P}_3\text{N}_{10}\text{X}$ (X = Cl, Br, I)	1/2	HP: Multianvil	Azide route (P_3N_5 , BaX_3)	$\text{Ba}_3\text{P}_3\text{N}_{10}\text{Br}$ (JOZ-zeolite FW)	Framework	-	2015	[55]	
$\text{BaM}_4\text{P}_6\text{N}_6$ (M = Ca, Sr)	1/2	HP: Multianvil	Azide route (P_3N_5)	HP- CaB_2O_4	Framework	-	2006	[56]	
Transition metals									
$\text{M}_{1-x}\text{PO}_{3+4x}\text{N}_{1-4x}$ (M = Zr, Hf)	1/4	HP: Multianvil	Metathesis	ZrSiO_4	NC tetrahedra	-	2018	[57]	
$\text{Hf}_{6-x}\text{P}_{24}\text{N}_{12-4x}\text{O}_{4x}$	6/13	HP: Multianvil	Metathesis	$\text{Ti}_5\text{P}_{12}\text{O}_{26}$	Interpenetrating frameworks	-	2018	[58]	
Rare-earth									
$\text{Ce}_x\text{Li}_3\text{P}_{18}\text{N}_{35}$	18/35	HP: Multianvil	Metathesis	$\text{Ce}_x\text{Li}_3\text{P}_{18}\text{N}_{35}$	Framework	Triply-bridging N	2017	[59]	
LiNdP_4N_6	1/2	HP: Multianvil	Metathesis	Paracelsian $\text{BaSi}_2\text{Al}_2\text{O}_8$	Framework	-	2015	[60]	
$\text{Ho}_3[\text{PN}_4]\text{O}$	1/4	HP: Multianvil	Metathesis	Cs_3CoCl_5	NC tetrahedra	-	2016	[61]	
Multinary									
Group 1									
$\text{Li}_x\text{H}_{12-x}\text{P}_{12}\text{O}_6\text{N}_{24-x}\text{X}_x$ (X = Cl, Br)	1/2	MP: Ampoule	$\text{Li}_2\text{S}/\text{HPN}_3/\text{OP}(\text{NH}_3)_2/\text{LiX}$	NPO Zeolite	Framework	-	2003	[62]	
Group 2									
$\text{MgSrP}_3\text{N}_5\text{O}_2$	3/7	HP: Multianvil	$\text{Mg}_3\text{N}_2/\text{Sr}(\text{N}_3)_2/\text{PON}/\text{P}_3\text{N}_5$	$\text{MgSrP}_3\text{N}_5\text{O}_2$	Framework	-	2014	[63]	
$\text{CaMg}_2\text{P}_6\text{O}_3\text{N}_{10}$	6/13	HP: Multianvil	$\text{Ca}(\text{N}_3)_2/\text{Mg}_3\text{N}_2/\text{P}_3\text{N}_5/\text{PON}$	$\text{Ti}_5\text{B}_{12}\text{O}_{26}$	Interpenetrating frameworks	-	2014	[64]	
$\text{Ba}_1\text{P}_{19}\text{O}_{36}\text{N}_{6+4x}\text{N}_{66-x}\text{Cl}_{8+4x}$	1/2	MP: Ampoule	$\text{BaS}/\text{OP}(\text{NH}_3)_2/\text{SP}(\text{NH}_3)_2/\text{NH}_4\text{Cl}$	NPT Zeolite	Framework	-	2011	[65]	
$\text{Ba}_6\text{P}_{12}\text{N}_{17}\text{O}_9\text{Br}_3$	6/13	MP: Ampoule	$\text{BaBr}_2/\text{OP}(\text{NH}_3)_2/\text{SP}(\text{NH}_3)_2/\text{NH}_4\text{Cl}$	$\text{Ba}_6\text{P}_{12}\text{N}_{17}\text{O}_9\text{Br}_3$	Chain	Triangular columns of $[\text{P}_{12}\text{N}_{17}\text{O}_9]^{9-}$	2012	[66]	
Group 13									
$\text{AlP}_6\text{O}_{36}(\text{NH})_{3-3x}\text{N}_6$	1/2	HP: Multianvil	$\text{Al/O}_2/\text{HPN}_2$	$\text{AlP}_6\text{O}_{36}(\text{NH})_{3-3x}\text{N}_6$	Layer	-	2017	[67]	

Rare-earth LiPr ₂ P ₄ N ₂ O ₃	2/5	HP: Multianvil	Metathesis	LiPr ₂ P ₄ N ₂ O ₃ (NW apophyllite)	Layer	2018	[68]
Sodalites							
Ternary							
Zn ₈ [P ₁₂ N ₂₄]	1/2	AP: Ampoule MP: Ampoule	Nitride route (P ₃ N ₅) Zn + HPN ₂	Sodalite	Framework	1997	[69]
Sn ₈ [P ₁₂ N ₂₄]	1/2	MP: Ampoule	Sn/HPN ₂	Sodalite	Framework	2015	[70]
Chalcogenides							
M ₈ [P ₁₂ N ₂₄ IS ₂] (M = Mg, Fe, Co)	1/2	AP: Gas flow	MS/P ₄ S ₁₀	Sodalite	Framework	1989	[71]
Zn ₈ [P ₁₂ N ₂₄]O ₂	1/2	MP: Ampoule	ZnO/Zn/HPN ₂	Sodalite	Framework	2007	[72]
Zn ₈ [P ₁₂ N ₂₄]X ₂ (X = S, Se, Te)	1/2	MP: Ampoule	ZnX/HPN ₂	Sodalite	Framework	1997	[73]
Cd ₈ [P ₁₂ N ₂₄]S ₂	1/2	AP: Gas flow	CdS/P ₄ S ₁₀	Sodalite	Framework	1988	[74]
Halides							
M _(6+10/2-3) H _{2x} [P ₁₂ N ₂₄]X _y (M = Fe, Co, Ni, Mn; X = Cl, Br, I)	1/2	MP: Ampoule	MCl ₂ /NH ₄ Cl/(PNX) ₂	Sodalite	Framework	1995	[75]
Zn _{7-x} H _{2x} [P ₁₂ N ₂₄]Cl ₂	1/2	MP: Ampoule	P ₃ N ₃ /Zn ₃ N ₂ /NH ₄ Cl	Sodalite	Framework	1994	[76]
Zn ₇ [P ₁₂ N ₂₄]Cl ₂	1/2	MP: Ampoule	ZnCl ₂ /NH ₄ Cl/(PNCl) ₃	Sodalite	Framework	1992	[77]
M _(6-n) H _{10n} [P ₁₂ N ₁₈ O ₆]X ₅ (M = Li, Cu; X = Cl, Br, I)	1/2	MP: Ampoule	LiCl/(NH ₂) ₂ P(O)NP(NH ₂) ₂ /NH ₄ Cl	Sodalite	Framework	1998	[78]
Oxygen-rich							
M ₃ M ^{III} P ₃ O ₅ N (M ^I = Na, K, (Na, K); M ^{III} = Al, Ga, In, Tl, V, Cr, Mn, Fe, (Al, Cr), (Al, V))	3/10	AP/MP: Various	Various	M ₃ M ^{III} P ₃ O ₅ N	Complex ionic	1987- 1994	[79]

$M_2M^{II}_3P_3O_6N$ ($M^I = Na, M^{II} = Mg, Mn, Fe, Co$)	3/10	AP/MP: Various	Various	$M_3M^{II}P_3O_6N$	Complex ionic	$[P_3O_6]^{6-}$ anions	1987- 1994	[79]
$Cs_3M^I P_6O_{17}N$ ($M^I = Mg, Fe, Co$)	1/3	AP: Gas flow	$CsPO_3/NH_4H_2PO_4/(MO/MCO_3)$	$Cs_3M^I P_6O_{17}N$	Complex ionic	cyclic $[P_6O_{17}]^{17-}$ anions	1998- 1999	[79]
$M_2M^I P_3O_8N$ ($M^I = K, Ti; M^{II} = Mg, Mn, Fe$)*	1/3	AP/MP: Various	Various	*	Chain	$[P_3O_8]^{4-}$ chain	1996	[79]

*Crystal structure not elucidated yet.

A.2 References

- [1] S. Horstmann, E. Irran, W. Schnick, *Angew. Chem., Int. Ed. Engl.* **1997**, *36*, 1873–1875; *Angew. Chem.* **1997**, *109*, 1938–1940.
- [2] K. Landskron, H. Huppertz, J. Senker, W. Schnick, *Angew. Chem., Int. Ed.* **2001**, *40*, 2643–2645; *Angew. Chem.* **2001**, *113*, 2713–2716.
- [3] J. Ronis, B. Bondars, A. Vitola, T. Millers, *J. Solid State Chem.* **1995**, *115*, 265–269.
- [4] L. Boukbir, R. Marchand, Y. Laurent, P. Bacher, G. Roullet, *Ann. Chim. Fr.* **1989**, *14*, 475–481.
- [5] D. Baumann, R. Niklaus, W. Schnick, *Angew. Chem., Int. Ed.* **2015**, *54*, 4388–4391; *Angew. Chem.* **2015**, *127*, 4463–4466.
- [6] J. Haines, C. Chateau, J. M. Léger, A. Le Sauze, N. Diot, R. Marchand, S. Hull, *Acta Crystallogr., Sect. B: Struct. Sci.* **1999**, *55*, 677–682.
- [7] D. Baumann, S. J. Sedlmaier, W. Schnick, *Angew. Chem., Int. Ed.* **2012**, *51*, 4707–4709; *Angew. Chem.* **2012**, *124*, 4785–4787.
- [8] J.-M. Léger, J. Haines, L. S. de Oliveira, C. Chateau, A. Le Sauze, R. Marchand, S. Hull, *J. Phys. Chem. Solids* **1999**, *60*, 145–152.
- [9] S. Vogel, D. Baumann, R. Niklaus, E. Bykova, M. Bykov, N. Dubrovinskaia, L. Dubrovinsky, W. Schnick, *Angew. Chem., Int. Ed.* **2018**, *57*, 6691–6695; *Angew. Chem.* **2018**, *130*, 6801–6805.
- [10] H. P. Baldus, W. Schnick, J. Lücke, U. Wannagat, G. Bogedain, *Chem. Mater.* **1993**, *5*, 845–850.
- [11] S. Vogel, A. T. Buda, W. Schnick, *Angew. Chem., Int. Ed.* **2018**, *57*, 13202–13205; *Angew. Chem.* **2018**, *130*, 13386–13389.
- [12] S. W., J. Lücke, *Z. Anorg. Allg. Chem.* **1992**, *610*, 121–126.
- [13] A. Marchuk, F. J. Pucher, F. W. Karau, W. Schnick, *Angew. Chem., Int. Ed.* **2014**, *53*, 2469–2472; *Angew. Chem.* **2014**, *126*, 2501–2504.
- [14] S. Horstmann, E. Irran, W. Schnick, *Angew. Chem., Int. Ed. Engl.* **1997**, *36*, 1992–1994; *Angew. Chem.* **1997**, *109*, 2085–2087.
- [15] D. Baumann, W. Schnick, *Inorg. Chem.* **2014**, *53*, 7977–7982.
- [16] D. Baumann, W. Schnick, *Angew. Chem., Int. Ed.* **2014**, *53*, 14490–14493; *Angew. Chem.* **2014**, *126*, 14718–14721.
- [17] W. Schnick, J. Lücke, *Z. Anorg. Allg. Chem.* **1990**, *588*, 19–25.

- [18] W. Schnick, U. Berger, *Angew. Chem., Int. Ed. Engl.* **1991**, *30*, 830–831; *Angew. Chem.* **1991**, *103*, 857–858.
- [19] E.-M. Bertschler, C. Dietrich, T. Leichtweiß, J. Janek, W. Schnick, *Chem. - Eur. J.* **2018**, *24*, 196–205.
- [20] E.-M. Bertschler, R. Niklaus, W. Schnick, *Chem. - Eur. J.* **2018**, *24*, 736–742.
- [21] E. M. Bertschler, C. Dietrich, J. Janek, W. Schnick, *Chem. - Eur. J.* **2017**, *23*, 2185–2191.
- [22] E.-M. Bertschler, R. Niklaus, W. Schnick, *Chem. - Eur. J.* **2017**, *23*, 9592–9599.
- [23] W. Schnick, J. Luecke, *J. Solid State Chem.* **1990**, *87*, 101–106.
- [24] K. Landskron, E. Irran, W. Schnick, *Chem. - Eur. J.* **1999**, *5*, 2548–2553.
- [25] A. Vitola, J. Ronis, T. Millers, *Latv. PSR Zinat. Akad. Vestis, Kim. Ser.* **1990**, *90*, 299–301.
- [26] K. Landskron, S. Schmid, W. Schnick, *Z. Anorg. Allg. Chem.* **2001**, *627*, 2469–2472.
- [27] R. Nymwegen, H. Jacobs, *Z. Anorg. Allg. Chem.* **1997**, *623*, 429–433.
- [28] K. Landskron, W. Schnick, *J. Solid State Chem.* **2001**, *156*, 390–393.
- [29] F. Karau, W. Schnick, *Angew. Chem., Int. Ed.* **2006**, *45*, 4505–4508; *Angew. Chem.* **2006**, *118*, 4617–4620.
- [30] F. J. Pucher, S. Rebecca Römer, F. W. Karau, W. Schnick, *Chem. - Eur. J.* **2010**, *16*, 7208–7214.
- [31] (a) V. Schultz-Coulon, W. Schnick, *Z. Anorg. Allg. Chem.* **1997**, *623*, 69–74. (b) V. Schultz-Coulon, W. Schnick, *Angew. Chem., Int. Ed.* **1993**, *32*, 280–281; *Angew. Chem.* **1993**, *105*, 308–309.
- [32] F. J. Pucher, A. Marchuk, P. J. Schmidt, D. Wiechert, W. Schnick, *Chem. - Eur. J.* **2015**, *21*, 6443–6448.
- [33] F. W. Karau, L. Seyfarth, O. Oeckler, J. Senker, K. Landskron, W. Schnick, *Chem. - Eur. J.* **2007**, *13*, 6841–6852.
- [34] S. Wendl, W. Schnick, *Chem. - Eur. J.* **2018**, *24*, 1497–1502.
- [35] F. W. Karau, W. Schnick, *J. Solid State Chem.* **2005**, *178*, 135–141.
- [36] F. J. Pucher, F. W. Karau, J. Schmedt auf der Günne, W. Schnick, *Eur. J. Inorg. Chem.* **2016**, 1497–1502.
- [37] S. D. Kloß, O. Janka, T. Block, R. Pöttgen, R. Glaum, W. Schnick, *Angew. Chem., Int. Ed.* <https://doi.org/10.1002/anie.201809146>; *Angew. Chem.*

- <https://doi.org/10.1002/ange.201809146>.
- [38] F. J. Pucher, F. Hummel, W. Schnick, *Eur. J. Inorg. Chem.* **2015**, 1886–1891.
- [39] S. J. Sedlmaier, M. Eberspächer, W. Schnick, *Z. Anorg. Allg. Chem.* **2011**, 637, 362–367.
- [40] S. D. Kloß, N. Weidmann, R. Niklaus, W. Schnick, *Inorg. Chem.* **2016**, 55, 9400–9409.
- [41] S. J. Sedlmaier, V. R. Celinski, J. Schmedt auf der Günne, W. Schnick, *Chem. - Eur. J.* **2012**, 18, 4358–4366.
- [42] E. M. Bertschler, T. Bräuniger, C. Dietrich, J. Janek, W. Schnick, *Angew. Chem., Int. Ed.* **2017**, 56, 4806–4809; *Angew. Chem.* **2017**, 129, 4884–4887.
- [43] K. Senevirathne, C. S. Day, M. D. Gross, A. Lachgar, N. A. W. Holzwarth, *Solid State Ionics* **2013**, 233, 95–101.
- [44] B. Wang, B. C. Chakoumakos, B. C. Sales, B. S. Kwak, J. B. Bates, *J. Solid State Chem.* **1995**, 115, 313–323.
- [45] D. Baumann, W. Schnick, *Eur. J. Inorg. Chem.* **2015**, 2015, 617–621.
- [46] H. Jacobs, S. Pollok, F. Golinski, *Z. Anorg. Allg. Chem.* **1994**, 620, 1213–1218.
- [47] F. Golinski, H. Jacobs, *Z. Anorg. Allg. Chem.* **1995**, 621, 29–33.
- [48] H. Jacobs, F. Golinski, *Z. Anorg. Allg. Chem.* **1994**, 620, 531–534.
- [49] A. Marchuk, V. R. Celinski, J. Schmedt auf der Günne, W. Schnick, *Chem. - Eur. J.* **2015**, 21, 5836–5842.
- [50] A. Marchuk, P. Schultz, C. Hoch, O. Oeckler, W. Schnick, *Inorg. Chem.* **2016**, 55, 974–982.
- [51] S. Vogel, W. Schnick, *Chem. - Eur. J.* **2018**, 24, 14275–14281.
- [52] S. J. Sedlmaier, E. Mugnaioli, O. Oeckler, U. Kolb, W. Schnick, *Chem. - Eur. J.* **2011**, 17, 11258–11265.
- [53] S. J. Sedlmaier, J. Schmedt auf der Günne, W. Schnick, *Dalton Trans.* **2009**, 4081.
- [54] S. J. Sedlmaier, D. Weber, W. Schnick, *Z. Kristallogr. - New Cryst. Struct.* **2012**, 227, 1–2.
- [55] (a) A. Marchuk, W. Schnick, *Angew. Chem., Int. Ed.* **2015**, 54, 2383–2387; *Angew. Chem.* **2015**, 127, 2413–2417. (b) A. Marchuk, S. Wendl, N. Imamovic, F. Tambornino, D. Wiechert, P. J. Schmidt, W. Schnick, *Chem. Mater.*, **2015**, 27, 6432–6441.
- [56] F. Karau, W. Schnick, *Z. Anorg. Allg. Chem.* **2006**, 632, 231–237.
- [57] S. D. Kloß, A. Weis, S. Wandelt, W. Schnick, *Inorg. Chem.* **2018**, 57, 4164–4170.

- [58] S. D. Kloß, S. Wandelt, A. Weis, W. Schnick, *Angew. Chem., Int. Ed.* **2018**, *57*, 3192–3195; *Angew. Chem.* **2018**, *130*, 3246–3249.
- [59] S. D. Kloß, L. Neudert, M. Döblinger, M. Nentwig, O. Oeckler, W. Schnick, *J. Am. Chem. Soc.* **2017**, *139*, 12724–12735.
- [60] S. D. Kloß, W. Schnick, *Angew. Chem., Int. Ed.* **2015**, *54*, 11250–11253; *Angew. Chem.* **2015**, *127*, 11402–11405.
- [61] S. D. Kloß, N. Weidmann, W. Schnick, *Eur. J. Inorg. Chem.* **2017**, 1930–1937.
- [62] (a) S. Correll, O. Oeckler, N. Stock, W. Schnick, *Angew. Chem., Int. Ed.* **2003**, *42*, 3549–3552; *Angew. Chem.* **2003**, *115*, 3674–3677. (b) S. Correll, N. Stock, O. Oeckler, J. Senker, T. Nilges, W. Schnick, *Z. Anorg. Allg. Chem.*, **2004**, *630*, 2205–2217.
- [63] F. J. Pucher, W. Schnick, *Z. Anorg. Allg. Chem.* **2014**, *640*, 2708–2713.
- [64] A. Marchuk, L. Neudert, O. Oeckler, W. Schnick, *Eur. J. Inorg. Chem.* **2014**, 3427–3434.
- [65] S. J. Sedlmaier, M. Doeblinger, O. Oeckler, J. Weber, J. S. A. Der Guenne, W. Schnick, *J. Am. Chem. Soc.* **2011**, *133*, 12069–12078.
- [66] E. Mugnaioli, S. J. Sedlmaier, O. Oeckler, U. Kolb, W. Schnick, *Eur. J. Inorg. Chem.* **2012**, 121–125.
- [67] L. Neudert, F. Heinke, T. Bräuniger, F. J. Pucher, G. B. Vaughan, O. Oeckler, W. Schnick, *Chem. Commun.* **2017**, *53*, 2709–2712.
- [68] S. D. Kloß, W. Schnick, *Inorg. Chem.* **2018**, *57*, 4189–4195.
- [69] J. Weitkamp, S. Ernst, F. Cubero, F. Wester, W. Schnick, *Adv. Mater.* **1997**, *9*, 247–248.
- [70] F. J. Pucher, C. Frhr. von Schirnding, F. Hummel, V. R. Celinski, J. Schmedt auf der Günne, B. Gerke, R. Pöttgen, W. Schnick, *Eur. J. Inorg. Chem.* **2015**, 382–388.
- [71] J. Ronis, V. Krasnikov, B. Bondars, A. Vitola, T. Millers, *Latv. PSR Zinat. Akad. Vestis, Kim. Ser.* **1989**, *1989*, 139–144.
- [72] F. Karau, O. Oeckler, F. Schäfers, R. Niewa, W. Schnick, *Z. Anorg. Allg. Chem.* **2007**, *633*, 1333–1338.
- [73] F. Wester, W. Schnick, *Z. Anorg. Allg. Chem.* **1996**, *622*, 1281–1286.
- [74] J. Ronis, V. V. Krasnikov, B. Y. Bondars, A. A. Vitola, T. Millers, *Latv. PSR Zinat. Akad. Vestis, Kim. Ser.* **1988**, *1988*, 643–646.

- [75] N. Stock, J. Lücke, M. Volkmann, M. Jansen, W. Schnick, *Z. Anorg. Allg. Chem.* **1995**, *621*, 987–992.
- [76] W. Schnick, J. Lücke, *Z. Anorg. Allg. Chem.* **1994**, *620*, 2014–2019.
- [77] W. Schnick, J. Lücke, *Angew. Chem., Int. Ed. Engl.* **1992**, *31*, 213–215; *Angew. Chem.* **1992**, *104*, 208–209.
- [78] N. Stock, E. Irran, W. Schnick, *Chem. - Eur. J.* **1998**, *4*, 1822–1828.
- [79] R. Marchand, W. Schnick, N. Stock, *Adv. Inorg. Chem.* **2000**, *50*, 193–233.

Appendix B. Supporting Information for Chapter 2

B.1 Experimental details of the HP/HT-metathesis of LiNdP₄N₈

P₃N₅. The binary starting material P₃N₅, needed for preparation of LiPN₂, was synthesized by reaction of phosphorous pentasulfide (P₄S₁₀, 99%, Sigma-Aldrich) in a constant ammonia flow (NH₃, 5.0, Air-Liquide).^[1] A quartz tube-type furnace and a quartz crucible were dried in vacuum for 5 h at 1000 °C. The quartz crucible was loaded with 8 g of P₄S₁₀ and placed in the tube furnace. The sample was saturated with ammonia for 4 h. After saturation the furnace was heated to 850 °C with a ramp of 5°C/min. The sample was fired for 4 h before ramping down to room temperature with 5 °C/min. The furnace was flushed with Ar gas and the orange product was isolated and washed with water/ethanol/acetone.

LiPN₂. LiPN₂ was prepared by reaction of 1.2 equivalents of Li₃N with P₃N₅ in a quartz ampoule under N₂ atmosphere. The starting materials were mixed and thoroughly ground under inert conditions. The reaction mixture was transferred into a Ta crucible, which was beforehand placed in a dried quartz tube, in a N₂ counter flow. The ampoule was molten off and fired in a furnace at 800 °C for 90 h. The reaction product was washed with diluted hydrochloric acid, water and ethanol.

LiNdP₄N₈. LiNdP₄N₈ was prepared by metathesis reaction of stoichiometric amounts of NdF₃ (99.99 %, Alfa Aesar) and LiPN₂ in a high-temperature high-pressure experiment using a modified walker-type multianvil assembly. The starting materials were thoroughly mixed and ground under inert conditions before being packed in an h-BN crucible. The crucible was transferred in a specially prepared MgO octahedron (Ceramic Substrates & Components, Isle of Wight, UK) with an edge length of 18 mm. Additional details about the high-pressure setup might be found in literature.^[2-6] The reaction was carried out at 5 GPa of pressure and 1300 °C. The pressure was built up using a 1000 t hydraulic press (Voggenreiter, Mainleus, Germany). Eight tungsten carbide cubes (Hawedia, Marklkofen, Germany) with truncated edges were used to create quasi-hydrostatic conditions within the sample octahedron. The temperature was built up over 60 min, maintained for 300 min and eventually dropped to RT in 40 min. The reaction product was washed with H₂O to remove the LiF, formed during the reaction. The product was obtained as colorless crystals.

B.2 Information on data collection and structure elucidation of LiNdP_4N_8

X-ray diffraction on a single crystal of LiNdP_4N_8 was carried out with a D8 Venture diffractometer (Bruker, Billerica MA, USA) using Mo-K_α radiation from a fine-focused sealed tube X-ray source. The cell determination and integration was executed using the Bruker program APEX2 as well as a multi-scan absorption correction. The space group was determined with XPREP^[7] and structure solution was carried out with SHELXS-97 using direct methods and structure refinement with SHELXL-97.^[8-10] Structure solution resulted in identification of Nd and P atom positions. Missing crystallographic atom sites were identified from the difference Fourier map. All atoms were refined anisotropically. Crystal structures were visualized using VESTA.^[11]

X-ray powder diffraction for bulk analysis and structure confirmation was conducted on a StadiP diffractometer (Stoe & Cie, Darmstadt, Germany) in parafocussing Debye-Scherrer geometry using a Cu anode. The Cu-K_α radiation was selected from the raw X-ray spectrum with a Ge(111) single-crystal monochromator. The diffracted radiation was detected using a Mythen 1K Si-strip detector (Dectris, Baden, Switzerland). Rietveld refinement^[12] on the obtained powder diffraction data was carried out using TOPAS-Academic V4.1.^[13] The background was handled using a shifted-Chebyshev function, while the peak shapes were described using the fundamental parameters approach.^[14,15]

Temperature dependent powder X-ray diffraction was carried out on a STOE StadiP diffractometer equipped with a high-temperature graphite furnace and an image plate position sensitive detector. The Mo-K_α ($\lambda = 0.70930 \text{ \AA}$) radiation used was selected by a Ge(111) monochromator. Diffraction patterns were collected up to a 1000 °C with 25 °C increments. Temperature in between measurements was increased with a rate of 5 °C/min and the exposure time for each measurement was set to 10 min. Infrared spectroscopy was performed on a Spectrum BX II spectrometer (Perkin Elmer, Waltham MA, USA) with ATR geometry in the range of 600–4000 cm^{-1} . Scanning electron microscopy was performed with a JSM-6500F (JEOL, Tokyo, Japan) and energy dispersive X-ray spectra were recorded using a type 7418 X-ray detector (Oxford Instruments, Abington, UK).

Magnetic measurements were carried out with a MPM-XL SQUID-Magnetometer (Quantum Design, San Diego CA, USA). The temperature could be varied between 1.8 K and 400 K while the magnetic field strength could be varied between –50 and 50 kOe. The measured susceptibilities were not

corrected with diamagnetic increments. Phase pure samples of known weight were placed in gelatine capsules with known diamagnetic properties. The measurement was carried out using the MPMS MultiVi software.^[16] The conversion of the data was carried out with the program SQUID Processor^[17], which corrected the data for the diamagnetic contribution of the gelatine capsule and core electrons. Magnetic field dependent measurements with fields varying between -50 and 50 kOe were carried out at 1.8 and 300 K. For susceptibility measurements the temperature was varied between 1.8 and 300 K at constant magnetic field strengths of 100 , 1000 , 5000 , 10000 and 50000 Oe. A zero-field-cooled, field-cooled experiment was carried out at 30 Oe.

A VHX-5000 (Keyence, Osaka, Japan) microscope with Z20 T objective was used to image samples.

B.3 Details of scanning electron microscopy

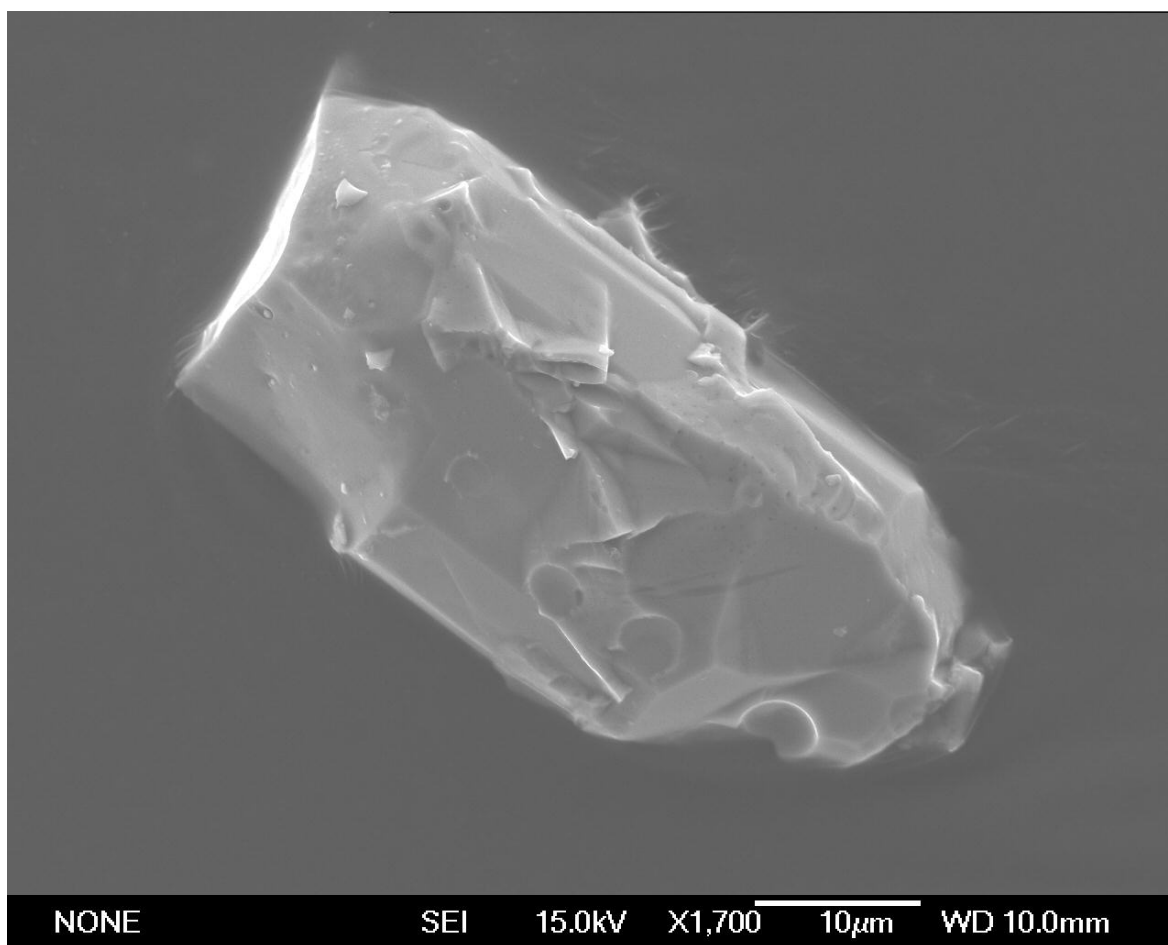


Figure B.1. Scanning electron micrograph of a LiNdP_4N_8 single crystal.

Table B.1. EDX analysis of LiNdP_4N_8 single crystal shown in Figure B.1.

atom	experimental / at-%	theoretical / at-%
Nd	9	7.7
P	32.8	30.8
N	55.8	61.5
O	2.5	0

B.4 Additional crystallographic data for LiNdP₄N₈

Table B.2. Crystallographic information for LiNdP₄N₈.

Formula	LiNdP ₄ N ₈
Crystal system	orthorhombic
Space group	<i>Pnma</i> (no. 62)
	$a = 8.7305(17)$
Cell parameters / Å	$b = 7.8783(16)$
	$c = 9.0881(18)$
Cell Volume / Å ³	625.1(2)
Formula units per unit cell Z	4
Calculated density / g·cm ⁻³	4.114
Absorption coefficient μ / mm ⁻¹	9.278
Radiation	Mo-K α ($\lambda = 0.71073$ Å)
Temperature \ K	293(2)
F(000)	716
θ range \ °	$3.24 \leq \theta \leq 33.15$
Total no. of reflections	12131
Independent reflections	1262
Refined parameters	70
Goodness of fit	1.160
R_1 (all data), R_1 [$F^2 > 2\sigma(F^2)$]	0.0135, 0.0129
wR_2 (all data), wR_2 [$F^2 > 2\sigma(F^2)$]	0.0344, 0.0342
$\Delta\rho_{\max}$, $\Delta\rho_{\min}$ / e·Å ⁻³	0.578, -0.631

$w = 1/[\sigma^2(F_o^2) + (0.0144 \cdot P)^2 + 0.95 \cdot P]$ with $P = (F_o^2 + 2F_c^2)/3$

Table B.3. Fractional atomic coordinates, isotropic thermal displacement parameters, and site occupancies for LiNdP₄N₈.

Atom	Wyckoff Symbol	x	y	z	U_{eq} / Å ²	Occupancy
Nd1	4c	0.912102(13)	1/4	0.414285(12)	0.00555(4)	1
P1	8d	0.72930(4)	0.94042(5)	0.58227(4)	0.00298(7)	1
P2	8d	0.93054(4)	0.06226(5)	0.80856(4)	0.00306(7)	1
N1	4c	0.9798(2)	1/4	0.8608(2)	0.0056(3)	1
N2	4c	1.1977(2)	1/4	0.4181(2)	0.0055(3)	1
N3	8d	0.69691(15)	0.02375(18)	0.42088(13)	0.0049(2)	1
N4	8d	0.57752(14)	0.93351(17)	0.68531(15)	0.0048(2)	1
N5	8d	0.87080(15)	0.05857(17)	0.63951(14)	0.0052(2)	1
Li1	4c	1.0550(6)	1/4	1.0666(5)	0.0134(8)	1

Table B.4. Anisotropic displacement parameters occurring in LiNdP₄N₈.

Atom	$U_{11} / \text{\AA}^2$	$U_{22} / \text{\AA}^2$	$U_{33} / \text{\AA}^2$	$U_{12} / \text{\AA}^2$	$U_{13} / \text{\AA}^2$	$U_{23} / \text{\AA}^2$
Nd1	0.00667(6)	0.00548(6)	0.00449(6)	0	-0.00034(3)	0
P1	0.00351(14)	0.00320(15)	0.00246(15)	0.00010(12)	-0.00015(11)	0.00014(11)
P2	0.00299(15)	0.00302(16)	0.00294(15)	0.00016(11)	-0.00013(11)	-0.00019(11)
N1	0.0064(5)	0.0060(5)	0.0033(5)	-0.0007(4)	-0.0009(4)	0.0026(4)
N2	0.0058(5)	0.0053(5)	0.0036(5)	-0.0008(4)	0.0009(4)	-0.0016(4)
N3	0.0042(5)	0.0050(5)	0.0053(5)	0.0014(4)	0.0009(4)	0.0009(4)
N4	0.0060(7)	0.0019(7)	0.0086(8)	0	0.0007(6)	0
N5	0.0085(7)	0.0038(7)	0.0045(7)	0	0.0015(6)	0
Li1	0.014(2)	0.013(2)	0.0127(19)	0	0.0007(16)	0

Table B.5. List of interatomic distances / \AA for LiNdP₄N₈.

Nd1–N2	2.493(2)	P1–N5	1.6320(14)	N4–P2	1.6367(13)
Nd1–N4	2.5354(14)	P1–Li1	2.904(4)	N4–Li1	2.143(4)
Nd1–N4	2.5355(14)	P2–N1	1.6120(9)	N4–Nd1	2.5355(14)
Nd1–N5	2.5679(13)	P2–N5	1.6227(14)	Li1–N4	2.143(4)
Nd1–N5	2.5680(13)	P2–N4	1.6367(13)	Li1–N4	2.143(4)
Nd1–N3	2.5905(14)	P2–N3	1.6550(14)	Li1–N3	2.174(3)
Nd1–N3	2.5905(14)	P2–Li1	2.712(2)	Li1–N3	2.174(3)
Nd1–Li1	3.122(5)	P2–Li1	2.978(4)	Li1–P2	2.712(2)
Nd1–P1	3.2904(6)	N1–P2	1.6120(9)	Li1–P2	2.712(2)
Nd1–P1	3.2904(6)	N1–Li1	1.982(5)	Li1–P1	2.904(4)
Nd1–Li1	3.397(5)	N2–P1	1.6300(9)	Li1–P1	2.904(4)
P1–N4	1.6235(13)	N2–P1	1.6301(9)	Li1–P2	2.978(4)
P1–N2	1.6300(9)	N3–P2	1.6550(14)	Li1–Nd1	3.122(5)
P1–N3	1.6317(13)	N3–Li1	2.174(3)		

Table B.6. List of bond angles / $^\circ$ for LiNdP₄N₈.

N–P–N				P–N–P	
N2–P1–N3	115.85(8)	N1–P2–N3	111.92(9)	P2–N1–P2	133.13(12)
N2–P1–N5	103.27(8)	N1–P2–N4	110.45(8)	P1–N2–P1	133.94(13)
N3–P1–N5	100.85(7)	N1–P2–N5	112.42(8)	P1–N3–P2	120.41(9)
N4–P1–N2	106.84(8)	N4–P2–N3	104.62(7)	P1–N4–P2	129.70(9)
N4–P1–N3	112.99(7)	N5–P2–N3	111.13(7)	P2–N5–P2	129.7(8)
N4–P1–N5	116.95(7)	N5–P2–N4	105.85(7)		

B.5 Details of the Rietveld refinement

Table B.7. Details of the Rietveld refinement of LiNdP_4N_8 for space groups $Pnma$ and $P2_1/c$.

Formula	LiNdP_4N_8	
Formula mass / $\text{g} \cdot \text{mol}^{-1}$	387.13	
Crystal system / space group	orthorhombic, $Pnma$ (no. 62)	monoclinic, $P2_1/c$ (no. 14)
Lattice parameters / $\text{Å}, ^\circ$	$a = 8.733300(85)$	$a = 8.73336(8)$
	$b = 7.883310(85)$	$b = 7.88341(8)$
	$c = 9.091160(97)$	$c = 9.09117(8)$
		$\beta = 89.99759(88)$
Cell volume / Å^3	625.902(11)	625.915(11)
Formula units per cell Z	4	
X-ray density / $\text{g} \cdot \text{cm}^{-3}$	4.108	
Linear absorption coefficient / cm^{-1}	728.61	
Radiation	Cu-K α_1 ($\lambda = 154.059$ pm)	
Monochromator	Ge(111)	
Diffractionmeter	Stoe StadiP	
Detector	MYTHEN 1K	
2θ -range / $^\circ$	5–92.420	
Temperature / K	298 (2)	
Data points	5829	
Number of observed reflections	294	536
Number of parameters	70	91
Constraints	0	0
Program used	TOPAS Academic	
Structure refinement	Rietveld-Method	
Profile function	fundamental parameters model	
Background function	shifted Chebychev	
R_{wp}	0.02766	0.02655
R_{exp}	0.01956	0.01952
R_{p}	0.01963	0.01880
R_{Bragg}	0.01984	0.01461
χ^2	1.414	1.360

B.6 Detailed Rietveld plot

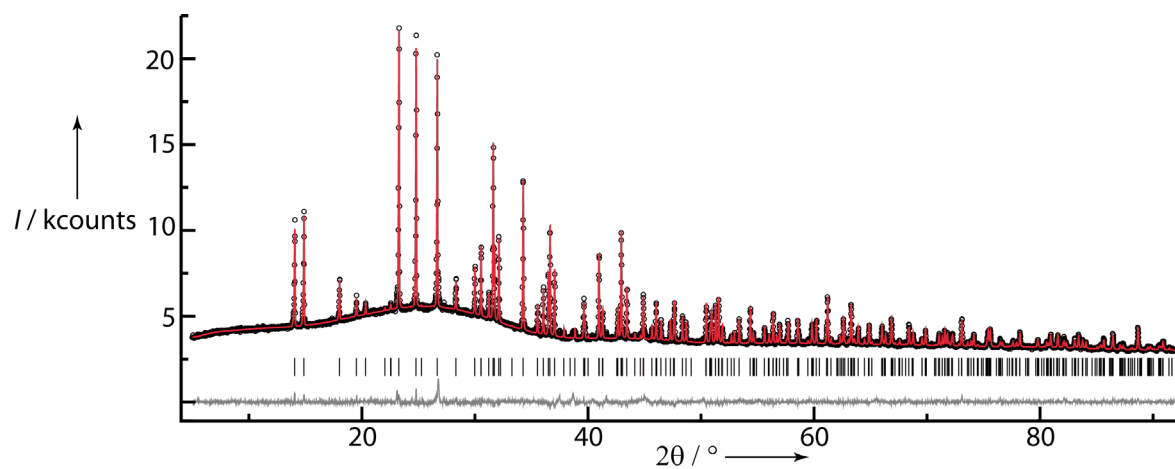


Figure B.2. Rietveld refinement of LiNdP_4N_8 in space group $Pnma$ (no. 62). Observed (black circles) and calculated (red line) powder diffraction pattern of LiNdP_4N_8 . The theoretical reflection positions (black vertical bars) and the difference plot (gray line) are displayed below the refinement. The heightened scattering background may stem from the glass capillary or an amorphous side phase.

B.7 Additional information on the structure

The P–N bond lengths within the two PN_4 tetrahedra (Figure 2.2) (1.63 to 1.66 Å) coincide with the value range found in other nitridophosphates.^[18,19] The N–P–N angles varying from 104.6–112.4° are close to the regular tetrahedral angle of 109.5°. The P2 centered tetrahedra with angles ranging from 100.9 to 117.0° are more distorted, which may be caused by an edge-sharing with the NdN_7 polyhedron. For olivines it was shown that edge-sharing of tetrahedra and cation polyhedra can cause a cation size dependent distortion.^[20] This distortion is attributed to bond angles, which are more flexible than bond lengths and follow the cation size change. Comparably, $\text{BaAl}_2\text{Si}_2\text{O}_8$ exhibits less distorted (Si/Al) O_4 tetrahedra^[21] than LiNdP_4N_8 due to the larger ionic radius of Ba ($r(\text{Ba}^{2+}) = 1.38 \text{ \AA}$, $r(\text{Nd}^{3+}) \approx 1 \text{ \AA}$).

The aforementioned paracelsian crystallizes in the maximal non-isomorphic subgroup $P2_1/a$ (no. 14) of $Pnma$ with a pseudo-orthorhombic metric.^[21] A structure with space group $P2_1/a$ may emulate $Pnma$ through merohedral twinning. To rule out such pseudo-orthorhombic metric in LiNdP_4N_8 , X-ray diffraction with Cu- $K\alpha_1$ radiation was carried out on a powdered sample. The recorded data (Figure B.3) reveals no obvious peak separation at high angles. An artificial monoclinic structure model with space group $P2_1/a$ (no. 14) was created by symmetry reduction. The fit of this model to the data by the Rietveld method gave further indication of an orthorhombic metric since the monoclinic angle β converged towards 90° and the isotropic thermal parameters could not be refined freely.

The paracelsian structure type is closely related to the feldspar type, which is an important class of rock-forming minerals. The feldspar structure can be obtained from paracelsian by a 90° rotation of the double crankshaft chains. Detailed information regarding structure similarity can be found in literature.^[21,22]

B.8 Detailed high-angle Rietveld plot

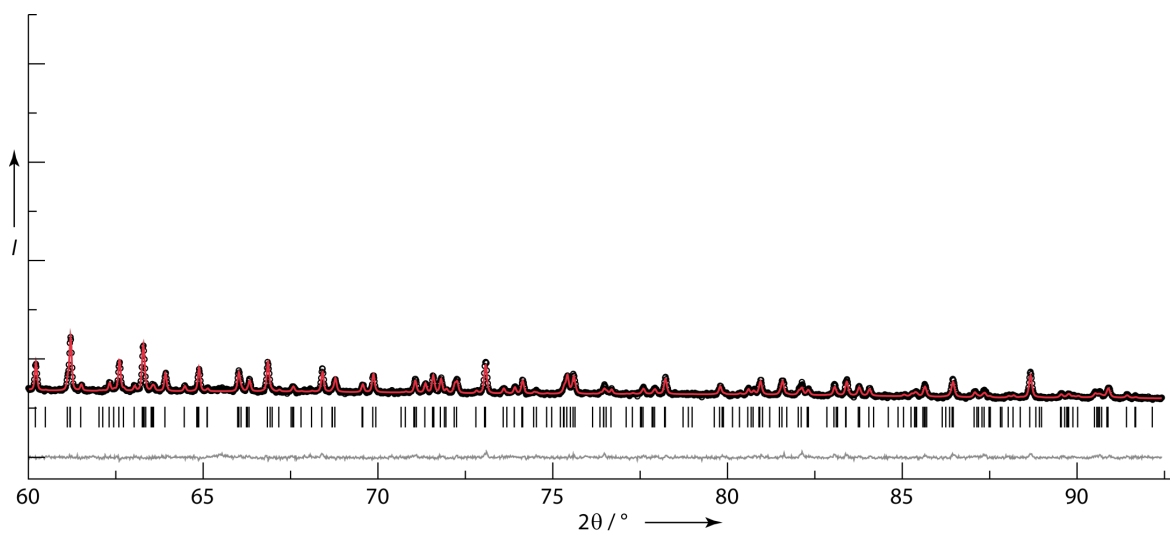


Figure B.3. Rietveld refinement of LiNdP_4N_8 in space group $Pnma$ (no. 62) in the range of $2\theta = 60$ – 93.5° .

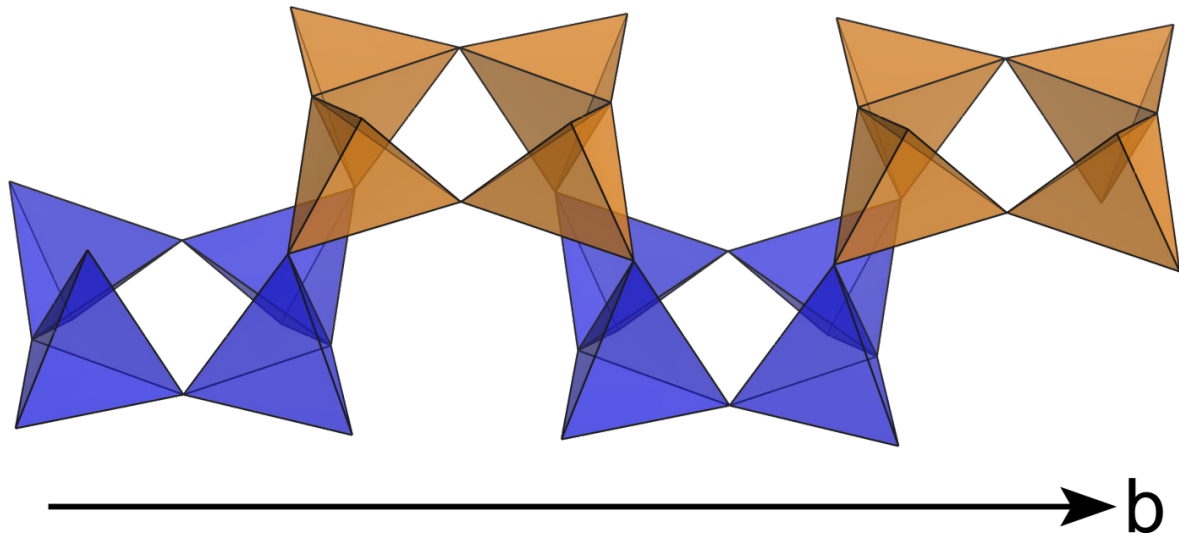


Figure B.4. Double Crankshaft chain running along $[010]$. Two orange and blue tetrahedra form the four-membered rings visible in projection on the (010) plane.

B.9 Comparison of paracelsian-type $\text{BaAl}_2\text{Si}_2\text{O}_8$ and LiNdP_4N_8

Table B.8. Fractional coordinates of atom sites in (a) paracelsian-type $\text{BaAl}_2\text{Si}_2\text{O}_8$ ^[21] and (b) LiNdP_4N_8 are compared.

Wyckoff position	Atom $\text{BaAl}_2\text{Si}_2\text{O}_8^a$	x	y	z	Atom $\text{LiNdP}_4\text{N}_8^b$	x	y	z	Displacement $ \mathbf{u} / \text{pm}$
4c	Ba1	0.8973	1/4	0.4123	Nd1	0.9121	1/4	0.4143	0.1305
8d	(Al,Si)1	0.7283	0.9337	0.5827	P1	0.7293	0.9404	0.5823	0.0536
8d	(Al,Si)2	0.935	0.0646	0.8039	P2	0.9305	0.0623	0.8086	0.0608
4c	O1	0.9933	1/4	0.827	N1	0.9798	1/4	0.8608	0.3290
4c	O2	0.209	1/4	0.412	N2	0.1977	1/4	0.4181	0.1132
8d	O3	0.693	0.998	0.4117	N3	0.6969	0.0237	0.4209	0.2217
8d	O4	0.575	0.9354	0.6875	N4	0.5775	0.9335	0.6853	0.0332
8d	O5	0.8713	0.046	0.638	N5	0.8708	0.0586	0.6395	0.1003

a) lattice parameters: $a = 9.02$, $b = 8.47$, $c = 9.50 \text{ \AA}$, $\beta = 90.0^\circ$ ^[21], b) lattice parameters: $a = 8.7305$, $b = 7.8783$, $c = 9.0881 \text{ \AA}$

B.10 Temperature dependent powder X-ray diffraction

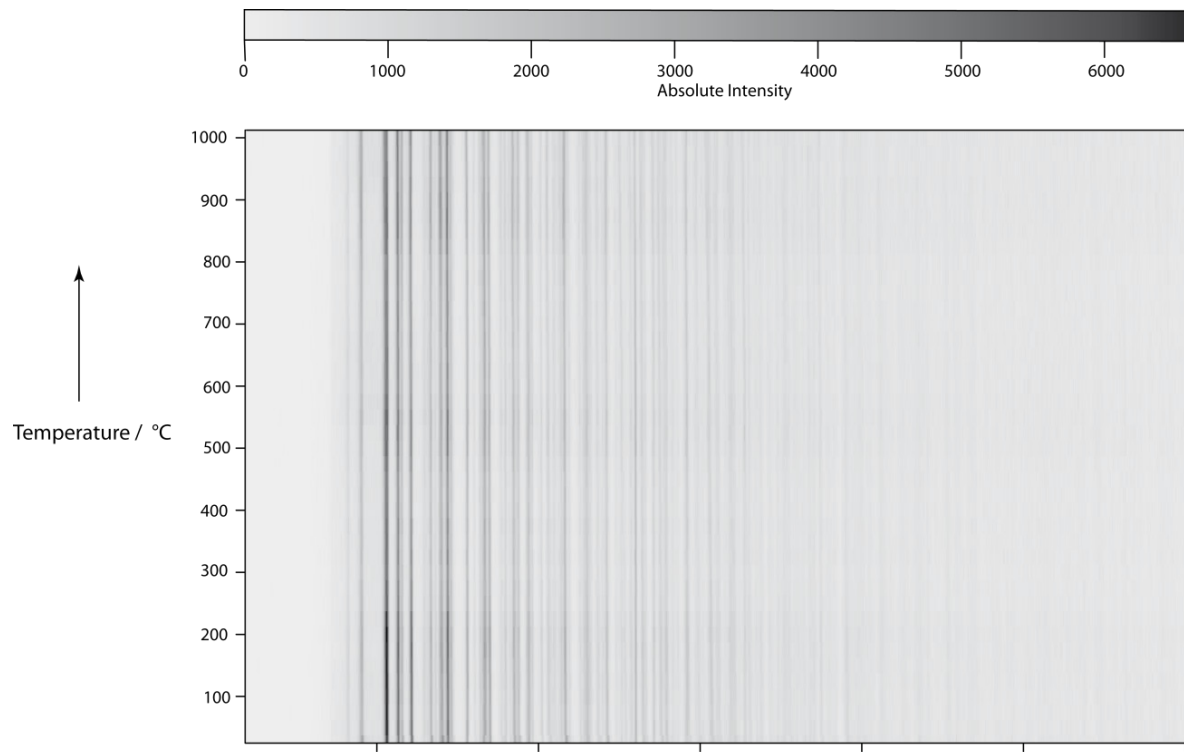
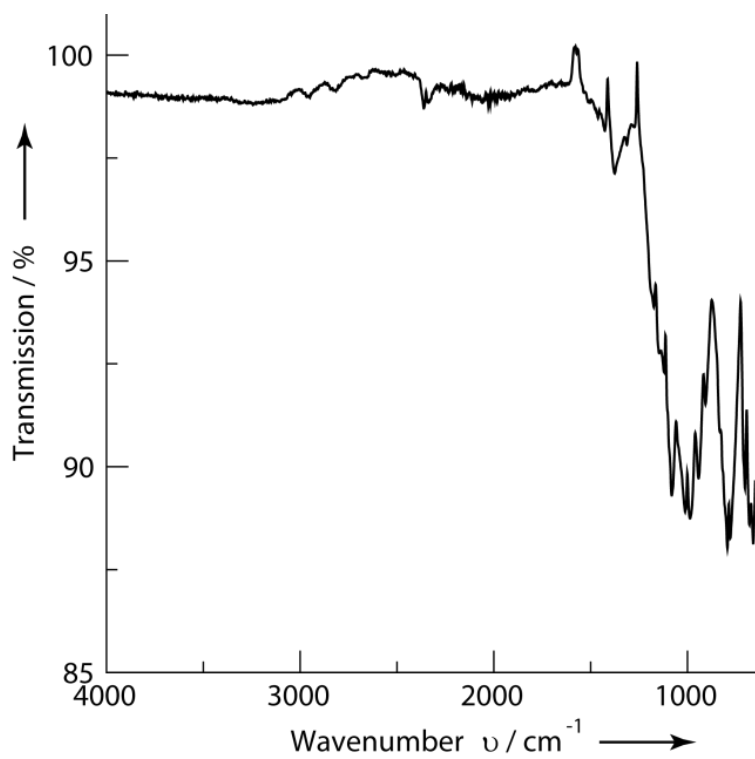


Figure B.5. Temperature dependent powder X-ray diffractogram of LiNdP_4N_8 .

B.11 FTIR spectrum**Figure B.6.** FTIR spectrum of LiNdP₄N₈

B.12 Details on the magnetic characterization of LiNdP₄N₈

The susceptibility data obtained from the magnetization of the sample at varying temperatures and a constant magnetic field strength of 20 kOe is displayed in Figure 2.4. The data is plotted as χ_m vs. T in red and χ_m^{-1} vs. T in blue. Examination of the data reveals no magnetic ordering in the range of 300 to 1.8 K. The data follows the expected trend for paramagnetic substances, which is an increase in magnetic susceptibility at lower temperatures. The effective magnetic moment was calculated from the slope of the black regression line in the χ_m^{-1} vs. T plot. The linear regression was fit to the data in the temperature range of 300 to 50 K since Curie's law is only valid for higher temperatures. The regression line can be described by the following equation.

The standard deviations are given in parentheses. The experimental effective magnetic moment μ_{eff} was calculated to be $3.815 \mu_B$, which is close to the theoretical value of $3.618 \mu_B$. The Curie temperature Θ can be calculated from the ordinate axis intercept at 2.20. The abscissa intercept Θ is at -4.00 K. This is close to the theoretical value for paramagnetic compounds of 0 K. The difference in μ_{eff} and Θ may be attributed to measurement accuracy. Moreover, additional magnetic contributions may stem from an amorphous phase which can be seen in the Rietveld plot in Figure B.2. Susceptibility measurements carried out at lower field strengths (Figure B.7) reveal no visible change in the magnetic behavior, thus paramagnetism is the only form of magnetism present in the sample.

Field-dependent measurements at 1.8 and 300 K (Figure B.8) are in agreement with these results. The magnetization follows the characteristic wave-shape at low temperatures.

A zero-field-cooled, field-cooled experiment conducted at 30 Oe (Figure B.9) shows no magnetic ordering phenomena.

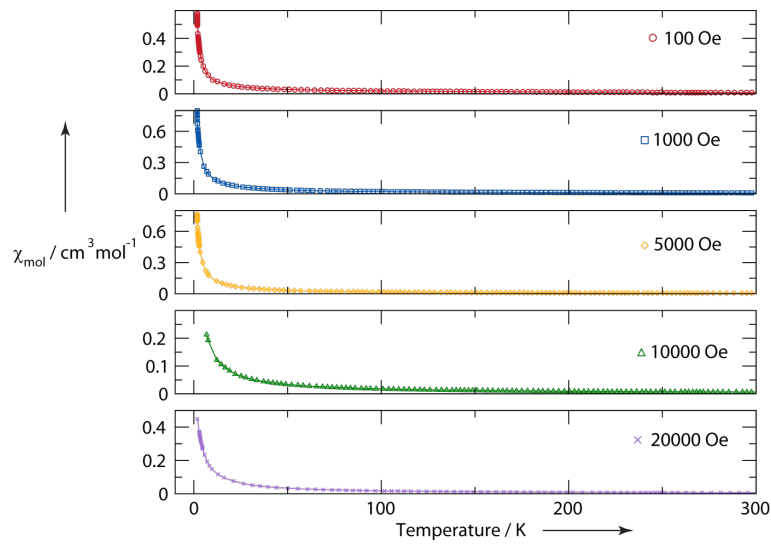


Figure B.7. Susceptibility measurements of LiNdP_4N_8 carried out at 0.1, 1, 5, 10 and 20 kOe.

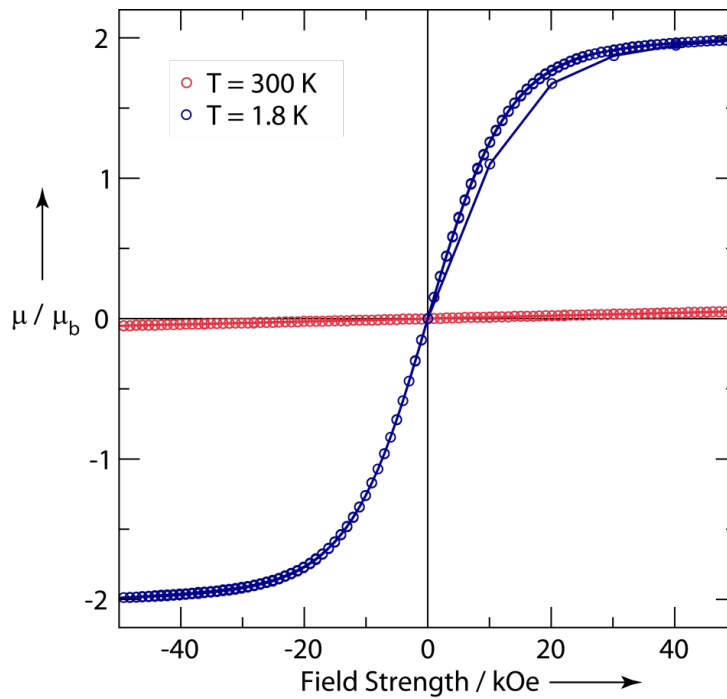


Figure B.8. Field dependent magnetization measurement of LiNdP_4N_8 carried out at 1.8 and 300 K.

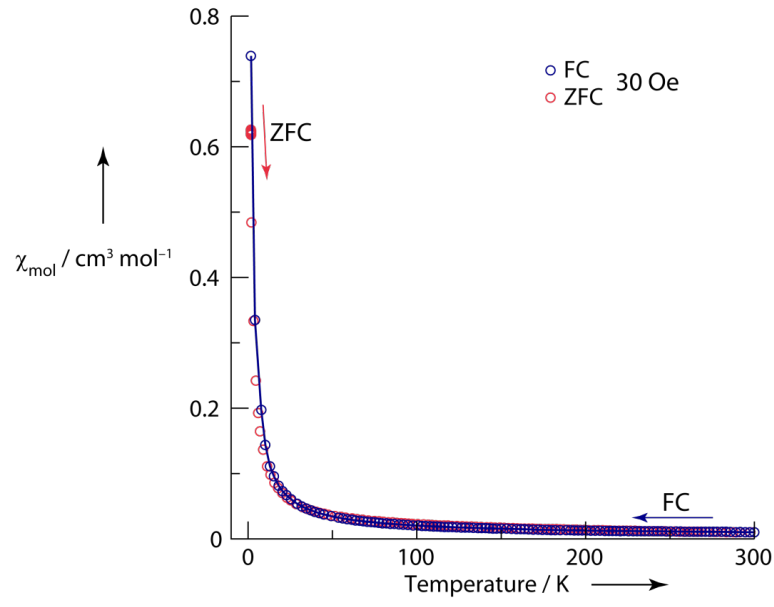


Figure B.9. Field-cooled, Zero-field-cooled magnetization measurement of LiNdP_4N_8 carried out at 30 Oe.

B.13 Light-microscopy of a LiNdP_4N_8 sample

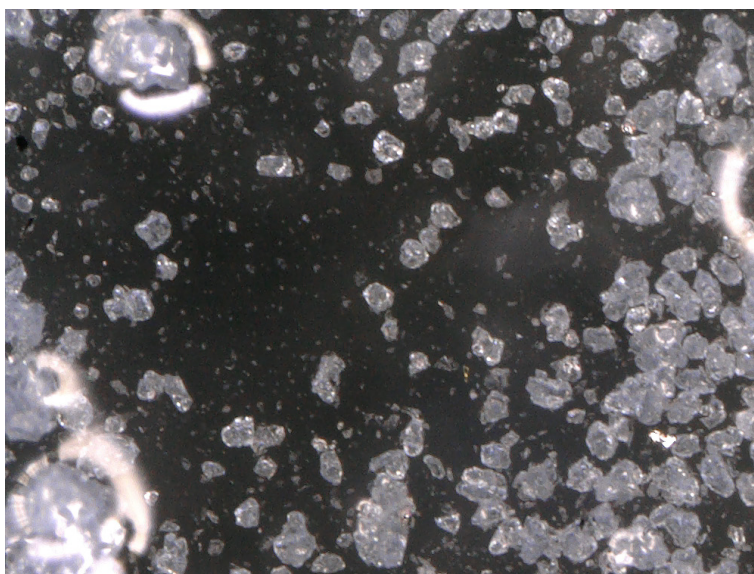


Figure B.10. Light-microscope image of a representative LiNdP_4N_8 sample.

B.14 References

- [1] A. Stock, H. Grüneberg, *Ber. Dtsch. Chem. Ges.* **1907**, 40, 2573–2578.
- [2] N. Kawai, S. Endo, *Rev. Sci. Instrum.* **1970**, 41, 1178–1181.
- [3] D. Walker, M. A. Carpenter, C. M. Hitch, *Am. Mineral.* **1990**, 75, 1020–1028.
- [4] D. Walker, *Am. Mineral.* **1991**, 76, 1092–1100.
- [5] H. Huppertz, *Z. Kristallogr.* **2004**, 219, 330–338.
- [6] D. C. Rubie, *Phase Transit.* **1999**, 68, 431–451.
- [7] Bruker-AXS, *XPREP*, Karlsruhe, **2001**.
- [8] G. M. Sheldrick, *SHELXS*, University of Göttingen, **1997**.
- [9] G. M. Sheldrick, *Acta Crystallogr., Sect. A: Found. Crystallogr.* **2008**, 64, 112.
- [10] L. J. Farrugia, *J. Appl. Crystallogr.* **1999**, 32, 837–838.
- [11] K. Momma, F. Izumi, *J. Appl. Crystallogr.* **2011**, 44, 1272–1276.
- [12] H. M. Rietveld, *J. Appl. Crystallogr.* **1969**, 2, 65–71.
- [13] A. A. Coelho, *TOPAS-Academic*, **2007**.
- [14] R. W. Cheary, A. A. Coelho, *J. Appl. Crystallogr.* **1992**, 25, 109–121.
- [15] R. W. Cheary, A. A. Coelho, J. P. Cline, *J. Res. Natl. Inst. Stand. Technol.* **2007**, 109, 1–25.
- [16] Quantum Design, *MPMS MultiVu*, 1.56 Built 72 ed., **2005**.
- [17] M. Tegel, *Squid Processor*, 0.2 ed., **2010**.
- [18] A. Marchuk, W. Schnick, *Angew. Chem., Int. Ed.* **2015**, 54, 2383–2387; *Angew. Chem.* **2015**, 127, 2413–2417.
- [19] F. W. Karau, W. Schnick, *J. Solid State Chem.* **2005**, 178, 135–141.
- [20] K. Robinson, G. V. Gibbs, P. H. Ribbe, *Science* **1971**, 172, 567–570.
- [21] J. V. Smith, *Acta Crystallogr.* **1953**, 6, 613–620.
- [22] F. Liebau, *Structural Chemistry of Silicates: Structure, Bonding, and Classification*, Springer, Berlin, Germany, **1985**.

Appendix C. Supporting Information for Chapter 3

C.1 *bex*-La₂P₃N₇

Tables

Table C.1. Crystallographic information on *bex*-La₂P₃N₇.

Formula	La ₂ P ₃ N ₇
Formula mass / g · mol ⁻¹	468.80
Crystal system, space group	monoclinic, C2/c (no. 15)
Lattice parameters / Å, °	<i>a</i> = 7.8414(8)
	<i>b</i> = 10.3698(10)
	<i>c</i> = 7.8214(8)
	β = 111.116(4)
Cell volume / Å ³	593.27(10)
Formula units per cell <i>Z</i>	4
Calculated density / g · cm ⁻³	5.248(1)
F(000)	832
Absorption coefficient μ / cm ⁻¹	14.946
Radiation	Mo-K α_1 (λ = 70.9300 pm)
Monochromator	Ge(111)
Diffractionmeter	Stoe StadiP
Detector	MYTHEN 1K
2 θ -range / °	2–56
Temperature / K	297(2)
Data points	3618
Number of observed reflections	750
Number of parameters	61
Constraints	0
Program used	TOPAS Academic
Structure refinement	Rietveld method
Profile function	Fundamental parameters model
Background function	Shifted Chebychev
R_{Bragg}	0.0404

Table C.2. Sites, positions and isotropic displacement parameters of *bex*-La₂P₃N₇, standard deviations in parentheses.

Atom	Wyckoff site	<i>x</i>	<i>y</i>	<i>z</i>	$U_{\text{iso}} / \text{\AA}^2$	Occupancy
La1	8 <i>f</i>	0.2289(4)	0.0421(3)	0.4810(4)	0.0088(9)	1
P1	4 <i>e</i>	0	0.7377(19)	1/4	0.009(4)	1
P2	8 <i>f</i>	0.123(2)	0.2728(12)	0.146(2)	0.016(3)	1
N1	4 <i>e</i>	0	0.342(4)	1/4	0.0063	1
N2	8 <i>f</i>	0.473(5)	0.150(4)	0.074(5)	0.0063	1
N3	8 <i>f</i>	0.319(5)	0.340(4)	0.238(5)	0.0063	1

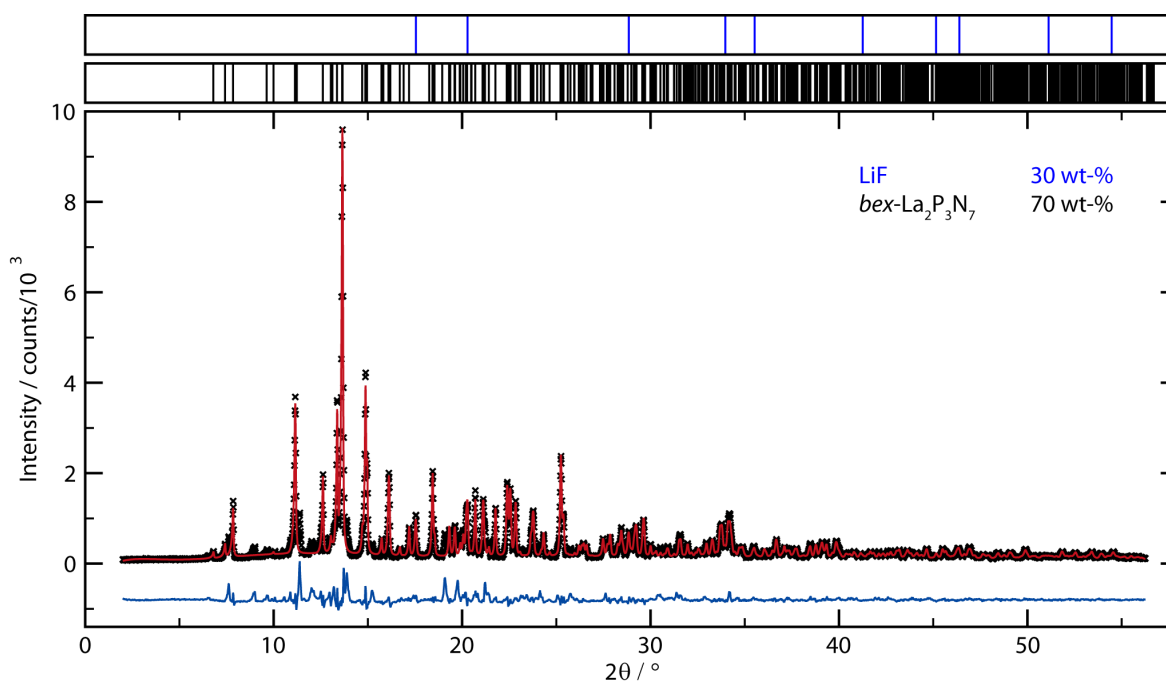
Table C.3. Bond lengths (Å) occurring in *bex*-La₂P₂N₇, standard deviations in parentheses.

La1–N4	2.56(4)	La1–N1	2.677(19)	P2–N1	1.64(2)
La1–N4	2.58(4)	La1–N3	2.66(4)	P2–N3	1.60(4)
La1–N2	2.76(4)	P1–N2	1.60(4)	P2–N4	1.60(3)
La1–N2	2.68(4)	P1–N3	1.75(4)	P2–N2	1.80(4)
La1–N4	2.51(4)	P1–N2	1.60(4)		
La1–N3	2.64(4)	P1–N3	1.75(4)		

Table C.4. Bond angles (°) occurring in *bex*-La₂P₂N₇, standard deviations in parentheses.

N–P–N		P–N–P			
N2–P1–N3	116.5(19)	N1–P2–N3	103.2(18)	P2–N1–P2	128(3)
N2–P1–N2	111(2)	N1–P2–N4	112(2)	P1–N2–P2	117(3)
N2–P1–N3	104.4(19)	N1–P2–N2	99.3(17)	P1–N3–P2	113(2)
N2–P1–N3	104(2)	N3–P2–N4	120(2)		
N3–P1–N3	105(2)	N2–P2–N3	104(2)		
N2–P1–N3	116.3(19)	N2–P2–N4	116(2)		

Rietveld Plot

**Figure C.1.** Rietveld plot of *bex*-La₂P₃N₇. Measured data is plotted as small black crosses, calculated model as the red line, difference plot as the blue line on the bottom; theoretical Bragg positions are located as vertical bars above the Rietveld plot. The difference profile shows an unidentified byproduct.

C.2 *bex*-Ce₂P₃N₇

Tables

Table C.5. Crystallographic information on *bex*-Ce₂P₃N₇.

Formula	Ce ₂ P ₃ N ₇
Crystal system	monoclinic
Space group	C2/c (no. 15)
Cell parameters / Å, °	$a = 7.8008(16)$ $b = 10.265(2)$ $c = 7.7868(16)$ $\beta = 111.08(3)$
Cell Volume / Å ³	581.8(2)
Formula units per unit cell Z	4
Formula mass / g·mol ⁻¹	471.22
Calculated density / g·cm ⁻³	5.380
Absorption coefficient μ / mm ⁻¹	16.203
Diffractometer	Stoe IPDS 1
Radiation	Mo-K α ($\lambda = 71.073$ pm)
Temperature \ K	293(2)
F(000)	840
θ range \ °	$3.741 \leq \theta \leq 32.519$
Total no. of reflections	4345
Independent reflections	1051
Refined parameters	56
Goodness of fit	1.204
R_{intr} R_{sigma}	0.0263, 0.0172
R_1 (all data), $R_1 [F^2 > 2\sigma(F^2)]$	0.0226, 0.0189
wR_2 (all data), $wR_2 [F^2 > 2\sigma(F^2)]$	0.0417, 0.0410
$\Delta\rho_{\text{max}}$ $\Delta\rho_{\text{min}}$ / e·Å ⁻³	1.201, -2.125

Table C.6. Sites, positions and isotropic displacement parameters of *bex*-Ce₂P₃N₇, standard deviations in parentheses.

Atom	Wyckoff Symbol	x	y	z	U _{iso} / Å ²	Occupancy
Ce1	8f	0.22642(2)	0.04233(2)	0.47871(2)	0.00589(6)	1
P1	4e	0	0.74318(10)	1/4	0.00496(17)	1
P2	8f	0.11411(9)	0.27395(8)	0.13412(10)	0.00485(12)	1
N1	4e	0	0.3475(4)	1/4	0.0078(6)	1
N2	8f	0.1069(3)	0.1198(3)	0.1349(3)	0.0064(4)	1
N3	8f	0.3235(3)	0.3387(2)	0.2295(3)	0.0059(4)	1
N4	8f	0.4716(3)	0.1505(2)	0.0697(3)	0.0061(4)	1

Table C.7. Anisotropic displacement parameters occurring in *bex*-Ce₂P₂N₇, standard deviations in parentheses.

Atom	$U_{11} / \text{Å}^2$	$U_{22} / \text{Å}^2$	$U_{33} / \text{Å}^2$	$U_{12} / \text{Å}^2$	$U_{13} / \text{Å}^2$	$U_{23} / \text{Å}^2$
Ce1	0.00642(8)	0.00570(8)	0.00557(8)	-0.00015(5)	0.00218(6)	-0.00010(5)
P1	0.0050(4)	0.0055(4)	0.0039(4)	0	0.0011(3)	0
P2	0.0052(3)	0.0050(3)	0.0042(3)	-0.0002(2)	0.0015(2)	0.0000(2)
N1	0.0105(13)	0.0066(15)	0.0079(13)	0	0.0054(12)	0
N2	0.0076(9)	0.0052(10)	0.0063(9)	-0.0004(8)	0.0024(7)	0.0000(8)
N3	0.0054(9)	0.0048(10)	0.0075(9)	-0.0001(8)	0.0024(8)	0.0000(7)
N4	0.0083(9)	0.0058(10)	0.0037(9)	-0.0002(8)	0.0017(7)	0.0006(7)

Table C.8. Bond lengths (Å) occurring in *bex*-Ce₂P₂N₇, standard deviations in parentheses.

Ce1–N2	2.436(2)	P1–N4	1.643(2)	N1–Ce1	2.6559(18)
Ce1–N2	2.554(2)	P1–N4	1.643(2)	N1–Ce1	2.6559(18)
Ce1–N3	2.587(3)	P1–N3	1.651(2)	N2–Ce1	2.436(2)
Ce1–N2	2.622(3)	P1–N3	1.651(2)	N2–Ce1	2.554(2)
Ce1–N1	2.6559(18)	P2–N2	1.583(3)	N3–P1	1.651(2)
Ce1–N4	2.665(2)	P2–N1	1.6595(19)	N3–Ce1	2.587(3)
Ce1–N3	2.728(2)	P2–N3	1.670(2)	N3–Ce1	2.728(2)
Ce1–N4	2.750(2)	P2–N4	1.674(2)	N4–P1	1.643(2)
Ce1–P2	3.2703(9)	P2–Ce1	3.2703(9)	N4–P2	1.674(2)
Ce1–P2	3.3905(11)	P2–Ce1	3.3905(11)	N4–Ce1	2.665(2)
Ce1–P2	3.3963(10)	P2–Ce1	3.3963(10)	N4–Ce1	2.750(2)
Ce1–Ce1	3.7664(8)	N1–P2	1.6596(19)		

Table C.9. Bond angles (°) occurring in *bex*-Ce₂P₂N₇, standard deviations in parentheses.

N–P–N		P–N–P			
N4–P1–N4	109.28(18)	N2–P2–N1	115.18(15)	P2–N1–P2	125.9(2)
N4–P1–N3	106.14(12)	N2–P2–N3	115.25(13)	P1–N3–P2	117.06(15)
N4–P1–N3	114.18(12)	N1–P2–N3	101.96(11)	P1–N4–P2	115.29(15)
N4–P1–N3	114.18(12)	N2–P2–N4	117.62(13)		
N4–P1–N3	106.14(12)	N1–P2–N4	101.28(12)		
N3–P1–N3	107.11(18)	N3–P2–N4	103.33(12)		

Rietveld Plot

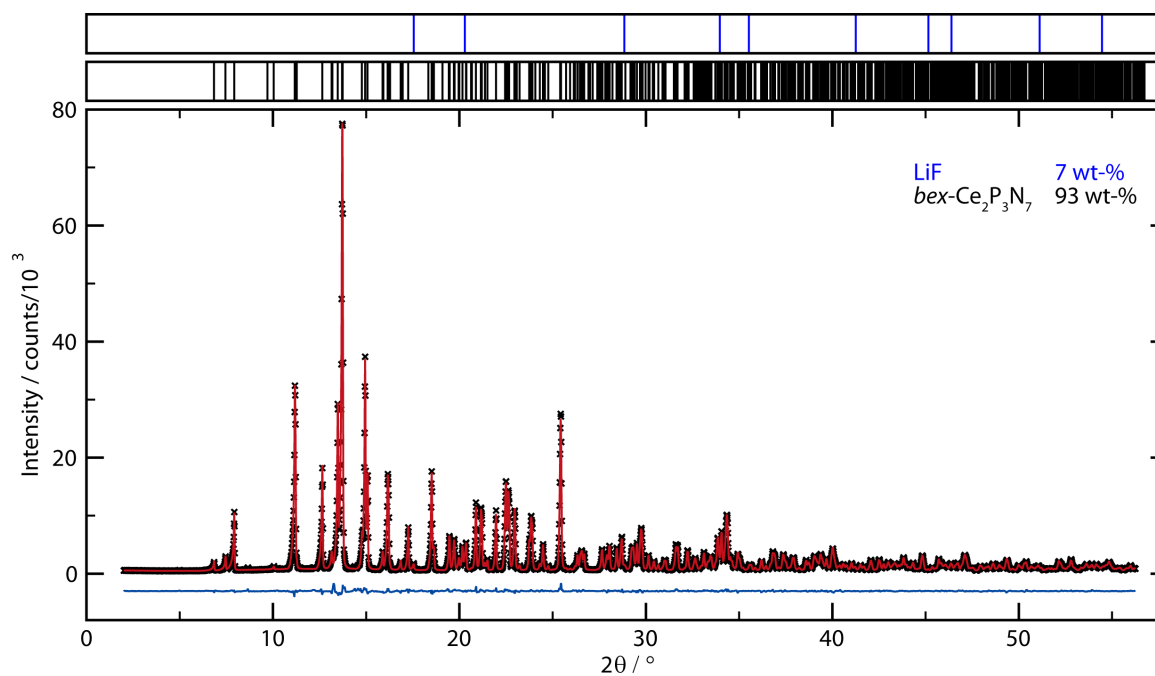


Figure C.2. Rietveld plot of $bex\text{-Ce}_2\text{P}_3\text{N}_7$. Measured data is plotted as small black crosses, calculated model as the red line, difference plot as the blue line on the bottom; theoretical Bragg positions are located as vertical bars of respective phase color above the Rietveld plot.

Table C.10. Crystallographic information for the Rietveld refinement of *bex*-Ce₂P₂N₇.

Formula	Ce ₂ P ₃ N ₇
Formula mass / g · mol ⁻¹	471.22
Crystal system / space group	monoclinic, C2/c (no. 15)
	<i>a</i> = 7.81724(8)
	<i>b</i> = 10.26970(9)
Lattice parameters / Å, °	<i>c</i> = 7.79472(7)
	β = 111.1896(6)
Cell volume / Å ³	583.457(10)
Formula units per cell <i>Z</i>	4
Calculated density / g · cm ⁻³	5.365
F(000)	832
Absorption coefficient μ / cm ⁻¹	16.157
Radiation	Mo-K α_1 (λ = 70.9300 pm)
Monochromator	Ge(111)
Diffractometer	Stoe StadiP
Detector	MYTHEN 1K
2 θ -range / °	2–56
Temperature / K	297(2)
Data points	3618
Number of observed reflections	736
Number of parameters	65
Constraints	0
Program used	TOPAS Academic
Structure refinement	Rietveld method
Profile function	Fundamental parameters model
Background function	Shifted Chebychev
R_{wp}	0.04951
R_{exp}	0.02214
R_p	0.03335
R_{Bragg}	0.01530
χ^2	2.236

C.3 *bex-Pr₂P₃N₇*

Tables

Table C.11. Sites, positions and isotropic displacement parameters of *bex-Pr₂P₂N₇*, standard deviations in parentheses.

Atom	Wyckoff Symbol	<i>x</i>	<i>y</i>	<i>z</i>	<i>U</i> _{iso} / Å ²	Occupancy
Pr1	8 <i>f</i>	0.22579(2)	0.04123(2)	0.47877(2)	0.00412(3)	1
P1	4 <i>e</i>	0	0.74283(6)	1/4	0.00278(9)	1
P2	8 <i>f</i>	0.11384(6)	0.27433(4)	0.13422(6)	0.00310(7)	1
N1	4 <i>e</i>	0	0.34835(19)	1/4	0.0047(3)	1
N2	8 <i>f</i>	0.4723(2)	0.14938(13)	0.07005(19)	0.00430(19)	1
N3	8 <i>f</i>	0.32359(19)	0.33926(14)	0.2294(2)	0.00432(19)	1
N4	8 <i>f</i>	0.1063(2)	0.12017(14)	0.1350(2)	0.0052(2)	1

Table C.12. Anisotropic displacement parameters occurring in *bex-Pr₂P₂N₇*, standard deviations in parentheses.

Atom	<i>U</i> ₁₁ / Å ²	<i>U</i> ₂₂ / Å ²	<i>U</i> ₃₃ / Å ²	<i>U</i> ₁₂ / Å ²	<i>U</i> ₁₃ / Å ²	<i>U</i> ₂₃ / Å ²
Pr1	0.00426(5)	0.00386(5)	0.00430(5)	-0.00007(2)	0.00163(3)	-0.00008(2)
P1	0.00284(19)	0.0034(2)	0.00215(19)	0	0.00103(16)	0
P2	0.00313(14)	0.00334(14)	0.00290(14)	-0.00003(11)	0.00120(12)	-0.00014(11)
N1	0.0061(7)	0.0039(7)	0.0054(7)	0	0.0038(6)	0
N2	0.0059(5)	0.0041(5)	0.0027(4)	-0.0001(4)	0.0012(4)	0.0004(4)
N3	0.0027(4)	0.0044(5)	0.0052(5)	-0.0003(4)	0.0007(4)	0.0002(4)
N4	0.0059(5)	0.0040(5)	0.0062(5)	-0.0003(4)	0.0026(4)	0.0000(4)

Table C.13. Bond lengths (Å) occurring in *bex-Pr₂P₂N₇*, standard deviations in parentheses.

Pr1–N4	2.4274(14)	Pr1–Pr1	3.7515(2)	N1–P2	1.6594(10)
Pr1–N4	2.5455(15)	P1–N2	1.6430(14)	N1–Pr1	2.6501(9)
Pr1–N3	2.5652(14)	P1–N3	1.6525(14)	N2–P1	1.6430(14)
Pr1–N4	2.6192(15)	P1–N3	1.6525(14)	N2–P2	1.6761(14)
Pr1–N2	2.6467(14)	P2–N4	1.5770(15)	N2–Pr1	2.6467(14)
Pr1–N1	2.6501(9)	P2–N1	1.6594(10)	N2–Pr1	2.7503(14)
Pr1–N3	2.7260(14)	P2–N3	1.6691(14)	N3–P1	1.6525(14)
Pr1–N2	2.7503(14)	P2–N2	1.6761(14)	N3–Pr1	2.5652(14)
Pr1–P2	3.2527(4)	P2–Pr1	3.2527(4)	N3–Pr1	2.7260(14)
Pr1–P2	3.3836(4)	P2–Pr1	3.3835(4)	N4–Pr1	2.4274(14)
Pr1–P2	3.3942(4)	P2–Pr1	3.3942(4)	N4–Pr1	2.5455(15)

Table C.14. Bond angles ($^{\circ}$) occurring in *bex*-Pr₂P₂N₇, standard deviations in parentheses.

N–P–N				P–N–P	
N2–P1–N2	108.89(10)	N4–P2–N1	115.17(8)	P2–N1–P2	125.74(13)
N2–P1–N3	106.07(7)	N4–P2–N3	115.31(8)	P1–N2–P2	114.88(8)
N2–P1–N3	114.64(7)	N1–P2–N3	102.10(6)	P1–N3–P2	116.97(9)
N2–P1–N3	114.64(7)	N4–P2–N2	117.78(8)		
N2–P1–N3	106.07(7)	N1–P2–N2	101.15(6)		
N3–P1–N3	106.76(10)	N3–P2–N2	103.07(7)		

Rietveld Plot

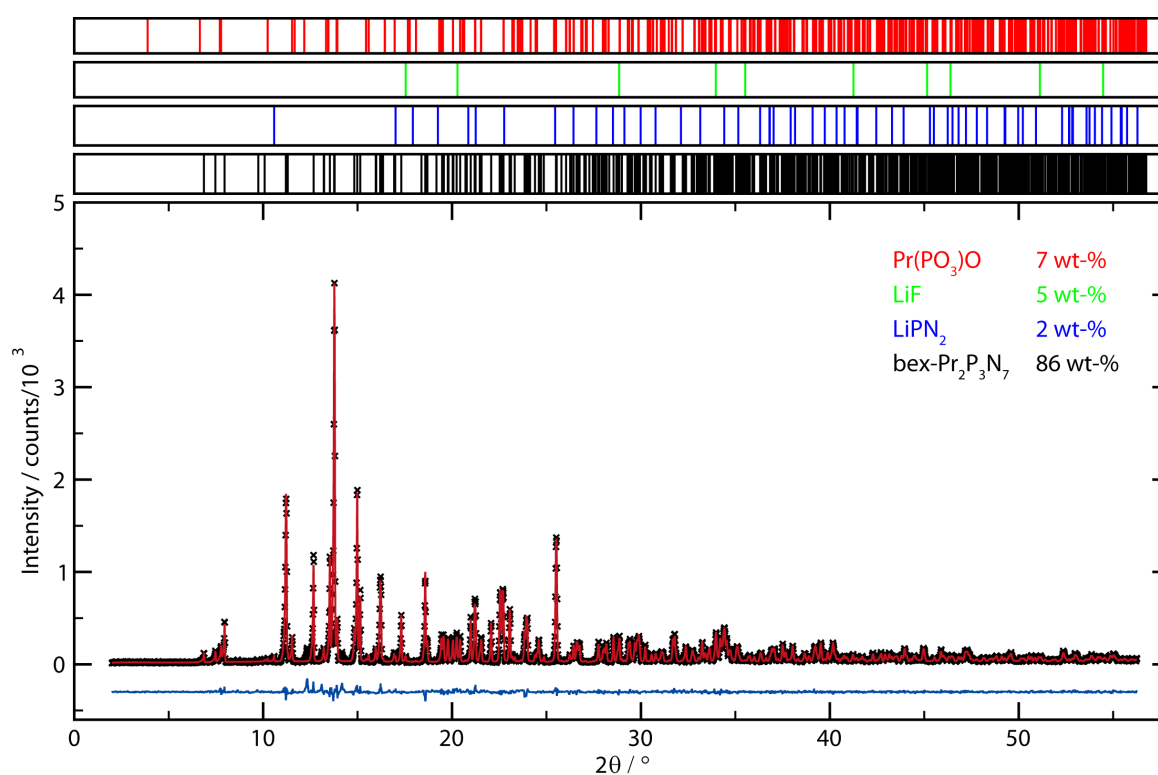


Figure C.3. Rietveld plot of *bex*-Pr₂P₃N₇. Measured data is plotted as small black crosses, calculated model as the red line, difference plot as the blue line on the bottom; theoretical Bragg positions are located as vertical bars of respective phase color above the Rietveld plot. LiPN₂ is unreacted starting material. The byproduct Pr(PO₃)O can be traced back to side reactions with the boron nitride crucible, which slowly hydrolyses in air to boric acid.

Table C.15. Crystallographic information on the Rietveld refinement of *bex*-Pr₂P₂N₇.

Formula	Pr ₂ P ₃ N ₇
Formula mass / g · mol ⁻¹	472.80
Crystal system / space group	monoclinic, C2/c (no. 15)
Lattice parameters / Å, °	$a = 7.79638(16)$ $b = 10.2156(2)$ $c = 7.77530(15)$ $\beta = 111.2965(12)$
Cell volume / Å ³	576.97(2)
Formula units per cell Z	4
Calculated density / g · cm ⁻³	5.443
F(000)	848
Absorption coefficient μ / cm ⁻¹	17.448
Radiation	Mo-K α_1 ($\lambda = 70.9300$ pm)
Monochromator	Ge(111)
Diffractometer	Stoe StadiP
Detector	MYTHEN 1K
2 θ -range / °	2–56
Temperature / K	297(2)
Data points	3618
Number of observed reflections	728
Number of parameters	91
Constraints	0
Program used	TOPAS Academic
Structure refinement	Rietveld method
Profile function	Fundamental parameters model
Background function	Shifted Chebychev
R_{wp}	0.12186
R_{exp}	0.10117
R_p	0.08076
R_{Bragg}	0.02789
χ^2	1.204

Infrared Spectroscopy

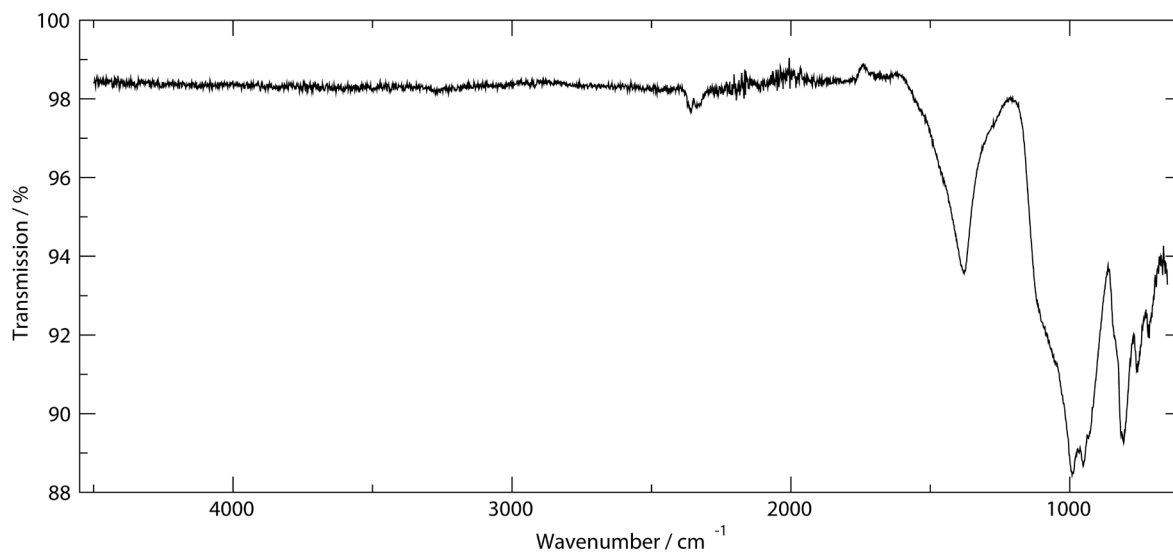


Figure C.4. IR spectrum of *bex*-Pr₂P₃N₇ obtained in ATR geometry.

High-temperature powder X-ray diffraction

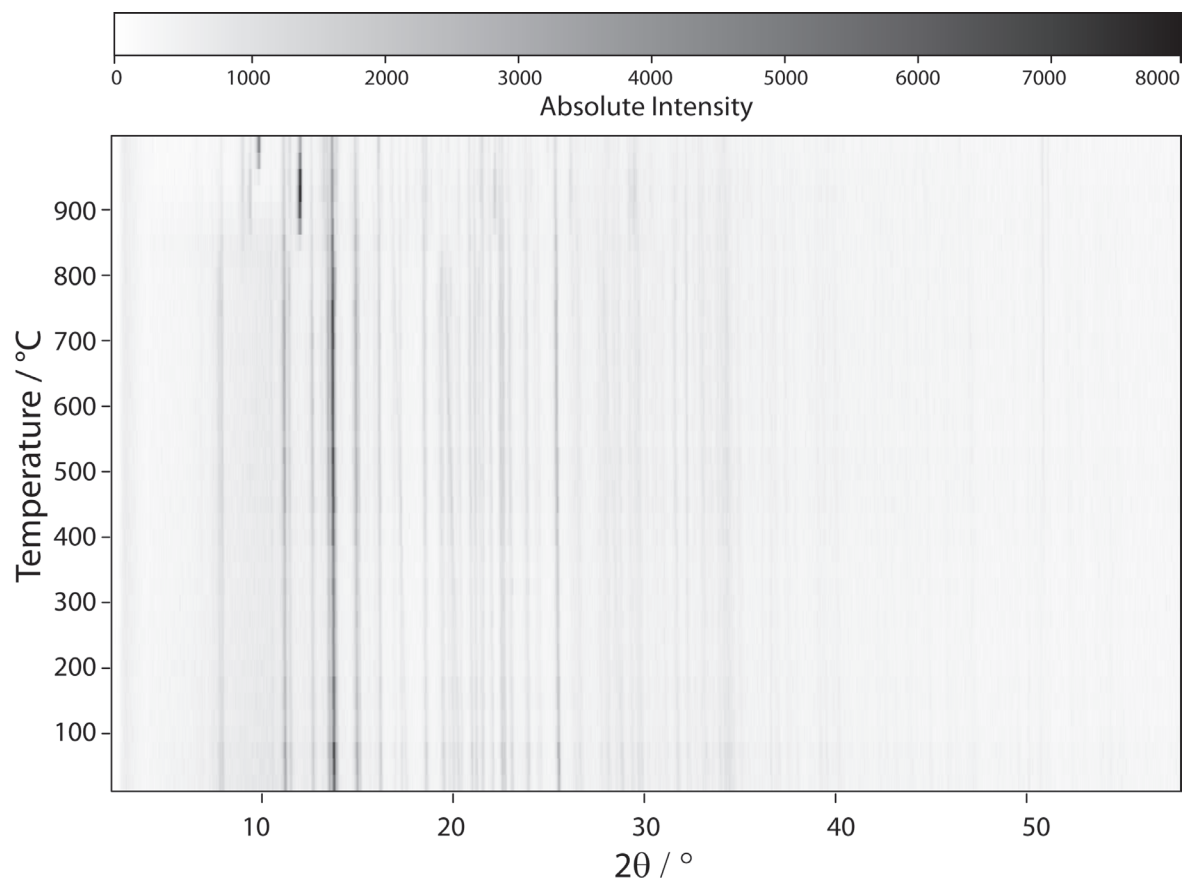


Figure C.5. Temperature Programmed PXRD of a *bex*-Pr₂P₃N₇ sample.

EDX**Table C.16.** EDX measurement on a single crystal of *bex*-Pr₂P₂N₇.

Atom	Theory / at-%	Experiment / at-%
Pr	16.7	20
P	25	26
N	58.3	52
O	0	0

C.4 *mcm*-Pr₂P₃N₇

Tables

Table C.17. Crystallographic information on *mcm*-Pr₂P₃N₇.

Formula	Pr ₂ P ₃ N ₇
Formula mass / g · mol ⁻¹	472.80
Crystal system / space group	tetragonal, $P\bar{4}2_1m$ (no. 113)
Lattice parameters / Å	a = 7.4915(7) c = 5.1880(7)
Cell volume / Å ³	291.16(8)
Formula units per cell Z	2
Calculated density / g · cm ⁻³	5.393(1)
F(000)	440
Absorption coefficient μ / cm ⁻¹	17.288
Radiation	Mo-K α_1 (λ = 70.9300 pm)
Monochromator	Ge(111)
Diffractometer	Stoe StadiP
Detector	MYTHEN 1K
2 θ -range / °	2–56
Temperature / K	297(2)
Data points	3618
Number of observed reflections	249
Number of parameters	40
Constraints	0
Program used	TOPAS Academic
Structure refinement	Rietveld method
Profile function	Fundamental parameters model
Background function	Shifted Chebychev
R_{Bragg}	0.025056

Table C.18. Sites, positions and isotropic displacement parameters of *mcm*-Pr₂P₃N₇, standard deviations in parentheses.

Atom	Wyckoff Symbol	x	y	z	U _{iso} / Å ²	Occupancy
Pr1	4e	0.1652(5)	0.6652(5)	0.506(2)	0.0017	1
P1	4e	0.6386(18)	0.1386(18)	0.946(8)	0.0101	1
P2	2a	0	0	0	0.0051	1
N1	2c	0	1/2	0.17(2)	0.0118	1
N2	4e	0.646(8)	0.146(8)	0.25(2)	0.0132	1
N3	8f	0.078(13)	0.165(4)	0.186(6)	0.0043	1

Table C.19. Bond lengths (Å) occurring in *bex*-Pr₂P₂N₇, standard deviations in parentheses.

Pr1–N1	2.47(7)	Pr1–N2	2.40(8)	P1–N3	1.69(4)
Pr1–N2	2.66(7)	Pr1–N2	2.66(7)	P1–N3	1.69(4)
Pr1–N3	2.50(8)	Pr1–N3	2.77(7)	P2–N3	1.67(5)
Pr1–Pr1	3.501(5)	Pr1–N3	2.50(8)	P2–N3	1.67(4)
Pr1–N3	2.77(7)	P1–N2	1.58(11)	P2–N3	1.67(4)
Pr1–P1	3.09(3)	P1–N1	1.59(4)	P2–N3	1.67(5)

Table C.20. Bond angles (°) occurring in *mcm*-Pr₂P₂N₇, standard deviations in parentheses.

N–P–N		P–N–P	
N1–P1–N2	115(4)	N3–P2–N3	109(4)
N2–P1–N3	113(3)	N3–P2–N3	109.6(18)
N2–P1–N3	113(3)	N3–P2–N3	109(4)
N1–P1–N3	104(4)	N3–P2–N3	109(4)
N1–P1–N3	104(4)	N3–P2–N3	109.6(19)
N3–P1–N3	108(4)	N3–P2–N3	109(4)
		P1–N1–P1	135(7)
		P1–N3–P2	120(2)

Rietveld Plot

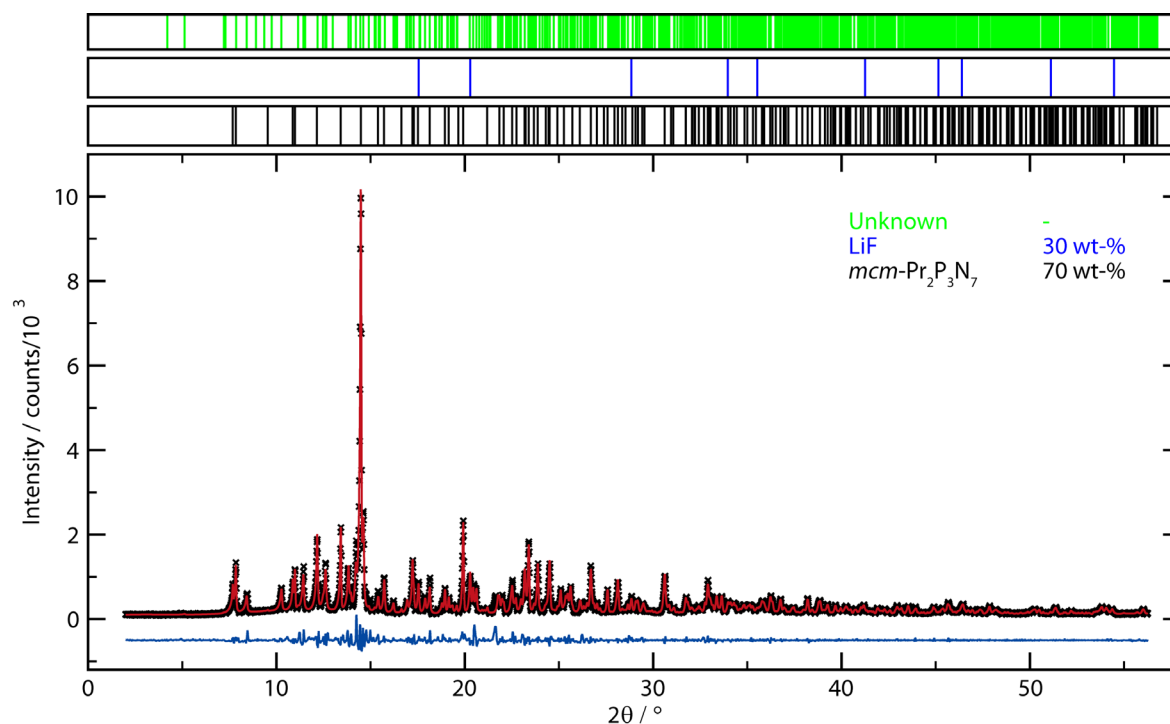


Figure C.6. Rietveld plot of $mcm\text{-Pr}_2\text{P}_3\text{N}_7$. Measured data is plotted as small black crosses, calculated model as the red line, difference plot as the blue line on the bottom; theoretical Bragg positions are located as vertical bars of respective phase color above the Rietveld plot. An yet unidentified byproduct complicates structure refinement. A preliminary hexagonal unit cell ($a = 11.153(3) \text{ \AA}$, $c = 13.881(1) \text{ \AA}$) was indexed from the difference plot but. Structure solution was not possible since the phase only occurred as a minor side phase.

C.5 *mcm*-Nd₂P₃N₇

Tables

Table C.21. Crystallographic information on *mcm*-Nd₂P₂N₇.

Formula	Nd ₂ P ₃ N ₇
Formula mass / g · mol ⁻¹	479.46
Crystal system, space group	tetragonal, $P4_2/m$ (no. 113)
Lattice parameters / Å	$a = 7.4642(3)$ $c = 5.1654(3)$
Cell volume / Å ³	287.78(3)
Formula units per cell Z	2
Calculated density / g · cm ⁻³	5.53295(59)
F(000)	444
Absorption coefficient μ / cm ⁻¹	18.603
Radiation	Mo-K α_1 ($\lambda = 70.9300$ pm)
Monochromator	Ge(111)
Diffractionmeter	Stoe StadiP
Detector	MYTHEN 1K
2 θ -range / °	2–56
Temperature / K	297(2)
Data points	3618
Number of observed reflections	242
Number of parameters	56
Constraints	0
Program used	TOPAS Academic
Structure refinement	Rietveld method
Profile function	Fundamental parameters model
Background function	Shifted Chebychev
R_{Bragg}	0.036074

Table C.22. Sites, positions and isotropic displacement parameters of *mcm*-Nd₂P₂N₇, standard deviations in parentheses.

Atom	Wyckoff Symbol	x	y	z	$U_{\text{iso}} / \text{Å}^2$	Occupancy
Nd1	4e	0.1630(2)	0.6630(2)	0.5089(11)	0.0039(8)	1
P1	4e	0.6430(11)	0.1430(11)	0.967(4)	0.012(4)	1
P2	2a	0	0	0	0.007(4)	1
N1	2c	0	1/2	0.180(10)	0.0063	1
N2	4e	0.643(4)	0.143(4)	0.272(6)	0.0063	1
N3	8f	0.083(3)	0.153(4)	0.185(5)	0.0063	1

Table C.23. Bond lengths (Å) occurring in *mcm*-Nd₂P₂N₇, standard deviations in parentheses.

Nd1–N1	2.42(4)	Nd1–N2	2.39(3)	P1–N3	1.77(3)
Nd1–N2	2.55(3)	Nd1–N2	2.55(3)	P1–N3	1.77(3)
Nd1–N3	2.48(2)	Nd1–N3	2.83(3)	P2–N3	1.61(3)
Nd1–Nd1	3.441(2)	Nd1–N3	2.48(2)	P2–N3	1.61(3)
Nd1–N3	2.84(3)	P1–N2	1.58(4)	P2–N3	1.61(3)
Nd1–P1	3.129(17)	P1–N1	1.69(3)	P2–N3	1.61(3)

Table C.24. Bond angles (°) occurring in *mcm*-Nd₂P₂N₇, standard deviations in parentheses.

N–P–N		P–N–P			
N1–P1–N2	117(2)	N3–P2–N3	110.6(12)	P1–N1–P1	127(3)
N2–P1–N3	116.3(16)	N3–P2–N3	107.3(13)	P1–N3–P2	116.3(16)
N2–P1–N3	116.3(16)	N3–P2–N3	110.6(12)		
N1–P1–N3	100.6(15)	N3–P2–N3	110.6(13)		
N1–P1–N3	100.6(15)	N3–P2–N3	107.3(14)		
N3–P1–N3	103.8(14)	N3–P2–N3	110.6(13)		

Rietveld Plot

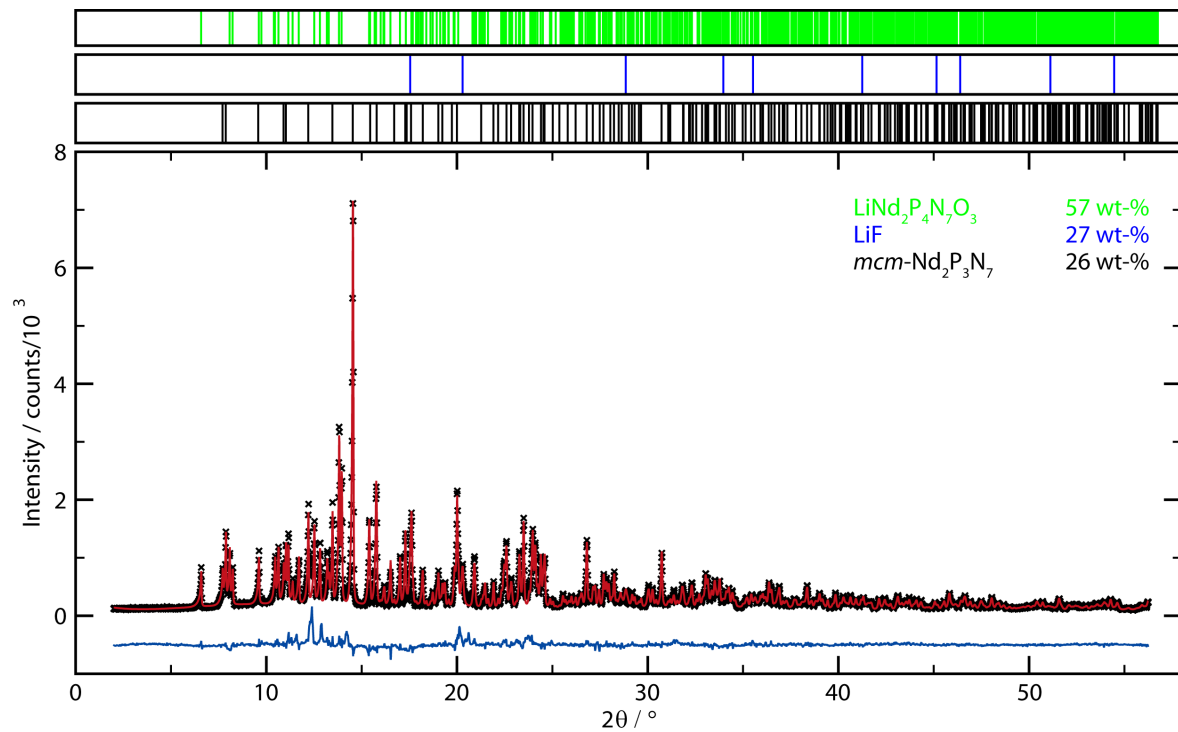


Figure C.7. Rietveld plot of $mcm\text{-Nd}_2\text{P}_3\text{N}_7$. Measured data is plotted as small black crosses, calculated model as the red line, difference plot as the blue line on the bottom; theoretical Bragg positions are located as vertical bars of respective phase color above the Rietveld plot. The oxygen containing side product might form due to a side reaction with the boron nitride crucible, which slowly hydrolyses to boric acid in air.

C.6 *mcm*-Sm₂P₃N₇

Tables

Table C.25. Crystallographic information on *mcm*-Sm₂P₃N₇.

Formula	Sm ₂ P ₃ N ₇
Formula mass / g · mol ⁻¹	491.69
Crystal system, space group	tetragonal, $P4_2m$ (no. 113)
Lattice parameters / Å	$a = 7.42914(9)$ $c = 5.11099(9)$
Cell volume / Å ³	282.086(10)
Formula units per cell Z	2
Calculated density / g · cm ⁻³	5.78883
F(000)	448
Absorption coefficient μ / cm ⁻¹	21.389
Radiation	Mo-K α_1 ($\lambda = 70.9300$ pm)
Monochromator	Ge(111)
Diffractometer	Stoe StadiP
Detector	MYTHEN 1K
2 θ -range / °	2–56
Temperature / K	297(2)
Data points	3618
Number of observed reflections	242
Number of parameters	54
Constraints	1
Program used	TOPAS Academic
Structure refinement	Rietveld method
Profile function	Fundamental parameters model
Background function	Shifted Chebychev
R_{Bragg}	0.01747

Table C.26. Sites, positions and isotropic displacement parameters of *mcm*-Sm₂P₃N₇, standard deviations in parentheses.

Atom	Wyckoff Symbol	x	y	z	$U_{\text{iso}} / \text{Å}^2$	Occupancy
Sm1	4e	0.16259(11)	0.66259(11)	0.5080(5)	0.0035(4)	1
P1	4e	0.6415(5)	0.1415(5)	0.9703(18)	0.0051(16)	1
P2	2a	0	0	0	0.0041(16)	1
N1	2c	0	1/2	0.180(5)	0.002(2)	1
N2	4e	0.6410(18)	0.1410(18)	0.277(3)	0.002(2)	1
N3	8f	0.0802(17)	0.1651(19)	0.186(2)	0.002(2)	1

Table C.27. Bond lengths (Å) occurring in *mcm*-Sm₂P₂N₇, standard deviations in parentheses.

Sm1-N1	2.393(18)	Sm1-N2	2.377(14)	P1-N3	1.704(14)
Sm1-N2	2.514(14)	Sm1-N2	2.514(14)	P1-N3	1.704(14)
Sm1-N3	2.473(12)	Sm1-N3	2.757(12)	P2-N3	1.662(13)
Sm1-Sm1	3.4165(12)	Sm1-N3	2.473(12)	P2-N3	1.662(13)
Sm1-N3	2.757(12)	P1-N2	1.568(18)	P2-N3	1.662(13)
Sm1-P1	3.134(8)	P1-N1	1.673(13)	P2-N3	1.662(13)

Table C.28. Bond angles (°) occurring in *mcm*-Sm₂P₂N₇, standard deviations in parentheses.

N-P-N		P-N-P			
N1-P1-N2	117.1(10)	N3-P2-N3	109.1(6)	P1-N1-P1	125.4(16)
N2-P1-N3	117.9(7)	N3-P2-N3	110.2(6)	P1-N3-P2	116.7(7)
N2-P1-N3	117.9(7)	N3-P2-N3	109.1(6)		
N1-P1-N3	98.5(7)	N3-P2-N3	109.1(6)		
N1-P1-N3	98.5(7)	N3-P2-N3	110.2(6)		
N3-P1-N3	103.5(7)	N3-P2-N3	109.1(6)		

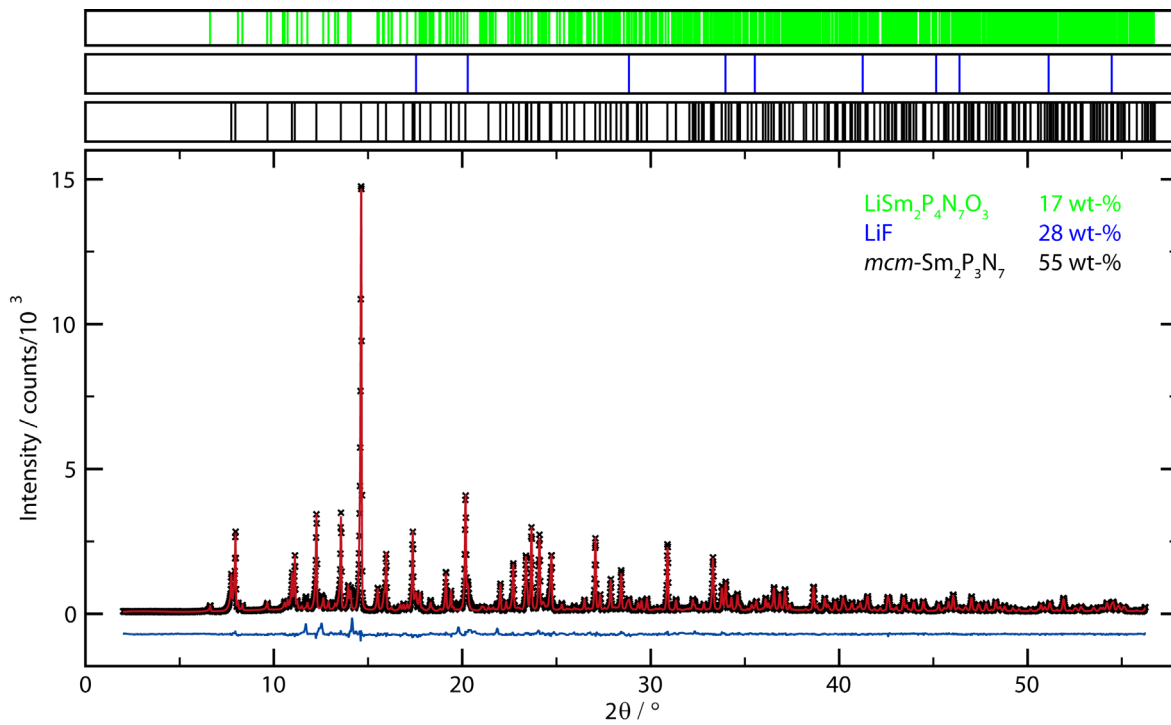
Rietveld Plot

Figure C.8. Rietveld plot of $mcm\text{-Sm}_2\text{P}_3\text{N}_7$. Measured data is plotted as small black crosses, calculated model as the red line, difference plot as the blue line on the bottom; theoretical Bragg positions are located as vertical bars of respective phase color above the Rietveld plot. The oxygen containing side product might form due to a side reaction with the boron nitride crucible, which slowly hydrolyses to boric acid in air.

C.7 *mcm*-Eu₂P₃N₇

Tables

Table C.29. Crystallographic information on *mcm*-Eu₂P₃N₇.

Formula	Eu ₂ P ₃ N ₇
Formula mass / g · mol ⁻¹	494.90
Crystal system, space group	tetragonal, $P4_2m$ (no. 113)
Lattice parameters / Å	$a = 7.4173(6)$ $c = 5.0899(4)$
Cell volume / Å ³	280.02(7)
Formula units per cell Z	2
Calculated density / g · cm ⁻³	5.86948
F(000)	452
Absorption coefficient μ / cm ⁻¹	22.975
Radiation	Mo-K α_1 ($\lambda = 70.9300$ pm)
Monochromator	Ge(111)
Diffractometer	Stoe StadiP
Detector	MYTHEN 1K
2 θ -range / °	2–56
Temperature / K	297(2)
Data points	3618
Number of observed reflections	238
Number of parameters	54
Constraints	0
Program used	TOPAS Academic
Structure refinement	Rietveld method Fundamental parameters
Profile function	model
Background function	Shifted Chebychev
R_{Bragg}	0.03536

Table C.30. Sites, positions and isotropic displacement parameters of *mcm*-Eu₂P₃N₇, standard deviations in parentheses.

Atom	Wyckoff Symbol	x	y	z	U _{iso} / Å ²	Occupancy
Eu1	4e	0.1624(2)	0.6624(2)	0.5080(12)	0.0080(8)	1
P1	4e	0.6436(12)	0.1436(12)	0.963(4)	0.016(4)	1
P2	2a	0	0	0	0.018(4)	1
N1	2c	0	1/2	0.153(10)	0.002(5)	1
N2	4e	0.631(4)	0.131(4)	0.272(7)	0.002(5)	1
N3	8f	0.067(4)	0.172(4)	0.189(5)	0.002(5)	1

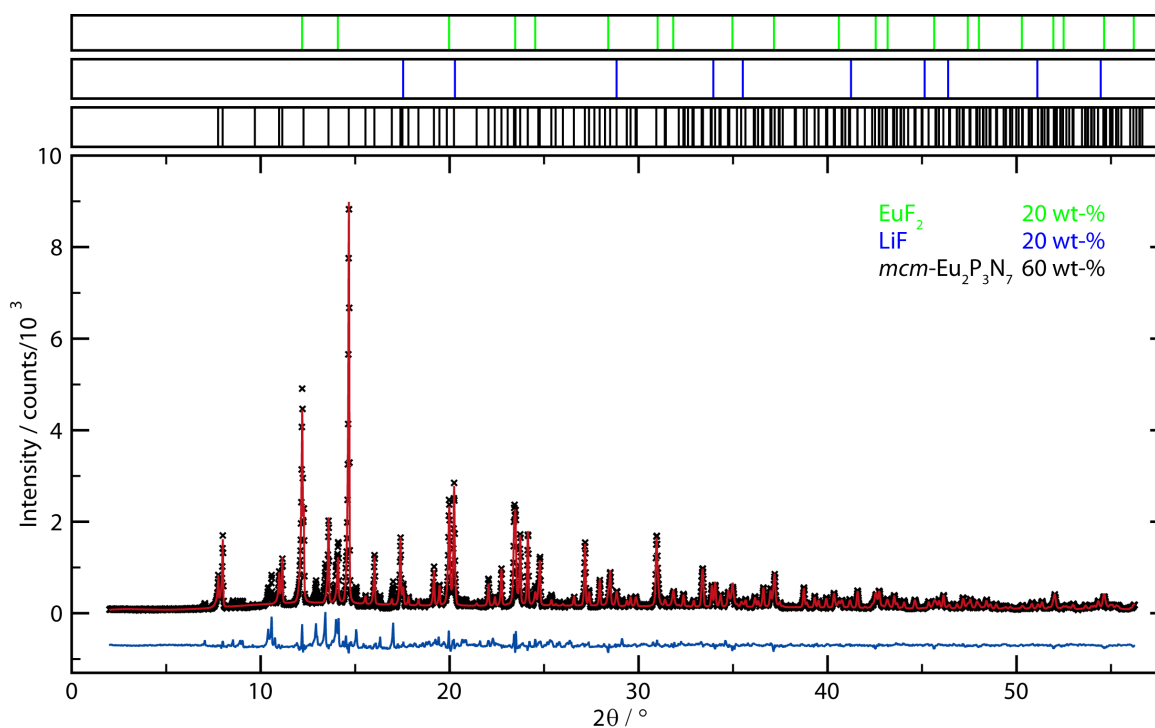
Table C.31. Bond lengths (Å) occurring in $mcm\text{-Eu}_2\text{P}_2\text{N}_7$, standard deviations in parentheses.

Eu1–N1	2.48(4)	Eu1–N3	2.65(3)	P1–N3	1.67(3)
Eu1–Eu1	3.931(2)	Eu1–N2	2.48(3)	P2–N3	1.67(3)
Eu1–P1	3.304(17)	Eu1–N3	2.65(3)	P2–N3	1.67(3)
Eu1–N2	2.46(3)	Eu1–N3	2.53(3)	P2–N3	1.67(3)
Eu1–N3	2.53(3)	P1–N2	1.58(4)		
Eu1–Eu1	3.407(2)	P1–N1	1.62(2)		

Table C.32. Bond angles (°) occurring in $mcm\text{-Eu}_2\text{P}_2\text{N}_7$, standard deviations in parentheses.

N–P–N		P–N–P	
N1–P1–N2	107(2)	N3–P2–N3	109.3(14)
N2–P1–N3	119.3(16)	N3–P2–N3	109.8(13)
N2–P1–N3	119.3(16)	N3–P2–N3	109.3(14)
N1–P1–N3	98.4(16)	N3–P2–N3	109.3(14)
N1–P1–N3	98.4(16)	N3–P2–N3	109.8(13)
N3–P1–N3	110.0(17)	N3–P2–N3	109.3(14)
		P1–N1–P1	137(3)
		P1–N3–P2	117.3(16)

Rietveld Plot

**Figure C.9.** Rietveld plot of $mcm\text{-Eu}_2\text{P}_3\text{N}_7$. Measured data is plotted as small black crosses, calculated model as the red line, difference plot as the blue line on the bottom; theoretical Bragg positions are located as vertical bars of respective phase color above the Rietveld plot. EuF_2 can form since the reaction conditions are highly reductive due to the presence of nitride.

C.8 *mcm*-Ho₂P₃N₇

Tables

Table C.33. Sites, positions and isotropic displacement parameters of *mcm*-Ho₂P₂N₇, standard deviations in parentheses.

Atom	Wyckoff Symbol	x	y	z	$U_{iso} / \text{\AA}^2$	Occupancy
Ho1	4e	0.16107(2)	0.66107(2)	0.50948(7)	0.00446(6)	1
P1	2a	0	0	0	0.0034(3)	1
P2	4e	0.64200(13)	0.14200(14)	0.9678(3)	0.0033(3)	1
N1	2c	0	1/2	0.1730(15)	0.0053(12)	1
N2	4e	0.6425(5)	0.1425(5)	0.2820(10)	0.0051(9)	1
N3	8f	0.0830(5)	0.1643(5)	0.1886(7)	0.0053(6)	1

Table C.34. Anisotropic displacement parameters occurring in *mcm*-Ho₂P₂N₇, standard deviations in parentheses.

Atom	$U_{11} / \text{\AA}^2$	$U_{22} / \text{\AA}^2$	$U_{33} / \text{\AA}^2$	$U_{12} / \text{\AA}^2$	$U_{13} / \text{\AA}^2$	$U_{23} / \text{\AA}^2$
Ho1	0.00420(6)	0.00420(6)	0.00497(10)	-0.00029(9)	-0.00029(9)	-0.00088(8)
P1	0.0030(4)	0.0030(4)	0.0042(7)	0	0	0
P2	0.0031(3)	0.0031(3)	0.0038(7)	-0.0002(4)	-0.0002(4)	0.0002(4)
N1	0.0041(18)	0.0041(18)	0.008(3)	0	0	0.003(3)
N2	0.0052(14)	0.0052(14)	0.005(2)	-0.0011(12)	-0.0011(12)	-0.0002(19)
N3	0.0078(15)	0.0033(13)	0.0046(14)	0.0003(14)	-0.0005(11)	-0.0020(13)

Table C.35. Bond lengths (Å) occurring in *mcm*-Ho₂P₂N₇, standard deviations in parentheses.

Ho1–N2	2.339(5)	Ho1–Ho1	3.3526(5)	P2–Ho1	3.2688(15)
Ho1–N1	2.375(5)	P1–N3	1.651(4)	N1–P2	1.637(4)
Ho1–N3	2.414(4)	P1–N3	1.651(4)	N1–P2	1.637(4)
Ho1–N3	2.414(4)	P1–N3	1.651(4)	N1–Ho1	2.375(5)
Ho1–N2	2.469(4)	P1–N3	1.651(4)	N2–P2	1.570(5)
Ho1–N2	2.469(4)	P2–N2	1.570(5)	N2–Ho1	2.339(5)
Ho1–N3	2.729(4)	P2–N1	1.637(4)	N2–Ho1	2.469(4)
Ho1–N3	2.729(4)	P2–N3	1.683(4)	N2–Ho1	2.469(4)
Ho1–P2	3.0738(14)	P2–N3	1.683(4)	N3–P2	1.683(4)
Ho1–P2	3.2688(15)	P2–Ho1	3.0738(14)	N3–Ho1	2.414(4)
Ho1–P2	3.2688(15)	P2–Ho1	3.2688(15)	N3–Ho1	2.729(4)

Table C.36. Bond angles (°) occurring in $mcm\text{-Ho}_2\text{P}_2\text{N}_7$, standard deviations in parentheses.

N-P-N				P-N-P	
N3-P1-N3	109.05(13)	N2-P2-N1	115.7(3)	P2-N1-P2	129.1(5)
N3-P1-N3	110.3(3)	N2-P2-N3	117.59(17)	P1-N3-P2	116.8(2)
N3-P1-N3	109.05(13)	N1-P2-N3	100.1(2)		
N3-P1-N3	109.05(13)	N2-P2-N3	117.59(17)		
N3-P1-N3	110.3(3)	N1-P2-N3	100.1(2)		
N3-P1-N3	109.05(13)	N3-P2-N3	102.8(3)		

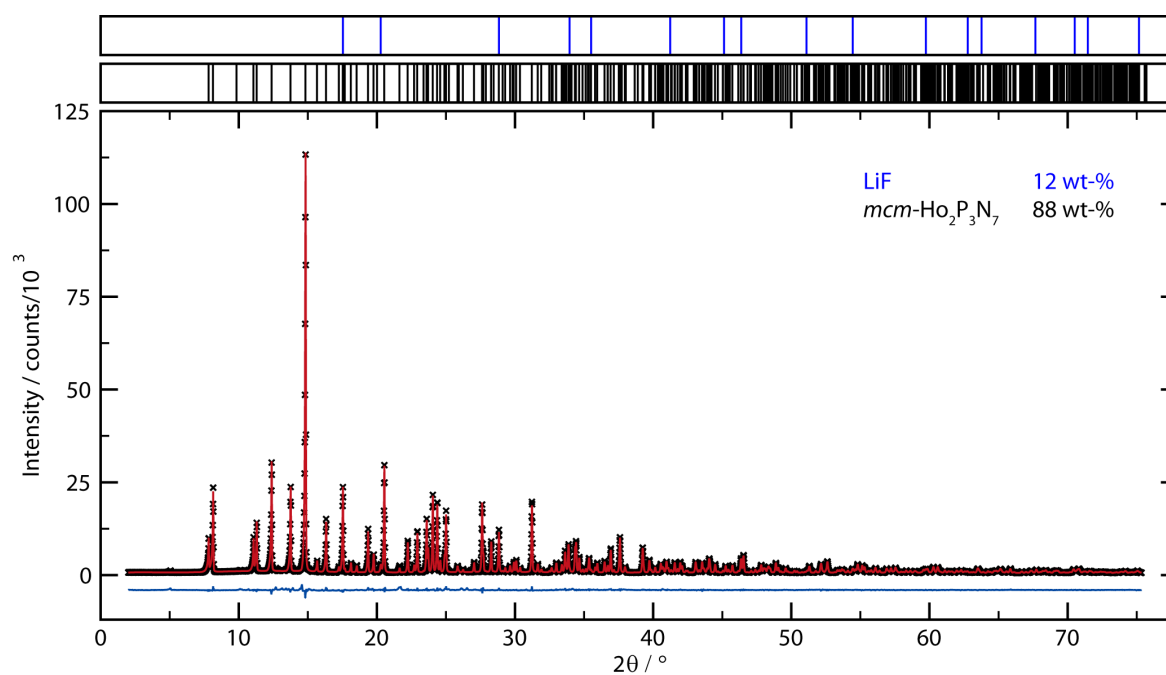
Rietveld Plot**Figure C.10.** Rietveld plot of $mcm\text{-Ho}_2\text{P}_3\text{N}_7$. Measured data is plotted as small black crosses, calculated model as the red line, difference plot as the blue line on the bottom; theoretical Bragg positions are located as vertical bars of respective phase color above the Rietveld plot.

Table C.37. Crystallographic information on the Rietveld refinement of *mcm*-Ho₂P₂N₇.

Formula	Ho ₂ P ₃ N ₇
Formula mass / g · mol ⁻¹	520.84
Crystal system, space group	tetragonal, $P4_2m$ (no. 113)
Lattice parameters / Å	$a = 7.35935(6)$ $c = 4.99757(5)$
Cell volume / Å ³	270.669(7)
Formula units per cell Z	2
Calculated density / g · cm ⁻³	6.391
F(000)	456
Absorption coefficient μ / cm ⁻¹	29.828
Radiation	Mo-K α_1 ($\lambda = 70.9300$ pm)
Monochromator	Ge(111)
Diffractometer	Stoe StadiP
Detector	MYTHEN 1K
2θ -range / °	2–76
Temperature / K	297(2)
Data points	4878
Number of observed reflections	474
Number of parameters	50
Constraints	0
Program used	TOPAS Academic
Structure refinement	Rietveld method
Profile function	Fundamental parameters model
Background function	Shifted Chebychev
R_{wp}	0.06258
R_{exp}	0.02427
R_p	0.03942
R_{Bragg}	0.01537
χ^2	2.578

Infrared Spectroscopy

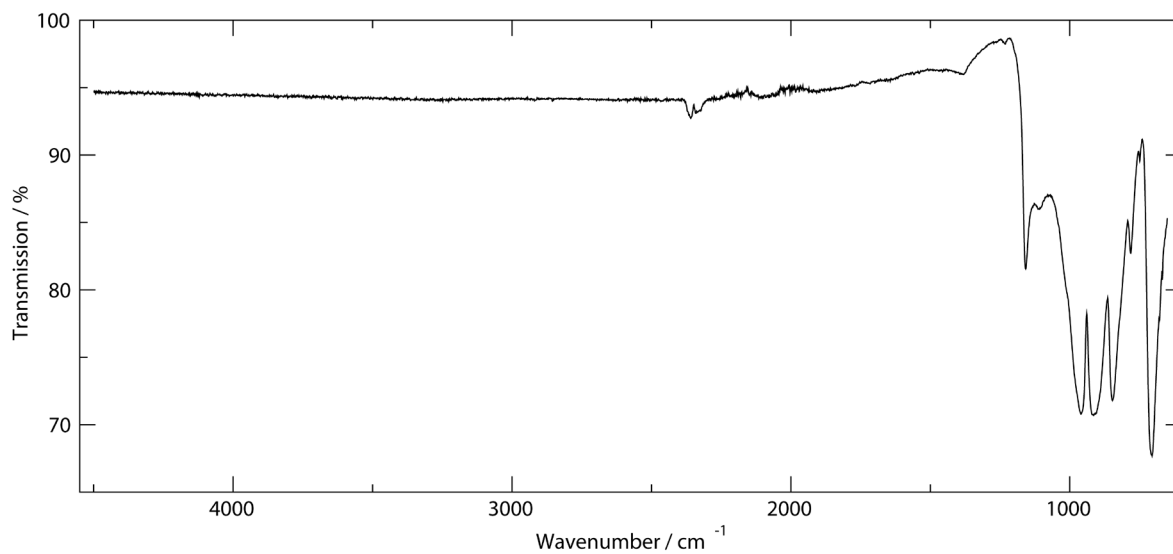


Figure C.11. IR spectrum of *mcm*- $\text{Ho}_2\text{P}_3\text{N}_7$ obtained in ATR Geometry.

High-temperature X-ray powder diffraction

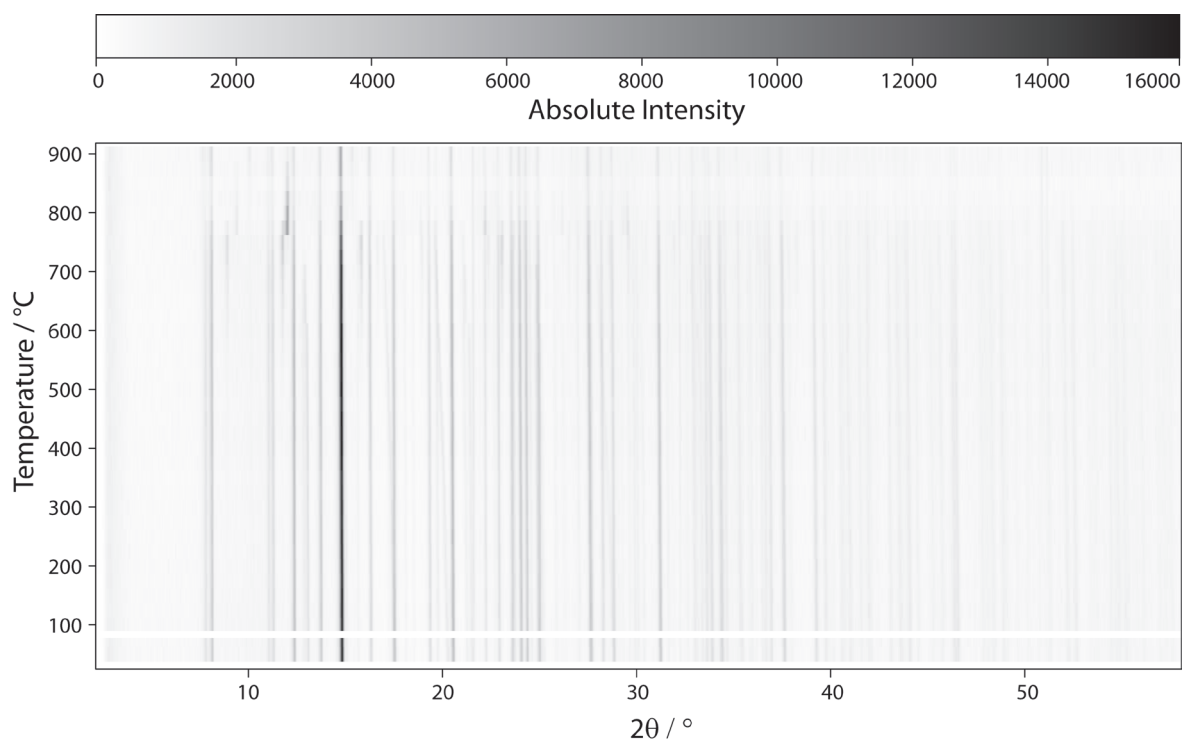


Figure C.12. Temperature Programmed PXRD of a *mcm*- $\text{Ho}_2\text{P}_3\text{N}_7$ sample.

EDX**Table C.38.** EDX measurement on a single crystal of *mcm*-Ho₂P₂N₇.

Atom	Theory / at-%	Experiment / at-%
Pr	16.7	17
P	25	22
N	58.3	57
O	0	5

C.9 *mcm*-Yb₂P₃N₇

Tables

Table C.39. Crystallographic information on *mcm*-Yb₂P₃N₇.

Formula	Yb ₂ P ₃ N ₇
Formula mass / g · mol ⁻¹	537.06
Crystal system, space group	tetragonal, $P\bar{4}2_1m$ (no. 113)
Lattice parameters / Å	$a = 7.32442(7)$ $c = 4.94453(5)$
Cell volume / Å ³	265.260(8)
Formula units per cell Z	2
Calculated density / g · cm ⁻³	6.7239(1)
F(000)	460
Absorption coefficient μ / cm ⁻¹	35.865
Radiation	Mo-K α_1 ($\lambda = 70.9300$ pm)
Monochromator	Ge(111)
Diffractometer	Stoe StadiP
Detector	MYTHEN 1K
2 θ -range / °	2–76
Temperature / K	297(2)
Data points	4958
Number of observed reflections	483
Number of parameters	68
Constraints	0
Program used	TOPAS Academic
Structure refinement	Rietveld method
Profile function	Fundamental parameters model
Background function	Shifted Chebychev
R_{wp}	0.02561
R_{exp}	0.02312
R_p	0.02561
R_{Bragg}	0.00927
χ^2	1.699

Table C.40. Sites, positions and isotropic displacement parameters of *mcm*-Yb₂P₂N₇, standard deviations in parentheses.

Atom	Wyckoff Symbol	x	y	z	$U_{iso} / \text{\AA}^2$	Occupancy
Yb1	4e	0.16073(4)	0.66073(4)	0.51060(15)	0.00889(12)	1
P1	4e	0.6427(2)	0.1427(2)	0.9659(6)	0.0080(5)	1
P2	2a	0	0	0	0.0086(6)	1
N1	2c	0	1/2	0.178(2)	0.007(3)	1
N2	4e	0.6427(7)	0.1427(7)	0.2840(12)	0.0071(18)	1
N3	8f	0.0831(7)	0.1648(7)	0.1933(9)	0.0049(10)	1

Table C.41. Bond lengths (Å) occurring in *mcm*-Yb₂P₂N₇, standard deviations in parentheses.

Yb1–N1	2.340(7)	Yb1–N2	2.447(5)	P1–N3	1.673(5)
Yb1–N2	2.447(5)	Yb1–N3	2.699(5)	P2–N3	1.656(5)
Yb1–N3	2.380(5)	Yb1–N3	2.380(5)	P2–N3	1.656(5)
Yb1–Yb1	3.3298(4)	P1–N2	1.573(7)	P2–N3	1.656(5)
Yb1–N3	2.699(5)	P1–N1	1.641(5)	P2–N3	1.656(5)
Yb1–N2	2.324(5)	P1–N3	1.673(5)		

Table C.42. Bond angles (°) occurring in *mcm*-Yb₂P₂N₇, standard deviations in parentheses.

N–P–N		P–N–P			
N1–P1–N2	115.7(4)	N3–P2–N3	109.5(2)	P1–N1–P1	128.6(6)
N2–P1–N3	118.1(3)	N3–P2–N3	109.5(2)	P1–N3–P2	116.0(3)
N2–P1–N3	118.1(3)	N3–P2–N3	109.5(2)		
N1–P1–N3	99.6(3)	N3–P2–N3	109.5(2)		
N1–P1–N3	99.6(3)	N3–P2–N3	109.5(2)		
N3–P1–N3	102.6(3)	N3–P2–N3	109.5(2)		

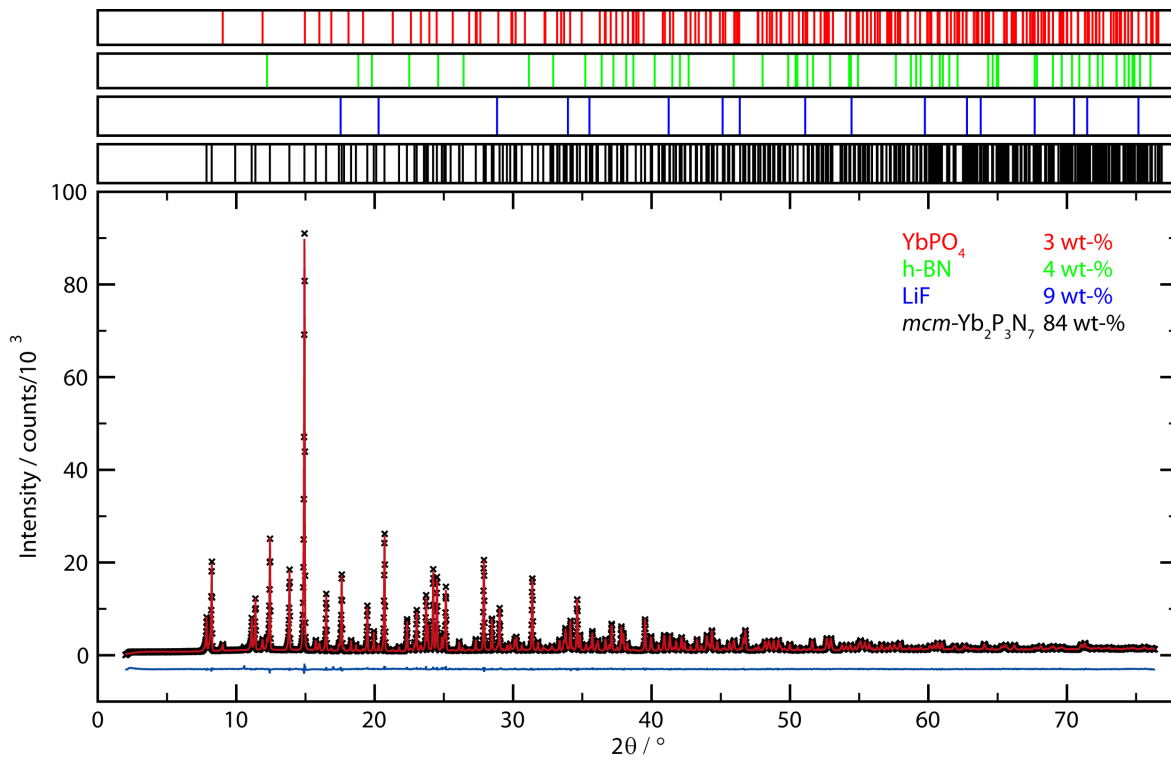
Rietveld Plot

Figure C.13. Rietveld plot of $mcm\text{-Yb}_2\text{P}_3\text{N}_7$. Measured data is plotted as small black crosses, calculated model as the red line, difference plot as the blue line on the bottom; theoretical Bragg positions are located as vertical bars of respective phase color above the Rietveld plot. YbPO_4 might form due to a side reaction with the boron nitride crucible, which slowly hydrolyzes to boric acid in air.

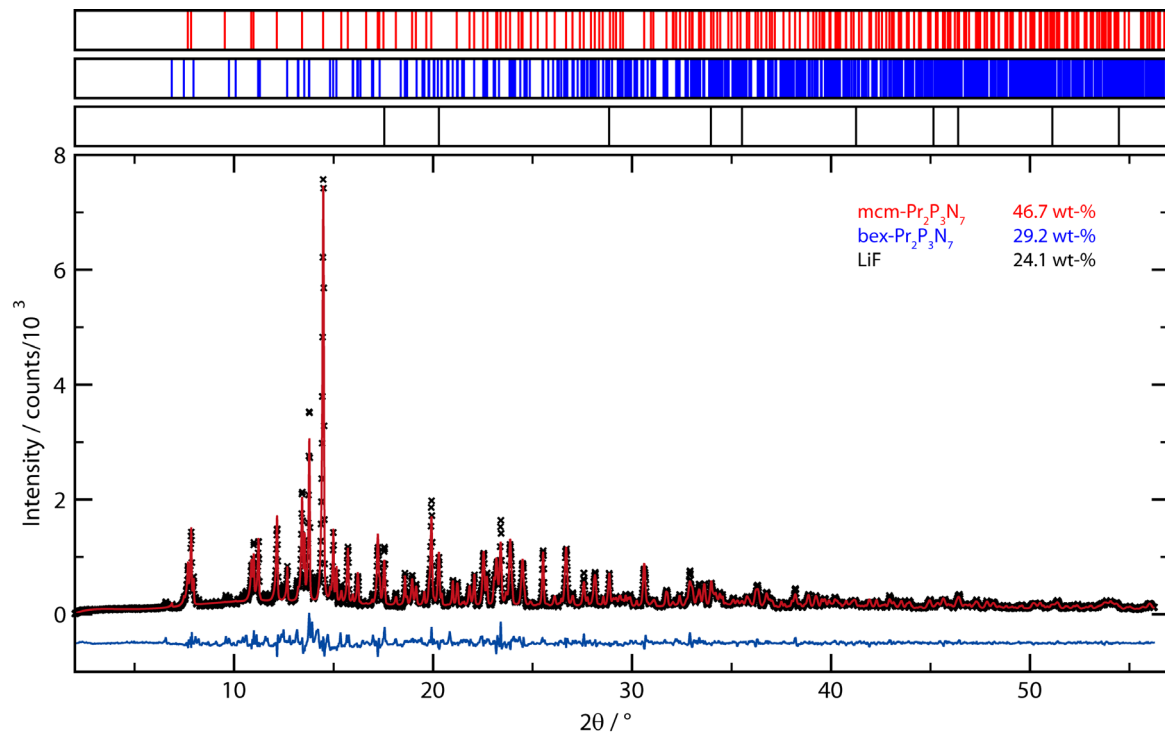
C.10 Rietveld Refinement of a *mcm/bex*-Pr₂P₃N₇ phase mixture

Figure C.14. Rietveld plot of *mcm*- and *bex*-Pr₂P₃N₇. Measured data is plotted as small black crosses, calculated model as the red line, difference plot as the blue line on the bottom; theoretical Bragg positions are located as vertical bars of respective phase color above the Rietveld plot.

Appendix D. Supporting Information for Chapter 4

D.1 Chemical analysis table containing EDX and ICP data

Table D.1. Table of chemical analysis by EDX and ICP of a $\text{Ho}_3[\text{PN}_4]\text{O}$ sample.

EDX	Ho / at-%	P / at-%	O / at-%	N / at-%	Li / at-%
Measured	24	9	19	48	-
Theory	33	11	11	44	-
ICP-OES	Ho / mol/g	P / mol/g	O / mol/g	N / mol/g	Li / mol/g
	2.922	0.977	-	-	9.222
Ratio:	2.993	1	-	-	9.447

D.2 Additional crystallographic information on Ho₃[PN₄]O

Table D.2. Anisotropic displacement parameters in Ho₃[PN₄]O, standard deviation in parenthesis.

Atom	$U_{11} / \text{Å}^2$	$U_{22} / \text{Å}^2$	$U_{33} / \text{Å}^2$	$U_{12} / \text{Å}^2$	$U_{13} / \text{Å}^2$	$U_{23} / \text{Å}^2$
Ho1	0.0122(4)	0.0122(4)	0.0111(5)	0	0	0
Ho2	0.0090(4)	0.0090(4)	0.0081(4)	0	0	-0.0005(2)
P1	0.0092(11)	0.0092(11)	0.0024(16)	0	0	0
O1	0.006(3)	0.006(3)	0.081(10)	0	0	0.000(5)
N1	0.0070(18)	0.0070(18)	0.009(3)	-0.005(2)	0.003(4)	-0.005(2)

Table D.3. Atomic distances in Ho₃[PN₄]O, standard deviation in parenthesis.

P1–N1	1.642(4)
Ho1–N1	2.673(4)
Ho2–N1	2.569(4)
Ho2–N1	2.295(4)
Ho1–O1	2.6393(1)
Ho2–O1	2.3465(6)
Ho2–Ho2	3.3184(9)

Table D.4. Important bond angles occurring in Ho₃[PN₄]O, standard deviation in parenthesis.

N–P–N		Ho–O–Ho	
N1–P1–N1	100.3(2)	Ho2–O1–Ho2	90.00(2)
N1–P1–N1	114.26(19)	Ho2–O1–Ho2	180

D.3 Maple calculations

Table D.5. MAPLE calculations of $\text{Ho}_3[\text{PN}_4]\text{O}$ and the formal division in its constituents.

	$\text{Ho}^{3+} / \text{kJ}\cdot\text{mol}^{-1}$	$\text{P}^{5+} / \text{kJ}\cdot\text{mol}^{-1}$	$\text{N}^{3-} / \text{kJ}\cdot\text{mol}^{-1}$	$\text{O}^{2-} / \text{kJ}\cdot\text{mol}^{-1}$	Total / $\text{kJ}\cdot\text{mol}^{-1}$
$\text{Ho}_3[\text{PN}_4]\text{O}$	4432.6830	15419.0034	5265.4558	1973.2635	51933.4162
$\text{HoN}^{[1]}$	4482.9252	-	4482.9252	-	8964.1394
$\text{Ho}_2\text{P}_3\text{N}_7^{[2]}$	4794.8200	14873.2235	5909.9533	-	95437.7488
$\text{Ho}_2\text{O}_3^{[3]}$	4462.2020	-	-	2114.2871	15275.7332
Sum			$S = 5x\text{HoN} + 1x \text{Ho}_2\text{O}_3 + 1x\text{Ho}_2\text{P}_3\text{N}_7 = 155534.179 \text{ kJ}\cdot\text{mol}^{-1}$		
			$3x \text{Ho}_3[\text{PN}_4]\text{O} = 155800.2486 \text{ kJ}\cdot\text{mol}^{-1}$		
Deviation	-	-	-	-	0.171 %

D.4 Rietveld refinement of $\text{Ho}_3[\text{PN}_4]\text{O}$ at 123 K

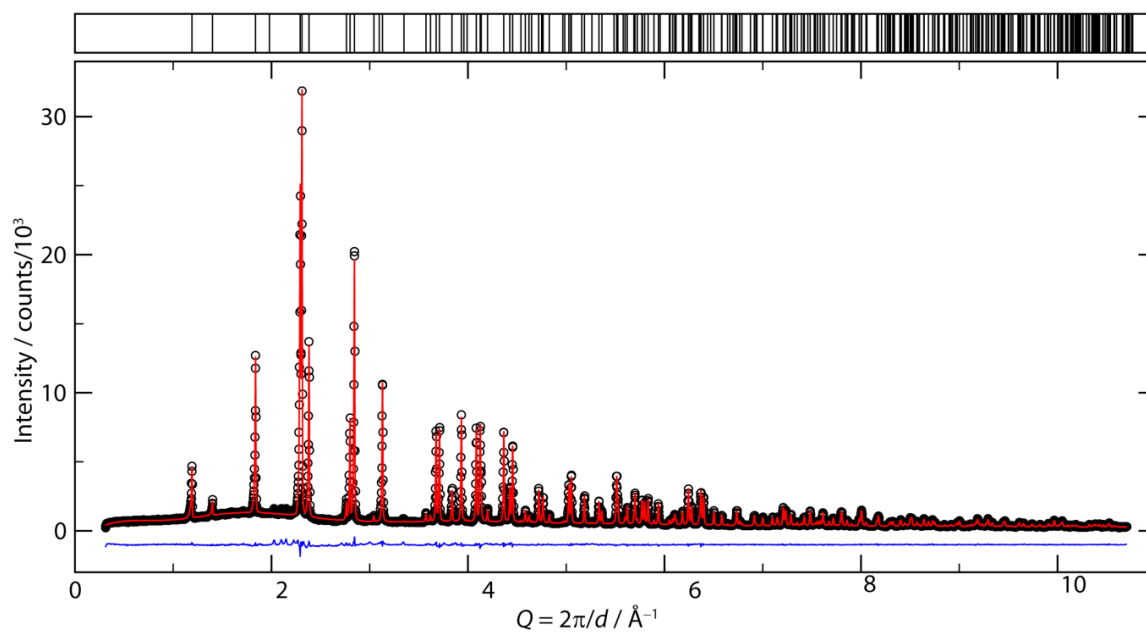


Figure D.1. Rietveld refinement of data from a $\text{Ho}_3[\text{PN}_4]\text{O}$ sample, collected at 123 K.

Table D.6. Crystallographic data table of low temperature Rietveld refinement on Ho₃[PN₄]O.

Formula	Ho ₃ [PN ₄]O
Formula weight / g·mol ⁻¹	597.80
Crystal system / space group	tetragonal, <i>I4/mcm</i> (no. 140)
Lattice parameters / Å	<i>a</i> = 6.34898(3) <i>c</i> = 10.55186(8)
Cell volume / Å ³	425.340(5)
Formula units per cell <i>Z</i>	4
X-ray density / g·cm ⁻³	9.35(1)
Abs. coefficient / mm ⁻¹	55.504
Radiation	Mo-Kα ₁ (λ = 70.9300 pm)
Monochromator	Ge(111)
Diffractionmeter	Stoe StadiP
Detector	MYTHEN 1K
<i>F</i> (000)	1008
2θ-range / °	2–75
Temperature / K	123(2)
Data points	4824
Number of observed reflections	325
Number of parameters	50
Constraints	0
Program used	TOPAS Academic V4
Structure refinement	Rietveld-Method
Profile function	fundamental parameters model
Background function	shifted Chebychev with 18 polynomials
<i>R</i> _{wp}	0.05008
<i>R</i> _{exp}	0.03318
<i>R</i> _p	0.03502
<i>R</i> _{Bragg}	0.01009
χ ²	1.509

D.5 References

- [1] W. Klemm, G. Winkelmann, *Z. Anorg. Allg. Chem.* **1956**, 288, 87–90.
- [2] S. D. Kloß, N. Weidmann, R. Niklaus, W. Schnick, *Inorg. Chem.* **2016**, 55, 9400-9409.
- [3] H. Bommer, *Z. Anorg. Allg. Chem.* **1939**, 241, 273–280.

Appendix E. Supporting Information for Chapter 5

E.1 Infrared spectroscopy

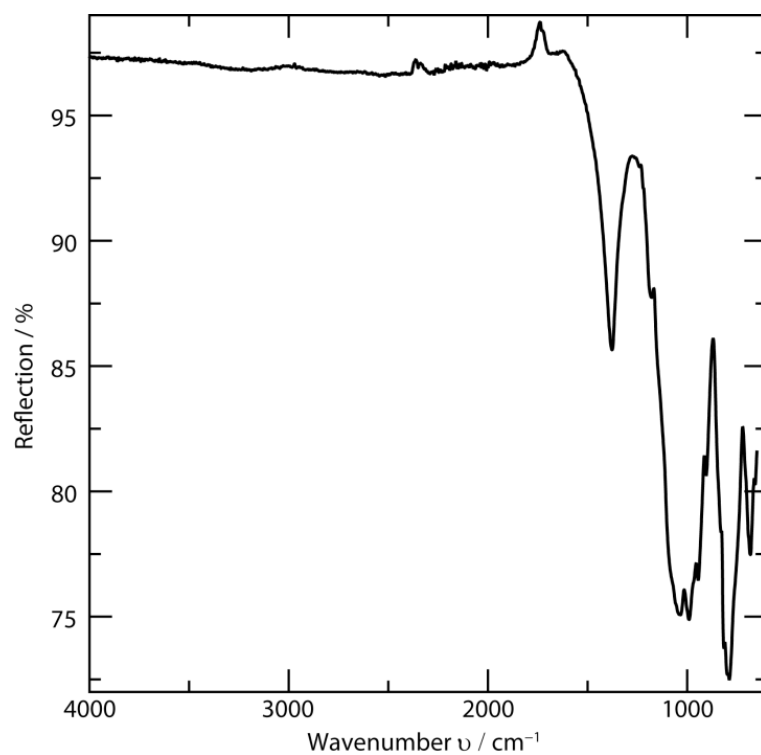


Figure E.1. FTIR spectrum of $\text{Ce}_{4-0.5x}\text{Li}_3\text{P}_{18}\text{N}_{35-1.5x}\text{O}_{1.5x}$.

E.2 High-Temperature Powder XRD

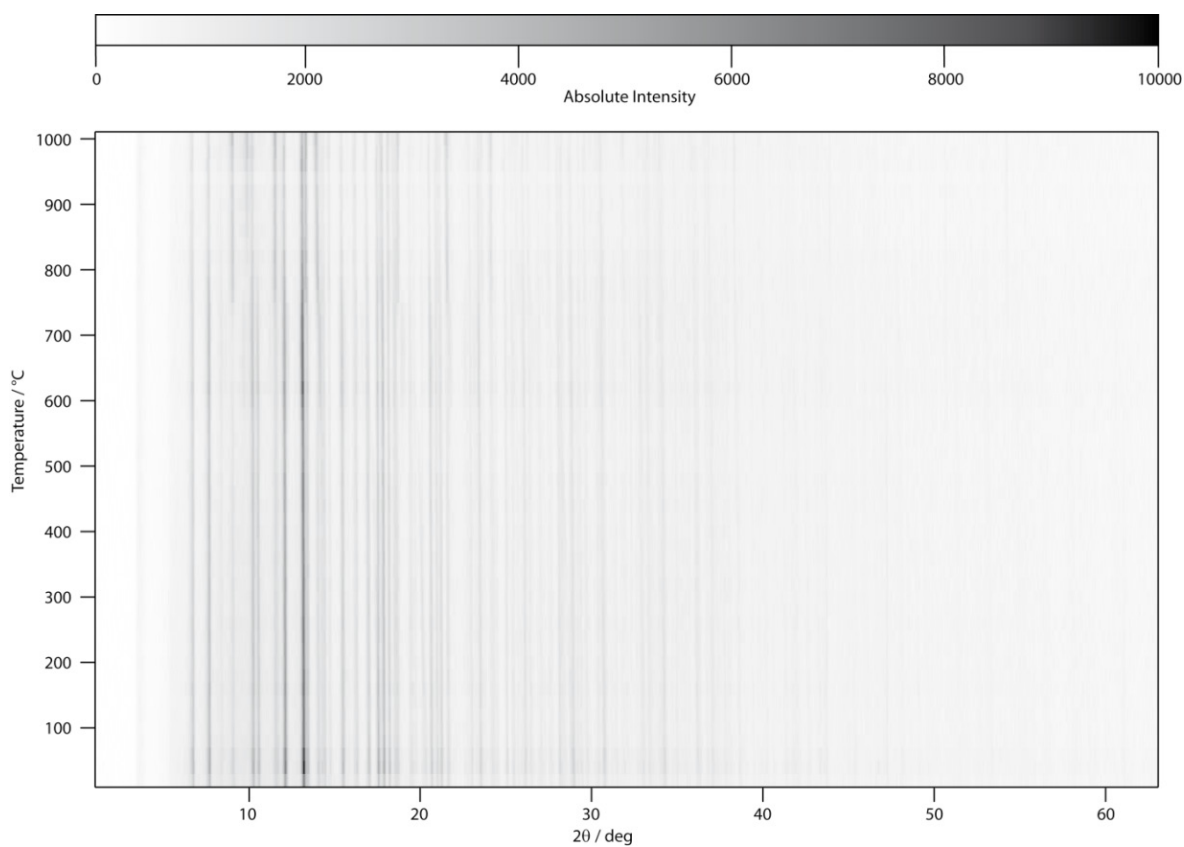


Figure E.2. Top view of high-temperature powder X-ray diffraction patterns of $\text{Ce}_{4-0.5x}\text{Li}_3\text{P}_{18}\text{N}_{35-x}\text{O}_{1.5x}$. LiPN_2 was present as a side phase (main reflection at $2\theta = 10.5^\circ$ marked by an arrow), which decomposed at around 800 °C.

E.3 Details of Rietveld refinement

Table E.1. Crystallographic data for the Rietveld refinement of $\text{Ce}_{4-0.5x}\text{Li}_3\text{P}_{18}\text{N}_{35-1.5x}\text{O}_{1.5x}$ ($x \approx 0.72$).

Crystal Data	
Formula	$\text{Ce}_{4-0.5x}\text{Li}_3\text{P}_{18}\text{N}_{35-1.5x}\text{O}_{1.5x}$ ($x \approx 0.72$)
Crystal system, space group	hexagonal, $P6_3/m$ (no. 173)
Lattice parameters / Å	$a = 13.92153(9)$ $c = 8.12855(6)$
Cell volume / Å ³	1364.32(2)
Formula units per cell Z	2
Data Collection	
Radiation	Mo-K α_1 ($\lambda = 0.7093$ Å)
Monochromator	Ge(111)
Diffractometer	Stoe StadiP
Detector	MYTHEN 1K
2 θ -range / °	2–76
Temperature / K	297(2)
Data points	4958
Number of observed reflections	2706
Refinement	
Number of parameters	108
Constraints	0
Program used	TOPAS Academic V4.1
Structure refinement	Rietveld-Method
Profile function	fundamental parameters model
Background function	shifted Chebychev polynomial with 14 terms
R_{wp}	0.041
R_{exp}	0.008
R_{p}	0.028
R_{Bragg}	0.015

E.4 Additional Crystallographic data for $\text{Ce}_{4-0.5x}\text{Li}_3\text{P}_{18}\text{N}_{35-1.5x}\text{O}_{1.5x}$

Table E.2. Anisotropic displacement parameters of $\text{Ce}_{4-0.5x}\text{Li}_3\text{P}_{18}\text{N}_{35-1.5x}\text{O}_{1.5x}$ ($x \approx 0.72$), standard deviations in parentheses, based on single crystal analysis.

Atom	$U_{11} / \text{\AA}^2$	$U_{22} / \text{\AA}^2$	$U_{33} / \text{\AA}^2$	$U_{12} / \text{\AA}^2$	$U_{13} / \text{\AA}^2$	$U_{23} / \text{\AA}^2$
Ce1	0.01017(8)	0.00809(8)	0.00726(8)	0	0	0.00421(5)
Ce2	0.00781(16)	0.00781(16)	0.0450(4)	0	0	0.00391(8)
P1	0.00742(18)	0.00627(18)	0.0091(2)	0.00069(15)	0.00075(15)	0.00311(15)
P2	0.00599(18)	0.00650(18)	0.00609(19)	-0.00031(14)	-0.00003(14)	0.00339(15)
P3	0.00678(18)	0.00669(18)	0.00579(19)	0.00005(14)	0.00007(14)	0.00334(15)
N1	0.0053(6)	0.0053(6)	0.0092(11)	0	0	0.0026(3)
N2	0.0095(9)	0.0074(9)	0.0066(9)	0	0	0.0038(7)
N3	0.0120(7)	0.0087(6)	0.0084(7)	0.0012(5)	0.0036(5)	0.0058(5)
N4	0.0129(10)	0.0092(9)	0.0107(9)	0	0	0.0048(8)
O4	0.0129(10)	0.0092(9)	0.0107(9)	0	0	0.0048(8)
N5	0.0076(6)	0.0073(6)	0.0132(7)	-0.0026(5)	0.0003(5)	0.0032(5)
N6	0.0259(13)	0.0160(11)	0.0069(10)	0	0	0.0157(10)
N7	0.0283(10)	0.0102(7)	0.0204(9)	0.0072(7)	0.0141(8)	0.0120(7)
N8	0.0403(14)	0.084(2)	0.0196(10)	0.0256(13)	0.0169(10)	0.0546(16)
Li1	0.020(3)	0.011(2)	0.033(3)	0	0	0.008(2)

Table E.3. Bond lengths (\AA) in $\text{Ce}_{4-0.5x}\text{Li}_3\text{P}_{18}\text{N}_{35-1.5x}\text{O}_{1.5x}$ standard deviations in parentheses.

Ce1		P1	
Ce1–N7	2.5394(19)	P1–N7	1.6059(19)
Ce1–N3	2.6069(17)	P1–N8	1.614(2)
Ce1–N6	2.727(3)	P1–N8	1.615(2)
Ce1–N5	2.7315(17)	P1–N4	1.6544(12)
Ce1–N5	2.8592(18)		
Ce1–P2	3.3358(5)	P2	
Ce1–P3	3.3784(5)	P2–N5	1.6053(17)
		P2–N2	1.6078(12)
Ce2		P2–N3	1.6103(18)
Ce2–N4	2.665(2)	P2–N1	1.6988(5)
Ce2–N8	2.792(3)		
		P3	
Li1		P3–N7	1.611(2)
Li1–N2	2.093(6)	P3–N6	1.6197(11)
Li1–N6	2.279(7)	P3–N3	1.6243(17)
Li1–N8	2.260(6)	P3–N5	1.6509(17)

Table E.4. Selected bond angles (in °) in $Ce_{4-0.5x}Li_3P_{18}N_{35-1.5x}O_{1.5x}$, standard deviations in parentheses.

N-P1-N		N-P2-N		N-P3-N		P-N-P	
N7-P1-N8	109.15(16)	N5-P2-N2	112.84(11)	N7-P3-N6	109.89(13)	P2-N1-P2	120
N7-P1-N8	113.38(15)	N5-P2-N3	108.54(9)	N7-P3-N3	116.14(10)	P2-N2-P2	124.58(15)
N8-P1-N8	111.2(2)	N2-P2-N3	110.23(10)	N6-P3-N3	111.74(11)	P2-N3-P3	117.30(10)
N7-P1-N4	106.59(11)	N5-P2-N1	107.09(7)	N7-P3-N5	99.14(9)	P1-N4-P1	127.33(15)
N8-P1-N4	109.34(11)	N2-P2-N1	109.91(12)	N6-P3-N5	107.36(12)	P2-N5-P3	129.06(11)
N8-P1-N4	106.96(12)	N3-P2-N1	108.07(10)	N3-P3-N5	111.62(9)	P3-N6-P3	134.80(17)
						P1-N7-P3	138.41(13)
						P1-N8-P1	133.67(16)

E.5 MAPLE and BVS

Madelung part of the lattice energy (MAPLE) calculations were carried out with MAPLE based on an idealized structure model of $\text{Ce}_4\text{Li}_3\text{P}_{18}\text{N}_{35}$, as not fully occupied atom positions cannot be taken into account. To evaluate the calculated values, $\text{Ce}_4\text{Li}_3\text{P}_{18}\text{N}_{35}$ was formally decomposed into 4 CeN, 3 LiPN_2 , and 5 $\gamma\text{-P}_3\text{N}_5$.^[1-3]

Table E.5. MAPLE calculations for $\text{Ce}_4\text{Li}_3\text{P}_{18}\text{N}_{35}$.

Compound	Multiplicator	MAPLE / $\text{kJ}\cdot\text{mol}^{-1}$	MAPLE · Multiplicator / $\text{kJ}\cdot\text{mol}^{-1}$
CeN	4	8686.1263	34744.5052
LiPN_2	3	28084.5637	84253.6911
P_3N_5	5	76829.8841	384149.421
Σ			503147.617
$\text{Ce}_4\text{Li}_3\text{P}_{18}\text{N}_{35}$	1	508459.308	508840.538
Deviation / %			1.13 %

Table E.6. Partial MAPLE values for $\text{Ce}_4\text{Li}_3\text{P}_{18}\text{N}_{35}$. Typical values: N^{3-} 5000–6000 $\text{kJ}\cdot\text{mol}^{-1}$, O^{2-} 2000–2800 $\text{kJ}\cdot\text{mol}^{-1}$.^[4]

Atom	Partial MAPLE / $\text{kJ}\cdot\text{mol}^{-1}$
Ce1	4473
Ce2	3318
P1	15533
P2	14458
P3	15434
N1	7674
N2	6384
N3	6227
N4	5851
N5	6151
N6	5948
N7	5931
N8	6206
Li1	881

Table E.7. Bond-valence sums for $\text{Ce}_{4-0.5x}\text{Li}_3\text{P}_{18}\text{N}_{35-1.5x}\text{O}_{1.5x}$.

Atom	Ce1	Ce2	Li1	P1	P2	P3	N1
BVS	2.44	1.93	0.86	5.0	4.93	4.94	3.09
Occupancy	1	0.64	1	1	1	1	1

Atom	N2	N3	N4	O4	N5	N6	N7
BVS	2.83	2.86	2.57	2.13	2.87	2.88	3.01
Occupancy	1	1	0.44	0.56	1	1	1

E.6 Difference Fourier Maps

Atom sites N6, N7 and N8 have strongly (Figure 5.3, 5.4 and 5.6) prolate displacement parameters, potentially caused by symmetry elements of the space group $P6_3/m$, which do not apply for the local structure. The ellipsoids might be explained by two independent N atoms that have slightly different x and y coordinates and are mapped onto each other by the mirror plane perpendicular to c . To falsify this suggested lower symmetry for the average long-range ordered structure, the structure refinement was repeated by systematically removing symmetry elements down to space group $P1$ under consideration of all relevant twin laws. Omission of the inversion center and the mirror plane perpendicular to $[001]$ (in the $t2$ subgroup $P6_3$, no. 173) theoretically suffices for crystallographic splitting of the N8 site. Difference Fourier maps calculated in $P6_3$ revealed a mirror- and centrosymmetric electron density (Figure E.3, E.4), indicating that the N8 position is best described with $P6_3/m$ symmetry.

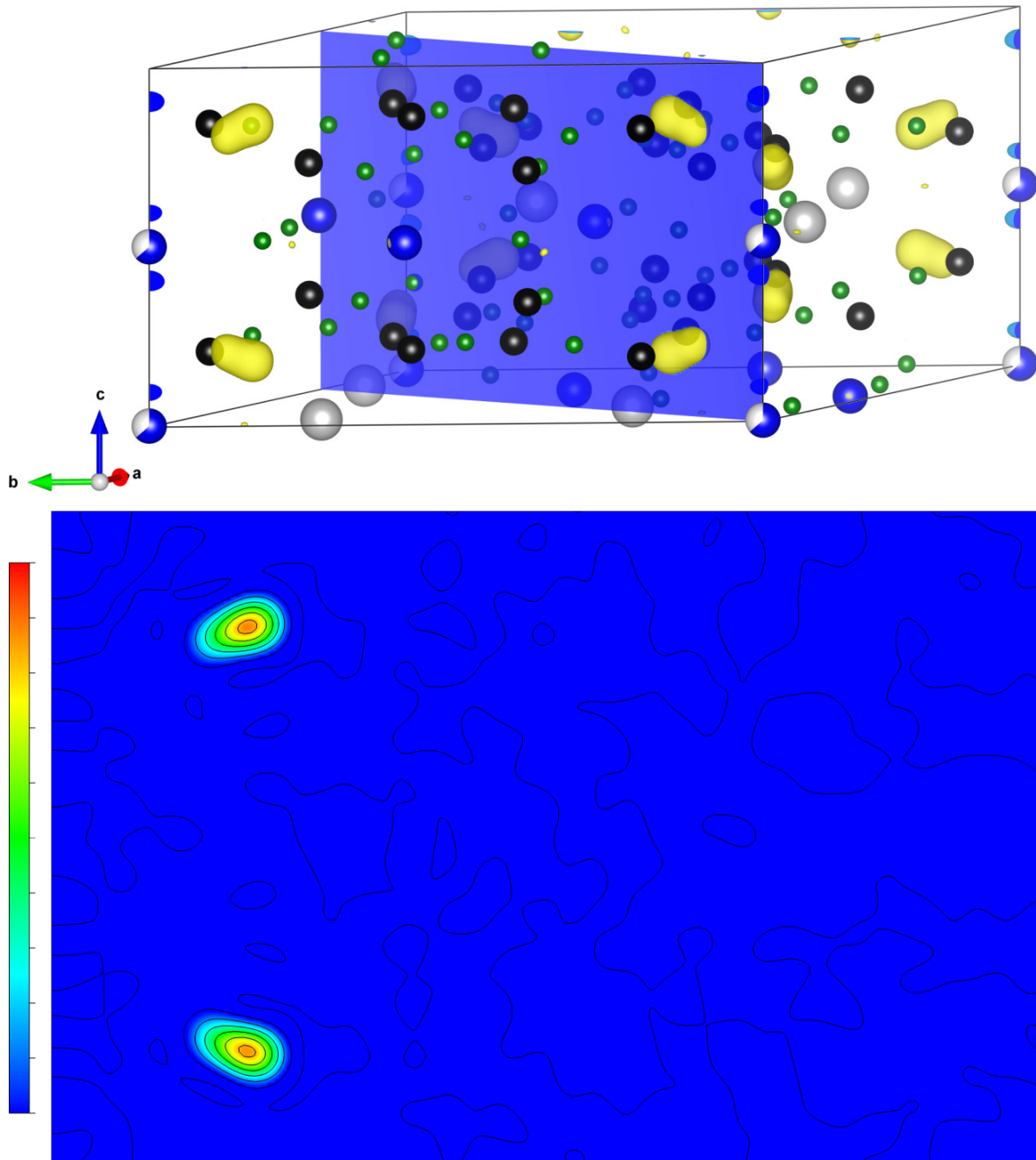
Difference Fourier maps in $P6_3$ 

Figure E.3. Difference Fourier maps ($F_{\text{obs}} - F_{\text{calc}}$) calculated for a structure model in space group $P6_3$, in which the atom positions of the inter-tetrahedra-bridging N were deleted. The top image shows the $F_{\text{obs}} - F_{\text{calc}}$ map of the unit cell, positive electron density in yellow, negative in blue. A plane $(-1.5 \ 1 \ 0)$ is highlighted in blue. The 2D contour $F_{\text{obs}} - F_{\text{calc}}$ plot through this plane is presented in the bottom part. It runs through the N8 atom positions. $F_{\text{obs}} - F_{\text{calc}}$ maps were calculated with VESTA.^[5]

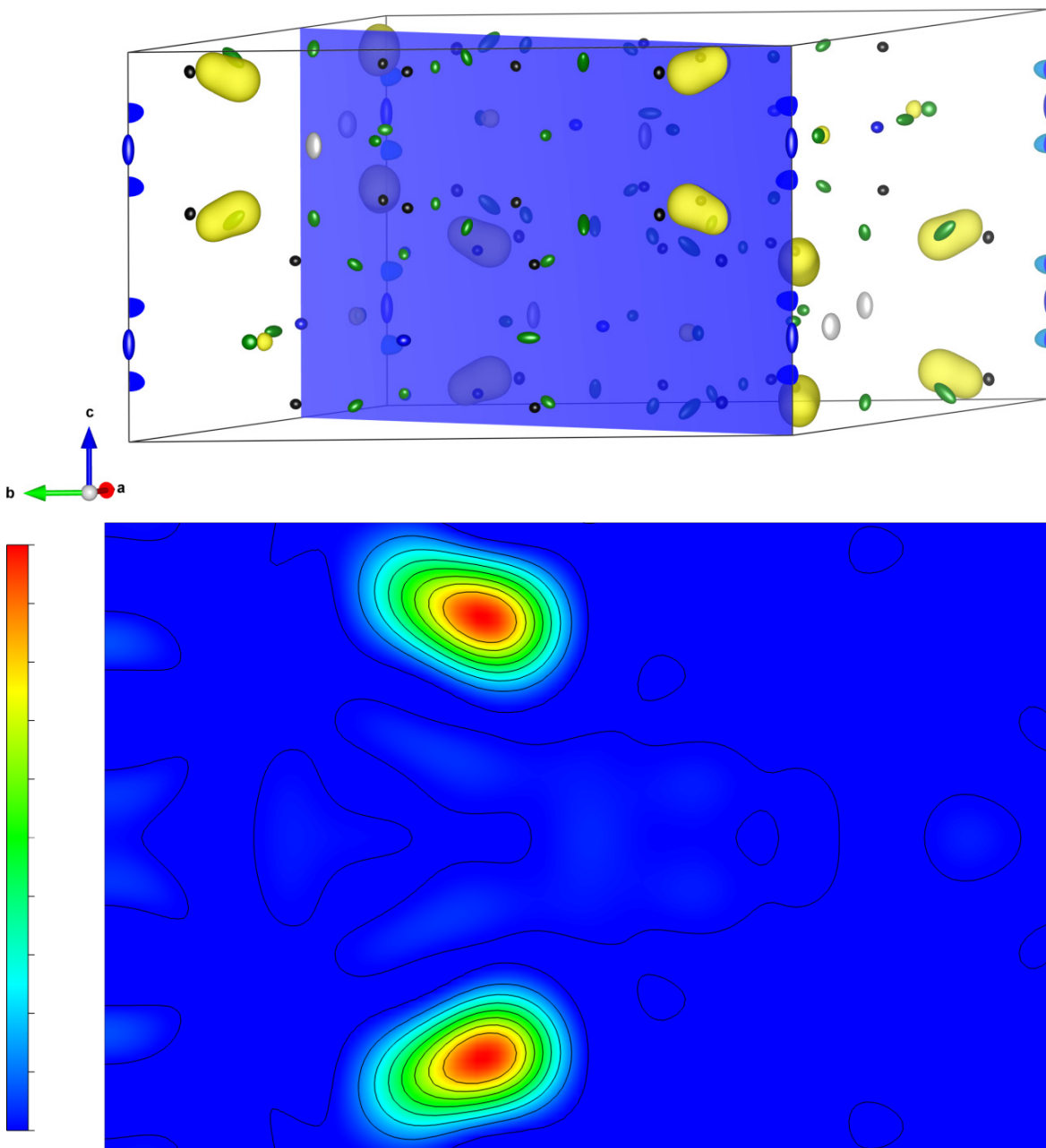
Difference Fourier maps in $P6_3/m$ 

Figure E.4. Difference Fourier maps ($F_{\text{obs}} - F_{\text{calc}}$) calculated for a structure model in space group $P6_3/m$, in which the atom positions of the inter-tetrahedra bridging N were deleted. The top image shows the $F_{\text{obs}} - F_{\text{calc}}$ map of the unit cell, positive electron density in yellow, negative in blue. A plane $(-1.5 \ 1 \ 0)$ is highlighted in blue. The 2D contour $F_{\text{obs}} - F_{\text{calc}}$ plot through this plane is presented in the bottom part. It runs through the N8 atom positions. $F_{\text{obs}} - F_{\text{calc}}$ maps were calculated with VESTA.^[5]

E.7 Network topology

Vertex Symbol

The vertex symbol of the PN net of $\text{Ce}_{4-0.5x}\text{Li}_3\text{P}_{18}\text{N}_{35-1.5x}\text{O}_{1.5x}$ was calculated with TOPOS with ring sizes up to 12, larger ring sizes were neglected and the corresponding angle marked with an asterisk.^[5]

P1: (6.6₂.6.6₂.6₂.6₂)

P2: (3.3.3.4.4.6.6.6.*.*)

P3: (3.6₂.6.6.6.6)

The framework's fundamental building units are essential rings of size 3 to 6, and no 10-membered rings are listed in the point as might contrarily be suggested by the structure's projection along [001] (Figure 5.3); vertex symbols only list the shortest rings and their number contained in the respective angle.^[6]

Tiling

All six tiles occurring in the maximum symmetry embedding of the PN net of $\text{Ce}_{4-0.5x}\text{Li}_3\text{P}_{18}\text{N}_{35-1.5x}\text{O}_{1.5x}$ are presented along with their wireframe representation and face symbol as well as their volume occupation in the real crystal structure (Figure E.5). Data calculated with TOPOS, tiles drawn with *3dt*.^[6,7]

Table E.8. Face symbols and volume of the tiles shown in Figure E.5.

Tile	Face Symbol	Volume / Å ³
a	[6 ⁵ .10 ²]	147.9
b	[3 ² .4 ³]	10.6
c	[6 ³]	17.0
d	[6 ⁵]	62.1
e	[3 ² .4.6 ²]	17.8
f	[3 ⁸ .6 ³]	59.6

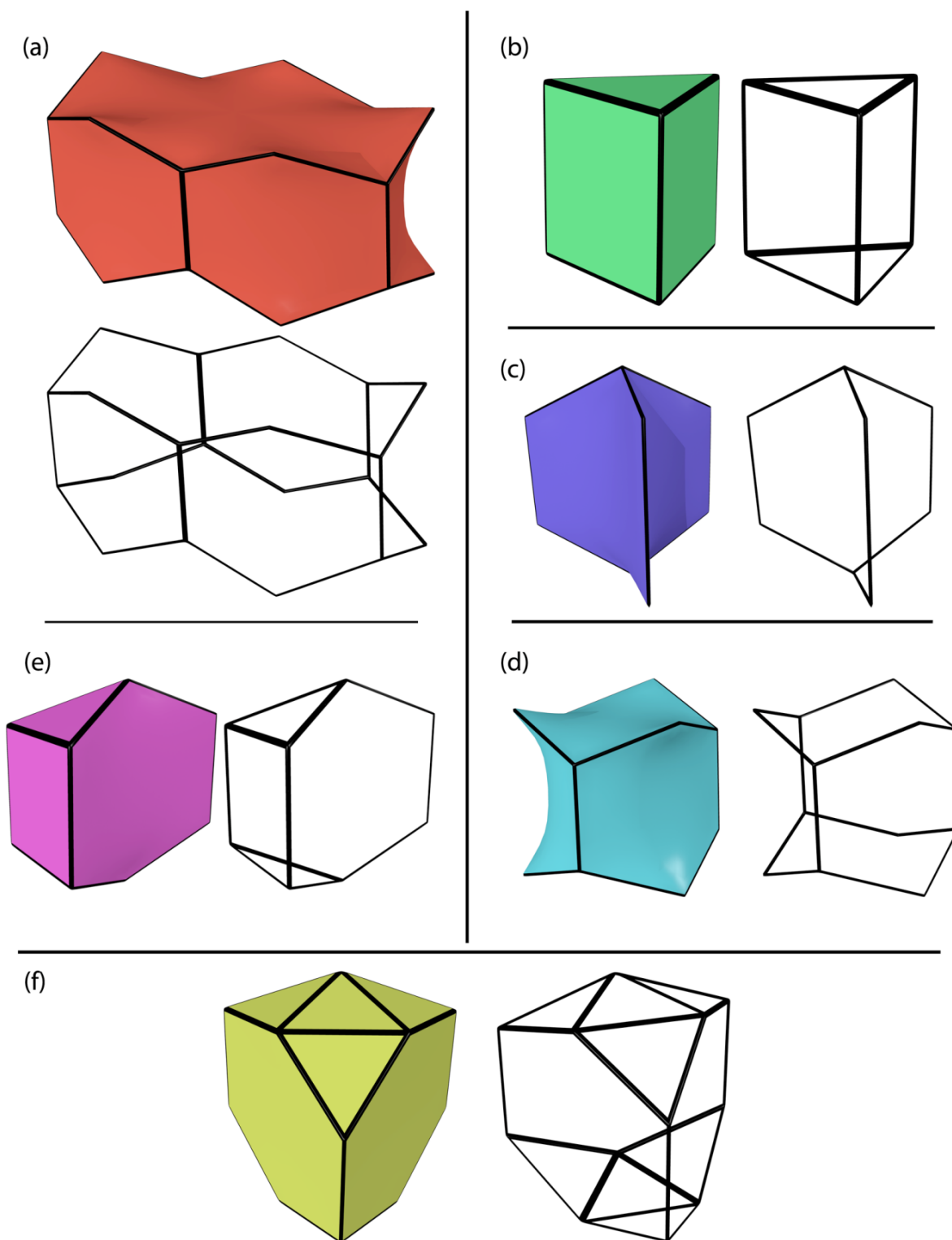


Figure E.5. Tiles occurring in $\text{Ce}_{4-0.5x}\text{Li}_3\text{P}_{18}\text{N}_{35-1.5x}\text{O}_{1.5x}$ face symbols and volume given in Table E.8.

E.8 Coordination polyhedra

Li2 coordination

The pentagonal pyramid belongs to the class of Johnson solids, polyhedra that are not transitive on its faces, edges and vertices but constitute regular polygons.^[8] It is classified as Johnson solid J_2 with vertex symbol $(3^2.5)_5(3^5)$ and C_{5v} symmetry in Schönflies notation. According to site symmetry $m..$ of the Li1 position, distortions in the LiN_6 polyhedron removed the five-fold rotation axis, which is in any case non-crystallographic, but maintained one vertical mirror plane. Common Li–N bond lengths range from 2.0 to 2.4 Å (e. g. NdLiP_4N_8 $d(\text{Li–N}) = 1.96$ to 2.17 Å, $\text{B}_3\text{Ca}_4\text{LiN}_6$ $d(\text{Li–N}) = 2.22$ Å).^[9,10] The values found here reveal a large distance variation ($d(\text{Li–N}) = 2.09$ – 2.80 , $d_\infty(\text{Li–N}) = 2.41$ Å) leading to an effective coordination number of 3.6. Hence, the coordination might better be represented by a tetrahedron. However, the prolate Li atom displacement, which shows a displacement towards the remote N7 ($d(\text{Li1–N7}) = 2.747(4)$ Å), is illustrated by the distortion of the pentagonal pyramid.

Ce1 coordination

Ce1 resides inside the ten-membered-ring channels and is coordinated in an irregular CeN_9 polyhedron, which is not one of the Johnson solids. A mathematically devised holohedral polygon with regular polygon faces, therefore, cannot be constructed. Through determination of faces based on shortest N–N distances, the face symbol could be $[3^7.4^2.5]$, describing the polyhedron as an arrangement of 4 N below and 5 N above Ce1 (depicted in Figure 5.6b). The corresponding vertex symbol is $(3^3.4)_2(3^2.4^2)_2(3.4.5)_2(3^3.5)_3$. The Ce1–N distances in the range of $d(\text{Ce1–N}) = 2.54$ – 2.93 Å coincide well with values of $\text{Ba}_2\text{Cu}[\text{Si}_2\text{O}_7]$ -type $\text{Ce}_2\text{P}_3\text{N}_7$ with $d(\text{Ce–N}) = 2.44$ – 2.75 Å.^[11] The coordination number in $\text{Ce}_2\text{P}_3\text{N}_7$ is $\text{CN} = 8$, hence the bond lengths are slightly shorter.

Ce2 coordination

Ce2, which is not fully occupied (*s.o.f.* = 0.635), resides in the six-membered-ring channels and is coordinated by nine N atoms arranged after Johnson solid J_{51} , a triaugmented triangular prism (Figure 5.6c).^[8] J_{51} belongs to the class of deltahedra, polyhedra constructed solely by equilateral triangles. Its vertex symbol is therefore $(3^4)_3(3^5)_6$ and its holohedral symmetry group is D_{3h} , which is a crystallogra-

phic point group denoted $m2$ in Hermann-Mauguin notation. While space group $P6_3/mmc$, the maximal symmetry group of the net, features $am2$ Wyckoff position, its $t2$ subgroup $P6_3/m$ does not and Ce2 is located on a 2 -fold symmetry axis in $P6_3/m$. Hence, symmetry of the triaugmented triangular prism surrounding Ce2 is reduced. Though two equilateral triangles comprise the triangular prism, which preserve the horizontal mirror plane and inversion center, the capping N4 atoms are not centered above the rectangular faces of the prism, thus eliminating the mirror plane and 2-fold rotation perpendicular to the main rotation axis. The symmetry group is thus C_{3h} in Schönflies notation. Two Ce2–N bond distances are found, $d(\text{Ce2–N4}) = 2.656 \text{ \AA}$ and $d(\text{Ce2–N8}) = 2.792 \text{ \AA}$.

E.9 TEM

Table E.9. TEM EDX of $\text{Ce}_{4-0.5x}\text{Li}_3\text{P}_{18}\text{N}_{35-1.5x}\text{O}_{1.5x}$ ($x \approx 0.72$) in atom% (standard deviations), mean values based on 9 measurement points each. All experiments showed more O than theoretically predicted. This might be due to hydrolysis of the surface. The experimental values, however, are to be understood in relation between the two domains.

Edge	average value	mean value of domains	
	from model	with low O content	with higher O content
N (K)	60.9	53(4)	52(1)
O (K)	1.0	2(1)	5(1)
P (K)	31.8	39(5)	36(3)
Ce (L)	6.4	6(1)	7(2)

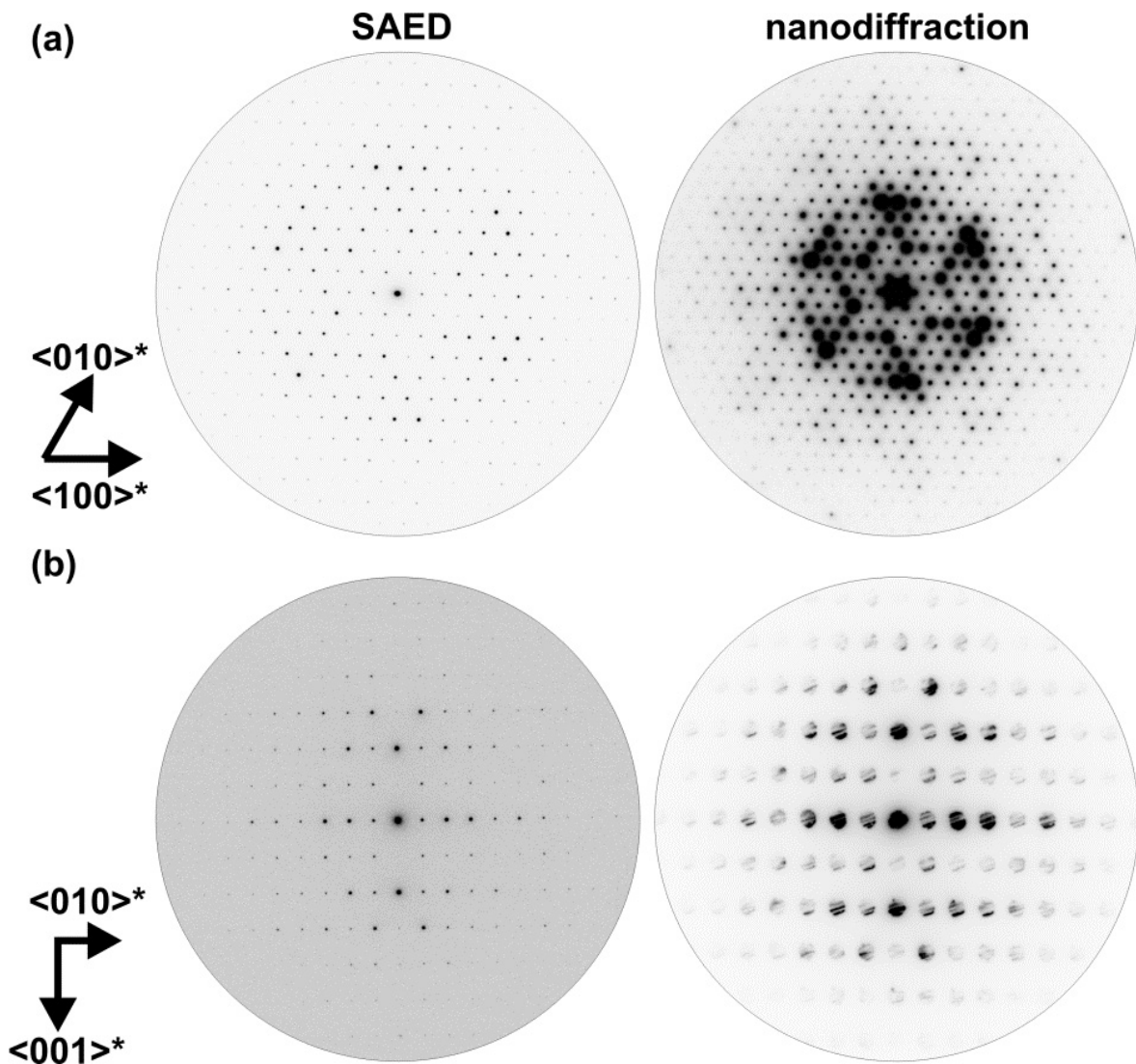


Figure E.6. Electron diffraction along [001] (a) and [100] (b), both SAED (left) and nanodiffraction (right) whole pattern symmetry in accordance to space group $P6_3/m$ derived from X-ray data.

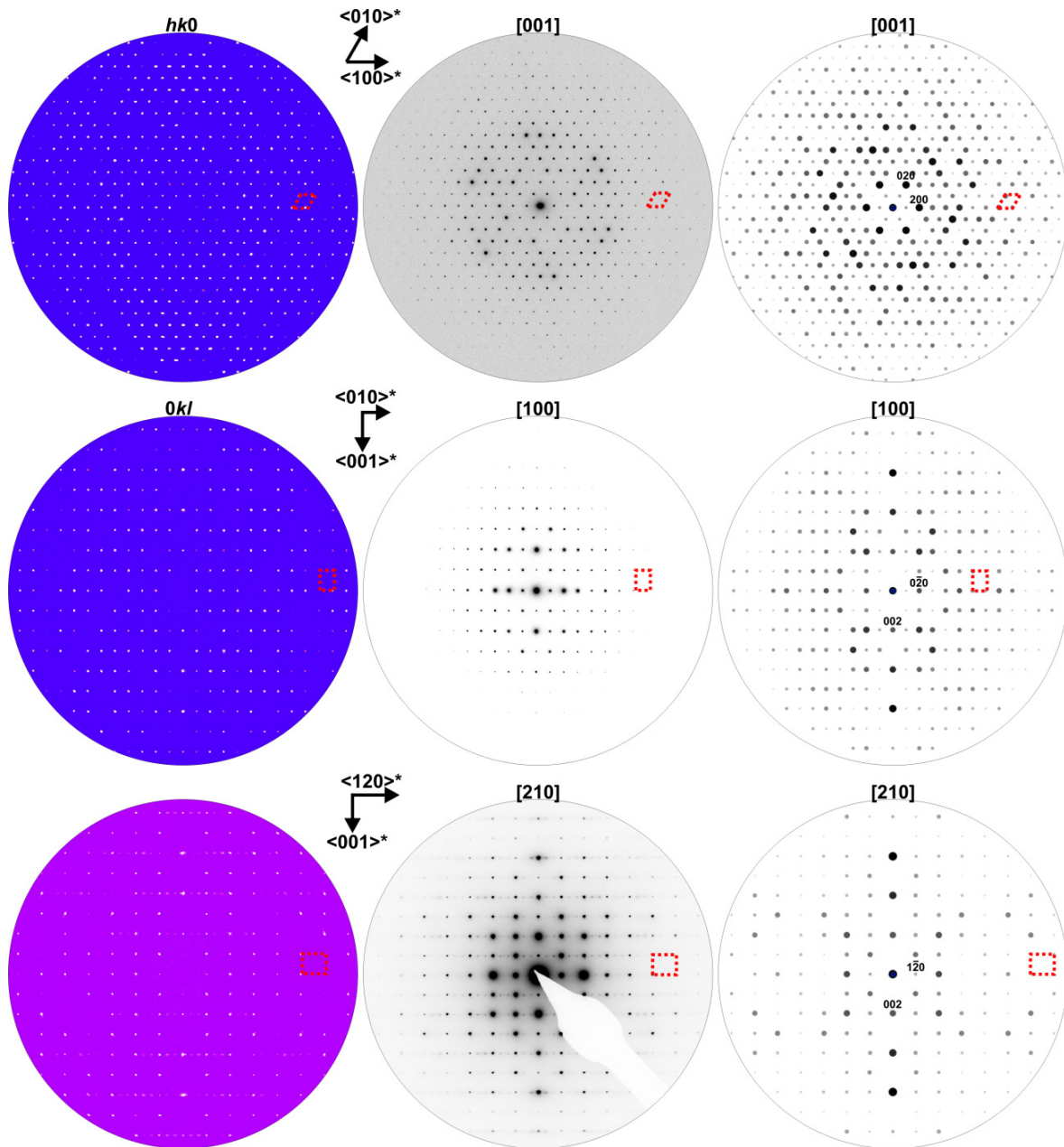


Figure E.7. Reciprocal lattice sections (see also Figure E.12, E.13) reconstructed from single crystal X-ray diffraction data (left) compared to SAED patterns along special directions from different crystallites (middle) with corresponding simulations (right) based on single crystal X-ray data, all each unit cell highlighted in red.

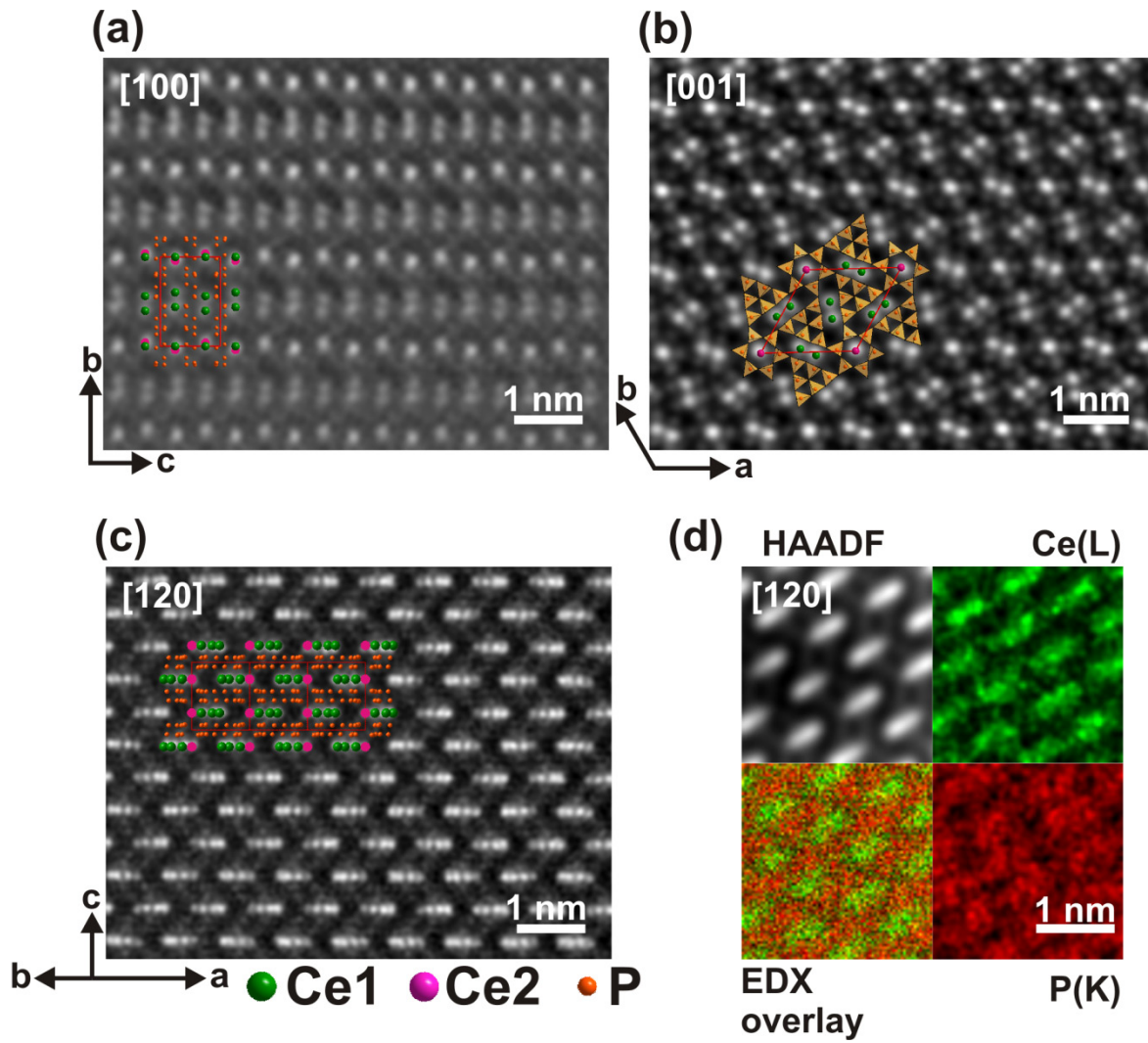


Figure E.8. Fourier filtered STEM-HAADF images (a-c) including structure projection as overlay (P atoms in orange, Ce1 atoms in green, Ce2 atoms in light green) and drift corrected EDX mappings (d) both with atomic resolution viewed along zone axis [100], [001] and [120], bright contrasts correspond to Ce, darker ones to P.

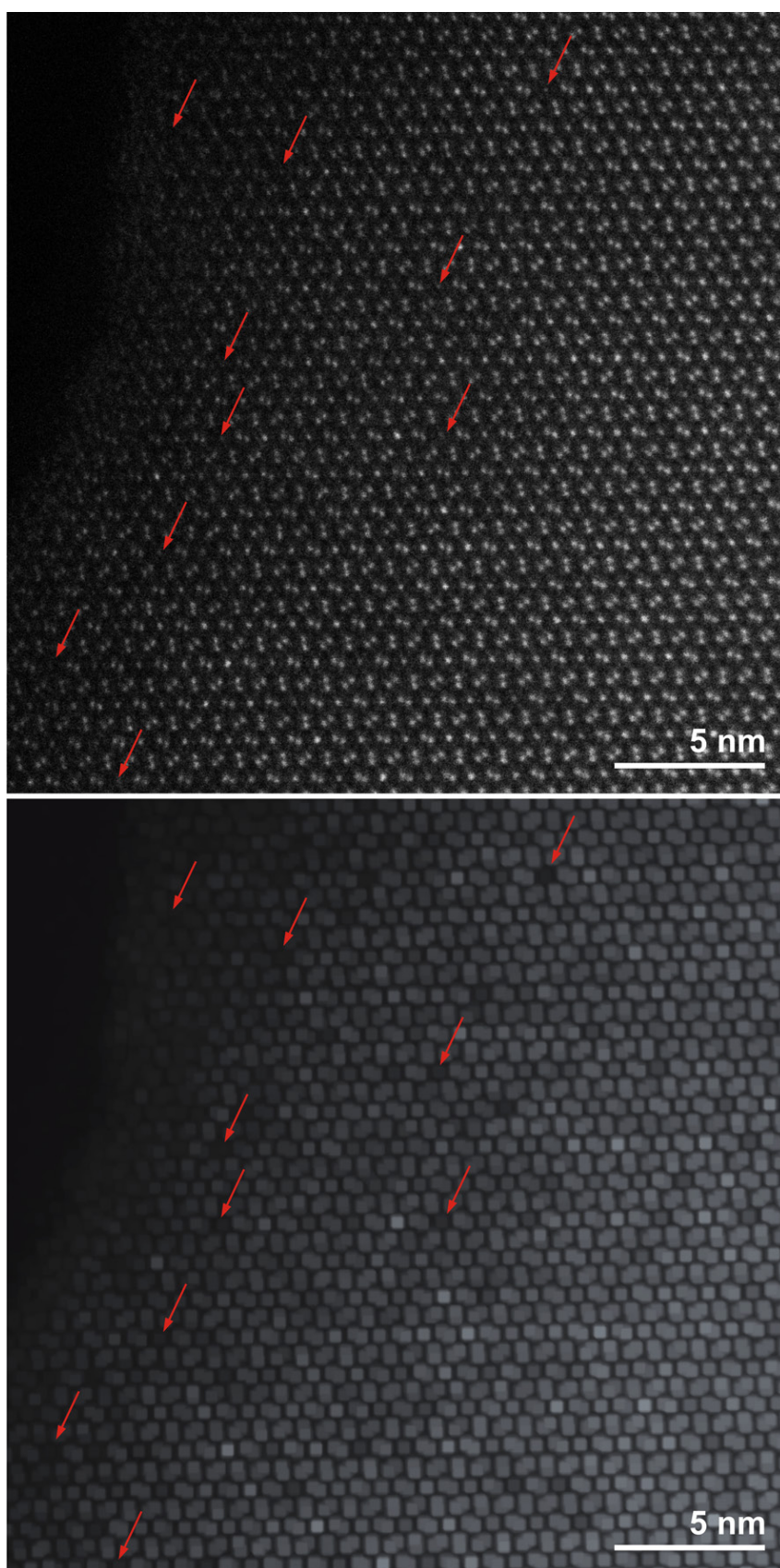


Figure E.9. Top: Experimental unfiltered STEM-HAADF image along [001] showing Ce₂ atom columns with varying intensity (some marked by red arrows). Bottom: Same figure, visually enhanced by interpolating brightness over four pixels, followed by extrapolation of bright areas over nine pixels (with Photoshop).

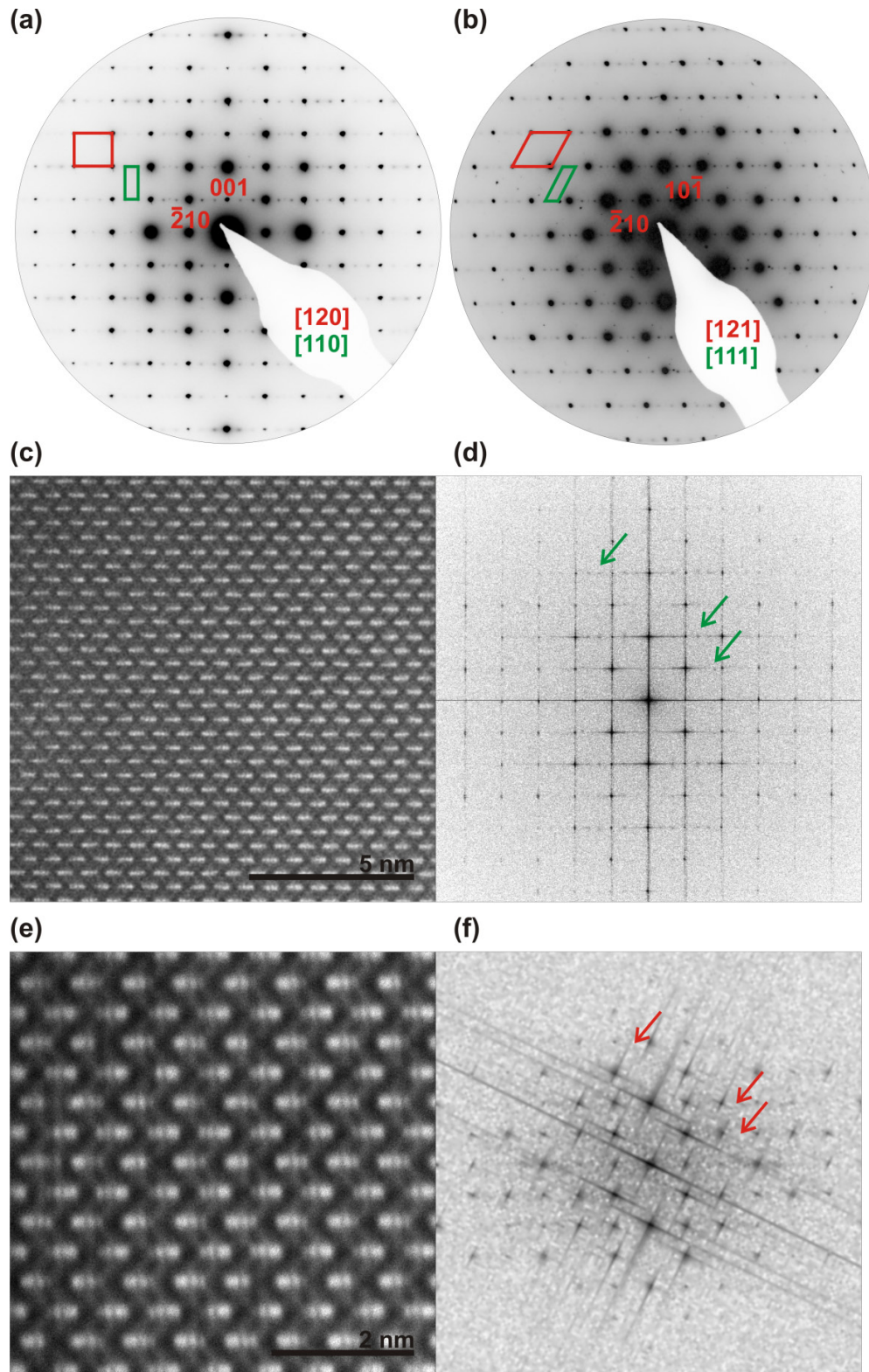


Figure E.10. SAED patterns along [120] (a) and [121] (b) zone axis containing superstructure reflections, pattern indexed with the average structure model (red), supercell highlighted in green. Unfiltered STEM-HAADF image (c) along [120] with corresponding Fourier transform (d) showing superstructure reflections (green arrows) similar to those in SAED above based on different Ce2 positions. STEM-HAADF image (e) along [120] with corresponding Fourier transform (e) of a domain without superstructure, superstructure reflections are missing (red arrows) and no different Ce2 positions can be observed.

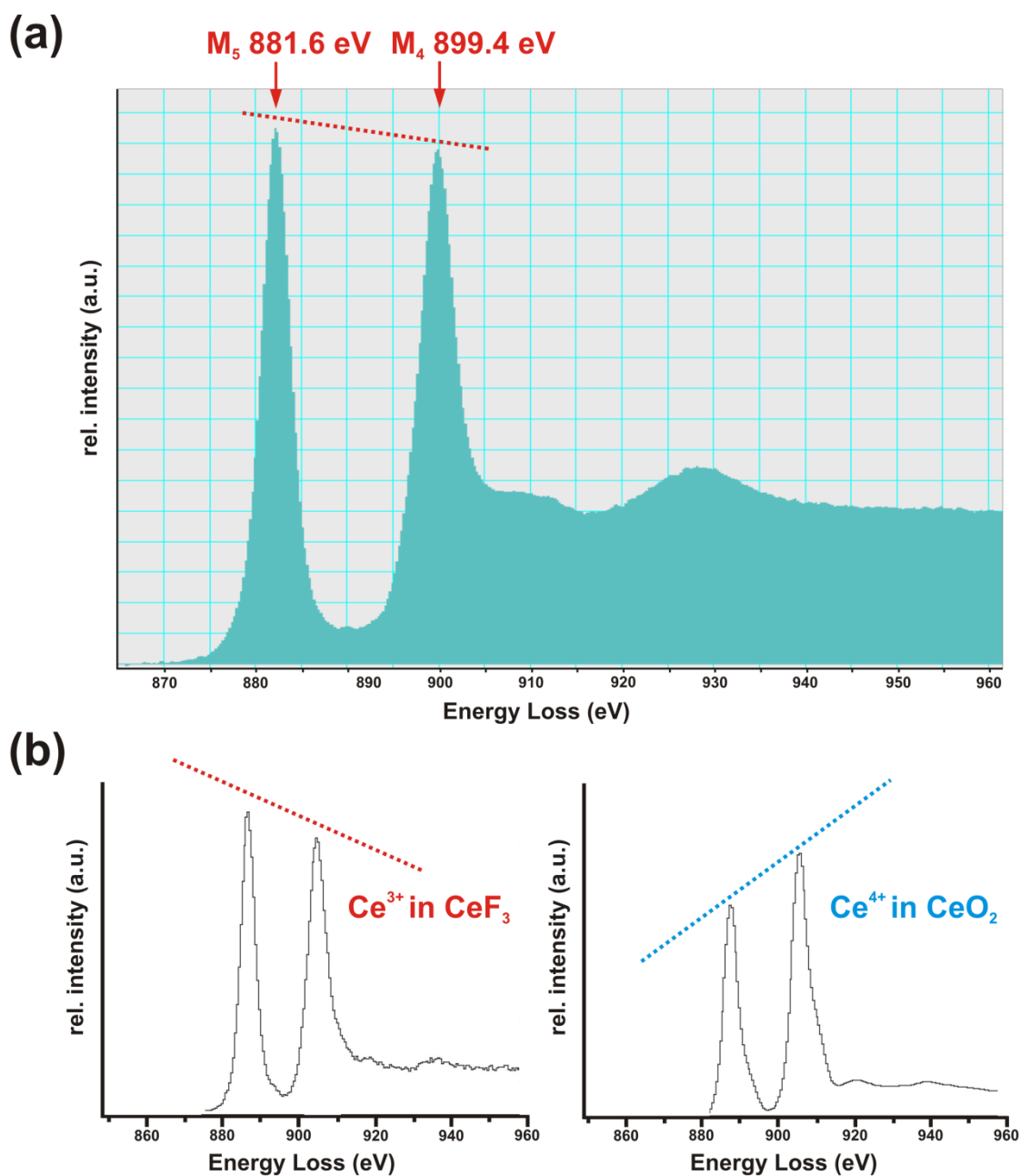


Figure E.11. (a) EELS spectrum of $\text{Ce}_{4-0.5x}\text{Li}_3\text{P}_{18}\text{N}_{35-1.5x}\text{O}_{1.5x}$ ($x \approx 0.72$), red arrows represent positions of the $\text{Ce}^{3+}\text{-M}_5$ and $\text{Ce}^{3+}\text{-M}_4$ edges. (b) Reference EELS spectra of CeF_3 and CeO_2 from Arai et al.^[12] Blue and red dotted lines illustrate different M_5/M_4 ratios in correspondence to Ce^{3+} and Ce^{4+} .

Off-axis EELS spectra do not suggest the presence of Ce^{4+} in $\text{Ce}_{4-0.5x}\text{Li}_3\text{P}_{18}\text{N}_{35-1.5x}\text{O}_{1.5x}$ (Figure E.11). They show relative to the zero loss peak the Ce- M_5 and Ce- M_4 edges at 881.6 eV and 899.4 eV energy loss, respectively. These positions of the Ce signals are very close to typical values for Ce^{3+} (M_5 at 882.0 eV, M_4 at 899.7 eV) in $\text{Ce}_2\text{Zr}_2\text{O}_8$ or CeO_2 . The Ce^{4+} peaks occur at lightly increased energy loss. The M_5 to M_4 ratio is nearly one with the M_5 edge showing more intensity than the M_4 edge. This is in accordance with the higher M_5/M_4 ratio of Ce^{3+} compared to the lower M_5/M_4 ratio of Ce^{4+} known from the literature. The more asymmetrically shaped M_4 edge compared to the M_5 is also characteristic for Ce^{3+} .^[12,13,14]

Ce2 Displacement Measurement

Position deviation of the Ce2 atoms along [001] of 0.3(1) Å is the mean value of 10 directly measured distances from a representative STEM-HAADF micrograph (cf. Figure 5.10). In order to determine the maximum distance between two deflected Ce2 atoms (atoms A and C in Figure 5.10), in a first step the centers of gravity of the Ce2 atoms and a horizontal neutral axis perpendicular to [001] were defined. The distance of 0.3(1) Å is then the sum of the deviations of the centers of gravities of two Ce2 atoms (one above and one below) from the neutral axis in [001] direction.

E.10 Synchrotron Data

Supercell model refinement procedure

Data were integrated (see Experimental section) with the supercell parameters and absorption corrected with SADABS in Laue class $6/m$.^[15] Two *hkl*-files were manually generated for the use with two scale factors; one *hkl*-file contained the average structure reflections and one contained the superstructure reflections ($-h+k = 3n$ are average structure reflections).

Initially, only the z coordinates of all Ce2 atoms within the supercell model were refined (with JANA2006)^[16] on the superstructure reflections, neglecting all symmetry restrictions ($P1$ symmetry). The other atom sites were kept fixed, which is feasible because the superstructure reflections carry information on the Ce2 distortion only and because the average structure is already well-established. The average structure scale factor was refined prior to including the satellite reflections and was kept constant for the following refinement steps since both scale factors were highly correlated. The scale factor of the superstructure reflections was set to the average structure scale factor and kept constant since it is to 100 % correlated to the Ce2 atom displacement. The refinement converged in an R-value of ≈ 30 %. The refined Ce2 displacement of 0.1 \AA corresponds to the minimal value since in this scenario the whole crystal would be modulated. The satellite reflection scale factor scales linearly with the displacement parameters; as the satellite reflection scale factor decreased to a fraction of the average structure scale factor the displacement gets larger ($\approx 0.1 \text{ \AA}$ at same scale factor, $\approx 0.3 \text{ \AA}$ at one third of the average structure scale factor). Since the real superstructure reflection scale factor is unknown the accurate displacement cannot be determined.

A subsequent refinement was carried out in which all atoms were refined, but symmetry restrictions were applied. Those restrained the symmetry to $P6_3/m$ for all non-Ce2 atoms and additional translational symmetry was added to treat the unit cell enlargement.

Reconstructed reciprocal lattice planes

The following reciprocal lattice planes are once shown as originally calculated (with linear intensity scaling) with the program CrysAlis^[17] and once visually enhanced by conversion to gray-scale and optimization of the tonal correction with Adobe Photoshop.

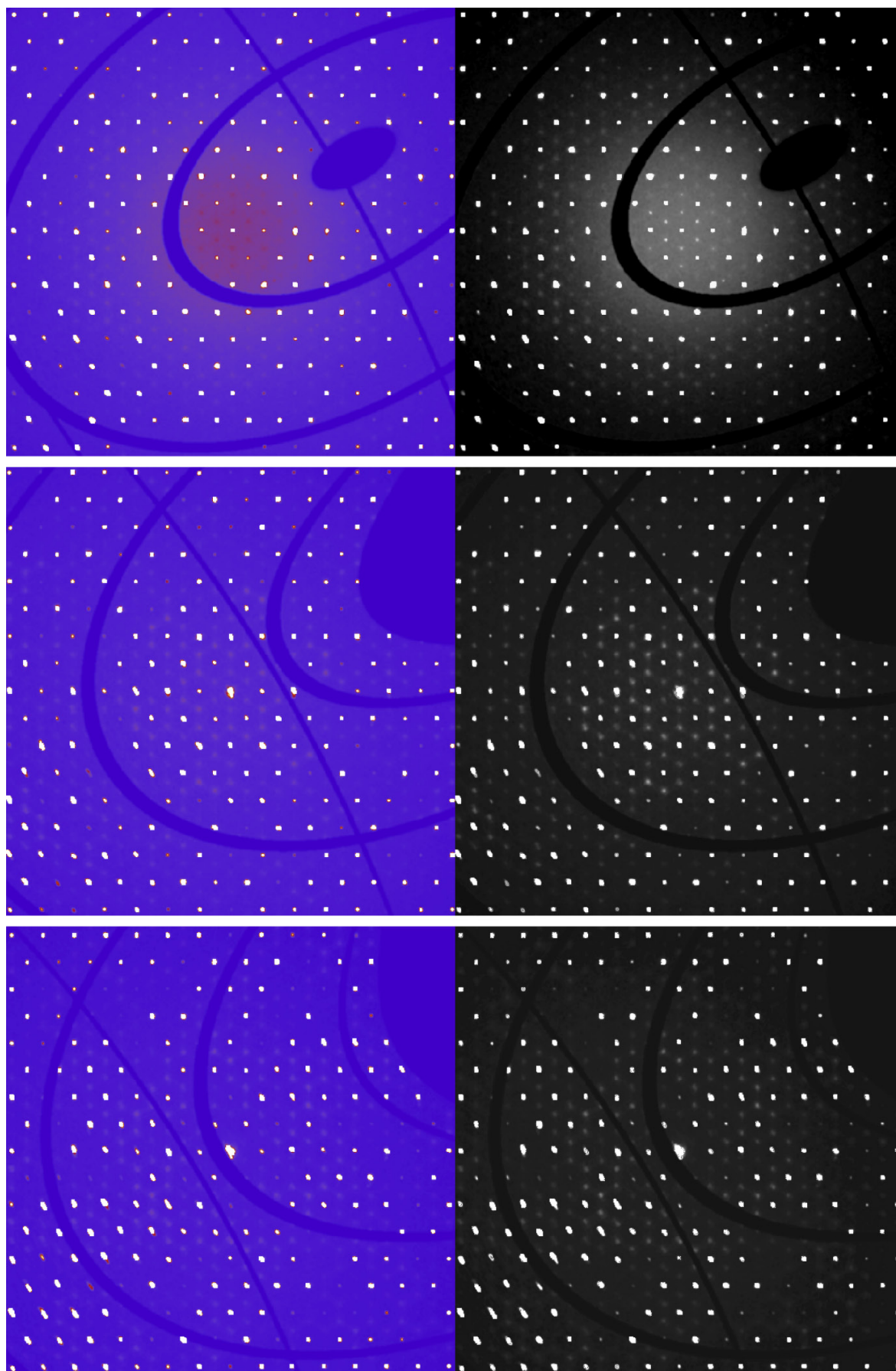


Figure E.12. Top to bottom: hk_2 , hk_4 and hk_6 planes.

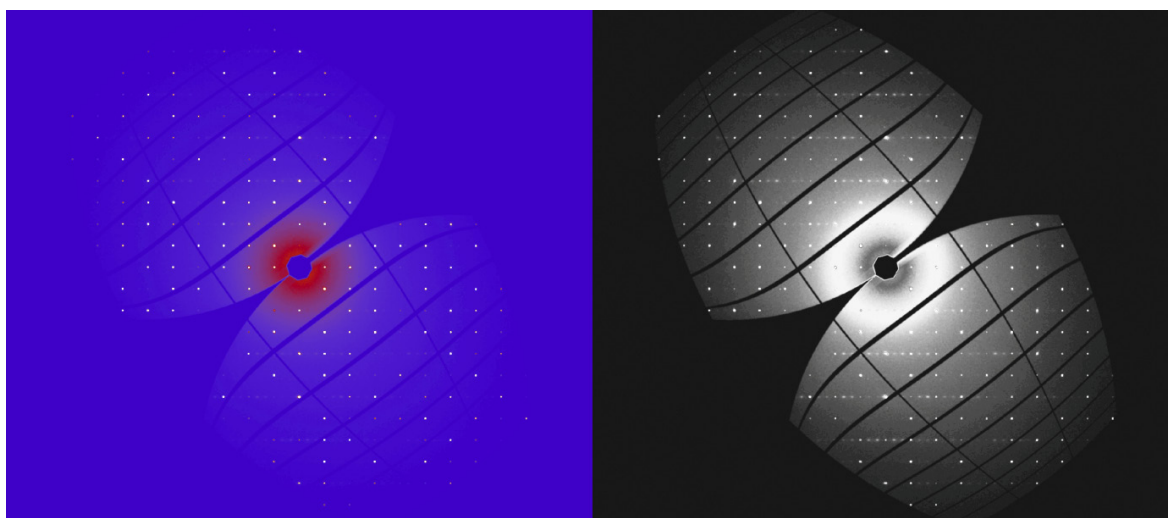


Figure E.13. hhl plane. Visual enhancement (as stated above) reveals superstructure reflections for every lattice plane hkl with $l = 2n$, except for the $hk0$ plane.

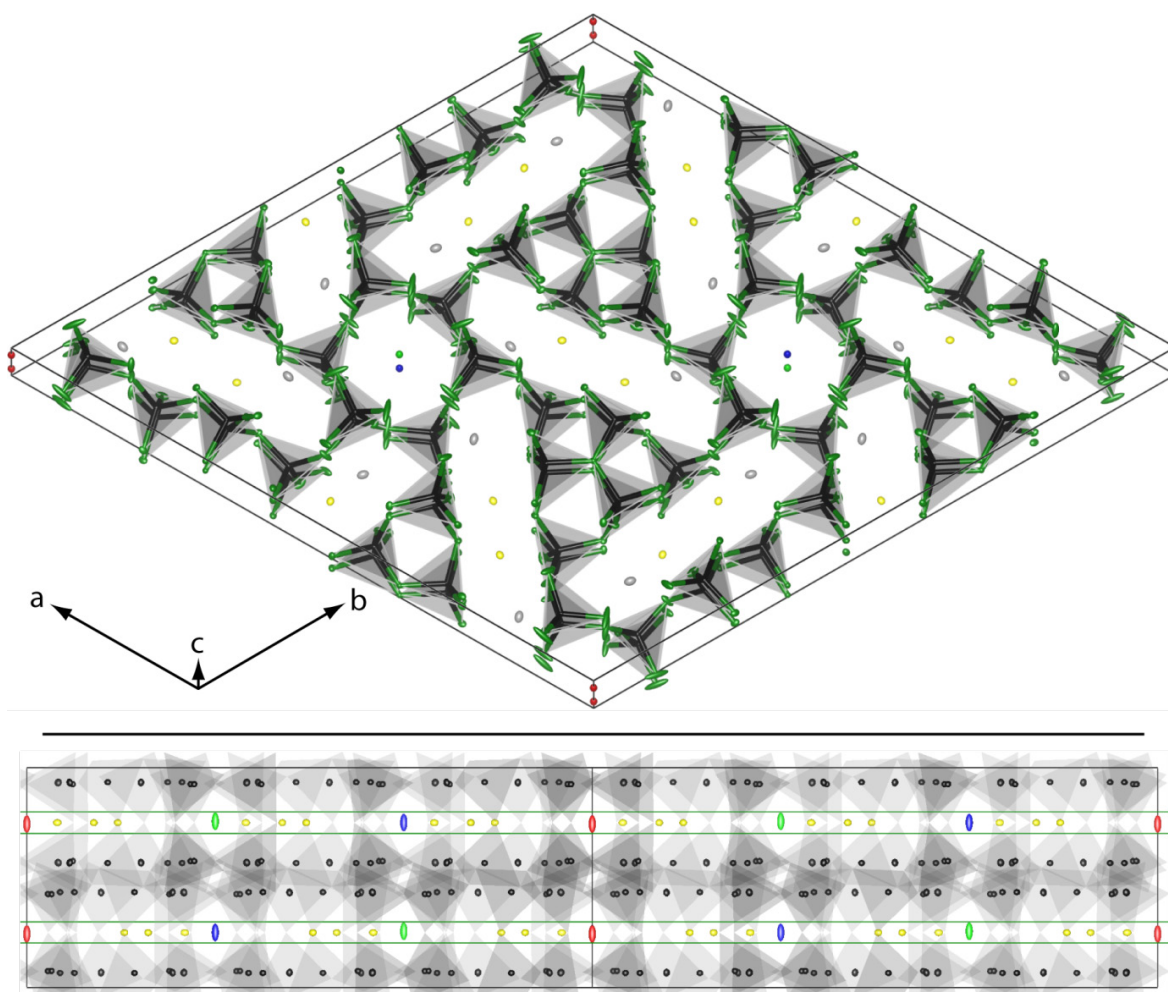


Figure E.14. Results of the superstructure refinement: Ce2 atoms related by symmetry highlighted by the same color. Bottom: viewed along $\langle 110 \rangle$, Ce2 displacement is highlighted by green lines perpendicular $[001]$, N and Li atoms were not displayed for clarity.

Structure Description in (3+2)D superspace

Lattice, symmetry and modulation vectors

Since the superstructure refinement revealed $P6_3$ symmetry for the displaced Ce2 atoms, the superspace group $P6_3(\alpha, \beta, 0)0(-\alpha-\beta, \alpha, 0)0$ was chosen for the (3+2)D modulation description. The diffraction pattern was indexed based on the basic cell with two modulation vectors $\mathbf{q}_1 = (1/3, 1/3, 0)$ and $\mathbf{q}_2 = (-2/3, 1/3, 0)$ (Figure 5.11). The diffraction vector then is:

$$\mathbf{h} = h\mathbf{a}^* + k\mathbf{b}^* + l\mathbf{c}^* + m\mathbf{q}_1 + n\mathbf{q}_2$$

It is apparent that due to the commensurateness of the superstructure an unambiguous indexing is not possible as one satellite is shared by three basic structure reflections. This might be regarded as merohedry in 5D but does not impede structure refinement as the reflections were treated as overlapped.^[18] Hence, a set of three symmetry-equivalent modulation waves is obtained with directions \mathbf{q}_1 , \mathbf{q}_2 and the linear combination $\mathbf{q}_1 + \mathbf{q}_2$. Since the indexing is ambiguous, the maximum satellite order of the reflections $hklmn$ was set to $m = n = 1$. To retain the same satellite order for reflections of the symmetry equivalent direction $\mathbf{q}_1 + \mathbf{q}_2$, the order o is defined as

$$o = \frac{1}{2} (|m| + |n| + |n-m|)$$

Concluding from the superstructure refinement described above, a purely z-polarized modulation function $\mathbf{u}^{\text{Ce2}}(\mathbf{x}_4, \mathbf{x}_5)$ is considered for the displacement of Ce2. Following Fourier's theorem, any wave-like function can be expanded in a basis of periodic sine and cosine functions.

$$\mathbf{u}^{\text{Ce2}}(\mathbf{x}_4, \mathbf{x}_5) = \sum_m \sum_n [A_{mn} \cdot \sin(2\pi \cdot m \cdot \mathbf{x}_4 + 2\pi \cdot n \cdot \mathbf{x}_5) + B_{mn} \cdot \cos(2\pi \cdot m \cdot \mathbf{x}_4 + 2\pi \cdot n \cdot \mathbf{x}_5)]$$

Here, $\mathbf{x}_4 = \mathbf{q} \cdot \mathbf{r} + t$ and $\mathbf{x}_5 = \mathbf{q} \cdot \mathbf{r} + u$, in which \mathbf{r} is the position of the Ce2 atom in unit cell $\mathbf{L} = l_1\mathbf{x} + l_2\mathbf{y} + l_3\mathbf{z}$ and phase shifts t and u denote the distance to physical space.

Of the six amplitudes A_{10} , B_{10} , A_{01} , B_{01} , A_{11} , and B_{11} only two, e.g. A_{10} and B_{10} , have to be determined since the others are related by symmetry. The number of parameters to describe the commensurately modulated structure is two and therefore one less than in the supercell refinement.

Refinement

For the refinement in $P6_3(\alpha, \beta, 0)0(-\alpha-\beta, \alpha, 0)0$, the basic structure model was first transformed to $P6_3$. For all non-modulated atoms, however, the inversion center and mirror plane were manually rein-

roduced by setting local symmetry restrictions. All atomic positions and anisotropic displacement parameters were refined. The amplitudes A_{10} and B_{10} were refined to a significance of 0.004370(15) and 0.00223(3), respectively. The x_3 – x_4 and x_3 – x_5 F_{obs} Fourier maps are shown in Figure E.15. In this refinement, the scale factor of the average structure and the satellite reflection scale factor were assumed to be equal. Therefore, the resulting Ce2 displacement is the minimal value, as for the supercell refinement, since this assumes that the whole crystal is modulated. The site occupancy factors of Ce2 cannot be refined since they are also to 100 % correlated with the scale factor. From TEM EDX data (Table E.10) we inferred that the superstructure domains contain very little oxygen that might just stem from surface hydrolysis. Hence, modulated domains with a fully occupied Ce2 are fathomable, in which local structure has sum formula $\text{Ce}_4\text{Li}_3\text{P}_{36}\text{N}_{70}$.

Superspace Symmetry Discussion

Both the supercell and superspace refinement yielded the same qualitative result and little uncertainty remains about the superstructure. However, in the superspace description, another interpretation of the modulation is possible, since the modulation vectors \mathbf{q}_1 , \mathbf{q}_2 , and $\mathbf{q}_1+\mathbf{q}_2$ are commensurate. In fact, the chosen Bravais class $P6/m(\alpha, \beta, 0)(-\alpha-\beta, \alpha, 0)$ does not contain the full symmetry of the observed lattice. Since $\alpha = \beta = 1/3$, the actual Bravais class should be $P6/mmm(\alpha, \alpha, 0)(-2\alpha, \alpha, 0)$. However, no incommensurate (3+2)D superspace group within this class is compatible with the superstructure.

The case that all components of the wave vectors in (3+2)D dimensions are commensurate can result in a (3+1)D modulation; for those special wave-vectors, *van Smaalen* derived additional commensurate (3+1)D Bravais-classes.^[19] Bravais-class $P6/mmm(1/3, 1/3, 0)$ fits the present problem and therefore the modulation could also be described in an adequate (3+1)D superspace group with $\mathbf{q} = (1/3, 1/3, 0)$.

The commensurate (3+1)D superspace groups are not tabulated, but all space groups in 4D have been derived and are in principle accessible via the program CARAT (including 5D and 6D space groups).^[20–22] However, the deduction of (3+1)D spacegroups with the program is not straightforward so that we rather established it ourselves. Since the superstructure symmetry is known from previous analysis and a superspace group is determined by the arithmetic crystal class and translational components, one can formulate the commensurate (3+1)D superspace group $P6_3(1/3\ 1/3\ 0)0$ with

non-lattice generator $(x_1-x_2, x_1, x_3+1/2, x_4)$. As can be verified by visual inspection of Figure 5.12 and D.14, this superspace group describes the structure as well as the (3+2)D group. The (3+1)D group also resolves the indexing ambiguities since for satellite order $o = 1$, all reflections are then unique. The modulation is then described by one wave triplicated by space group symmetry.

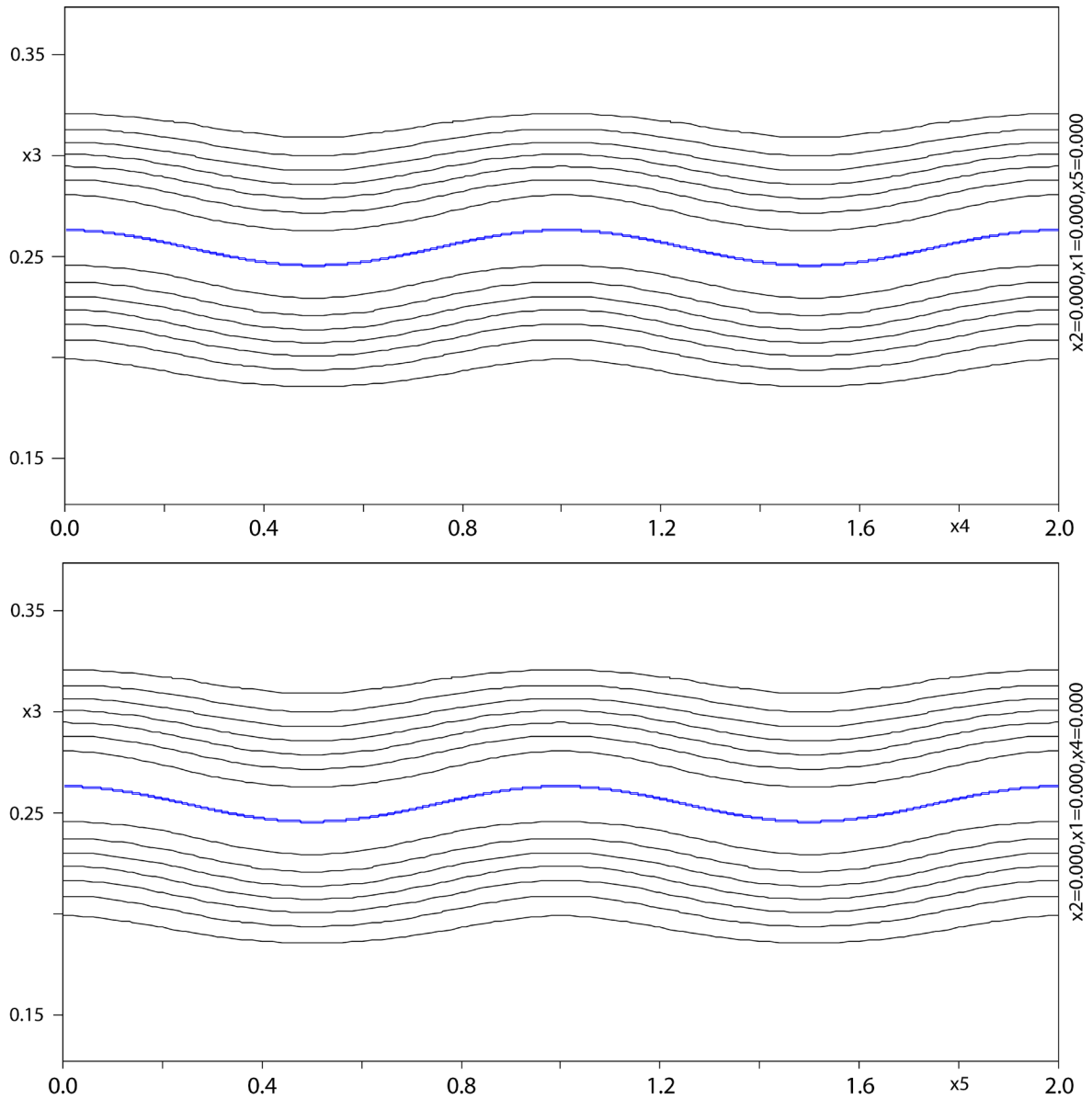


Figure E.15. F_{obs} maps of the Ce2 position (blue line) in superspace. Top: x_3 vs. x_4 ; bottom: x_3 vs. x_5 map. Black lines indicate the electron density profile.

E.11 References

- [1] W. Klemm, G. Z. Winkelmann *Anorg. Allg. Chem.* **1956**, 288, 87–90.
- [2] W. Schnick, J. Z. Lücke *Anorg. Allg. Chem.* **1990**, 588, 19–25.
- [3] K. Landskron, H. Huppertz, J. Senker, W. Schnick *Angew. Chem., Int. Ed.* **2001**, 40, 2643–2645; *Angew. Chem.* **2001**, 113, 2713–2716.
- [4] K. Köllisch, *Dissertation*, “*Neue Beiträge Zur Strukturchemie Der Sione Und Sialone*”, LMU Munich, **2001**.
- [5] K. Momma, F. J. Izumi, *Appl. Crystallogr.* **2011**, 44, 1272–1276.
- [6] V. A. Blatov, A. P. Shevchenko, D. M. Proserpio, *Cryst. Growth Des.* **2014**, 14, 3576–3586.
- [7] O. Delgado-Friedrichs, *3dt*, <http://www.gavrog.org/>, **2013**.
- [8] N. W. Johnson, *Can. J. Math.* **1966**, 18, 169–200.
- [9] S. D. Kloß, W. Schnick, *Angew. Chem., Int. Ed.* **2015**, 54, 11250–11253; *Angew. Chem.* **2015**, 127, 11402–11405.
- [10] M. Somer, U. Herterich, J. Curda, K. Peters, H. G. von Schnering, *Z. Kristallogr.* **1994**, 209, 182.
- [11] S. D. Kloß, N. Weidmann, R. Niklaus, W. Schnick, *Inorg. Chem.* **2016**, 55, 9400–9409.
- [12] S. Arai, S. Muto, J. Murai, T. Sasaki, Y. Ukyo, K. Kuroda, H. Saka, *Mater. Trans.* **2004**, 45, 2951–2955.
- [13] L. A. J. Gravier, P. R. Buseck, *J. Phys. Chem. Solids* **1999**, 60, 1943–1947.
- [14] A. M. D’Angelo, A. C. Y. Liu, A. L. Chaffee, *J. Phys. Chem. C* **2016**, 120, 14382–14389.
- [15] Bruker AXS, Inc., *SADABS*, Madison, Wisconsin, USA, **2001**.
- [16] V. Petříček, M. Dušek, L. Palatinus, *Z. Kristallogr. – Cryst. Mater.* **2014**, 229, 345–352.
- [17] Agilent Technologies, *CrysAlis Pro*, Yarnton, Oxfordshire, England, **2011**.
- [18] L. Bindi, P. Bonazzi, M. Dušek, V. Petříček, G. Chapuis, *Acta Crystallogr., Sect. B: Struct. Sci.* **2001**, 57, 739–746.
- [19] S. Van Smaalen, *Acta Crystallogr., Sect. A: Found. Crystallogr.* **1987**, 43, 202–207.
- [20] W. Plesken, T. Schulz, *Exp. Math.* **2000**, 9, 407–411.
- [21] T. Janssen, A. Janner, E. Ascher, *Physica* **1969**, 42, 41–70.
- [22] G. Fast, T. Janssen, *J. Comput. Phys.* **1971**, 7, 1–11.

Appendix F. Supporting Information for Chapter 6

F.1 Rietveld refinement

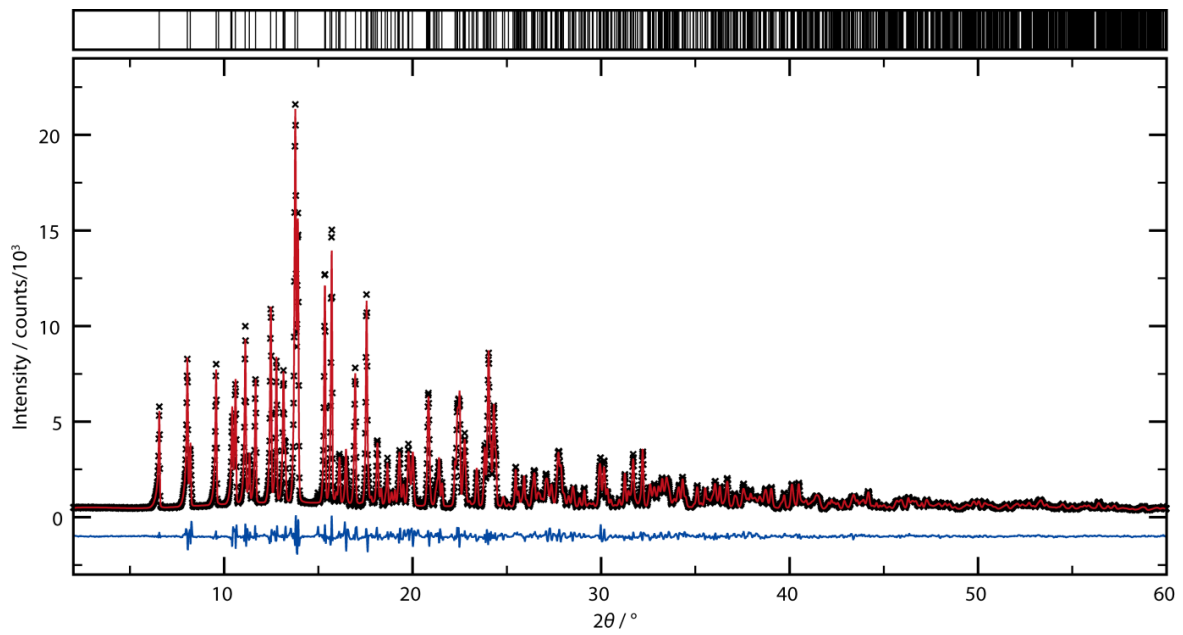


Figure F.1. Rietveld refinement of $\text{LiPr}_2\text{P}_4\text{N}_7\text{O}_3$. Experimental data as black crosses, Rietveld fit in red, difference plot in blue. Positions of Bragg-reflections marked by black vertical drop lines.

Table F.1. Crystallographic data for the Rietveld refinement of $\text{LiPr}_2\text{P}_4\text{N}_7\text{O}_3$.

Crystal Data	
Formula	$\text{LiPr}_2\text{P}_4\text{N}_7\text{O}_3$
Crystal system, space group	monoclinic, $P2_1/c$ (no. 14)
Lattice parameters / Å, °	$a = 4.9617(3)$ $b = 7.8600(4)$ $c = 10.1065(6)$ $\beta = 91.646(3)$
Cell volume / Å ³	393.98(4)
Formula units per cell Z	2
Data Collection	
Radiation	Mo-K α_1 ($\lambda = 0.7093$ Å)
Monochromator	Ge(111)
Diffractometer	Stoe StadiP
Detector	MYTHEN 1K
2 θ -range / °	2–60
Temperature / K	297(2)
Data points	3886
Number of observed reflections	1193
Refinement	
Number of parameters	103
Program used	TOPAS Academic V4.1
Structure refinement	Rietveld-Method
Profile function	fundamental parameters model
Background function	shifted Chebychev polynomial (14 terms)
R_{wp}	0.116
R_{exp}	0.028
R_{p}	0.057
R_{Bragg}	0.020
GoF	2.692

F.2 Infrared spectroscopy

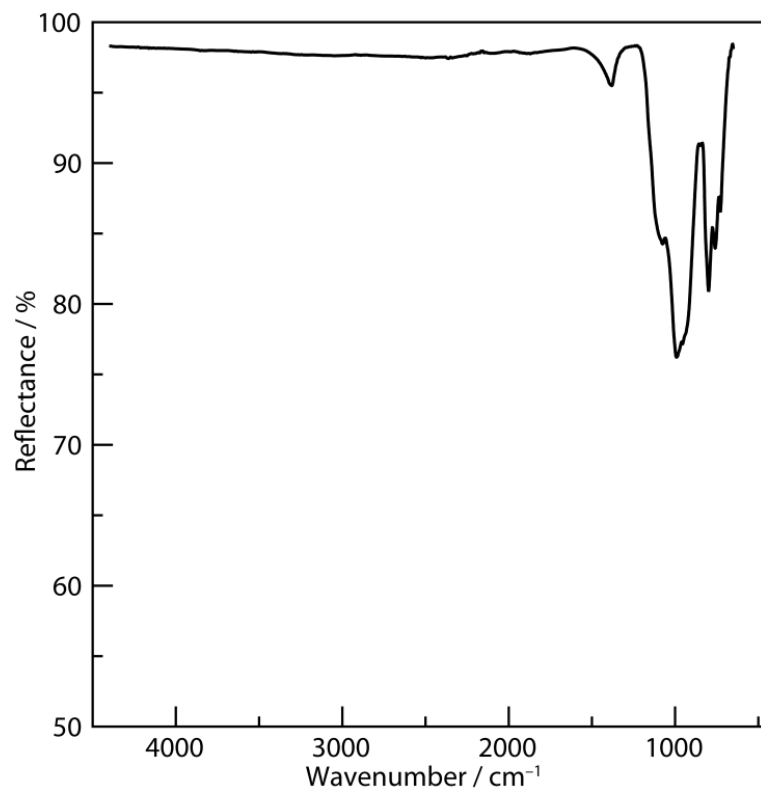


Figure F.2. FTIR spectrum of $\text{LiPr}_2\text{P}_4\text{N}_7\text{O}_3$ obtained in ATR geometry.

F.3 Crystallographic tables

Table F.2. Anisotropic displacement parameters occurring in $\text{LiPr}_2\text{P}_4\text{N}_7\text{O}_3$. Sites N1/O1 and N5/O5 are shared positions.

Atom	$U_{11} / \text{\AA}^2$	$U_{22} / \text{\AA}^2$	$U_{33} / \text{\AA}^2$	$U_{23} / \text{\AA}^2$	$U_{13} / \text{\AA}^2$	$U_{12} / \text{\AA}^2$
Pr1	0.00797(4)	0.00867(3)	0.00665(3)	-0.00017(2)	0.00137(2)	-0.00110(2)
P1	0.00719(13)	0.00526(12)	0.00433(12)	0.00044(9)	0.00053(10)	0.00044(10)
P2	0.00736(13)	0.00603(13)	0.00535(12)	-0.00023(9)	0.00092(10)	-0.00023(10)
O1	0.0100(4)	0.0084(4)	0.0082(4)	0.0000(3)	-0.0013(3)	-0.0028(3)
N1	0.0100(4)	0.0084(4)	0.0082(4)	0.0000(3)	-0.0013(3)	-0.0028(3)
N2	0.0095(5)	0.0061(4)	0.0098(4)	-0.0008(3)	0.0032(3)	0.0000(3)
N3	0.0107(5)	0.0091(4)	0.0072(4)	0.0025(3)	0.0034(3)	0.0033(4)
N4	0.0081(4)	0.0094(4)	0.0063(4)	0.0019(3)	0.0005(3)	0.0013(3)
O5	0.0097(4)	0.0105(4)	0.0083(4)	-0.0002(3)	-0.0004(3)	-0.0009(3)
N5	0.0097(4)	0.0105(4)	0.0083(4)	-0.0002(3)	-0.0004(3)	-0.0009(3)
Li1	0.016(2)	0.034(3)	0.013(2)	0.000(2)	-0.0028(17)	-0.007(2)

Table F.3. Bond lengths [\AA] occurring in $\text{LiPr}_2\text{P}_4\text{N}_7\text{O}_3$.

Pr1–(N/O)		P1–(N/O)	
Pr1–N1/O1	2.4556(14)	P1–N1/O1	1.5579(13)
Pr1–N1/O1	2.4895(13)	P1–N2	1.6323(13)
Pr1–N2	2.5128(15)	P1–N3	1.6312(14)
Pr1–N3	2.5321(14)	P1–N4	1.6449(14)
Pr1–N4	2.6520(14)		
Pr1–N4	2.7251(15)	P2–(N/O)	
Pr1–N5/O5	2.4820(13)	P2–N2	1.6441(14)
Pr1–N5/O5	2.6013(14)	P2–N3	1.6529(14)
		P2–N4	1.6679(13)
		P2–N5/O5	1.5610(14)
Li1–(N/O)			
Li1–N5/O5	2.1586(14)		
Li1–N2	2.2219(15)		
Li1–N3	2.4349(15)		

Table F.4. Angles [°] occurring in $\text{LiPr}_2\text{P}_4\text{N}_7\text{O}_3$.

(N/O)–P1–(N/O)		P–N–P	
N1/O1–P1–N3	110.08(7)	P1–N2–P2	124.89(9)
N1/O1–P1–N2	106.10(7)	P1–N3–P2	119.55(8)
N3–P1–N2	112.22(7)	P1–N4–P2	117.99(8)
N1/O1–P1–N4	111.78(7)		
N3–P1–N4	107.71(7)		
N2–P1–N4	109.01(7)		
(N/O)–P2–(N/O)			
N5/O5–P2–N2	114.67(7)		
N5/O5–P2–N3	112.27(7)		
N2–P2–N3	107.73(8)		
N5/O5–P2–N4	113.64(7)		
N2–P2–N4	102.13(7)		
N3–P2–N4	105.51(7)		

F.4 Electrostatics

Bond valence sums (BVS)

Table F.5. Bond valence sums calculated with ValList for the anions of the $\text{LiPr}_2\text{P}_4\text{N}_7\text{O}_3$ structure model.^[1] Atom positions, which might partially be occupied by oxygen, are marked with green color.

Atom	N1	O1	N2	O2	N3	O3	N4	O4	N5	O5
BVS	2.54	2.029	3.076	2.42	2.933	2.315	2.859	2.273	2.611	2.058

Charge distribution (CHARDI) calculations

CHARDI calculations were performed with VESTA, following the theory of Hoppe et al.^[2,3] Table F.6 contains the CHARDI values for each cation, Pr1, Li1, P1, and P2. The CHARDI values for N1/O1 and N5/O5 show a lower Q value than the other N positions. This might indicate a mixed occupancy of O and N on this position, in accordance with the findings of BVS.

Table F.6. CHARDI values calculated for each of the cations. With Δq as the fraction of the charge received by the ion, Q the total charge received by the ion, and q the formal charge.

Cation/Atom site	Δq	Q	q
Pr1			
N5/O5	0.332	-2.581	-2.25
N1/O1	0.467	-2.431	-2.25
N2	0.413	-2.965	-3
N4	0.288	-2.709	-3
N4	0.228	-2.709	-3
N1/O1	0.435	-2.431	-2.25
N5/O5	0.442	-2.581	-2.25
N3	0.395	-2.813	-3
Pr1		2.92	3
Li1			
N2	0.188	-2.965	-3
N5/O5	0.22	-2.581	-2.25
N3	0.091	-2.813	-3
N2	0.188	-2.965	-3
N5/O5	0.22	-2.581	-2.25
N3	0.091	-2.813	-3
Li1		0.96	1
P1			
N1/O1	1.529	-2.431	-2.25
N2	1.175	-2.965	-3
N3	1.18	-2.813	-3
N4	1.116	-2.709	-3
P1		5.098	5
P2			
N5/O5	1.587	-2.581	-2.25
N3	1.147	-2.813	-3
N2	1.188	-2.965	-3
N4	1.078	-2.709	-3
P2		5.002	5

F.5 High-temperature X-ray powder diffraction

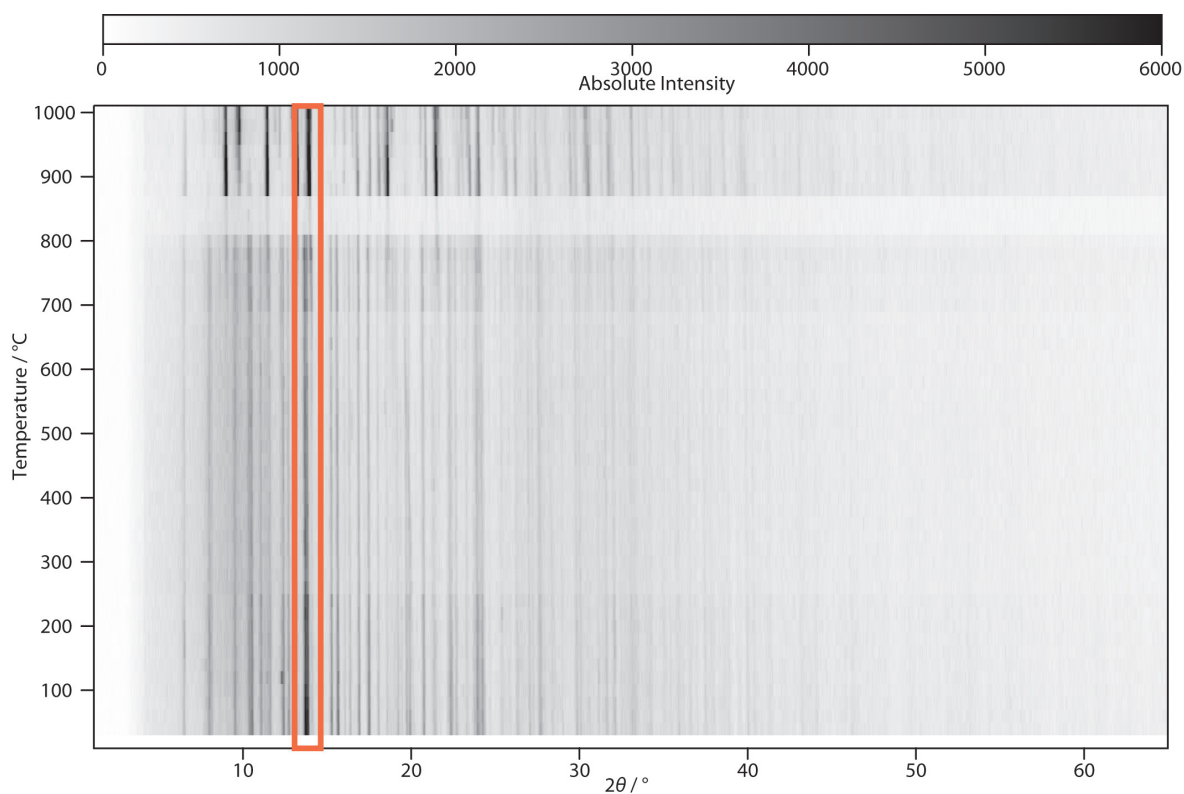


Figure F.3. Temperature-dependent powder diffraction pattern. Data collected in steps of 20 °C up to 1000 °C in air. Orange-bordered area highlights the main reflection of $\text{LiPr}_2\text{P}_4\text{N}_7\text{O}_3$ (left peak) and Pr_2O_3 (right peak).^[4] The Pr_2O_3 intensity is first observed at ca 500 °C. Diffractograms in the range of 820 °C to 860 °C have weaker intensity, which is due to a measurement artifact.

F.6 References

- [1] A. S. Wills, *Valist*, Program available from www.ccp14.ac.uk, **2011**.
- [2] K. Momma, F. Izumi, *J. Appl. Crystallogr.* **2011**, *44*, 1272–1276.
- [3] R. Hoppe, S. Voigt, H. Glaum, J. Kissel, H. P. Müller, and K. Bernet, *J. Less-Common Met.*, **1989**, *156*, 105-122.
- [4] O. Greis, R. Ziel, B. Breidenstein, A. Haase, T. Petzel, *J. Alloys Compd.* **1995**, *216*, 255–258.

Appendix G. Supporting Information for Chapter 7

G.1 Experimental

P₃N₅. P₃N₅ is starting material for the synthesis of LiPN₂ and was prepared by ammonolysis (NH₃, Air Liquide 5.0) of phosphorus pentasulfide P₄S₁₀ (Sigma-Aldrich, 99.99 %) in a tube furnace lined with a fused silica tube.^[1] Prior to the reaction, a fused silica boat was dried at 1000 °C in a dynamic vacuum maintained at < 10⁻³ mbar for 4 h. The fused silica boat was loaded with P₄S₁₀ in an Ar counterflow, after which the tubing and the P₄S₁₀ was saturated with ammonia gas for 4 h. The reaction was conducted at 850 °C with temperature ramps of 5 °C/min while a constant flow of ammonia was maintained. The residual ammonia was purged with ammonia and the product was obtained after step wise washing with water/ethanol/acetone in form of an orange powder. The product was characterized by PXRD and IR.

LiPN₂. LiPN₂ was prepared by reaction of P₃N₅ with a 1.2 times excess of Li₃N (94 %, Rockwood Lithium, Langelsheim, Germany) in a Ta crucible residing in a sealed fused silica ampoule.^[2] The starting materials were thoroughly mixed and ground under the inert conditions of a glovebox with concentrations of O₂ and H₂O < 1 ppm. The sealed of ampoule was fired at 800 °C with a 90 h dwell and 5 °C/min temperature ramps. The obtained brownish product was consecutively washed with water/ethanol/acetone and characterized by IR and PXRD.

Li₂O. Li₂O was prepared by thermal decarboxylation of Li₂CO₃ (Sigma-Aldrich 99.99 %) under dynamic vacuum conditions at 700 °C. An Ag boat was loaded with Li₂CO₃ and transferred in a fused silica tube connected to the vacuum/inert gas line.^[3] The Li₂CO₃ was decarboxylated for 72 h or reaction finish, then stored in the glovebox. The purity of the reaction product was verified by PXRD.

Hf_{9-x}P₂₄N_{52-4x}O_{4x} (x ≈ 1.84). The title compound was prepared by high-pressure metathesis starting from stoichiometric amounts of HfCl₄ (99.9 %, abcr GmbH), LiPN₂, and Li₂O. The starting materials were handled under the inert conditions of a glovebox. The reaction conditions of 8 GPa and 1300 °C were achieved with a hydraulic 1000 t press (Voggenreiter, Mainleus, Germany) using the multi-anvil technique. The multianvil setup resided inside a modified Walker-type module and consisted of six steel wedges driving the usual octahedron-within-cube setup. The 18/11-size setup comprised

eight 7-% Co-doped tungsten carbide cubes (Hawedia, Marklkofen, Germany) and a 6-% Cr₂O₃-doped MgO octahedron (Ceramic Substrates & Components, Isle of Wight, U.K.). The sample resided within an h-BN crucible (Henze, Kempten, Germany), while temperature was controlled with a graphite sleeve resistance-heating assembly. (Schunk Kohlenstofftechnik GmbH, Zolling, Germany). Additional information regarding high-pressure techniques can be found in the literature.^[4-8]

Spectroscopy. Scanning electron microscopy (SEM) with attached energy dispersive X-ray (EDX) spectroscopy was carried out with a Helios Nanolab G3 Dualbeam UC (FEI, Hillsboro, OR, United States) equipped with a X-Max 80 SDD detector (Oxford Instruments, Abingdon, United Kingdom). Samples were coated with carbon and resided on an adhesive conducting carbon foil affixed to a metal carrier

Infrared spectra were recorded on a Spectrum BX II spectrometer (PerkinElmer Waltham, MA, United States) with DuraSampler ATR-unit in the range of 650–4500 cm⁻¹.

A V-650 UV-Vis spectrophotometer (JASCO, Gross-Umstadt, Germany) equipped with a photomultiplier tube detector and a single monochromator with 1200 lines/mm was used for recording UV-Vis spectra in the range of 240 to 800 nm. A deuterium (240–330 nm) and a halogen lamp (330–880 nm) was used with a 2 nm resolution and a scan speed of 400 nm/min controlled by the Spectra Manager II software. Samples were affixed between a fused silica glass slide and a BaSO₄-coated stamp.

Single-Crystal Diffraction. Single-crystal diffraction was carried out on a D8 Quest (Bruker, Billerica, MA, United States) diffractometer. Cell determination, data reduction, semiempirical absorption correction (SADABS), and reconstruction of reciprocal lattice planes was performed with the APEX3 software.^[9,10] Space group determination was based on analysis of systematically absent reflections with XPREP, structure solution and refinement were carried out with SHELX-97.^[11-13] Suitable crystals were affixed on MicroMounts (MiTeGen, Ithaca, NY, United States) for the measurement. Crystal structures and electron density maps were visualized with VESTA.^[14]

Powder X-ray diffraction. PXRD data were collected on a Stadi P diffractometer (Stoe & Cie GmbH, Darmstadt, Germany) with MYTHEN 1K (Dectris, Baden, Switzerland) in parafocusing Debye-Sher-

rer geometry. Mo- $K_{\alpha 1}$ radiation ($\lambda = 0.709300 \text{ \AA}$) was used, selected by a Ge single-crystal monochromator. Microcrystalline samples were loaded to glass capillaries with 0.3 mm outer and 0.28 mm inner diameter (Hilgenberg GmbH, Malsfeld, Germany). Diffractograms were recorded in the range of $2\theta = 2\text{--}76^\circ$.

Data was analyzed by Rietveld refinement carried out with TOPAS-Academic V4.1.^[15,16] Peak profiles were modeled by a fundamental parameters approach consisting of a direct convolution of axial instrument contributions, source emission profile, crystallite size, and microstrain effects. The background was approximated with a shifted-Chebyshev polynomial.

High-temperature PXRD was recorded on a Stadi P diffractometer (Stoe & Cie GmbH, Darmstadt, Germany) in the range of $2\theta = 2\text{--}55^\circ$ using Mo- $K_{\alpha 1}$ radiation ($\lambda = 0.709300 \text{ \AA}$). X-ray were detected with an image-plate position-sensitive detector. Diffractograms were collected in 20 °C steps up to 1000 °C. Samples resided in fused silica capillaries with a 0.5 mm outer and 0.48 mm inner diameter (Hilgenberg GmbH, Malsfeld, Germany).

Magnetometry. Magnetic susceptibility and isothermal magnetization measurements were conducted with a Quantum Design PPMS EverCool-II measurement system with a 9 T magnet and a vibrating sample magnetometer (VSM). Susceptibility measurements were carried out at a magnetic field of 1000 Oe in the temperature range between 1.9 and 300 K. Isothermal magnetization curves were recorded at 1.9 and 300 K with magnetic field strengths up to 50 kOe. Samples were affixed in plastic capsules (QD-P125E, Quantum Design Inc.). Data were recorded with the program PPMS MultiVu.^[17]

Electron energy loss spectroscopy. Energy dispersive X-ray (EDX) spectroscopy and electron energy loss spectroscopy (EELS) were performed on a Titan Themis at 300 kV. For EDX spectroscopy, a windowless Super X detector was used. EELS was performed with a Gatan Enfium spectrometer at a convergence angle of 16.6 mrad and a collection angle of 44 mrad.

Solid state NMR. ^7Li NMR spectra were recorded on a DSX Avance spectrometer (Bruker) at a magnetic field of 11.7 T. The samples were loaded into a 2.5 mm rotor made of ZrO_2 . The rotor was moun-

ted on a commercial MAS probe (Bruker). Spectra were recorded at a rotation frequency of 20 kHz and at room temperature. The raw data were analyzed with the device-specific software.

G.2 Additional information on synthesis

The endmember of $\text{Hf}_{9-x}\text{P}_{24}\text{N}_{52-4x}\text{O}_{4x}$ with $x = 0$ could not be prepared by stoichiometric reaction as the two heavy atom positions (as discussed later) in the structure always have a Hf deficiency. The compound seems to have a broad phase stability regarding the amount of Hf offered during reaction. Crystallographic pure compounds (see Figure G.1) were even obtained after reaction of starting materials with the element ratio Hf:P:N:O 4:25.6:41.6:9.6, less than half of the Hf needed for a stoichiometric reaction. Rietveld refinement of such powders, however, did not suggest that such an actual composition; the excess P/N/O might react with the boron nitride crucible or forms an amorphous byproduct. A certain flexibility in the Hf:N:O ratio is to be expected, but the actual range was not determined.

G.3 Powder X-ray diffraction

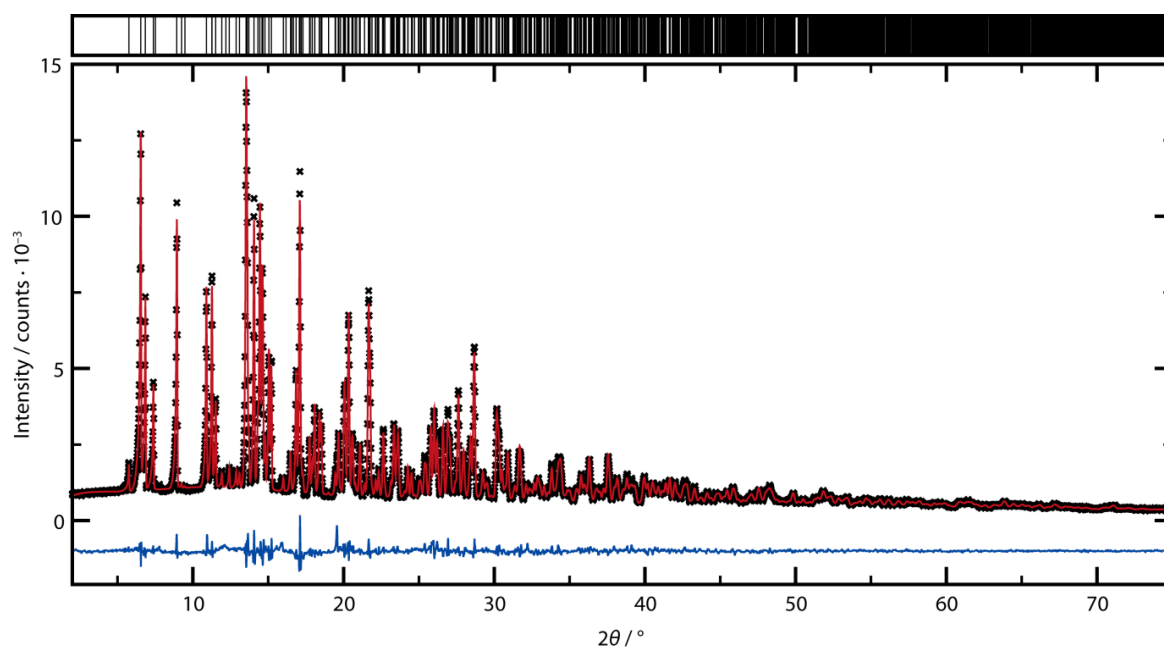


Figure G.1. Rietveld refinement of a $\text{Hf}_{9-x}\text{P}_{24}\text{N}_{52-4x}\text{O}_{4x}$ ($x \approx 1.84$) sample, datapoints as black crosses, fit as red line, difference plot as blue line, ($\lambda(\text{Mo-K}_{\alpha 1}) = 0.709300 \text{ \AA}$). The background is non-linear but slightly curved, indicative of an amorphous phase.

Table G.1. Crystallographic data for the Rietveld refinement of $\text{Hf}_{9-x}\text{P}_{24}\text{N}_{52-4x}\text{O}_{4x}$ ($x \approx 1.84$).

Crystal Data	
Formula	$\text{Hf}_{9-x}\text{P}_{24}\text{N}_{52-4x}\text{O}_{4x}$ ($x \approx 1.84$)
Crystal system, space group	Tetragonal, $I4_1/acd$ (no. 142, origin choice 2)
Lattice parameters / Å	$a = 12.4443(2)$ $c = 23.7674(4)$
Cell volume / Å ³	3680.6(1)
Formula units per cell Z	4
Data Collection	
Radiation	Mo-K α_1 ($\lambda = 0.7093$ Å)
Monochromator	Ge(111)
Diffractometer	Stoe StadiP
Detector	MYTHEN 1K
2θ -range / °	2–76
Temperature / K	297(2)
Data points	4958
Number of observed reflections	2523
Refinement	
Number of parameters	62
Constraints	0
Program used	TOPAS Academic V4.1
Structure refinement	Rietveld-Method
Profile function	fundamental parameters model
Background function	shifted Chebychev polynomial with 14 terms
R_{wp}	0.052
R_{exp}	0.029
R_{p}	0.039
R_{Bragg}	0.017
GoF	1.785

G.4 Scanning Electron Microscopy

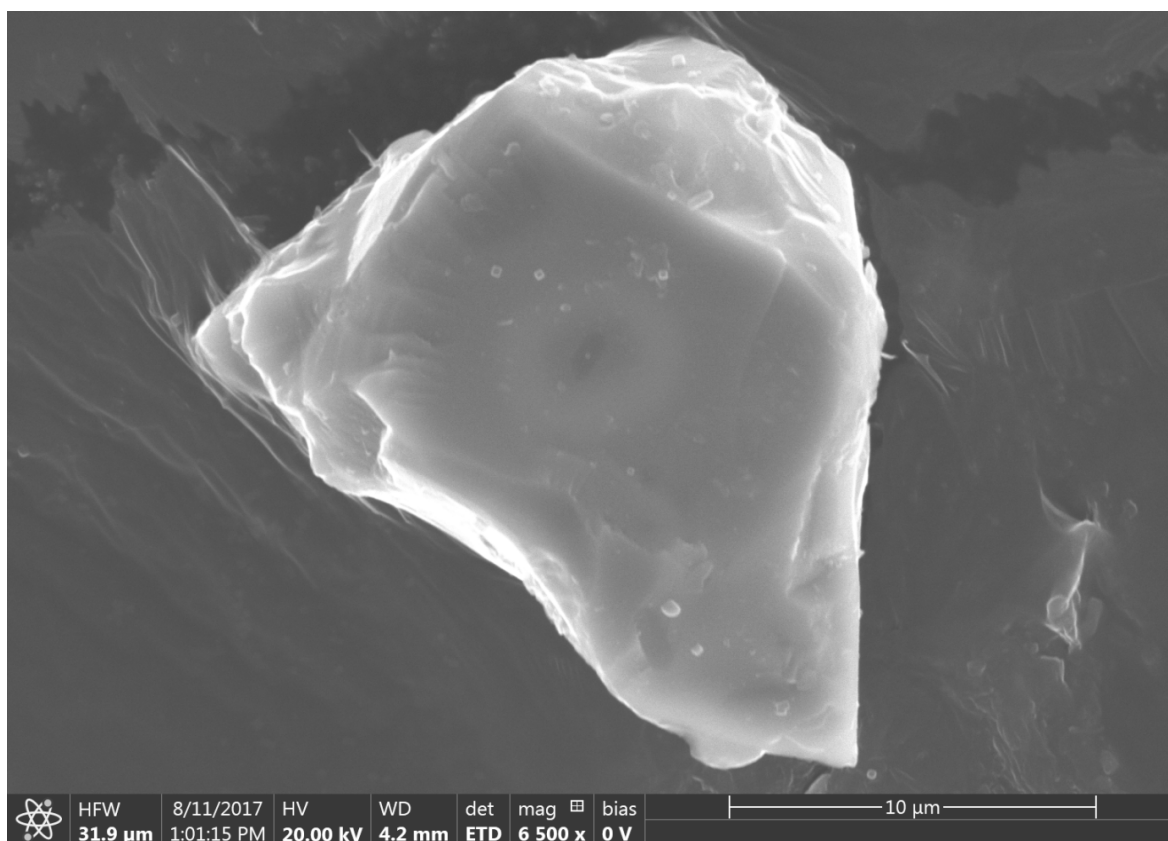


Figure G.2. SEM micrograph of a $\text{Hf}_{9-x}\text{P}_{24}\text{N}_{52-4x}\text{O}_{4x}$ ($x \approx 1.84$) crystal.

G.5 Crystallographic tables

Table G.2. Crystallographic data for $\text{Hf}_{9-x}\text{P}_{24}\text{N}_{52-4x}\text{O}_{4x}$ ($x \approx 1.84$).

Crystal Data	
Formula	$\text{Hf}_{7.16}\text{P}_{24}\text{N}_{44.64}\text{O}_{7.36}$
Formula mass / $\text{g}\cdot\text{mol}^{-1}$	2765.32
Crystal system	tetragonal
Space group	$I4_1/acd$ (no. 142, origin choice 2)
Cell parameters / \AA	$a = 12.466(1)$ $c = 23.719(2)$
Cell volume / \AA^3	3685.7(9)
Formula units per unit cell Z	4
$F(000)$	4989
Calculated density ρ / $\text{g}\cdot\text{cm}^{-3}$	4.984
Abs. coefficient μ / mm^{-1}	21.251
Data Collection	
Radiation	Mo- K_α
Temperature / K	293(2)
θ range / deg.	$2.879 \leq \theta \leq 32.576$
Total no. of reflections	86876
Independent reflections	1684
Absorption correction	semiempirical ^[9]
R_{intr} R_{sigma}	0.076, 0.018
Refinement	
Refined parameters	107
Goodness of fit	1.113
R_1 (all data), $R_1 [F^2 > 2\sigma(F^2)]$	0.025, 0.021
wR_2 (all data), $wR_2 [F^2 > 2\sigma(F^2)]$	0.048, 0.046
$\Delta\rho_{\text{max}}$ $\Delta\rho_{\text{min}}$ / $\text{e}\cdot\text{\AA}^{-3}$	1.39, -1.37

Table G.3. Atom position of $\text{Hf}_{9-x}\text{P}_{24}\text{N}_{52-4x}\text{O}_{4x}$ ($x \approx 1.84$).

Atom	Wyckoff Position	<i>a</i>	<i>b</i>	<i>c</i>	$U_{\text{eq}} / \text{\AA}^2$	Occupancy
Hf1	32g	0.36275(2)	0.04603(2)	0.04216(2)	0.01036(5)	0.881(3)
Hf2	8b	0	1/4	1/8	0.128(11)	0.059(3)
P1	32g	0.26113(7)	0.30245(7)	0.08491(3)	0.00644(18)	1
P2	32g	0.26893(7)	0.14409(7)	0.17049(4)	0.00750(18)	1
P3	32g	0.09255(6)	0.31077(6)	0.00232(3)	0.00656(18)	1
N1	32g	0.0158(2)	0.0920(2)	0.29294(12)	0.0105(5)	0.696(1)
O1	32g	0.0158(2)	0.0920(2)	0.29294(12)	0.0105(5)	0.304(1)
N2	32g	0.1842(2)	0.0568(2)	0.04496(11)	0.0102(5)	0.689(1)
O2	32g	0.1842(2)	0.0568(2)	0.04496(11)	0.0102(5)	0.311(1)
N3	32g	0.0173(2)	0.0429(2)	0.11577(13)	0.0156(6)	0.694(1)
O3	32g	0.0173(2)	0.0429(2)	0.11577(13)	0.0156(6)	0.306(1)
N4	32g	0.3537(2)	0.0777(2)	0.13186(12)	0.0089(5)	1
N5	32g	0.1709(2)	0.3681(2)	0.04869(12)	0.0080(5)	1
N6	32g	0.1640(2)	0.2891(2)	0.28038(13)	0.0106(5)	1
N7	16d	0	1/4	0.03541(16)	0.0080(7)	1

Table G.4. List of anisotropic displacement parameters of $\text{Hf}_{9-x}\text{P}_{24}\text{N}_{52-4x}\text{O}_{4x}$ ($x \approx 1.84$).

Atom	$U_{11} / \text{\AA}^2$	$U_{22} / \text{\AA}^2$	$U_{33} / \text{\AA}^2$	$U_{23} / \text{\AA}^2$	$U_{13} / \text{\AA}^2$	$U_{12} / \text{\AA}^2$
Hf1	0.01253(8)	0.00999(8)	0.00857(8)	-0.00100(5)	0.00135(5)	-0.00237(5)
Hf2	0.178(16)	0.178(16)	0.027(6)	0	0	-0.048(18)
P1	0.0064(3)	0.0078(3)	0.0051(3)	-0.0001(3)	0.0000(3)	0.0002(3)
P2	0.0094(4)	0.0070(3)	0.0061(3)	0.0001(3)	-0.0005(3)	0.0002(3)
P3	0.0067(3)	0.0075(3)	0.0055(3)	-0.0005(3)	0.0004(3)	-0.0005(3)
N1	0.0111(12)	0.0102(12)	0.0103(12)	0.0017(9)	0.0014(10)	-0.0003(9)
O1	0.0111(12)	0.0102(12)	0.0103(12)	0.0017(9)	0.0014(10)	-0.0003(9)
N2	0.0114(12)	0.0116(12)	0.0076(11)	0.0007(9)	0.0021(9)	-0.0019(9)
O2	0.0114(12)	0.0116(12)	0.0076(11)	0.0007(9)	0.0021(9)	-0.0019(9)
N3	0.0175(14)	0.0133(13)	0.0161(14)	0.0047(10)	0.0083(11)	0.0054(11)
O3	0.0175(14)	0.0133(13)	0.0161(14)	0.0047(10)	0.0083(11)	0.0054(11)
N4	0.0113(12)	0.0082(11)	0.0072(12)	0.0004(9)	-0.0003(9)	0.0007(10)
N5	0.0091(12)	0.0080(11)	0.0068(11)	-0.0007(9)	-0.0013(9)	-0.0002(9)
N6	0.0113(12)	0.0100(12)	0.0105(12)	-0.0029(10)	-0.0022(10)	0.0028(10)
N7	0.0099(17)	0.0081(16)	0.0060(15)	0	0	-0.0019(13)

Table G.5. List of interatomic distances occurring in $\text{Hf}_{9-x}\text{P}_{24}\text{N}_{52-4x}\text{O}_{4x}$ ($x \approx 1.84$), [Å].

Hf1-(N/O)		P1-(N/O)	
Hf1-N1	2.360(3)	P1-N1	1.653(3)
Hf1-N2	2.152(3)	P1-N3	1.605(3)
Hf1-N2	2.230(3)	P1-N4	1.637(3)
Hf1-N4	2.167(3)	P1-N5	1.635(3)
Hf1-N5	2.263(3)		
Hf1-N6	2.271(3)	P2-(N/O)	
Hf1-N6	2.677(3)	P2-N2	1.586(3)
		P2-N3	1.599(3)
Hf2-(N/O)		P2-N4	1.625(3)
Hf2-N3	2.600(3)	P2-N6	1.659(3)
Hf2-N3	2.600(3)		
Hf2-N3	2.600(3)	P3-(N/O)	
Hf2-N3	2.600(3)	P3-N1	1.652(3)
Hf2-N7	2.125(4)	P3-N5	1.635(3)
Hf2-N7	2.125(4)	P3-N6	1.643(3)
		P3-N7	1.588(2)

Table G.6. List of bond angles occurring in $\text{Hf}_{9-x}\text{P}_{24}\text{N}_{52-4x}\text{O}_{4x}$ ($x \approx 1.84$), [deg].

(N/O)-P1-(N/O)		(N/O)-P3-(N/O)	
N3-P1-N5	111.41(15)	N7-P3-N5	108.06(16)
N3-P1-N4	104.41(16)	N7-P3-N6	108.17(12)
N5-P1-N4	104.14(15)	N5-P3-N6	102.58(15)
N3-P1-N1	114.61(15)	N7-P3-N1	113.85(13)
N5-P1-N1	111.15(15)	N5-P3-N1	113.25(15)
N4-P1-N1	110.39(15)	N6-P3-N1	110.24(15)
(N/O)-P2-(N/O)		P-(N/O)-P	
N2-P2-N3	114.61(16)	P3-N1-P1	113.28(17)
N2-P2-N4	111.41(15)	P2-N3-P1	124.33(19)
N3-P2-N4	111.23(15)	P2-N4-P1	116.84(18)
N2-P2-N6	104.27(15)	P1-N5-P3	123.07(18)
N3-P2-N6	105.89(16)	P3-N6-P2	121.49(18)
N4-P2-N6	108.89(15)	P3-N7-P3	120.8(2)

G.6 EEL and NMR spectroscopy

Prior to the EELS measurements, the sample composition was determined with EDX spectroscopy on thin samples, which confirms that the majority phase present is the title compound. Additional material found mainly contains B, N, and O, which can be attributed to partly hydrolyzed boron nitride. Thin sample areas of the majority phase show EDX compositions close to $\text{Hf}_{0.06}\text{P}_{0.28}\text{N}_{0.47}\text{O}_{0.18}$ (theory based on single crystal refinement: $\text{Hf}_{0.086}\text{P}_{0.289}\text{N}_{0.537}\text{O}_{0.089}$). The N/O to P ratio is close to the theoretical value. Since the Hf content may vary because of two not fully occupied Hf positions, the here found slight changes in the Hf to P and the N to O ratio can be explained.

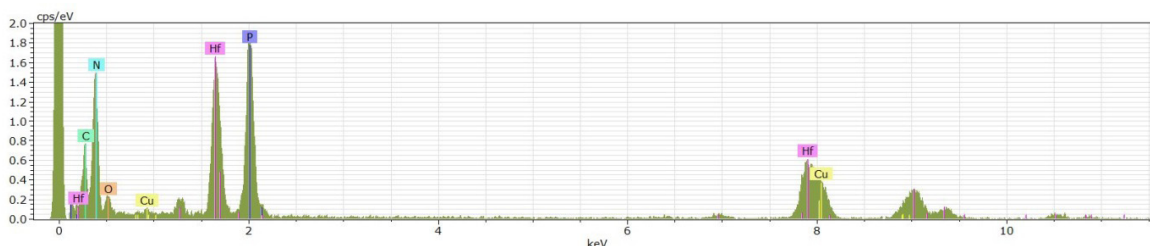


Figure G.3. EDX spectrum of the title compound. C and Cu stem from the sample support.

In the areas of the majority phase, as identified by EDX spectroscopy, EEL spectroscopy detected Hf, P, N, and O, but no experimental evidence was found for Li or other elements (Figures G.4 to G.6). As discussed in the manuscript, Li might be present in a mixed position with Hf on the Hf2 site. The maximum Li content, representing a full Li position, would be 2.35 at-%. The Li K-edge (close to 60 eV) is in the low-loss region of the spectrum where strong plasmon excitations might obscure the presence of small amounts of Li. Having not found evidence for the Li K edge therefore does not exclude the presence of Li but indicates that Li is either absent or only present at very low concentrations.

Bulk methods to verify the presence of small amounts of Li can be misleading in the present case as the high-pressure metathesis reaction also produced LiCl in situ. The LiCl might react under the high-pressure/high-temperature conditions with the boron nitride crucible forming amorphous Li-containing byproducts. Powder X-ray diffraction revealed a slightly curved background indicative of an amorphous phase. Traces of Li, however, can be detected with ^7Li solid state NMR. We performed magic angle spinning (MAS) solid-state ^7Li NMR on two different samples of the compound and detected signals at a chemical shift of -0.65 and -0.54 ppm (Figure G.7). Since NMR probes the lo-

cal environment of the observed nuclei, assignment of signals to specific phases is not unequivocal. However, a qualitative argument may be made as follows. The ${}^7\text{Li}$ NMR spectra of the compound exhibit an extensive spinning sideband (SSB) pattern, spanning more than 800 ppm, as can be seen in Figure G.8. The only possible explanation for this is the existence of a comparatively large quadrupolar interaction for ${}^7\text{Li}$, which has spin $I=3/2$. This partitions the spectrum in a strong and narrow central-transition (CT) component (as shown in Figure G.7), and widely stretched satellite transition (ST) components, which appear in the SSB pattern. This can be compared to the spectrum of LiCl (Figure G.8), where the quadrupolar interaction is absent because of the cubic symmetry (the remaining small SSBs in this spectrum are most likely due to dipolar couplings). As the quadrupole moment of the ${}^7\text{Li}$ nucleus is small, the presence of a strong quadrupolar coupling reveals that the electronic environment of the ${}^7\text{Li}$ has very low symmetry, as one would expect for amorphous phases. Low symmetry environments also occur in crystalline phases, but in these cases one would expect the CT resonance to show a well-defined, canonical powder pattern reflecting the magnitude and the asymmetry of the quadrupole coupling tensor.^[18] The fact that the two samples of the compound show slightly different CT line shapes also supports the hypothesis that the ${}^7\text{Li}$ NMR signals arise from additional amorphous phases that emerge in different ratios and/or compositions from the synthesis.

Moreover, the range of observed chemical shifts in ${}^7\text{Li}$ NMR is only a few ppm but typical values for Li nitridophosphates lie in the range of $\delta = 1.6$ to 4.9 ppm.^[19–23] These observations also indicate that the Li detected here at chemical shifts of -0.54 and -0.65 ppm (Figure G.7) might not be embedded in a nitridophosphate matrix. As mentioned above, EELS detected areas with element combinations other than the title compound. Synthesis carried out in large volume presses at such high-pressures and temperatures, as we have done here, is prone to side reactions, sometimes with the crucible. Hence it is difficult to prepare high-purity samples with high-pressure metathesis. We cannot rule out an incorporation of Li in the structure, however, the combination of single-crystal diffraction, EELS, indicate that either no or only very small amounts of Li are present in the main phase. By solid state NMR we cannot unambiguously attribute the found ${}^7\text{Li}$ signal to a specific phase, only exclude the incorporation into a highly symmetric crystalline environment. Proving the absence of Li in the main phase might require neutron scattering experiments, which are, given that the multianvil technique only produces ca. 30 mg sample per experiment, beyond the scope of this report.

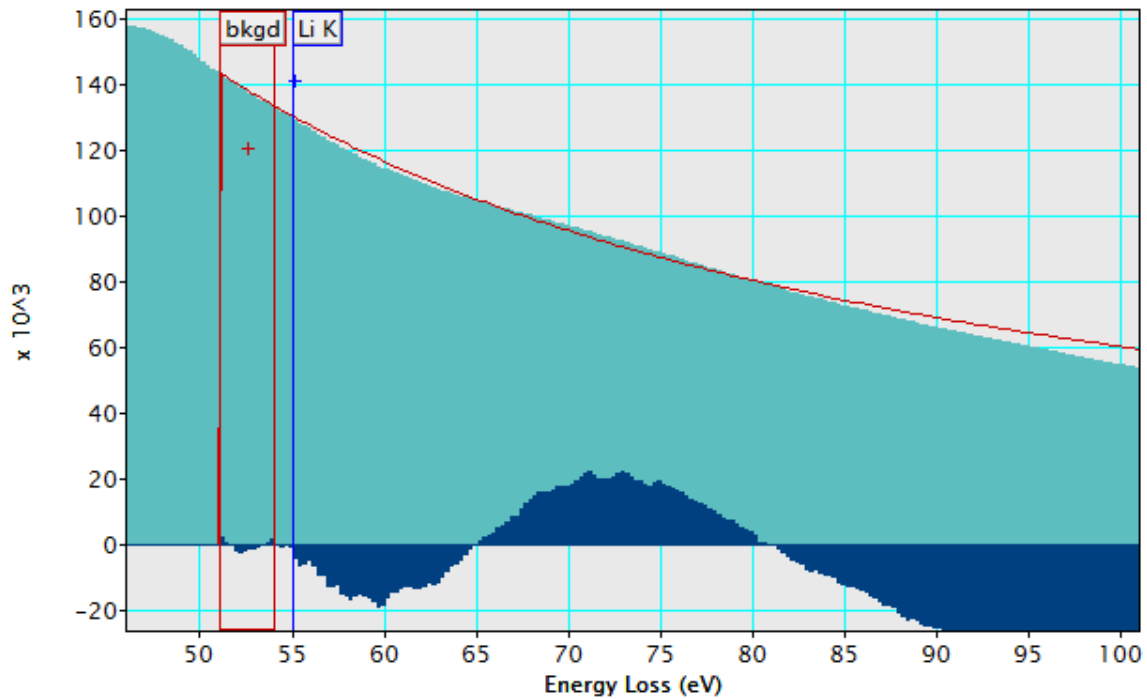


Figure G.4. EEL spectrum in light blue, background subtracted spectrum dark blue, red line background. The maximum of the Li K-edge is expected at around 60 eV. The weak peak at around 72 eV is a multiple of the plasmon excitation around 24 eV.

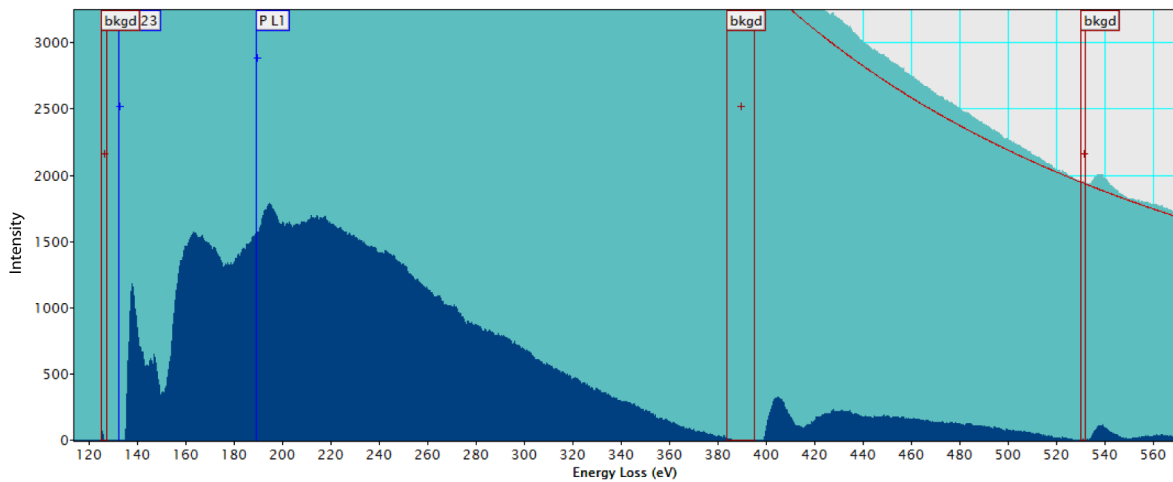


Figure G.5. EEL spectrum in light blue, background subtracted spectrum dark blue, red line background. The background subtracted spectrum shows the L edge of P (onset 132 eV), and the K edges of N and O with onset energies of 401 eV and 532 eV.

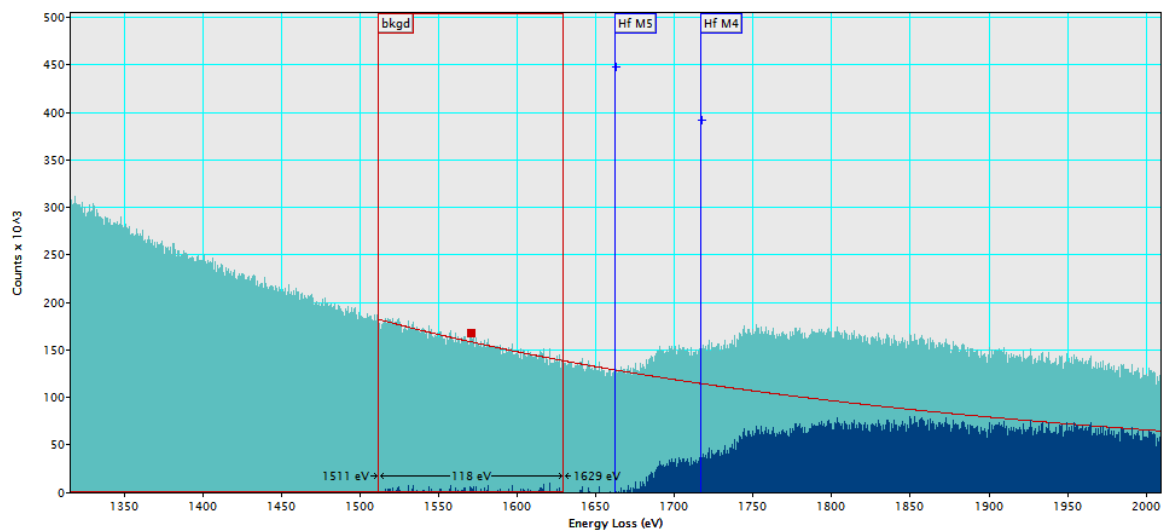


Figure G.6. High-loss EEL spectrum in light blue, background subtracted spectrum dark blue, red line background. The spectrum shows the M_{4,5} edge of Hf with an onset of 1662 and 1716 eV.

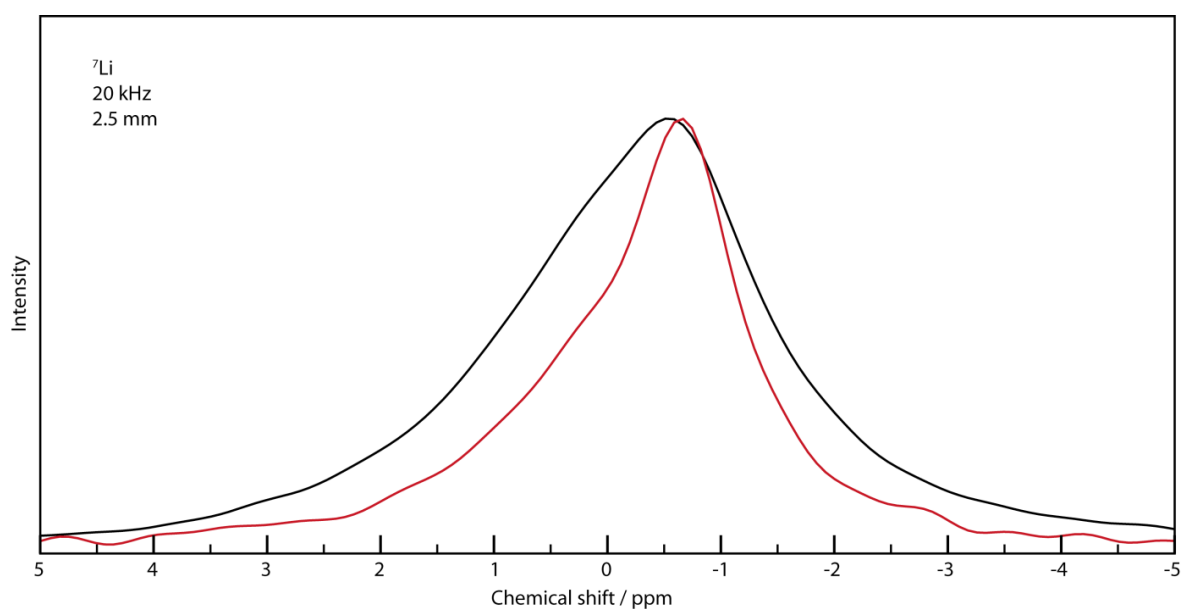


Figure G.7. ⁷Li NMR spectra of two samples of the title compound recorded at room temperature. Peak maxima at -0.54 (black) and -0.65 (red) ppm.

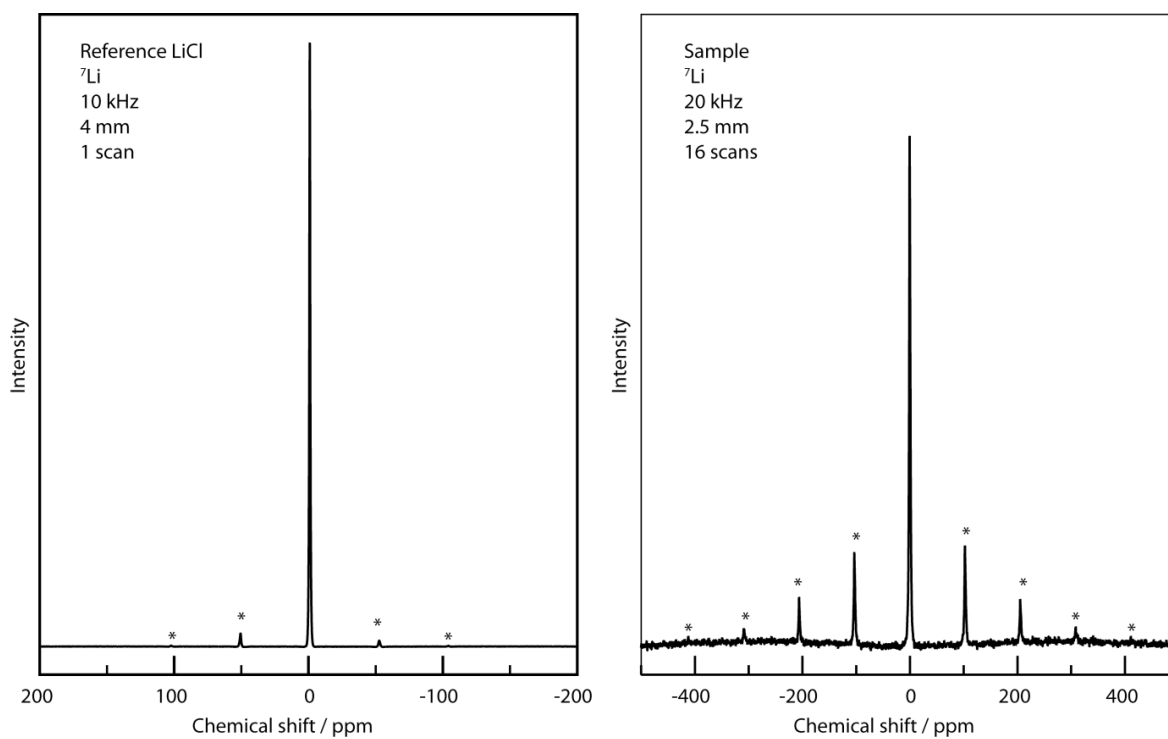


Figure G.8. ${}^7\text{Li}$ NMR spectra of a LiCl reference (left) and the sample (right) recorded at room temperature. Peak maxima at -0.95 (LiCl reference) and -0.65 (sample) ppm. Spinning sidebands marked by asterisks.

G.7 Magnetic measurements

The magnetic properties of a crystallographically pure sample of $\text{Hf}_{9-x}\text{P}_{24}\text{N}_{52-4x}\text{O}_{4x}$ ($x \approx 1.84$) were determined by isothermal magnetization measurements at 300 and 1.9 K, respectively, and by a susceptibility measurement in a field of 1000 Oe (Figure G.3). The isothermal magnetization at 300 and 1.9 K indicate a diamagnetic behavior of the sample, the observed magnetic moments are very small and directed against the applied magnetic field. A small ferromagnetic impurity, however, can be discerned in the measurements. At 300 K, in the region between 0 and ca. 2000 Oe, an increase in magnetic moment is observed. This behavior is more clearly visible at 1.9 K, at which temperature the increase in magnetic moment is extended to 10000 Oe, after which the diamagnetism exceeds and the magnetic moment begins to decline again. The susceptibility measurement conducted at 1000 Oe is in the region, in which the ferromagnetic behavior is predominant; it shows a very small magnetization of the sample. One reason for this odd magnetic behavior of the sample could be a minor ferromagnetic impurity, maybe due to the usage of a metallic spatula. The gross of the $\text{Hf}_{9-x}\text{P}_{24}\text{N}_{52-4x}\text{O}_{4x}$ ($x \approx 1.84$) sample, however, is diamagnetic, probably stemming from paired core electrons. Hence, these data indicate the presence of Hf in formal oxidation state +IV within $\text{Hf}_{9-x}\text{P}_{24}\text{N}_{52-4x}\text{O}_{4x}$ ($x \approx 1.84$).

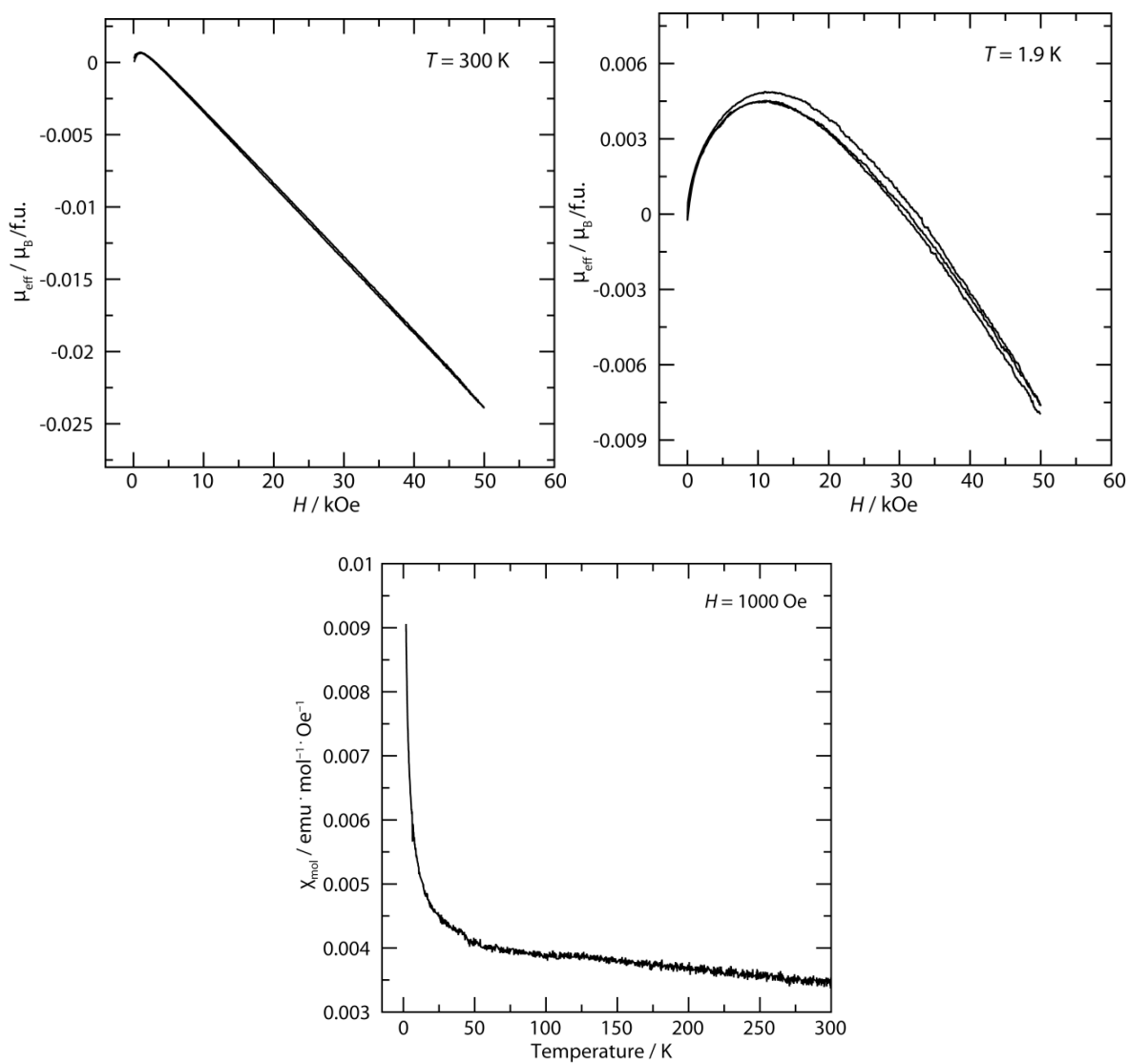


Figure G.9. Top left: effective magnetic moment per formula unit at 300 K. Top right: effective magnetic moment per formula unit at 1.9 K. Bottom: molar susceptibility obtained in the temperature range of 1.9 to 300 K.

G.8 Infrared spectroscopy

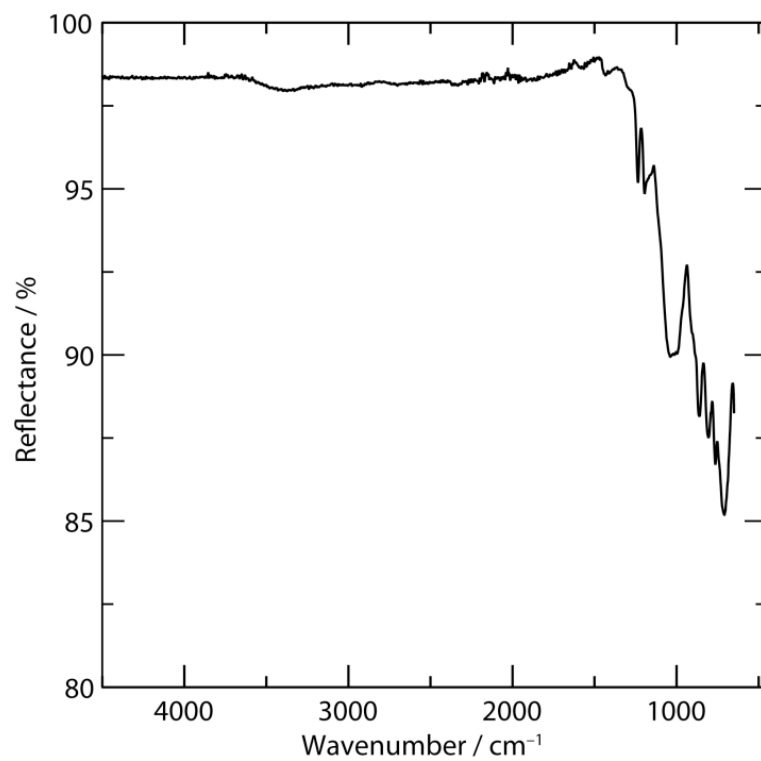
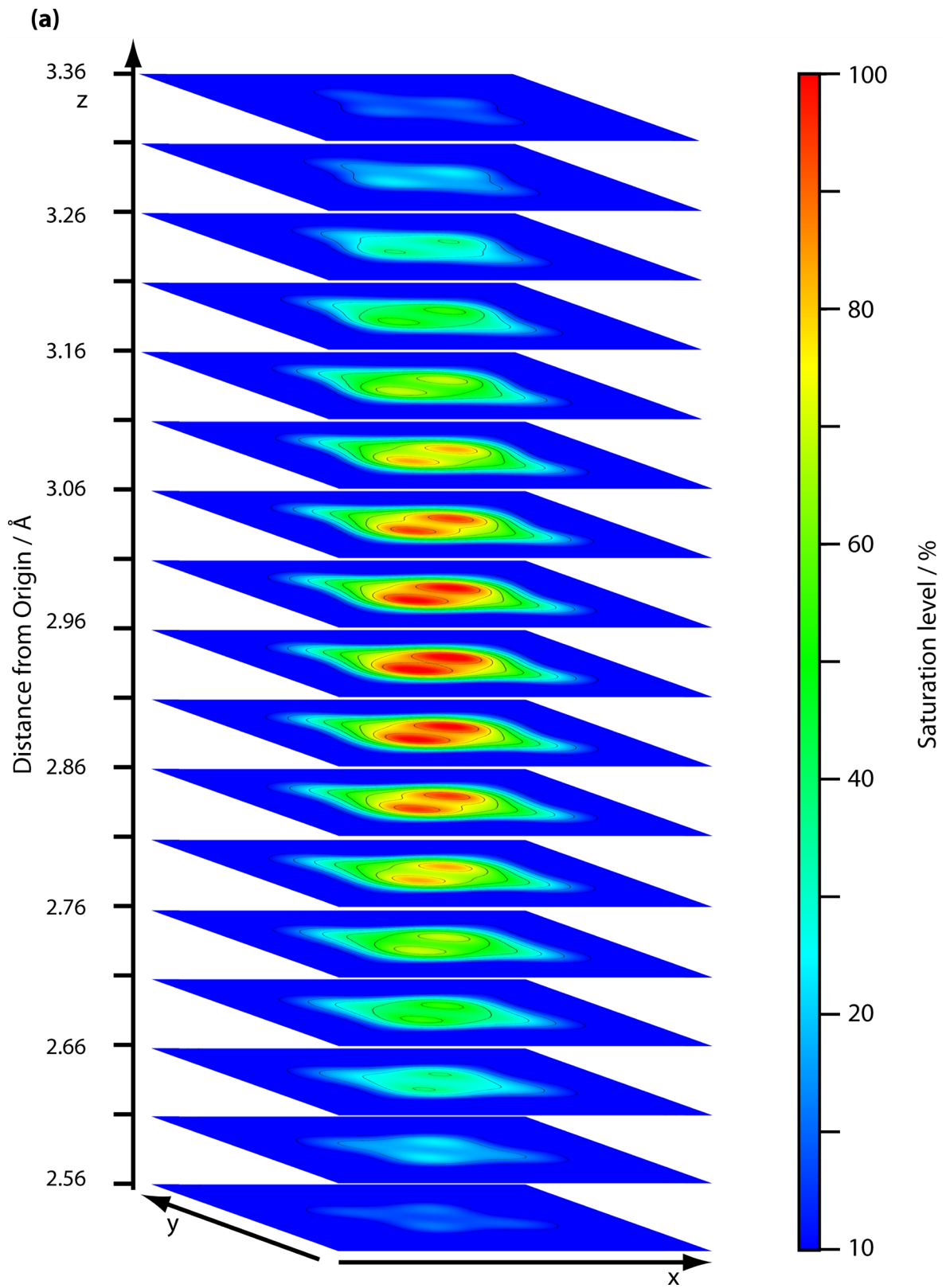


Figure G.10. Fourier transform infrared spectrum of a $\text{Hf}_{9-x}\text{P}_{24}\text{N}_{52-4x}\text{O}_{4x}$ ($x \approx 1.84$) sample measured in ATR geometry.

G.9 Bond valence sums

Table G.7. Bond valence sums calculated with VaList for the anions of the $\text{Hf}_{9-x}\text{P}_{24}\text{N}_{52-4x}\text{O}_{4x}$ ($x \approx 1.84$) structure model.^[24] Atom positions, which might be occupied by oxygen, are marked with green color.

Atom	N1	O1	N2	O2	N3	O3	N4	O4
BVS	2.79	2.14	2.78	1.99	2.81	2.20	3.26	2.44
Atom	N5	O5	N6	O6	N7	O7		
BVS	3.03	2.31	3.08	2.32	2.86	2.25		

G.10 Additional information on structure solution

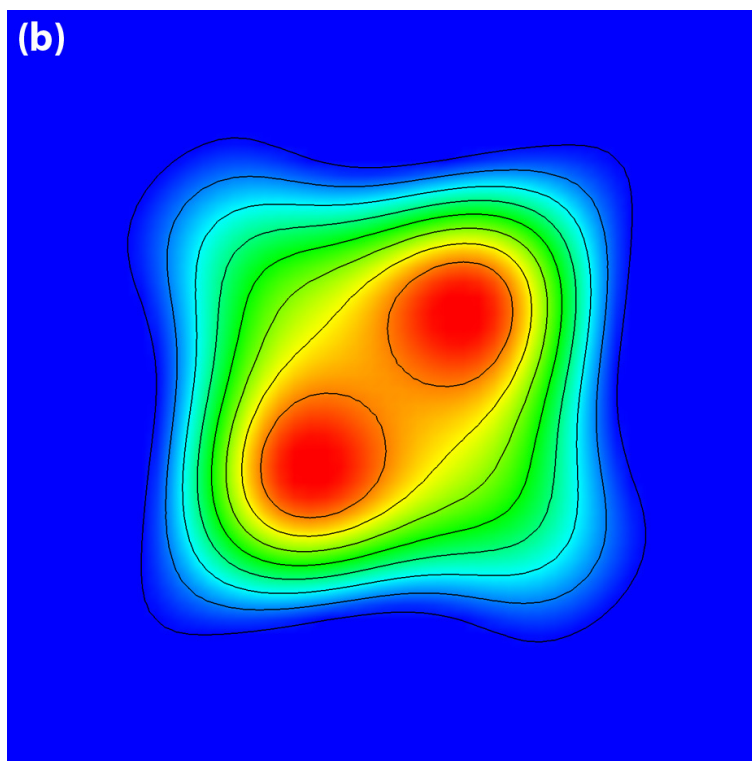


Figure G.11. (a) Planes through a Hf₂ electron density distribution. (b) One plane through the Hf₂ electron density distribution at 2.9 Å from origin. Two large peaks are discernible, highlighted by the red electron density spikes. Two smaller shoulders in the top left and bottom right are also visible, leading to a cushion-like electron density distribution. Saturation level 10 % represents 1.5, 100 % 4.5 electrons/ a_0^3 (a_0 = Bohr radius).

Whether the observed electron density of Figure G.11 is an artifact of too high assumed space group symmetry can be tested by removal of symmetry elements mapping the electron density peaks upon each other. We considered the two cases of retaining Laue class $4/m\bar{3}m$ and lowering the Laue class to $4/m$, the latter including the merohedry twin law completing the $4/m\bar{3}m$ symmetry.

In the first case, t_2 transition to $I4_122$ (no. 98) leads to the crystallographic splitting of Hf₂'s Wyckoff position $8b$ into the two positions $4a$ and $4b$. The difference Fourier maps show a very similar split position (Figure G.12), indicating the same four Hf positions.

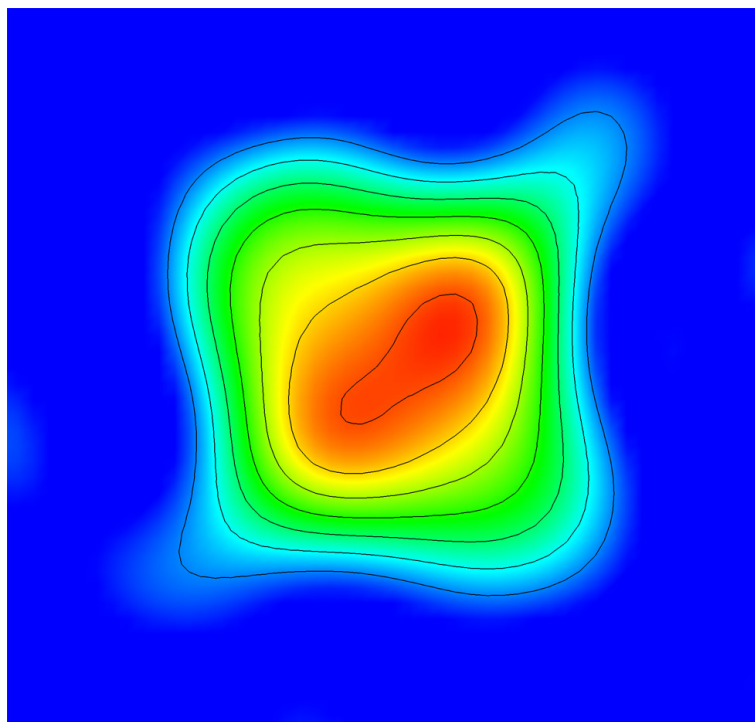


Figure G.12. Difference Fourier map at Hf2's position in projection along [001] obtained from refinement in space group $I4_122$ (no. 98).

In the second case, a $t2$ transition to $I4_1/a$ (no. 88) without splitting of the crystallographic site ($8b$ to $8e$) followed by another $t2$ transition to $\bar{I}4$ (no. 82) splits the Hf2 position in two ($8e$ to $4e$ and $4f$). The difference Fourier map (Figure G.13) again shows the split position, the electron density distorted in comparison to the higher symmetric ones due to the symmetry reduction.

A further reduced symmetry of the Hf2 position has been investigated by refinement in $P1$. The electron density is distorted due to serious parameter correlation, which is due to lowering the symmetry from $I4_1/acd$ to $P1$. Two electron density maxima, however, are still discernible, indicating a regular split position with randomly distributed Hf atoms (Figure G.14). Twinning with domain sizes smaller than the X-ray coherence length cannot be ruled out with X-ray studies alone and would necessitate transmission electron microscopy studies. There is, however, no chemical reason for a twinning that only affects the Hf2 position. The Hf2 positions are too far spaced to be influencing each other ($d(\text{Hf2-Hf2}) = 8.6029(7) \text{ \AA}$). No obvious structural distortion emanating from the Hf2 position can be discerned, which might carry information from one Hf2 position to the next. Hence, a random distribution of Hf atoms is a more probable explanation and fits the X-ray data.

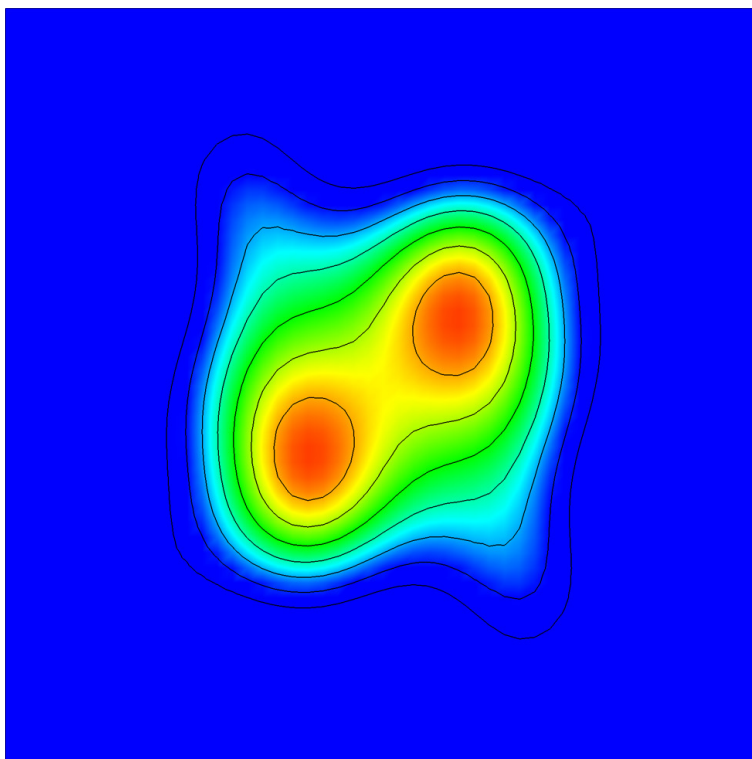


Figure G.13. Difference Fourier map at Hf2's position in projection along [001] obtained from refinement in space group $I\bar{4}$ (no. 82).

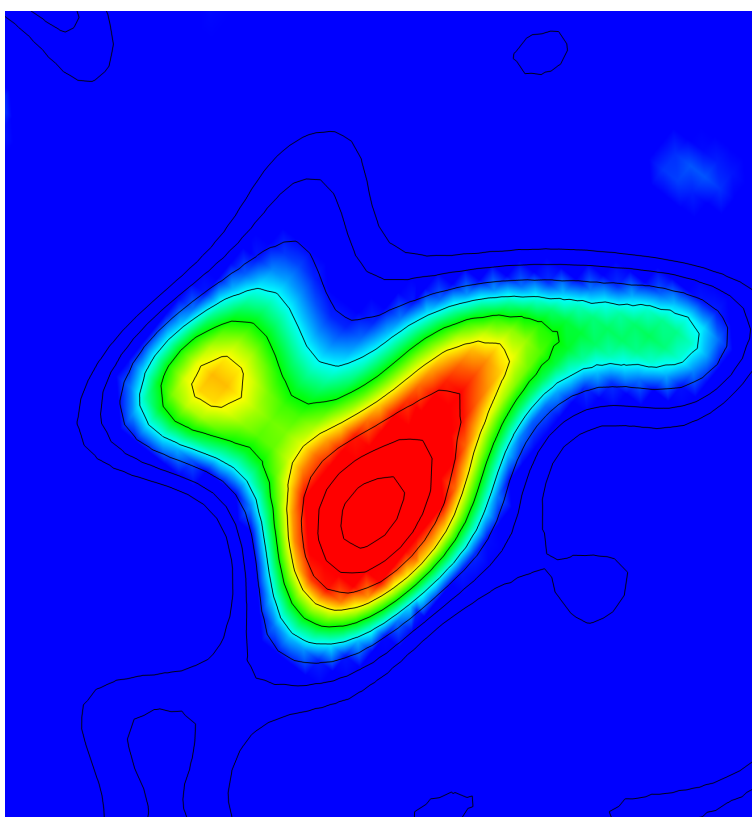


Figure G.14. Difference Fourier map at Hf2's position obtained from refinement in space group $P1$ (no. 1).

G.11 High-temperature PXRD

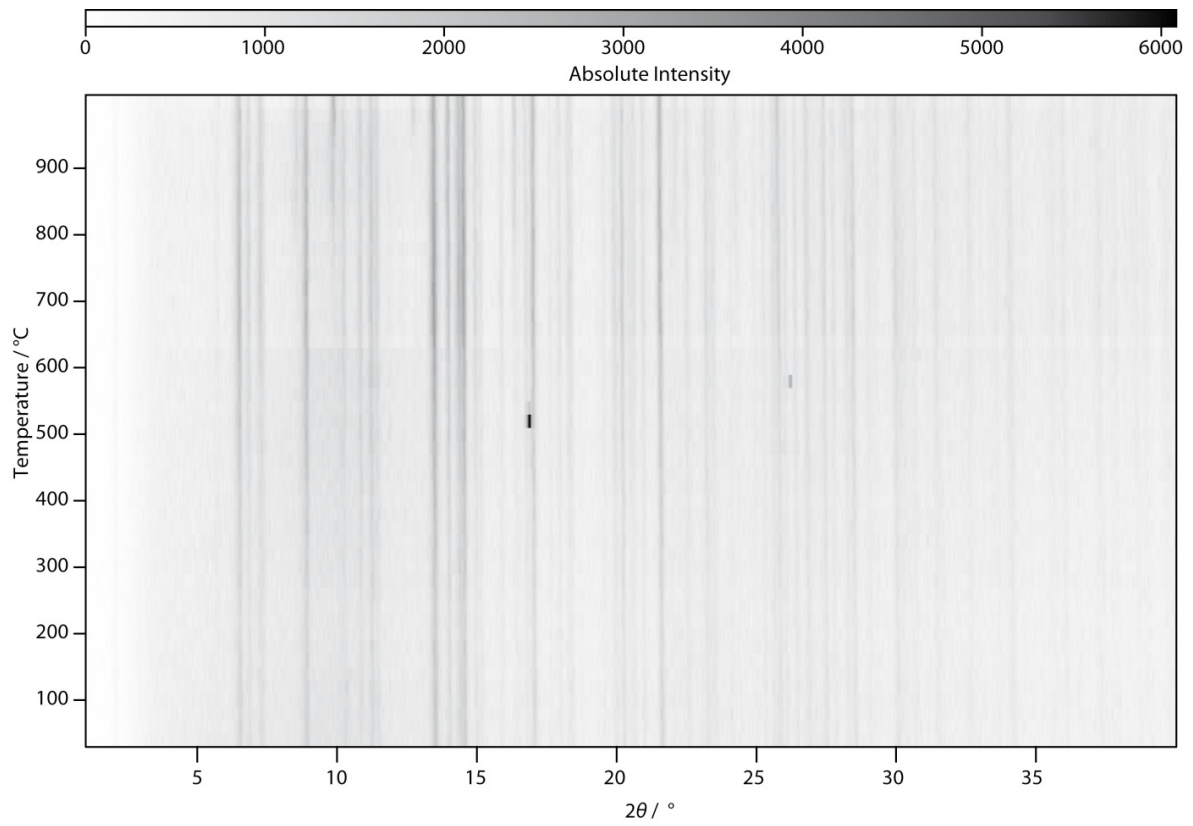


Figure G.15. High-temperature powder diffraction patterns of a $\text{Hf}_{9-x}\text{P}_{24}\text{N}_{52-4x}\text{O}_{4x}$ ($x \approx 1.84$) sample ($\lambda(\text{Mo-K}\alpha_1) = 0.709300 \text{ \AA}$).

G.12 References

- [1] A. Stock, H. Grüneberg, *Ber. Dtsch. Chem Ges.* **1907**, *40*, 2573–2578.
- [2] W. Schnick, J. Lücke, *Z. Anorg. Allg. Chem.* **1990**, *588*, 19–25.
- [3] E. Zintl, A. Harder, B. Dauth, *Ztschr. Elektrochem.* **1934**, *40*, 588–593.
- [4] H. Huppertz, *Z. Kristallogr.* **2004**, *219*, 330–338.
- [5] N. Kawai, S. Endo, *Rev. Sci. Instrum.* **1970**, *41*, 1178–1181.
- [6] D. Walker, M. A. Carpenter, C. M. Hitch, *Am. Miner.* **1990**, *75*, 1020–1028.
- [7] D. Walker, *Am. Mineral.* **1991**, *76*, 1092–1100.
- [8] D. C. Rubie, *Phase Transitions* **1999**, *68*, 431–451.
- [9] Bruker AXS, Inc., SADABS, Madison, Wisconsin, USA, **2001**.
- [10] Bruker AXS, Inc., APEX3, Madison, Wisconsin, USA, **2016**.
- [11] Bruker AXS, Inc., XPREP, Karlsruhe, Germany, **2001**.
- [12] G. M. Sheldrick, *Acta Crystallogr., Sect. A: Found. Crystallogr.* **2008**, *64*, 112–122.
- [13] G. M. Sheldrick, *SHELXS – A Programm for Crystal structure Solution*, University of Göttingen, Germany, **1997**.
- [14] K. Momma, F. Izumi, *J. Appl. Crystallogr.* **2011**, *44*, 1272–1276.
- [15] H. M. Rietveld, *J. Appl. Crystallogr.* **1969**, *2*, 65–71.
- [16] A. A. Coelho, *TOPAS-Academic V4.1*, Coelho Software, Brisbane, Australia, **2007**.
- [17] Quantum Design, *MultiVu V1.5.11*, **2013**.
- [18] T. Bräuniger, M. Jansen, *Z. Anorg. Allg. Chem.* **2013**, *639*, 857–879.
- [19] E.-M. Bertschler, T. Bräuniger, C. Dietrich, J. Janek, W. Schnick, *Angew. Chem., Int. Ed.* **2017**, *56*, 4806–4809; *Angew. Chem.* **2017**, *129*, 4884–4887.
- [20] E.-M. Bertschler, R. Niklaus, W. Schnick, *Chem. - Eur. J.* **2017**, *23*, 9592–9599.
- [21] E. M. Bertschler, C. Dietrich, J. Janek, W. Schnick, *Chem. - Eur. J.* **2017**, *23*, 2185–2191.
- [22] E.-M. Bertschler, R. Niklaus, W. Schnick, *Chem. - Eur. J.* **2018**, *24*, 736–742.
- [23] E.-M. Bertschler, C. Dietrich, T. Leichtweiß, J. Janek, W. Schnick, *Chem. - Eur. J.* **2018**, *24*, 196–205.
- [24] A. S. Wills, *Valist*, Program available from www.ccp14.ac.uk, **2011**.

Appendix H. Supporting information for Chapter 8.

H.1 Rietveld refinement data

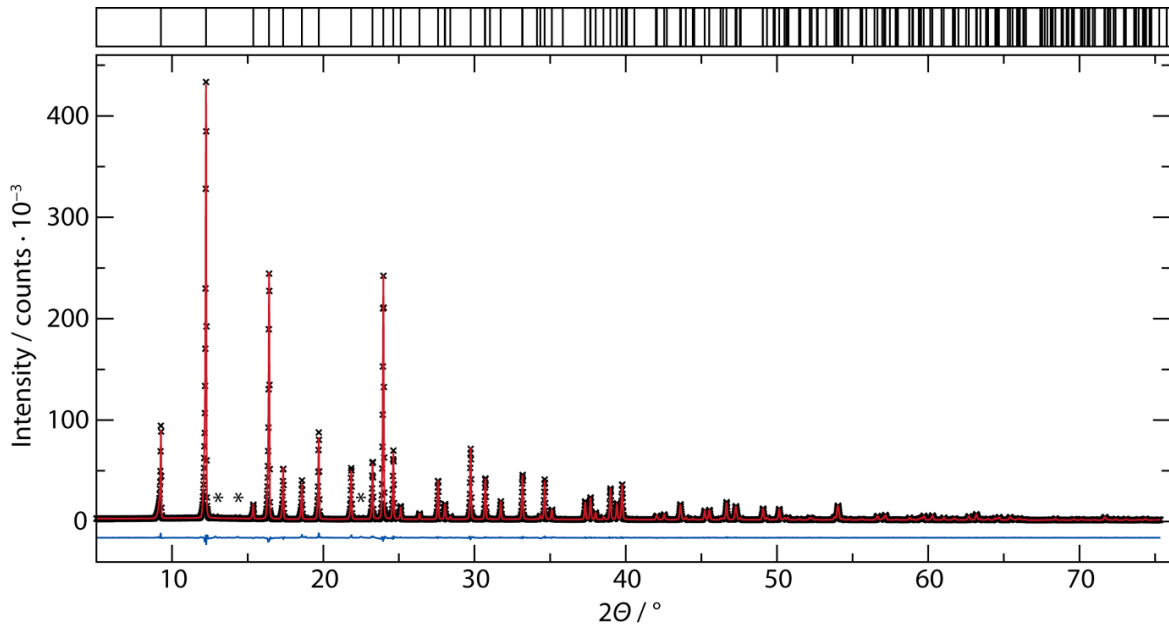


Figure H.1. Rietveld refinement of a $\text{Zr}_{1-x}\text{PO}_{3+4x}\text{N}_{1-4x}$ sample. Data points as black crosses, model fit as red line, difference plot as blue line. Positions of theoretical Bragg reflections are marked by black vertical drop lines. Minor ZrO_2 impurity marked by asterisks (*).^[1]

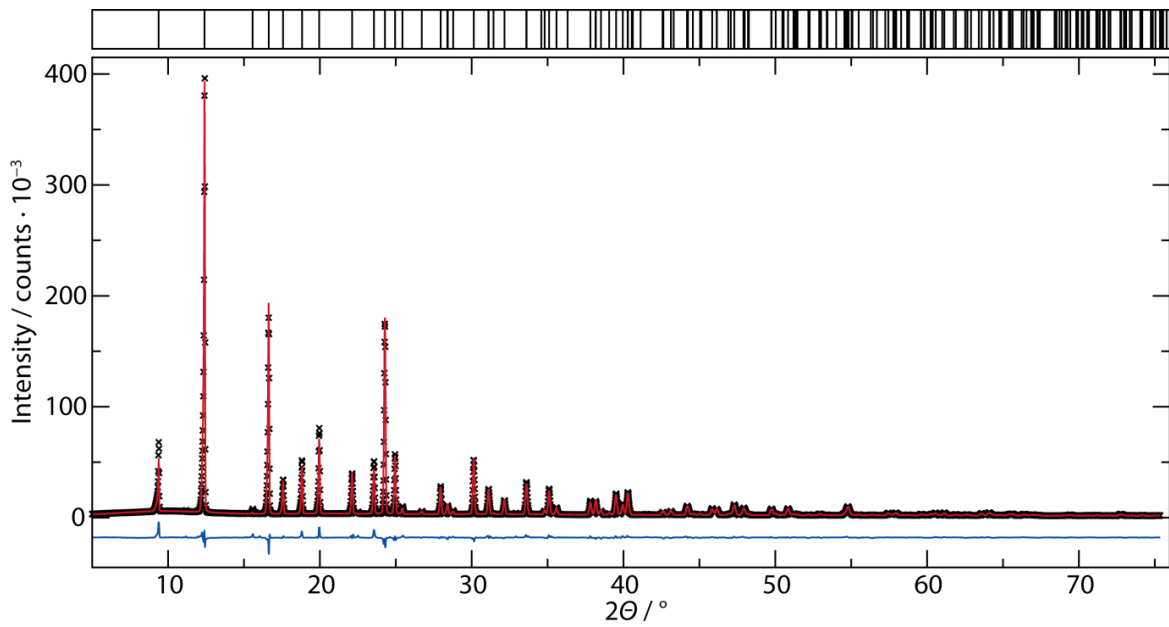


Figure H.2. Rietveld refinement of a $\text{Zr}_{0.75}\text{PO}_4$ sample. Data points as black crosses, model fit as red line, difference plot as blue line. Positions of theoretical Bragg reflections are marked by black vertical drop lines.

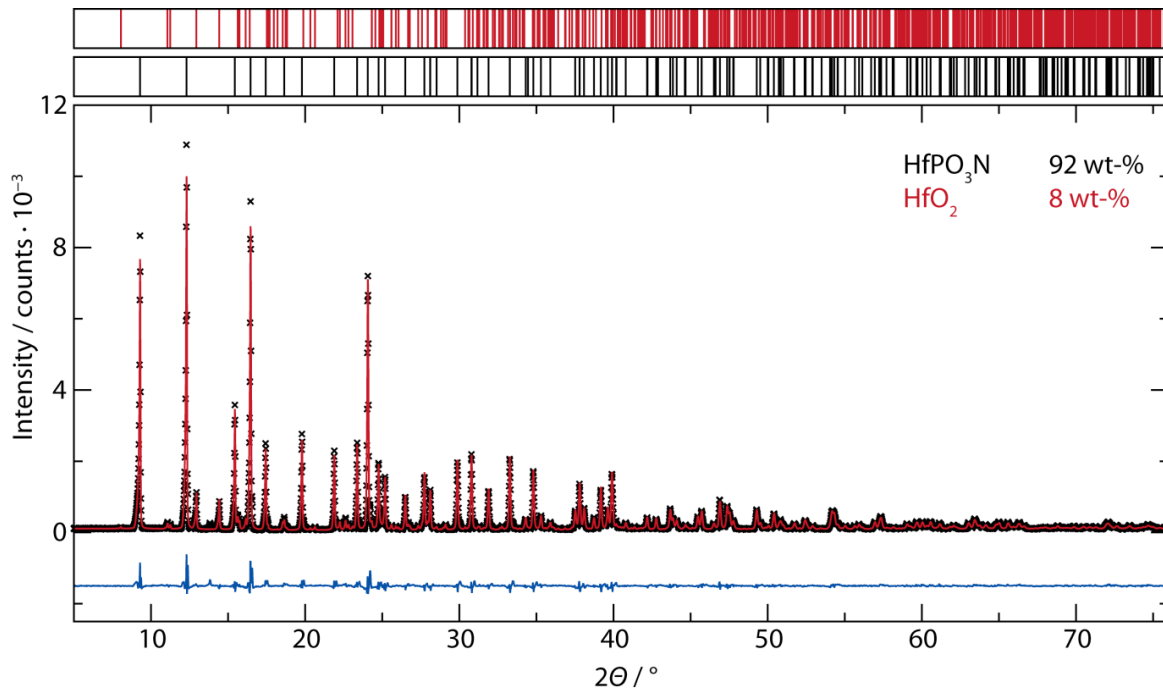


Figure H.3. Rietveld refinement of a $\text{Hf}_{1-x}\text{PO}_{3+4x}\text{N}_{1-4x}$ sample. Data points as black crosses, model fit as red line, difference plot as blue line. Positions of theoretical Bragg reflections are marked by black ($\text{Hf}_{1-x}\text{PO}_{3+4x}\text{N}_{1-4x}$) and red (baddeleyite HfO_2) vertical drop lines.^[1]

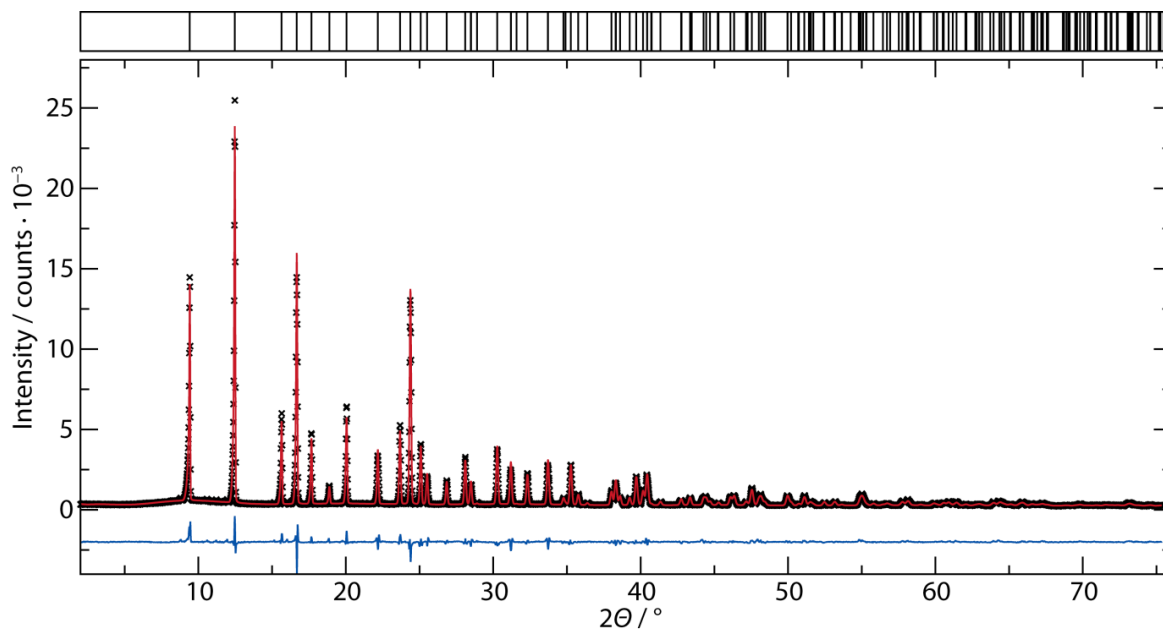


Figure H.4. Rietveld refinement of a $\text{Hf}_{0.75}\text{PO}_4$ sample. Data points as black crosses, model fit as red line, difference plot as blue line. Positions of theoretical Bragg reflections are marked by black vertical drop lines.

Table H.1. Crystallographic data for the Rietveld refinements of all compounds.

Crystal Data				
Formula	Zr _{1-x} PO _{3+4x} N _{1-4x}	Zr _{0.75} PO ₄	Hf _{1-x} PO _{3+4x} N _{1-4x}	Hf _{0.75} PO ₄
Formula mass / g·mol ⁻¹	180.04	163.39	271.47	228.84
Crystal system, space group	Tetragonal, <i>I</i> ₄ / <i>amd</i> (no. 141)			
Lattice parameters / Å	<i>a</i> = 6.65183(3) <i>c</i> = 5.85204(3)	<i>a</i> = 6.56621(8) <i>c</i> = 5.77808(8)	<i>a</i> = 6.61732(13) <i>c</i> = 5.84230(13)	<i>a</i> = 6.53266(9) <i>c</i> = 5.76781(11)
Cell volume / Å ³	258.934(2)	249.122(7)	255.83(1)	246.14(1)
Calculated density ρ / g·cm ⁻³	4.604(3)	4.3563(1)	7.0483(3)	6.1752(2)
Data Collection				
Radiation	Mo-K α_1 ($\lambda = 0.709300$ Å)			
Monochromator	Ge(111)			
Diffractometer	Stoe StadiP			
Detector	MYTHEN 1K			
2 θ -range / °	2–76			
Temperature / K	297(2)			
Data points	4958			
No. observed reflections	202	197	206	194
Refinement				
Number of parameters	46	42	47	44
Constraints	0	0	0	0
Program used	TOPAS Academic V4.1			
Structure refinement	Rietveld-Method			
Profile function	fundamental parameters model			
Background function	shifted Chebychev polynomial with			
	22 terms	20 terms	14 terms	22 terms
R_p	0.027	0.049	0.079	0.060
R_{wp}	0.043	0.067	0.116	0.078
R_{exp}	0.015	0.013	0.063	0.041
R_{Bragg}	0.013	0.043	0.029	0.032
$\chi = R_{wp}/R_{exp}$	2.943	4.924	1.844	1.916

H.2 Infrared spectroscopy

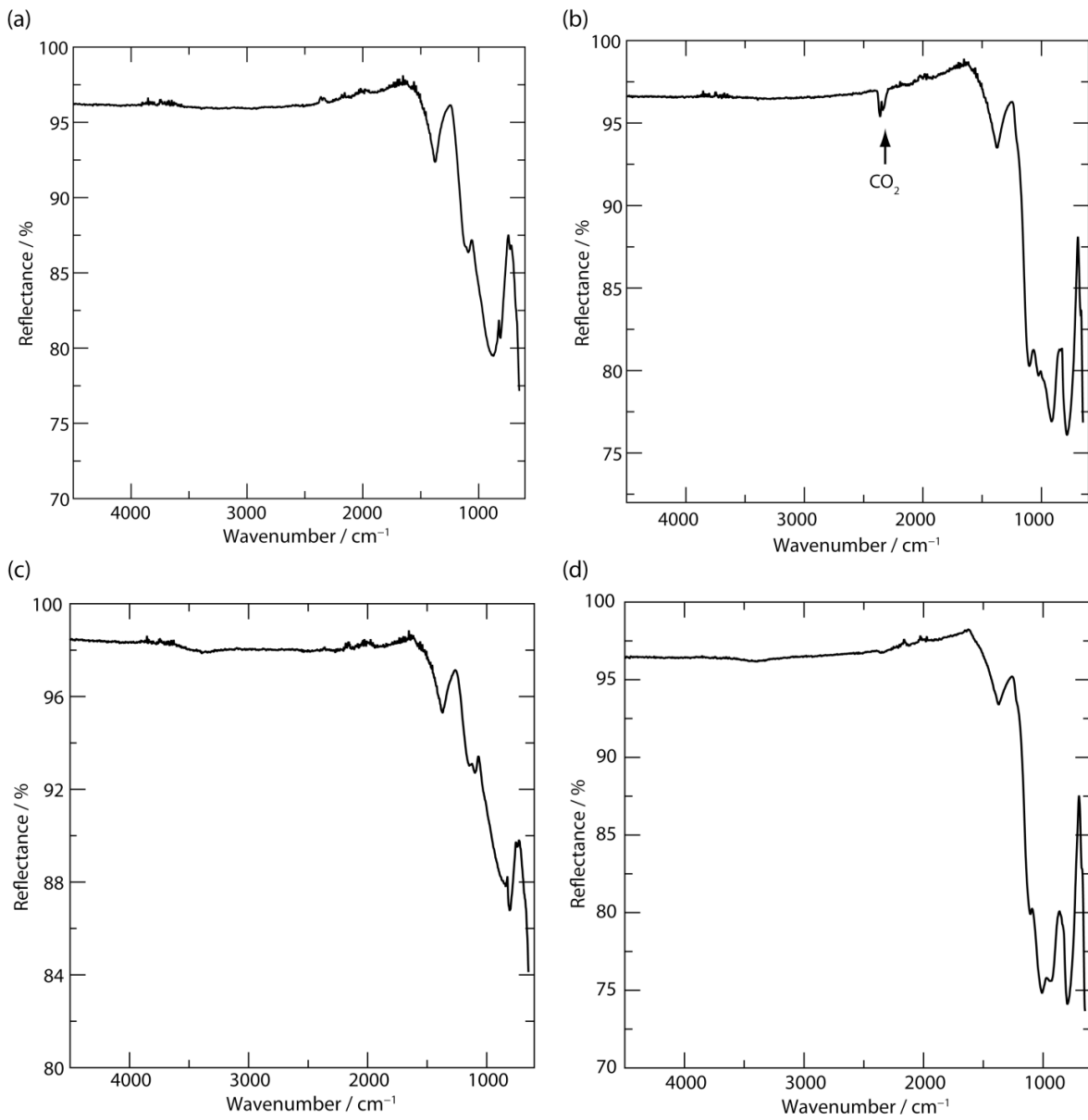


Figure H.5. Infrared spectra of samples of (a) $\text{Zr}_{1-x}\text{PO}_{3+4x}\text{N}_{1-4xr}$ (b) $\text{Zr}_{0.75}\text{PO}_4$, (c) $\text{Hf}_{1-x}\text{PO}_{3+4x}\text{N}_{1-4xr}$ (d) $\text{Hf}_{0.75}\text{PO}_4$.

H.3 Crystallographic tables

Table H.2. Crystallographic data for $M_{1-x}PO_{3+4x}N_{1-4x}$ ($x \approx 0.05$) and $M_{0.75}PO_4$ ($M = \text{Zr, Hf}$).

Crystal Data				
Formula	$\text{Zr}_{0.950(6)}\text{PO}_{3.2}\text{N}_{0.8}$	$\text{Zr}_{0.75}\text{PO}_4$	$\text{Hf}_{0.947(4)}\text{PO}_{3.2}\text{N}_{0.8}$	$\text{Hf}_{0.75}\text{PO}_4$
Formula mass / $\text{g}\cdot\text{mol}^{-1}$	180.04	163.39	262.51	228.84
Crystal system, space group	tetragonal, $I4_1/amd$ (no. 141)			
Cell parameters / Å	$a = 6.596(1)$	$a = 6.567(1)$	$a = 6.6178(12)$	$a = 6.5335(7)$
	$c = 5.805(1)$	$c = 5.783(2)$	$c = 5.8409(9)$	$c = 5.7699(7)$
Cell volume / Å ³	252.59(9)	249.3(1)	255.8(1)	246.30(6)
Z	4			
F(000)	336.8	308	458	404
Calc. density ρ / $\text{g}\cdot\text{cm}^{-3}$	4.734	4.353	6.820	6.171
Abs. coefficient μ / mm^{-1}	4.555	3.839	39.084	32.302
Data Collection				
Radiation	Mo-K α			
Temperature / K	293(2)			
θ min/ θ max / deg.	4.677/36.442	4.697/32.489	4.655/34.327	4.713/42.083
Total no. of reflections	1555	1459	3137	4543
Independent reflections	173	133	156	246
Absorption correction	Semiempirical ³⁴			
$R_{\text{int}}, R_{\text{sigma}}$	0.032, 0.022	0.034, 0.019	0.037, 0.014	0.039, 0.019
Refinement				
Extinction coefficient	none	0.025(7)	0.0026(3)	0.014(2)
Refined parameters	12	12	13	12
Goodness of fit	1.247	1.359	1.188	1.471
R_1 (all data), $R_1 [F_2 > 2s(F_2)]$	0.022, 0.020	0.035, 0.029	0.009, 0.007	0.020, 0.019
wR_2 (all data), $wR_2 [F_2 > 2s(F_2)]$	0.040, 0.040	0.072, 0.070	0.015, 0.015	0.044, 0.044
$\Delta\rho_{\text{max}}, \Delta\rho_{\text{min}}$ / $\text{e}\cdot\text{Å}^{-3}$	0.66, -0.80	0.57, -0.45	0.62, -0.53	0.97, -0.93

Table H.3. Atom positions, displacement parameters, and occupancy of the title compounds. O1 and N1 is the split anion position in $Zr_{1-x}PO_{3+4x}N_{1-4x}$ and $Hf_{1-x}PO_{3+4x}N_{1-4x}$, respectively.

Compound/Atom	Wyckoff Position	x	y	z	$U_{eq} / \text{\AA}^3$	Occupancy
$Zr_{1-x}PO_{3+4x}N_{1-4x}$						
Zr1	4a	0	3/4	1/8	0.00688(13)	0.950(6)
P1	4b	0	1/4	3/8	0.0055(3)	1
O1	16h	0	0.0704(2)	0.2046(3)	0.0078(3)	0.800
N1	16h	0	0.0704(2)	0.2046(3)	0.0078(3)	0.200
$Zr_{0.75}PO_4$						
Zr1	4a	0	3/4	1/8	0.0109(4)	3/4
P1	4b	0	1/4	3/8	0.0088(4)	1
O1	16h	0	0.0688(4)	0.2081(4)	0.0088(5)	1
$Hf_{1-x}PO_{3+4x}N_{1-4x}$						
Hf1	4a	0	3/4	1/8	0.00831(7)	0.947(4)
P1	4b	0	1/4	3/8	0.0078(2)	1
O1	16h	0	0.0701(9)	0.2018(8)	0.0113(4)	0.198
N1	16h	0	0.0701(9)	0.2018(8)	0.0113(4)	0.802
$Hf_{0.75}PO_4$						
Hf1	4a	0	3/4	1/8	0.01035(11)	3/4
P1	4b	0	1/4	3/8	0.0069(2)	1
O1	16h	0	0.0686(3)	0.2070(4)	0.0075(3)	1

Table H.4. Anisotropic displacement parameters for all four compounds.

Compound/Atom	$U_{11}/\text{\AA}^2$	$U_{22}/\text{\AA}^2$	$U_{33}/\text{\AA}^2$	$U_{12}/\text{\AA}^2$	$U_{13}/\text{\AA}^2$	$U_{23}/\text{\AA}^2$
Zr_{1-x}PO_{3+4x}N_{1-4x}						
Zr1	0.00727(15)	0.00727(15)	0.00611(19)	0	0	0
P1	0.0061(3)	0.0061(3)	0.0045(4)	0	0	0
O1	0.0102(6)	0.0058(6)	0.0075(6)	-0.0011(5)	0	0
N1	0.0102(6)	0.0058(6)	0.0075(6)	-0.0011(5)	0	0
Zr_{0.75}PO₄						
Zr1	0.0108(4)	0.0108(4)	0.0110(5)	0	0	0
P1	0.0093(5)	0.0093(5)	0.0079(7)	0	0	0
O1	0.0100(12)	0.0085(10)	0.0079(11)	-0.0009(9)	0	0
Hf_{1-x}PO_{3+4x}N_{1-4x}						
Hf1	0.00863(8)	0.00863(8)	0.00767(9)	0	0	0
P1	0.0082(3)	0.0082(3)	0.0069(4)	0	0	0
O1	0.0138(8)	0.0095(7)	0.0105(6)	-0.0007(6)	0	0
N1	0.0138(8)	0.0095(7)	0.0105(6)	-0.0007(6)	0	0
Hf_{0.75}PO₄						
Hf1	0.00975(12)	0.00975(12)	0.01153(15)	0	0	0
P1	0.0072(3)	0.0072(3)	0.0064(5)	0	0	0
O1	0.0088(7)	0.0065(6)	0.0072(6)	-0.0018(6)	0	0

Table H.5. List of bond lengths occurring in all four compounds, [\AA].

Zr_{1-x}PO_{3+4x}N_{1-4x}		Zr_{0.75}PO₄		Hf_{1-x}PO_{3+4x}N_{1-4x}		Hf_{0.75}PO₄	
Zr1–(O1/N1)	2.1634(15)	Zr1–O1	2.147(2)	Hf1–(O1/N1)	2.1652(16)	Hf1–O1	2.135(2)
Zr1–(O1/N1)	2.2502(16)	Zr1–O1	2.264(3)	Hf1–(O1/N1)	2.2572(15)	Hf1–O1	2.253(2)
Zr1–P1	2.9027(4)	Zr1–P1	2.8916(8)	Hf1–P1	2.9204(4)	Hf1–P1	2.8849(4)
Zr1–Zr1	3.6033(5)	Zr1–Zr1	3.5872(5)	Hf1–Hf1	3.6168(6)	Hf1–Hf1	3.5710(3)
P1–(O1/N1)	1.5435(15)	P1–O1	1.532(2)	P1–(O1/N1)	1.5586(15)	P1–O1	1.531(2)

Table H.6. List of X–P–X angles occurring in all four compounds, [Å].

Zr_{1-x}PO_{3+4x}N_{1-4x}		Zr_{0.75}PO₄	
(O1/N1)–P–(O1/N1)	100.25(11)	O1–P1–O1	113.39(10)
(O1/N1)–P–(O1/N1)	114.27(6)	O1–P1–O1	113.39(10)
(O1/N1)–P–(O1/N1)	114.27(6)	O1–P1–O1	101.90(19)
(O1/N1)–P–(O1/N1)	114.27(6)	O1–P1–O1	101.90(19)
(O1/N1)–P–(O1/N1)	114.27(6)	O1–P1–O1	113.39(10)
(O1/N1)–P–(O1/N1)	100.25(11)	O1–P1–O1	113.39(10)
Hf_{1-x}PO_{3+4x}N_{1-4x}		Hf_{0.75}PO₄	
(O1/N1)–P–(O1/N1)	114.51(6)	O1–P1–O1	113.62(9)
(O1/N1)–P–(O1/N1)	114.51(6)	O1–P1–O1	113.62(9)
(O1/N1)–P–(O1/N1)	99.81(11)	O1–P1–O1	101.46(16)
(O1/N1)–P–(O1/N1)	99.81(11)	O1–P1–O1	101.46(16)
(O1/N1)–P–(O1/N1)	114.51(6)	O1–P1–O1	113.62(9)
(O1/N1)–P–(O1/N1)	114.51(6)	O1–P1–O1	113.62(9)

H.4 Details on structure determination

Precedence case in the pyrophosphate $Ta_{0.899}P_{1.901}O_7$ shows that P sites might feature vacancies in the presence of oxophilic metals.^[2] To test for such P vacancies in the $M_{0.75}PO_4$ structure models, which could have electrostatic consistency in an $MP_{0.8}O_4$ composition, additional refinements were carried out:

1) “ $M^{IV}P_{0.8}O_4$ ” structure models with fixed composition.

The refinement of fixed composition $MP_{0.8}O_4$ resulted in quite large R1 values (“ $ZrP_{0.8}O_4$ ”, R1 = 18 %; “ $HfP_{0.8}O_4$ ”, R1 = 5 %) and negative displacement parameters of P and O, which clearly indicates a wrong structure model.

2) “ $M^{IV}P_{0.8}O_4$ ” structure models with fixed *M* s.o.f. of 1 and refined P s.o.f.

The free refinement of P obviously improves the resulting R values (“ $ZrP_{0.8}O_4$ ”, R1 = 6.9 %; “ $HfP_{0.8}O_4$ ”, R1 = 3.5 %), but they are still large and the P position has now an s.o.f. of 1.5, which is physically impossible.

3) “ $M_x^{IV}P_yO_4$ ” structure model with refined *M* s.o.f. and refined P s.o.f.

The last possibility is to co-refine the occupancies of the heavy atom position and the P position, which would correspond to a situation, in which both, the M and the P position are not fully occupied. Since the overall structure factor is now only coupled to the weak scatterer O, large correlations between the occupancy of M and P and the OSF are the result. The free refinement of physically significant occupancies is therefore not possible. However, the ratio of the s.o.f.'s of M and P can still be determined as the OSF is just a factor. The ratio of the s.o.f.'s of M and P are 0.80:1 ($Zr_{0.75}PO_4$) and 0.78:1 ($Hf_{0.75}PO_4$), which is close to the expected 0.75:1. Deviations can be explained since the free refinement of the s.o.f.'s allows to fit the counting statistic error that comes from data collection. The refined ratio of the occupancies clearly indicate $M_{0.75}PO_4$ (M = Zr, Hf) structure models. Structure models with less than 0.75 M and 1 P are not possible through electrostatic charge balancing (FTIR spectra indicated no presence of H).

Reciprocal lattice planes

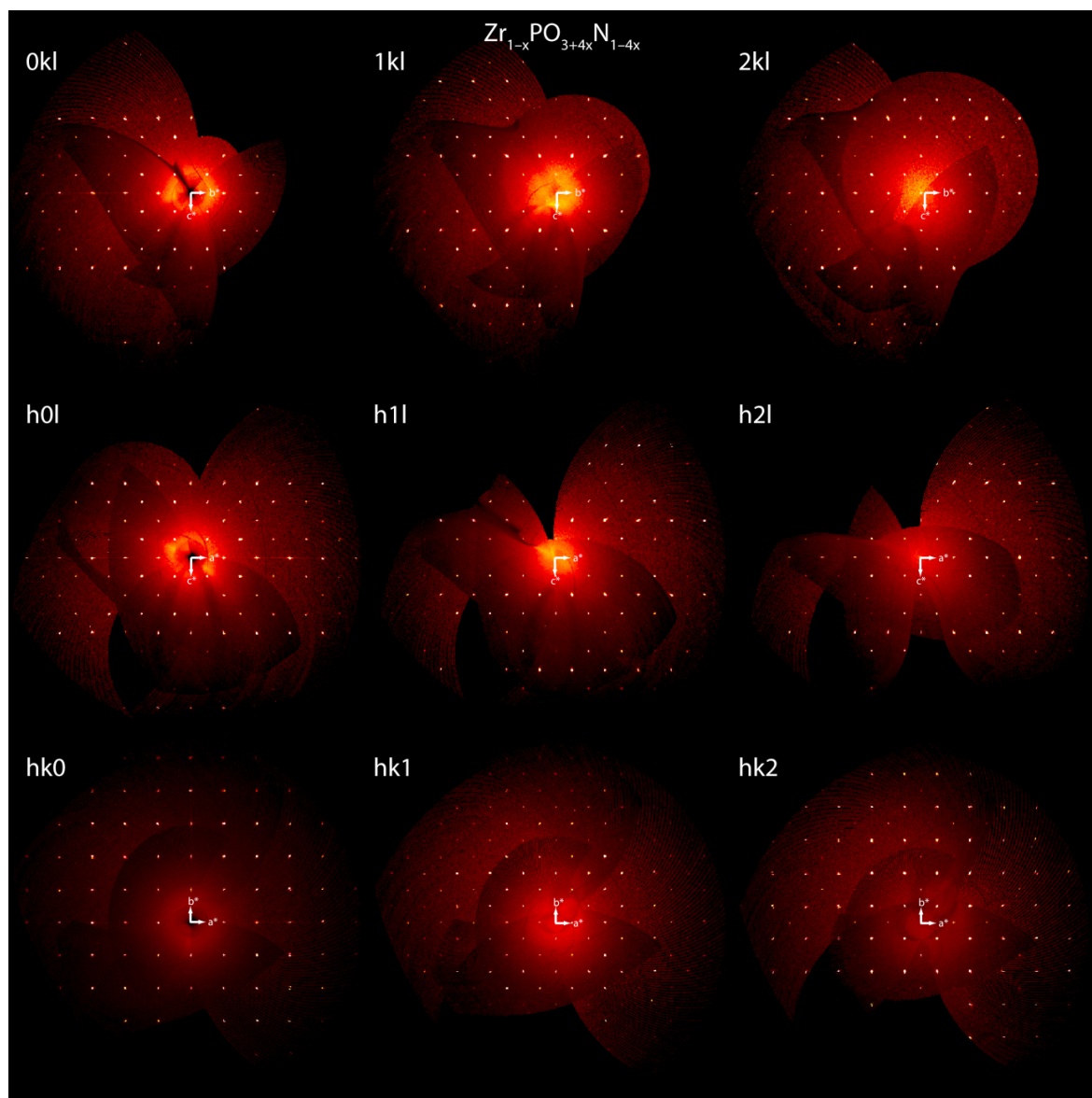


Figure H.6. Reconstructed reciprocal lattice planes of $\text{Zr}_{1-x}\text{PO}_{3+4x}\text{N}_{1-4x}$, maximum index is two. Reciprocal unit cell vectors displayed as white arrows. Magnification of picture possible by zooming.

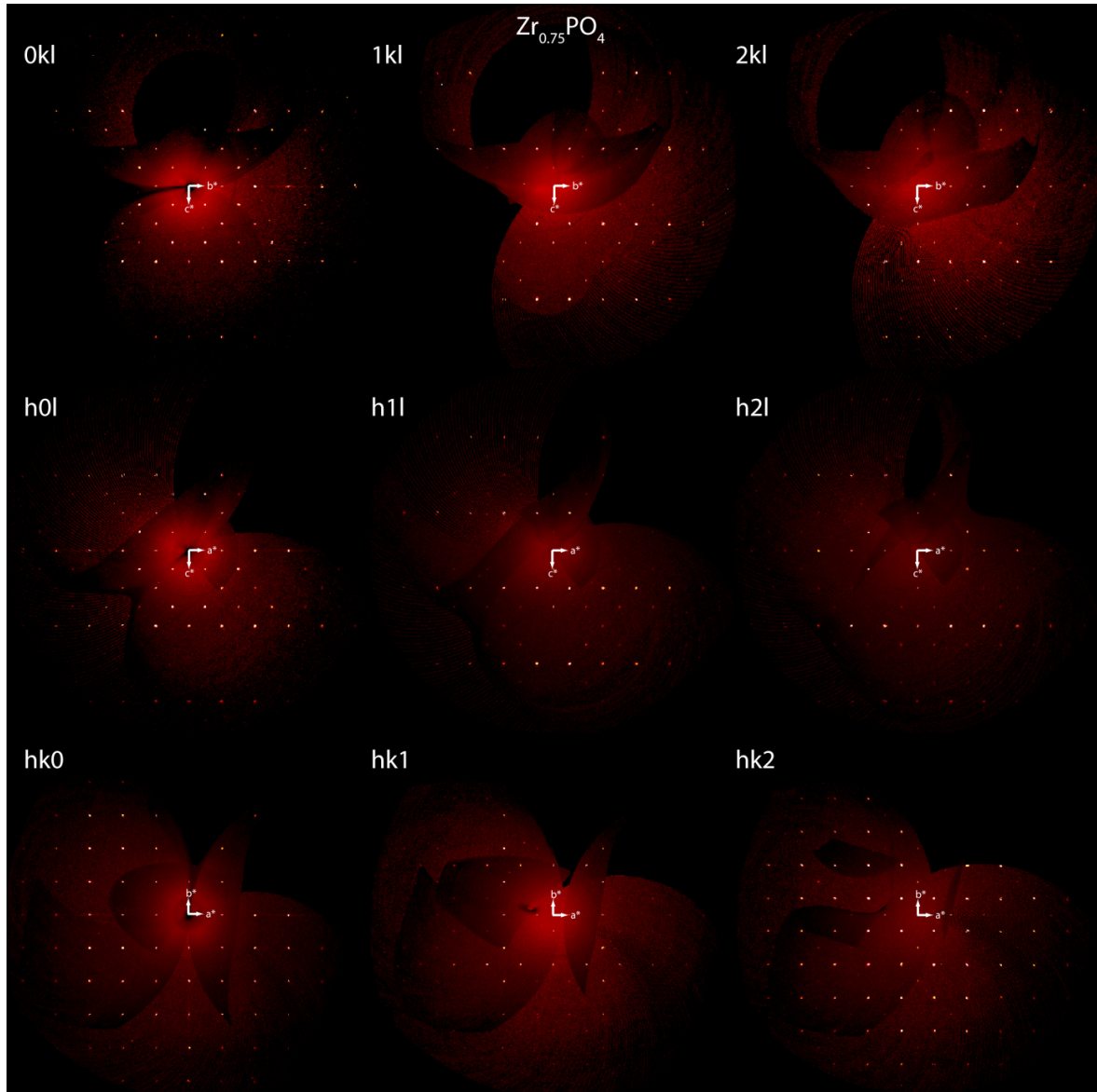


Figure H.7. Reconstructed reciprocal lattice planes of $\text{Zr}_{0.75}\text{PO}_4$, maximum index is two. Reciprocal unit cell vectors displayed as white arrows. Magnification of picture possible by zooming.

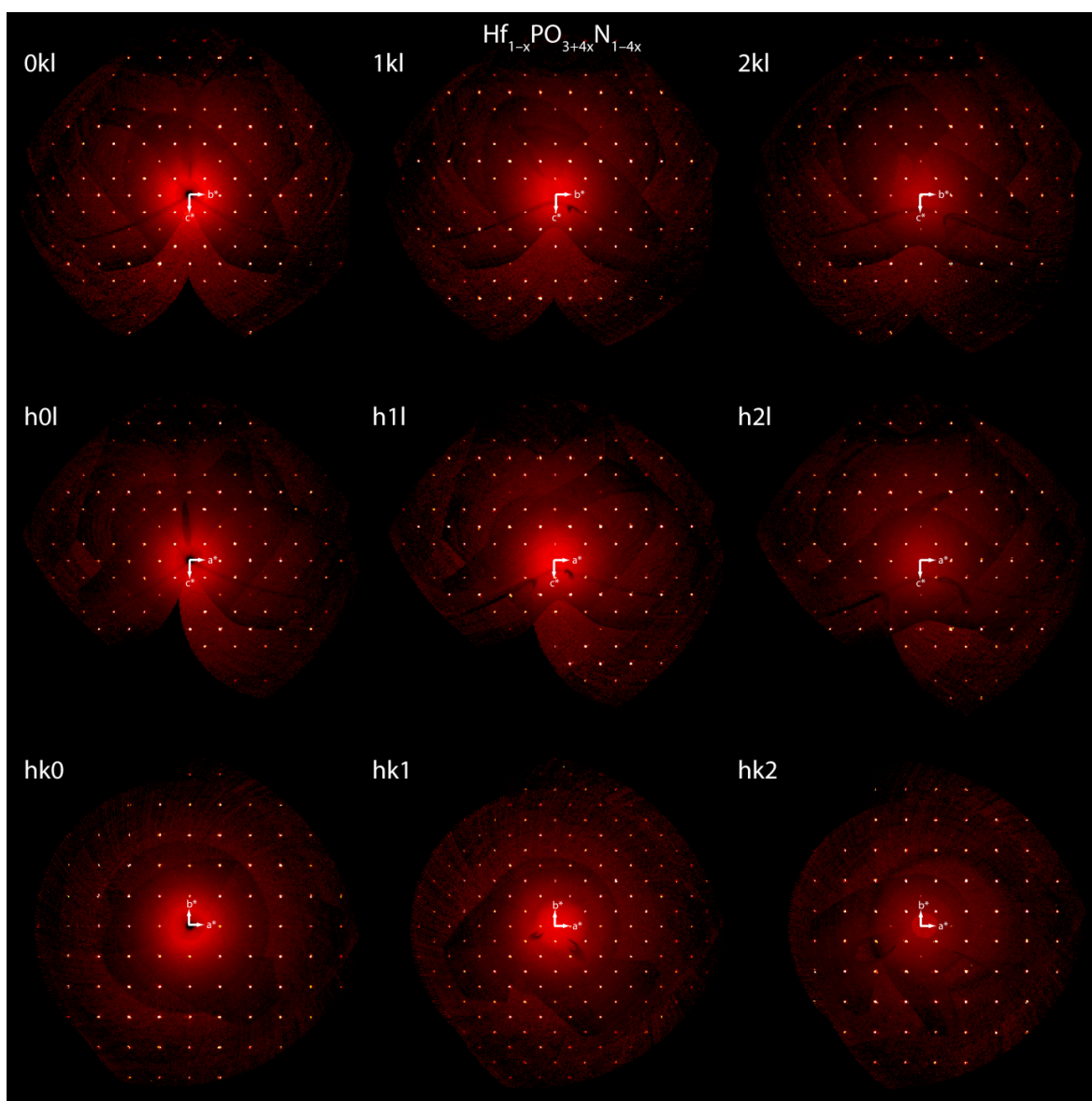


Figure H.8. Reconstructed reciprocal lattice planes of $\text{Hf}_{1-x}\text{PO}_{3+4x}\text{N}_{1-4x}$, maximum index is two. Reciprocal unit cell vectors displayed as white arrows. Magnification of picture possible by zooming.

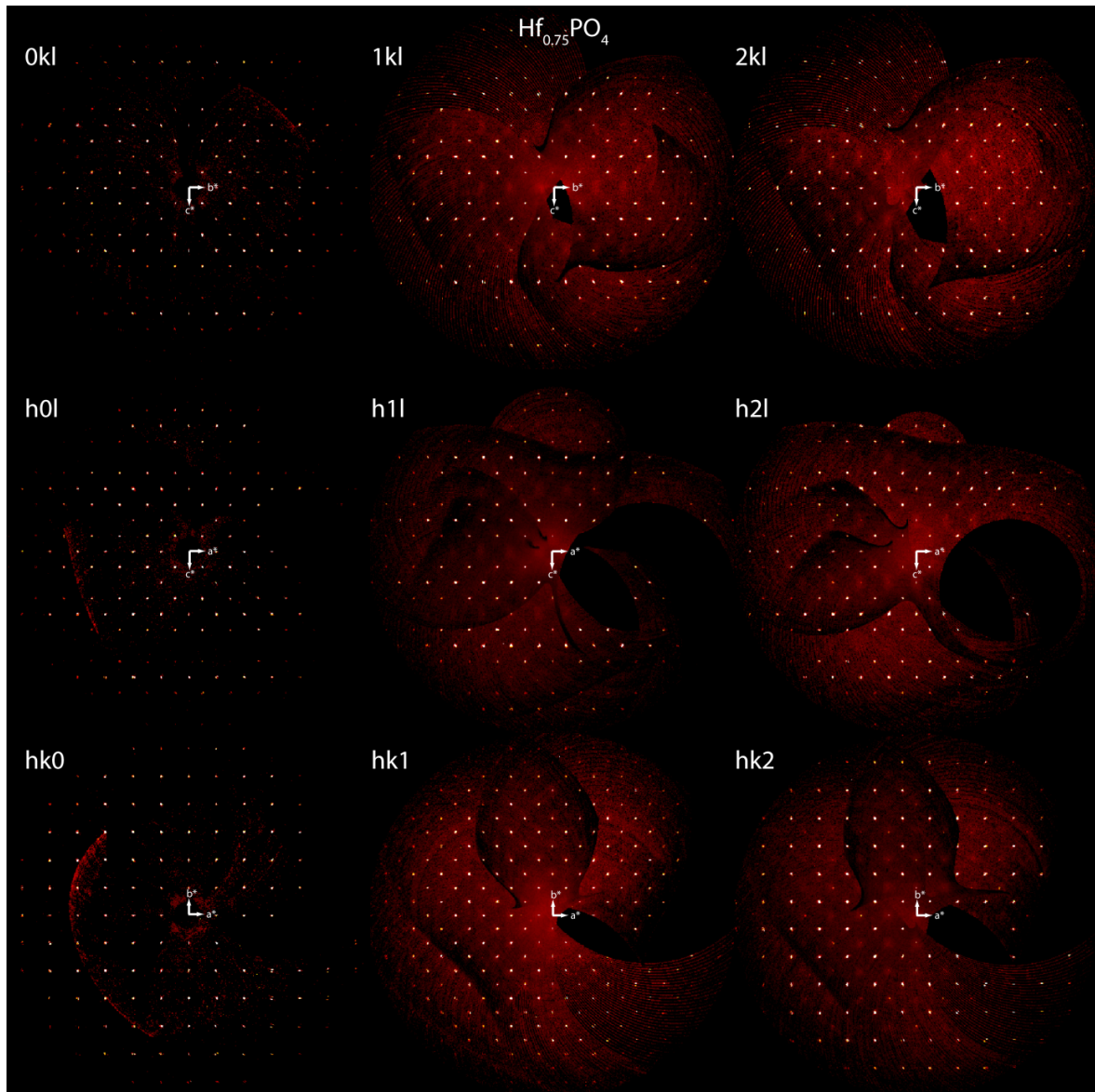


Figure H.9. Reconstructed reciprocal lattice planes of $\text{Hf}_{0.75}\text{PO}_4$, maximum index is two. Reciprocal unit cell vectors displayed as white arrows. Magnification of picture possible by zooming.

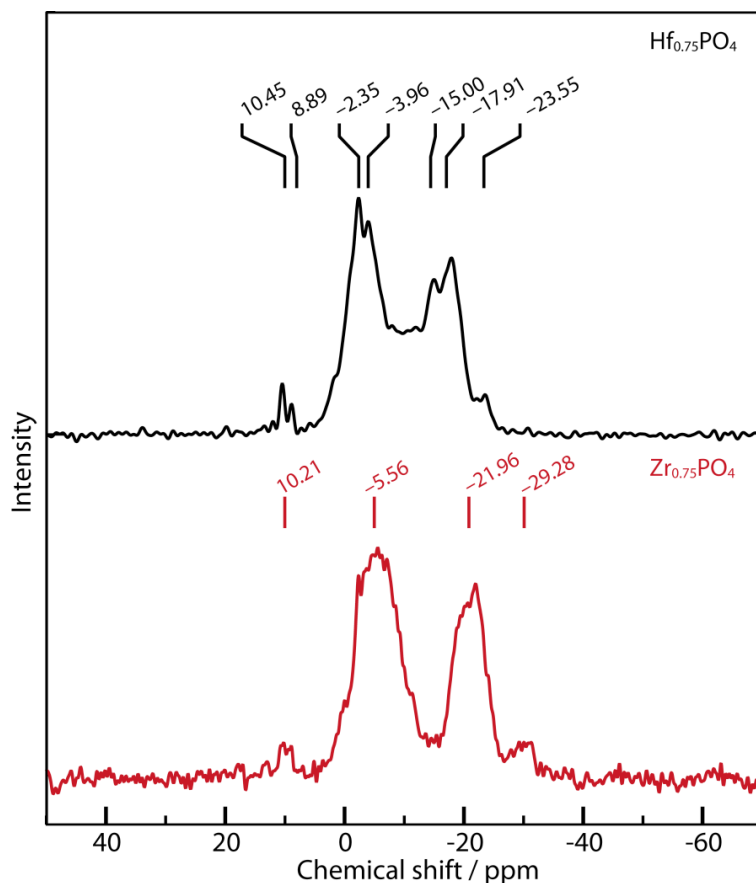
Nuclear magnetic resonance (NMR) measurements.

Figure H.10. ³¹P MAS NMR spectra of the $M_{0.75}PO_4$ ($M = Zr, Hf$) samples. Several peaks (chemical shift marked in figure) are discernible with differing intensities.

³¹P MAS NMR spectra (Figure H.10) were recorded of the $M_{0.75}PO_4$ ($M = Zr, Hf$) samples. As the heavy metal positions, Zr1 and Hf1, are not fully occupied the ³¹P MAS NMR spectra show not one single peak, which would be in accordance with the single P atom position of the average-structure model, but several signals. The most straightforward explanation for the appearance of several ³¹P resonances is to assume different local chemical environments of the P atoms, which stem from random heavy metal vacancies (s.o.f. (Zr1/Hf1) = 0.75). In the second coordination sphere, displayed in Figure H.11, P is surrounded by six M atoms ($M = Zr, Hf$), two of them closer (Hf_{0.75}PO₄: 2.885(1) Å, Zr_{0.75}PO₄: 2.892(1) Å) and four of them further away (Hf_{0.75}PO₄: 3.571(3) Å, Zr_{0.75}PO₄: 3.587(1) Å). Based on the probability of 75 % to find an M atom at its site, this generates several possible chemical environments. We calculated the probabilities for each combination assuming a random distribution. We first calculated the probabilities to find two, one, or zero of the close M atoms in the local envi-

ronment of a P atom. Within these three cases we further differentiated the simultaneously present number of remote M atoms, which can be four, three, two, one, or zero. This sums to a total of 15 chemical environments, whose probabilities are summarized in Table H.7. Six combinations have a larger probability, which correspond to the cases of either two or one close M atom and four, three, or two remote M atoms present. A quantitative assignment of the chemical environments to the spectra cannot be made, however, a qualitative statement is possible. Several different chemical environments are generated by the partial occupancy model, which is in accordance with the several observed ^{31}P signals. The spectra are therefore in accordance with the structure model suggested by single-crystal diffraction.

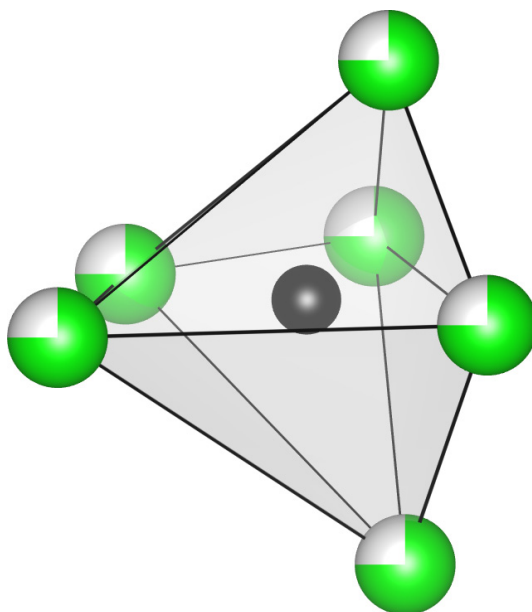


Figure H.11. Second coordination sphere around P in $M_{0.75}\text{PO}_4$ ($M = \text{Zr}, \text{Hf}$). P in black, M in green, three-quarter filled spheres indicate an occupancy of 75 %, picture obtained from the $\text{Hf}_{0.75}\text{PO}_4$ structure model.

Table H.7. Mathematical probabilities for each coordination environment. Labels are understood the following way: A: 2 close *M* atoms, B: 1 close *M* atom, C: 0 close *M* atoms, a: zero remote *M* atoms, b: 1 remote *M* atom, c: 2 remote *M* atoms, d: 3 remote *M* atoms, e: 4 remote *M* atoms.

Combination	Probability / %
Aa	0.22
Ab	2.64
Ac	11.87
Ad	23.73
Ae	17.80
Ba	0.15
Bb	1.76
Bc	7.91
Bd	15.82
Be	11.87
Ca	0.02
Cb	0.29
Cc	1.32
Cd	2.64
Ce	1.98
Σ	1

H.5 Temperature-dependent powder X-ray diffraction

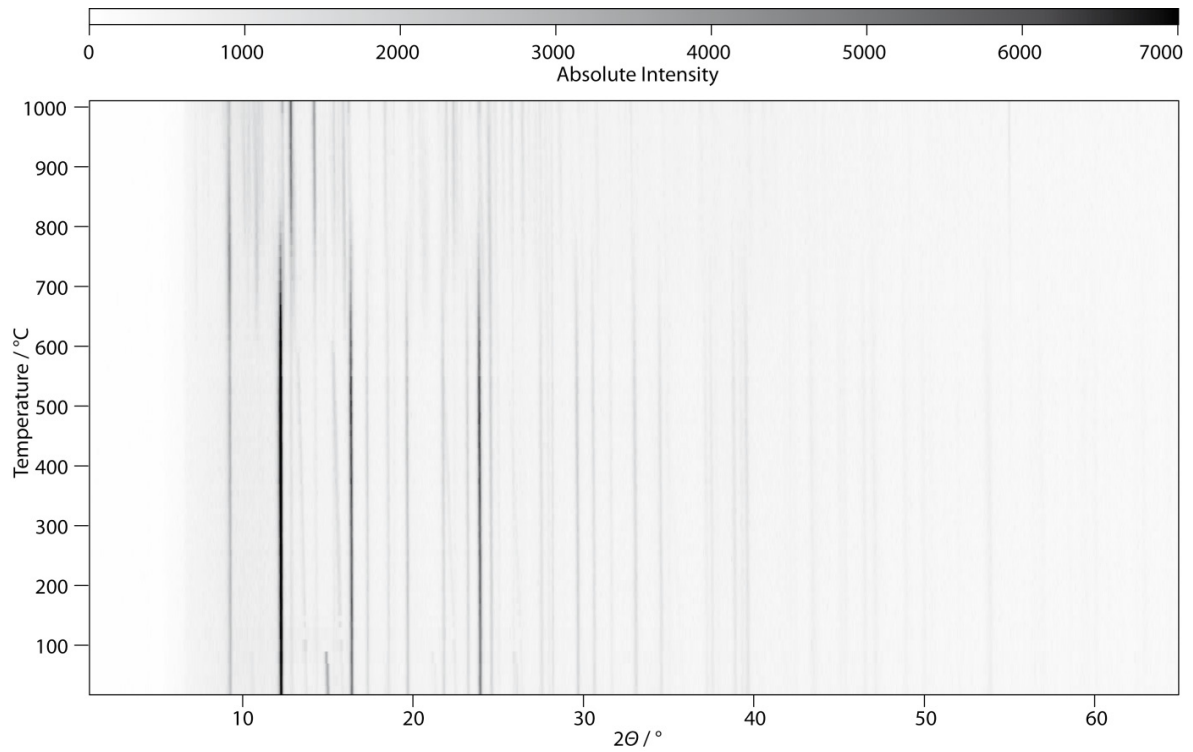


Figure H.12. High-temperature powder diffraction patterns of $\text{Zr}_{1-x}\text{PO}_{3+4x}\text{N}_{1-4x}$.

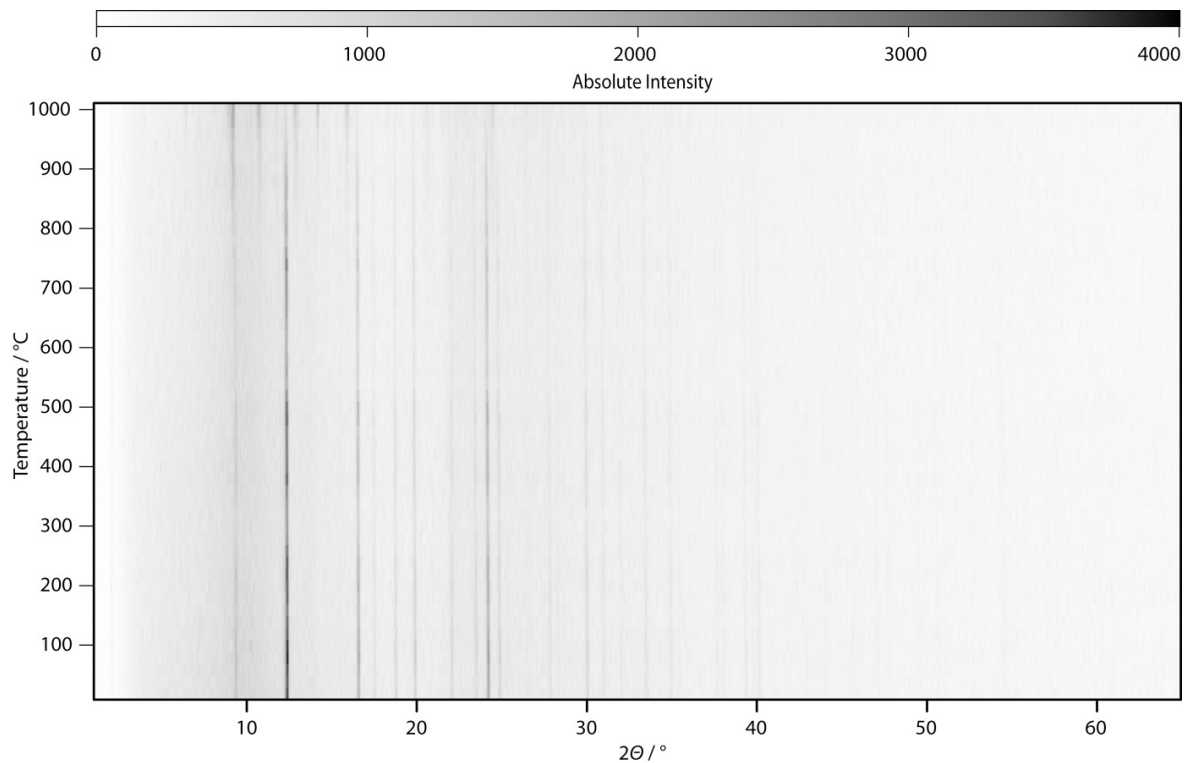


Figure H.13. High-temperature powder diffraction patterns of $\text{Zr}_{0.75}\text{PO}_4$.

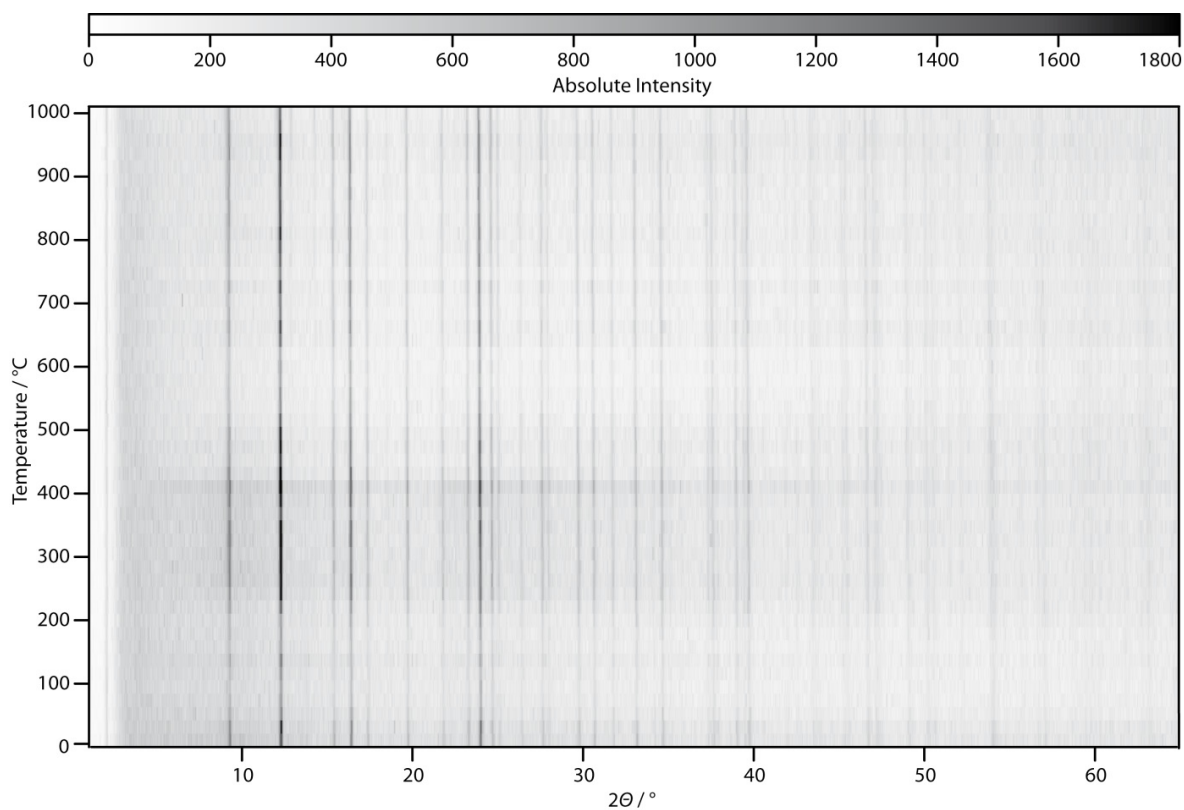


Figure H.14. High-temperature powder diffraction patterns of $\text{Hf}_{1-x}\text{PO}_{3+4x}\text{N}_{1-4x}$.

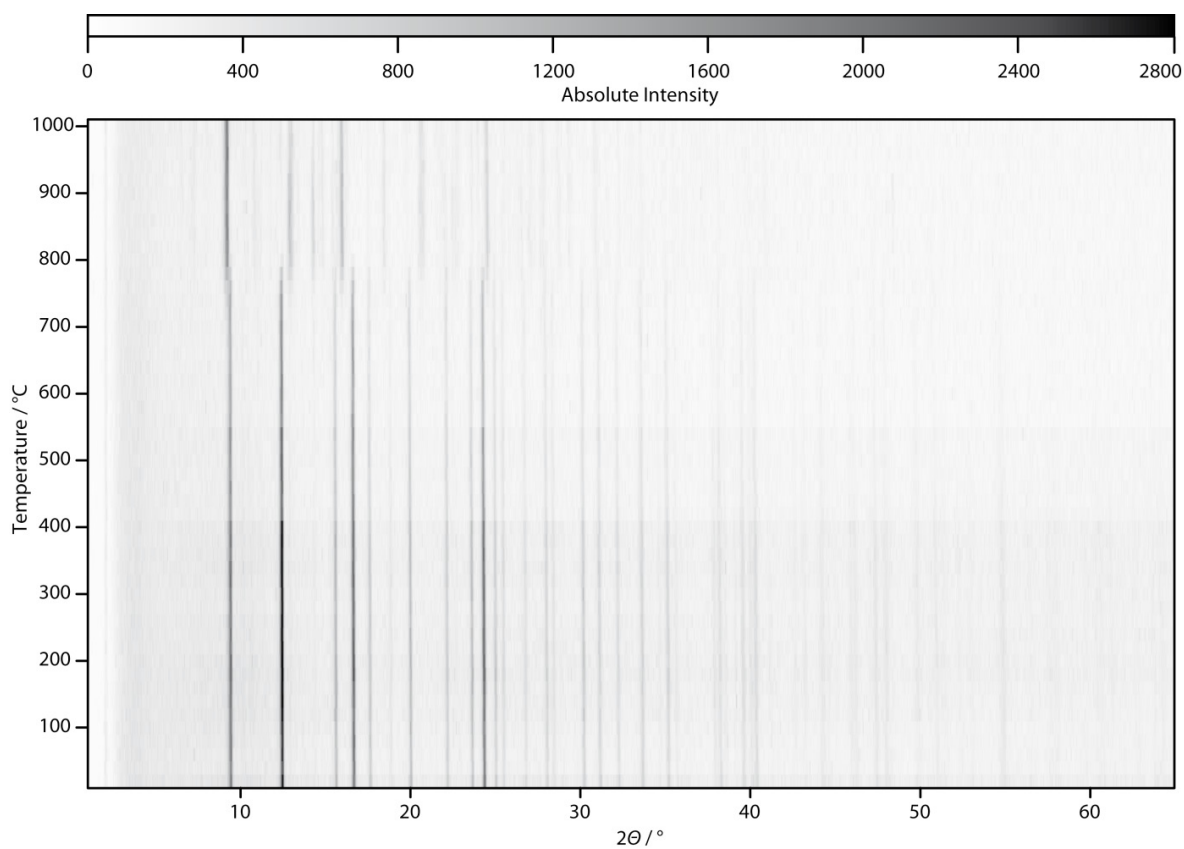


Figure H.15. High-temperature powder diffraction pattern of $\text{Hf}_{0.75}\text{PO}_4$.

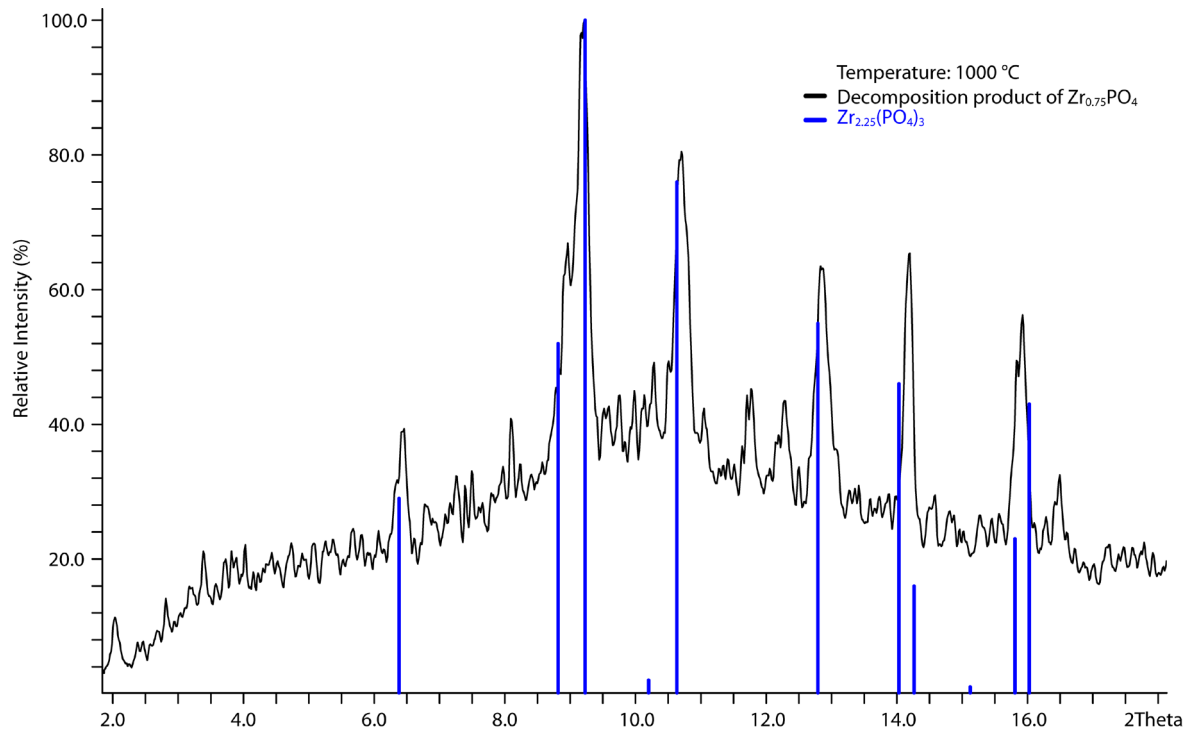


Figure H.16. Powder diffraction pattern of the phase transformation product of $Zr_{0.75}PO_4$ at 1000 °C. Blue reference from ICDD [00-038-0017].^[3]

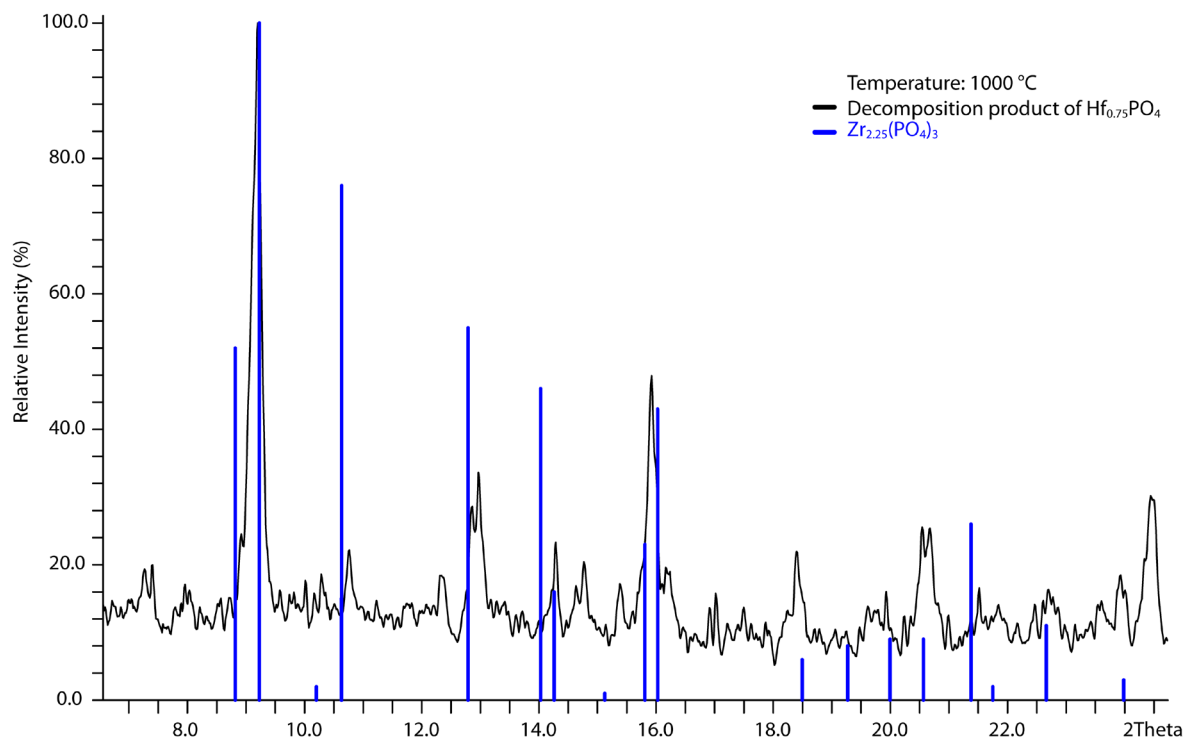


Figure H.17. Powder diffraction pattern of the phase transformation product of $Hf_{0.75}PO_4$ at 1000 °C. Blue reference from ICDD [00-038-0017].^[3]

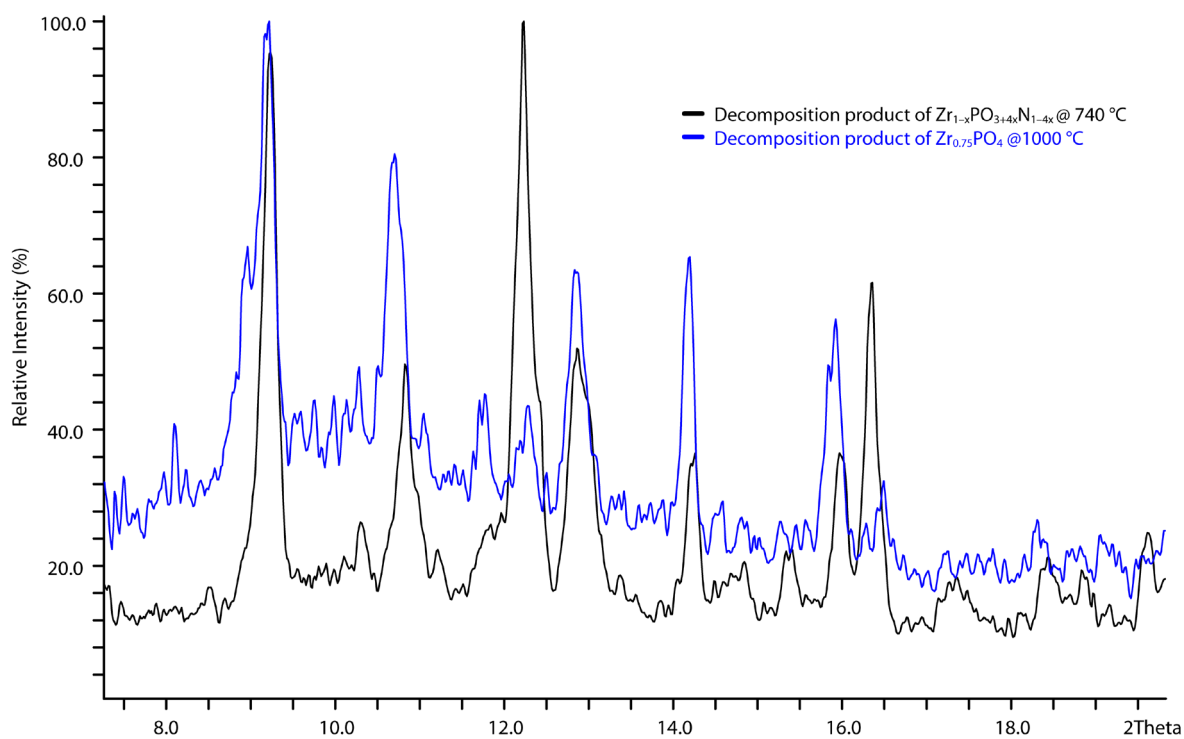


Figure H.18. Powder diffraction pattern of the phase transformation product of $Zr_{1-x}PO_{3+4x}N_{1-4x}$ and $Zr_{0.75}PO_4$ at 740 and 1000 °C. Strong reflections at ca. $2\theta = 12.5$ and 16.5° cannot be explained by a $Zr_{2.25}(PO_4)_3$ phase.^[3]

H.6 UV-vis spectroscopy

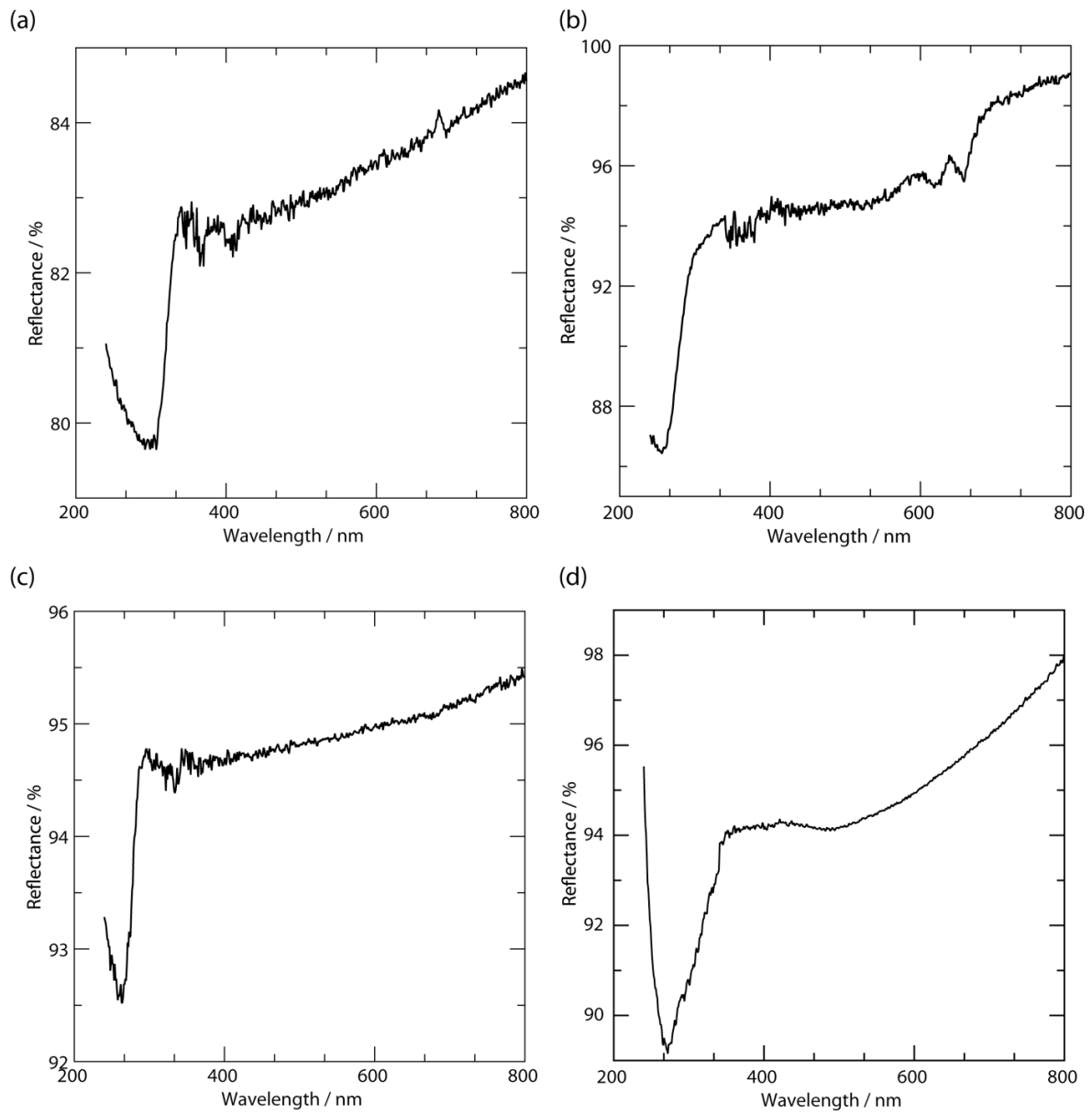


Figure H.19. UV-vis spectra of samples of (a) $Zr_{1-x}PO_{3+4x}N_{1-4x}r$ (b) $Zr_{0.75}PO_{4r}$ (c) $Hf_{1-x}PO_{3+4x}N_{1-4x}r$ (d) $Hf_{0.75}PO_{4r}$.

H.7 References

- [1] J. Adam, M. D. Rogers, *Acta Crystallogr.* **1959**, *12*, 951–951.
- [2] S. Oyetola, A. Verbaere, D. Guyomard, M. P. Crosnier, Y. Piffard, M. Tournoux, *Eur. J. Solid State Inorg. Chem.* **1991**, *28*, 23–36.
- [3] J. Alamo, R. Rustum, *J. Am. Ceram. Soc.* **1984**, *67*, 80–82.

Appendix I. Supporting information for Chapter 9.

I.1 Experimental Procedures

Preparation of P_3N_5

P_3N_5 was prepared following the method of Stock *et al.* by firing P_4S_{10} (Sigma-Aldrich, 99.99 %) in a constant flow of ammonia gas (5.0, Air Liquide).^[1] A fused silica tube with a fused silica boat was dried in a tube furnace under dynamic vacuum ($< 10^{-3}$ mbar) and at 1273 K for 4 h. After loading the boat with P_4S_{10} in an Ar counter flow, the tubing and the starting material was saturated with a constant flow of ammonia for 4 h. The temperature was raised to 1123 K and maintained for additional 4 h, then cooled to room temperature. Temperature ramps were set to 5 K/min. The product was obtained as an orange/brown powder and its purity confirmed by PXRD, IR spectroscopy, and CHNS analysis.

Preparation of $LiPN_2$

A mixture of P_3N_5 and a 1.2 times excess of Li_3N (Rockwood Lithium, 94 %) was ground in a glove box ($H_2O, O_2 < 1$ ppm) and then transferred to a Ta crucible residing in a dried fused silica ampoule.^[2] The sealed ampoule was fired at 1073 K for 90 h with temperature ramps of 5 K/min. After washing with diluted hydrochloric acid/ H_2O /acetone, the product was obtained as a light brown powder. Its purity was confirmed by PXRD and IR spectroscopy.

Preparation of MP_8N_{14} ($M = Fe, Co, Ni$)

For the preparation of the MP_8N_{14} ($M = Fe, Co, Ni$) samples a modified Walker-type multianvil setup driven by a 1000 t hydraulic press (Voggenreiter, Mainleus, Germany) was used.^[3-7] The payload consisted of the octahedron-within-cubes arrangement driven by steel wedges, size 18/11, representing an 18 mm octahedron edge with an 11 mm truncation of the cubes. Materials used were Cr_2O_3 -substituted (6 %) MgO octahedra (Ceramic Substrates & Components, Isle of Wight, U.K), pyrophyllite gas-kets (Ceramic Substrates & Components, Isle of Wight, U.K), Co-substituted (7 %) tungsten carbide cubes (Hawedia, Marklkofen, Germany), h-BN crucibles (Henze, Kempten, Germany), and graphite sleeves for heating (Schunk, Heuchelheim, Germany).

The starting materials $FeCl_2$ (Alfa Aesar, 99.99 %), $CoBr_2$ (Sigma-Aldrich, 99.99 %), $NiCl_2$ (Sigma-Aldrich, 99.99 %), $LiPN_2$, and P_3N_5 were mixed and ground in a glovebox ($H_2O, O_2 < 1$ ppm), then

transferred into the octahedron assembly. Reactions were carried out at 9 GPa and ca. 1473 K, with a 4 h dwell for $\text{FeP}_8\text{N}_{14}$ and $\text{NiP}_8\text{N}_{14}$, and a 2 h dwell for $\text{CoP}_8\text{N}_{14}$. Temperature was increased over 30 min for all compounds and decreased over 4 h for $\text{FeP}_8\text{N}_{14}$ and $\text{NiP}_8\text{N}_{14}$, and over 2 h for $\text{CoP}_8\text{N}_{14}$. Samples were recovered and washed with water to remove the Li halide byproduct.

Powder X-ray diffraction

Powder X-ray diffraction was carried out on a StadiP diffractometer (STOE & Cie, Darmstadt, Germany) equipped with a MYTHEN 1K detector (Dectris, Baden, Switzerland; angular range $\Delta 2\theta = 12.5^\circ$), a Mo-source, and a Ge(111) monochromator singling out the Mo- $K\alpha_1$ radiation. Samples were loaded into glass capillaries with 0.3 mm diameter and 0.01 mm wall thickness (Hilgenberg GmbH, Malsfeld, Germany). Data was recorded in the angular range between $2\theta = 2-76^\circ$ with a step width of $0.015^\circ/\text{step}$.

Diffraction data was analyzed with the TOPAS-Academic V4.1 software.^[8] Patterns were indexed with the SVD-algorithm, tentative space group determination was based on missing/present reflections.^[9] Intensities were extracted with the Pawley method and structure solution was performed with the charge-flipping algorithm.^[10-13] Structure models were refined with the Rietveld method.^[14,15] The estimated standard deviations were calculated by TOPAS-Academic using the matrix inversion method. Crystal structures and electron density maps were visualized with VESTA.^[16]

Further details on the crystal structure investigations may be obtained from the Fachinformationszentrum Karlsruhe, 76344 Eggenstein-Leopoldshafen, Germany (fax: (+49)7247-808-666; email: @fiz-karlsruhe.de), on quoting the depository numbers CSD-1856625-1856627 for $\text{FeP}_8\text{N}_{14}$, $\text{CoP}_8\text{N}_{14}$, and $\text{NiP}_8\text{N}_{14}$ respectively. Temperature-dependent X-ray powder diffraction was obtained on a StadiP diffractometer with Mo- $K\alpha_1$ radiation, attached graphite furnace and an image plate position-sensitive detector. Data was recorded in the temperature range of 298 to 1273 K in steps of 20 K.

Spectroscopy

Infrared spectroscopy was performed with a Spectrum BX II spectrometer (PerkinElmer Waltham, MA, United States) with DuraSampler ATR-unit in the range of $650-4500\text{ cm}^{-1}$.

UV-vis spectra were recorded in reflection geometry on a V-650 UV-Vis spectrophotometer (JASCO, Gross-Umstadt, Germany) equipped with a photomultiplier tube detector and a single monochromator with 1200 lines/mm in the range of 240–800 nm. The scan speed was set to 400 nm/min with a 2 nm resolution, a deuterium lamp (240–330 nm) and a halogen lamp (330–880 nm) were used. The spectrometer was controlled with the Spectra Manager II software. Samples were placed between a fused silica glass slide and a BaSO₄-coated stamp.

UV-vis-NIR spectra were recorded in reflection geometry on a Varian Cary 500 photospectrometer with a scan rate of 600 nm/min and a data interval of 0.33 nm in the range of 175–2000 nm. Source changeover at 350 nm, detector changeover at 800 nm, and corrected baseline. BaSO₄ was used as white standard, and the samples were diluted with BaSO₄.

A Helios Nanolab G3 Dualbeam UC (FEI, Hillsboro, OR, United States) with attached X-Max 80 SDD detector (Oxford Instruments, Abingdon, United Kingdom) was used for scanning electron microscopy (SEM) and energy dispersive X-ray (EDX) spectroscopy. Samples were placed on conducting carbon foil and coated with carbon.

Mössbauer Spectroscopy

A ⁵⁷Co/Rh source was used for the Mössbauer spectroscopic measurement of FeP₈N₁₄. The measurement was conducted in the usual transmission geometry in a continuous flow cryostat system (Janis Research Co LLC) at 6 K while the source was kept at room temperature. The powdered sample was placed in a PMMA container with an optimized thickness as described by Long *et al.*^[17] The WINNORMOS routine^[18] was used to fit the spectrum.

Magnetic Properties

Powdered samples of FeP₈N₁₄, CoP₈N₁₄ and NiP₈N₁₄ were packed in polyethylene (PE) capsules and attached to the sample holder rod of a Vibrating Sample Magnetometer unit (VSM) for measuring the magnetization $M(T,H)$ in a Quantum Design Physical Property Measurement System (PPMS). The samples were investigated in the temperature range of 2.5–300 K and with external magnetic fields up to 80 kOe.

I.2 Structure Determination

The structure of the isotypic MP_8N_{14} ($M = \text{Fe, Co, Ni}$) compounds was initially solved for the data set of $\text{FeP}_8\text{N}_{14}$. Indexing with the SVD-algorithm lead to the cell $a = 8.26930(13)$, $b = 5.10147(8)$ $c = 23.0776(4)$ Å (exact data from the final refinement) in the tentative space group $Cmc2_1$. The structure was solved with charge-flipping in $Cmc2_1$ and the structure model completed through difference Fourier maps. The structure model was transformed to the supergroup $Cmce$ and refined with the method of Rietveld leading to the final structure model (Table I.1 and Figures I.1–I.4). The structures of the Co and Ni compound were deduced from Rietveld refinements starting from the $\text{FeP}_8\text{N}_{14}$ model. Atom positions in Tables I.2–I.4, interatomic distances in Tables I.6–I.8, and angles in Tables I.9–I.11.

The quality of the data did not allow refinement of anisotropic displacement parameters. In $\text{FeP}_8\text{N}_{14}$ all atoms were refined isotropically, constraining all N atoms to a single value and restraining them to a reasonable value. The N atoms in $\text{CoP}_8\text{N}_{14}$ and $\text{NiP}_8\text{N}_{14}$ were treated as the N atoms in $\text{FeP}_8\text{N}_{14}$.

The displacement parameters of the metal atoms are enlarged compared to those of the non-metal positions (cf. Tables I.2–I.5). Since the metal atoms reside in MN_6 octahedra that are elongated along one axis (cf. structure description in the manuscript, Figure 9.1, Tables I.6–I.8), the metal atoms might show an anisotropic behavior. To get an estimate of the displacement anisotropic displacement parameter refinement was tried for the metal atoms. The data quality was insufficient for the refinement on $\text{FeP}_8\text{N}_{14}$, but values for Co and Ni could be obtained and are reported here (Table I.5). To get a visual estimate of the observed electron density, 3D isosurface maps (F_{obs}) of the CoN_6 and NiN_6 octahedra are displayed in Figure I.4. The map suggests a not perfectly spherical electron distribution of the metal atoms, they are slightly elongated towards the axial N atoms, which are ca. 0.42 Å ($\text{CoP}_8\text{N}_{14}$) and 0.37 Å ($\text{NiP}_8\text{N}_{14}$) further from the metal atom than the respective equatorial N atoms.

Several reasons for the low degree of information on the displacement ellipsoids of metal, P, and N atoms might play a role. First off, powder diffraction data always has limited information in that regard due to the collapse of 3D data onto 1D. Moreover, the small crystallite size of the compounds has to be taken into account (Figure I.5). Small crystallites usually indicate bad crystallization, stacking-faults might occur, which impede the collection of accurate high-angle data and so the determination of accurate displacement ellipsoids. The high-angle data are further burdened by the long c -axis of the unit cell, which leads to a lot of reflection overlap in the high-angle region. Hence, the

values for the anisotropically refined metal atoms reported here, should only serve as an indicator for a displacement of the metal atoms from the center of the N_6 octahedra.

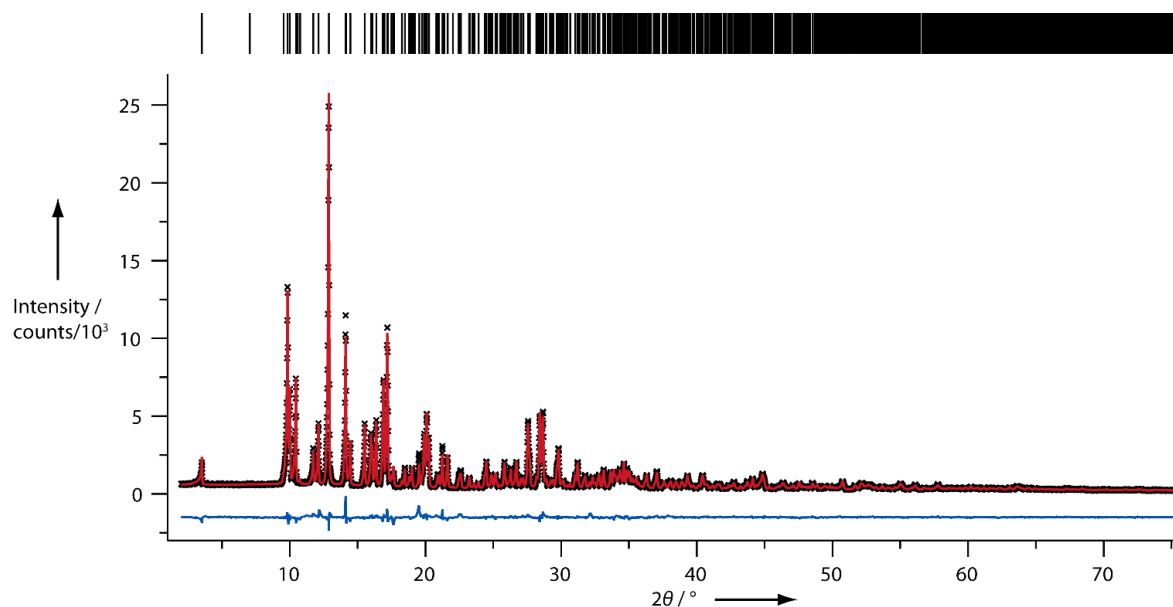


Figure I.1. Rietveld refinement of FeP_8N_{14} . Experimental data as black crosses, Rietveld fit as red line, difference plot in blue, black drop lines indicate theoretical reflection positions; Mo- $K\alpha_1$ radiation.

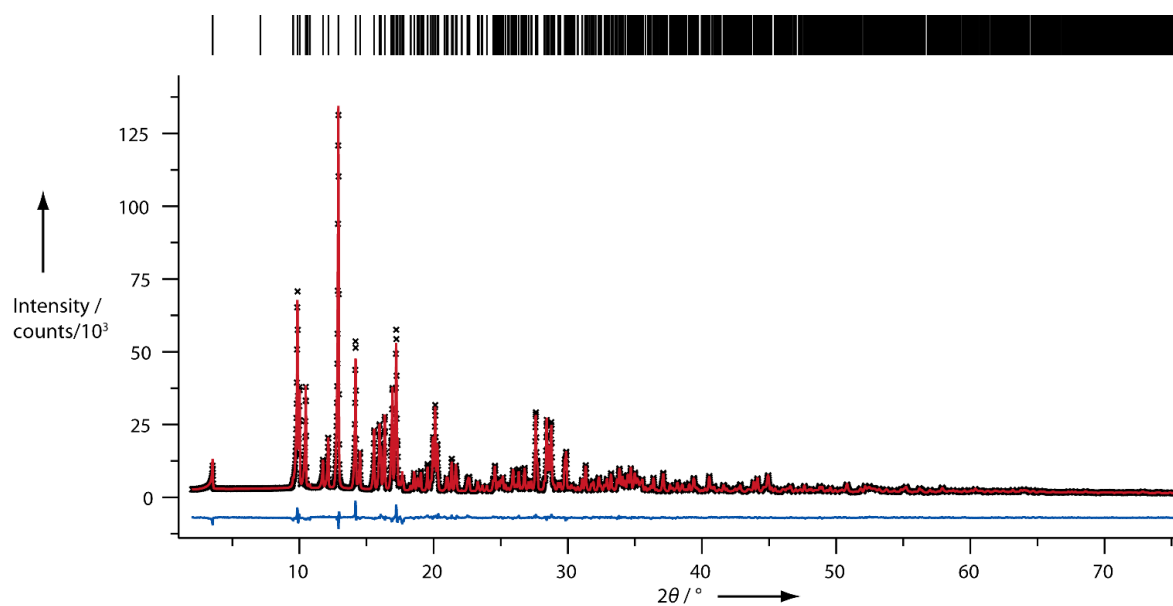


Figure I.2. Rietveld refinement of CoP_8N_{14} . Experimental data as black crosses, Rietveld fit as red line, difference plot in blue, black drop lines indicate theoretical reflection positions; Mo- $K\alpha_1$ radiation.

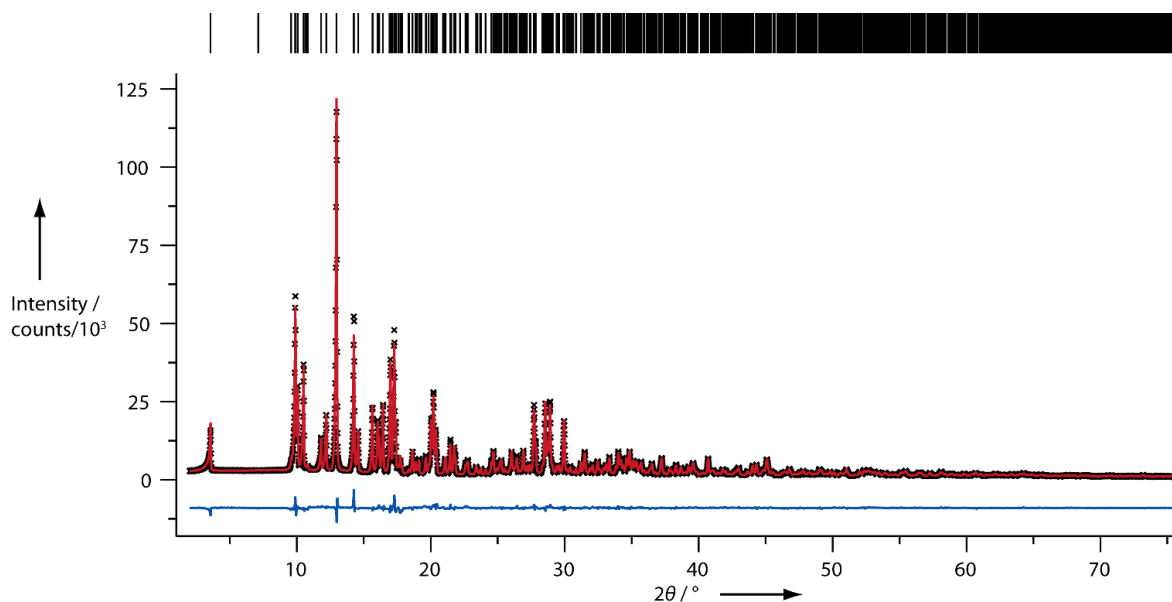


Figure I.3. Rietveld refinement of $\text{NiP}_8\text{N}_{14}$. Experimental data as black crosses, Rietveld fit as red line, difference plot in blue, black drop lines indicate theoretical reflection positions; Mo- $\text{K}\alpha_1$ radiation.

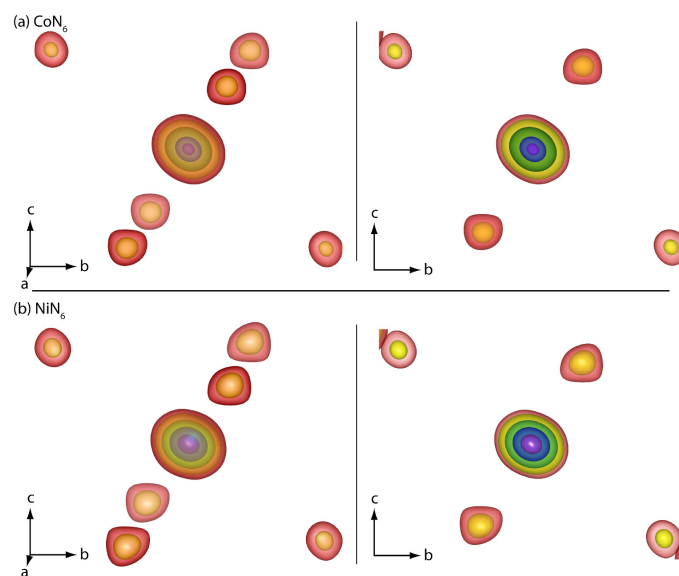


Figure I.4. (a) Observed electron density (F_{obs}) map with boundaries around a CoN_6 octahedron obtained from the $\text{CoP}_8\text{N}_{14}$ powder data. Left: section $-0.25 \leq x \leq 0.25$, $-0.475 \leq y \leq 0.475$, $-0.08 \leq z \leq 0.08$ in an orientation highlighting the elongated octahedral coordination. Axial N5 atoms aligned along the [011] direction. Right: section $-0.25 \leq x \leq 0$, $-0.475 \leq y \leq 0.475$, $-0.08 \leq z \leq 0.08$ in projection along [100]. (b) Observed electron density (F_{obs}) map with boundaries around a NiN_6 octahedron obtained from the $\text{NiP}_8\text{N}_{14}$ powder data. Left: section $-0.25 \leq x \leq 0.25$, $-0.475 \leq y \leq 0.475$, $-0.08 \leq z \leq 0.08$ in an orientation highlighting the elongated octahedral coordination. Axial N5 atoms aligned along the [011] direction. Right: section $-0.25 \leq x \leq 0$, $-0.475 \leq y \leq 0.475$, $-0.08 \leq z \leq 0.08$ in projection along [100]. Isosurfaces are displayed at 5 (red), 8 (yellow), 15 (green), 25 (blue) electrons/ a_0^3 (a_0 = Bohr radius). Purple isosurface at 30 electrons/ a_0^3 for $\text{CoP}_8\text{N}_{14}$, and 35 electrons/ a_0^3 for $\text{NiP}_8\text{N}_{14}$. Electron density in the selected region not belonging to the MN_6 octahedra has been omitted for clarity.

I.3 Crystallographic tables

Table I.1. Crystallographic data for the Rietveld refinement of the MP_8N_{14} ($M = \text{Fe, Co, Ni}$) compounds.

Crystal Data			
Formula	$\text{FeP}_8\text{N}_{14}$	$\text{CoP}_8\text{N}_{14}$	$\text{NiP}_8\text{N}_{14}$
Formula mass / $\text{g}\cdot\text{mol}^{-1}$	499.75	502.83	502.59
Crystal system, space group	orthorhombic, $Cmce$ (no. 64)		
Formula units per unit cell, Z	4		
Lattice parameters / Å	$a = 8.26930(13)$ $b = 5.10147(8)$ $c = 23.0776(4)$	$a = 8.25183(8)$ $b = 5.10337(5)$ $c = 22.9675(2)$	$a = 8.23105(9)$ $b = 5.08252(6)$ $c = 22.8516(3)$
Cell volume / Å^3	973.54(3)	967.21(2)	955.99(2)
Calculated density ρ / $\text{g}\cdot\text{cm}^{-3}$	3.41	3.45	3.49
Absorption coefficient, μ / mm^{-1}	2.9	3.1	3.4
F(000)	976	980	984
Data Collection			
Radiation	Mo-K α_1		
Monochromator	Ge(111)		
Diffractometer	Stoe Stadi P		
Detector	MYTHEN 1K		
2θ -range / $^\circ$	2–75	2–75	2–76
Temperature / K	297(2)		
Data points	4891	4891	4958
No. observed reflections	1401	1391	1426
Refinement/Solution			
Program used	TOPAS Academic V4.1		
Number of parameters	61	64	64
Constraints, restraints	4, 1	4, 1	4, 1
Structure solution	Charge-flipping	-	-
Structure refinement	Rietveld-Method		
Profile function	fundamental parameters model		
Background function	shifted Chebychev polynomial with 14 terms		
R_p	4.5	3.2	3.6
R_{wp}	6.5	4.5	4.9
R_{exp}	3.6	1.6	1.7
R_{Bragg}	2.8	2.3	2.3
$\chi = R_{wp}/R_{exp}$	1.8	2.8	2.9

Table I.2. Atom positions and isotropic displacement parameters for $\text{FeP}_8\text{N}_{14}$.

Atom	Wyckoff position	x	y	z	$U_{\text{iso}} / \text{\AA}^2$	Occupancy
Fe1	4a	0	0	0	0.0185(6)	1
P1	16g	0.1770(2)	0.1534(4)	0.19036(6)	0.0031(4)	1
P2	16g	0.17300(18)	0.4586(4)	0.08118(6)	0.0020(4)	1
N1	16g	0.1871(5)	0.1589(9)	0.0580(2)	0.0051(6)	1
N2	16g	0.2038(4)	0.4388(8)	0.15426(16)	0.0051(6)	1
N3	8e	1/4	0.2128(13)	1/4	0.0051(6)	1
N4	8f	0	0.0489(11)	0.1845(2)	0.0051(6)	1
N5	8f	0	0.0926(10)	0.4334(4)	0.0051(6)	1

Table I.3. Atom positions and isotropic (equivalent for Co1) displacement parameters for $\text{CoP}_8\text{N}_{14}$.

Atom	Wyckoff position	x	y	z	$U_{\text{iso(eq)}} / \text{\AA}^2$	Occupancy
Co1	4a	0	0	0	0.0239(6)	1
P1	16g	0.17667(14)	0.14831(17)	0.18998(4)	0.0023(2)	1
P2	16g	0.17322(13)	0.45547(18)	0.08034(4)	0.0031(2)	1
N1	16g	0.1877(4)	0.1531(5)	0.05807(13)	0.0051(4)	1
N2	16g	0.2019(4)	0.4334(5)	0.15448(11)	0.0051(4)	1
N3	8e	1/4	0.2197(8)	1/4	0.0051(4)	1
N4	8f	0	0.0436(7)	0.18431(16)	0.0051(4)	1
N5	8f	0	0.0825(7)	0.43474(17)	0.0051(4)	1

Table I.4. Atom positions and isotropic (equivalent for Ni1) displacement parameters for $\text{NiP}_8\text{N}_{14}$.

Atom	Wyckoff position	x	y	z	$U_{\text{iso(eq)}} / \text{\AA}^2$	Occupancy
Ni1	4a	0	0	0	0.0192(5)	1
P1	16g	0.17610(16)	0.1537(2)	0.18969(4)	0.0030(3)	1
P2	16g	0.17290(13)	0.4624(2)	0.07939(4)	0.0032(3)	1
N1	16g	0.1857(4)	0.1578(7)	0.05714(14)	0.0051(4)	1
N2	16g	0.2015(4)	0.4400(7)	0.15399(11)	0.0051(4)	1
N3	8e	1/4	0.2287(10)	1/4	0.0051(4)	1
N4	8f	0	0.0461(8)	0.18457(16)	0.0051(4)	1
N5	8f	0	0.0927(8)	0.4360(2)	0.0051(4)	1

Table I.5. Anisotropic displacement parameters of Co and Ni in MP_8N_{14} ($M = \text{Co}, \text{Ni}$).

Atom	$U_{11} / \text{\AA}^2$	$U_{22} / \text{\AA}^2$	$U_{33} / \text{\AA}^2$	$U_{23} / \text{\AA}^2$	$U_{13} / \text{\AA}^2$	$U_{12} / \text{\AA}^2$
CoP₈N₁₄						
Co1	0.0139(8)	0.0291(10)	0.0287(11)	0	-0.0101(8)	0
NiP₈N₁₄						
Ni1	0.0108(7)	0.0270(10)	0.0198(10)	0	-0.0086(8)	0

Table I.6. List of interatomic distances [\AA] occurring in $\text{FeP}_8\text{N}_{14}$

Fe1-N		P1-N	
Fe1-N1	2.201(4)	P1-N2	1.692(4)
Fe1-N1	2.201(4)	P1-N3	1.533(2)
Fe1-N1	2.201(4)	P1-N4	1.564(3)
Fe1-N1	2.201(4)	P1-N2	1.692(4)
Fe1-N5	2.585(7)		
Fe1-N5	2.585(7)		
		P2-N	
		P2-N1	1.624(5)
		P2-N2	1.709(4)
		P2-N5	1.621(3)
		P2-N1	1.634(5)

Table I.7. List of interatomic distances [\AA] occurring in $\text{CoP}_8\text{N}_{14}$

Co1–N		P1–N	
Co1–N1	2.188(3)	P1–N2	1.681(3)
Co1–N1	2.188(3)	P1–N3	1.5489(14)
Co1–N1	2.188(3)	P1–N4	1.5582(17)
Co1–N1	2.188(3)	P1–N2	1.695(3)
Co1–N5	2.605(4)		
Co1–N5	2.605(4)		
		P2–N	
		P2–N1	1.630(3)
		P2–N2	1.723(3)
		P2–N5	1.607(2)
		P2–N1	1.611(3)

Table I.8. List of interatomic distances [\AA] occurring in $\text{NiP}_8\text{N}_{14}$

Ni1–N		P1–N	
Ni1–N1	2.164(3)	P1–N2	1.681(3)
Ni1–N1	2.164(3)	P1–N3	1.5539(16)
Ni1–N1	2.164(3)	P1–N4	1.5536(19)
Ni1–N1	2.164(3)	P1–N2	1.691(3)
Ni1–N5	2.535(4)		
Ni1–N5	2.535(4)		
		P2–N	
		P2–N1	1.633(4)
		P2–N2	1.725(3)
		P2–N5	1.609(2)
		P2–N1	1.612(4)

Table I.9. List of bond angles [$^\circ$] occurring in $\text{FeP}_8\text{N}_{14}$

N–P1–N		N–P2–N		P–N–P	
N2–P1–N3	102.7(3)	N1–P2–N2	105.0(2)	P2–N1–P2	122.1(3)
N2–P1–N4	111.9(2)	N1–P2–N5	113.1(3)	P1–N2–P2	121.2(2)
N2–P1–N2	103.8(2)	N1–P2–N1	115.5(2)	P1–N2–P1	113.0(2)
N3–P1–N4	120.9(2)	N2–P2–N5	111.2(4)	P1–N2–P2	122.3(2)
N2–P1–N3	109.9(2)	N1–P2–N2	104.8(2)	P1–N3–P1	157.2(5)
N2–P1–N4	106.4(2)	N1–P2–N5	107.1(3)	P1–N4–P1	138.8(4)
				P2–N5–P2	123.9(4)

Table I.10. List of bond angles [°] occurring in $\text{CoP}_8\text{N}_{14}$

N-P1-N		N-P2-N		P-N-P	
N2-P1-N3	100.35(17)	N1-P2-N2	103.78(14)	P2-N1-P2	123.0(2)
N2-P1-N4	111.85(18)	N1-P2-N5	112.30(18)	P1-N2-P2	121.27(16)
N2-P1-N2	104.69(14)	N1-P2-N1	116.15(16)	P1-N2-P1	113.58(16)
N3-P1-N4	121.37(15)	N2-P2-N5	111.19(18)	P1-N2-P2	120.96(16)
N2-P1-N3	110.45(15)	N1-P2-N2	104.88(16)	P1-N3-P1	152.8(3)
N2-P1-N4	106.92(17)	N1-P2-N5	108.21(17)	P1-N4-P1	138.7(3)
				P2-N5-P2	125.6(2)

Table I.11. List of bond angles [°] occurring in $\text{NiP}_8\text{N}_{14}$

N-P1-N		N-P2-N		P-N-P	
N2-P1-N3	99.8(2)	N1-P2-N2	103.67(17)	P2-N1-P2	122.2(2)
N2-P1-N4	112.59(19)	N1-P2-N5	112.29(19)	P1-N2-P2	121.3(2)
N2-P1-N2	104.34(16)	N1-P2-N1	116.06(18)	P1-N2-P1	113.32(16)
N3-P1-N4	121.22(16)	N2-P2-N5	111.4(2)	P1-N2-P2	121.1(2)
N2-P1-N3	110.62(16)	N1-P2-N2	104.71(17)	P1-N3-P1	151.6(4)
N2-P1-N4	107.06(19)	N1-P2-N5	108.43(19)	P1-N4-P1	137.8(3)
				P2-N5-P2	124.4(3)

I.4 Charge distribution (CHARDI) calculations

Table I.12. CHARDI calculations for $\text{FeP}_8\text{N}_{14}$.

Cation/Atom site	Δq	Q	q
Fe1			
N1	0.449	-3.111	-3
N1	0.449	-3.111	-3
N5	0.102	-2.839	-3
N1	0.449	-3.111	-3
N1	0.449	-3.111	-3
N5	0.102	-2.839	-3
Fe1		1.947	2
P1			
N2	0.891	-2.751	-3
N4	1.53	-3.059	-3
N3	1.689	-3.378	-3
N2	0.89	-2.751	-3
P1		4.943	5
P2			
N1	1.309	-3.111	-3
N1	1.354	-3.111	-3
N2	0.969	-2.751	-3
N5	1.368	-2.839	-3
P2		5.07	5

Table I.13. CHARDI calculations for $\text{CoP}_8\text{N}_{14}$.

Cation/Atom site	Δq	Q	q
Co1			
N1	0.458	-3.159	-3
N1	0.458	-3.159	-3
N5	0.084	-2.912	-3
N1	0.458	-3.159	-3
N1	0.458	-3.159	-3
N5	0.084	-2.912	-3
Co1		1.913	2
P1			
N2	0.889	-2.726	-3
N3	1.604	-3.207	-3
N2	0.951	-2.726	-3
N4	1.556	-3.113	-3
P1		5.025	5
P2			
N1	1.395	-3.159	-3
N1	1.306	-3.159	-3
N2	0.885	-2.726	-3
N5	1.414	-2.912	-3
P2		4.996	5

Table I.14. CHARDI calculations for $\text{NiP}_8\text{N}_{14}$.

Cation/Atom site	Δq	Q	q
Ni1			
N1	0.447	-3.146	-3
N1	0.447	-3.146	-3
N5	0.106	-2.938	-3
N1	0.447	-3.146	-3
N1	0.447	-3.146	-3
N5	0.106	-2.938	-3
Ni1		1.922	2
P1			
N4	1.576	-3.151	-3
N2	0.948	-2.736	-3
N2	0.903	-2.736	-3
N3	1.574	-3.148	-3
P1		5.029	5
P2			
N1	1.3	-3.146	-3
N2	0.885	-2.736	-3
N5	1.416	-2.938	-3
N1	1.398	-3.146	-3
P2		4.991	5

I.5 Scanning electron microscopy

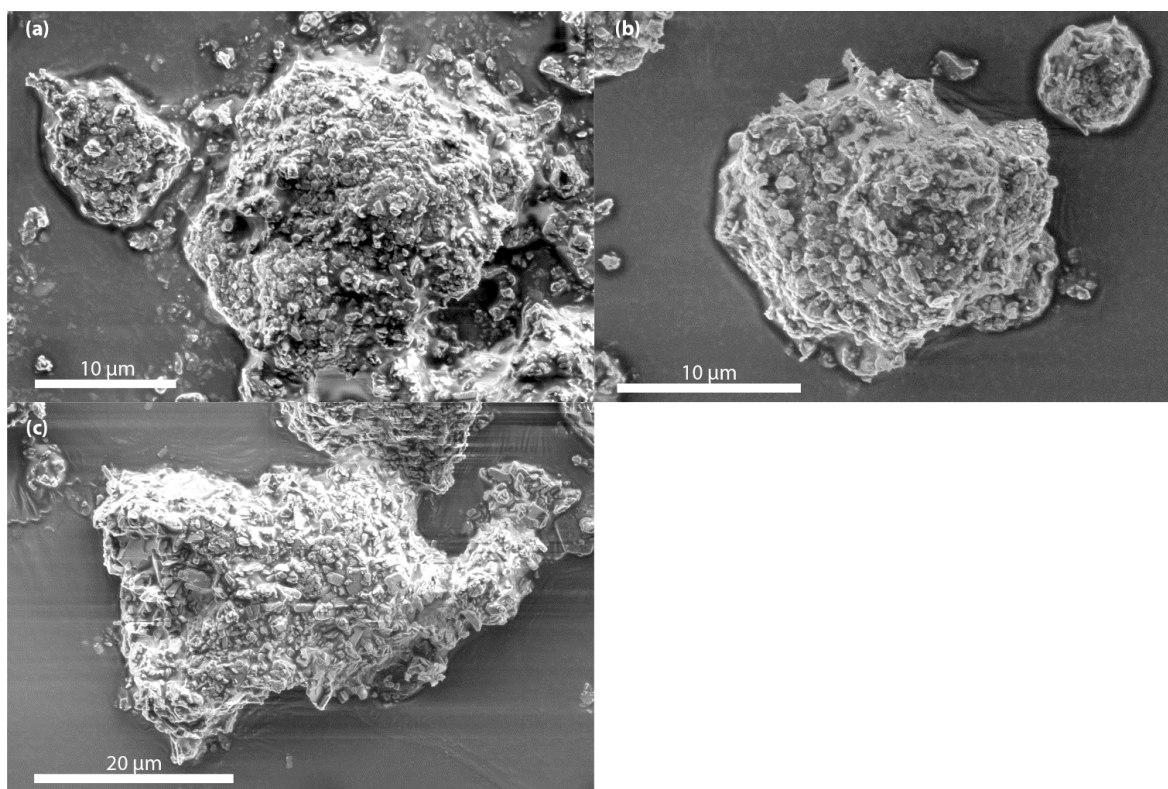


Figure I.5. Scanning electron microscopy micrographs of representative samples of (a) $\text{FeP}_8\text{N}_{14}$, (b) $\text{CoP}_8\text{N}_{14}$, (c) $\text{NiP}_8\text{N}_{14}$.

I.6 Fourier transform infrared spectroscopy

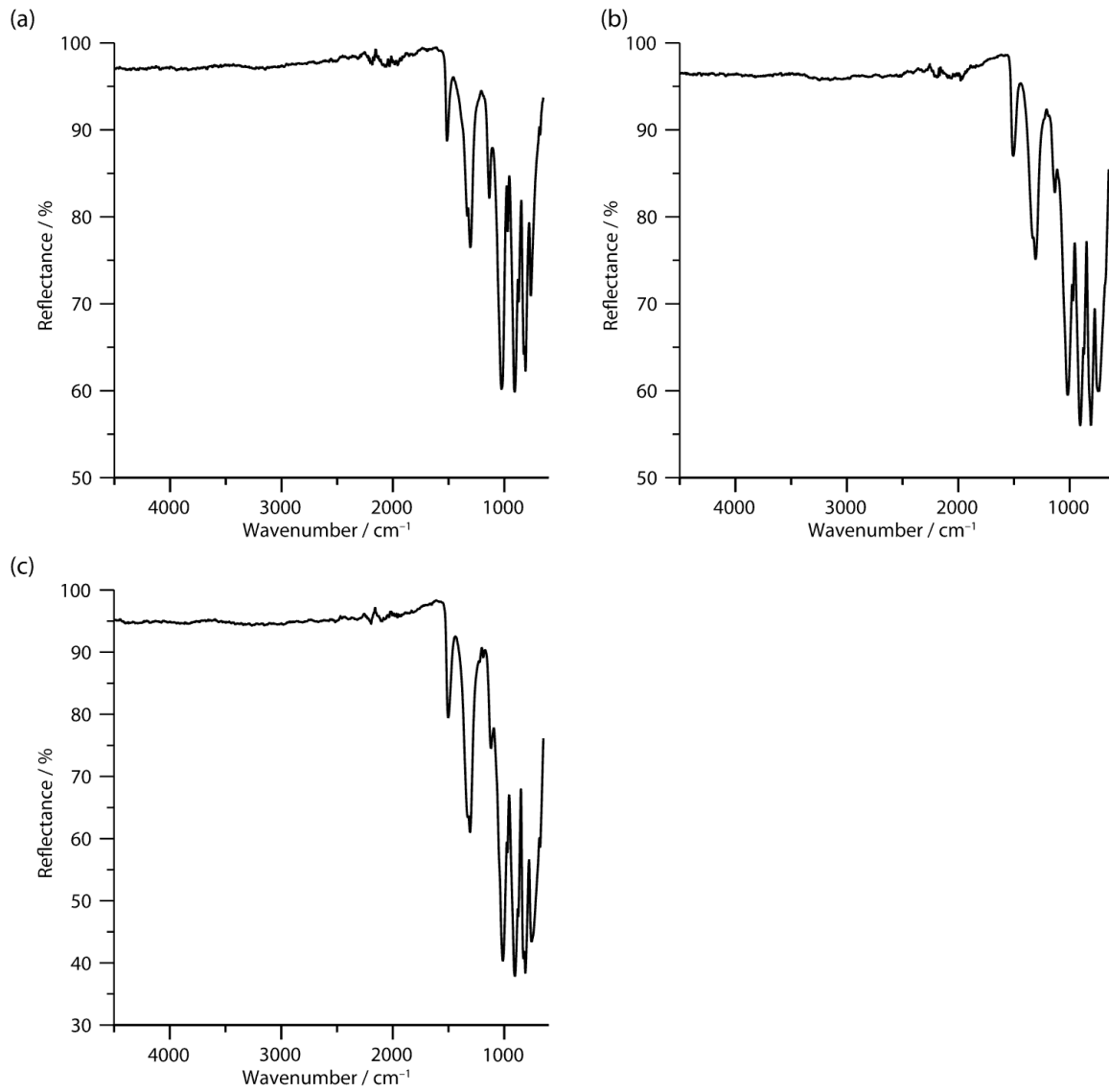


Figure I.6. FTIR spectra of (a) FeP₈N₁₄, (b) CoP₈N₁₄, (c) NiP₈N₁₄ obtained in ATR geometry.

I.7 Temperature-dependent powder X-ray diffraction

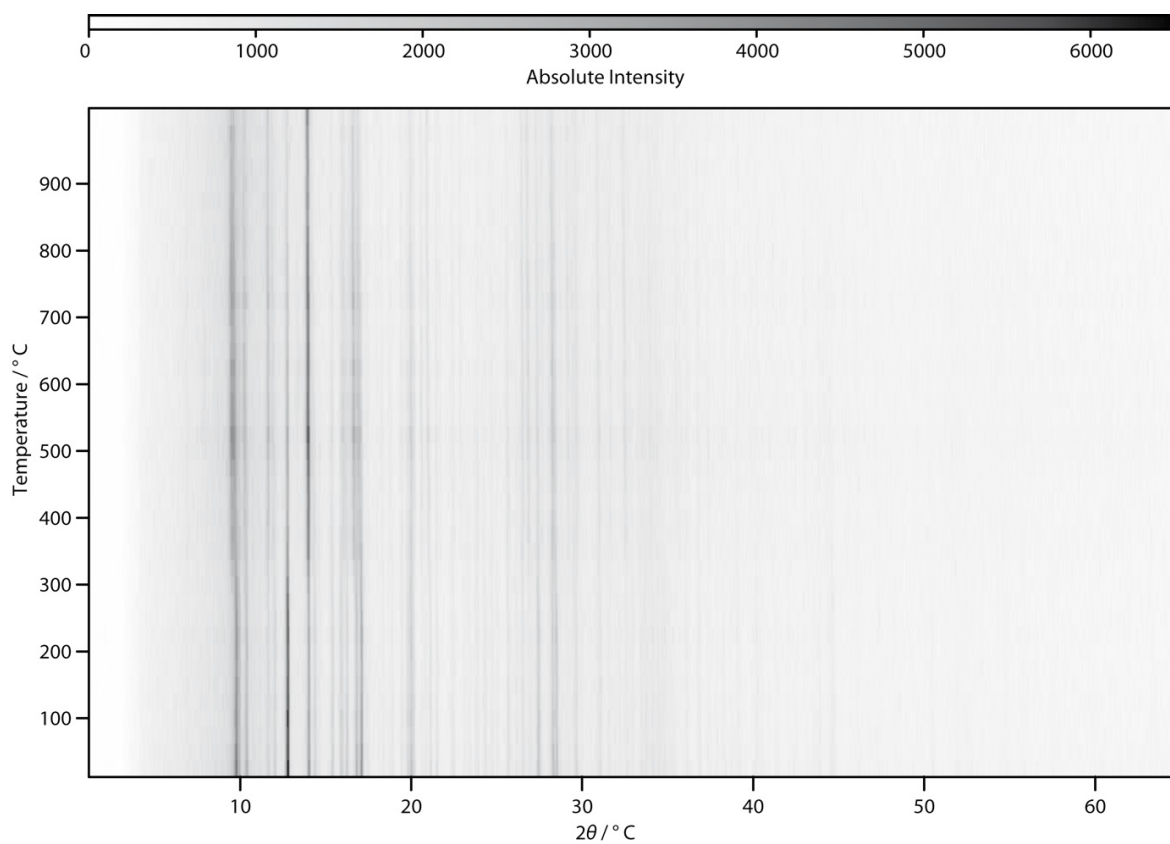


Figure I.7. Temperature-dependent powder X-ray diffraction pattern of $\text{FeP}_8\text{N}_{14}$.

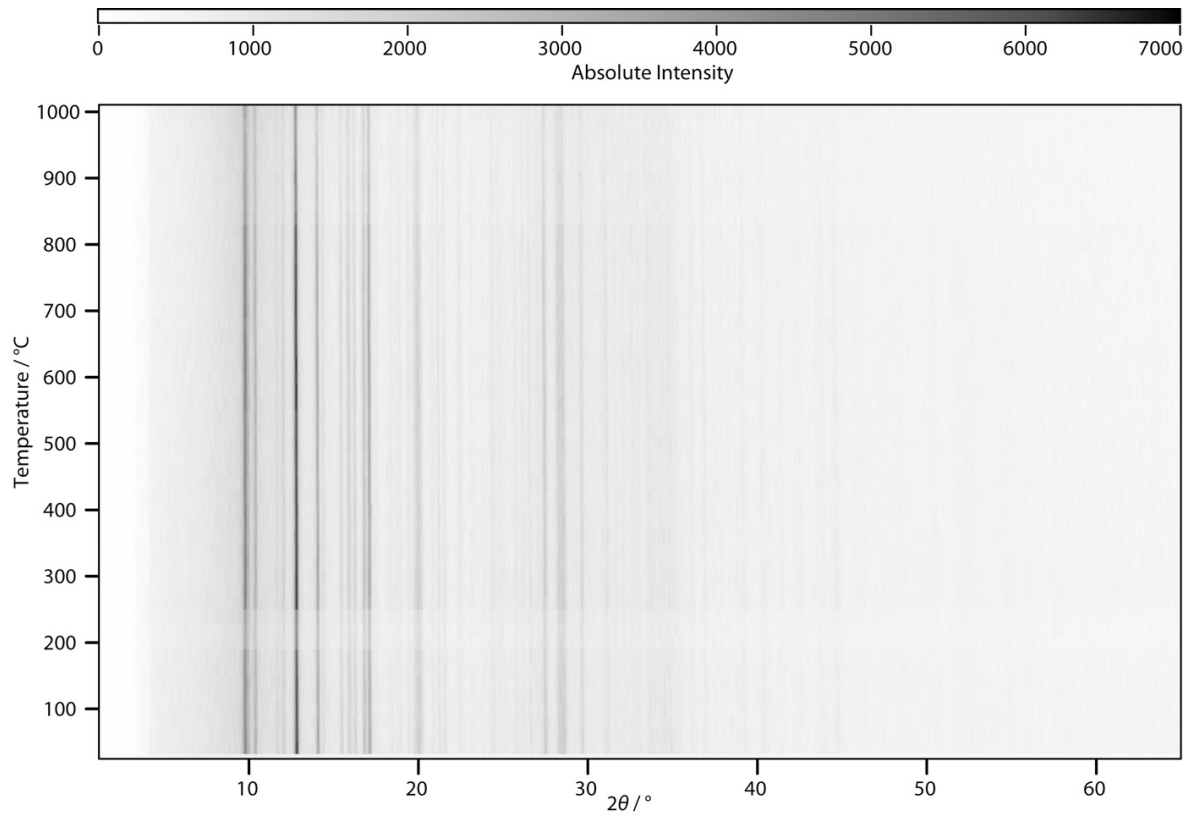


Figure I.8. Temperature-dependent powder X-ray diffraction pattern of CoP₈N₁₄.

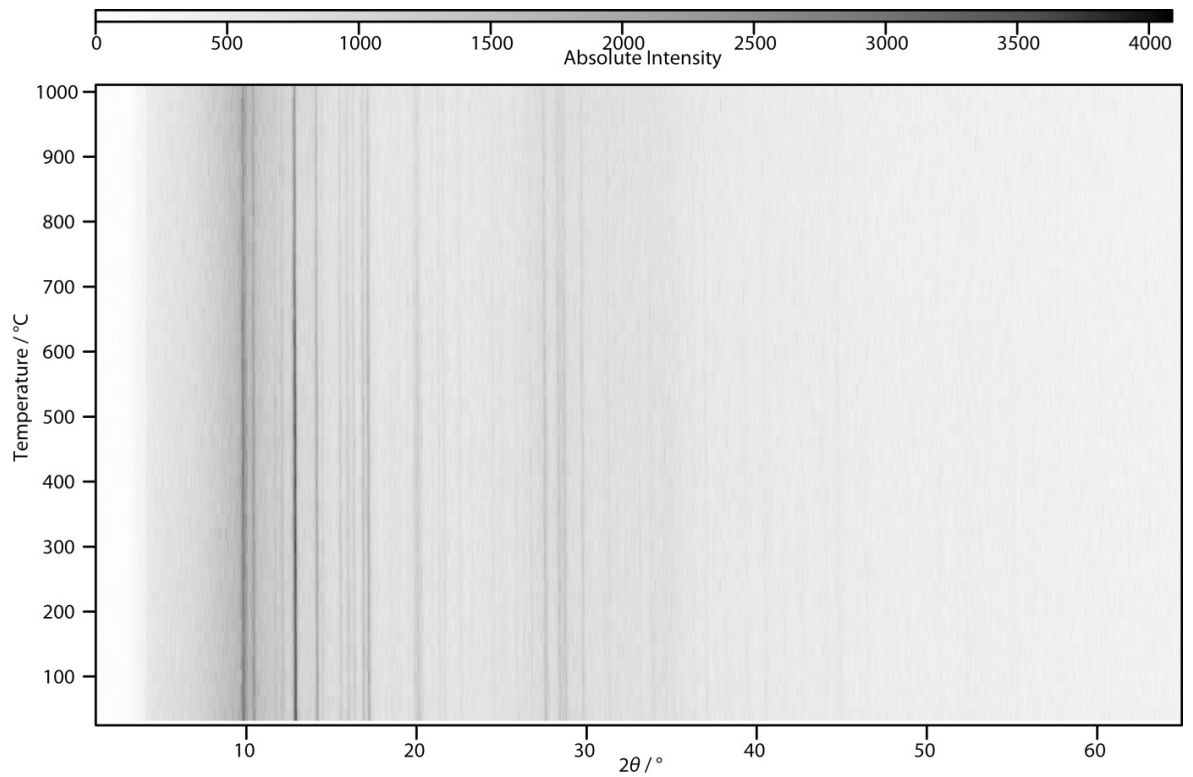


Figure I.9. Temperature-dependent powder X-ray diffraction pattern of NiP₈N₁₄.

I.8 Addition to the structure discussion

The structure of the MP_8N_{14} ($M = \text{Fe, Co, Ni}$) compounds is similar to $\text{SrP}_8\text{N}_{14}$, which also consists of tetra-layers, but differently arranged, probably due to the larger Sr^{2+} ions. In $\text{SrP}_8\text{N}_{14}$, the second and third layers are related by the mirror plane perpendicular to c of space group $Cmcm$ resulting in a mirror-symmetric $ABA'B'$ stacking. The individual layer stacking sequences lead to different point symbols for one of the two vertices in the P–P connection pattern: MP_8N_{14} $M = \text{Fe, Co, Ni}$ ($3^3.4^5.5^5.6^2$) ($3^3.4^3.5^3.6$), $\text{SrP}_8\text{N}_{14} = (3^3.4^6.5^5.6)(3^3.4^3.5^3.6)$.^[19,20]

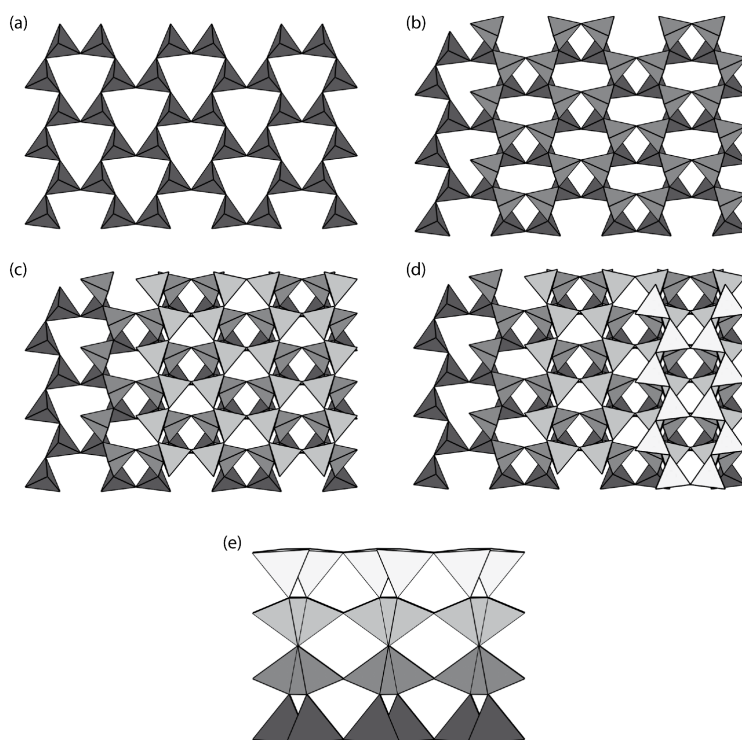


Figure I.10. (a)–(d) Honeycomb-type layers of PN_4 tetrahedra forming the tetra-layers of the MP_8N_{14} structures along $[001]$. Each layer is added stepwise onto the next forming the ABCD stacking. Layers C and D are related to A and B by the e -glide plane of space group $Cmce$. (e) Tetra-layer along the $[010]$ direction.

I.9 Magnetic measurements

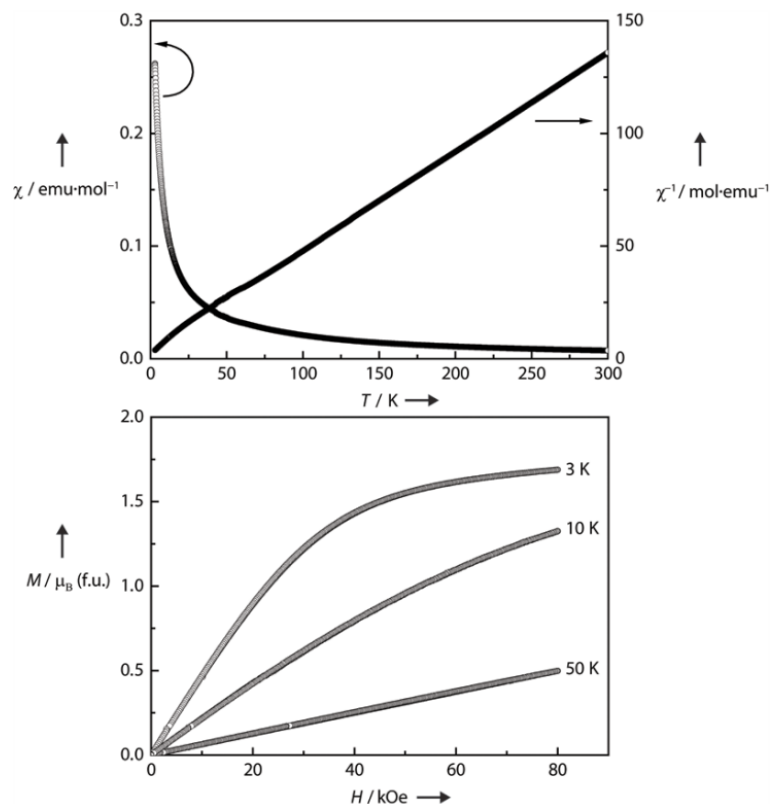


Figure I.11. Magnetic properties of $\text{CoP}_8\text{N}_{14}$: (top) χ and χ^{-1} data measured at 10 kOe and (bottom) magnetization isotherms recorded at 3, 10 and 50 K.

For $\text{CoP}_8\text{N}_{14}$, the measured effective magnetic moment of $\mu_{\text{eff}} = 4.27(1) \mu_B$ is well above the spin-only value of $\mu_{\text{calc}} = 3.87 \mu_B$ for an octahedrally coordinated Co^{2+} ion. Yet, it is nicely matched by $4.15 \leq \mu_{\text{calc}}/\mu_B \leq 4.30$ (for $25 \leq T \leq 300$ K) obtained by AOM allowing for spin-orbit coupling and low-symmetry ligand field effects (see section SI 2.10 for details). In other divalent Co compounds even larger effective magnetic moments have been found; e.g. $\mu_{\text{eff}} = 5.28 \mu_B$ for $\alpha\text{-Co}_2\text{P}_2\text{O}_7$ ^[21], $\mu_{\text{eff}} = 5.16 \mu_B$ for $\text{Co}_2\text{P}_4\text{O}_{12}$ ^[22] or $\mu_{\text{eff}} = 5.65 \mu_B$ for CoSO_4 ^[23].

For the nickel compound also an enhanced magnetic moment has been found. This suggests a contribution from the orbital angular momentum as found for the cobalt compound. In the literature, similar increased moments have been found, e.g. $\mu_{\text{eff}} = 3.30 \mu_B$ for $\alpha\text{-Ni}_2\text{P}_2\text{O}_7$ ^[21], $\mu_{\text{eff}} = 3.28 \mu_B$ for $\text{Ni}_2\text{P}_4\text{O}_{12}$ ^[24], $\mu_{\text{eff}} = 3.82 \mu_B$ for NiSO_4 ^[23] or in the borates $\gamma\text{-NiB}_4\text{O}_7$ ^[21] ($\mu_{\text{eff}} = 2.98\text{--}3.08(1) \mu_B$), $\text{NiB}_5\text{O}_5(\text{OH})$ ($\mu_{\text{eff}} = 3.30(1) \mu_B$)^[24] or $\text{Ni}_3\text{B}_{18}\text{O}_{28}(\text{OH})_4\cdot\text{H}_2\text{O}$ ($\mu_{\text{eff}} = 3.20(1) \mu_B$)^[25]. The magnetic moment measured for $\text{NiP}_8\text{N}_{14}$ is also matched by ligand field analysis via AOM (see section SI 2.10 for details) which leads to $3.13 \leq \mu_{\text{calc}}/\mu_B \leq 3.22$ (for $25 \leq T \leq 300$ K). Some iron compounds also show an increased magne-

tic moment; e.g. α - $\text{Fe}_2\text{P}_2\text{O}_7$ ^[23] ($\mu_{\text{eff}} = 5.33 \mu_{\text{B}}$),^[11] FeTa_2O_6 ($\mu_{\text{eff}} = 5.10 \mu_{\text{B}}$),^[24] FeSO_4 ($\mu_{\text{eff}} = 5.20 \mu_{\text{B}}$)^[23] or $\text{Fe}_2\text{P}_4\text{O}_{12}$ ($\mu_{\text{eff}} = 5.46 \mu_{\text{B}}$).^[25] The Weiss constants are negative ($\text{FeP}_8\text{N}_{14}$: $\theta_{\text{p}} = -0.9(1)$ K; $\text{CoP}_8\text{N}_{14}$: $\theta_{\text{p}} = -9.6(1)$ K; $\text{NiP}_8\text{N}_{14}$: $\theta_{\text{p}} = -12.8(1)$ K), suggesting antiferromagnetic correlations in the paramagnetic temperature range.

For $\text{NiP}_8\text{N}_{14}$ a small bifurcation in the ZFC/FC measurements is observed along with a subtle maximum either suggesting weak AFM ordering or traces of impurities (Figure I.12). Magnetization isotherms for all compounds were recorded at 3, 10 and 50 K (Figures 9.2c, I.11, I.12); that of the iron compound discussed in the manuscript. For $\text{CoP}_8\text{N}_{14}$ a bent 3 K isotherm is observed, suggesting saturation at high fields, the 10 K isotherm is only slightly bent while the 50 K isotherm is linear indicating paramagnetism. For $\text{NiP}_8\text{N}_{14}$ all isotherms are linear as expected for a paramagnetic material.

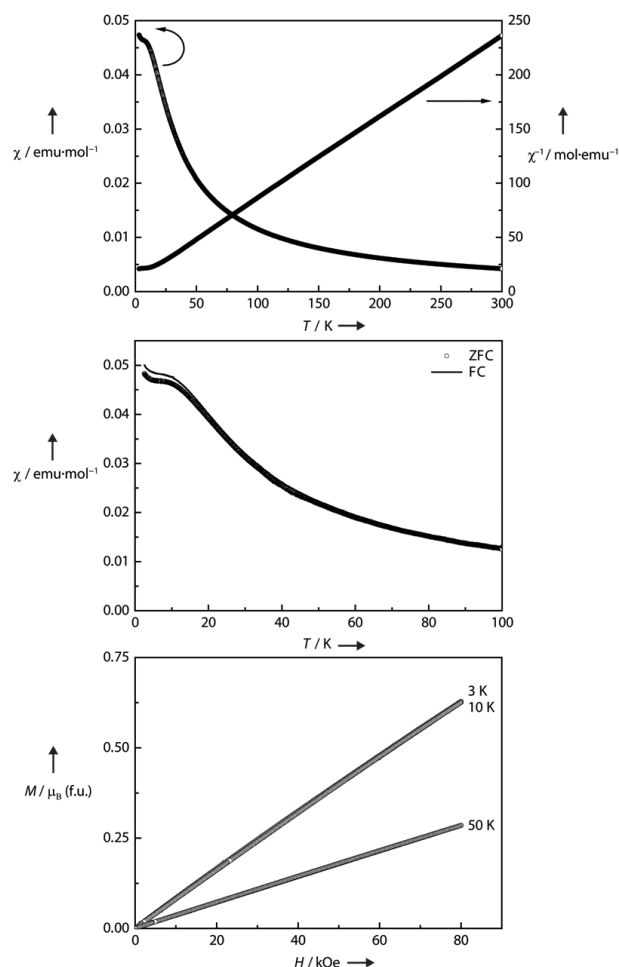


Figure I.12. Magnetic properties of $\text{NiP}_8\text{N}_{14}$: (top) χ and χ^{-1} data measured at 10 kOe, (middle) zero-field-cooled / field-cooled measurements (ZFC/FC) at 100 Oe and (bottom) magnetization isotherms recorded at 3, 10 and 50 K.

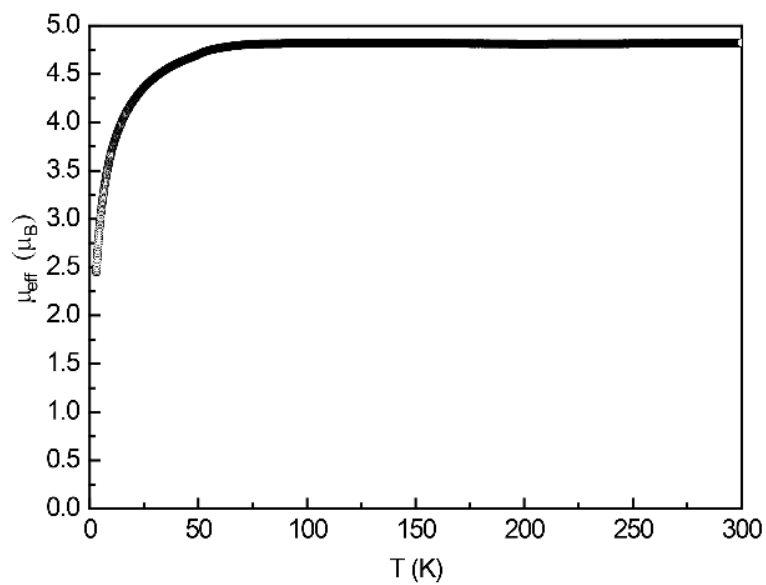


Figure I.13. Temperature dependence of the effective magnetic moment of the Fe^{2+} cations in $\text{FeP}_8\text{N}_{14}$.

I.10 Mössbauer spectroscopy

$\text{FeP}_8\text{N}_{14}$ was further characterized through its ^{57}Fe Mössbauer spectrum. The 6 K spectrum is shown in Figure I.14 and could be well reproduced with one doublet signal with an isomeric shift of $\delta = 1.14(1) \text{ mm s}^{-1}$ indicating the presence of Fe(II) in a high-spin state. The observed shift is in line with other Fe(II)-compounds, e.g. Fe_2SiO_4 and FeSO_4 ($\delta = 1.01\text{-}1.32 \text{ mm s}^{-1}$)^[26] or $\text{Fe}_3(\text{PO}_4)_2 \cdot 8\text{H}_2\text{O}$ ($\delta = 1.10 \text{ mm s}^{-1}$).^[27] The line width of $\Gamma = 0.31(1) \text{ mm s}^{-1}$ is in the usual range for iron containing compounds. The quadrupole splitting of $\Delta E_Q = 2.13(1) \text{ mm s}^{-1}$ is in good agreement with the non-cubic site symmetry of the iron atoms. Although $\text{FeP}_8\text{N}_{14}$ exhibits an AFM transition at $T_N = 3.5(1) \text{ K}$, the 6 K spectrum shows no magnetic hyperfine field splitting due to the temperature difference. Additional measurements at 40 and 78 K yielded identical results.

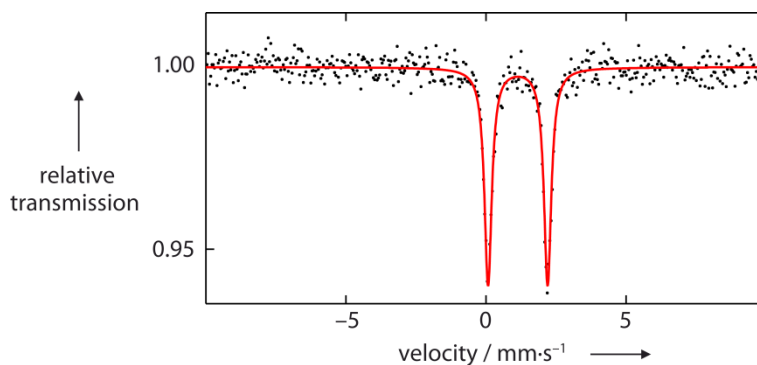


Figure I.14. Experimental (dots) and simulated (red line) ^{57}Fe Mössbauer spectrum of $\text{FeP}_8\text{N}_{14}$ at 6 K.

I.11 Electronic absorption spectra

Tanabe and Sugano Analysis of $\text{CoP}_8\text{N}_{14}$ and $\text{NiP}_8\text{N}_{14}$

For the determination of the ligand field splitting Δ_o (energy difference between t_{2g} and e_g orbitals) and the Racah-parameter B (measure of interelectronic repulsion of the d-electrons) with Tanabe-Sugano Diagrams, the observed absorption bands have to be attributed to the corresponding term symbols.^[28] This is outlined in the manuscript and as mentioned there, for both compounds, $\text{CoP}_8\text{N}_{14}$ and $\text{NiP}_8\text{N}_{14}$, one transition is split in two. This is possibly due to the geometric distortion of the $[\text{CoN}_6]$ and $[\text{NiN}_6]$ chromophores (Figure I.16, Tables I.6–11) and the corresponding d-electron energies are shown in Figure I.15. For both cases, d^7 and d^8 , the ground state and the corresponding excited state, which suffers from the severe energy splitting, are shown. Though the point symmetry of the chromophores is $2/m$, its geometry is in first approximation D_{4h} . Similar splitting for the d^8 case has been observed in $[\text{Ni}^{\text{II}}\text{O}_6]$ chromophores.^[29] With this qualitative representation of the splitting of the ${}^4\text{T}_1(\text{P})$ (d^7) and ${}^3\text{T}_{2g}(\text{F})$ (d^8) states, and with the Tanabe-Sugano diagrams the observed absorptions can be assigned to spin-allowed transitions (Table I.16, Table I.15 shows the ones used for Tanabe-Sugano analysis).^[28] To evaluate the spectra according to Tanabe-Sugano, the mean energy values of the split states were taken (Table 9.2). This is a source of error and one reason angular overlap modeling was performed for these chromophores.

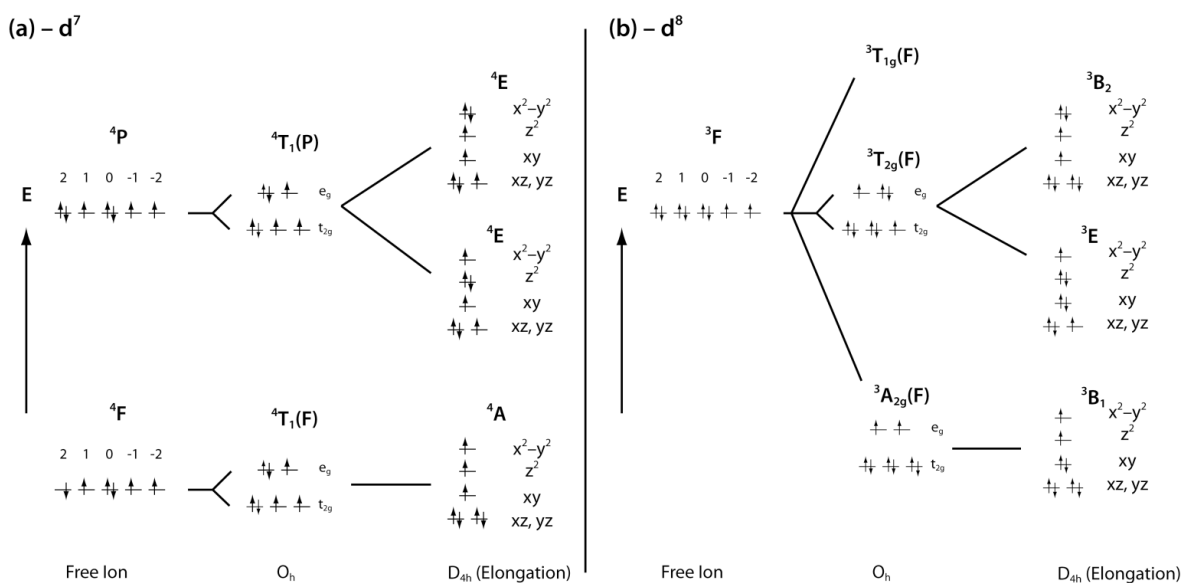


Figure I.15. Orbital energies in coordination environments of different symmetry compared to the free ion for (a) a d^7 system and (b) a d^8 system.

Table I.15. Assignment of electronic transitions observed for $\text{CoP}_8\text{N}_{14}$ and $\text{NiP}_8\text{N}_{14}$ ($\tilde{\nu}_{\text{obs.}}$) and used for Tanabe-Sugano analysis. Mulliken-Plažek symbols given for O_h symmetry.

Transition	$\tilde{\nu}_{\text{obs}} / \text{cm}^{-1}$
$\text{CoP}_8\text{N}_{14}$	
${}^4\text{T}_{1g}(\text{F}) \rightarrow {}^4\text{A}_{2g}(\text{F})$	14862
${}^4\text{T}_{1g}(\text{F}) \rightarrow {}^4\text{T}_{1g}(\text{P})$	16838
	21711
$\text{NiP}_8\text{N}_{14}$	
${}^3\text{A}_{2g}(\text{F}) \rightarrow {}^3\text{T}_{1g}(\text{F})$	12200
${}^3\text{A}_{2g}(\text{F}) \rightarrow {}^3\text{T}_{2g}(\text{F})$	19900
	22750

Angular Overlap Modelling of $\text{CoP}_8\text{N}_{14}$ and $\text{NiP}_8\text{N}_{14}$

The chromophores $[\text{Co}^{\text{II}}\text{N}_6]$ and $[\text{Ni}^{\text{II}}\text{N}_6]$ show strong radial “elongated octahedral” distortion. Furthermore, due to the trigonal-planar coordination of the N ligator atoms (Figure I.16) anisotropy in the π -interaction between the nitride ions and the metal d-orbitals might be anticipated. Both, geometric and electronic, effects will contribute low-symmetry components to the ligand-field.

Thus, evaluation according to the two-parameter model (Δ_o , B) can be only a rough approximation. For a better understanding of the ligand-field effects in these chromophores and their influence on the d-electron energies, calculations within the framework of the angular overlap model (AOM) were performed.^[30,31,32] An advantage of this model is its ability to use the chromophores with their actual geometry, as determined from crystal structure analysis. Instead of using global parameters, like 10Dq or Δ_o , one σ - and two π -interactions of each ligand (in total 18 bonding parameters for an octahedral chromophore) with the five 3d-orbitals of the central ion are introduced for the fitting between calculated and observed transition energies. The decomposition of the global ligand field parameter permits also accounting for second-sphere ligand field effects, e.g. anisotropic π -bonding of ligands.^[33] To reduce the number of independent bonding parameters, constraints on these parameters were introduced. Thus, for the energy $e_\sigma(M^{\text{II}}-\text{N})$, proportionality to the distance $d(M-\text{N})^{-5.0}$ is assumed.^[34] In general, the energy of e_π is set to one quarter of the corresponding energy e_σ in the case of “undisturbed” π -interaction.^[30,33] For the particular bonding situation encountered in the nitridophosphates $M^{\text{II}}\text{P}_8\text{N}_{14}$ a strong anisotropy of π -bonding has been assumed, since all N-ligand atoms show *c.n.*(N^{3-}) = 3.

Thus, it is assumed that the trigonal-planar coordination of the N-ligand atoms leads to sp^2 hybridization, leaving just one p-orbital perpendicular to this plane for π -interaction with the metals d-orbitals.^[33,35] Table I.17 gives a summary of the AOM parameters that led to the best match with the experimental data for CoP_8N_{14} and NiP_8N_{14} (UV/vis spectra, Bohr magneton numbers μ/μ_B).

For the AOM calculations the computer program *CAMMAG* in a modified PC version was used.^[36,37,38]

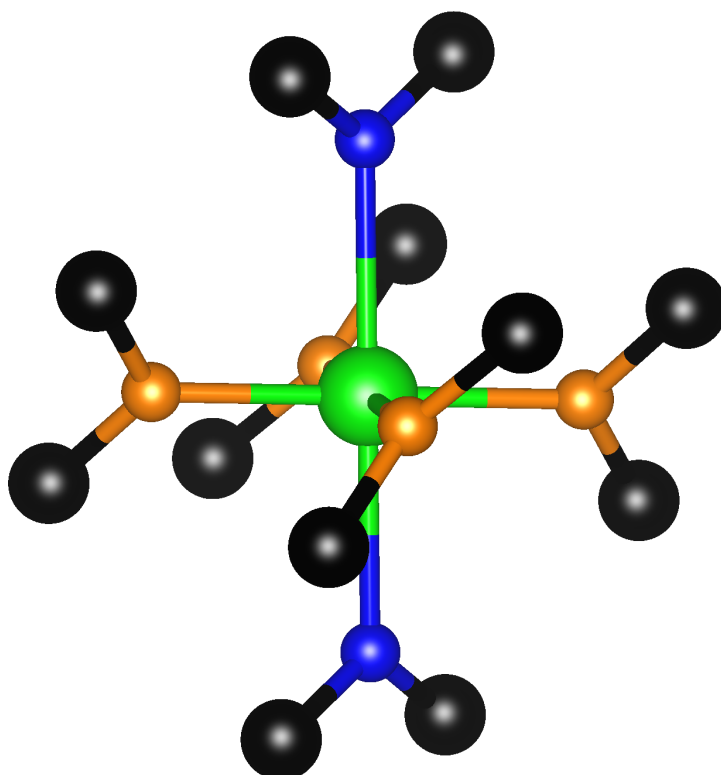


Figure I.16. MN_6 octahedra of MP_8N_{14} ($M = Fe, Co, Ni$) with second coordination sphere, visualizing the trigonal-planar [$c.n.(N^{3-}) = 3$] coordination of N by one metal atom M and two P atoms. Metal atoms in green, P in black, equatorial N (N1) in orange, and axial N (N5) in blue.

Conclusions

Even though it would have been desirable for the detailed ligand field analysis to have also good quality spectroscopic data for the NIR spectral range combination of available optical spectra and magnetic data allows several interesting insights into the ligand behaviour of nitrogen in nitridophosphates in general and in CoP_8N_{14} and NiP_8N_{14} in particular.

1) The ligand-field splittings Δ_o and the corresponding AOM parameters $e_\sigma(M^{II}-N)$ ($M^{II} = (Fe), Co,$

Ni) are surprisingly similar to the values for the corresponding $e_{\sigma}(M^{II}-O)$ ($M^{II} = (Fe), Co^{[39]}, Ni^{[29]}$) in oxophosphates and other complex oxo-anions (e.g. borates, silicates, sulfates).^[40–43]

Table I.16. Assignment of electronic transitions observed for CoP_8N_{14} and NiP_8N_{14} ($\tilde{\nu}_{obs.}$) and comparison to energies calculated within the AOM framework ($\tilde{\nu}_{calc.}$).

transition ^a	$\tilde{\nu}_{obs.}/\text{cm}^{-1}$	$\tilde{\nu}_{calc.}/\text{cm}^{-1}$
CoP₈N₁₄		
${}^4T_{1g}(F) \rightarrow {}^4T_{2g}(F)$	not obs.	5816, 8068, 8271
${}^4T_{1g}(F) \rightarrow {}^4A_{2g}(F)$	14862	14613
${}^4T_{1g}(F) \rightarrow {}^4_aT_{1g}(P)$	16838	16650, 17200
${}^4T_{1g}(F) \rightarrow {}^2G, {}^2H, {}^2P$	18918	17780–20300
${}^4T_{1g}(F) \rightarrow {}^4_bT_{1g}(P)$	21711	20430
NiP₈N₁₄		
${}^3A_{2g}(F) \rightarrow {}^3T_{2g}(F)$	not obs., 8260	5400, 6200, 8250
${}^3A_{2g}(F) \rightarrow {}^3T_{1g}(F)$	11700, 12640	10500, 12600
??	15400, 17260	
${}^3A_{2g}(F) \rightarrow {}^3T_{1g}(P)$	19900, 22713	20360, 22500
${}^3A_{2g}(F) \rightarrow {}^1T_{2g}(G)$	26500, 27000	26000, 28700
${}^3A_{2g}(F) \rightarrow {}^1T_{2g}(G)$		

^a Mulliken-Plažek symbols given for O_h symmetry.

Table I.17. Parameters used for AOM of CoP_8N_{14} and NiP_8N_{14} . $B, C, B_{fi.}, C_{fi.}$ being the Racah-parameters of the chromophor and of the free ion, respectively; ζ and $\zeta_{fi.}$ being the spin-orbit coupling constant of the chromophor and the free ion; k being the Stevens-orbital reduction factor, d the $M-N$ interatomic distances, e_{σ} and e_{π} the interaction energies.

	FeP ₈ N ₁₄	CoP ₈ N ₁₄	NiP ₈ N ₁₄
$B, C, \zeta / \text{cm}^{-1}$	700, 3008, 312	739, 2883, 340	820, 3805, 498
$B_{fi.}, C_{fi.}, \zeta_{fi.} / \text{cm}^{-1}$ ^[26]	897, 3857, 400	989, 4253, 515	1042, 4835, 630
$\beta = B/B_{fi.}$	0.78	0.75	0.78
k	0.78	0.75	0.78
$d(M-N1) / \text{Å}$	2.201	2.189	2.164
$e_{\sigma}(M-N1) / \text{cm}^{-1}$	3600	3500	3400
$e_{\pi x}(M-N1), e_{\pi y}(M-N1) / \text{cm}^{-1}$	0, 900	0, 875	0, 850
$d(M-N5) / \text{Å}$	2.585	2.606	2.535
$e_{\sigma}(M-N5) / \text{cm}^{-1}$	1609	1589	1544
$e_{\pi x}(M-N5), e_{\pi y}(M-N5) / \text{cm}^{-1}$	0, 403	0, 399	0, 388

2) For nitridophosphates second-sphere ligand-field effects (e.g. anisotropic π -interaction between N and the metal d-orbitals) are observed similar to those occurring in solids containing complex oxo-anions.^[33,41,43]

3) As one might have anticipated due to its higher polarizability, the nitrodiphosphate framework exerts a slightly stronger nephelauxetic effect (β well below 0.8) as it is typically observed for solids containing complex oxo-anions (β equal or above 0.8). Note: We refer to the values of B and hence, β obtained from AOM. In particular, B for $\text{CoP}_8\text{N}_{14}$ determined from the two-parameter model (Tanabe-Sugano) suffers from the low-symmetry ligand-field.

4) The quite large splitting observed for the excited state ${}^4\text{T}_{1g}(\text{P})$ of the Co^{2+} ions in $\text{CoP}_8\text{N}_{14}$ (bands at $\tilde{\nu}_{3a} = 16838 \text{ cm}^{-1}$ and $\tilde{\nu}_{3b} = 21711 \text{ cm}^{-1}$; Figure 9.3) is mainly caused by the geometric distortion of the chromophore (strongly elongated octahedron). Yet, the assumed anisotropic π -bonding behavior of the N-ligand atoms is the only way to explain the strong splitting of the electronic ground state ${}^4\text{T}_{1g}(\text{P})$ of the Co^{2+} ions which is evidenced by the magnitude of the experimentally observed Bohr magneton number of $\mu_{\text{exp}}/\mu_{\text{B}} = 4.27$ and their rather small temperature dependence. Without allowing for the π -anisotropy in AOM much higher values $\mu_{\text{exp}}/\mu_{\text{B}} \approx 4.8$ at 300 K and significant temperature dependency for $\mu_{\text{exp}}/\mu_{\text{B}}$ are calculated.

5) The comparison of ligand-field analyses for $\text{CoP}_8\text{N}_{14}$ and $\text{NiP}_8\text{N}_{14}$ shows the great advantage of AOM over other approaches. Based on the “real” (from crystal structure analysis) structure of the chromophores a chemically reasonable and transferable parameterization with a limited number of parameters is achieved. The bonding model introduced for both nitridophosphates is the same. Even the observed slight differences in LF parameters [$\beta(\text{Co}^{2+}, \text{CoP}_8\text{N}_{14}) < \beta(\text{Ni}^{2+}, \text{NiP}_8\text{N}_{14})$, $e_{\sigma}(\text{Co-N}) > e_{\sigma}(\text{Ni-N})$ despite $d(\text{Co-N}) > d(\text{Ni-N})$] can be rationalized along the lines of classical ligand-field theory.

6) Eventually, AOM with the bonding model used for $\text{CoP}_8\text{N}_{14}$ and $\text{NiP}_8\text{N}_{14}$ allows prediction of the ligand-field effects encountered by the Fe^{2+} ions in $\text{FeP}_8\text{N}_{14}$. Clearly, AOM with parameters very similar to those used for $\text{CoP}_8\text{N}_{14}$ and $\text{NiP}_8\text{N}_{14}$ (Table I.16) supports the high-spin configuration for the $[\text{Fe}^{\text{II}}\text{N}_6]$ chromophore. AOM predicts electronic transitions to the sublevels of the ${}^5\text{E}_g$ excited state at 6400 and 10400 cm^{-1} . Furthermore, a strong ground state splitting (due to the anisotropic π -bonding) is expected, leading to $\mu_{\text{calc}}/\mu_{\text{B}} = 5.30$ (80 to 300 K) strongly decreasing to lower temperatures. This ground state splitting should also lead to a highly anisotropic g tensor, a point that might be subject of further investigation.

I.12 References

- [1] A. Stock, H. Grüneberg, *Ber. Dtsch. Chem. Ges.* **1907**, *40*, 2573–2578.
- [2] W. Schnick, J. Lücke, *Z. Anorg. Allg. Chem.* **1990**, *588*, 19–25.
- [3] H. Huppertz, *Z. Kristallogr.* **2004**, *219*, 330–338.
- [4] D. Walker, *Am. Mineral.* **1991**, *76*, 1092–1100.
- [5] D. Walker, M. A. Carpenter, C. M. Hitch, *Am. Mineral.* **1990**, *75*, 1020–1028.
- [6] D. C. Rubie, *Phase Trans.* **1999**, *68*, 431–451.
- [7] N. Kawai, S. Endo, *Rev. Sci. Instrum.* **1970**, *41*, 1178–1181.
- [8] A. A. Coelho, TOPAS-Academic V4.1, Coelho Software, Brisbane, Australia, **2007**.
- [9] A. A. Coelho, *J. Appl. Crystallogr.* **2003**, *36*, 86–95.
- [10] G. S. Pawley, *J. Appl. Crystallogr.* **1981**, *14*, 357–361.
- [11] A. A. Coelho, *Acta Crystallogr., Sect. A: Found. Crystallogr.* **2007**, *63*, 400–406.
- [12] G. Oszlányi, A. Süto, *Acta Crystallogr., Sect. A: Found. Crystallogr.* **2008**, *64*, 123–134.
- [13] G. Oszlányi, A. Süto, *Acta Crystallogr., Sect. A: Found. Crystallogr.* **2004**, *60*, 134–141.
- [14] H. M. Rietveld, *Z. Kristallogr.* **2010**, *225*, 545–547.
- [15] H. M. Rietveld, *J. Appl. Crystallogr.* **1969**, *2*, 65–71.
- [16] K. Momma, F. Izumi, *J. Appl. Crystallogr.* **2011**, *44*, 1272–1276.
- [17] G. J. Long, T. E. Cranshaw, G. Longworth, *Mössbauer Eff. Ref. Data J.* **1983**, *6*, 42.
- [18] R. A. Brand, *WinNormos for Igor6, Version for Igor 6.2 or above: 22.02.2017*, Universität Duisburg, Duisburg, Germany, **2017**.
- [19] S. Wendl, W. Schnick, *Chem. - Eur. J.*, **2018**, *24*, 15889–15896
- [20] V. A. Blatov, A. P. Shevchenko, D. M. Proserpio, *Cryst. Growth Des.* **2014**, *14*, 3576–3586.
- [21] M. Gerk, *Ph.D. thesis*, University of Giessen, Giessen **1996**.
- [22] a) K. Rohwer, A. Wiedenmann, W. Gunßer, *Physica* **1986**, *136B*, 341–345. b) W. Gunßer, D. Fruehauf, K. Rohwer, A. Zimmermann, A. Wiedenmann, *J. Solid State Chem.* **1989**, *82*, 43–51.
- [23] B. C. Frazer, P. J. Brown, *Phys. Rev.* **1962**, *125*, 1283–1291.
- [24] E. M. L. Chung, M. R. Lees, G. J. McIntyre, C. Wilkinson, G. Balakrishnan, J. P. Hague, D. Visser, D. M. Paul, *J. Phys.: Condens. Matter* **2004**, *16*, 7837–7852.
- [25] W. Gunßer, B. R. Röhl, A. Schütze, E. Gmelin, A. Wiedenmann, *Ber. Bunsenges. Phys. Chem.*

- 1992, 96, 1698-1700.
- [26] G. K. Shenoy, F. E. Wagner, *Mößbauer Isomer Shifts*, North-Holland Publishing Company, Amsterdam, 1978.
- [27] C. Piña, H. Arriola, N. Nava, *J. Phys.: Conf. Ser.* **2010**, 217, 012037.
- [28] Y. Tanabe, S. Sugano, *J. Phys. Soc. Jpn.* **1954**, 9, 753-766.
- [29] K. Maaß, Dissertation, *Neues von quaternären Phosphaten der zweiwertigen 3d-Übergangsmetalle: Darstellung, Kristallstrukturen und spektroskopische Charakterisierung von quaternären Chrom(II)-phosphaten und isotypen Verbindungen mit einer ausführlichen Behandlung der Farbe von Nickel(II)-oxoverbindungen* (in German), Gießen University, Gießen, Germany, 2002. URL: <http://geb.uni-giessen.de/geb/volltexte/2002/819/>
- [30] B. N. Figgis, M. A. Hitchman, *Ligand Field Theory and Its Applications*, Wiley-VCH, Weinheim, Germany, 2000.
- [31] C.K. Jorgensen, R. Pappalardo, H. H. Schmidtke, *J. Chem. Phys.* **1963**, 39, 1422-1430.
- [32] D. E. Richardson, *J. Chem. Educ.* **1993**, 70, 372-380.
- [33] D. Reinen, M. Atanasov, S. L. Lee, *Coord. Chem. Rev.* **1998**, 175, 91-158.
- [34] M. Bermejo, L. Pueyo, *J. Chem. Phys.* **1983**, 78, 854-857.
- [35] H. Thauern, R. Glaum, *Inorg. Chem.* **2007**, 46, 2057-2066.
- [36] D. A. Cruse, J. E. Davies, J. H. Harding, M. Gerloch, D. J. Mackey, R. F. McMeeking CAMMAG, a FORTRAN program, Cambridge, UK, 1980.
- [37] M. Gerloch, *Magnetism and Ligand Field Theory*; Cambridge Univ. Press 1983.
- [38] M. Riley, CAMMAG for PC, v4.0, University of Queensland, St. Lucia, Australia, 1997.
- [39] A. Schmidt, Dissertation, *Phosphide und Phosphate des Cobalts: Kristallisation, Thermodynamik, Strukturen und Farben* (in German), Gießen University, Gießen, Germany 2002. URL: <http://geb.uni-giessen.de/geb/volltexte/2002/805/>
- [40] M. K. Schmitt, O. Janka, O. Niehaus, T. Dresselhaus, R. Pöttgen, F. Pielnhöfer, R. Wehrich, M. Krzhizhanovskaya, S. Filatov, R. Bubnova, L. Bayarjargal, B. Winkler, R. Glaum, H. Huppertz, *H. Inorg. Chem.* **2017**, 56, 4217-4228.
- [41] M. Schöneborn, R. Glaum, *Z. Anorg. Allg. Chem.* **2007**, 633, 2568-2578.

- [42] M. Funke, M. Blum, R. Glaum, B. ElBali, *Z. Anorg. Allg. Chem.* **2004**, 630, 1040–1047.
- [43] R. Glaum, M. A. Hitchman, *Aus. J. Chem.* **1996**, 49, 1221–1228.

Appendix J. Miscellaneous

J.1 List of Publications

The following list contains all publications of this dissertation, including authors, citation, and author contributions.

1. Rare-Earth-Metal Nitridophosphates Through High-Pressure Metathesis

Simon D. Kloß, Wolfgang Schnick

published in: *Angew. Chem., Int. Ed.* **2015**, *54*, 11250–11253.

published in: *Angew. Chem.* **2015**, *127*, 11402–11405.

Synthesis and analysis, as well as writing of the manuscript were done by Simon D. Kloß. Wolfgang Schnick directed and supervised the work. All authors revised the manuscript.

2. High-pressure Synthesis of Melilite-Type Rare-Earth Nitridophosphates $RE_2P_3N_7$ and a $Ba_2Cu[Si_2O_7]$ -type Polymorph

Simon D. Kloß, Niels Weidmann, Robin Niklaus, Wolfgang Schnick

published in: *Inorg. Chem.* **2016**, *55*, 9400–9409.

Major part of synthesis was done by Simon D. Kloß. For $mcm-Ho_2P_3N_7$ the preparation and measurements of physical properties was carried out by Niels Weidmann under supervision of Simon D. Kloß. Collection of data for the other compounds and analysis of all measured data was carried out by Simon D. Kloß. DFT calculations and evaluation thereof as well as writing the DFT part of the manuscript was done by Robin Niklaus. Conceptualization and writing most part of the manuscript was done by Simon D. Kloß. Wolfgang Schnick directed and supervised the work. All authors revised the manuscript.

3. Antiperovskite Nitridophosphate Oxide $Ho_3[PN_4]O$ by High-Pressure Metathesis

Simon D. Kloß, Niels Weidmann, Wolfgang Schnick

published in: *Eur. J. Inorg. Chem.* **2017**, 1930–1937.

Preparation and measurements of physical properties were carried out by Niels Weidmann under supervision of Simon D. Kloß. Analysis of data and DFT calculations were as well as writing of the manuscript were carried out by Simon D. Kloß. Wolfgang Schnick directed and supervised the work. All authors revised the manuscript.

4. Puzzling Intergrowth in Cerium Nitridophosphate Unraveled by Joint Venture of Aberration-Corrected Scanning Transmission Electron Microscopy and Synchrotron Diffraction

Simon D. Kloß, Lukas Neudert, Markus Döblinger, Markus Nentwig, Oliver Oeckler, Wolfgang Schnick

published in: *J. Am. Chem. Soc.* **2017**, 139, 12724–12735.

Project was conceptualized by Simon D. Kloß. Sample preparation and determination of physical properties and average structure performed by Simon D. Kloß. Synchrotron diffraction data collection and data reduction was performed by Oliver Oeckler and Markus Nentwig. Synchrotron diffraction data analysis, determination of the superstructure by supercell and superspace description done in leading role by Simon D. Kloß, and in supporting role by Oliver Oeckler. STEM and HRTEM characterization performed by Lukas Neudert and Markus Döblinger. Analysis of STEM data done by Lukas Neudert in leading role, and Simon D. Kloß and Oliver Oeckler in supporting role. Topology analysis was done by Simon D. Kloß. Manuscript was written by Simon D. Kloß, except for the TEM part, which was written by Lukas Neudert. Wolfgang Schnick directed and supervised the work. All authors revised the manuscript.

5. $\text{LiPr}_2\text{P}_4\text{N}_7\text{O}_3$: Structural Diversity of Oxonitridophosphates Accessed by High-Pressure Metathesis

Simon D. Kloß, Wolfgang Schnick

published in: *Inorg. Chem.* **2018**, 57, 4189–4195.

Conceptualization, synthesis, analysis, and composition of the article were done by Simon D. Kloß. Wolfgang Schnick directed and supervised the work. All authors revised the manuscript.

6. Accessing Tetravalent Transition-Metal Nitridophosphates through High-Pressure Metathesis

Simon D. Kloß, Sophia Wandelt, Andreas Weis, Wolfgang Schnick

published in: *Angew. Chem., Int. Ed.* **2018**, 57, 3192–3195.

published in: *Angew. Chem.* **2018**, 130, 3246–3249.

Conceptualization of the project was executed by Simon D. Kloß. Sophia Wandelt and Andreas Weis carried out synthesis and measurements of physical properties under supervision of Simon D. Kloß. Data were analyzed by Simon D. Kloß. The manuscript was written by Simon D. Kloß. Wolfgang Schnick directed and supervised the work. All authors revised the manuscript.

7. High-Pressure Metathesis of the $M_{1-x}PO_{3+4x}N_{1-4x}$ ($x \approx 0.05$) and $M_{0.75}PO_4$ ($M = Zr, Hf$) Orthophosphates

Simon D. Kloß, Andreas Weis, Sophia Wandelt, Wolfgang Schnick

published in: *Inorg. Chem.* **2018**, 57, 4164–4170.

Conceptualization of the project was executed by Simon D. Kloß. Sophia Wandelt and Andreas Weis carried out the synthesis and, except for NMR, the measurements of physical properties under supervision of Simon D. Kloß. Data were analyzed by Simon D. Kloß. The manuscript was written by Simon D. Kloß. Wolfgang Schnick directed and supervised the work. All authors revised the manuscript.

8. Open-shell 3d Transition Metal Nitridophosphates $M^{II}P_8N_{14}$ ($M^{II} = Fe, Co, Ni$) by High-pressure Metathesis

Simon D. Kloß, Oliver Janka, Theresa Block, Rainer Pöttgen, Robert Glaum, Wolfgang Schnick

published in: *Angew. Chem., Int. Ed.* **2018**, DOI: 10.1002/anie.201809146

published in: *Angew. Chem.* **2018**, DOI: 10.1002/ange.201809146

Conceptualization, synthesis, and organization of the project was done by Simon D. Kloß. Oliver Janka performed magnetic characterization, Theresa Block performed Mössbauer spectroscopy. Rainer Pöttgen supervised the magnetic and Mössbauer characterization. Robert Glaum performed the Angular Overlap Modelling and supervised the UV/Vis/NIR characterization. The manuscript was written by Simon D. Kloß in a leading role with support of all co-authors. Wolfgang Schnick supervised the project. All authors revised the manuscript.

J.2 Contributions to Conferences and Seminars

13. Ternary Transition Metal Nitridophosphates

Simon D. Kloß, Oliver Janka, Theresa Block, Rainer Pöttgen, Robert Glaum, Wolfgang Schnick

Poster presentation, 19. Vortragstagung für Anorganische Chemie der Fachgruppen Wöhler-Vereinigung und Festkörperchemie und Materialforschung, 2018, Regensburg, Germany.

12. Übung zur Bestimmung von Raumgruppen anhand von Schnitten durchs reziproke Gitter

Simon D. Kloß, Wolfgang Schnick

Seminar Schnick Group, 2015, Munich, Germany.

11. Accessing Nitridophosphates through High-Pressure Metathesis

Simon D. Kloß, Wolfgang Schnick

Oral presentation, VCI Stipendiatentreffen, 2018, LMU Munich, Munich, Germany

10. Accessing High-Valency Metal Nitridophosphates through High-Pressure Metathesis

Simon D. Kloß, Wolfgang Schnick

Oral presentation, 15th European Conference on Solid State Chemistry (ECSSC16), 2017, Glasgow, Scotland

9. Cer-Nitridophosphat mit Problemen

Simon D. Kloß, Lukas Neudert, Oliver Oeckler

Oral presentation, 43. Hirschegg-Seminar Festkörperchemie, 2017, Hirschegg, Österreich

8. Neue Übergangsmetall-(Oxo)Nitridophosphate

Simon D. Kloß, Wolfgang Schnick

Seminar Schnick Group, 2015, Munich, Germany.

7. Two Modifications of $RE_2P_3N_7$ Rare-Earth Nitridophosphates

Simon D. Kloß, Niels Weidmann, Robin Niklaus and W. Schnick

Poster presentation, 18. Vortragstagung der Fachgruppe Festkörperchemie und Materialforschung, 2016, Innsbruck, Austria

6. Neues aus dem High-Pressure Lab — Topologie, Topologie - Mathematische Beschreibung von Kristallstrukturen

Simon D. Kloß, Wolfgang Schnick

Seminar Schnick Group, 2015, Munich, Germany.

5. $SE_2P_3N_7$ im Melilith-Typ und seine Hochdruckmodifikation

Simon D. Kloß, Wolfgang Schnick

Oral presentation, 42. Hirschegg-Seminar Festkörperchemie, 2016, Hirschegg, Österreich

4. $Yb_2P_3N_7$ — Ein niedrigkondensiertes Nitridophosphat

Simon D. Kloß, Wolfgang Schnick

Oral presentation, 2. Obergurgl-Seminar Festkörperchemie, 2016, Obergurgl, Österreich

3. Metathese — Ein Vielfältiges Werkzeug

Simon D. Kloß, Wolfgang Schnick

Seminar Schnick Group, 2015, Munich, Germany.

2. $NdLiP_4N_8$ — The First Rare Earth Nitridophosphate by Metathesis

Simon D. Kloß, Wolfgang Schnick

Poster presentation, 15th European Conference on Solid State Chemistry (ECSSC15), 2015, Vienna, Austria.

1. Masterarbeit — Mit Hochdruck-Metathese zu neuen Nitridophosphaten

Simon D. Kloß, Wolfgang Schnick

Seminar Schnick Group, 2014, Munich, Germany.

J.3 Deposited crystallographic data

The crystallographic data of the compounds contained in this dissertation theses can be acquired through the Fachinformationszentrum (FIZ) Karlsruhe, Germany (fax: +49-7247-808-666, email:crysdata@fiz-karlsruhe.de) or the Cambridge Crystallographic Data Centre upon quoting the corresponding CSD or CCDC depository number.

Table J.1. Depository numbers of all compounds within this dissertation. CSD-numbers correspond to FIZ, CCDC-numbers to Cambridge Crystallographic Data Centre depositories.

Compound	CSD-Number	CCDC-Number
LiNdP₄N₈	429542	–
bex-Ce₂P₃N₇	431287	–
bex-Pr₂P₃N₇	431288	–
mcm-Ho₂P₃N₇	431289	–
Ho₃[PN₄]O	432168	–
Ce_{4-0.5x}Li₃P₁₈N_{35-1.5x}O_{1.5x} (X ≈ 0.72)	433141	–
Hf_{9-x}P₂₄N_{52-4x}O_{4x} (X ≈ 1.84)	433753	–
Zr_{1-x}PO_{3+4x}N_{1-4x} (X ≈ 0.05)	433854	1816010
Zr_{0.75}PO₄	433855	1816011
Hf_{1-x}PO_{3+4x}N_{1-4x} (X ≈ 0.05)	433856	1816012
Hf_{0.75}PO₄	433857	1816013
LiPr₂P₄N₇O₃	434268	1824687
FeP₈N₁₄		1856625
CoP₈N₁₄		1856626
NiP₈N₁₄		1856627

J.4 Curriculum Vitae

Personal Details

Name	Simon David Kloß
Date of Birth	04/06/1990
Place of Birth	Geseke, Germany
Nationality	German

Education

Since 01/2015	<p>Research assistant in the group of Prof. Dr. Wolfgang Schnick (Department of Chemistry, Ludwig-Maximilians-Universität München, Germany)</p> <p>Doctoral thesis: “<i>The High-Pressure Metathesis Route for the Preparation of Rare-Earth and Transition Metal Nitridophosphates</i>”</p>
05/2014–11/2014	<p>Masters thesis (Inorganic Chemistry)</p> <p>Ludwig-Maximilians-Universität München, Prof. Dr. Wolfgang Schnick. Title: “<i>Accessing novel nitridophosphates through high-pressure metathesis</i>”</p>
09/2013–11/2013	<p>Research internship (Inorganic Chemistry)</p> <p>University of California, Santa Barbara (UCSB), Santa Barbara, California, USA, Prof. Dr. Ram Seshadri</p>
10/2012–11/2014	<p>Master of Science (Chemistry)</p> <p>Ludwig-Maximilians-Universität München, Germany Main areas Inorganic Chemistry and Physical Chemistry</p>
03/2012–07/2012	<p>Bachelor thesis (Inorganic Chemistry)</p> <p>Ludwig-Maximilians-Universität München, Prof. Dr. Wolfgang Schnick. Title: “<i>Synthese und Charakterisierung neuer Alkalimetall-P-O-N Verbindungen</i>”</p>

10/2009–07/2012 **Bachelor of Science** (Chemistry and Biochemistry)
Ludwig-Maximilians-Universität München, Germany

06/2009 **Allgemeine Hochschulreife**
Advanced courses English and Mathematics

08/2000–06/2009 **Secondary School**
Städtisches Gymnasium Erwitte, Erwitte, Germany

Fellowships and Awards

09/2018 Poster-prize
For poster „Ternary Transition Metal Nitridophosphates“ presented at the 19. Vortragstagung für Anorganische Chemie der Fachgruppen Wöhler-Vereinigung und Festkörperchemie und Materialforschung (J.2 contribution no. 13)

11/2015–07/2017 Chemiefonds-Stipendium of the Stiftung Stipendien-Fonds
Full doctoral scholarship of the Fonds der Chemischen Industrie (FCI)

09/2013–11/2013 PROSA LMU
Fellowship financially supporting the research internship in the group of Prof. Dr. Ram Seshadri at the University of California, Santa Barbara (UCSB)

09/2013–11/2013 Unterstützung zur individuellen Studiengestaltung
Scholarship of the Faculty of Chemistry of the LMU Munich financially supporting the research internship in the group of Prof. Dr. Ram Seshadri at the University of California, Santa Barbara (UCSB)

03/2012 Oskar-Karl-Forster-Stipendium
Scholarship financially supporting the acquisition of chemistry textbooks

List of Publications

10. Open-shell 3d Transition Metal Nitridophosphates $M^{\text{II}}\text{P}_8\text{N}_{14}$ ($M^{\text{II}} = \text{Fe, Co, Ni}$) by High-pressure Metathesis
S. D. Kloß, O. Janka, T. Block, R. Pöttgen, R. Glaum, W. Schnick, *Angew. Chem., Int. Ed.* 2018; *Angew. Chem.* 2018
DOI: 10.1002/anie.201809146
DOI: 10.1002/ange.201809146

9. $\text{LiPr}_2\text{P}_4\text{N}_7\text{O}_3$: Structural Diversity of Oxonitridophosphates Accessed by High-Pressure Metathesis
S. D. Kloß, W. Schnick, *Inorg. Chem.* 2018, 57, 4189–4195.
DOI: 10.1021/acs.inorgchem.8b00455

8. High-Pressure Metathesis of the $M_{1-x}\text{PO}_{3+4x}\text{N}_{1-4x}$ ($x \approx 0.05$) and $M_{0.75}\text{PO}_4$ ($M = \text{Zr, Hf}$) Orthophosphates
S. D. Kloß, A. Weis, S. Wandelt, W. Schnick, *Inorg. Chem.* 2018, 57, 4164–4170.
DOI: 10.1021/acs.inorgchem.8b00373

7. Accessing Tetravalent Transition-Metal Nitridophosphates through High-Pressure Metathesis
S. D. Kloß, S. Wandelt, A. Weis, W. Schnick, *Angew. Chem., Int. Ed.* 2018, 57, 3192–3195; *Angew. Chem.* 2018, 130, 3246–3249.
DOI: 10.1002/anie.201712006 / DOI: 10.1002/ange.201712006

6. Puzzling Intergrowth in Cerium Nitridophosphate Unraveled by Joint Venture of Aberration-Corrected Scanning Transmission Electron Microscopy and Synchrotron Diffraction
S. D. Kloß, L. Neudert, M. Döblinger, M. Nentwig, O. Oeckler, W. Schnick, *J. Am. Chem. Soc.* 2017, 139, 12724–12735.
DOI: 10.1021/Jacs.7b07075

5. Antiperovskite Nitridophosphate Oxide $\text{Ho}_3[\text{PN}_4]\text{O}$ by High-Pressure Metathesis
S. D. Kloß, N. Weidmann, W. Schnick, *Eur. J. Inorg. Chem.* 2017, 1930–1937.
DOI: 10.1002/ejic.201601425

4. High-pressure Synthesis of Melilite-Type Rare-Earth Nitridophosphates $RE_2P_3N_7$ and a $Ba_2Cu[Si_2O_7]$ -type Polymorph
S. D. Kloß, N. Weidmann, R. Niklaus, W. Schnick, *Inorg. Chem.* **2016**, *55*, 9400–9409.
DOI: 10.1021/acs.inorgchem.6b01611

3. Rare-Earth-Metal Nitridophosphates Through High-Pressure Metathesis
S. D. Kloß, W. Schnick, *Angew. Chem., Int. Ed.* **2015**, *54*, 11250–11253; *Angew. Chem.* **2015**, *127*, 11402–11405.
DOI: 10.1002/anie.201504844 / DOI: 10.1002/ange.201504844

2. Average and Local Structure, Debye Temperature, and Structural Rigidity in Some Oxide Compounds Related to Phosphor Hosts
K. A. Denault, J. Brgoch, **S. D. Kloß**, M. W. Gaultois, J. Siewenie, K. Page, R. Seshadri, *ACS Appl. Mater. Inter.* **2015**, *7*, 7264–7272.
DOI: 10.1021/acsami.5b00445

1. Accessing $(Ba_{1-x}Sr_x) Al_2Si_2O_8:Eu$ Phosphors for Solid State White Lighting via Microwave- assisted Preparation: Tuning Emission Color by Coordination Environment
J. Brgoch, **S. D. Kloß**, K. A. Denault, R. Seshadri, *Z. Anorg. Allg. Chem.* **2014**, *640*, 1182–1189.
DOI: 10.1002/zaac.201400003

